

Lecture Notes in Mechanical Engineering

Somashekhar S. Hiremath
N. Siva Shanmugam
B. R. Ramesh Babu *Editors*

Advances in Manufacturing Technology

Select Proceedings of ICAMT 2018

 Springer

Lecture Notes in Mechanical Engineering

Lecture Notes in Mechanical Engineering (LNME) publishes the latest developments in Mechanical Engineering - quickly, informally and with high quality. Original research reported in proceedings and post-proceedings represents the core of LNME. Volumes published in LNME embrace all aspects, subfields and new challenges of mechanical engineering. Topics in the series include:

- Engineering Design
- Machinery and Machine Elements
- Mechanical Structures and Stress Analysis
- Automotive Engineering
- Engine Technology
- Aerospace Technology and Astronautics
- Nanotechnology and Microengineering
- Control, Robotics, Mechatronics
- MEMS
- Theoretical and Applied Mechanics
- Dynamical Systems, Control
- Fluid Mechanics
- Engineering Thermodynamics, Heat and Mass Transfer
- Manufacturing
- Precision Engineering, Instrumentation, Measurement
- Materials Engineering
- Tribology and Surface Technology

To submit a proposal or request further information, please contact the Springer Editor in your country:

China: Li Shen at li.shen@springer.com

India: Dr. Akash Chakraborty at akash.chakraborty@springernature.com

Rest of Asia, Australia, New Zealand: Swati Meherishi at swati.meherishi@springer.com

All other countries: Dr. Leontina Di Cecco at Leontina.dicecco@springer.com

To submit a proposal for a monograph, please check our Springer Tracts in Mechanical Engineering at <http://www.springer.com/series/11693> or contact Leontina.dicecco@springer.com

Indexed by SCOPUS. The books of the series are submitted for indexing to Web of Science.

More information about this series at <http://www.springer.com/series/11236>

Somashekhar S. Hiremath ·
N. Siva Shanmugam · B. R. Ramesh Babu
Editors

Advances in Manufacturing Technology

Select Proceedings of ICAMT 2018

 Springer

Editors

Somashekhar S. Hiremath
Indian Institute of Technology Madras
Chennai, Tamil Nadu, India

N. Siva Shanmugam
National Institute of Technology
Tiruchirappalli, Tamil Nadu, India

B. R. Ramesh Babu
Chennai Institute of Technology
Chennai, Tamil Nadu, India

ISSN 2195-4356 ISSN 2195-4364 (electronic)
Lecture Notes in Mechanical Engineering
ISBN 978-981-13-6373-3 ISBN 978-981-13-6374-0 (eBook)
<https://doi.org/10.1007/978-981-13-6374-0>

Library of Congress Control Number: 2019931857

© Springer Nature Singapore Pte Ltd. 2019

This work is subject to copyright. All rights are reserved by the Publisher, whether the whole or part of the material is concerned, specifically the rights of translation, reprinting, reuse of illustrations, recitation, broadcasting, reproduction on microfilms or in any other physical way, and transmission or information storage and retrieval, electronic adaptation, computer software, or by similar or dissimilar methodology now known or hereafter developed.

The use of general descriptive names, registered names, trademarks, service marks, etc. in this publication does not imply, even in the absence of a specific statement, that such names are exempt from the relevant protective laws and regulations and therefore free for general use.

The publisher, the authors and the editors are safe to assume that the advice and information in this book are believed to be true and accurate at the date of publication. Neither the publisher nor the authors or the editors give a warranty, expressed or implied, with respect to the material contained herein or for any errors or omissions that may have been made. The publisher remains neutral with regard to jurisdictional claims in published maps and institutional affiliations.

This Springer imprint is published by the registered company Springer Nature Singapore Pte Ltd. The registered company address is: 152 Beach Road, #21-01/04 Gateway East, Singapore 189721, Singapore

Organizing Committee

Chief Patron

Shri P. Sriram, Chairman, Chennai Institute of Technology, Chennai

Patrons

Shri P. Janakiraman, Vice Chairman, Chennai Institute of Technology, Chennai

Smt. S. Sridevi, Secretary, Chennai Institute of Technology, Chennai

Co-Patron

Prof. Dr. K. S. Srinivasan, Principal, Chennai Institute of Technology, Chennai

Conveners

Dr. B. R. Ramesh Babu, Professor, Department of Mechanical Engineering

Dr. K. Vimalanathan, Professor, Department of Mechanical Engineering

Organizing Secretary

Dr. V. Dhinakaran, Professor, Department of Mechanical Engineering

Committee Members

Prof. M. D. Vijayakumar, Professor and Head, Mechanical Engineering

Dr. G. Gopalarama Subramanian, Professor, Mechanical Engineering

Dr. M. Ravichandram, Professor, Mechanical Engineering

Dr. K. Karthikeyan, Professor, Mechanical Engineering

Dr. S. Rajarasalnath, Professor, Mechanical Engineering

Prof. Prince Packiaraj, Professor, Mechanical Engineering

Dr. A. Dhanasekaran, Professor, Mechanical Engineering

International Advisory Committee

Dr. Angappa Gunasekaran, California State University, Bakersfield, USA

Dr. Moraru Roland, University of Petrosani, Romania

Dr. Joerg Niemann, University of Applied Sciences, Dusseldorf, Germany

Dr. Yuriy N. Saraev, Russian Academy of Sciences, Russia
 Dr. Mikhail Slobodyan, Tomsk Polytechnic University, Russia
 Dr. M. A. Rashid Sarkar, BUET, Dhaka, Bangladesh
 Dr. Krishnaswami Srihari, Binghamton University, USA
 Dr. Mohammad T. Khasawneh, Watson Institute for Systems Excellence (WISE), USA

National Advisory Committee

Chairman

Mr. P. Kaniappan, Managing Director, WABCO India Ltd

Advisory

Dr. K. Sanakaranarayananasamy, NIT Tiruchirappalli
 Dr. N. Siva Shanmugam, NIT Tiruchirappalli
 Dr. S. Murugan, NIT Rourkela
 Dr. N. Ramesh Babu, IIT Madras
 Dr. Somashekhar S. Hiremath, IIT Madras
 Dr. B. Muthukumar, IIT Guwahati
 Dr. I. A. Palani, IIT Indore
 Dr. L. Karunamoorthy, Anna University, Chennai
 Dr. M. Kanthababu, Anna University, Chennai
 Dr. N. Alagumurthi, Pondicherry Engineering College, Puducherry
 Dr. V. Balasubramani, Annamalai University, Chidambaram
 Dr. S. R. Devadasan, PSG College of Technology, Coimbatore
 Dr. K. M. Paramasivam, MIT, Anna University, Chennai
 Dr. K. Parthiban, NIT Tiruchirappalli
 Dr. T. Ramesh, NIT Tiruchirappalli
 Dr. V. Anandakrishnan, NIT Tiruchirappalli
 Dr. S. Babu, PSG College of Technology, Coimbatore
 Dr. K. Tamil Mannan, IGNOU, Delhi

List of Contributors and Reviewers

Dr. A. Arockiarajan, IIT Madras
 Dr. Somashekhar S. Hiremath, IIT Madras
 Dr. N. Siva Shanmugam, NIT Tiruchirappalli
 Dr. B. Ravisankar, NIT Tiruchirappalli
 Dr. V. Dhinakaran, Chennai Institute of Technology, Chennai
 Dr. Jagadeesha, NIT Calicut
 Dr. V. Pandu Ranga, IIT Bhubaneswar
 Dr. Harpreet Singh, IIT Ropar
 Dr. C. Sathiya Narayanan, NIT Tiruchirappalli
 Dr. I. A. Palani, IIT Roorkee
 Dr. P. Muthukumar, IIT Guwahati
 Dr. V. P. Chandramohan, NIT Warangal

- Dr. T. Radha Ramanan, NIT Calicut
- Dr. T. Ramesh, NIT Tiruchirappalli
- Dr. A. Krishnaveni, Government College of Engineering, Tirunelveli
- Dr. Anathakrishnan, NIT Tiruchirappalli
- Dr. S. Senthilkumaran, Anna University, Chennai
- Dr. S. Periyasamy, Government College of Technology, Coimbatore
- Dr. K. S. P. Rao, DMS SVH College of Engineering, Machilipatnam
- Dr. S. Babu, PSG College of Technology, Coimbatore
- Dr. N. M. Sivaraman, NIT Puducherry
- Dr. A. John Rajan, VIT, Vellore
- Dr. K. Jayaraman, IIT Madras
- Dr. V. Raghuraman, VIT, Vellore
- Dr. R. Bharanidaran, VIT, Vellore
- Dr. J. Arunkumar, Auckland University of Technology, New Zealand
- Dr. S. Sundar Pethaiah, Singapore Power, Singapore
- Dr. V. Rajkumar, Singapore University of Technology and Design, Singapore

Foreword

This book published by Springer is an outcome of the International Conference on Advances in Manufacturing Technology—ICAMT 2018—that assimilates the research work of some prominent researchers in the extensive area of manufacturing technology.

This book presents an anthology of works presented at ICAMT 2018, covering subjects in the areas, such as material process, machine tools, cutting tools, manufacturing systems, optimization technologies, 3D scanning and re-engineering and 3D printing, and computer applications in design, as well as exciting subjects in contemporary manufacturing such as robotics and intelligent materials.

I am also grateful to Chairman Mr. P. Sriram and Principal Dr. K. S. Srinivasan, Chennai Institute of Technology; members of the ICAMT 2018 Committee; and the researchers who have actively participated in the elaboration of this book. A special thanks to Dr. Somashekhar S. Hiremath, Associate Professor, IIT Madras; Dr. N. Siva Shanmugam, Associate Professor, National Institute of Technology Tiruchirappalli; and Dr. B. R. Ramesh Babu, Dean, Chennai Institute of Technology, who took the responsibility of being the editors of this book.

I would like to extend my sincere thanks to MK Autocomponents India Limited, ACMEE 2018, 13th International Machine Tool Exhibition (an initiative of AIEMA—Ambattur Industrial Estate Manufacturers' Association) for their support.

Chennai, India

Dr. V. Dhinakaran
Organizing Secretary-ICAMT 2018
Professor, Chennai Institute of Technology

Preface

Chennai Institute of Technology organized the International Conference on Advances in Manufacturing Technology—ICAMT 2018—in association with ACMEE on June 22–23, 2018. ICAMT 2018 was held for the third successive time in Chennai. The mission of ICAMT 2018 is to bridge the gap between academics and industry in the field of manufacturing technology. ICAMT 2018 includes oral, poster, and tutorial sessions given by experts in state-of-the-art topics.

ICAMT 2018 brings leading researchers from academia, R&D organizations, and industries from various countries together under one roof and at one time to discuss new opportunities, emerging trends of new technologies, machine tools, cutting tools, manufacturing systems, and simulation tools for solving manufacturing technology problems at various levels starting from material design to complex manufacturing system.

Sessions explore innovative as well as revered technologies, research, development and optimization, workforce efficiency, and productivity. Special emphasis is placed on expressing application trends, progress, and future course of manufacturing technology. ICAMT is planned to be held once in 2 years and will reflect the changing scenario in manufacturing and empower the future growth in a sustainable manner.

Chennai, India

Somashekhar S. Hiremath
N. Siva Shanmugam
B. R. Ramesh Babu

About This Book

The present issue of Lecture Notes in Mechanical Engineering from Springer is the outcome of International Conference on Advances in Manufacturing Technology (ICAMT 2018) held at **Chennai Institute of Technology, Chennai, Tamil Nadu, India**, on June 22–23, 2018, as a parallel event with ACMEE, an international machine tool exhibition conducted in association with Ambattur Industrial Estate Manufacturers' Association (AIEMA). This edition of the ICAMT proceedings provides the in-depth work of different researchers and practicing engineers who are all working in the field of manufacturing industries and academic institutions throughout the globe. This book covers diversified topics of contemporary manufacturing technology such as:

Material process

Machine tools

Cutting tools

Robotics and automation

Manufacturing systems

Optimization technologies

3D scanning and re-engineering and 3D printing

Computer applications in design

Analysis and simulation tools for solving manufacturing technology problems at various levels starting from material designs to complex manufacturing systems.

Contents

Evaluation of Tensile Properties of Nanoclay-Filled Madar Fiber-Reinforced Polyester Hybrid Composites	1
Gunti Rajesh, M. V. Raghavendra Rao, K. Vijay and S. Gopinath	
Characterization of Economical Aluminium MMC Reinforced with Weld Slag Particles	9
P. Paranthaman, P. M. Gopal and N. Sathiesh Kumar	
Optimization of Weld-Bead Parameters of Plasma Arc Welding Using GA and IWO	17
Kadivendi Srinivas, Pandu R. Vundavilli and M. Manzoor Hussain	
Experimental Studies on the Effect of Basalt Powder Inclusion on Mechanical Properties of Hybrid Epoxy and Polyester Composites Reinforced with Glass Fiber	25
S. Mahesh Babu and M. Venkateswara Rao	
An Experimental Investigation on Tensile Properties of Hybrid BioPolyurethane Composite: Modeling and Optimization	33
A. Soundhar, M. Rajesh, K. Jayakrishna and M. T. H. Sultan	
Improvement of Machining Characteristics by EDM with Graphite Powder-Mixed Dielectric Medium	41
V. Srinivasa Sai, K. Gnana Sundari, P. Gangadhara Rao and B. Surekha	
Measuring Industrial Symbiosis Index Using Multi-Grade Fuzzy Approach	49
C. Kalyan, T. Abhirama, Neyara Radwan Mohammed, S. Aravind Raj and K. Jayakrishna	
Fabrication and Machining Characteristics of Al7075-Red Mud and Al7075-TiC Metal Matrix Composites	59
Chinmayee Kar and B. Surekha	

Multicriteria Optimization of Machining Parameters in WEDM of Titanium Alloy 6242	65
R. Prasanna, P. M. Gopal, M. Uthayakumar and S. Aravind	
Water Absorption and Density Tests on the Water Hyacinth-Based Partial Green Composite	77
Rakesh Potluri and M. Sreenivasa Rao	
Experimental Analysis on the Mechanical Properties of Dissimilar Material Joint During PCTIG Welding	89
B. Kamesh Srikar, Raghuraman Srinivasan, Venkatraman Ramamoorthi, Sivachidambaram Pichumani and J. Durga Venkata Satyanarayana	
Influence of Flux Coating During Dissimilar Welding of Copper with Brass Using ATIG Welding Process	95
J. Durga Venkata Satyanarayana, Raghuraman Srinivasan, Venkatraman Ramamoorthi, Sivachidambaram Pichumani and B. Kamesh Srikar	
Innovative Nitride Film Deposition on Copper Interconnects of MEMS Devices Using Plasma-Enhanced Chemical Vapor Deposition Techniques	105
T. Jagadeesha and Louis Kim	
Sleep Detection and Alert System for Automobiles	113
T. Babu, S. Ashwin, Mukul Naidu, C. Muthukumaaran and C. Ravi Raghavan	
Numerical Analysis and Design Optimization of Lip Seal Opening Pressure for Automotive Valves	119
T. Sukumar, B. R. Ramesh Bapu, B. Durga Prasad and B. R. Vijay Prithiv	
Mechanical and Microstructural Properties of Multi-Axially Forged LM6 Aluminium Alloy	131
Sudheer S. Sajjan, Mithun V. Kulkarni, S. Ramesh, P. C. Sharath, R. Rajesh and Vasantha Kumar	
Implementation of Lean Concepts Using Value Stream Mapping in Automotive Firm	141
Abhishek Deokar, S. Aravind Raj, K. Jayakrishna and H. Abdul Zubar	
Fabrication of Automated Scrap Collector Cum Scrubber for Production Industries	149
R. Bhoopathi, K. Karthikeyan, J. Balamurugan, S. Krishnakanth and T. Dharan Raj	

Enhancement of Mechanical Properties Through Spheroidization Annealing for Low-Carbon Steel 159
 D. Venkatesan and R. Chandramouli

Effect of Rolling Reduction on Microstructure and Mechanical Properties Cu-3%Ti Alloy 167
 Prabhjot Singh, S. Ramesh, Gajanan Anne and H. Shivananda Nayaka

An Investigative Approach to Study the Corrosion Response of Copper–Brass TIG Welded Samples Using Nitric Acid as the Corroding Agent 177
 Aparna Vinayan, Sourabh S. Nair, Raghuraman Srinivasan and Sivachidambaram Pichumani

A Review on Mechanical Properties, Tribological, Corrosion, and Weldability Studies of Aluminium Composites Processed Using Stir Casting and ECAP Methods 187
 Aravind Muralitharan, Krishna Madhavan, Raghuraman Srinivasan, Venkatraman Ramamoorthi and Sivachidambaram Pichumani

Characterization and Comparison of Functionally Graded Al/Mg and Al/Al 7075 Metal Matrix Composites Manufactured by Die Casting 193
 Goutam Mondal, Pradipta Kumar Rout, Gourab Mohanty and B. Surekha

Statistical Quality Control of Torque Wrenches Used in Automotive Assembly Department 199
 Soham Kulkarni, Chaitanya Kulkarni, K. E. K. Vimal and K. Jayakrishna

Optimal Sequence Identification in Parallel Flow Line Environment Using Heuristics 209
 N. Rajeswari and K. Balasubramanian

Design and Analysis of Stringer on the Chassis Frame in Load Carrying Vehicle 219
 B. Stalin, M. Ravichandran, C. Ramesh Kannan and K. Sathiya Moorthi

Design and Analysis of Active Controlled Prosthetic Hand 227
 E. Vijayaragavan, Nikhar Khandelwal and Pathan Aftab Altaf

Biodegradable Composites from Leaf Wastes for Packing Applications 233
 S. Renold Elsen, R. Bharanidaran and S. Surendarnath

A Comparative Study of Flow Characteristics of BMW M6 and AUDI R8 Commercial Sports Car Using Flow Design Software 243
 S. Renold Elsen, K. Jegadeesan and J. Ronald Aseer

Mechanical Characterization of Glass Fiber-Strengthened Balsa–Depron Composite	255
Nallusamy Tamilselvam, S. Varsha, D. S. Seema and B. Indhumathy	
Milling Cutter Flank Wear Prediction Using Ensemble of PSO-Optimized SVM and GLM Regression Models	265
B. Stalin, M. Ravichandran, S. Marichamy and C. Anandavel Murugan	
Investigation on the Corrosion Resistance Characteristics of Automobile Lug Nuts	273
K. Sridharan, B. Muthuselvan, R. Gopinath and M. Umamaheswari	
Optimization of Process Parameters of Electrochemical Machining of TiC-Reinforced AA6063 Composites	281
S. Saravanan, M. Ravichandran, B. Stalin, S. Saravanel and S. Sukumar	
Performance Analysis of SS304 Steel Hat Stringer on the Chassis Frame	289
C. Ramesh Kannan, B. Stalin, M. Ravichandran and K. Sathiya Moorthi	
Finite Element Modeling of Single Spark Material Removal and Heat Flux Distribution in Micro-Electro Discharge Machining Process	297
Ishwar Bhiradi, Leera Raju and Somashekhar S. Hiremath	
Electrochemical Micromachining of Aluminium Alloy Composite	309
S. Ramesh and V. Subburam	
Analysis on Mechanical Behaviour of Binary and Hybrid Al2014 Metal Matrix Composites	319
S. Arivukkarasan, B. Stalin, A. Suresh Babu and M. Pandiyarajan	
Study of Forces, Surface Finish, and Tool Life on Machining of Inconel 718	327
K. Venkatesan, S. Devendiran, Biplav Bijoy Goswami, Prafful Kumar and Shakya Rishabhsingh Tejpalsinng	
Investigations on Corrosion Behaviour of AA 8011-ZrB₂ in Situ Metal Matrix Composites	335
B. M. Muthamizh Selvan and V. Anandkrishnan	
Introducing Various Image Processing Techniques to Improve Topology Optimization Process to Develop Compliant Mechanism-Based Microgripper	343
S. P. Banu Murthy, R. Bharanidaran, T. Ramesh and S. Renoldelsen	
Study on Tensile Strength of GFRP Nanocomposites by VARTM	351
A. Thiagarajan, K. Jagadish Chandra Bose, K. Velmurugan and V. S. K. Venkatachalapathy	

Investigations on Wire Spark Erosion Machining of Aluminum-Based Metal Matrix Composites 361
 N. Manikandan, J. S. Binoj, K. C. Varaprasad, S. Sree Sabari and Ramesh Raju

Optimization of Coefficient of Friction for Direct Metal Laser Sintered Inconel 718 371
 S. Sathish, V. Anandkrishnan, V. Dillibabu, Duraiselvam Muthukannan and N. Balamuralikrishnan

Experimental and Numerical Investigation on Incremental Forming of IS513Cr3 381
 M. D. Vijayakumar and G. Gopalaramasubramanian

Modeling of Support Vector Mechanism for Green Manufacturability Quantification of Production 391
 T. Sathish

Experimental Study on Surface Roughness and Optimization of Process Parameters Using ANN-GA in Milling of Super-Duplex Stainless Steel Under Dry and Wet Conditions 399
 Soumya Sambedana, N. Subhash, P. Nithin Raj and T. Jagadeesha

Experimental Study on Tool Wear and Optimization of Process Parameters Using ANN-GA in Turning of Super-Duplex Stainless Steel Under Dry and Wet Conditions 411
 N. Subhash, Soumya Sambedana, P. Nithin Raj and T. Jagadeesha

Multi-Response Optimization Using Grey Relation Analysis in Mechanical Micro Drilling (MMD) of Titanium Alloy—(CP-Ti) Grade II 421
 P. Prashanth and Somashekhar S. Hiremath

A Glance Through History of Automobile Industry and Current Market Study of Some of the Legendary Models in India 433
 Muthu Ajay, Sridhar Kannan, P. Prem Narayan and R. Deepak Suresh Kumar

Effect of Twist Angle and RPM on the Natural Vibration of Composite Beams Made up of Hybrid Laminates 443
 Rakesh Potluri, V. Diwakar, K. Venkatesh and R. Sravani

Tribological Behavior of AZ91–Al₂O₃ Composites by Powder Metallurgy 453
 N. Keerthivasan, S. Selvaraj, V. Anandkrishnan and E. Thayumanvan

Annealing and ZnO Doping Effects on Hydrophilicity and Mechanical Strength of PVDF Nanocomposite Thin Films	463
Mani Sathiyaraju, T. Ramesh and Kumarasamy Jagatheswaran	
Optimization of Transient State Temperature Distribution Analysis on Diffusion-Bonded Joints of Ti-6Al-4V With SS304L Stainless Steel Alloy	473
K. Muthukumar, R. B. Durairaj, G. Mageshwaran, J. Jayajeevahan, V. Sriram and Vikram Naidu	
Optimization of Tribological Properties of Al6061/9%Gr/WC Hybrid Metal Matrix Composites Using FGRA	485
Gangadhara Rao Ponugoti, Pandu R. Vundavilli and Alluru Gopala Krishna	
Experimental Study on Mechanical Properties of Superelastic Alloy	493
M. Sangeetha, P. Ponnusamy, Durgajeevitha and S. Shiva Ganesh	
Framework Execution and Schematic of Jounce Bumper in Two-Wheeler Fork	503
T. Babu, R. Sudharshan, Mohammed Suhail, K. Pradeep and S. Sanjay Arun	
Finite Element Analysis of Bending and Dynamic Response of a Power Transmission Spur Gear	511
A. Saravanan and P. Suresh	
Design and Analysis of Composite Parabolic Leaf Spring Under Fatigue Load Condition	527
Priyadarshi Dutt, T. Babu, M. Murugan, P. Anbarasu and Bala Subramani	
Optimizing Headlamp Focusing Through Intelligent System as Safety Assistance in Automobiles	533
S. K. Rajesh Kanna, N. Lingaraj, P. Sivasankar, C. K. Raghul Khanna and M. Mohanakrishnan	
Modeling and Validation of Ride Characteristics of All-Terrain Vehicle (ATV)	547
Mallikarjuna Reddy, Sanyam Kakkar, Prabhu Pal Singh and Uma Shankar Lath	
Influence of Tool Rotation Speed on Soundness of Water-Cooled Friction Stir Welded Armour Grade Al-Cu Joint	557
S. Sree Sabari, J. S. Binoj, Felix Xavier Muthu, S. Malarvizhi and V. Balasubramanian	

Investigation of Hardness and Tribological Behaviour of Aluminium Alloy LM30 Reinforced with Silicon Carbide, Boron Carbide and Graphite 569
 P. Shanmugaselvam, R. Sasikumar and S. Sivaraj

Friction and Wear Properties of Bio-Based Abrasive in a High-Friction Composite Material..... 577
 S. Stephen Bernard, Md. Javeed Ahmed, J. Dasaprakash, M. R. Saroj Nitin, S. Vivek and G. K. Kannan

Parametric Optimization of Single-Cylinder Four-Stroke Spark Ignition Engine Crankshaft Using Four Different Materials—AISI 1040, AISI 4340, AISI 4140 and AISI 4615 587
 A. Pandiyan, G. Arun Kumar, S. Shaik Asif and Amit Patel

Evaluation and Optimization of Surface Roughness and Metal Removal Rate Through RSM, GRA, and TOPSIS Techniques in Turning PTFE Polymers 595
 N. Sathiya Narayanan, N. Baskar, M. Ganesan, M. P. Jenarathanan and S. Praveen

Effect of Sintering Temperature on the Microstructure and Forming Behavior of AA8079 (Al–Cu–Fe–Si–Zn) 607
 M. Meignanamoorthy, M. Ravichandran, A. Elmariung and S. Dinesh Kumar

Studies on the Influence of Welding Parameters in Cladding of ERNiCrMo-10 on AISI 4140 Using GMAW Process 615
 G. Britto Joseph, T. N. Valarmathi, G. Mageshwaran, Jeya Jeevahan, V. Sriram and R. B. Durai Raj

Review on Corrosion Behavior of Copper–Brass Weldment Samples During Welding with the Different Corrosive Environment 623
 Sourabh S. Nair, Aparna Vinayan, Raghuraman Srinivasan and Sivachidambaram Pichumani

Effect on Mechanical Properties of Aluminum Composites by Inclusion of Silicon Carbide 635
 V. Senthil Kannan and K. Lenin

About the Editors

Dr. Somashekhar S. Hiremath is Associate Professor at the Department of Mechanical Engineering, Indian Institute of Technology (IIT) Madras. He received his doctoral degree in 2004 from IIT Madras. He has published more than 150 papers in national and international journals. He has delivered more than 75 Invited talks on various topics of his research at engineering colleges, universities, research centers, industries, and conferences. Dr. Somashekhar also worked as a visiting Professor at Ecole Centrale de Nantes, France and Warsaw University of Technology, Poland. Currently, he is handling many consultancy and sponsored projects of various industries and R&D institutions of defense, Government of India. His current research areas are mechatronic system design, system simulation and modeling, robotics, finite element modeling, micromachining, fluid structure interactions, and fluid power systems.

Dr. N. Siva Shanmugam is affiliated to the Mechanical Engineering department, National Institute of Technology (NIT), Tiruchirappalli, India where he is currently working as Associate Professor. He received his doctoral degree in 2012 from NIT Tiruchirappalli. He has published numerous papers in reputed national and international peer-reviewed journals. He is actively associated with different national and international societies and academies. He has delivered several invited talks at various engineering institutions and industries located in different parts of India such as Tamil Nadu, Kerala and Andhra Pradesh. He has completed several research and consultancy projects, further he is handling multiple consultancy and sponsored projects for Bharat Heavy Electrical Limited (BHEL) and ISRO, Government of India. His research interests include FE simulation of welding processes, ergonomics study, and biomechanics.

Dr. B. R. Ramesh Babu is currently working as Professor and Dean (R&D) at the Department of Mechanical Engineering at Chennai Institute of Technology, Chennai, Tamil Nadu, India. He received his bachelor's degree in Mechanical Engineering from Madurai Kamaraj University, in 1989, and his Master of Engineering Degree from the University of Madras and BITS (Pilani). He has 30

years of teaching experience and he has published 80 papers in reputed national and international journals, and conference proceedings. He is member of IE (I), SAE, IIPE and ISTE. He is also a Research Supervisor of Anna University, Chennai, JNTU Ananthapur, JNTU Kakinada, Sathyabama University and St. Peter's University. He has guided six doctoral scholars. His research areas of interest include thermal, renewable energy, high temperature coating, and alternate fuels.

Evaluation of Tensile Properties of Nanoclay-Filled Madar Fiber-Reinforced Polyester Hybrid Composites



Gunti Rajesh, M. V. Raghavendra Rao, K. Vijay and S. Gopinath

Abstract In the present work, an effort has been made to improve the mechanical properties of natural fiber-reinforced polyester composite using nanoclay. The composite specimens were prepared with varying weight proportions of short-madar fiber in the polyester matrix from 2.5 to 15% at an interval of 2.5% without and with nanoclay of 1%. The samples were then tested for tensile properties and the results were analyzed. The results showed that the tensile strength of composite was increased with increased fiber loading up to 10%, and with further addition of fibers, there was decrease in the tensile strength. The maximum value attained for 10% fiber loading was 23.33 MPa. The tensile strength of nanoclay-filled madar fiber-reinforced composite is increased to a value of 25.16 MPa up to 10% fiber loading and then with further addition of fibers along with nanoclay, the tensile strength is reduced. It is also observed that there increase in the modulus of madar fiber composite to a value of 520.2 MPa up to fiber loading of 15% and the tensile modulus of nanofilled fiber composites is increased to a value of 460.35 MPa up to fiber loading of 15% which is 11.5% less compared to that of composite without nanoclay. It is observed that there is reduction in the percentage elongation at break for madar fiber-reinforced polyester composite with and without nanoclay filler. The drop is 43.7% in madar fiber composite and it is much higher in composite filled with nanoclay.

Keywords Polyester · Madar fiber · Nanoclay · Tensile strength

1 Introduction

From several decades, lignocellulosic natural fibers have been widely used in the development and fabrication of partially degradable polymer composites. Environmental safety and use of renewable materials for making greener world have lead

G. Rajesh (✉) · M. V. Raghavendra Rao · K. Vijay · S. Gopinath
Department of Mechanical Engineering, DVR & Dr. HS MIC College of Technology,
Kanchikacherla 521180, Andhra Pradesh, India
e-mail: rajesh.mtech@gmail.com

© Springer Nature Singapore Pte Ltd. 2019
S. S. Hiremath et al. (eds.), *Advances in Manufacturing Technology*,
Lecture Notes in Mechanical Engineering,
https://doi.org/10.1007/978-981-13-6374-0_1

industries to use natural fibers as reinforcing materials in composites [1]. Natural fibers have attractive and possible advantages, such as cheaper in cost, reduced tool wear, lower density, and reasonable specific strength, apart from their inbuilt features such as renewability and degradability. A huge number of natural fibers were available in the nature those are being used as reinforcements.

Nowadays, polymer nanocomposites reinforced with natural fibers are widely used for automobile, aerospace, sports, and military applications due to their multi-functional characteristics such as high specific strength, improved mechanical properties, flame retardancy, high corrosion resistance, and low cost when compared to synthetic fiber-reinforced polymer composites [2]. The hybridization is the practice that can eliminate the shortcomings of the present composites reinforced either by natural fibers or clay particles, like low durability and higher water absorption by natural fibers that make them unbalanced with non-polar polymer matrix and non-degradable characteristic of plastics based on clay particles [3].

The nanocomposites were fabricated with varying compositions (0, 0.5, 1, 1.5, and 2 wt%) of Cloisite15A as nanofiller along with glass fiber reinforcement in the polyester. The consequences of addition of nanoclay on the thermal, mechanical, and dynamic mechanical properties of nanocomposites were investigated [4]. The results of tensile and impact tests have obtained 1% as the best possible percentage of clay content in the composite for better mechanical properties. However, the storage modulus of composite was improved for 1% nanoclay fill. Thermogravimetric analysis indicated the initial degradation that starts at 200 °C for all the samples. The tensile fractured surfaces analyzed by SEM indicated brittle fracture for glass fiber-reinforced polyester without nanoclay, whereas by the addition of nanoclay the fracture has changed to ductile nature. Various categories of nanoclay along with natural fiber-based composites giving particular importance to their applications as food packaging and a summary of the most advanced and emerging characteristics of nano technology to develop eco-friendly hybrid composites compatible for food packaging were presented [5].

Wild cane grass fiber up to 40% volume fraction and organically modified montmorillonite (MMT) nanoclay of 4% were added to polyester resin to prepare hybrid composite, and their mechanical properties were investigated [6]. The results indicated that the use of nanoclay has shown noteworthy improvement in tensile, flexural, and impact properties of wild cane grass fiber-reinforced composites. The consequences in addition of nanoclay filler on mechanical and morphological properties of Napier/epoxy composites were examined [7]. The Napier/epoxy composites were fabricated with 2–5 wt% of montmorillonite (MMT) nanoclay by vacuum infusion technique and tested for flexural properties. The results depicted that flexural strength of composite was increased when 3% of nanoclay was added to it. However, there was an increase of 180% in flexural modulus of composite with 5% of nanoclay filler. The biocomposites from unsaturated polyester (UP) resin and chemically modified bamboo fibers were fabricated with hand layup method [8]. In this study, nanocomposite was prepared initially from UP and nanoclay by solution method. Then, that solution was poured on to the selective mat layers to prepare hybrid composite. Com-

posites showed good properties at 90% of bamboo fibers modified by vinyl silane solution of 0.7 and 1% of nanoclay filler.

A relative study was made on the fracture toughness of woven glass fiber/polypropylene, chopped glass fiber/polypropylene, and nanoclay-filled polypropylene composites [9]. The technology of nano and microscale particle reinforcement in various polymeric fiber-reinforced composites with polyamides (PA), polyurethanes, polyesters, polypropylenes, and high-performance/temperature engineering polymers such as poly(ether-ether ketone) (PEEK), polyimide (PI), polyary-lacetylene (PAA), and poly p-phenylene benzobisoxazole (PBO) was examined [10]. The effect of amount of nanoclay and alkali treatment of wood flour on physical and mechanical properties of low-density polyethylene (LDPE) composites with beech flour was studied [11]. In this study, 40% of wood flour chemically treated with 2% alkaline was added to LDPE. Cloisite 15A nanoclay particles were added to the composite in different weight ratios. The results indicated a reduced water absorption rate by increasing the nanoclay content and alkaline treatment on flour. The tensile strength was also increased with increasing the nanoclay content, besides using the chemical treatments on flour. Also, the impact strength was improved by 3% with increased nanoclay content.

The effect of addition of nanoclay particles on the flame retarding properties of wood-fiber/plastic composites (WPC) were investigated [12]. This study indicated that the structure of nanocomposites and the clay content used had a great impact on the flame retardancy of WPC. Effect of addition of nanoclay on the fiber/matrix adhesion in epoxy/glass composites was investigated [13]. In this study, different organically modified clays were added at different weight fractions in the epoxy matrix. The results depicted that the formation of intercalated microstructures due to nanoclay led to considerable improvement in mechanical and thermal properties of the epoxy matrix.

Though several researchers have explored the advantages of addition of nanoclay in the natural fiber composites, there is still ample scope for the development of nanofilled composites reinforced with new natural fiber composites. In this study, a new mixture of natural fiber and matrix, i.e. madar fiber and polyester with 1% nanoclay were considered to fabricate hybrid composite. The short fibers with varying weight fraction in polyester were considered along with nanoclay, and tensile properties were evaluated.

2 Materials and Methods

2.1 Materials

The polyester resin of the grade ECMALON 4413 with viscosity of 500–600 cPs (Brookfield viscometer) and a specific gravity of 1334 kg/m³ at 25 °C was purchased from Bindu Agencies Pvt. Ltd., Vijayawada, India. Methyl ethyl ketone per-

Table 1 Composite sample fabrication

S. no.	Fiber, wt%	Nanoclay, wt%	Polyester, wt%
1	2.5	1	96.5
2	5	1	94.0
3	7.5	1	91.5
4	10	1	89.0
5	12.5	1	86.5
6	15	1	84.0

oxide (MEKP) accelerator and cobalt octoate ($C_{16}H_{30}CoO_4$) catalysts namely were obtained from local market. The organically modified montmorillonite (MMT) nanoclay used was supplied by sigma Aldrich, Hyderabad.

Extraction of Madar Fibers

Stem is collected from the madar (*Calotropis Gigantea*) plant and the fiber from the stem is extracted by water retting process. Here, the stalks of stems were submerged in water for 15 days. Then, the stems were taken out of water and were beaten gently using wooden mallet. The fibers were then extracted and dried in the sunlight for 48 h. The fibers were then chopped to a length of 3–4 mm.

2.2 Fabrication of Composite

The modified nanoclay and polyester were dried in oven for about 2 h before use. The MMT particles have a fine particle-size distribution and exceptional dispersion in the matrix. An amount of 1% organically modified MMT nanoclay was mixed with the polyester resin by means of a sonicator for a period of 30 min at room temperature to obtain a homogenous mixture.

The madar fibers of size 3–4 mm were then added at various weight ratios from 2.5 to 15% to the mixture of polyester and nanoclay. The samples were prepared by filling the mixture in the mold prepared using rubber as per ASTM D638 for tensile properties using hand layup technique. For each weight ratio of fiber, five samples were prepared and an average of these was considered to calculate tensile strength. The detailed ratio of reinforcements and matrix to fabricate the composite was shown in Table 1.

2.3 Testing of Composite Samples

The samples were tested for tensile strength on a universal testing machine as per ASTM standard D638. The samples were loaded on the machine with maximum load set to 200 kg and the samples were tested at a crosshead speed of 0.5 mm/min



Fig. 1 Tensile fractured samples of nanofilled polyester composites with 7.5 and 10% madar fibers

and the strain was measured with an extensometer of the machine. The elongation and their respective loads were noted (Fig. 1).

3 Results and Discussion

From the Fig. 2, it is observed that the tensile strength of untreated madar fiber-reinforced polyester composite was increased with increased fiber loading up to 10%, and with further addition of fibers, there was decrease in the tensile strength. The maximum value attained for 10% fiber loading was 23.33 MPa. The tensile strength of nanoclay-filled madar fiber-reinforced composite is increased to a value

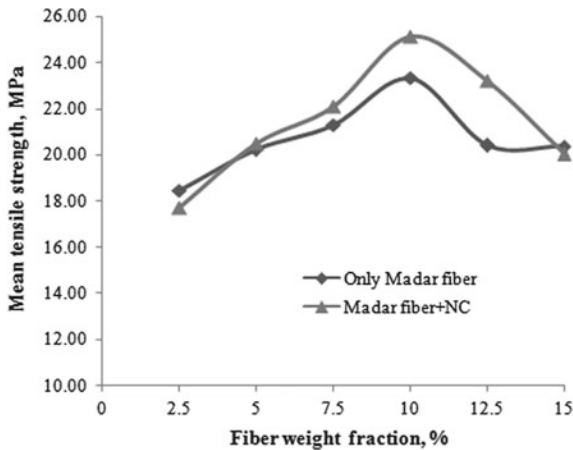


Fig. 2 Variation of tensile strength of nanoclay-filled and unfilled madar fiber-reinforced polyester composites with fiber loading

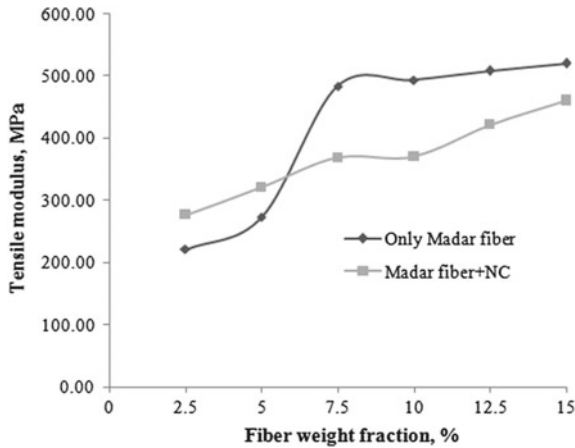


Fig. 3 Variation of tensile modulus of nanoclay-filled and normal madar fiber-reinforced polyester composites with fiber loading

of 25.16 MPa at 10% fiber loading which is 7.8% higher than madar fiber composite without nanoclay.

The increase in the tensile strength with increased fiber loading is due to better interaction between fiber and matrix and the drop in tensile strength with further addition of fiber beyond 10% is the fact that there is more fiber-fiber interaction than that of fiber–matrix interaction. It is observed that the addition of nanoclay in the madar fiber-reinforced composite has considerable effect on tensile strength of the composite.

From Fig. 3, it is observed that there was an increase in tensile modulus of madar fiber polyester composite without nanoclay to a value of 520.20 MPa at fiber loading of 15%. The tensile modulus of nanofilled fiber composites is increased to a value of 460.35 MPa at fiber loading of 15% which is 11.5% less compared to that of fiber-reinforced composite without nanoclay.

From Fig. 4, it is observed that there was reduction in the percentage elongation at break for madar fiber-reinforced polyester with and without nanoclay filler. The drop in the madar fiber-reinforced composite without nanoclay is 8.35–4.7%, i.e. the drop is 43.7%. The drop is much higher for nanofilled madar fiber-reinforced composite. The increase in the stiffness of the composite with the addition of nanoclay might be the reason for drop in elongation at break of the composite.

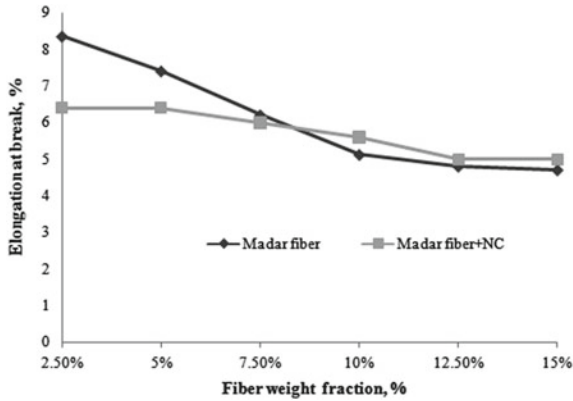


Fig. 4 Variation of % elongation of nanoclay-filled and normal madar fiber-reinforced polyester composites with fiber loading

4 Conclusions

With the results obtained from the experimental procedure, the following conclusions were made.

- The tensile strength of madar fiber-reinforced polyester composite with and without nanoclay was increased with increased fiber loading up to 10%, and with further addition of fibers, there was decrease in the tensile strength. The tensile strength of nanoclay-filled madar fiber-reinforced composite is increased to a value of 25.16 MPa at 10% fiber loading which is 7.8% higher than madar fiber composite without nanoclay.
- There was an increase in tensile modulus of madar fiber polyester composite without nanoclay to a value of 520.20 MPa at fiber loading of 15%. The tensile modulus of nanofilled fiber composites is increased to a value of 460.35 MPa at fiber loading of 15% which is 11.5% less compared to that of fiber-reinforced composite without nanoclay.
- It is observed that there is reduction in the percentage elongation at break for madar fiber-reinforced polyester with and without nanoclay filler. The drop in the madar fiber-reinforced composite without nanoclay is 8.35–4.7%, i.e. the drop is 43.7%. The drop is much higher for nanofilled madar fiber-reinforced composite.
- Finally, it is concluded that the fiber loading has influenced the properties of composite and also there is significant role of adding nanoclay of 1% in improving the strength of the composite.

References

1. Saba N, Tahir PM, Jawaid M (2014) A review on potentiality of nano filler/natural fiber filled polymer hybrid composites. *Polymers* 6(8):2247–2273
2. Arulmurugan S, Venkateshwaran NR (2016) Vibration analysis of nanoclay filled natural fiber composites. *Polym Polym Compos* 24(7):507–516
3. Essabir H, Raji M, Bouhfid R, Qaiss AEK (2016) Nanoclay and natural fibers based hybrid composites: mechanical, morphological, thermal and rheological properties. In: *Engineering materials—nanoclay reinforced polymer composites*. Springer Science, Singapore
4. Binu PP, George KE, Vinodkumar MN (2016) Effect of nanoclay, Cloisite15A on the mechanical properties and thermal behavior of glass fiber reinforced polyester. *Procedia Technol* 25(2016):846–853
5. Majeed K, Jawaid M, Hassan A, Abu Bakar A, Abdul Khalil HPS, Salema AA, Inuwa I (2013) Potential materials for food packaging from nanoclay/natural fibres filled hybrid composites. *Mater Des* 46(6):391–410
6. Ratna Prasad AV, Balakotesara Rao K, Mohana Rao K, Ramanaiah K, Kumar Gudapati SP (2015) Influence of nanoclay on the mechanical performance of wild cane grass fiber-reinforced polyester nanocomposites. *Int J Polym Anal Charact* 20(6):541–556
7. Lim KM, Majid MSA, Ridzuan MJM, Basaruddin KS, Afendi M (2017) Effect of nano-clay fillers on mechanical and morphological properties of Napier/epoxy composites. *IOP Conf Ser J Phys Conf Ser* 908:1–9
8. Thanh T, Mao N, Ngan N, Thanh N, Tai D (2011) Effect of nanoclay on properties of the biocomposite based on unsaturated polyester resin and bamboo fibers. *VNU J Sci Math Phys* 27(3):165–173
9. Ramsaroop A, Kanny K, Mohan TP (2010) Fracture toughness studies of polypropylene—clay nanocomposites and glass fibre reinforced polypropylene composites. *Mater Sci Appl* 1:301–309
10. Njuguna J, Pielichowski K, Desai S (2008) Nanofiller fibre-reinforced polymer nanocomposites. *Polym Adv Technol* 19(8):947–959
11. Nozari O, Madanipour M, Farsi M, Tabei A (2013) Mechanical properties and water uptake of nanoclay/wood flour/LDPE composites after fiber surfacemergerization. *Cellul Chem Technol* 47(3–4):295–301
12. Guo G, Park C, Lee Y, Kim Y, Sain M (2007) Flame retarding effects of nanoclay on wood–fiber composites. *Polym Eng Sci* 47(3):330–336
13. Dorigato A, Morandi S, Pegoretti A (2011) Effect of nanoclay addition on the fiber/matrix adhesion in epoxy/glass composites. *J Compos Mater* 46(12):1439–1451

Characterization of Economical Aluminium MMC Reinforced with Weld Slag Particles



P. Paranthaman, P. M. Gopal and N. Sathiesh Kumar

Abstract Rapid advancement in technology forces the researchers to search for advanced materials with higher performance like composites. The composites are known for their better mechanical properties and less weight, but the cost is the major factor that hinders the wider application of these materials. In this study, welding slag is reused as reinforcement to produce economical metal matrix composites, because slag is produced in enormous amount during welding of materials which causes pollution. The aluminium alloy (Al 6063) is used as base material. Weld slag of different weight proportions (0, 5 10 and 15 wt%) is mixed with Al 6063 through stir casting process, and samples are taken for investigation. The mechanical properties of the composites like tensile strength, compression strength and its wear behaviour are analysed. And also, the microstructure of the MMC is analyzed through optical microscope (OM) to determine the weld slag distribution in aluminium matrix material. The observed result indicates that the addition of weld slag particles with aluminium increases the mechanical properties. The composite having 15% of welding slag exhibits the best tensile and wear resistance.

Keywords Composite · Weld slag · Stir casting · Tensile strength · Compressive strength

1 Introduction

Metal matrix composites (MMCs) gain significant importance worldwide due to their superior mechanical properties, because materials with better strength and less weight are well suitable and necessary for engineering applications [1]. Further, the development of sustainable and reusable materials from existing things has observed

P. Paranthaman (✉) · P. M. Gopal · N. Sathiesh Kumar
Department of Mechanical Engineering, Karpagam Academy of Higher Education,
Coimbatore 641021, India
e-mail: paranth.ponnusamy@gmail.com

© Springer Nature Singapore Pte Ltd. 2019
S. S. Hiremath et al. (eds.), *Advances in Manufacturing Technology*,
Lecture Notes in Mechanical Engineering,
https://doi.org/10.1007/978-981-13-6374-0_2

an ideal global attention and importance from engineers as well as the wide-ranging community and government [2, 3].

Aluminium and its alloys have superior mechanical properties while adding reinforcements during metal matrix composite (MMC) development. The wide spectrum of unique properties can be attained with Al MMCs at comparatively low processing expenditure. The Al-based MMCs have superior specific stiffness and strength, enhanced elevated temperature properties (concerning its monolithic alloy) and thermal conductivity. The multi-functional characteristic of Al-based composites has seen its exploitation in aerospace technology, electronic heat sinks, antenna reflectors, automobile drive shafts fins and engine machineries, along with others [4]. Properties of these Al-based matrix composites majorly subject to (1) composition of the base alloy, (2) the character of material reinforced and (3) the techniques opted for MMC processing.

Thus, a large amount of research works reported in the literature have attempted to address how these facets influence the properties and behaviour of aluminium matrix composites. The majority of research works reported on the literature on Al composites has been committed frequently only on some of the aluminium alloys, such as A357, A359, 2618, 2254, 6061 and 7075. However, not much study has been reported on the exploitation of Al 6063 as matrix material for the Al MMC fabrication. Al 6063 alloy is the most readily obtainable aluminium alloy in the global metal markets. It is processed in soaring quantities at small price by the majority of aluminium processing industries for applications such as the production of glazing bars and window sections, wind screen and sliding roof sections for the automobile industry, pipes and tubing and for furniture also. The perspective for developing aluminium-based MMC with superior performance by using Al 6063 alloy as base material has created the thrust of this research exertion.

In recent past, an enormous amount of research works are carried on waste particle-reinforced MMCs. Currently, fly ash cenosphere [5], rock dust [6, 7] and CRT glass [7, 8] like waste particles are tried as reinforcement, and good results were obtained. Similar to these wastes, welding slag is noteworthy and is produced while joining metals which cause the pollution and leftover of resources. But, an effective recycling technique for this industrial waste is not yet discussed widely.

Hence, the current research intents to reuse welding slag as reinforcement to produce the composite materials. Further, among various MMC development methodologies, stir casting furnishes superior matrix particle attachment as a result of stirring action of particles into the metals. The studies in the literature described that the uniform mixing and wetting be able to obtain by choosing suitable parameters while MMC processing [9].

The present research investigation explores the mechanical and wear behaviour of welding slag-reinforced Al 6063 MMCs. The effect of reinforcement percentage on mechanical and wear behaviour of MMC has been investigated experimentally.

2 Materials and Methods

Al 6063 is selected as base material due to its availability, low cost and its wider applications. Aluminium 6063 is the most commonly available metal which is in pre-tempered grades. It is mostly used in aircraft structures and all complicated extrusions. It has a good surface finish, high resistance to corrosion, suitable for welding and can be anodized effortlessly. The typical elements of the aluminium alloys are copper, manganese, silicon, magnesium and zinc, wherein silicon and magnesium play key role.

The reinforcement material used in this study is welding slag which is a residue after welding. The slag is collected for the nearby industries and ball milled to obtain uniform size of 50 μm . The ball milled welding slag is shown in Fig. 1, and the chemical composition is given in Table 1.

The MMC is developed through stir casting method by reinforcing welding slag at three weight percentages (5, 10 and 15). Along with MMCs, one base metal sample also is developed for reference. A calculated amount of welding slag is kept in a furnace and heated up to 600 $^{\circ}\text{C}$ (preheating). Then, these preheated particles were put into Al 6063 molten metal. Then, the mixture is heated to around 720 $^{\circ}\text{C}$. Degassing agent (hexachloroethane) was used to reduce gas porosities. The melt is consequently stirred at 900 r/min with the aid of a mechanical stirrer that is fastened with adjustable speed motor. Then, the temperature in the furnace was maintained constant for 10 min at 720 $^{\circ}\text{C}$; subsequently, the composite mixture is poured into

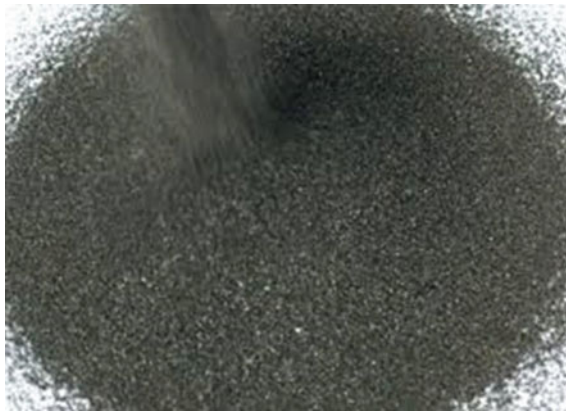


Fig. 1 Welding slag

Table 1 Chemical composition of welding slag

Constitution	CaO	SiO ₂	FeO	MnO	MgO	Al ₂ O ₃	Others
Composition (%)	43.21	17.15	21.43	5.22	7.18	3.43	Remaining

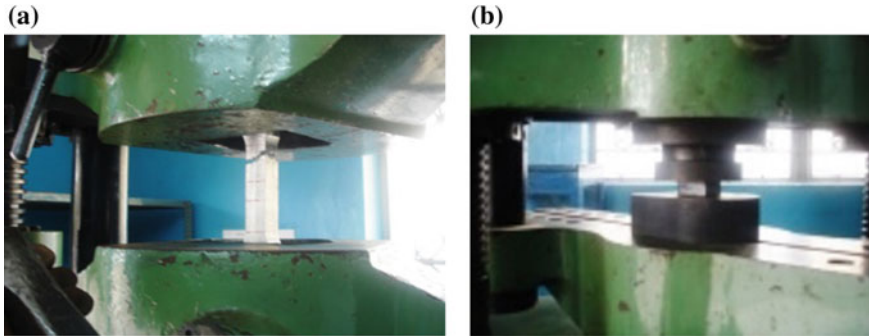


Fig. 2 a Tensile testing and b compression testing

the mould cavity of 200 mm × 40 mm × 30 mm, and the required composite is obtained. The die was released after 5 h, and the cast specimens were taken out.

Brinell hardness method is followed for measuring hardness of the developed MMC as per the ASTM standards. Hardness is measured at the five distinct places of the polished MMC surface, and average value is taken into consideration. Tensile and compression test are also performed on the specimens prepared based on ASTM standard. Three specimens were prepared from each MMC samples for both tensile and compression test. Then, the average values are taken for the analysis. Figure 2 shows the tensile and compression testing procedures for the developed specimens. Wear analysis for the developed MMC is performed under dry conditions through pin-on-disc apparatus. The counter disc material used is hardened EN31 steel.

3 Result and Discussion

3.1 Microstructure

The Al composites produced were examined for its microstructure using an optical microscope (OM). A series of emery papers of grit sizes ranging from 1000 μm is utilized for polishing the specimens of optical microscopy inspection. Polycrystalline diamond suspension of particle size varying from 10 to 0.5 μm with ethanol solvent is utilized for fine polishing. The samples were etched with 0.5% HF solution by swabbing for 3–6 min (subsequently rinsing in water and drying) prior to OM inspection. An optical microscopic image obtained from the analysis is shown in Fig. 3.

The optical microscopic images clearly show the presence of welding slag reinforcement particles in the aluminium matrix. The existence of reinforcement particles at the grain boundaries can be clearly identified from Fig. 3a. These reinforcement

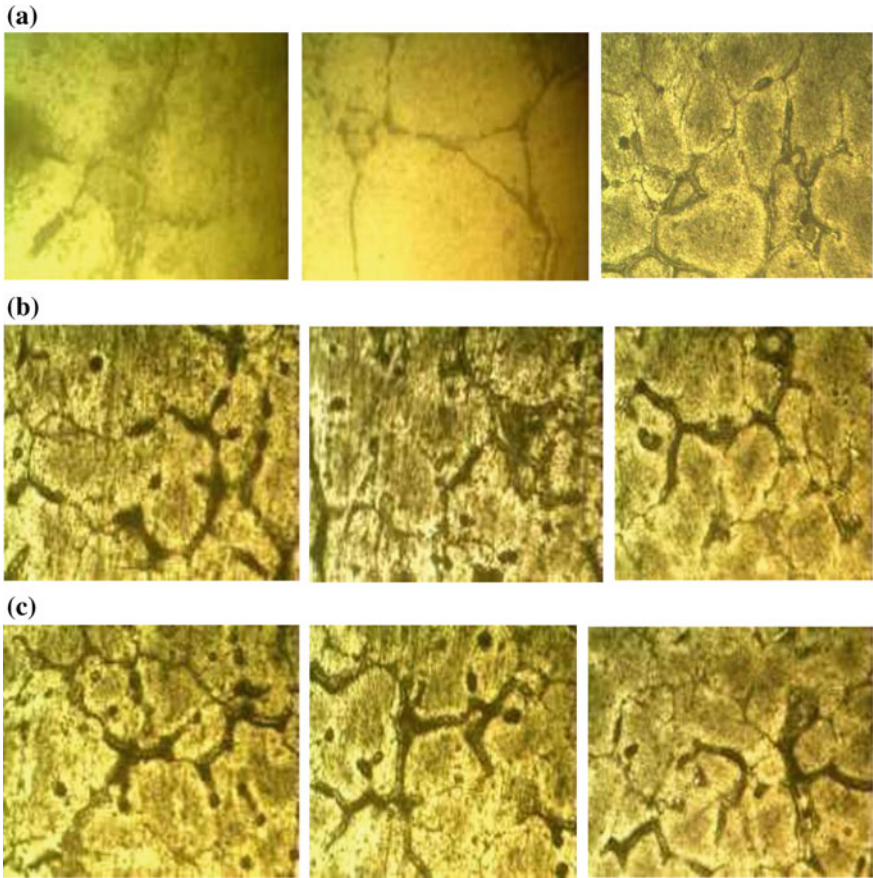


Fig. 3 a Microstructure of 5% welding slag-reinforced MMC. b Microstructure of 10% welding slag-reinforced MMC. c Microstructure of 15% welding slag-reinforced MMC

particles help to hinder the dislocation motion during plastic deformation which will increase the properties of the aluminium.

3.2 Hardness

Hardness of the aluminium is increased when the welding slag is added, and it increases with every rise in welding slag percentage. Hardness of the aluminium base material is 35 BHN, and it increases to 55 BHN when 15 wt% of welding slag is introduced to the aluminium matrix which is found to be 57% increase. As stated earlier, the presence of reinforcement particles at the grain boundaries hinders the motion of dislocation during plastic deformation (indentation during hardness test).

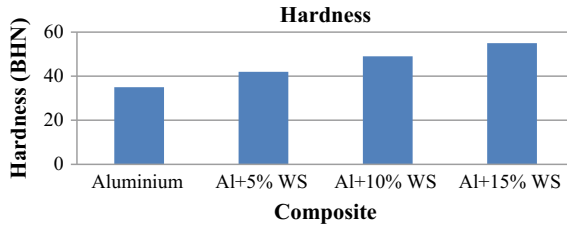


Fig. 4 Hardness of the base material and MMC

Table 2 Tensile test results

Description and units	Observed values/results			
	Base material	Al + 5% WS	Al + 10% WS	Al + 15% WS
Tensile stress (N/mm ²)	80.12	90.05	107.05	112.27
% of elongation	7.1	5.4	4.2	3.4

Hence, higher energy is required to move the dislocation; i.e., hardness of the material is increased. Enhancement in Al hardness with respect to reinforcement percentage is shown in Fig. 4.

3.3 Tensile Strength

The variation in mean tensile strength with respect to slag percentage is represented in Table 2. Tensile strength of the aluminium increases greatly up to 10% welding slag addition, and further increase in reinforcement did not give significant effect; i.e., the tensile strength only increases to 112.27 from 107.05 N/mm². Addition of welding slag reinforcement into the aluminium base material results in elongation loss. The elongation of aluminium decreases with increase in welding slag percentage. This loss of ductility may be due to rise in aluminium hardness as a result of reinforcement addition.

3.4 Compression Strength

Compression test is also carried out on UTM in accordance with ASTM standard. Compression test results of the developed MMC are publicized in Fig. 5. It clearly depicts that the compressive strength of the aluminium increases up to 10% welding slag addition, whereas further addition of reinforcement results in a slight decrement in compressive strength. The effect of welding slag reinforcement over the compression strength of the aluminium is not high as that of tensile strength.

Fig. 5 Compressive strength of the base material and MMC

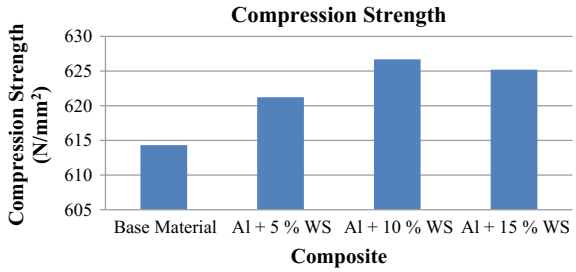
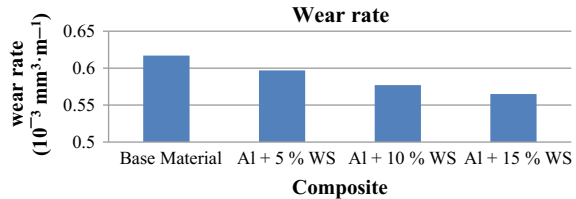


Fig. 6 Wear behaviour of the base material and MMC



3.5 Wear Behaviour

Wear rate of the specimens tested under same experimental conditions, i.e. same load, sliding speed and distance, is shown in Fig. 6. The wear analysis parameters are 10 N load, 1 m/s sliding velocity and 1000 m sliding distance. Resistance to wear capability of the aluminium is found to be greater than before with the addition of welding slag reinforcements. MMC hardness increment with respect to weld slag weight percentage results in increased wear resistance. It is a well-known fact that the harder material always gives the better wear resistance [10].

4 Conclusion

Composite technologies offer a way of lightweight and high-strength components. In the view of economy, the developed composite material gives extreme output. From the investigation and results, it can be able to conclude that

- The tensile stress was increased due to presence of welding slag compare to other metals.
- The compression property of Al 6063 with welding slag (10%) is found to be good due to presence of welding slag compare to other metals.
- The microstructure result confirms that the particulate distribution is better in developed Al 6063 composite and also shows the signs of healthier interfacial bonding.

- Compression and tensile strength of Al 6063/welding slag MMC are getting improved with an increase in weight per cent of the reinforcing phase at the cost of ductility decrement.
- Wear rate of the aluminium decreases with respect to the welding slag percentage.

References

1. Alaneme KK, Bodunrin MO, Awe AA (2018) Microstructure, mechanical and fracture properties of groundnut shell ash and silicon carbide dispersion strengthened aluminium matrix composites. *J King Saud Univ Eng Sci* 30(1):96–103
2. Ashori A (2008) Wood–plastic composites as promising green-composites for automotive industries. *Bioresour Technol* 99(11):4661–4667
3. Karthikeyan S, Paranthaman P, Gopi Kanna J, Karthick G (2015) Evaluation of natural fiber reinforced composite by varying hybrid ratio. *Int J App Eng Res* 10(85):694–703
4. Singh S (2017) Wear behavior of Al-6063/SiC metal matrix composites reinforced with different particles sizes using Taguchi's methodology. *Mater Today Proc* 4(9):10148–10152
5. Kumarasamy SP, Vijayananth K, Thankachan T, Muthukutti GP (2017) Investigations on mechanical and machinability behavior of aluminum/flyash cenosphere/Gr hybrid composites processed through compocasting. *J Appl Res Technol* 15(5):430–441
6. Prakash KS, Kanagaraj A, Gopal PM (2015) Dry sliding wear characterization of Al 6061/rock dust composite. *Trans Nonferrous Met Soc China* 25(12):3893–3903
7. Prakash KS, Gopal PM, Kavimani V (2017) Effect of rock dust, cenosphere and E-waste glass addition on mechanical, wear and machinability behaviour of Al 6061 hybrid composites. *Indian J Eng Mater Sci* 24:270–282
8. Gopal PM, Prakash KS, Jayaraj S (2018) WEDM of Mg/CRT/BN composites. Effect of materials and machining parameters. *Mater Manuf Processes* 33(1):77–84
9. Hariprasad T, Varatharajan K, Ravi S (2014) Wear characteristics of B4C and Al₂O₃ reinforced with Al 5083 metal matrix based hybrid composite. *Procedia Eng* 97:925–929
10. Gopal PM, Prakash KS, Nagaraja S, Aravindh NK (2017) Effect of weight fraction and particle size of CRT glass on the tribological behaviour of Mg-CRT-BN hybrid composites. *Tribol Int* 116:338–350

Optimization of Weld-Bead Parameters of Plasma Arc Welding Using GA and IWO



Kadivendi Srinivas, Pandu R. Vundavilli and M. Manzoor Hussain

Abstract Plasma arc welding (PAW) of Inconel 617 plates is an important and critical process for many engineering applications such as combustion cans, high-temperature nuclear reactors, and transition liners in aircraft due to its high depth-to-width ratio. Therefore, finding the combination of optimal input process parameters of the said welding process is an essential task to be carried out before employing it in various applications. In the present study, bead-on-plate (BoP) trails of PAW are performed on Inconel 617 plates after conducting the experiments designed based on the central composite design of experiments (CCD). During experimentation, welding speed, welding current, and gas flow rate are considered as input process parameters, and bead width and bead height of BoP trails are treated as responses of the PAW process. The nonlinear regression equations developed for both the bead width and bead height are optimized with the help of two population-based optimization algorithms, namely genetic algorithm (GA) and invasive weed optimization (IWO) algorithms.

Keywords Plasma arc welding · Bead-on-plate trails · Optimization · Genetic algorithm · Invasive weed optimization

K. Srinivas (✉)

Department of Mechanical Engineering, DVR & Dr. HS MIC College of Technology,
Kanchikacherla 521180, AP, India
e-mail: kadivendi@gmail.com

P. R. Vundavilli

School of Mechanical Sciences, Indian Institute of Technology Bhubaneswar, Bhubaneswar
752050, Odisha, India

M. Manzoor Hussain

Department of Mechanical Engineering, Jawaharlal Nehru Technological University, Hyderabad
500085, Telangana, India

© Springer Nature Singapore Pte Ltd. 2019

S. S. Hiremath et al. (eds.), *Advances in Manufacturing Technology*,

Lecture Notes in Mechanical Engineering,

https://doi.org/10.1007/978-981-13-6374-0_3

1 Introduction

It is always important to determine the optimal process parameters of any manufacturing process to minimize the cost as well as the time invested in manufacturing the part. Particularly, welding is such a manufacturing technique with more number of input process parameters and output responses. On the other hand, superalloys are high-strength materials that exhibit creep, corrosion, and oxidization resistance. It is important to note that the Ni-based superalloy, Inconel 617, exhibited high strength and oxidation resistance at elevated temperatures over 1800 °F. Further, Inconel 617 offers attractive properties for the machinery of nuclear fossil-fueled power generating plants. Therefore, the selection of welding process parameters that are essential to produce high temperatures and concentrated arc plays a key role in joining of superalloys.

The plasma transferred arc welding produces high energy density with high velocity that causes deep and narrow penetration and improves the weld quality. It is important to set the best possible process parameters for achieving the essential bead dimensions like bead width and depth of penetration. Babu et al. [1] obtained the optimal process parameters using a genetic algorithm in friction stir welding of cryo-rolled AA2219 alloy. Nagaraju et al. [2] performed experimentation on 9Cr–1Mo steel using the A-TIG welding process. Further, they used RSM and GA techniques to optimize the process parameters. In that work, they concluded that the GA-based tournament selection is an accurate method of optimization for the A-TIG welding process. Pal et al. [3] used the neuro-genetic algorithm technique to optimize the process parameters in pulsed metal inert gas welding for desired weld quality. Satpathy et al. [4] conducted experimentation on ultrasonic welding machine to join the dissimilar metals, namely AA1100 and UNS C27000. Later on, they optimized the process parameters using fuzzy logic and genetic algorithm approaches. They reported that logic-based optimization yields better results than GA. Furthermore, Kanigalpula et al. [5] performed welding of precipitation-hardened Cu–0.804Cr–0.063Zr alloy using electron beam welding. In their work, they optimized the weld area by considering the constraints, such as maximum weld penetration and micro-hardness. Moreover, they also reported that GA is a useful tool to optimize constraint problems with reasonably good accuracy. Vasudevan et al. [6] developed a GA-based computational model to obtain the best suitable process parameter combination that is responsible for achieving target-based bead geometry. They conducted experimentation on 316L (N) and 304L (N) material after using the A-TIG welding process. Dey et al. [7] had done bead-on-plate experimentation on austenitic steels using electron beam welding. Further, they determined the solution for the constrained problem, which gives optimal weld-bead geometry using a GA-based penalty function approach. Kim et al. [8] investigated the weld-bead geometry of mild steel material in the CO₂ welding process. In their study, they have used the desirability function approach to find the optimal weld conditions after applying GA and RSM. Meran [9] developed a nonlinear process parameter estimation models after using a couple of variables of GA, named as genetic algorithm welding current estimation model and genetic

algorithm welding velocity estimation model to optimize the weld-bead geometry of brass material. Correia et al. [10] compared the response surface methodology and genetic algorithm techniques for the optimization of the GMAW process. They reported that both the techniques were capable of providing optimal values of process parameters with limited input data. Mehrabian and Lucas [11] introduced a new optimization algorithm called invasive weed optimization (IWO) and compared with the other evolutionary algorithms like GA, memetic algorithms, PSO, and shuffled frog leaping. In their work, they suggested that the IWO has performed the optimization of engineering problems with a high level of satisfaction. Pourjafari and Mojallali [12] also suggested the IWO algorithm for solving nonlinear engineering problems for various practical applications like chemical systems, robotics, and other geometry problems.

From the literature, it has been observed that many of the researchers had given an attempt to optimize the welding process parameters using different optimization techniques. But, none of the researchers has used the IWO algorithm to perform the optimization of the PAW process. In the present work, an attempt has been made to optimize the bead geometry of plasma arc welded Inconel 617 plates using two different techniques, namely GA and IWO.

2 Materials and Methods

2.1 Experimentation

In the present research, Inconel 617 superalloy plates of thickness 2 mm is used as the base material. Plasma arc welding in melt in mode is used to conduct bead-on-plate (BoP) experiments on the Inconel material. Initially, trial/pilot experiments are conducted to determine the range of the input parameters at full depth of penetration. The welding speed, welding current, and plasma gas flow rate are considered as the input process parameters [13]. The working ranges of the input process parameters are given in Table 1.

Central composite design (CCD) is used to conduct the experiments. After experimentation, the plates are cross-sectioned using wire-cut electric discharge machine to measure the bead dimensions [14]. The sectioned pieces are mounted with the help of specimen mounting machine, and then, proper etching is applied on the round specimen. The mounted specimens are used to measure the weld-bead dimensions,

Table 1 Input parameters and their working ranges

Input parameter	Low value	High value
Welding current (I)	80 A	105 A
Welding speed (N)	250 mm/min	300 mm/min
Plasma gas flow rate (G)	2 LPM	2.5 LPM

namely bead width and bead height. The measured data are fed into the MINITAB software to analyze it and to establish the nonlinear regression equations.

2.2 *Statement of the Problem*

The formulation of the problem is discussed in this section. Among the bead parameters, bead width and bead height are to be minimized for the quality of the weld. At the same time, the constraint has been taken that the maximum bead height should be less than or equal to 2 mm (plate thickness) to avoid the weld sag, which is not recommended in the welded component. The objective function related to the weld-bead geometry is given below.

$$\begin{aligned} \text{Minimize } (Z) &= BW + BH \\ \text{Constraint } BH &\leq 2 \\ \text{Subjected to} \\ 80 &\leq I \leq 105 \\ 250 &\leq N \leq 300 \\ 2 &\leq G \leq 2.5 \end{aligned}$$

2.3 *Optimization Methods*

In the present work, two non-traditional optimization methods, namely GA and IWO, are used to optimize the welding bead parameters of plasma arc welded Inconel 617 sheets. The algorithms used in the present work are discussed in the subsequent subsections.

Genetic Algorithm

Genetic algorithm [15] is a population-based search and optimization procedure, which is capable of finding close proximity to an optimal solution to the real world problems. It is used to solve constrained as well as unconstrained problems. In the present study, a binary-coded GA is used to derive the process parameters that are responsible for optimizing the bead parameters of PA welded Inconel plates. A parametric study is conducting to perform the said task. During the optimization, the population is initiated randomly and evaluated by performing mutation and crossover operations. This procedure is repeated until the maximum number of generations is reached.

Invasive Weed Optimization

Invasive weed optimization is a stochastic optimization algorithm that is constructed using the theory of weed biology and ecology developed by Mehrabian and Lucas [11]. In a crop field, weeds are spread randomly and they grow up to become flowering weeds and generate new weeds by taking unused resources. The fitness of the

flowering weed is decided the number of weeds to be generated by each flowering weed. The weeds with a good adaptation in the location will consume additional unexploited resources from the field and grow faster and harvest additional new seeds. Further, the newly formed seeds dispersed arbitrarily throughout the field and grow to a flowering weed. The above process will continue to reach the maximum number of weeds in the field by using limited resources. Finally, the weeds having better fitness/qualification could continue and harvest new weeds. Initialization, reproduction, and spatial dispersal are three major procedural steps of the algorithm.

3 Results and Discussions

The nonlinear regression equations that represent the bead width and bead height of PAW of Inconel plates are given in Eqs. (1) and (2), respectively.

$$\begin{aligned} BW = & 45.76 + 0.1263I - 0.3217N - 1.82G \\ & + 0.00186I^*I + 0.000626N^*N + 1.294G^*G \\ & - 0.00072I^*N - 0.10044I^*G + 0.01635N^*G \end{aligned} \quad (1)$$

$$\begin{aligned} BH = & -22.76 - 0.6486I + 0.5473N - 17.70G \\ & + 0.001970I^*I - 0.000953N^*N + 4.767G^*G \\ & + 0.000507I^*N + 0.06872I^*G - 0.03507N^*G \end{aligned} \quad (2)$$

The parameters of GA and IWO that are responsible for the optima BW and BH are determined by conducting a parametric study. In genetic algorithm, the parametric study has been conducted by varying mutation percentage {0.01–0.09}, crossover percentage {0.1–0.9}, population size {10–100}, and number of iterations {10–100}. Whereas in IWO, the sigma initial {2/100–10/100}, exponent {2–9}, maximum number of seeds {10–70}, maximum population size {10–50}, and maximum number of generations {10–100} are considered as variables for the parametric study. Figure 1a, b shows the convergence plots for the GA and IWO, respectively. The optimal parameters {Pm, Pc, population size, number of generations} and {Smin, Smax, sigma initial, sigma final, initial population, final population, number of generations} for GA and IWO are seen to be equal to {0.03, 0.3, 20, 38} and {10, 17, 2%, 0.001%, 5, 50, 20}, respectively.

The optimal values of the welding parameters and corresponding bead parameters are given in Table 2. It has been observed that IWO is found to perform better than GA in terms of both the bead parameters. It is interesting to note that the IWO has shown a 1.16% increase in the value of bead width and a 2.23% decrease in the value of bead height. The better performance of IWO is due to its reproduction procedure in which both the fit and unfit seeds will contribute toward the generation of new seeds.

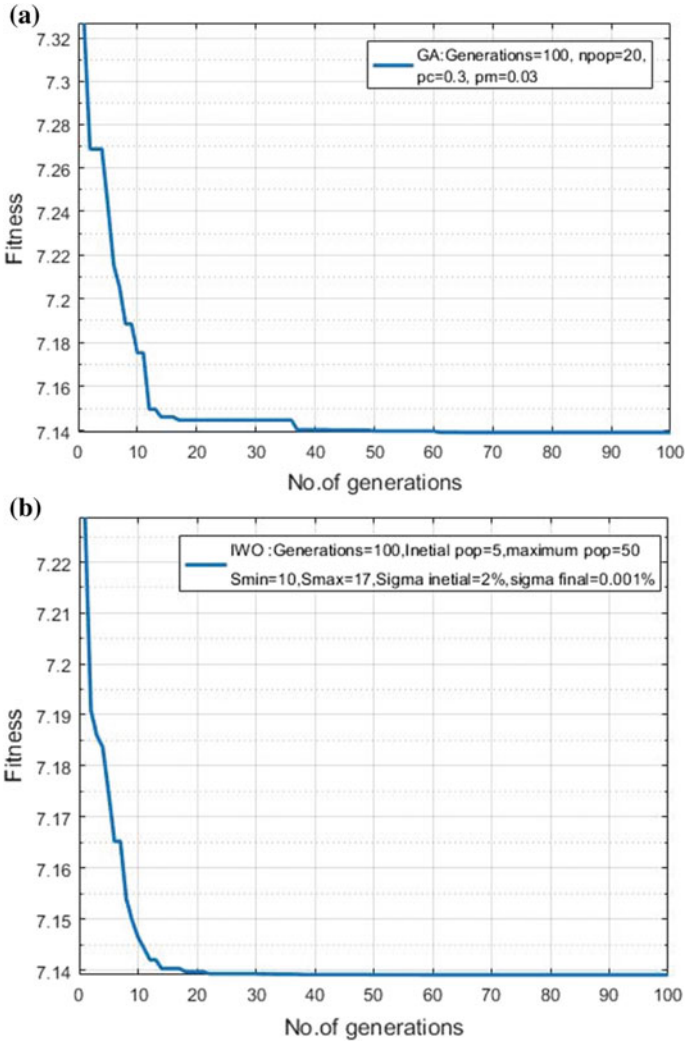


Fig. 1 Convergence graphs for **a** GA and **b** IWO algorithms

Table 2 Optimal values of the process parameters and their responses

Optimization method	Welding current (<i>I</i>)	Welding speed (<i>N</i>)	Plasma gas flow rate (<i>G</i>)	Bead width (BW) in mm	Bead height (BH) in mm
GA	86.001	300.00	2.296	5.600	1.656
IWO	86.049	300.00	2.298	5.666	1.620

4 Conclusions

In the present work, an attempt has been made to optimize the bead profile of the plasma arc welded BoP weld geometry of Inconel 617 plates using two non-traditional optimization techniques, namely GA and IWO. The regression equations obtained with the help of the response surface methodology are used to establish the objective functions for the study. It is observed that both the optimization methods are seen to perform with reasonably good accuracy. But the convergence rate of IWO is faster when are compared with GA. The results of optimization also show that IWO algorithm is found to perform better than GA in terms of both the bead width and bead height of the BoP weld.

References

1. Babu KK, Panneerselvam K, Sathiyaraj P, Haq AN, Sundararajan S, Mastanaiah P, Murthy CS (2018) Parameter optimization of friction stir welding of cryorolled AA2219 alloy using artificial neural network modeling with genetic algorithm. *Int J Adv Manuf Technol* 94(9–12):3117–3129
2. Nagaraju S, Vasantharaja P, Chandrasekhar N, Vasudevan M, Jayakumar T (2016) Optimization of welding process parameters for 9Cr-1Mo steel using RSM and GA. *Mater Manuf Processes* 31(3):319–327
3. Pal S, Pal SK, Samantaray AK (2010) Determination of optimal pulse metal inert gas welding parameters with a neuro-GA technique. *Mater Manuf Processes* 25(7):606–615
4. Satpathy MP, Moharana BR, Dewangan S, Sahoo SK (2015) Modeling and optimization of ultrasonic metal welding on dissimilar sheets using fuzzy based genetic algorithm approach. *Eng Sci Technol Int J* 18(4):634–647
5. Kanigalpula PKC, Pratihar DK, Jha MN, Derose J, Bapat AV, Pal AR (2016) Experimental investigations, input-output modeling and optimization for electron beam welding of Cu-Cr-Zr alloy plates. *Int J Adv Manuf Technol* 85(1–4):711–726
6. Vasudevan M, Bhaduri AK, Raj B, Rao KP (2007) Genetic-algorithm-based computational models for optimizing the process parameters of A-TIG welding to achieve target bead geometry in type 304 L (N) and 316 L (N) stainless steels. *Mater Manuf Processes* 22(5):641–649
7. Dey V, Pratihar DK, Datta GL, Jha MN, Saha TK, Bapat AV (2009) Optimization of bead geometry in electron beam welding using a genetic algorithm. *J Mater Process Technol* 209(3):1151–1157
8. Kim D, Rhee S, Park H (2002) Modelling and optimization of a GMA welding process by genetic algorithm and response surface methodology. *Int J Prod Res* 40(7):1699–1711
9. Meran C (2006) Prediction of the optimized welding parameters for the joined brass plates using genetic algorithm. *Mater Des* 27(5):356–363
10. Correia DS, Gonçalves CV, da Cunha Jr SS, Ferraresi VA (2005) Comparison between genetic algorithms and response surface methodology in GMAW welding optimization. *J Mater Process Technol* 160(1):70–76
11. Mehrabian AR, Lucas C (2006) A novel numerical optimization algorithm inspired from weed colonization. *Ecol Inform* 1(4):355–366
12. Pourjafari E, Mojallali H (2012) Solving nonlinear equations systems with a new approach based on invasive weed optimization algorithm and clustering. *Swarm Evol Comput* 4:33–43
13. Dhinakaran V, Shanmugam NS, Sankaranarayanan K (2017) Experimental investigation and numerical simulation of weld bead geometry and temperature distribution during plasma arc welding of thin Ti-6Al-4V sheets. *J Strain Anal Eng Des* 52(1):30–44

14. Dhinakaran V, Shanmugam NS, Sankaranarayanan K (2017) Some studies on temperature field during plasma arc welding of thin titanium alloy sheets using parabolic Gaussian heat source model. *Proc Inst Mech Eng Part C J Mech Eng Sci* 231(4):695–711
15. Pratihari DK (2014) *Soft computing: fundamentals and applications*. Alpha Science International Ltd., Oxford, U.K

Experimental Studies on the Effect of Basalt Powder Inclusion on Mechanical Properties of Hybrid Epoxy and Polyester Composites Reinforced with Glass Fiber



S. Mahesh Babu and M. Venkateswara Rao

Abstract The studies of new material development require specific properties for easy fabrication of high-quality products in research as well as in industrial applications. In this paper, the effect of basalt powder addition on mechanical properties of glass fiber reinforcement of polymer composites was experimentally investigated. The samples were prepared as per ASTM standards using by hand layup process. The mechanical properties and comparative studies of on these hybrid composites were predicted by means of tensile test, flexural test, Charpy impact strength method and hardness test. In the present work, results showed that the inclusion of basalt powder improves strength of the hybrid polymer composites reinforced with glass fiber.

Keywords Glass fiber · Basalt powder · Polymer composites · Mechanical properties

1 Introduction

In the present era, all over the world the mineral fillers have been interesting to engineers, researchers, professionals and scientists as a substitute reinforcement of fiber-reinforced polymer composites, due to its superior properties such as low cost, high specific strength, fairly good mechanical properties, non-abrasive, low weight, eco-friendly and biodegradable characteristics. Ajaj et al. [1] investigated the influence of SiO₂ nanoparticles on the fatigue behavior of chopped glass fiber reinforcement. Devendra et al. [2] presented the effect of different fillers such as magnesium hydrox-

S. Mahesh Babu (✉)

Department of Mechanical Engineering, Acharya Nagarjuna University College of Engineering and Technology, Guntur, India
e-mail: maresh0025@gmail.com

M. Venkateswara Rao

Department of Mechanical Engineering, Bapatla Engineering College, Bapatla, Guntur, India

© Springer Nature Singapore Pte Ltd. 2019

S. S. Hiremath et al. (eds.), *Advances in Manufacturing Technology*,
Lecture Notes in Mechanical Engineering,
https://doi.org/10.1007/978-981-13-6374-0_4

Table 1 Preparation details of the test samples

Composite 1	Composite 2 [wt in %]	Glass fiber	Basalt powder [wt in %]
Glass fiber–epoxy (GFE) composites	Glass fiber polyester (GFP) composites	40	0
		40	2.5
		40	5
		40	7.5
		40	10

ide, fly ash, hematite, aluminum oxide on mechanical properties of reinforcement of glass fiber–epoxy composites. Nayak et al. [3] investigated the mechanical properties of epoxy modifier with SiO₂, TiO₂ and Al₂O₃ particles reinforced with glass fiber composites. Mohammed et al. [4] introduced the natural fillers of bagasse fiber (B.F)/bagasse ash (B.A)/coal powder (C.P)/coal fly ash (C.F.A) in epoxy composites reinforced with glass fiber of glass. Matykiewicz et al. [5] studied the mechanical and thermal properties of basalt powder and reinforced basalt fiber–epoxy composites.

Even though plenty of work has been completed on various synthetic fibers and its composites, a small effort is attempted in the present work to introduce basalt powder in polymer matrices reinforced with glass fiber. The aim of this investigation was to study the influence of basalt powder on mechanical properties of polymer composites reinforced with glass fiber. Table 1 indicates the compositions of matrix and reinforcement (wt.%) of the two composites considered in this study. The mechanical properties of these two composites are compared and evaluated. First type of the composites was prepared as the basalt powder of weight percentage was varied from 0 to 10%wt in the difference of 2.5%wt in epoxy matrix reinforced with glass fiber, and second type of the composites was prepared as the basalt powder of weight percentage was varied from 0 to 10%wt in the difference of 2.5%wt in polyester matrix reinforced with glass fiber. The weight percentage of glass fiber was fixed to 40%wt, and remaining 60%wt was polymer matrices which decreased the weight percentage by addition of basalt powder. The mechanical properties were conducted through tensile test, flexural test (three-point bending), impact Charpy method and hardness test.

2 Experimental Methodology

2.1 Development of New Composite Materials

Woven fabric-type glass fiber is used for reinforcement in the composite material. Epoxy and polyester matrices are used in the present study. The raw materials con-

sidered in this study such as fiber and matrices were procured from Bindu Agency, Vijayawada, India. Whereas, basalt rocks were procured from Almin Rocks, Bangalore, India. Basalt powder is used as the mineral filler which is blending in two matrices; hence, new modified matrices are obtained.

Hydraulic press was used for the crushing of the basalt in order to obtain the basalt powder and basalt powder composition [5], and then it sieved to 75 μm using sieving machine in our laboratory. The particle size of the basalt powder (75 μm) is used because there is no extensive change in composition, structure or water content and also the spectral gap reduction is controlled by variations in the ratio of scattering to absorption.

2.2 Method and Preparation of Composite Materials

Hand layup process was used for the fabrication of the composites which were prepared as per ASTM standards. Table 1 represents the glass fiber, basalt powder weight percentages and remaining weight percentage corresponding to the polymer matrices. Firstly, the molds with the standard dimensions were prepared to fabricate the composite material. Secondly, glass fiber mat was prepared as per the mold. Thirdly, basalt powder was stirred in polymer matrices using mechanical stirrer before mixing up the hardener into the matrices. Modified matrices were obtained by the addition of the basalt powder into polymer matrices which were applied in the mold and also layer by layer up to six layers placed over the mold. Mild steel roller was used during placing of the layers in order to avoid the entrapped air in the composite. Moreover, 72 h is required for curing of the composite at room temperature. The same procedure was employed for the composite without addition of basalt power.

Tensile properties are tested from the universal testing machine [UTM] with TUE-C-machine, series number 2013/50 as model number. Tensile test specimens were prepared according to ASTM D-638 (Type-I) standards. All tensile tests were done at room temperature with a testing speed of 5 mm/min and load cell of 30 kN.

Flexural properties are tested on the universal testing machine [UTM] with TUE-C-200 and machine series number 2013/50 as model number. Flexural strength and inter-linear shear strength [ILSS] of samples were calculated using Eqs. (1) and (2), respectively, and tested as per the ASTM D-790. Flexural strength formulae and inter-laminar shear strength [ILSS] are given by

$$\text{Flexural strength} = \frac{3Pl}{2bd^2} \quad (1)$$

$$\text{Inter - laminar shear strength[ILSS]} = \frac{3P}{4bd} \quad (2)$$

where P = maximum applied load on the specimen in kN, l = specimen length in mm, b = specimen width in mm, and d = specimen thickness in mm.

Impact test (Charpy method) is carried out on impact testing machine at room temperature. The specifications of the machine model are: FIT 300 [EN] and machine serial number 2008/105[1]. The specimen was notched at appropriate point on the surface.

Hardness test is carried out on Rockwell's hardness tester as per ASTM D 2240-2003.

3 Result and Discussion

3.1 Mechanical Properties

The percentage of basalt powder is influenced by the tensile strength of the GFE and GFP composites as shown in Fig. 1. The GFE composites have low tensile strengths than the GFP composites up to 5% basalt powder (B.P). Then, the GFE composites showed the higher tensile strengths for 7.5 and 10% B.P when compared to the GFP composites. Thus, it was observed that the inclusion of 0–5% basalt powder (B.P) in polyester composites showed better tensile values than the epoxy composites because of the good interfacial bonding between fiber and matrix. On the other hand, it was noticed that the addition of 7.5–10% basalt powder (B.P) in epoxy composites exhibited the good tensile values than the polyester composites due to the good interaction of fiber and matrix. Tensile strength values decrease due to more fiber–fiber and particle–particle interactions rather than the fiber and matrix interactions [6, 7].

The percentage of basalt powder (B.P) versus flexural strengths of GFE and GFP composites is plotted in Fig. 2. The flexural strength of the GFE composites revealed the higher values than the GFP composites. Thus, the basalt powder addition for each combination of epoxy composites indicated the more flexural values than the polyester composites because of the good interfacial adhesion between matrix and fiber. Decrease in flexural values indicated the huge amount of fiber–fiber interactions

Fig. 1 Tensile strength versus % of B.P

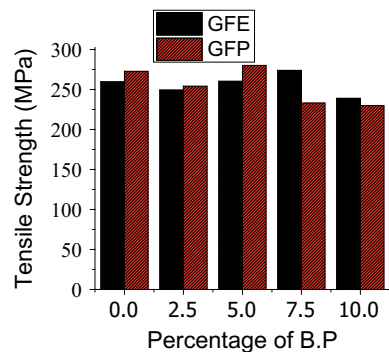


Fig. 2 Flexural strength versus % of B.P

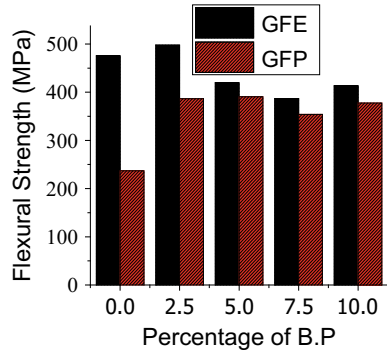
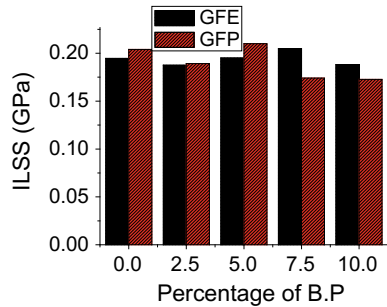


Fig. 3 ILSS versus % of B.P



rather than the fiber–matrix interactions, and the rigid particles could not transfer to the matrix by the applied load [8].

Figure 3 presents the percentage of basalt powder (B.P) with reference to inter-laminar shear stress (ILSS). From Fig. 3, it was seen that the GFP composites have more ILSS values than the GFE composites by the blending of 0–5% basalt powder in polymer matrix. Moreover, 7.5 and 10% B.P of GFE composites recorded the higher ILSS values than the GFP composites [9–12].

The influence of the basalt powder (B.P) on impact strength of the GFE and GFP composites is presented in Fig. 4. In Fig. 4, it was observed that GFP composites offered more impact strength than the GFE composites for containing 0, 2.5 and 5% and lower values for containing 7.5 and 10% B.P. Enhancement in the impact strength is attributed to the steadiness in the fiber dimension and homogeneity. Moreover, the reduction of impact strength with increase in basalt powder content is influenced by the breaking of fibers rather than their pullout.

The plot of graphs of hardness number versus basalt powder (B.P) is shown in Fig. 5. The increase in addition of basalt powder into polymer matrices increases the hardness number of the GFE and GFP composites. GFE composites have higher hardness number values when compared to the GFP composites. Therefore, increase in the addition of basalt powder in polymer matrix, enhances the hardness property. It is caused by the uniform dispersion of these particles in the matrix. Further, the dispersion of particles are anticipated to object the propagation to failure of the

Fig. 4 Impact strength versus % of B.P

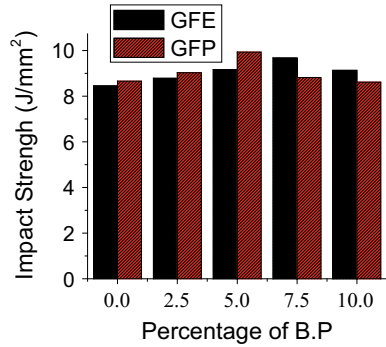
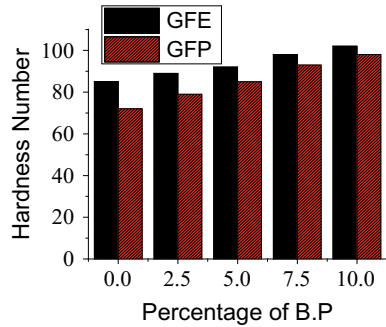


Fig. 5 Hardness number versus % of B.P



composite along the applied load. The propagation of failure in a direction was noted by the concentration of the dispersion of filler material in the polymer matrix [13, 14].

4 Conclusion

The salient features of the present work are as follows

- Tensile strengths of the GFP composites reached higher values when compared to the GFE composites for 0, 2.5 and 5% of B.P and lower values for 7.5 and 10% B.P.
- Flexural strengths of the GFE composites obtained higher values when compared to the GFP composites for 0, 2.5, 5, 7.5 and 10% B.P.
- Inter-laminar shear stresses (ILSSs) of the GFP composites attained higher values when compared to the GFE composites for 0, 2.5 and 5% of B.P and lower values for 7.5 and 10% B.P.
- Impact strengths of the GFP composites attained higher values when compared to the GFE composites for 0, 2.5 and 5% of B.P and lower values for 7.5 and 10% B.P.

- Hardness number of the GFE composites obtained higher values when compared to the GFP composites for 0, 2.5, 5, 7.5 and 10% B.P.

References

1. Ajaj EA, Jubier NJ, Majeed KJ (2013) Fatigue behavior of epoxy/SiO₂ nanocomposites reinforced with E-glass fiber. *Int J Appl Innovation Eng Manage [IJAIEM]* 2(9):62–69
2. Devendra K, Rangaswamy T (2013) Strength characterization of E-GFRP epoxy composites with filler materials. *J Miner Mater Charact Eng* 1:353–357
3. Nayak RK, Dash A, Ray BC (2014) Effect of epoxy modifiers on mechanical performance of epoxy/glass fiber hybrid composites. *Procedia Mater Sci* 6:1359–1364. In: 3rd international conference on materials processing and characterization [ICMPC 2014]. Elsevier Ltd
4. Mohammed R, Reddy BRG, Reddy VS, Ali MA (2015) Effect of epoxy modifiers [bagasse fiber/bagasse ash/coal powder/coal fly ash] on mechanical properties of epoxy/glass fiber hybrid composites. *Int J Appl Eng Res* 10(24):45625–45630
5. Matykiewicz D, Barczewski M, Knapski D, Skórczewska K (2017) Hybrid effects of basalt fibers and basalt powder on thermomechanical properties of epoxy composites. *Compos Part B*. <https://doi.org/10.1016/j.compositesb.2017.05.060>
6. Suresh JS, Devi MP, Mohammed R (2017) Characterization of epoxy/polyester based composites. *Int J Adv Sci Eng Technol* 5(1):114–116
7. Velmurugan K, Gopinath R (2015) Characterization of polyester based composites. *Int J Sci Eng Technol Res (IJSETR)* 4(7):2466–2469
8. Pol AS, Chanshetti N, Ashok (2016) Mechanical properties of TiO₂ and WC reinforced epoxy resin composites. *Int J Sci Res Dev* 4(6):162–164
9. Stevanovic MM, Stecenko TB (1992) Mechanical behaviour of carbon and glass hybrid reinforced polyester composites. *J Mater Sci* 27:941–946
10. Chen C-H, Lien K-C (2006) Pultruded hybrid fibre (glass/carbon) reinforced unsaturated polyester composites: mechanical and thermal properties. *Polym Polym Compos* 14(2):154–164
11. Uma Devi L, Bhagawan S, Thomas S (2009) Dynamic mechanical analysis of pineapple leaf/glass hybrid fiber reinforced polyester composites. Society of Plastics Engineers. <https://doi.org/10.1002/pc.20880>
12. Sapuana SM, Lokb HY, Ishakc MR, Misria S (2013) Mechanical properties of hybrid glass/sugar palm fibre reinforced unsaturated polyester composites. *Chin J Polym Sci*. <https://doi.org/10.1007/s10118-013-1342-4>
13. Idicula M, Joseph K, Thomas S (2014) Mechanical performance of short banana/sisal hybrid fiber reinforced polyester composites. *J Reinf Plast Compos*. <https://doi.org/10.1177/0731684408095033>
14. Suresha B, Chandramohan G, Renukappa NM, Siddaramaiah (2006) Mechanical and tribological properties of glass–epoxy composites with and without graphite particulate filler. *J Appl Polym Sci*. <https://doi.org/10.1002/app.25413>

An Experimental Investigation on Tensile Properties of Hybrid BioPolyurethane Composite: Modeling and Optimization



A. Soundhar, M. Rajesh, K. Jayakrishna and M. T. H. Sultan

Abstract The primary objective of this study is to investigate the influence of different weight percentages of natural fibers on mechanical properties when reinforced with polyurethane foam. This experiment studies were systematically designed and analyzed by response surface methodology (RSM) using Box–Behnken design (BBD) approach. As per the design of experiments, the hybrid polyurethane composites were prepared by using one-shot process. Tensile tests of the hybrid composites were performed over a total of 17 specimens prepared as per ASTM standards. The mathematical models developed to predict the results obtained were in good coherence with the experimental results that are within 95% confidence level for tensile strength. The suggested model's trustworthiness was evaluated using Analysis of Variance (ANOVA). The optimum weight percentages of groundnut, Roselle, and pineapple leaf fiber are 2, 2, and 5 with 15.7 MPa as tensile strength.

Keywords Hybrid polyurethane foam · Roselle · Pineapple leaf fiber · Groundnut shell · Response surface mechanism · Tensile properties

1 Introduction

The developing worldwide problem in connection with the global ecological protection of natural resources has fascinated researchers from different fields to come up with products based on ecological balance. Nowadays, the use of polyurethane foam combined with natural fibers has drawn mind of researchers. The advantages of using natural fibers are their low cost, flexibility, stiffness, and less weight [1].

A. Soundhar · M. Rajesh · K. Jayakrishna (✉)
School of Mechanical Engineering, VIT University, Vellore 632014, Tamil Nadu, India
e-mail: mail2jaikrish@gmail.com

M. T. H. Sultan
Laboratory of Biocomposite Technology (BIOCOMPOSITE), Institute of Tropical Forestry and Forest Products (INTROP), Universiti Putra Malaysia, 43400 Seri Kembangan, Malaysia

© Springer Nature Singapore Pte Ltd. 2019
S. S. Hiremath et al. (eds.), *Advances in Manufacturing Technology*,
Lecture Notes in Mechanical Engineering,
https://doi.org/10.1007/978-981-13-6374-0_5

Different types of natural fibers are studied as fillers for polyurethane foam composites. Roselle fiber, pineapple leaf fiber, and groundnut shell have been identified as the ones which serve the purpose. Roselle fibers are coarse and possess good tensile and durability [2]. Pineapple leaf fiber (PALF) has a high amount of cellulose content due to which it is hydrophilic nature. It also has high strength and stiffness.

Polyurethane foam is a preferred choice of polymer because of its low cost, and relatively low heat conduction coefficient, with low density has very less weight, with low water absorption property makes it preferable in water travel, relatively better mechanical properties with excellent an insulation property and good adherence with other types of materials [3]. Natural fibers found extensive automotive applications for the past few decades, on account of its low cost and weight [4]. Parts made from natural fibers not only save natural resources but also are quite economical. The porous structure of polyurethane foam systems improves the acoustic properties in comparison with parts made from thermoplastics [5]. Previous studies were made on polyurethane foam with Kenaf [6], Talc, zinc borate and aluminum hydroxide and sisal [7]. This paper investigates the tensile properties of hybrid polyurethane foam composites with Roselle, groundnut, and pineapple leaf fiber.

2 Experimental

2.1 Materials

Polyurethane foam produced using polyol and isocyanides with a ratio of 1:1 at room temperature was supplied by GSRR Resins and Polymers, Madurai. Pineapple leaf fiber, Roselle powder, and groundnut shell powder were supplied by Counts, Coimbatore.

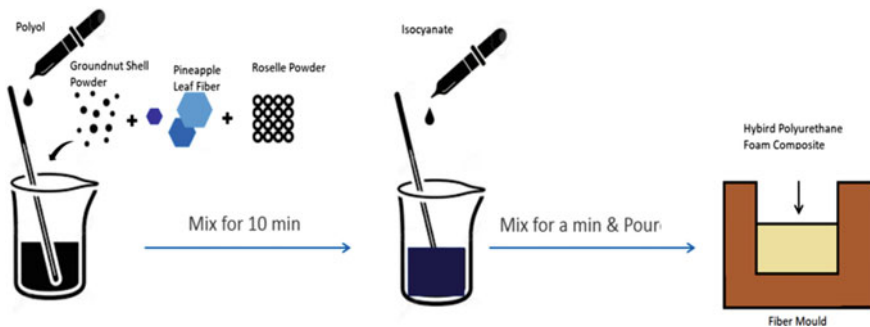


Fig. 1 Preparation of hybrid polyurethane foam composites

2.2 Hybrid Polyurethane Foam

Hybrid polyurethane foam composites were prepared using one-shot process. Initially, Polyol is mixed with the fillers for about 10 min using overhead stirrer at speed of 200–1000 rpm. Later, isocyanides were added to the mixed solution in a ratio of 1:1 with polyol for about a minute. Then, the prepared solution was poured into a mold with dimensions $250 \times 2000 \times 50 \text{ mm}^3$ to allow a free rise of Polyurethane foam as shown in Fig. 1. Response surface methodology of Box–Behnken design using Design Expert (Version 11) was used to design the experiments. Roselle powder (RP), groundnut shell powder (GSP), and pineapple leaf fiber (PALF) were used as fillers to polyurethane foam at various weight percentages.

2.3 Tensile Testing

The specimens were prepared with the different weight percentages based on the design of experiments. Dumbbell-shaped samples were cut according to ASTM D-638 dimensions ($150 \times 25 \times 10 \text{ mm}$). Tensile test was conducted according to ASTM



Fig. 2 Tensile testing of specimen

standards using INSTRON 8801 at 25 °C, and relative humidity of 60 and tensile strength were taken at crosshead speed of 1.3 mm/min (Fig. 2).

3 Design of Experiments (DoE)

The experimental results obtained from the tests conducted above were used to generate optimal condition for the preparation of composite with maximum desirability using response surface regression. Table 1 shows the weight percentage levels obtained using DoE.

3.1 Box–Behnken Design (BBD)

In this research, depending on Box–Behnken design (BBD), a total of 17 experiments were designed in order to study the influence of different weight percentages of natural fiber fillers on the tensile properties of the reinforced composite. The following Table 2 shows the results obtained after performing tensile tests on 17 specimens.

3.2 Analysis of Variance (ANOVA)

ANOVA for tensile strength was done and presented in Table 3. The value of P obtained is less than 0.05 denotes that the effects of parameters are significant. In order to comment on the model reasonableness P -value, lack of fit and R^2 are considered.

Table 1 Levels of produced hybrid polyurethane foam composite

Natural fibers	Level –1	Level 0	Level +1
Roselle (wt%)	1	1.5	2
Pineapple leaf fiber (wt%)	1	3	5
Groundnut shell (wt%)	2	4	6

Table 2 Weight percentages obtained using DoE and tensile values measured

Specimen	GSP (wt%)	RP (wt%)	PALF (wt%)	Tensile (MPa)
1	4	1.5	3	13.67
2	4	2	5	14.83
3	6	2	3	12.12
4	4	1	5	11.99
5	4	1.5	3	15.63
6	4	1.5	3	16.03
7	6	1	3	13.51
8	6	1.5	5	15.94
9	2	2	3	12.77
10	4	2	1	11.49
11	2	1.5	1	17.08
12	6	1.5	1	15.32
13	2	1.5	5	16.5
14	2	1	3	14.17
15	4	1.5	3	13.08
16	4	1	1	16.47
17	4	1.5	3	13.36

Table 3 ANOVA for tensile strength

Source	Sum of squares	df	Mean square	F value	p-value Prob > F	
Model	41.87	9	4.65	4.14	0.0372	Significant
A-Groundnut shell powder	1.65	1	1.65	1.46	0.2654	
B-Roselle powder	3.04	1	3.04	2.7	0.1442	
C-Pineapple leaf fiber	0.15	1	0.15	0.13	0.7246	
AB	2.50E-05	1	2.50E-05	2.22E-05	0.9964	
AC	0.36	1	0.36	0.32	0.5892	
BC	15.29	1	15.29	13.6	0.0078	
A ²	1.79	1	1.79	1.59	0.2476	
B ²	14.62	1	14.62	13	0.0087	
C ²	6.11	1	6.11	5.43	0.0526	
Residual	7.87	7	1.12			
Lack of fit	0.35	3	0.12	0.063	0.9768	Not significant
Pure error	7.52	4	1.88			
Cor. total	49.74	16				

$R^2 = 0.8418$, Adjusted $R^2 = 0.6383$

4 Results

4.1 Tensile Properties

The main effects of differing weight percentage of RP, GSP, and PALF on tensile strength of polyurethane foam are shown in Figs. 3, 4, and 5, respectively. Figure 3 shows the effect of PALF and RP on the tensile strength. From Fig. 4, it can be noted that for weight percentage of PALF up to 3 wt% tensile strength of composite increased slightly. In case of addition of RP, the tensile strength value increased to a maximum of 17.08 at 1.5 wt%. Further increase in weight percentage of RP decreased the tensile strength of the composite. A similar trend can also be shown in Figs. 4 and 5. The tensile strength value decreased up to 11.99 MPa for four weight percentages of GSP and further increase in the weight percentage of groundnut shell helped the composite to increase the tensile strength (Fig. 4). The maximum tensile strength value observed was 17.08 MPa, and the lowest being 11.49 MPa.

$$\begin{aligned} \text{TENSILE} = & 15.57631 - 1.75912 * G + 15.25150 * R \\ & - 5.10763 * \text{PLF} + 2.50000E - 003 * G * R \end{aligned}$$

Fig. 3 Effect of pineapple leaf fiber and Roselle powder on tensile strength

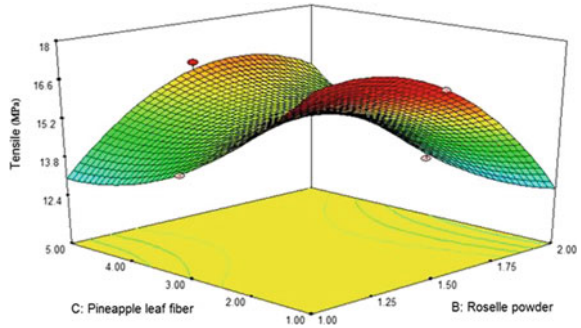
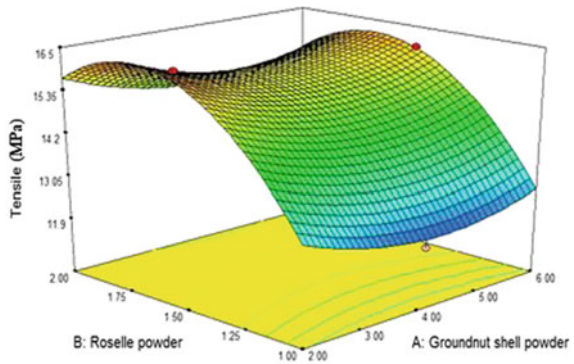


Fig. 4 Effect of groundnut shell powder and Roselle powder on tensile strength



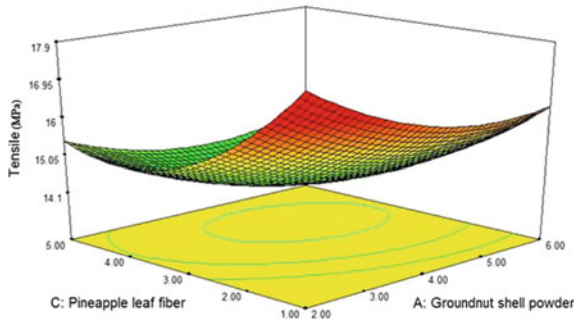


Fig. 5 Effect of groundnut shell powder and pineapple leaf fiber on tensile strength

Table 4 Optimum weight percentage of pineapple leaf fiber, Roselle powder, and groundnut shell powder

No.	GSP (wt%)	RP (wt%)	PALF (wt%)	Tensile (MPa)	Desirability
1	2	2.00	5.00	15.71	0.74

$$\begin{aligned}
 &+ 0.075000 * G * PLF + 1.95500 * R * PLF \\
 &+ 0.16294 * G^2 - 7.45300 * R^2 + 0.30106 * (PLF)^2 \quad (1)
 \end{aligned}$$

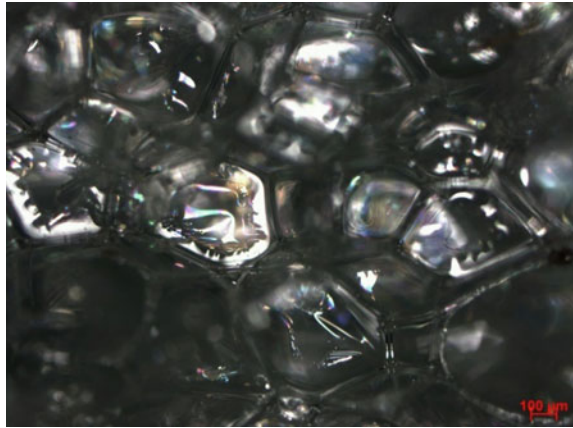
where G—groundnut shell powder, R—Roselle powder, and PLF—pineapple leaf fiber.

Equation 1 represents the relation between weight percentages of natural fillers and tensile strength.

The suggested model’s trustworthiness was evaluated using Analysis of Variance (ANOVA). The mathematical models establish to be significant with *P*-values of 0.0372 for tensile strength, respectively. This shows that the model is significantly fit to the experimental value and the lack of fit is not significant. From the variance analysis, *R*-squared value for tensile strength was found out to be 0.8418. Results show that the quadratic models can be used to predict the results with 95% confidence level. The optimum weight percentage values of tensile strength are shown in Table 4. From this, the desirability value closer to one was chosen as the optimal solution. Therefore, the optimum solution found to be two weight percentages of groundnut powder, two weight percentages of Roselle powder, and five weight percentages of pine apple leaf fiber.

The morphology of hybrid PU foam composites with different weight percentages of natural fibers was noted by optical microscope as shown in Fig. 6. From this figure, the cell shape displays polyhedral, spherical shape and also cell edges are sharply visible. But additions of filler materials make less uniform and uneven cell structure. The optimum weight percentage shows the good interfacial adhesion between fiber and matrix phase.

Fig. 6 Optical microscope image for hybrid biocomposite



5 Conclusion

This research proved that addition of natural fibers (PALF, RP and GSP) to the polyurethane foam to prepare hybrid composites enhances the tensile properties due to good adherence between natural fibers and PU foam. Conversely, after reaching an optimum level, further addition of natural fillers into polymer matrix remarkably reduced the mechanical properties, due to enormous agglomerations presents in the PU foam hybrid composites. The optimum weight percentages to prepare a hybrid composite to achieve maximum desirability using GSP, RP, and PALF are 2, 2, and 5%, respectively. These results were verified through mechanical characterization and statistical comparison using RSM.

References

1. Aridi N, Sapuan AM, Zainudin ES, Oqla FM (2016) Mechanical and morphological properties of injection-molded rice husk polypropylene composites. *Int J Polym Anal Charact* 21(4):305–313
2. Boland CS, Kleine R, Keoleian GA, Lee EC, Kim HC, Wallington TJ (2016) Life cycle impacts of natural fiber composites for automotive applications: effects of renewable energy content and lightweighting. *J Ind Ecol* 20(1):179–189
3. Hristozov D, Wroblewski L, Sadeghian P (2016) Long-term tensile properties of natural fibre-reinforced polymer composites: comparison of flax and glass fibres. *Compos B Eng* 95:82–95
4. Ishak MR, Sapuan SM, Leman Z, Rahman MZA, Anwar UMK (2011) Characterization of sugar palm (*Arenga pinnata*) fibres: tensile and thermal properties. *J Therm Anal Calorim* 109(2):981–989
5. Sanjay MR, Arpitha GR, Naik LL, Gopalakrishna K, Yogesha B (2016) Applications of natural fibers and its composites: an overview. *Nat Resour* 7(03):108
6. Sadeghian P, Hristozov D, Wroblewski L (2016) Experimental and analytical behavior of sandwich composite beams: comparison of natural and synthetic materials. *J Sandwich Struct Mater* 109(1):889–903
7. Saba N, Jawaid M, Alothman OY, Paridah MT (2016) A review on dynamic mechanical properties of natural fibre reinforced polymer composites. *Constr Build Mater* 106:149–159

Improvement of Machining Characteristics by EDM with Graphite Powder-Mixed Dielectric Medium



V. Srinivasa Sai, K. Gnana Sundari, P. Gangadhara Rao and B. Surekha

Abstract In the present research, experimental investigations are carried out to study the influence of graphite powder on the machining of EN-19 during electric discharge machining (EDM). During experimentation, paraffin is used as dielectric medium and brass rod is considered as electrode. The nonlinear regression models that represent the relationship between the input and output parameters are established by conducting the experiments after following the concept of central composite design (CCD) of experiments. The statistical acceptability of the established regression models is verified with the help of analysis of variance (ANOVA), and also the correctness in estimation of the developed models is tested with the help of experimental test cases.

Keywords PM-EDM · Graphite · Paraffin · Central composite design

1 Introduction

EN-19 is one of the hard and high-strength iron–carbon alloys that exhibited high resistance to wear. These properties of EN-19 alloy make the machining tough with the help of conservative methods. On the other hand, EDM is the most frequently used method for machining such high-strength and hard materials with good surface

V. Srinivasa Sai

Department of Mechanical Engineering, DVR & Dr. HS MIC College of Technology,
Kanchikacherla 521180, India

K. Gnana Sundari

School of Mechanical Engineering, Karunya University, Coimbatore 641114,
Tamil Nadu, India

P. Gangadhara Rao

Nalanda Institute of Engineering and Technology, Sattenapalli 522403, India

B. Surekha (✉)

School of Mechanical Engineering, KIIT Deemed to be University, Bhubaneswar 751024,
Odisha, India

e-mail: surekhafme@kiit.ac.in

© Springer Nature Singapore Pte Ltd. 2019

S. S. Hiremath et al. (eds.), *Advances in Manufacturing Technology*,

Lecture Notes in Mechanical Engineering,

https://doi.org/10.1007/978-981-13-6374-0_6

finish. Further, the surface quality of the machined component can be enriched to mirror finish by supplying the dielectric medium along with the powder particles to the machining zone with a properly selected flushing system [1]. To attain glossy-type machined surface, in the said research, electrode was coated with antimony-doped silicon and was provided with a planetary motion. It is also important to note that the surface finish can also be improved by the addition of various powders at different scales and levels [2]. In [3], the authors had added silicon powder to the dielectric fluid during the machining of AISI D2 steel. It was noted that the addition of powder particles and the value of current had increased the value of MRR. Further, they also conducted the ANOVA test to verify the statistical acceptability of the model. They also tested the prediction correctness of the model with the help of random experimental test cases other than those used for the design of experiments. Kumar and Uma [4] focused on the improvement of the surface characteristics by mixing the tungsten powder in the dielectric medium. They conducted experiments on different alloy steels and analyzed the effect of addition of powders through the hardness test and SEM analysis. They concluded that a significant quantity of matter was deposited on the machined surface through the added particles. Titanium alloys were used in enormous applications such as in chemical industry, ship building, automobile, medicine, and civil engineering because of its high strength, resistance to corrosion, and wear. Among all titanium alloys, Ti-6Al-4V is the one of the widely used alloys in various industrial applications because to its exceptional corrosion and fatigue resistance in many environments. Furthermore, Kolli and Kumar [5] conducted the experimental investigations to decide the effect of parameters like concentration of surfactant, graphite powder, and the peak current on the responses MRR, TWR, surface finish and the thickness of recast layer. Moreover, they also conducted ANOVA and F-test for the experimental data to reveal the effect of peak current and concentration of the surfactant on MRR and TWR. It was also observed that the values of RLT and SR were seen to be influenced by the peak current and the concentration of the graphite powder. Later on, Toshimitsu [6] had given an effort to study the surface characteristics during EDM of SKD7 alloy steel with copper electrode. In their work, they used chromium powder-mixed in kerosene as the dielectric fluid. They also performed spectroscopic analysis and SEM analysis to predict the effect of the chromium particles on the machined surface. Further, the researchers [7] made an attempt to study the machining characteristics of powder-mixed EDM and rotary electrode during EDM. They used Inconel as the workpiece material and rotary copper tungsten electrode as the tool material. Kumar [8] also conducted an experimental study on the EDM of Inconel 825 with the addition of aluminum oxide nanopowder to the dielectric medium. Various dielectric medium such as EDM oil [9], kerosene [10], and deionized water [11] were used as the dielectric medium in the EDM processes. They focused on the responses such as MRR, SR, and the surface topography with the help of FESM images and AFM analysis. However, no work is reported on the usage of paraffin oil as dielectric medium during EDM.

2 Materials and Methods

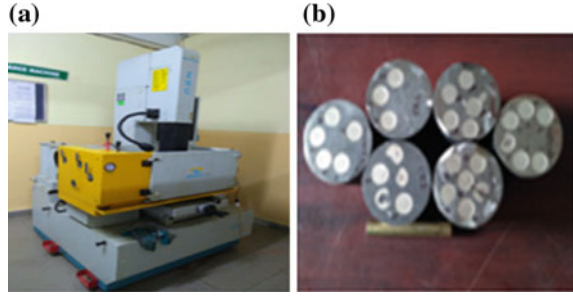
In the present experimental investigation, the authors have considered EN-19 as the workpiece material and brass rod as the electrode. Further, paraffin is used as the dielectric fluid and the graphite powder is chosen as the powder to be mixed in the dielectric medium. EN-19 is one of the high-strength alloys that exhibit high resistance to wear that can be used to produce various mechanical components, like gears, shafts, connecting rods, etc. It is understood that due to the high carbon, it is very difficult to machine EN-19 with the help of conventional manufacturing processes. Hence, it is chosen to use powder-mixed EDM to study the machining characteristics of EN-19 steel. In the present research, EN-19 steel of 50-mm-diameter and 40-mm-height cylindrical specimen is considered as the workpiece material. A brass rod is selected as electrode due to its good electrical conductivity. In the present work, the authors have used paraffin oil as the dielectric medium and the graphite powder is mixed in the dielectric medium to improve the SR and MRR. Two sets of experiments have been conducted under two different environments, such as plain dielectric (i.e., paraffin)-based EDM and powder-mixed (i.e., graphite powder-mixed with paraffin) EDM.

2.1 Experimental Setup

The experiments are conducted on a die-sinking EDM (ELECTRONICA—SMART ZNC, ref. to Fig. 1) with necessary adjustments for conducting powder-mixed EDM. The consumption of the dielectric medium was reduced by carrying out the experimentation in small machining tank of $27.5 \times 22.5 \times 15 \text{ cm}^3$ instead of the main tank of the EDM setup. Workpiece is held rigidly on the magnetic chuck placed at the bottom of the small tank. To perform machining, it is necessary that the workpiece should be finely polished and fully immersed in the dielectric medium. To achieve this, the surface of the workpiece is cleaned and flattened with the help of a suitable finishing process, and the required quantity of the fluid is filled in the container. Hence, a minimum of 5 L of paraffin oil with a fixed level of graphite powder is filled in the tank to initiate machining with the help of powder-mixed EDM. It is also important to see that there should not be any accumulation of the powder particles, and it is taken care by the circulation pump and a stirrer.

In addition to this, the dielectric medium is allowed to flush exactly at the machining zone with the help of a nozzle at certain pressure. It is expected that the material removal rate is improved by the addition of graphite particles that decrease the discharge gap and enhance the energy available for the removal of the metal particle at atomic level. In the present research, the parameters like peak current (I_p), gap voltage (V_g), pulse on time (T_{on}), and the concentration of the powder are considered as the input process parameters and TWR and MRR are considered as the responses.

Fig. 1 Schematic diagram showing the ELECTRONICA—SMART ZNC-EDM process. **a** EDM machine and **b** EN-19 workpieces and the brass electrode machined using PM-EDM



2.2 Design of Experiments

According to the current research objective, it is necessary to conduct the experiments with different combinations of the input parameters at different levels. Hence, it is necessary to decide the input parameters and their ranges for conducting the experiments. The input process parameters, such as peak current (I_p), pulse on time (T_{on}), gap voltage (V), and concentration of powder (%), are varied in the range of (6–10) A, (50–100) μ s, (40–60) V, and (2–6)%, respectively. A conventional methodology, named CCD of experiments, is used to decide the number of experiments to be conducted and to develop the nonlinear regression models for two sets of experimental scenarios.

2.3 Measurement of Responses

The process parameters, namely gap voltage (V_g), peak current (I_p), and pulse on time (T_{on}) concentration of graphite powder (g/liter of paraffin), are varied according to set range. The necessary readings have been noted down for the estimation of the responses. The MRR is calculated as shown below.

$$\text{MRR} = (W_b - W_a)/t \quad (1)$$

where t indicates the machining time, W_b represent the weight of the workpiece before machining, and W_a indicate the weight after machining. Moreover, the TWR is measured with the help of Eq. (2).

$$\text{TWR} = (T_b - T_a)/t \quad (2)$$

where T_a and T_b show the weight of tool after and before machining (g), respectively.

3 Results and Discussions

The experimental data obtained is analyzed with the help of Minitab 17 software. The nonlinear regression models established after using the response surface methodology for MRR and TWR of EDM and PM-EDM are given by Eqs. (3), (4) and (5), (6), respectively.

$$\begin{aligned} \text{MRR}_{\text{EDM}} = & -0.047 + 0.0040I_p - 0.00475V_g + 0.005003T_{\text{on}} \\ & - 0.00174I_p \times I_p + 0.000032V_g \times V_g - 0.000009T_{\text{on}} \times T_{\text{on}} \\ & + 0.000549I_p \times V_g - 0.000127I_p \times T_{\text{on}} - 0.000037V_g \times T_{\text{on}} \end{aligned} \quad (3)$$

$$\begin{aligned} \text{TWR}_{\text{EDM}} = & -0.1651 - 0.00716I_p + 0.00554V_g + 0.001344T_{\text{on}} \\ & + 0.001050I_p \times I_p - 0.000034V_g \times V_g - 0.000001T_{\text{on}} \times T_{\text{on}} \\ & - 0.000072I_p \times V_g - 0.000025I_p \times T_{\text{on}} - 0.000017V_g \times T_{\text{on}} \end{aligned} \quad (4)$$

$$\begin{aligned} \text{MRR}_{\text{PM-EDM}} = & 0.2974 + 0.0542I_p - 0.01874V_g + 0.000255T_{\text{on}} \\ & + 0.01561C - 0.004657I_p \times I_p + 0.000148V_g \times V_g \\ & - 0.000023T_{\text{on}} \times T_{\text{on}} - 0.006227C \times C + 0.000038I_p \times V_g \\ & + 0.000265I_p \times T_{\text{on}} - 0.000016I_p \times C + 0.000015V_g \times T_{\text{on}} \\ & + 0.000463V_g \times C + 0.000126T_{\text{on}} \times C \end{aligned} \quad (5)$$

$$\begin{aligned} \text{TWR}_{\text{PM-EDM}} = & -0.3680 + 0.0011I_p + 0.02424V_g - 0.001695T_{\text{on}} \\ & - 0.04583C + 0.000207I_p \times I_p - 0.000241V_g \times V_g \\ & + 0.000001T_{\text{on}} \times T_{\text{on}} + 0.002507C \times C - 0.000301I_p \times V_g \\ & + 0.000189I_p \times T_{\text{on}} - 0.000188I_p \times C - 0.000006V_g \times T_{\text{on}} \\ & + 0.000420V_g \times C + 0.000039T_{\text{on}} \times C \end{aligned} \quad (6)$$

The worth of developed models was gauged by analysis of variance (ANOVA). The results of ANOVA show that all the terms of input variables are found to be significant for both the EDM and graphite-mixed EDM processes. Furthermore, the experimental results also related the fact that the usage of paraffin as dielectric medium show that the TWR and MRR are found to increase with the escalation in the values of I_p and T_{on} . This is due to the high amount of energy available for the removal of the material with the increase in the values of the said variables. But the values of MRR and TWR are found to be inversely proportional to V_g which is in line with the findings observed in the earlier works. Similar study has also been conducted for the EDM method in which graphite powder is mixed with the paraffin dielectric. It has also been observed that the combined effect of increase in the values of peak current–concentration of graphite powder, peak current–pulse on time, has resulted in an increase in the values of MRR and TWR up to certain extent and then starts decreasing with the increase in the same. The reduction in the above responses

might have happened due to the increase in the concentration of graphite powder that reduces the energy available for the ionization of the dielectric medium. Further, the increase in the value of gap voltage results in decrease in the values of MRR and TWR. Moreover, the R^2 values for MRR and TWR for EDM and PM-EDM are found to be equal to {0.945, 0.956} and {0.984, 0.973}, respectively, and show good agreement with the experimental data.

4 Confirmation and Comparison Study

The prediction accuracy of the developed models is tested with the help of ten experimental test cases that are different from the data used in establishing the models.

Figure 2 shows the comparison of the percentage error in prediction of the responses, namely MRR and TWR for both the processes, namely EDM and PM-EDM. From the said graphs, it is observed that the range of percentage error for the responses MRR and TWR for EDM and PM-EDM processes is seen to be in the range of $\{(-6.319 \text{ to } 7.29), (-7.49 \text{ to } 7.837)\}$ and $\{(-8.17 \text{ to } 7.1311), (-9.615 \text{ to } 8.596)\}$, respectively. Further, a comparative study has been conducted in terms of average values of MRR and TWR that were obtained using EDM and PM-EDM processes (ref. to Fig. 3) in which pure paraffin and graphite-mixed paraffin are used as dielectric fluids. From Fig. 3, it is observed that the MRR and TWR values for PM-EDM process are seen to low when compared with the graphite powder-mixed EDM. This may be due to the fact that graphite powder might have decreased the discharge frequency that results in the availability of higher amounts of energy for removing the material from both the workpiece and the tool.

Fig. 2 Graph showing the percentage deviation of responses for EDM and PM-EDM processes

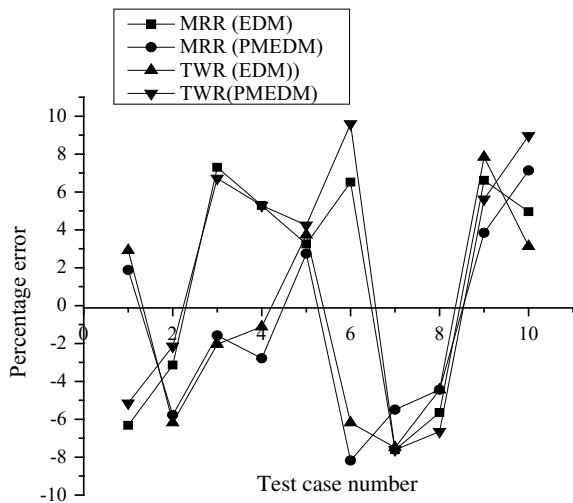
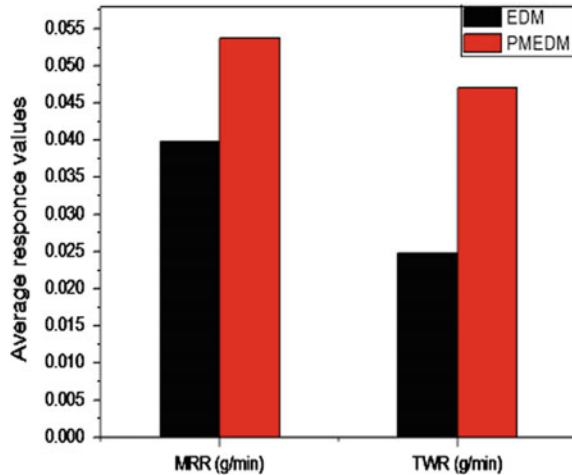


Fig. 3 Graph showing average response values of MRR and TWR for EDM and PM-EDM processes



5 Conclusions

Experimental investigations related to the machining of EN-19 steel are carried out during EDM and PM-EDM processes successfully. Further, nonlinear regression models are developed based on the results of experimentation. The results of ANOVA show that the nonlinear regression models are found to be statistically adequate to perform the predictions. From the experimental results, it has also been observed that the input parameters such as peak current, gap voltage, and pulse on time are directly proportional to the responses, MRR and TWR, and the gap voltage is seen to be inversely related to the responses. The prediction accuracy of the models suggests that the developed models are capable of predicting the responses with a reasonably good accuracy. Further, the average values of MRR and TWR for PM-EDM are seen to be higher when compared with the traditional EDM process.

References

1. Wong YS (1998) Near-mirror-finish phenomenon in EDM using powder-mixed dielectric. *J Mater Process Technol* 79:30–40
2. Zhao WS, Meng QG, Wang ZL (2002) The application of research on powder mixed EDM in rough machining. *J Mater Process Technol* 129:30–33
3. Kansal HK, Sehijpal S, Pradeep K (2007) Effect of silicon powder mixed EDM on machining rate of AISI D2 die steel. *J Manuf Proc* 9:3–22
4. Kumar S, Uma B (2012) Surface modification of die steel materials by EDM method using tungsten powder-mixed dielectric. *J Manuf Processes* 14:35–40
5. Kolli M, Kumar A (2015) Effect of dielectric fluid with surfactant and graphite powder on electrical discharge machining of titanium alloy using Taguchi method. *Eng Sci Technol Int J* 18:524–535

6. Toshimitsu R (2016) Improvement in surface characteristics by EDM with chromium powder mixed fluid. *Procedia CIRP* 42:231–235
7. Patel S, Dignesh T, Avadhoot R (2018) Aluminium powder mixed rotary electric discharge machining (PMEDM) on Inconel 718. *Aust J Mech Eng* 16:21–30
8. Kumar A (2017) Performance evaluation of Al₂O₃ nano powder mixed dielectric for electric discharge machining of Inconel 825. *Mater Manuf Processes* 33:1–10
9. Singh P (2010) Some experimental investigation on aluminum powder mixed EDM on machining performance of hastelloy steel. *Int J Adv Eng Technol* 1:28–45
10. Yue X, Yang X (2016) Study on the distribution of removal material of EDM in deionized water and gas with molecular dynamics simulation. *Procedia CIRP* 42:691–696
11. Anandakumar PA (2017) Analysis of copper mixed kerosene servotherm in EDM of Monel 400™. In: IOP conference series: materials science and engineering, vol 197

Measuring Industrial Symbiosis Index Using Multi-Grade Fuzzy Approach



C. Kalyan, T. Abhirama, Neyara Radwan Mohammed, S. Aravind Raj and K. Jayakrishna

Abstract The article reports a research that was carried out to measure the industrial symbiosis percentage of an industrial symbiotic setup utilising multi-grade fuzzy approach. Industrial symbiosis is a subclass of industrial ecology which describes how a cluster of assorted organizations can foster eco-innovation and long-term culture change, create, and share mutually profitable transactions and improve business and technical processes. A symbiosis measurement framework model incorporated accompanied by multi-grade fuzzy approach was developed. Successively, data congegated from the industrial symbiotic setup under study were substituted in this representation, and the improvement areas for symbiosis enhancement of the organization were elucidated. The application of this study reveals that the organization in question was symbiotic. Yet, there was further scope for improvement of symbiosis in the organizational cluster. On utilising, the model represented in this paper indicates that the symbiosis of the organization as well as the actions required to enhance its symbiotic level. This process is bound to accelerate the absorption of the symbiotic attributes of the organizations in Industry 4.0.

Keywords Industrial symbiosis · Symbiotic characteristics · Symbiosis percentage assessment · Fuzzy method M

1 Introduction

Every organisation exhaustively utilises its raw material, workforce and cash deposits in order to make finished goods or services with a lot of wastes and by-products. What if wastes and by-products of a company transform into raw material for another? As coined by Chertow, industrial symbiosis engages traditionally separate industries

C. Kalyan · T. Abhirama · S. Aravind Raj · K. Jayakrishna (✉)
School of Mechanical Engineering, VIT University, Vellore 632014, Tamil Nadu, India
e-mail: mail2jaikrish@gmail.com

N. R. Mohammed
Industrial Engineering Department, King Abdulaziz University, Jeddah 21589, Saudi Arabia

© Springer Nature Singapore Pte Ltd. 2019
S. S. Hiremath et al. (eds.), *Advances in Manufacturing Technology*,
Lecture Notes in Mechanical Engineering,
https://doi.org/10.1007/978-981-13-6374-0_7

in relatively close proximity to gain a competitive advantage involving physical exchange of materials, energy, water, and/or by-products through collaboration [1]. In this research, symbiosis of an industry was evaluated through the symbiotic characteristics or aspects like environmental benefits, policy benefits, management benefits, economic values, and customer feedback of an organization. In order to overcome the drawbacks of conventional methods, this study applies multi-grade fuzzy approach to evaluate symbiosis. To attain the given objectives, the study has been conducted by evaluating the symbiosis percentage of a tire-manufacturing organization.

2 Literature Review

Lombardi et al. discuss and redefine various interpretations of IS. Furthermore, this study posits that geographical proximity of industries is not necessarily sufficient or is a singular focus on physical resource exchange in Industry 4.0 [2]. Laybourn et al. discuss how National Industrial Symbiosis Program (NISP) of UK initiated by International Synergies Limited in 2003 had been successful in making multiple government and private bodies symbiotic all across Europe, Asia, Africa, and North and South America [3]. Desrochers takes an historical approach on how industrial symbiosis was nothing new and that it has existed during the Victorian times. It also sheds light on the reasons why industrial symbiosis did not take the limelight then and why it did in recent times [4]. Mantese et al. take the virtues of industrial symbiosis into the field of product development. They introduce and explain the concept of Design for Industrial Symbiosis (DFIS) [5]. Jensen in his study explored influences of industrial diversity geospatially and its effect on the working agreements of industrial symbiosis. The industrial diversity of a given geographical area in this paper was the primary driver behind how far a material travels from its point of origin to its point of reuse [6]. Ntaisou et al., in their study, shed light on various sustainability criteria, how geographic proximity and spatial principles affect the designing of an industrial park. They have also included a case study of sitting and designing a business park in Greece [7]. Novak et al., in their book, provide a formal theory of fuzzy logic. Generally, it is used to take care of the concept of partial truth, where the values range between entirely true and entirely false [8]. Cintula et al., in their article, explain and extoll about the virtues of fuzzy logic and its uses from an academic perspective with various real-world examples and case studies [9]. Vinodh et al. in his article assess the sustainability of an organization using multi-grade fuzzy approach with various sustainability enablers, criteria, and attributes mapped out [10].

2.1 Conceptual Model of Symbiosis Evaluation

As shown in Table 1, the conceptual model for industrial symbiosis is viewed from five perspectives namely environmental benefits, policy benefits, management benefits, economic values, and customer feedback. The proposed model of MGFA consists of two levels for the symbiosis evaluation. First level consists of the five symbiosis aspects (S_i) and the second in total deals with 25 symbiosis criteria (S_{ij}).

Table 1 Conceptual model for symbiosis evaluation

Symbiosis aspects (S_i)	Symbiosis criteria (S_{ij})
Environmental benefits	Recycle of waste resources
	Design for environment
	Solid waste management
	Utilization ratio of raw material
	Energy recycling
Policy benefits	Government policy
	Stakeholder involvement
	Voluntary agreement
	Existing policy
	Expected policy
Management benefits	Market structure management
	Enterprise management
	Waste management
	Information sharing
	Human resource management
Economic values	Growth rate
	Impact of R&D in GDP
	Capital investment
	Revenue generated
	Price and quantity control
Customer feedback	Customer satisfaction
	Serviceability
	Reverse logistics
	Quality control and assurance
	Customer acquisition

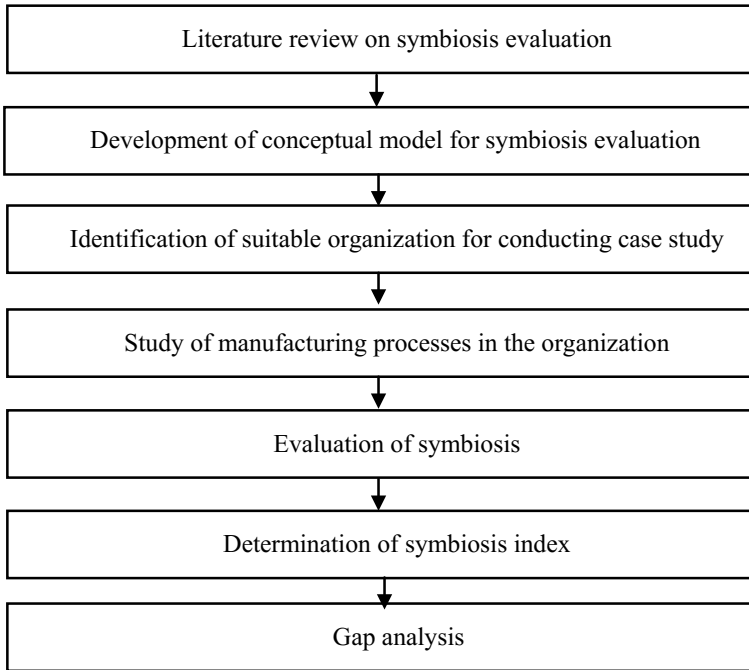


Fig. 1 Methodology

3 Methodology

As shown in Fig. 1, the methodology of this study initiates with a thorough literature review on symbiosis evaluation. Followed by the development of a conceptual model for carrying out the evaluation, identification of a case organisation to measure its industrial symbiosis using multi-grade fuzzy approach and finally determining its symbiosis index and summarising the results and key observations made.

4 Case Study

4.1 Case Company

The case company in this study is taken to be a tire-manufacturing company in Tamil Nadu. Hereafter, it is referred to as ABC Tire Company.

4.2 Evaluation of Symbiosis with the Help of Multi-grade Fuzzy Method

Multi-grade fuzzy approach was used in this study to measure the industrial symbiosis index to overcome the drawbacks of conventional crisp approaches [10]. Measurement of industrial symbiosis index using multi-grade fuzzy approach is a new contribution to the theory.

Symbiosis index of an organization, depicted by the variable S , is the matrix product of the overall assessment factor R and the overall weight W . The equation for symbiosis index is

$$S = W \times R \tag{1}$$

Five experts on a scale of 1–10 have performed the evaluation, where ‘1’ represents ‘extremely un-symbiotic’ and ‘10’ represents ‘extremely symbiotic.’ The experts have rated the symbiotic performance as shown in Table 2 for the criteria and aspects mentioned in Table 1.

4.3 Symbiosis Evaluation for the First Criteria

The calculation for the ‘environmental benefit’ criterion is as follows:

The weights concerned with ‘environmental benefit’ criterion are

$$W_1 = (0.1, 0.4, 0.15, 0.15, 0.2) \tag{2}$$

Evaluation vector related to ‘environmental benefit’ criterion is

$$R_1 = \begin{bmatrix} 8 & 6 & 8 & 6 & 9 \\ 7 & 9 & 8 & 5 & 6 \\ 6 & 8 & 9 & 5 & 7 \\ 9 & 6 & 6 & 6 & 7 \\ 5 & 7 & 9 & 7 & 9 \end{bmatrix} \tag{3}$$

Index related to environmental benefits is given by

$$S_1 = W_1 \times R_1 \tag{4}$$

$$S_1 = (6.85, 7.6, 8.05, 5.65, 7.2) \tag{5}$$

Using the same principle, the index related to the rest of the symbiosis criteria has been derived

Table 2 Matrix of evaluation vector and weights provided by experts

S_i	S_{ij}	$E1$	$E2$	$E3$	$E4$	$E5$	W_i	W_{ij}
S_1	S_{11}	8	5	8	6	9	0.10	0.3
	S_{12}	7	9	8	5	6	0.40	
	S_{13}	6	8	9	5	7	0.15	
	S_{14}	9	6	6	6	7	0.15	
	S_{15}	5	7	9	7	9	0.20	
S_2	S_{21}	6	7	7	5	7	0.20	0.05
	S_{22}	7	9	8	9	9	0.30	
	S_{23}	6	6	9	9	6	0.10	
	S_{24}	5	7	8	9	8	0.20	
	S_{25}	5	7	9	9	6	0.20	
S_3	S_{31}	8	5	8	8	7	0.25	0.2
	S_{32}	7	8	7	7	6	0.25	
	S_{33}	7	5	7	7	8	0.20	
	S_{34}	8	8	5	7	8	0.15	
	S_{35}	5	9	8	7	5	0.15	
S_4	S_{41}	9	9	7	5	6	0.20	0.2
	S_{42}	7	8	9	7	6	0.10	
	S_{43}	8	9	7	7	6	0.30	
	S_{44}	8	9	5	5	6	0.20	
	S_{45}	6	7	9	7	7	0.20	
S_5	S_{51}	5	5	6	8	9	0.30	0.25
	S_{52}	7	9	9	7	6	0.15	
	S_{53}	9	9	5	7	5	0.15	
	S_{54}	8	9	7	6	9	0.20	
	S_{55}	8	6	7	9	9	0.20	

$$S_2 = (5.9, 7.5, 8.1, 8.2, 7.5) \tag{6}$$

$$S_3 = (7.1, 6.8, 7.1, 7.25, 6.8) \tag{7}$$

$$S_4 = (7.7, 8.5, 7.2, 6.2, 6.2) \tag{8}$$

$$S_5 = (7.1, 7.2, 6.7, 7.5, 7.95) \tag{9}$$

4.4 Symbiosis Evaluation for the Secondary Criteria

The symbiosis index of ABC tire-manufacturing organization has been calculated to be:

Overall weight

$$W = (0.3, 0.05, 0.2, 0.2, 0.25) \tag{10}$$

Overall assessment vector is given by Eq. 11

$$R = \begin{bmatrix} 6.85 & 7.6 & 8.05 & 5.65 & 7.2 \\ 5.9 & 7.5 & 8.1 & 8.2 & 7.5 \\ 7.1 & 6.8 & 7.1 & 7.25 & 6.8 \\ 7.7 & 8.5 & 7.2 & 6.2 & 6.2 \\ 7.1 & 7.2 & 6.7 & 7.5 & 7.95 \end{bmatrix} \tag{11}$$

Symbiosis index

$$S = W \times R \tag{12}$$

$$S = (7.085, 7.515, 7.355, 6.67, 7.1225) \tag{13}$$

$$S_{avg} = 1/5(7.085, 7.515, 7.355, 6.67, 7.1225) \tag{14}$$

$$S_{avg} = 7.1495 \tag{15}$$

5 Results and Discussion

The industrial symbiosis index, which was calculated by utilizing multi-grade fuzzy approach, was 7.15. It indicates that the ABC tire-manufacturing organization is suitable for symbiosis. There is still scope for improvement of the symbiosis index in following areas.

- Government policy
- Revenue generated
- Customer satisfaction
- Waste management
- Human resource management
- Utilization of raw materials.

Table 3 Feedback from experts

Symbiosis aspects (S_i)	Likert scale rating of range 0–10					Mean response
	$E1$	$E2$	$E3$	$E4$	$E5$	
Environmental benefits	7	10	7	7	10	8.2
Policy benefits	9	8	10	7	8	8.4
Management benefits	7	7	10	9	9	8.4
Economic values	10	8	7	9	10	8.8
Customer feedback	7	8	10	8	10	8.6

5.1 Validation

In order to deem this study valid, a survey has been conducted and feedback from the experts was collected on the symbiosis aspects. The responses are recorded on a Likert scale of 0–10, and the results are as follows.

As shown in Table 3, the mean responses are 8.2 at the minimum for environmental benefits and 8.8 at the maximum for economic values. The mean response feedback points toward the possible implications and utilization of multi-grade fuzzy method in order to evaluate industrial symbiosis.

5.2 Industrial Implications

The implications of this study are reported in sustainability viewpoint, i.e., based on the triple-bottom line of sustainability (economic, environmental, and social) [11].

5.3 Economic Implications

Industrial symbiosis has huge economic advantages. The costs can be cut for the industries, which utilize the by-products and wastes of other industries as raw materials, as well as increase the revenue for the industries by selling their wastes and by-products at a price.

5.4 Environmental Implications

When multiple industries come together to be symbiotic, they make up an industrial corridor. This lets them cut down on the environmental impacts like reduced transportation.

5.5 *Social Implications*

Industrial symbiosis helps in an inclusive growth of the industries with sustainable future as a common goal, providing higher job opportunities and good relations between the industries in this extremely competitive Industry 4.0. It inculcates moral and ethical values to its employees as well as its partner industries providing a vision to grow and succeed.

6 Conclusion

The increased competition in Industry 4.0 has forced companies to collaborate and maintain good relations by being symbiotic. The contemporary or traditional industries are making an effort to evolve in order to survive be it by acquiring, merging, or collaborating. The symbiosis evaluation of ABC tire-manufacturing industry implies that ABC is symbiotic but still there is further scope to improve in the aspects of government policy, revenue generated, customer satisfaction, waste management, human resource management, and utilization of raw materials. In these perspectives, this study reports the measurement of industrial symbiosis index of a tire-manufacturing company using the conceptual model developed. The measurement indicates that the organization is symbiotic in nature. On the improvement of the identified weak areas, symbiosis of the organization could be improved which enables the organization to attain complete symbiosis under a circular economy.

6.1 *Limitations and Future Research Directions*

This study uses multi-grade fuzzy method for this study to evaluate symbiosis in a single industry. Advanced fuzzy logic methods can be utilized to evaluate for multiple industries. Further research can also be toward using different methods similar to multi-grade fuzzy logic.

References

1. Chertow MR (2000) Industrial symbiosis: literature and taxonomy. *Ann Rev Energy Environ* 25(1):313–337
2. Lombardi DR, Laybourn P (2012) Redefining industrial symbiosis. *J Ind Ecol* 16(1):28–37
3. Lombardi DR, Laybourn PT (2014) National industrial symbiosis programme (nisp): connecting industry, creating opportunity-2015. *ENEA* 2012(2013):22
4. Desrochers P (2004) Industrial symbiosis: the case for market coordination. *J Clean Prod* 12(8–10):1099–1110

5. Mantese GC, Bianchi MJ, Amaral DC (2018) The industrial symbiosis in the product development: an approach through the DFIS. *Proc Manuf* 21:862–869
6. Jensen PD et al (2011) Quantifying geographic proximity: experiences from the United Kingdom's national industrial symbiosis programme. *Resour Conserv Recycl* 55(7):703–712
7. Ntasiou M, Andreou E (2017) The standard of industrial symbiosis. Environmental Criteria and methodology on the establishment and operation of industrial and business parks. *Procedia Environ Sci* 38:744–751
8. Novák V, Perfilieva I, Mockor J (2012) *Mathematical principles of fuzzy logic*, vol 517. Springer Science & Business Media, Berlin
9. Cintula P, Fermüller C, Noguera C (2017) Fuzzy logic. In: Zalta EN (ed) *The Stanford Encyclopedia of Philosophy*
10. Vinodh S (2011) Assessment of sustainability using multi-grade fuzzy approach. *Clean Tech Environ Policy* 13(3):509–515
11. Savitz A (2006) *The triple bottom line*. Jossey-Bass, San Francisco

Fabrication and Machining Characteristics of Al7075-Red Mud and Al7075-TiC Metal Matrix Composites



Chinmayee Kar and B. Surekha

Abstract In the present research work, an attempt is made to fabricate two different aluminum-based metal matrix composites (AMMCs), namely Al7075-red mud and Al7075-TiC composites. The MMCs are made by adding 6 wt% of red mud and same percentage of TiC separately using stir casting method. Once the specimens are made, machining characteristics of the said AMMCs are studied by using electric discharge machining (EDM). During experimentation, investigations are carried out to study the effect of machining parameters such as peak current and pulse on time on the tool wear rate (TWR), material removal rate (MRR), and radial over cut (ROC) of two developed MMCs. It is observed that MRR is seen to be less, and TWR and ROC are found to be high for Al7075-TiC composites when compared to the Al7075-red mud composites.

Keywords Al7075-red mud MMC · Al7075-TiC MMC · Stir casting · Electric discharge machining

1 Introduction

Metal matrix composites (MMCs) are increasingly used in various latest industrial applications such as aerospace, aircraft, and automobile [1]. A large number of components in the said applications are made up of MMCs because of their high strength, resistance to wear and corrosion, and weight-to-strength ratio. The fabrication of metal matrix composites with fiber reinforcement, and with and without coatings was discussed by Richard [2]. In the last few decades, researchers were extending their research to introduce various reinforcing materials through the process of chemical reaction which is called as in situ metal matrix casting process. Tjong and Ma [3] fabricated the aluminum-based MMCs with TiC, and C as reinforcements. They

C. Kar · B. Surekha (✉)

School of Mechanical Engineering, KIIT Deemed to be University, Bhubaneswar 751024, Odisha, India

e-mail: surekhafme@kiit.ac.in

© Springer Nature Singapore Pte Ltd. 2019

S. S. Hiremath et al. (eds.), *Advances in Manufacturing Technology*,

Lecture Notes in Mechanical Engineering,

https://doi.org/10.1007/978-981-13-6374-0_8

discussed various aspects of MMCs, such as fabrication, mechanical and microstructural characteristics after utilizing different analysis methods, namely XRD, optical microscope, HREM, etc. It is to note that the stir casting process is also one of the important routes for fabrication of MMCs which was a simple and economic route. Kumar et al. [4] made MMCs by choosing A359 as matrix material and aluminum oxide as the reinforcement. After that, the mechanical and microstructural characterization of the sample specimens was performed and the tensile strength and hardness were found to increase with the increase in the weight fraction of the reinforcement. Another possible way to produce MMCs was the use of bottom-up approach. Some of the researchers [5] tried to fabricate the MMCs through powder metallurgy route. Once the component is produced, the machining characteristics of the MMCs were studied using EDM. Due to high strength-to-weight ratio and low density, Aluminum-based composites are produced by different methods, and various types of characterizations were needed to be performed. Rozenek et al. [6] tried to investigate the machining characteristics of the aluminum alloy reinforced with silicon carbide and aluminum oxide during WEDM. It was found that the cutting velocity and the surface roughness were seen to be inversely proportional to each other with the increase in the values of the input process parameters such as current, voltage, and pulse time. Few researchers [7] had made an attempt to fabricate the metal matrix composite with ceramic particle reinforcement and proved that EDM was suitable for powder-reinforced metal matrix composites (PRMMC) but that process was very slow. Furthermore, most of the researchers had used static electrode to investigate the machining characteristics during EDM process. But in some other studies, few investigations had also used rotary electrode [8] in the EDM process. In the present research, an attempt is made to study the machining characteristics of two developed MMCs, namely Al7075-red mud and Al7075-TiC MMCs during EDM.

2 Experimental Procedure

In the present experimentation, Aluminum 7075 is used as the matrix material because of its good cast ability and wear resistance. The chemical composition of Al7075 is shown in Table 1. Two different Al7075 metal matrix composites are made by considering 6 wt% of two different reinforcements such as red mud and titanium carbide (TiC). The composites are fabricated by adding the required quantity of reinforcement to the molten Al7075 matrix in a crucible maintained at 730–750 °C. The schematic view of the furnace along with stirrer and the preheating setup of the die is shown in Fig. 1.

Table 1 Chemical composition of Al7075

Composition	Fe ₂ O ₃	Al ₂ O ₃	SiO ₃	Na ₂ O	CaO
Percentages (%)	30–60	10–20	10–20	20–10	2–8



Fig. 1 Schematic view of the furnace along with stirrer and preheating setup of the die

Graphite crucible is used to melt Al70075 by keeping it in a pit furnace. When the aluminum alloy reaches to the molten state, pre-heated (1000–1500 °C) red mud is added to the melt and stirred properly at 350 rpm with the help of an electrical stirrer. Stirring will be continued for three times at the said speed for 1–2 min with 2 min interval. Two sets of experiments are conducted by considering red mud and TiC as reinforcements in Al7075. Once the MMCs are made through stir casting process, they are machined on EDM to estimate the effect of machining process parameters on the responses, namely TWR, MRR, and ROC.

Once the Al7075-red mud and Al7075-TiC MMCs are produced, the machining characteristics of these two developed materials are carried out using EDM after utilizing the brass electrode with the diameter equal to 10 mm. For the experimental investigations, two variables, namely peak current (I_p) and pulse on time (T_{on}), are considered as inputs and the responses material removal rate (MRR), tool wear rate (TWR), and radial over cut (ROC) are treated as outputs. It is to be noted that the range of the input process parameters is identified based on the material of the work piece, literature, and the limitations of the available EDM setup. Table 2 shows the input parameters and the measured responses for the two developed MMCs.

Table 2 Input parameters and responses of Al7075-red mud and Al7075-TiC MMCs

Exp. no	I_p	V_g	T_{on}	Al7075/red mud			Al7075/TiC		
				MRR	TWR	ROC	MRR	TWR	ROC
1	6	50	50	0.055	0.0012	0.0036	0.043	0.0256	0.0621
2	8	50	50	0.07	0.007	0.0071	0.05	0.027	0.0643
3	10	50	50	0.12	0.015	0.0288	0.069	0.0359	0.0686
4	6	50	100	0.077	0.0069	0.0219	0.049	0.0281	0.0669
5	8	50	100	0.122	0.0125	0.0252	0.06	0.030	0.067
6	10	50	100	0.176	0.0204	0.0417	0.075	0.0368	0.0699
7	6	50	150	0.087	0.0091	0.0297	0.052	0.0291	0.069
8	8	50	150	0.135	0.0147	0.0303	0.066	0.0310	0.0702
9	10	50	150	0.1974	0.0227	0.0496	0.082	0.0376	0.073

3 Results and Discussions

From the results of experiments, a study has been conducted to investigate the effect of peak current and pulse on time at constant voltage on the three responses, namely MRR, TWR, and ROC. Figure 2 shows the variation of MRR at different peak current and pulse on time during the electric discharge machining of developed composites, namely Al7075-red mud and Al7075-TiC composites. It is to be noted that the gap voltage is kept fixed at 50 V during the entire study.

From the graph (ref. to Fig. 2), it is observed that the MRR of Al7075-red mud MMC is higher than that of the Al7075-TiC MMC. This may be due to the fact that the hardness of the Al7075 alloy in the presence of carbide particles increases and leads to the increase in the time taken to remove the material (that is, decrease the value of MRR) when compared with the Al7075-red mud composites. It is also observed that the increase in the values of current and pulse on time increases the MRR. This might have happened due to the availability of higher amounts of energy with the increase in the value of current and pulse on time. This is true for both the red-mud- and TiC-reinforced composites. Figure 3 shows the variation TWR with the increase in the value of the current and pulse on time with constant value for gap voltage (50 V).

From the above plot (ref to Fig. 3), it is found that the TWR is high for high strength material (that is, Al7075-TiC) than the low strength material (Al7075-red mud). This might be due to the higher machining time requirement for the high strength material, which causes more erosion on the electrode and in turn increases the tool wear rate. It is also found that the TWR is increasing with the increase in the values of peak current and pulse on time. Furthermore, Fig. 4 shows the variation of radial over cut for the two developed MMCs.

It is observed that the ROC is also a function of machining time. As the machining time increases, the ROC is also seen to be increased. From the plot, it is also observed that the ROC of both the MMCs is increasing as the peak current and pulse on time are increasing. The reason for this is same as the one explained above.

Fig. 2 Variation of MRR against I_p and T_{on} of two MMCs (Al7075-TiC/Al7075-red mud)

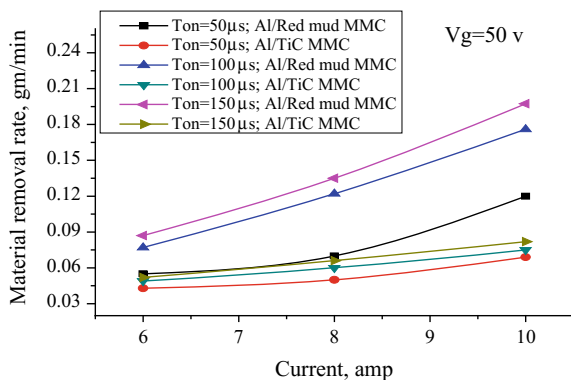


Fig. 3 Variation of TWR against I_p and T_{on} of two MMCs (Al7075-TiC/Al7075-red mud)

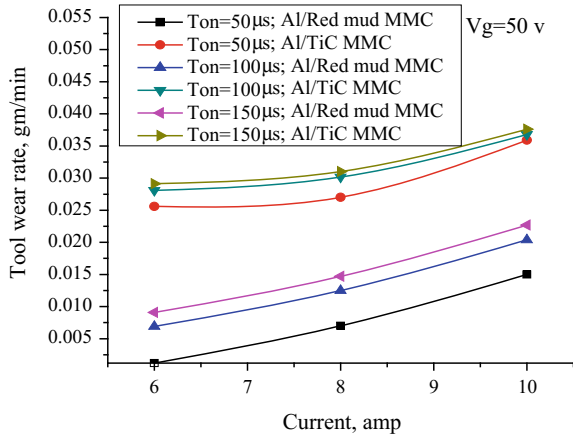
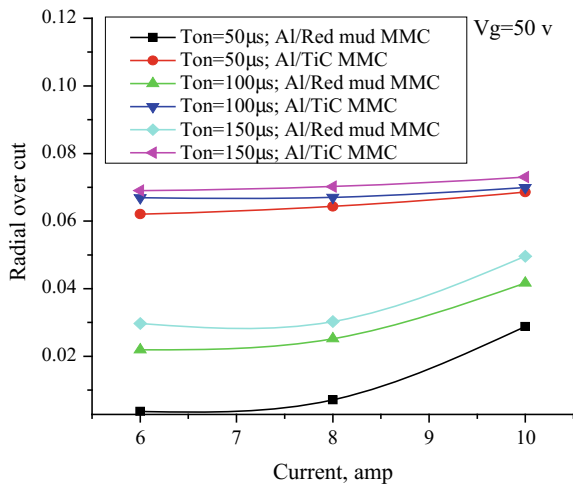


Fig. 4 Variation of ROC against I_p and T_{on} of two MMCs (Al7075-TiC/Al7075-red mud)



4 Conclusions

Two different metal matrix composites (Al7075-red mud and Al7075-TiC) have been fabricated through stir casting process successfully. The machining characteristics such as MRR, TWR, and ROC of the developed metal matrix composites have been studied during EDM by varying peak current and pulse on time. It is observed that the MRR is less in Al7075-TiC than Al7075-red mud composites. It is due to its high value of strength when compared with the red-mud-reinforced MMCs. As Al7075-TiC requires longer machining time when compared with Al7075-red mud composites, former composite shows increase in both the TWR and ROC when compared with the later. It is also found that the MRR, TWR, and ROC are seen to be increased with the increase in the values of peak current and pulse on time.

References

1. Bunk W, Esslinger P, Keller H (1989) *Aerospace materials: trends and potential*. Materials and processing Ð move into the 90's. Elsevier, Amsterdam, pp 327–341
2. Ricard TH (1968) Fabrication of metal matrix composites. *J Compos Mater* 2:32–42
3. Tjong SC, Ma ZY (2000) Microstructural and mechanical characteristics of in situ metal matrix composites. *Mater Sci Eng* 29:49–113
4. Kumar A, Lal S, Kumar S (2013) Fabrication and characterization of A359/Al₂O₃ metal matrix composite using electromagnetic stir casting method. *J Mater Res Technol* 2:250–254
5. Rozenek M, Kozak J, Browski LD, Lubkowski K (2001) Electrical discharge machining characteristics of metal matrix composites. *J Mater Process Technol* 109:367–370
6. Bodukuri AK, Eswaraiah K, Rajendar K, Sampath V (2016) Fabrication of Al–SiC–B₄C metal matrix composite by powder metallurgy technique and evaluating mechanical properties. *Perspect Sci* 8:428–431 (2016)
7. Müller F, Monaghan J (2000) Non-conventional machining of particle reinforced metal matrix composite. *Int J Mach Tools Manuf* 40:1351–1366
8. Mohan B, Rajadurai A, Satyanarayana KG (2004) Electric discharge machining of Al–SiC metal matrix composites using rotary tube electrode. *J Mater Process Technol* 153:978–985

Multicriteria Optimization of Machining Parameters in WEDM of Titanium Alloy 6242



R. Prasanna, P. M. Gopal, M. Uthayakumar and S. Aravind

Abstract This article deals with the optimization of process parameters in WCEDM of titanium alloy (Ti–6Al–2Sn–4Zr–2Mo). Material removal rate and surface roughness were studied against the wire cut EDM process parameters, namely pulse ON time, pulse OFF time, voltage and wire feed rate. The pulse ON time selected for the experiment was 4, 5, 6 μ s, and pulse OFF time is 6, 8, 10 μ s. The voltage values selected in the experiment are 50, 65 and 85 V, while wire feed rate used was 2, 4 and 6 m/min. The effect of pulse ON, pulse OFF, voltage and wire feed rate over material removal rate and surface roughness of the machined surface is backed up with scanning electron microscopy (SEM). The contribution of parameters on responses was determined by analysis of variance, and regression models were obtained for material removal rate and surface roughness.

Keyword ANOVA · DOE · GRA · Wire cut EDM · Material removal rate · Surface roughness · Ti-6242

1 Introduction

Machining plays a vital role in the manufacturing industry, and it is a process of removing excessive material from workpiece in order to achieve required size and shape by controlling the various parameters. Various machining methodologies like turning, milling and drilling are generally utilized for material removal in order to get the final product. However, it is difficult to machine hard and brittle products like punches, tool and dies through these conventional machining techniques.

R. Prasanna (✉) · P. M. Gopal · S. Aravind
Department of Mechanical Engineering, Karpagam Academy of Higher Education,
Coimbatore 641021, Tamil Nadu, India
e-mail: prasannaravi.g@gmail.com

M. Uthayakumar
Department of Mechanical Engineering, Kalasalingam University, Krishnan Kovil 626126,
Tamil Nadu, India

Titanium and its alloys are one among these kind of difficult to cut materials which is mainly used for biomedical implant and aerospace industry applications. Machining of titanium alloy using conventional (like milling and turning) and unconventional techniques (like WJM and AWJM) with precision is difficult. If titanium alloy is machined in traditional method like milling, broaching or grinding, it results in higher tool wear and also it is very difficult to machine economically. Nontraditional methodologies like plasma and AWJM are limited to linear cutting, and hence, WEDM is preferred over other nontraditional machining processes for the machining of titanium alloy (Ti-6Al-2Sn-4Zr-2Mo).

Wire cut electrical discharge machining (WEDM) is an effective unconventional machining (UCM) process which helps for machining hard materials. It has various distinct advantages over the other nontraditional cutting technologies such as high machining versatility, minimum stresses on the workpiece, high flexibility and small cutting forces. Using WEDM technology, the fabrication of extremely precise parts are possible (± 0.016), while other UCM methodologies such as water jet machining (WJM) is not very precise technology (± 0.13) as that of EDM. As much as minimal surface roughness of $0.72 \mu\text{m}$ is achieved while machining through WEDM, whereas the WJM gives the roughness value of $1.02 \mu\text{m}$ while machining the same material [1].

The selection of appropriate process parameter values in WEDM is an essential step towards achieving an effective process performance which includes pulse ON time, pulse OFF time, voltage and wire feed rate that are responsible for the output responses such as material removal rate and surface roughness [2]. It was reported that higher material removal rate can be achieved at higher pulse ON time, lower pulse OFF time, higher current and lower voltage. Maximum material removal rate for titanium alloy (Ti-6Al-4V) can be achieved by increasing the pulse ON time because the number of discharge in a given period is increased at higher pulse ON time [3, 4]. The roughness of the machined surface tends to increase with an increase in pulse ON time, and the increase in voltage results in reduced surface roughness, while surface roughness decreases with increase in wire tension for titanium alloy (Ti-6Al-4V) [5]. The most significant factors for material removal rate are discharge current, voltage and pulse ON time [6], while workpiece thickness and wire feed rate are found as least significant [7]. The most significant for the surface roughness are wire tension and servo voltage in which increase in wire tension leads to decreased surface roughness, while pulse OFF time, wire feed rate and flushing pressure are stated as least significant [8]. It can be identified from the literature that the output parameters or machining performance depends on various parameters which have to be maintained properly in order to achieve effective machining. Hence, this study intends to find optimal input parameter combination for better output performance such as surface roughness and material removal rate.

2 Materials and Experimentation

2.1 Work Material

Titanium alloys are metals containing a blend of titanium and other chemical compositions, and Grade 6Al 2Sn 4Zr 2Mo titanium alloy is a near alpha alloy. It was developed for the purpose of handling operations in high-temperature application up to 538 °C. Titanium 6242 alloy of 5 mm thickness is used as the work material. It possesses excellent strength and corrosion resistance with comparatively good weldability and fabricability.

2.2 Experimental Set-up

WEDM of titanium alloy was done by utilizing CNC electro-discharge machine that has the acceptable job size of 400 × 500 × 200 mm, maximum cutting speed of 120 mm/min and maximum taper cutting angle of ±30° on 50 mm job. Wire material used in this study is brass of diameter 0.25 mm, and de-ionized water is used as a dielectric medium. The process parameters such as pulse ON time, pulse OFF time, voltage and wire feed rate are selected as input parameters. Table 1 shows the selected process parameter and their levels, whereas L27 orthogonal array developed based on the input parameter levels through Taguchi method is given in Table 2. The material removal rate (MRR) for wire cut EDM is calculated by using the equation:

$$MRR = F \times D_w \times H \tag{1}$$

where *F* is cutting speed (mm/min), *D_w*—width of cut (mm), *H*—height of the workpiece (mm).

The average surface roughness (Ra) of WEDM machined Ti alloy samples was measured by using Mitutoyo SJ-310 surface roughness measurement device. The measurement was taken for a distance of 5 mm from the top, middle, bottom of the

Table 1 Parameters and their levels

S. No.	Parameter	Unit	Symbol	Level		
				L1	L2	L3
1	Pulse ON time	μs	A	4	5	6
2	Pulse OFF time	μs	B	6	8	10
3	Voltage	V	C	50	65	80
4	Wire feed rate	m/min	D	2	4	6

Table 2 Experimental responses with SN ratio

Run	A	B	C	D	MRR	SNR-MRR	Ra	SNR-Ra
1	4	6	50	2	2.742	8.760	2.635	-8.416
2	4	6	65	4	2.643	8.443	2.535	-8.081
3	4	6	80	6	2.546	8.119	2.440	-7.746
4	4	8	50	2	2.733	8.732	2.622	-8.372
5	4	8	65	4	2.636	8.418	2.530	-8.061
6	4	8	80	6	2.537	8.088	2.428	-7.703
7	4	10	50	2	2.723	8.702	2.618	-8.360
8	4	10	65	4	2.627	8.389	2.519	-8.026
9	4	10	80	6	2.528	8.057	2.416	-7.660
10	5	6	50	4	2.753	8.795	2.614	-8.345
11	5	6	65	6	2.654	8.478	2.516	-8.013
12	5	6	80	2	2.574	8.211	2.494	-7.938
13	5	8	50	4	2.747	8.778	2.603	-8.310
14	5	8	65	6	2.649	8.463	2.508	-7.986
15	5	8	80	2	2.562	8.171	2.486	-7.911
16	5	10	50	4	2.736	8.744	2.592	-8.272
17	5	10	65	6	2.634	8.411	2.496	-7.945
18	5	10	80	2	2.561	8.170	2.478	-7.882
19	6	6	50	6	2.766	8.835	2.593	-8.277
20	6	6	65	2	2.685	8.578	2.570	-8.199
21	6	6	80	4	2.590	8.265	2.472	-7.861
22	6	8	50	6	2.750	8.788	2.583	-8.242
23	6	8	65	2	2.674	8.542	2.569	-8.195
24	6	8	80	4	2.579	8.230	2.464	-7.832
25	6	10	50	6	2.740	8.756	2.578	-8.225
26	6	10	65	2	2.667	8.521	2.554	-8.143
27	6	10	80	4	2.573	8.210	2.452	-7.789

cut surface. Each test was carried out thrice, and the averages of the result are taken for the study.

2.3 Multicriteria Optimization

In this paper, multiple performance characteristics are analysed using grey relation analysis (GRA). In this method, multiple performance characteristics can be converted into a single grey relation grade.

Steps in grey relation analysis:

Step 1: Normalize Y_{ij} as Z_{ij} ($0 < Z_{ij} \leq 1$) by the following formula to avoid the effect of using different units and to reduce variability. Normalization is a transformation performed on a single input to disturb the data evenly and scale it into acceptable range for the further analysis.

Z_{ij} = Normalized value for i th experimental/trial j th dependent variable/response

$$Z_{ij} = \frac{Y_{ij} - \min(Y_{ij}, i = 1, 2, \dots, n)}{\max(Y_{ij}, i = 1, 2, \dots, n) - \min(Y_{ij}, i = 1, 2, \dots, n)}$$

(to be used for S/N ratio with larger – the better case) (2)

$$Z_{ij} = \frac{\max(Y_{ij}, i = 1, 2, \dots, n) - Y_{ij}}{\max(Y_{ij}, i = 1, 2, \dots, n) - \min(Y_{ij}, i = 1, 2, \dots, n)}$$

(to be used for S/N ratio with smaller – the better case) (3)

Step 2: Compute the grey relational coefficient (GC) for the normalized S/N ratio values.

$$GC_{ij} = GC_{ij} = \frac{\Delta_{\min} + \lambda \Delta_{\max}}{\Delta_{ij} + \lambda \Delta_{\max}} \tag{4}$$

- i 1, 2, 3, ..., n experiments.
- j 1, 2, 3, ..., m responses.
- GC_{ij} grey relation coefficient for the i th experiment/trial and j th dependent variable/response.
- Δ absolute difference between Y_{oj} and Y_{ij} which is a deviation from target value and can be treated as quality loss.
- Y_{oj} optimum performance value or the ideal normalized value of j th responses.
- Y_{ij} the i th normalized value of the j th response/dependent variable.
- Δ_{\min} minimum value of Δ .
- Δ_{\max} maximum value of Δ .
- λ is the distinguishing coefficient which is defined in the range $0 \leq \lambda \leq 1$ (the value may be adjusted on the practical needs of the system).

Step 3: The grey relational grade was determined by averaging the grey relational coefficient corresponding to each performance characteristic which is given in Table 5. The overall performance characteristic of the multiple response process depends on the calculated grey relational grade. The grey relational grade can be expressed as:

$$G_i = (1/m) \left[\sum GC_{ij} \right] \tag{5}$$

where m is the number of responses.

3 Results and Discussion

3.1 Effect of Input Parameters on MRR and Surface Roughness

The experimental results, namely MRR and surface roughness, while machining Ti alloy are reported in Table 2. In Taguchi method, the response values are initially converted into SN ratio values. Since the aim of this work is to reduce the roughness of the surface and increase the MRR, smaller the better criteria is followed for surface roughness whereas larger the better criteria is followed for MRR. By plotting the mean SN ratio values of each parameter level, the optimum parameter combination is identified.

The main effect plot for S/N ratio of MRR for wire cut EDM is represented in Fig. 1. Material removal rate is mainly controlled by pulse ON time, and it gets increased while increasing pulse ON time and decreasing the pulse OFF time, voltage and wire feed rate. It is fact that if spark time gets increased, there will be more discharge current which strikes the surface of the metal lead to maximum quantity of floating material for higher material removal rate. Optimal conditions for maximum material removal rate are achieved as pulse ON time 6 (μ s), pulse OFF time 6 (μ s), voltage 50 (V) and wire feed rate 2 (mm/min).

The main effect plot of S/N ratio of Ra for wire cut EDM is represented in Fig. 2. Surface roughness specifies the state of machined surface. The results indicate that

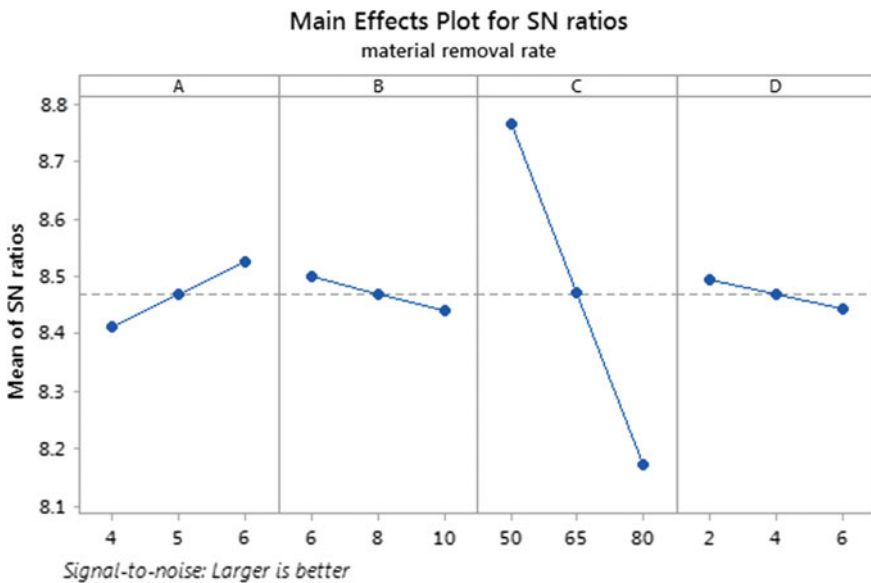


Fig. 1 Main effect plot for MRR (S/N ratio)

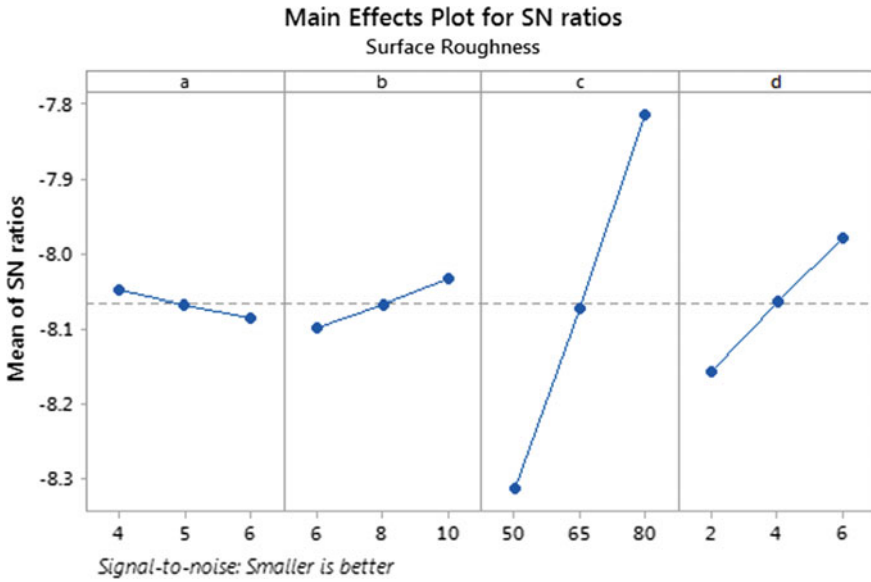


Fig. 2 Main effect plot for surface roughness (S/N ratio)

the surface roughness is minimal at higher level of pulse OFF time, voltage and wires feed rate and lower level of pulse ON time. At moderate level of spark time, spark strikes the surface of work piece for minimal time and creates less crater which results in minimum surface roughness. Optimal conditions for minimum surface roughness are achieved by as pulse ON time 4 (μ s), pulse OFF time 10 (μ s), voltage 80 (V) and wire feed rate 6 (mm/min).

3.2 Surface Topography

It was found that machined surface was not very uniform. This can be explained using micrographs. The SEM micrograph of the sample machined with pulse ON time 6 μ s, pulse OFF time 6 μ s, voltage 50 V and wire feed rate 2 mm/min (Fig. 3) shows that maximum material removal rate leads to surface peak, valley, microhole, microcrack and large debris. This is fact that, as pulse ON current increases more discharge spark and more powerful explosion strikes the surface which leads to deeper crater formation on the machined surface due to material removal at higher quantity [9]. The observation over Fig. 4 which belong to sample machined at Pulse ON time 4 μ s, Pulse OFF time 10 μ s, Voltage 80 V, Wire feed rate 6 mm/min shows minimum surface roughness due to minimum surface peak, valley and micro hole and small debris. At moderate pulse ON current which produces moderate spark strikes the surface uniformly which leads to better surface finish. From the observation

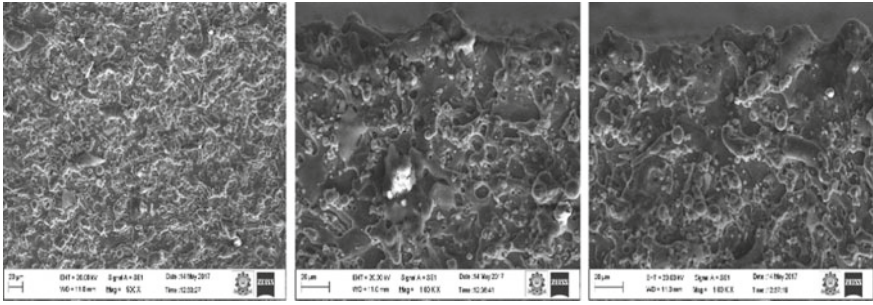


Fig. 3 SEM image of machined surface (pulse ON time 6 µs, pulse OFF time 6 µs, voltage 50 V and wire feed rate 2 mm/min)

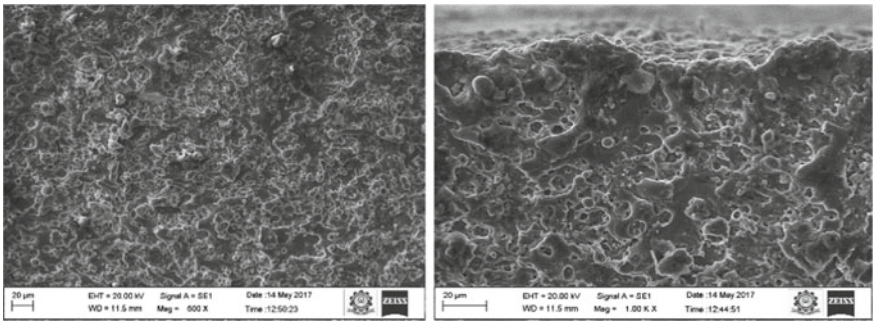


Fig. 4 SEM image of machined surface (pulse ON time 5 µs, pulse OFF time 8 µs, voltage 80 V and wire feed rate 6 mm/min)

of Figs. 3 and 4, this paper concludes that peak, valley, microhole and debris get increased when the process input parameter is increased. This article shows that the lower and moderate process parameters give better quality than higher level of process parameter.

3.3 ANOVA for MRR and Surface Roughness

General linear ANOVA is made using the popular software specifically used for the design of experiment application known as MINITAB 17. It is used to study the effect of machining parameter such as pulse ON, pulse OFF, voltage, wire feed rate and two output parameters such as material removal rate and surface roughness.

Table 3 shows the ANOVA for MRR, and it predicts that pulse ON, pulse OFF, voltage and wire feed rate are most significant (since P value < 0.05) for material removal rate. Voltage has more contribution than other process parameters (since the F value (10,445.19) of voltage is higher than other process parameters).

Table 3 ANOVA for (MRR) ($R\text{-sq}$ —0.9992 and $R\text{-sq}(\text{adj})$ —0.9988)

Analysis of variance					
Source	DF	Adj SS	Adj MS	F value	P value
A	2	0.005298	0.002649	370.96	0.000
B	2	0.001432	0.000716	100.28	0.000
C	2	0.149168	0.074584	10445.19	0.000
D	2	0.000764	0.000384	53.52	0.000
Error	18	0.000129	0.000007		
Total	26	0.156790			

DF—degree of freedom, SS—sum of square, MS—mean square

Table 4 ANOVA for surface roughness ($R\text{-sq}$ —0.9990 and $R\text{-sq}(\text{adj})$ —0.9986)

Analysis of variance					
Source	DF	Adj SS	Adj MS	F value	P value
A	2	0.000473	0.000237	39.37	0.000
B	2	0.001545	0.000773	128.51	0.000
C	2	0.095353	0.047676	7929.57	0.000
D	2	0.012265	0.006133	1019.99	0.000
Error	18	0.000108	0.000006		
Total	26	0.109745			

Table 4 shows that ANOVA for surface roughness (R_a). It predicts that pulse ON pulse OFF, voltage and wire feed rate are most significant (since P value < 0.05). Voltage has more contribution than other process parameters (since $F = 7929.57$ value higher than other process parameter).

3.4 Grey Relation Optimization

Table 5 shows that grey relation coefficient and grey relation grade; here, normalized S/N ratio for MRR and R_a is calculated by appropriate formula depending on the type of quality characteristic. ΔMRR and ΔR_a are calculated using Eqs. 1 and 2, respectively. GC_{MRR} and GC_{R_a} are calculated by Eq. 3. Finally, grey relation grade is calculated by Eq. 4. The higher value of grey relation grade 0.77642 shows the higher quality of machining parameters (pulse ON time 6 μm , pulse OFF 6 μm , voltage 50 V and wire feed rate 6 m/min). The main effect of MRPI (mean of MRPI) is tabulated in Table 6 which shows the machining parameter of maximum material removal rate and better surface roughness.

Table 5 Grey relation coefficient and grey relation grade

Run	Normalized SN ratio for (MRR)	Normalized SN ratio for (Ra)	$\Delta_{(MRR)}$	$\Delta_{(Ra)}$	GC _(MRR)	GC _(Ra)	G_i grade
1	0.899	0.000	0.101	1.000	0.908	0.500	0.704
2	0.485	0.454	0.515	0.546	0.660	0.647	0.653
3	0.076	0.891	0.924	0.109	0.520	0.902	0.711
4	0.862	0.061	0.138	0.939	0.878	0.516	0.697
5	0.452	0.481	0.548	0.519	0.646	0.658	0.652
6	0.038	0.945	0.962	0.055	0.510	0.948	0.729
7	0.822	0.078	0.178	0.922	0.849	0.520	0.685
8	0.415	0.528	0.585	0.472	0.631	0.679	0.655
9	0.000	1.000	1.000	0.000	0.500	1.000	0.750
10	0.946	0.098	0.054	0.902	0.948	0.526	0.737
11	0.530	0.544	0.470	0.456	0.680	0.687	0.684
12	0.191	0.643	0.809	0.357	0.553	0.737	0.645
13	0.924	0.146	0.076	0.854	0.929	0.539	0.734
14	0.510	0.579	0.490	0.421	0.671	0.704	0.688
15	0.141	0.678	0.859	0.322	0.538	0.756	0.647
16	0.877	0.197	0.123	0.803	0.891	0.555	0.723
17	0.444	0.633	0.556	0.367	0.643	0.732	0.687
18	0.139	0.716	0.861	0.284	0.537	0.779	0.658
19	1.000	0.191	0.000	0.809	1.000	0.553	0.776
20	0.659	0.296	0.341	0.704	0.746	0.587	0.666
21	0.259	0.743	0.741	0.257	0.574	0.795	0.685
22	0.936	0.238	0.064	0.762	0.940	0.567	0.754
23	0.613	0.301	0.387	0.699	0.721	0.589	0.655
24	0.215	0.781	0.785	0.219	0.560	0.820	0.690
25	0.894	0.261	0.106	0.739	0.904	0.575	0.740
26	0.585	0.371	0.415	0.629	0.707	0.614	0.660
27	0.190	0.835	0.810	0.165	0.552	0.859	0.705

Table 6 Mean table for MRPI values

Factors	Level 1	Level 2	Level 3
Pulse ON (μs)	0.6929	0.6891	0.7035
Pulse OFF (μs)	0.6957	0.6939	0.6959
Voltage (V)	0.7277	0.6667	0.6911
Wire feed rate (m/min)	0.6686	0.6928	0.7241

4 Conclusion

In this paper, optimum parameters of material removal rate and surface roughness of titanium alloy are studied. Experiments were conducted with different process parameters for the determination of optimum condition.

- Voltage plays an important role in material removal rate and surface roughness.
- In this paper, optimum parameters for material removal rate and surface roughness while machining titanium alloy is identified.
- The higher level of pulse ON time with lower pulse OFF time, voltage and wire feed rate leads to an increase in material removal rate and surface roughness. The optimum values are A3B1C1D1.
- The higher level of voltage and wire feed rate leads to minimum surface roughness. The optimum values are A1B3C3D3.
- It is observed from the SEM micrograph that lower and moderate levels of process parameter lead to higher material removal than higher level of process parameter. Higher level of process parameter leads to arching during machining.
- Maximum material removal rate leads to surface peak, valley and microhole. This is fact that as pulse on current increases more discharge spark strike the surface lead maximum quantity of molten and floating metal which result deterioration of the surface roughness which is observed through SEM micrograph.

References

1. Luca A, Popan I, Bala M, Blaga L, Balci N (2013) Comparison between the accuracy and efficiency of EDMWC and WJC. *Acad J Manuf Eng* 11:42–47
2. Rajurkar KP, Sundaram MM, Malshe AP (2013) Review of electrochemical and electro discharge machining. *Proc CIRP* 6:13–26
3. Rajurkar KP, Wang WM (1993) Thermal modeling and on-line monitoring of wire-EDM. *J Mater Process Technol* 38(1–2):417–430
4. Singh H, Garg R (2009) Effects of process parameters on material removal rate in WEDM. *J Achievements Mater Manuf Eng* 32:70–74
5. Sarkar S, Sekh M, Mitra S, Bhattacharyya B (2001) Modeling and optimization of wire electrical discharge machining of γ -TiAl in trim. *J Mater Process Technol* 118:1–3
6. Mahapatra SS, Patnaik A (2006) Optimization of wire electrical discharge machining (WEDM) process parameters using genetic algorithm. *Indian J Eng Mater Sci* 13:494–502
7. Shah A, Mufti AN, Rakwal D, Bamberg E (2011) Material removal rate, kerf, and surface roughness of tungsten carbide machined with wire electrical discharge machining. *J Mater Eng Perform* 20:71–76
8. Rao PS, Ramji K, Satyanarayana B (2011) Effect of WEDM conditions on surface roughness a parametric optimization using Taguchi method. *Int J Adv Eng Sci Technol* 6:041–048
9. Goswami A, Kumar J (2017) Optimization in wire cut EDM of Nimonic-80A using Taguchi's approach and utility concept. *Eng Sci Technol Int J* 236–246

Water Absorption and Density Tests on the Water Hyacinth-Based Partial Green Composite



Rakesh Potluri and M. Sreenivasa Rao

Abstract At present, natural composites have received a wide range of attention from the researchers due to the fact that fossil fuel resources are depleting rapidly, increase in global warming, and concern on environmental pollution. The development of the green composites is also increased for the fact that the properties of these are very similar to synthetic composites. Water hyacinth plant is an aquatic plant which causes several devastating problems to the ecosystem in which it grows. Removing this plant is a huge cost and time-consuming process, and this is not a permanent solution as it grows in a very short span. Utilizing such type of plants to prepare composite materials will be beneficial to society. In this paper, the water hyacinth (WH) plant is dried and powdered to manufacture a partial green composite. The water hyacinth powder is mixed with epoxy to prepare a partial green particulate composite. Experimental investigation of the density changes, mass savings, and water absorption behavior of the WH powder-based composite was performed, and its behavior has been presented in the current paper. Comparisons were made between the density and water absorption behavior of the normal epoxy with the WH powder-infused epoxy.

Keywords Water hyacinth (WH) · Epoxy · Particulate-reinforced composite · Partial green composite

1 Introduction

Composites are a material formed by the combination of two or more dissimilar materials at a macroscopic scale which results in a distinct interface being formed in between these materials. Usually, the composites were manufactured with the use of synthetic polymers and fibers, derived from petrochemicals. Environmental pollution

R. Potluri (✉) · M. Sreenivasa Rao
DVR & Dr. HS MIC College of Technology, Kanchikacherla, Krishna Dt.,
Andhra Pradesh, India
e-mail: y09me042@gmail.com

© Springer Nature Singapore Pte Ltd. 2019
S. S. Hiremath et al. (eds.), *Advances in Manufacturing Technology*,
Lecture Notes in Mechanical Engineering,
https://doi.org/10.1007/978-981-13-6374-0_10

is a great danger with which the whole world is trying to fight. Waste management and fossil fuel resource depletion are also other great global problems that are threatening the humans right now. To address these issues, in terms of materials, research on new sustainable and biodegradable materials that can be produced using the by-products or the products derived from the natural resources is on the rise. A lot of efforts are being focused toward the development of the composite materials with natural fiber or filler-reinforced composite materials.

Biocomposites are playing a major role in different application fields such as the automobile, aerospace, construction, sports, and industries. Researchers are not only looking for natural fibers that can act as a replacement for artificial fibers. They also are looking to utilize agricultural by-products like husk and woodworking byproduct of wood flour as an effective filler material in the composite materials. Polymers can also be developed from natural sources such as corn starch. But, the majority of the research interests are dedicated to finding natural fibers and filler materials for reinforcement in the composite materials to address the above-mentioned issues. Particulate reinforcements are one form of composite materials, where the particles are reinforced in the composite matrix instead of fiber. The particulates tend to increase the strength and wear resistance of the matrix materials by filling the voids and arresting the crack growth. That is why particulate fillers are mainly used for tweaking the wear and thermal properties of the matrix material rather than the mechanical properties.

Water hyacinth is an aquatic plant that typically grows in wetlands and surface of the water bodies. It is an invasive plant which has a very rapid growth rate. The development of this plant in the canals tends to clogs the flow of water as this plant grows rapidly in the form of large dense mats. This plant tends to threaten the marine life in the water bodies where it grows, by depriving the water of nutrients and oxygen. Its colony of plants is so dense that even sunlight cannot pass through them into the water. A lot of governments have tried to eradicate this plant, but none of the measures taken up by them were successful. In the present times, the stem part of the plant is dried, and it is being used to prepare items such as baskets, carpets... etc. But, the problem with this plant has not been addressed in a large context. In this research, we wanted to use the powder extracted from the water hyacinth plant as a filler material in the epoxy-based composite material and wanted to find out its effect on the density and water absorption behavior of the water hyacinth powder-filled particulate composite.

Flores Ramirez et al. [1] studied the effect of reinforcing water hyacinth fibers on the mechanical and thermal properties of the composite made from a polyester matrix material. They created composites with 5, 10, 15, and 20 wt% of water hyacinth fiber in the polyester matrix, using the technique of resin impregnation and hot curing methods. It was shown that the major effect of inclusion of water hyacinth was seen for wt% of 5 and 10. It has been concluded from the results that the water hyacinth fiber can be a good competitor for the other natural fibers as it has shown no negative effects on the mechanical and thermal characteristics of the polyester matrix material. Abral et al. [2] studied the effect of alkali treatment on the mechanical properties of the water hyacinth fiber-based composite material made up of the unsaturated

polyester matrix material. Different concentration of alkali solutions was used for treating the water hyacinth fibers, and it was concluded that the alkali solution treatment with 7% concentration for 1 h of treatment time expressed the best results. It was also noted through SEM examination that, if the raw water hyacinth fibers were used for reinforcing the matrix material, it was clear that the failure of the composite was due to the fiber pull out. It was also concluded that if a higher concentration of alkali solution was used for the treatment of the water hyacinth fibers, it has damaged the surface of the fiber leading to the decrement in the mechanical properties of the composite. Abral et al. [3] evaluated the effect of moisture absorption on the mechanical properties of water hyacinth fiber-based polyester composites. They also studied the effect of alkali treatment on the water absorption behavior of the water hyacinth fibers, and it was noted that there was no significant effect of this treatment on the water absorption behavior of the water hyacinth fibers. It was concluded that the mechanical properties of the water hyacinth fiber-based unsaturated polyester matrix composite were lower when immersed in the water compared to that of the dry ones. Supri et al. [4] studied the water absorption behavior and morphological characteristics of composite made up of low-density polyethylene with treated and untreated water hyacinth plant fibers. It was concluded that as the weight percentage of the fiber is increasing, the water absorption of the composite also increased. Treating with coupling agents has improved the interfacial adhesion between the fiber and the matrix material. Supri et al. [5] prepared composite materials with treated and untreated water hyacinth fibers in both low-density polyethylene and ABS polymers. The water hyacinth fibers are treated with an isophorone diisocyanate-polyhydroxyl group as the coupling agent. It was concluded that the composites with treated fibers exhibited higher tensile strength and modulus, resistance to water absorption and thermal properties in comparison with the composites made from untreated fibers. Supri et al. [6] prepared composites made out of low-density polyethylene/natural rubber/water hyacinth fiber composite. Poly(methyl methacrylate) was used for treating the water hyacinth fiber. The composite with treated water hyacinth fiber had showed higher tensile strength and modulus, higher glass transition temperature, and melting point in comparison with the composite filled with untreated water hyacinth fibers. Supri et al. [7] prepared composites made out of low-density polyethylene/natural rubber/water hyacinth fiber composite. Polyaniline was used for treating the water hyacinth fiber. The composite with treated water hyacinth fiber had exhibited higher tensile strength and modulus, melting point, and electrical conductivity but lower molar sorption, capacitance, percentage crystallinity in comparison with the composite filled with untreated water hyacinth fibers. Sathishkumar et al. [8] reviewed how to characterize different physical, chemical, mechanical, dynamic, and thermal properties of various natural fiber and natural fiber-based hybrid composite. Potluri et al. [9–11] prepared different natural fiber composites using the hand layup methods and characterized the mechanical properties of the respective natural fiber composite. Other literature about the natural fiber-based composite materials, their preparation, and testing were taken from the remaining references [10–19].

2 Composite Manufacturing

2.1 Preparation of Water Hyacinth Powder

Water hyacinth plants were collected from the canals of river Krishna and then transported to the laboratory. Then, the leaves and roots of the water hyacinth plant are removed leaving behind the trunk or stem of the plant. Then, the trunk/stem is dried for a period of 15 days in sunlight. Figure 1 shows the stem of the water hyacinth fiber plants being dried in the sun. The sunlight drying is essential as it removes the moisture content from the trunks. Then, the plant stems are again dried in a hot air oven at a temperature of about 60 °C for a period of about 8 h. This oven drying was performed to ensure the removal of any trace amount of moisture. Once the plant stems are dried, they are powdered using a crushing machine and a mixer. This cursing will yield a powder with different sizes of particles. The mixture of different particle sizes of water hyacinth powder was then passed through mechanical sieves, to obtain a powder where the particle sizes that vary between the 130 and 150 μm . Figure 2 shows the powdered water hyacinth after sieving was performed. These microparticles have been used as the filler inside the epoxy resin. The reason behind choosing the microparticles is that they are very cost-effective to produce.

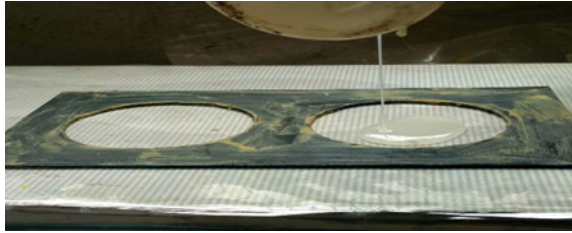
Fig. 1 Drying of WH stems



Fig. 2 Water hyacinth powder



Fig. 3 Water absorption test specimen manufacturing



2.2 Specimen Preparation

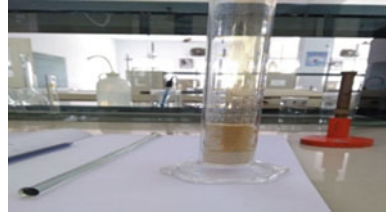
The matrix material used for the preparation of the composite is the epoxy LY556. This epoxy along with the suitable hardener was obtained from Ecmas resin Pvt. Ltd, Hyderabad. The specimens are prepared with using the hand lay-up process followed by the process of compression molding. Ceramic tiles were taken as the base plates. Then, a polyurethane sheet was glued to both the tiles to create a very smooth surface. A rubber sheet of the required thickness has been taken, and the holes were cut according to the size of the specimens. These rubber molds were then glued to one of the ceramic plates, and then, let it to dry under a pressure of 0.5 MPa for a period of about 24 h. Then, silicon spray was sprayed on to the rubber mold for easy removal of the specimens after manufacturing. Different weights of each epoxy and the powder were calculated according to the volume fraction requirements. Based upon these calculations, different weights of the powder are mixed with the epoxy matrix; this mixture was stirred for 2 h using a mechanical stirrer, and then, hardener was mixed. This mixture is then poured into the rubber mold. Then, a polyurethane sheet is placed upon it and rolling is performed to ensure the removal of excess material and also to get rid of the air bubbles that may have occurred while pouring the mixture into the mold cavity. Then, the other ceramic tile is placed upon the rubber mold and weights were kept on it to simulate a compression pressure of 0.5 MPa. The specimens were allowed to set for a time of 24 h. Once the specimens were removed from the die, and then dried in a hot air oven for a period of 6 h at a temp of 60 °C, for ensuring the removal of moisture from the specimen. Figure 3 shows the die used for manufacturing specimens for water absorption test.

3 Experimental Work

3.1 Density Tests for WH Powder

The density of the water hyacinth powder was found using the method of weight-to-volume ratio. A small volume measuring flask was taken and weighed at first, and then, some quantity of water hyacinth powder is taken in that measuring flask.

Fig. 4 Determination of density of WH powder



The powder is compacted inside the flask using a simple glass rod. This is to ensure that the volume of the powder is always right. Then again, the weight of the flask with the powder filled in is measured. The difference in the initial weight of the flask and the final weight of the flask with powder gives the weight of the water hyacinth powder. The volume of the powder is known from the measuring flask. From these two values, we can determine the density of the water hyacinth powder. This particular procedure was repeated for different volumes of the water hyacinth powder to ensure the accuracy of the density value determined using this procedure. The density of the water hyacinth powder is found to be 276.35 kg/m^3 .

The density of the epoxy matrix was taken from the data sheets provided by the supplier of the matrix material. Figure 4 shows the measuring flask with compacted water hyacinth powder.

3.2 Density of the Composite Specimens

Different specimens were manufactured according to different ASTM D792 standards for performing the various tests like the tensile, flexural, and impact. Extra specimens were prepared according to all these ASTM D792 standards that were used to perform the density tests for finding out the influence of inclusion of the water hyacinth powder on the density of the epoxy matrix material. These extra specimens were used to determine the density of the water hyacinth powder-based epoxy composite. Pycnometer procedure was used for determining the density of the powder-reinforced composite. The weight of the specimen is taken by using an electronic precision weight measuring machine. Then, these specimens are immersed in water, in a beaker with graduated volume readings. After immersing the specimen, the change in the level of water is noted from which the volume of the specimen is calculated. Then from the mass and the volume values for each specimen, the density was calculated. The density values for three different specimens were determined for each volume fraction of the water hyacinth powder, and the average of these three values was determined as the density of the composite. Figure 5 shows the density tests carried out for the specimens.

Fig. 5 Density test for composite specimen



3.3 Water Absorption Tests

The water absorption behavior of any composite mainly depends on several factors. The factors such as the type of matrix material, the reinforcement phase, the length of exposure to moisture, the temperature of the water, and types of additives used. All these factors affect the rate of water absorption of any composite material. The water absorption tests were carried out for a period of 24 h, according to the ASTM D570 standard. The specimens are circular in shape with a diameter of 51 mm in diameter with a thickness of about 6.35 mm. These specimens are dried in a hot air oven to remove the moisture and then cooled down to room temperature. Then, these specimens are weighed carefully on an electronic balance and then immersed in the water at room temperature. Then after 12 h, the specimens are taken out of the water and carefully tapped with a dry Lenin cloth and then weighed. This weighing was down for every 6 h until a total of six readings are taken. Three specimens for each volume fraction of the water hyacinth powder-based composite are taken, and the change in the water absorption behavior of the epoxy matrix material was noted down. The change in the weight of the specimen can be calculated by subtracting the weight of the dry specimen from the weight of the immersed specimen. The percentage of water absorption can be obtained by dividing the value of the change in the specimen by the initial dry weight of the specimen and then multiplying this value with 100.

$$\text{Percentage of water absorption} = \left(\frac{\text{Weight after immersion} - \text{Initial dry weight}}{\text{initial dry weight}} \right) \times 100. \quad (1)$$

The volume fraction of the water hyacinth powder that is required inside the epoxy matrix is first determined. Based on the volume fraction requirements, the corresponding volume fractions are converted into the weight fractions based on the densities of the corresponding materials. Depending on the densities and the volume of the specimen to be produced, the weight of each constituent material was determined.

4 Results

4.1 Density Test

Figure 6 shows the variation of the density of the composite material with respect to the increase in the volume fraction of the water hyacinth powder. It can be clearly observed that as the inclusion of the water hyacinth particles is increased, the density of the composite has decreased in a linear fashion. The density of the water hyacinth is so low because of the fact that it contains microscopic air pockets within its stem cell structure. The presence of air pockets in the water hyacinth stem structure was shown using SEM images by Supri et al. The decrease in the density of the composite is due to the fact that the epoxy matrix is a material with higher density (1.3065 kg/m^3) when compared to that of the water hyacinth powder. Thus, as the component of lower density is increasing in the whole composition, the density of the composite has decreased.

Figures 7, 8, 9, 10, 11, and 12 show the variation in the percentage of water absorption of the composite material with respect to the time for a particular volume fraction of the water hyacinth powder. Each unit of time corresponds to 6 h each. A total of six readings for every 6 h for a total period of 36 h have been noted. In the first case of water absorption for pure epoxy, the percentage of water absorption has increased along with the time. But the percentage of change in the water absorptivity is on an average of 1.02%. This slight percentage of water absorption is may be due to the presence of small microvoids that might have been created during the manufacturing process on the surface of the epoxy specimens.

Likewise, in the other specimens containing 10, 20, 30, 40, and 50% volume fractions of the water hyacinth powder that the water absorption percentage of the composites are increasing at an average rate of 1.018, 1.215, 1.066, 1.129, and 1.977%, respectively. Likewise, it can also be observed from Fig. 13 that as the volume fraction of the water hyacinth powder is increasing, the water absorptivity of the composite is also increasing. But on an actual scale, the change in the average rate of change in the water absorptivity of the composite with 50% volume fraction of water hyacinth

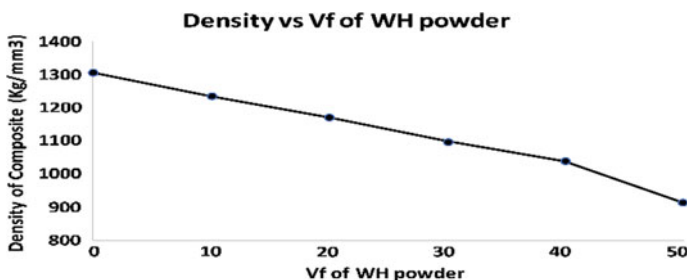


Fig. 6 Density versus volume fraction of WH powder

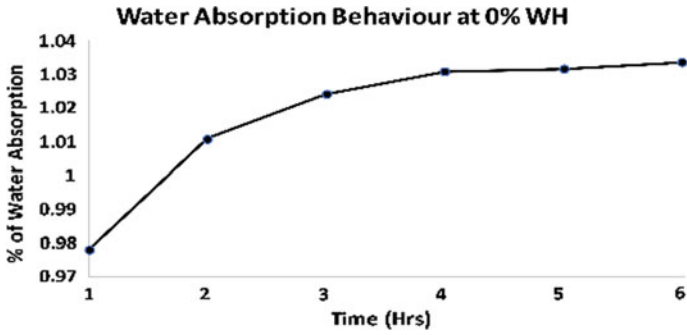


Fig. 7 % of water absorption at 0% Vf of WH powder

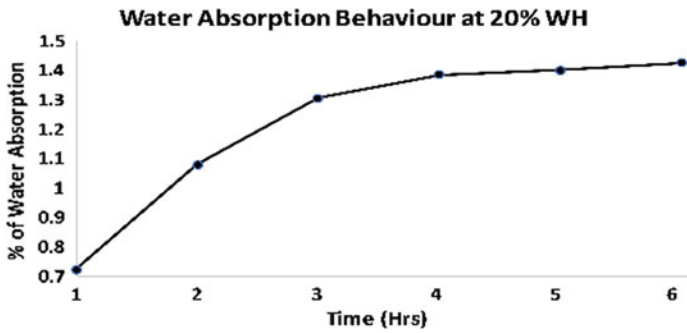


Fig. 8 % of water absorption at 10% Vf of WH powder

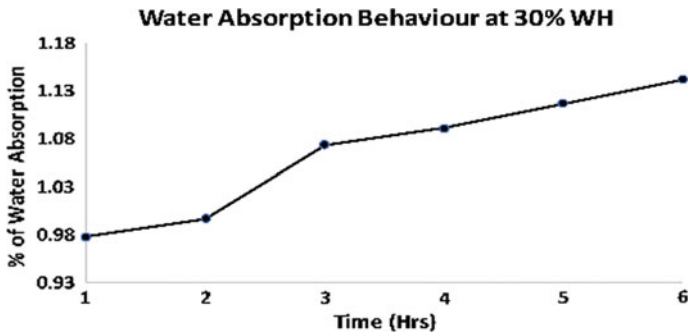


Fig. 9 % of water absorption at 20% Vf of WH powder

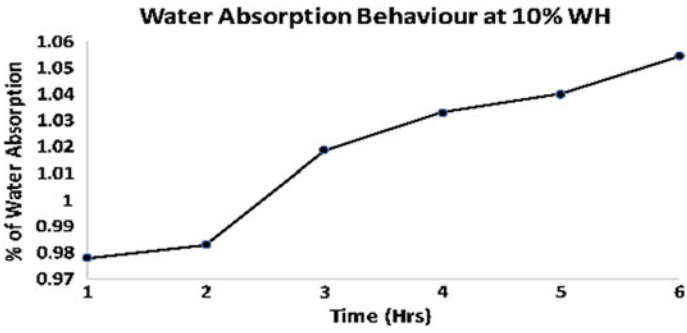


Fig. 10 % of water absorption at 30% Vf of WH powder

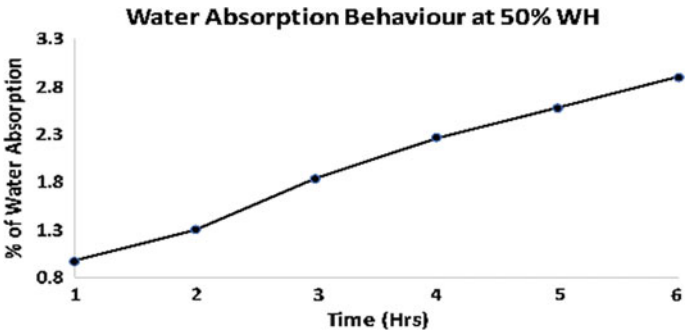


Fig. 11 % of water absorption at 40% Vf of WH powder

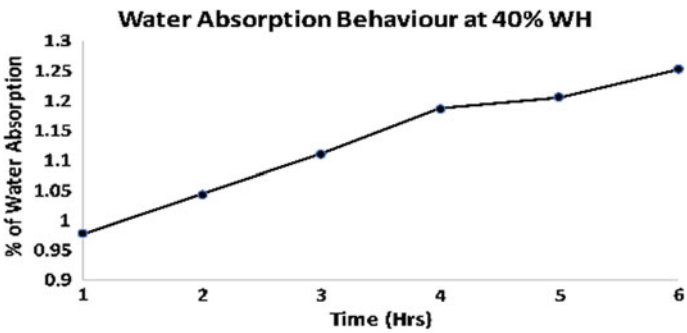


Fig. 12 % of water absorption at 50% Vf of WH powder

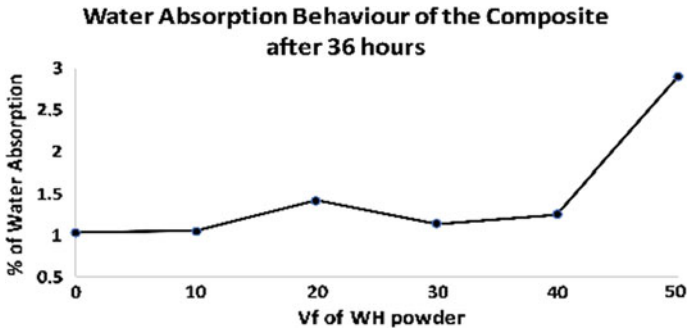


Fig. 13 % of water absorption at different Vf of WH powder after the last reading

powder is double to that of the pure epoxy composite. It can be also observed that the addition of 10, 20, and 30% of water hyacinth powder has no major effect on the change of the water absorption behavior of the epoxy. The major change in the water absorption behavior of the composites was observed at 40 and 50% volume fraction of water hyacinth powder. But overall, no major deviation in the water absorption behavior of the epoxy matrix has been observed with the inclusion of the water hyacinth powder up to 30%, with some exception to 20% volume fraction of water hyacinth powder.

5 Conclusion

Successful experimental work was carried out to find the effect of inclusion of different volume fractions of water hyacinth powder in epoxy matrix on the density and water absorption behavior of the composite. The density of the composite has decreased linearly with the increase in the volume fraction of the water hyacinth powder. This is beneficial as it decreases the weight of the composite material made out of epoxy matrix and water hyacinth powder, without a major increase in the cost of the composite material. The major change in the water absorption behavior of the composites was observed at 40 and 50% volume fraction of water hyacinth powder. But overall, no major deviation in the water absorption behavior of the epoxy matrix has been observed with the inclusion of the water hyacinth powder up to 30% volume fraction in the composite material. Adding water hyacinth powder has an effect on the water absorption behavior of epoxy matrix.

References

1. Flores Ramirez N, Sanchez Hernandez Y, Cruz de Leon J, Vasquez Garcia SR, Domratheva Lvova L, Garcia Gonzalez L (2015) Composites from water hyacinth (*Eichhornea crassipe*) and polyester resin. *Fibers Polym* 16:196–200
2. Abrial H, Kadriadi D, Rodianus A, Mastariyanto P, Ilhamdi, Arief S, Sapuan SM, Ishak MR (2014) Mechanical properties of water hyacinth fibers—polyester composites before and after immersion in water. *Mater Des* 58:125–129
3. Abrial H, Putra H, Sapuan SM, Ishak MR (2013) Effect of alkalization on mechanical properties of water hyacinth fibers-unsaturated polyester composites. *Polym Plast Technol Eng* 52:446–451
4. Supri A, Lim B (2009) Effect of treated and untreated filler loading on the mechanical, morphological, and water absorption properties of water hyacinth fibers-low density polyethylene. *J Phys Sci* 20:85–96
5. Supri AG, Ismail H (2011) The effect of isophorone diisocyanate-polyhydroxyl groups modified water hyacinth fibers (*Eichhornia crassiper*) on properties of low density polyethylene/acrylonitrile butadiene styrene (LDPE/ABS) composites. *Polym Plast Technol Eng* 50:113–120
6. Supri AG, Tan SJ, Ismail H, Teh PL (2011) Effect of poly(methyl methacrylate) modified water hyacinth fiber on properties of low density polyethylene/natural rubber/water hyacinth fiber composites. *Polym Plast Technol Eng* 50:898–906
7. Supri AG, Tan SJ, Ismail H, Teh PL (2014) Properties of (low-density polyethylene)/(natural rubber)/(water hyacinth fiber) composites: the effect of polyaniline. *J Vinyl Add Tech* 20:122–130
8. Sathishkumar TP, Navaneethakrishnan P, Shankar S, Rajasekar R, Rajini N (2013) Characterization of natural fiber and composites—a review. *J Reinf Plast Compos* 32:1457–1476
9. Potluri R (2017) Mechanical properties of pineapple leaf fiber reinforced epoxy infused with silicon carbide micro particles. *J Nat Fibers* 00:1–15
10. Potluri R, Diwakar V, Venkatesh K, Reddy BS (2018) Analytical model application for prediction of mechanical properties of natural fiber reinforced composites. *Mater Today Proc* 5:5809–5818
11. Potluri R, James Paul K, Abdul S, Prasanthi P (2017) Mechanical properties characterization of okra fiber based green composites & hybrid laminates. *Mater Today Proc* 4:2893–2902
12. Potluri R, Dheeraj RS, Vital GVVNG (2018) Effect of stacking sequence on the mechanical & thermal properties of hybrid laminates. *Mater Today Proc* 5:5876–5885
13. Potluri R, Eswara A, Raju MN, Prakash KR (2017) Finite element analysis of cellular foam core sandwich structures. *Mater Today Proc* 4:2501–2510
14. Potluri R, Eswara Kumar A, Navuri K, Nagaraju M, Rao DM (2016) Buckling analysis of a ring stiffened hybrid composite cylinder. In: IOP conference series: materials science and engineering
15. Potluri R, Rao UK (2017) Determination of elastic properties of reverted hexagonal honeycomb core: FEM approach. *Mater Today Proc* 4:8645–8653
16. Potluri R, Paul KJ, Babu BM (2018) Effect of silicon carbide particles embedment on the properties of Kevlar Fiber reinforced polymer composites. *Mater Today Proc* 5:6098–6108
17. Potluri R (2018) Mechanical properties evaluation of T800 carbon fiber reinforced hybrid composite embedded with silicon carbide microparticles: a micromechanical approach. *Multidiscip Model Mater Struct*
18. Potluri R (2015) Comparative study of pressure vessels made from laminated composite material (COPV) with the pressure vessels made with sandwich core composite material. *J Mater Sci Mech Eng* 2:203–207
19. Potluri R, Ketha KK (2015) Comparison between GFRP and CFRP composite power take-off shaft in helicopters for prescribed torque and geometrical constraints. *J Mater Sci Mech Eng* 2:214–219

Experimental Analysis on the Mechanical Properties of Dissimilar Material Joint During PCTIG Welding



B. Kamesh Srikar, Raghuraman Srinivasan, Venkatraman Ramamoorthi, Sivachidambaram Pichumani and J. Durga Venkata Satyanarayana

Abstract During TIG welding on dissimilar joint weldment between copper and brass, reduced mechanical strength is observed. To overcome these challenges, pulsed current tungsten inert gas (PCTIG) welding technique has been employed. Experimental investigations were carried out using TIG welding and PCTIG welding with AC and DC currents on dissimilar joints of copper and brass and mechanical properties such as microhardness were compared. AC-PCTIG with 5 Hz resulted in improved microhardness of 92.66 Hv on weld zone. DC-PCTIG with 100 Hz resulted in microhardness of 107.5 Hv on the weld zone. Mixed-mode current consisting of half-cycle of AC current and another half-cycle of DCEN mode was also carried out on PCTIG welding. Due to the influence of the DCEN current, the mechanical properties suffer reduction and weld strength lies between the AC and DCEN welded conditions.

Keywords TIG welding · PCTIG welding · Dissimilar joints

1 Introduction

The process of welding is a perpetual joining of distinctive materials like metals, alloys, composites, plastics combining together with their contacting surfaces by the applications of pressure and heat. At the welding area, the metal gets melted and solidified and forms a hard joint between the two surfaces. The weldability of the material relies on the various components i.e., metallurgical characteristics changes during the welding operation, it causes to increase the hardness of weld zone because of the fast rate of solidification, the degree of oxidation with air and other environmental gases leading to the development of breakage at the joining area of the weld [1]. TIG welding process is also called the gas tungsten arc welding; it

B. Kamesh Srikar · R. Srinivasan · V. Ramamoorthi · S. Pichumani (✉) ·
J. Durga Venkata Satyanarayana
School of Mechanical Engineering, SASTRA Deemed University, Thanjavur 613401,
Tamil Nadu, India
e-mail: sivaumaphd@gmail.com

© Springer Nature Singapore Pte Ltd. 2019
S. S. Hiremath et al. (eds.), *Advances in Manufacturing Technology*,
Lecture Notes in Mechanical Engineering,
https://doi.org/10.1007/978-981-13-6374-0_11

is suitable for the welding of the thin section. The TIG welding is widely used in the nonferrous metals like aluminum, copper, magnesium, and copper alloys. The TIG welding process is almost slower process compared to other welding techniques, like plasma welding and laser welding techniques [2]. TIG welding is an electric arc welding process in which the fusion energy is produced by an electric arc between the workpiece and the tungsten electrode. PCTIG welding involves cycling of welding current from a higher level (peak current) to lower level (base current) at a particular pulse frequency. This peak current gives adequate penetration and bead contour, while the base current helps in maintaining a stable arc throughout the welding process [3]. The pulse frequency helps in giving sufficient time to transfer heat from weld zone and heat-affected zone to the base material region. Also optimized PCTIG welding parameters gives reduced heat input and fine grain microstructure [4]. This can increase the weld strength of the dissimilar specimen when compared to TIG welding. PCTIG technology has progressed to give magnificent welding performance on the thin plate of aluminum, stainless, and other materials. A copper compound can be employed welded by general welding procedures using metal inert gas (MIG) and tungsten inert gas (TIG) [5].

2 Experimental Method

The PCTIG welding process is performed on copper and brass with a thickness of 6 mm by using ADOR CHAMPTIG 300AD weld machine. The process parameters used in a PCTIG welding process are shown in Table 1. Experimentation has been carried out at maximum and minimum frequency levels of 100 and 5 Hz and currents with both AC and DC for dissimilar welding on copper and brass using PCTIG welding process and the mechanical properties like microhardness. The microhardness

Table 1 PCTIG parameters

S. No.	Conditions	Value
1	Peak current	320 A
2	Base current	160 A
3	Pulse on time	50%
5	Weld speed	2 mm/s
6	Gas flow rate	20 L/min
7	Flow pressure	1 kg/cm ²
8	Electrode diameter	4 mm
9	Nozzle size	6
10	Collet and body	4 mm
11	Electrode type	2% thoriated tungsten
12	High and low frequencies	100 and 5 Hz



Fig. 1 Welded samples

test is performed on the various areas of the weld zone, HAZ, and base material on the weldments by utilizing the Shimadzu smaller-scale Vickers hardness analyzer equipment as per the standards of ASTM 384 (Fig. 1).

3 Results and Discussions

3.1 Hardness Test

It is observed that the hardness value of the base material is nearly equal for each and every base samples and it differs for weld zone and HAZ. Three trails of hardness test are carried out by utilizing Vickers hardness analyzer equipment. The brass base material is having the high hardness, whereas copper base metal is having the low hardness. The hardness values are shown in Table 2 (Fig. 2).

Table 2 Hardness test values

S. No.	Sample name	Copper base (HV)	Copper HAZ (HV)	Weld zone (HV)	Brass HAZ (HV)	Brass base (HV)
1	DC high frequency 100 Hz	61	64.5	107.5	150.5	140
2	Mixed high frequency 100 Hz	65.66	66	99.33	132.66	142
3	AC high frequency 100 Hz	58.33	66.33	95.33	117.33	141
4	DC low frequency 5 Hz	69	68.33	102.66	139.66	130
5	Mixed low frequency 5 Hz	65.33	73.33	96.33	159.33	139.66
6	AC low frequency 5 Hz	70	72	92.66	151.33	142.33
7	DC-TIG	66	72	86.33	148	146.33
8	AC-TIG	65.66	65	88.66	138.33	133.66

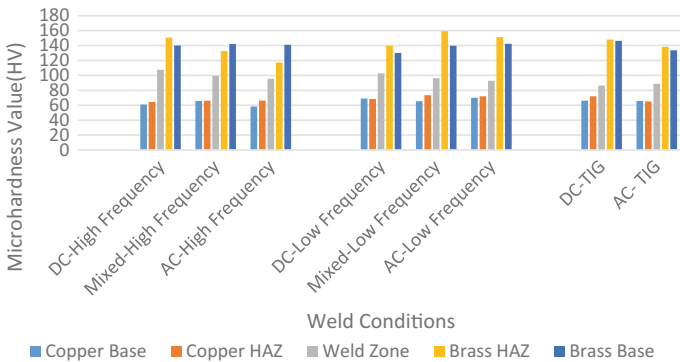


Fig. 2 Microhardness graph

3.2 Effect of Frequency on the Hardness

The hardness value varies according to two types of frequencies in PCTIG (5, 100 Hz) which are shown in Table 3. The hardness at different areas is examined and concluded that hardness decreases in the weld zone, when welded at 5 Hz than the weldments are welded at 100 Hz. Due to the formation of coarse grains, controlled heat input at 100 Hz PCTIG welding than 5 Hz and TIG welding.

Table 3 Effects of frequency variation in levels and types of current observed in microstructure

Hardness	Type of grains	High frequency—100 Hz	Low frequency—5 Hz
High	Coarse	DC	DC
Intermediate	Intermediate coarse dendritic	AC, mixed	Mixed
Low	Fine dendritic	–	AC

4 Conclusion

The PCTIG welding system provides uniform welding on the material joint. The tensile strength of the weldment depends on the welding parameters like welding current and frequency. In the first case, welding of copper and brass with the AC low frequency of 5 Hz gives low hardness value, and the results are 92.66 Hv. From this experiment, the AC low frequency of 5 Hz gives better results in mechanical properties. In the second case, the welding of copper and brass with DC high frequency—100 Hz—gives high hardness value, and the results are 107.5 Hv. Therefore, the DC high frequency of 100 Hz gives undesired results. Finally, we concluded that AC low frequency of 5 Hz gives better results compared to other cases in terms of hardness value of the weldment of copper and brass.

References

1. Indira Rani M, Marpu RN (2012) Effect of pulsed current TIG welding parameters on mechanical properties of J-joint strength of Aa6351. *Int J Eng Sci (IJES)* 1(1):1–5
2. Pichumani S, Raghuraman S, Venkatraman R (2015) Correlation between microstructure and microhardness on Al-Sic composite welded using pulsed current TIG welding. *ARPN J Eng Appl Sci* 10(18):8141–8149
3. Wang Q, Sun DL, Na Y, Zhou Y, Han XL, Wang J (2011) Effects of TIG welding parameters on morphology and mechanical properties of welded joint of Ni-base superalloy. *Proc Eng* 10:37–41
4. Kumar A, Sundarajan S (2009) Optimization of pulsed TIG welding process parameters on mechanical properties of AA 5456 aluminium alloy weldments. *Mater Des* 30:1288–1297
5. Senthil Kumar T, Balasubramanian V, Sanavullah MY (2007) Influences of pulsed current tungsten inert gas welding parameters on the tensile properties of AA 6061 aluminium alloy. *Mater Des* 28:2080–2092
6. Dhinakaran V, Shanmugam NS, Sankaranarayanan K (2017) Experimental investigation and numerical simulation of weld bead geometry and temperature distribution during plasma arc welding of thin Ti-6Al-4V sheets. *J Strain Anal Eng Des* 52(1):30–44
7. Dhinakaran V, Shanmugam NS, Sankaranarayanan K (2017) Some studies on temperature field during plasma arc welding of thin titanium alloy sheets using parabolic Gaussian heat source model. *Proc Inst Mech Eng Part C J Mech Eng Sci* 231(4):695–711

Influence of Flux Coating During Dissimilar Welding of Copper with Brass Using ATIG Welding Process



J. Durga Venkata Satyanarayana, Raghuraman Srinivasan, Venkatraman Ramamoorthi, Sivachidambaram Pichumani and B. Kamesh Srikar

Abstract Dissimilar joints between copper and brass are performed using TIG/AC-ATIG/DC-ATIG. There is a reduction in mechanical strength of the weldment while TIG welding of copper and brass. To overcome these challenges, activated TIG (ATIG) welding has been used. Here, DC current straight polarity DCEN has been used for improved weld penetration through higher heat input to weldment for better strength. It is also inferred that the usage of Al_2O_3 with active flux in ATIG is not suitable because of inert behavior which in turn hinders the heat flow during the process. During DC current straight polarity DCEN welding results in reduced mechanical properties than the AC current welding due to the formation of coarse columnar grain structure observed in the weldment. AC-ATIG with SiO_2 and TiO_2 fluxes, the intermediate dendritic grain structures are observed in the weld zone.

Keywords ATIG welding process · Dissimilar welding · Microstructures

1 Introduction

Welding is the way of joining two pieces of metals with or without using filler rods. At that point, two sections are to be combined with each other and result in developing the metallic bond between two metals by applying heat/pressure/both. Increasing the need for higher production rates and higher quality, the industries are fully mechanized and automated welding technologies are introduced in the welding field [1]. The automation is being introduced in the welding technologies is impress greatly and end of the century the more of automated machines in the welding manufacturing units are established. Moreover, the computers are playing a huge role, and through the use of automation in welding technologies, the automation machines

J. Durga Venkata Satyanarayana · R. Srinivasan (✉) · V. Ramamoorthi · S. Pichumani · B. Kamesh Srikar
School of Mechanical Engineering, SASTRA Deemed University, Thanjavur 613401, Tamil Nadu, India
e-mail: raghu@mech.sastra.edu

© Springer Nature Singapore Pte Ltd. 2019
S. S. Hiremath et al. (eds.), *Advances in Manufacturing Technology*,
Lecture Notes in Mechanical Engineering,
https://doi.org/10.1007/978-981-13-6374-0_12

are run by the computer instructions and computers are run by the programs [2]. Automation and the use of computers in welding result in the manufacturing of quality weld components. TIG welding process is also called the gas tungsten arc welding; it is suitable for the welding of the thin section. The TIG welding is widely used in the nonferrous metals like aluminum, copper, magnesium, and copper alloys. In TIG welding the weld can be created by the non-consumable electrode, the electrode and weld area are protected from the atmosphere contamination and oxidation using the shielding gas like argon or helium [3]. Generally, TIG welding process filler rods are used and in some situation like autogenous welding process do not require filler rods. The TIG welding process is almost slower process compared to other welding techniques, like plasma welding and laser welding techniques. TIG welding is an electric arc welding process in which the fusion energy is produced by an electric arc between the workpiece and the tungsten electrode. During the welding process, the electrode, the arc, and the weld pool are protected against the damaging effects of the atmospheric air by an inert shielding gas [4]. Activated flux TIG welding is a unique joining process, invented at Paton Institute of Electric Welding in 1960. ATIG welding process is also referred to as flux zoned TIG (FZTIG). Active flux is coated on the surface of the joint before performing welding facilitating deep penetration [5]. The table shows the variety of activated fluxes which are utilized in TIG welding to enhance the weld penetration. The flux is mixed with a binder (sodium silicate) and a solvent (acetone or methanol). This binds the flux paste on the metal surface the proper execution of coated layer. The weld penetration in ATIG process is doubled to that of the traditional TIG welding process [6]. The microstructure, shape, and mechanical properties of the weld are also improved when welded by this technique. Most of the copper and other materials like Al, Br, Ti, Mg, and stainless steels are welded by using resistance spot welding and electron beam welding [7]. Improve the mechanical properties of the structural application. From the literature survey, the research work of dissimilar weld joints on copper and brass are not addressed in this study attempt has been made by welding copper and brass using ATIG welding process. To achieve high penetration and weld depth using different fluxes Performing dissimilar welding on copper and brass using ATIG welding process using different process parameters and analyzing the mechanical properties. The main objective of this work is performing dissimilar welding on copper–brass by using ATIG welding process using different active fluxes and currents (AC and DC) through analyzing the microstructure of the weldments. Copper and brass are used as the base material, copper is chemical element available in nature, the atomic number of copper is 29, and atomic mass is 63. The copper is soft and ductile material, it is high-thermal conductivity material, and the pure copper is reddish orange in color. The brass is the alloy of copper; it is made up of copper and zinc [8]. By varying the percentage of zinc and copper in brass alloys leads to change in mechanical and electrical properties.

2 Methodologies

ATIG welding process is performed on copper and brass metals with a plate thickness of 6 mm as shown in Fig. 1, by using ADOR CHAMPTIG 300AD welding machine. Figure 2 shows the sequence of operations. The weldments are shown in Fig. 3. The flowchart shows the sequence of operations that are performed during the work. The process parameters used in an ATIG welding are shown in Table 1. Here, the powders like SiO_2 , Al_2O_3 , TiO_2 are used with both AC and DC currents to Performing dissimilar welding on copper and brass and microstructure of the weldments are analyzed. The standard metallographic method was used for capturing the microstructure of weldment. Microstructures are observed in different magnification ranges, utilizing high transmission trinocular metallurgical magnifying lens in KYOWA-ME-LUX 2.

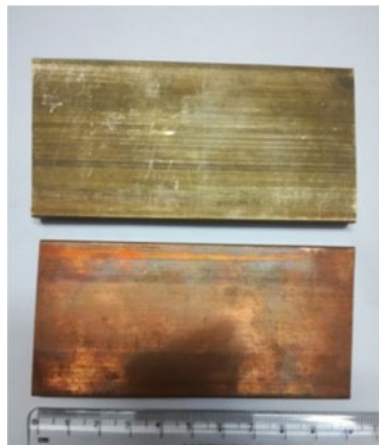


Fig. 1 Base metals

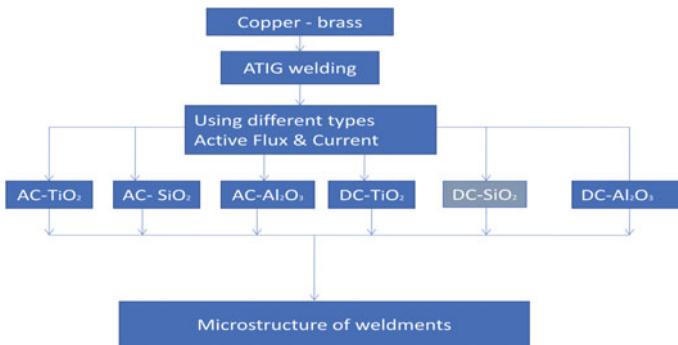


Fig. 2 Sequence of operations

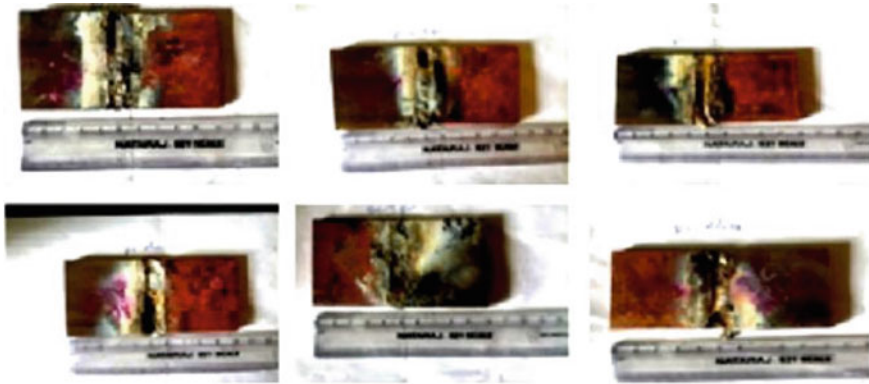


Fig. 3 Welded samples

Table 1 ATIG welding process parameters

S. No.	Parameters	Values
1	Weld current	240 A
2	Welding speed	2 mm/s
3	Gas flow rate	20 L/min
4	Gas flow pressure	1 kg/cm ²
5	Electrode diameter	4 mm
6	Nozzle size	8 mm
7	Electrode type	2% thoriated tungsten
8	Flux coating effect	1 mg/cm ²
9	Types of fluxes used	TiO ₂ , SiO ₂ , Al ₂ O ₃

3 Results and Discussions

3.1 Microstructure Analysis

The microstructures of AC-TIG, DC-TIG AC-ATIG-SiO₂, AC-ATIG-Al₂O₃, AC-ATIG-TiO₂, DC-ATIG-SiO₂, DC-ATIG-Al₂O₃, and DC-ATIG-TiO₂ are observed. Here, microstructure analysis is carried out using high transmission trinocular metallurgical microscope, KYOWA-ME-LUX 2. The fine dendritic grain structure is obtained during AC welding with TiO₂ flux and the coarse dendritic structures are obtained during AC welding with SiO₂ fluxes, the coarse columnar structure obtained during DC welding with Al₂O₃ flux. Figures 4 and 5 show the material microstructure for copper and brass base materials.

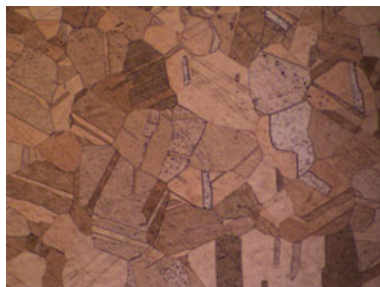


Fig. 4 Copper base material microstructure

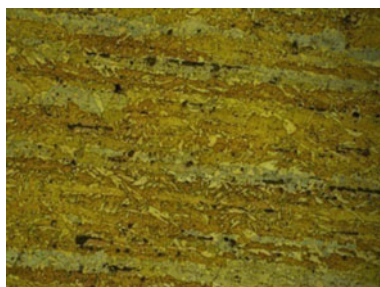


Fig. 5 Brass base material microstructure

3.2 DC-TIG

Base Metal: Micrograph shows the uniform fine grain structure for brass and copper materials.

HAZ: Micrograph shows the fine dendritic pattern in the brass side (right) and coarse grain structure in the copper side (left).

Weld Zone: Micrograph shows the non-uniform distribution of fine dendritic pattern.

3.3 AC-TIG

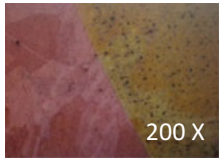

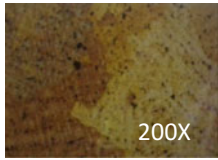
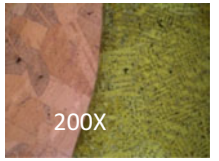
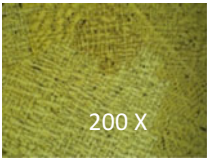
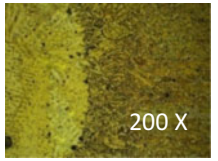
Base Metal: Micrograph shows uniform fine grain structure for brass and copper base material.

HAZ: Micrograph shows the fine dendritic pattern (right) and coarse grain structure (left).

Weld Zone: Micrograph shows the presence of the coarse columnar pattern.

Table 2 shows the microstructural images of DC-TIG welding.

Table 2 Microstructure images of TIG welding

S. No.	Sample	HAZ	Weld zone	HAZ
1	DC-TIG			
2	AC-TIG			

3.4 Effect of TiO₂ on ATIG Welding

The fine dendritic grain structure is obtained during AC welding with TiO₂ flux. Fine grain structure is obtained at heat-affected zone in brass and coarse grain structure at the heat-affected zone in copper. Due to fine dendritic grain structure, the tensile strength of the weldment was improved. The AC-ATIG-TiO₂ shows fine dendritic structure compared to DC-ATIG-TiO₂, and the hardness of the weld zone of DC-ATIG-TiO₂ is higher compared to AC-ATIG-TiO₂.

Table 3 shows the microstructural images of AC-ATIG welding of TiO₂.

Table 3 Microstructure images of TiO₂ flux



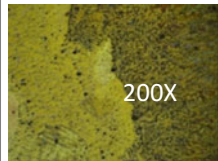
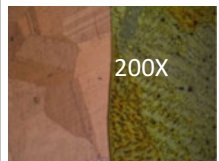


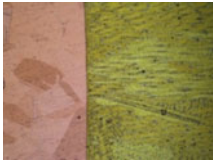
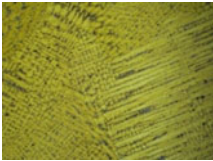
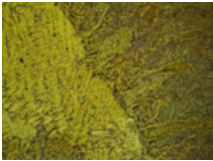
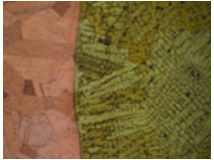
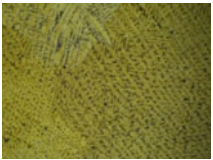
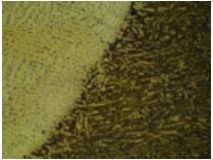
S. No.	Sample	HAZ	Weld zone	HAZ
1	AC-TiO ₂			
2.	DC-TiO ₂			

Table 4 Microstructure images of SiO₂ flux

S. No.	Sample	HAZ	Weld zone	HAZ
1	AC-SiO ₂			
2.	DC-SiO ₂			

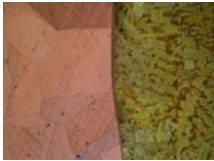
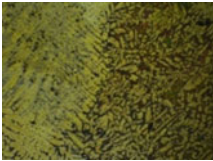
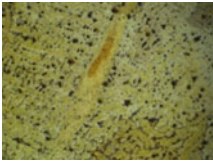
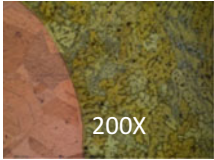
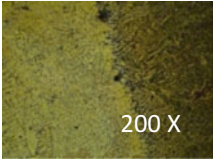
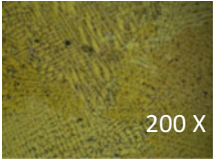
3.5 Effect of SiO₂ on ATIG Welding

The coarse dendritic structure is obtained during AC welding with SiO₂ flux. The coarse dendritic structure is obtained at heat-affected zone in brass and coarse grain structure at the heat-affected zone in copper. Due to coarse dendritic grain structure, the tensile strength of the weldment was improved. The AC-ATIG-SiO₂ shows coarse dendritic structure compared to DC-ATIG-SiO₂, and the hardness of the weld zone of DC-ATIG-SiO₂ is higher compared to AC-ATIG-SiO₂. Table 4 shows the microstructural images of AC-ATIG welding SiO₂.

3.6 Effect of Al₂O₃ on ATIG Welding

The coarse columnar structure is obtained during AC welding with Al₂O₃ flux. The coarse columnar structure is obtained at the heat-affected zone in brass and coarse columnar structure at the heat-affected zone in copper. Due to coarse columnar structure, the tensile strength of the weldment was improved. The AC-ATIG-Al₂O₃ shows coarse columnar structure compared to DC-ATIG-Al₂O₃, and the hardness of the weld zone of DC-ATIG-Al₂O₃ is higher compared to AC-ATIG-Al₂O₃. Table 5 shows the microstructural images of AC-ATIG welding of Al₂O₃.

Table 5 Microstructure images of Al₂O₃ flux

S. No.	Sample	HAZ	Weld zone	HAZ
1	AC-Al ₂ O ₃			
2.	DC-Al ₂ O ₃			

4 Conclusions

The ATIG welding is the advancement process in the TIG welding. Due to the presence of a thin layer of activating flux in ATIG welding, the weld penetration increased; thereby, the heat input and also the number of passes were reduced. Dissimilar weld joints on the nonferrous materials resulted in improved strength in the weldment using ATIG. ATIG on dissimilar welding of copper and brass has a tendency to improve the weld strength and weld penetration. Autogenous ATIG welding was performed on copper and brass material with a plate thickness of 6 mm. Here, active fluxes were used like SiO₂, Al₂O₃, and TiO₂ with both AC and DC. AC-ATIG welding with SiO₂ and TiO₂ fluxes shows intermediate dendritic grain structure, and DC-ATIG welding with Al₂O₃ flux shows coarse columnar structure at the weldments.

References

1. Zhou L, Luo LY, Tan CW, Li ZY, Song XG, Zhao HY, Huang YX, Feng JC (2018) Effect of welding speed on microstructural evolution and mechanical properties of laser welded-brazed Al/brass dissimilar joints. *Optics Laser Technol* 98:234–246
2. Gao Y, Nakata K, Nagatsuka K, Matsuyama T, Shibata Y, Amano M (2016) Microstructures and mechanical properties of friction stir welded brass/steel dissimilar lap joints at various welding speed. *Mater Des* 90:1018–1025
3. Luo J, Xiang J, Liu D, Li F, Xue K (2012) Radial friction welding interface between brass and high carbon steel. *J Mater Process Technol* 212:385–392
4. Li L, Xia H, Tan C, Mac N (2018) Effect of groove shape on laser welding-brazing Al to steel. *J Mater Process Tech* 252:573–581
5. Guo S, Zhou Q, Peng Y, Xu X, Diao C, Kong J, Luo TY, Wang KH, Zhu J (2017) Study on strengthening mechanism of Ti/Cu electron beam welding. *Mater Des* 121:51–60
6. Singh AK, Dey V, Rai RN (2017) Techniques to improve weld penetration in TIG welding (a review). *Mater Today Proc* 4:1252–1259

7. Arivazhagan B, Vasudevan M (2015) Studies on A-TIG welding of 2.25Cr-1Mo (P22) steel. *J Manuf Process* 18:55–59
8. Devendranath Ramkumar K, Siva Goutham P, Sai Radhakrishna V, Tiwari A, Anirudh S (2016) Studies on the structure-property relationships and corrosion behavior of the activated flux TIG welding of UNS S32750. *J Manuf Process* 23:231–241

Innovative Nitride Film Deposition on Copper Interconnects of MEMS Devices Using Plasma-Enhanced Chemical Vapor Deposition Techniques



T. Jagadeesha and Louis Kim

Abstract Advances in integrated circuit fabrication technology over the past two decades have resulted in integrated circuits with smaller device dimensions, larger area, and complexity. As the device size shrinks, process integration gets more complicated and interaction between the layers becomes very important. In this work, the silicon nitride layer is deposited on test wafers with different percentage of NH_3 to study the effect of NH_3 on film profile like step coverage and conformity. A stack of 5000 Å oxide was deposited on test wafers with low and H hydrogen nitride to study the effect of Cu diffusion and adhesion properties of nitride layer. The deposited wafers were etched to calculate the etch rate and etch rate dependence on hydrogen content. Furthermore, the low pressure CVD (LPCVD) process is used to deposit the nitride layer, and characteristics of low nitride with LPCVD layers are done using SEM analysis. Low H nitride developed in this work gives excellent copper diffusion resistance. Low H nitride gives good adhesion to the FSG layer. Low-H nitride film increases etch selectivity up to 30%. In addition, it also provides a larger process window for trench and via etching. In situ process developed in this work gives the highest productivity.

Keywords PMD · CVD · Passivation layer · Low H nitride · PMD nitride · Micro-fabrication

1 Introduction

Silicon nitride has been widely used in microelectronic device fabrication for many interconnect applications such as final passivation and mechanical protective layers for underlying circuits [1, 2], diffusion barriers against mobile ions and moisture

T. Jagadeesha (✉)
National Institute of Technology, Calicut, Kerala, India
e-mail: jagdishg@nitc.ac.in

L. Kim
Chartered Semiconductor Manufacturing, Woodlands Industrial Park, Singapore, Singapore

© Springer Nature Singapore Pte Ltd. 2019
S. S. Hiremath et al. (eds.), *Advances in Manufacturing Technology*,
Lecture Notes in Mechanical Engineering,
https://doi.org/10.1007/978-981-13-6374-0_13

[1, 2], in addition to anti-reflective coatings [3, 4], stop layers for both etch and chemical mechanical polishing (CMP) processes [5–7], and protective films against copper oxidation and diffusion. The most common method to deposit silicon nitride film for interconnect application is the plasma-enhanced chemical vapor deposition (CVD) method. However, plasma-enhanced CVD silicon nitride film is known to be non-stoichiometric and contains a substantial amount of hydrogen [1, 2] and in some cases, a small amount of oxygen [8, 9, 10]. The high hydrogen content results in a film that is actually $\text{Si}_x\text{N}_y\text{H}_z$ instead of Si_xN_y . This substantial amount of hydrogen can degrade the device performance if the hydrogen migrates to the Si– SiO_2 interface in devices, thus creating interface states [11–13]. In addition, the hydrogen also degrades the film characteristics, for example lower film density, higher etch rate, and lower thermal stability [1, 2]. Recently, a new method has been used to deposit silicon nitride [14]. This new method, high-density plasma CVD (HDP-CVD) has been used previously to deposit high-quality silicon dioxide films.

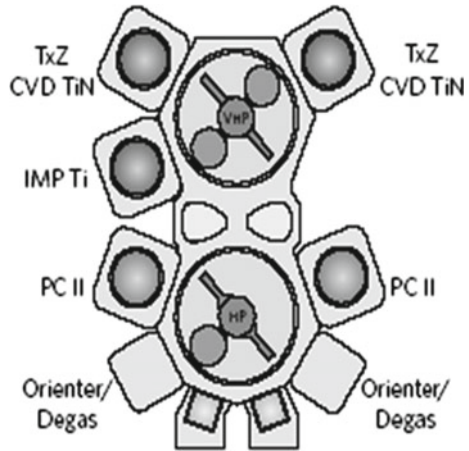
2 Experiment

Applied materials high-performance physical vapor deposition (HP PVD) tool is used for thin film deposition. Schematic configuration of HP PVD is shown in Fig. 1. Process chamber (PC) II pre-clean chamber provides in situ removal of residue and prevents native oxide re-growth, enabling excellent film adhesion and resistance performance. PC chamber utilizes dual radio frequency (RF) sources that independently control the plasma and sputter energies, minimizing plasma damage while maintaining high removal rates. PC also features an enhanced process kit to avoid accumulation of by-products at the wafer edge and a fan-cooled resonator for efficient thermal management to prevent re-deposition flaking. Advanced electrostatic capacitance (ESC) technology enables temperature control and stress modulations for the successful integration of interconnect metals.

In this work, the silicon nitride layer is deposited on 60 wafers with different percentage of NH_3 to study the effect of NH_3 on film profile like step coverage and conformity.

A stack of 5000 Å oxide was deposited on test wafers with low and H hydrogen nitride to study the effect of Cu diffusion. Nitride layer is also deposited on FSG layer to study the adhesion properties of nitride layer. The deposited wafers were etched to calculate the etch rate and etch rate dependence on hydrogen content. Furthermore, the low pressure CVD (LPCVD) process is used to deposit the nitride layer, and characteristics of low nitride with LPCVD layers are done using SEM analysis. Integrity test for both standard LPCVD and low H nitride was carried out to examine the sidewall quality.

Fig. 1 Tool configuration of applied materials HP PVD



3 Results and Discussion

Silicon nitride is usually used as the final passivation layer because it is a very good barrier material for moisture and mobile ions. Since nitride has a larger dielectric constant, $k \geq 7.0$, than oxide, it is not used for inter-metallic dielectric (IMD) gap fill but rather as a barrier layer. High-temperature nitride is used specifically at the PMD level, primarily as an etch stop layer. Due to the action of the plasma and the low temperature, the deposited film always contains large amounts of hydrogen. Hydrogen level in nitrides is proven to be correlated with device aging. Higher hydrogen content implies faster device aging. Firstly, the effect of NH_3 on step coverage and mechanism of the reaction was studied. Series of experiments were conducted with a variable amount of NH_3 , and results are shown in Fig. 2. NH_3 forms weak hydrogen bonds and physisorbs on the wafer surface without any need for plasma dissociation, thus improving step coverage as well as deposition rate. By contrast, N_2 with very strong bond energy has to be atomized by electron impact dissociation in order to engage in the deposition process. This leads to chemisorptions of N atoms on the wafer surface. The result is a low deposition rate, poor step coverage, but low hydrogen impurity content.

A stack of 5000 Å oxide was deposited on test wafers followed by TaN deposition and copper and nitride as shown in Fig. 3.

SIMS analysis was carried out on these stacks, and results are shown in Fig. 4. It can be observed that copper diffusion is very less in low H nitride.

A stack of fluorinated silicon glass (FSG) and low-H nitride stack was prepared as shown in Fig. 5 to study the H and F interactions.

Cross section of both low and high H contents nitride surfaces was studied, and results are shown in Fig. 6.

It is clear from Fig. 6a that low nitride process produces a very clean surface. When the hydrogen content was increased by 20%, wafer surfaces are observed with

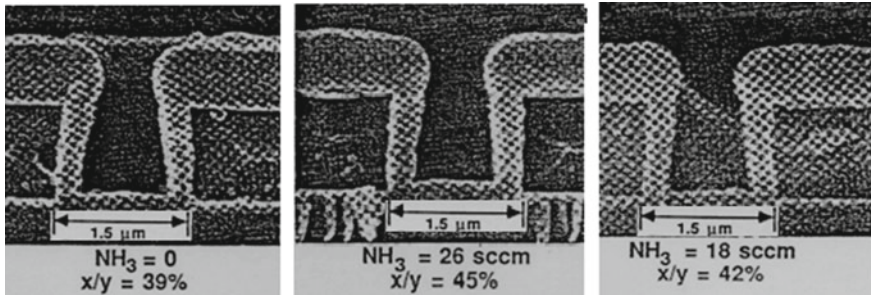


Fig. 2 Effect of NH₃ on step coverage

Fig. 3 Deposition on test wafers

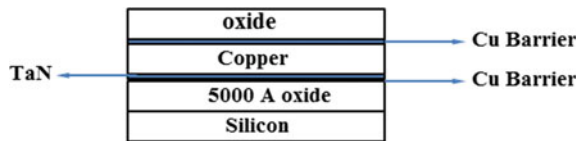


Fig. 4 SIMS analysis of oxide, nitride, and copper stacks

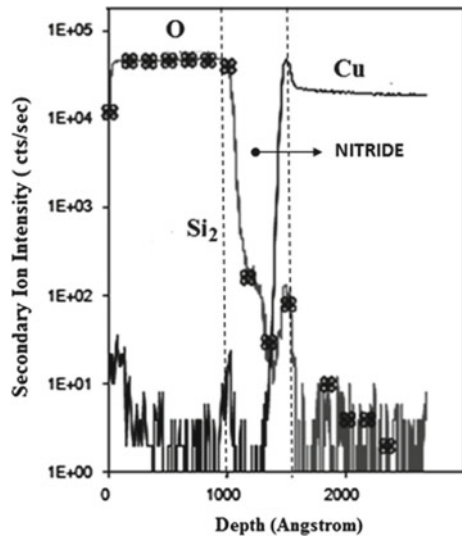
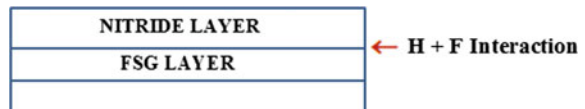


Fig. 5 FSG and low nitride stack deposition



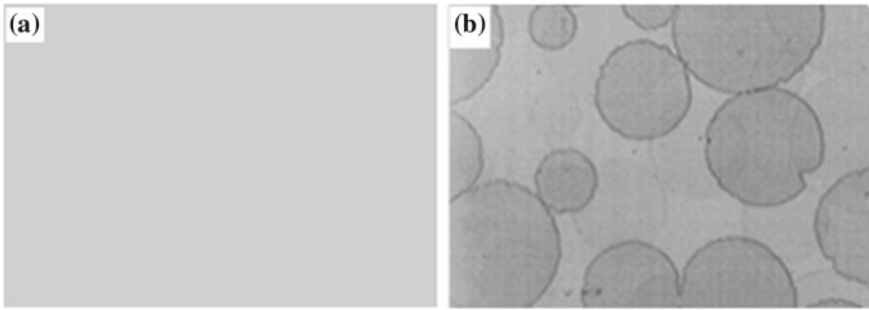


Fig. 6 a Low hydrogen nitride (9% H, RI = 1.94) b high hydrogen nitride (>20% H and RI = 2)

Fig. 7 Dependence of etch selectivity on hydrogen content of nitride

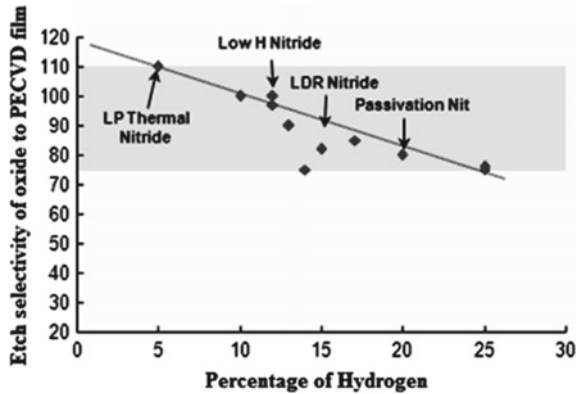


Table 1 Etch selectivity on hydrogen content of nitride for various etch chemistries

Etch rate (Å/min)	SiN	H SiN	% reduction
50 Ar diluent	497	364	27
50 C ₂ F ₆ trench/via main etch	3376	3039	10
50 CF ₆ trench/via main etch	6072	4264	30
30 C ₄ F ₈ trench/via main etch	322	260	20
15 C ₄ F ₈ trench/via main etch	1233	1098	11
15 CHF ₃ nitride	2244	2034	10
8C ₄ F ₈ /8O ₂ /150 CO over etch stop on nitride	1515	1105	27

patch marks on the wafers. Thus, we can conclude that low H nitrides give good adhesion to the previously deposited layer.

Several experiments were conducted to know the etch selectivity dependence on the effect of hydrogen content in the nitride layer. Results are shown in Fig. 7 and Table 1.

It is clear from both Fig. 6 and Table 1 that low-H nitride film increases etch selectivity up to 30% and provides a larger process window for trench and via etching.

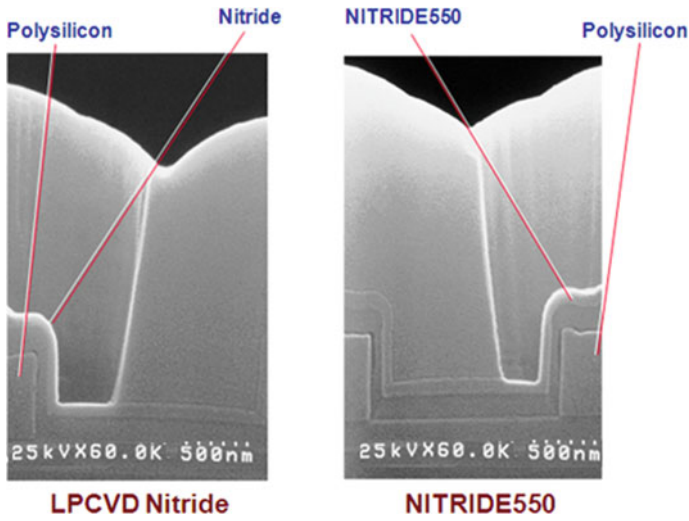


Fig. 8 SEM pictures of LPCVD nitride and nitride 550

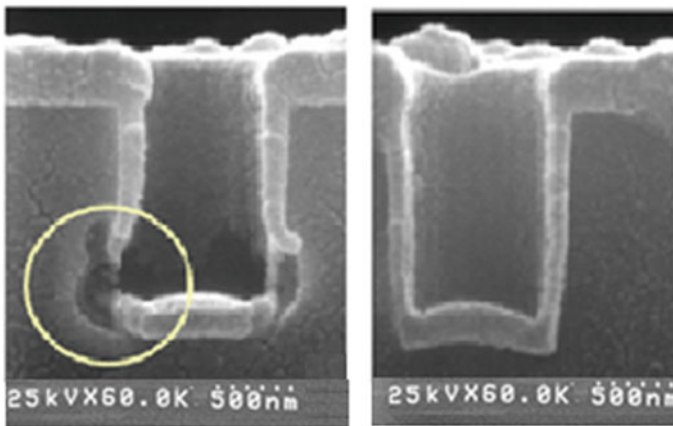


Fig. 9 SEM pictures of sidewall quality for LPCVD and nitride processes

It is also found that in situ removal of copper oxide and simultaneous deposition of nitride gives the highest productivity.

Several experiments were carried out to qualify and compare the process with the existing PECVD nitride process. Figure 8 shows SEM pictures of LPCVD nitride and low-H nitride process. It is observed that low H nitride (nitride 550) offers excellent etch stop performance.

Improved sidewall quality can also be achieved using nitride 550 layers. Results are shown in Fig. 9. High-temperature nitride layer improves film integrity.

4 Conclusions

In this work, the silicon nitride layer is deposited on test wafers with different percentage of NH_3 to study the effect of NH_3 on film profile like step coverage and conformity.

A stack of 5000 Å oxide was deposited on test wafers with low and H hydrogen nitride to study the effect of Cu diffusion. Nitride layer is also deposited on the FSG layer to study the adhesion properties of nitride layer. The deposited wafers were etched to calculate the etch rate and etch rate dependence on hydrogen content. Furthermore, the low pressure CVD (LPCVD) process is used to deposit the nitride layer, and characteristics of low nitride with LPCVD layers are done using SEM analysis. Integrity test for both standard LPCVD and low H nitride was carried out to examine the sidewall quality.

Low H nitride developed in this work gives excellent copper diffusion resistance. Low H nitride gives good adhesion to the FSG layer. Low-H nitride film increases etch selectivity up to 30%. In addition, it also provides a larger process window for trench and via etching. In situ process developed in this work gives the highest productivity.

In this work, it has been shown that nitride 550 can also be used for the PMD layer. It is enabling technology for $<0.18 \mu\text{m}$ devices. Use of nitride layer as PMD is demonstrated for borderless contact etches stop layer applications, and SEM data prove that it has excellent etches stop performance. Low H nitride is superior to conventional passivation nitride, and it is comparable to furnace nitride.

References

1. Wolf S, Tauber R (1986) Silicon processing for VLSI era, 2nd edn. Lattice, SA
2. Sze S (1988) VLSI technology, 1st edn. McGraw Hill, New York
3. Winderbaum S (2000) A comparative study on inductively-coupled plasma high-density plasma, plasma-enhanced and low pressure chemical vapor deposition silicon nitride films. *J Vac Sci Technol A* 18:372–375
4. Bhushan S, Sundrajan S (1998) Micro/nanoscale friction and wear mechanisms of thin films using atomic force and friction force microscopy. *Metal Acta* 46:3793–3804
5. Sankaran A, Kushner MJ (2004) Integrated feature scale modeling of plasma processing of porous and solid SiO_2 . I. Fluorocarbon etching. *J Vac Sci Technol A* 22:1242
6. Rueger NR, Doemling MF (1999) Selective etching of SiO_2 over polycrystalline silicon using CHF_3 in an inductively coupled plasma reactor. *J Vac Sci Technol A* 17:2492
7. Yota J (2000) A comparative study on inductively-coupled plasma high-density plasma, plasma-enhanced, and low pressure chemical vapor deposition silicon nitride films. *J Vac Sci Technol A* 18:372
8. Ross CA (1999) Fabrication of patterned media for high density magnetic storage. *J Vac Sci Technol* 17:3168
9. Flemish JR, Pfeffer RL (1993) Low hydrogen content silicon nitride films from electron cyclotron resonance plasmas. *J Appl Phys* 74:3277
10. Lapeyrade M, Besland MP (1999) Silicon nitride thin films deposited by electron cyclotron resonance plasma-enhanced chemical vapor deposition. *J Vac Sci Technol A* 17:433

11. Martin N, Rousselot C (1999) Instabilities of the reactive sputtering process involving one metallic target and two reactive gases. *J Vac Sci Technol A* 17:2869
12. Tiron V, Velicu I-L, Pana I, Cristea D, Rusu BG, Dinca P, Porosnicu C, Grigore E, Munteanu D, Tascu S (2018) HiPIMS deposition of silicon nitride for solar cell. *Surf Coat Technol* 344:197–203
13. Rai DK, Solanki CS, Balasubramaniam RK (2017) Growth of silicon nitride by nitridation of amorphous silicon at low temperature in hot-wire CVD. *Mater Sci Semiconductor Process* 67:46–54
14. Dasmahapatra A, Kroll P (2018) Modeling amorphous silicon nitride: a comparative study of empirical potentials. *Comput Mater Sci* 148:165–175

Sleep Detection and Alert System for Automobiles



T. Babu, S. Ashwin, Mukul Naidu, C. Muthukumaaran
and C. Ravi Raghavan

Abstract Driver sleep detection is a car safety technology which helps to prevent accidents when the driver gets drowsy. Various studies have suggested that around 20% of road accidents are fatigue related. A sleep alarm is used in a vehicle for detecting the condition indicative of the onset of sleepiness of a driver and for alerting the driver. An eye blink sensor is used to keep track of the driver's eyelid motion. If the predefined safety conditions are not met, then the driver is alerted by producing an alarming sound from the inbuilt car speakers primarily. Secondly, a vibrating device is incorporated within the driver's seat which activates when the conditions are not satisfied. Taking into account of the worst case scenario, that is, if the driver does not respond to any of these alarms then, using the proximity sensors, the obstacles around the vehicle is detected, and the brakes are automatically applied gradually.

Keywords Sleep detection · Eye blink · Drowsy · Driver · Eyelid

1 Introduction

A sleep detection and driver alert apparatus has a compact housing that can be placed in any automobile. It contains an eye blink sensor for monitoring the effects of early impending sleep by means of a microprocessor. This will alert the driver in case the system detects drowsiness while the vehicle is moving, in case the driver does not respond to the alert mechanisms, then the brakes are actuated to stop the vehicle in order to avoid a collision. This can take place due to sleepiness or any medical emergency of the driver. Thus, the main objective of this paper is to avoid fatal accidents. In this paper, we used the Arduino board as a major part to interact with sensors and actuators. Kusuma Kumari BM [1] discussed the non-intrusive method for detecting the drowsiness of the driver using webcam by getting a video image of the driver's mouth and eyes with the help of image processing techniques.

T. Babu (✉) · S. Ashwin · M. Naidu · C. Muthukumaaran · C. Ravi Raghavan
Department of Mechanical Engineering, Sri Sai Ram Engineering College, Chennai, India
e-mail: babu.prabu@gmail.com

© Springer Nature Singapore Pte Ltd. 2019
S. S. Hiremath et al. (eds.), *Advances in Manufacturing Technology*,
Lecture Notes in Mechanical Engineering,
https://doi.org/10.1007/978-981-13-6374-0_14

Choudhary [2] used state of eyes and position of irises that was monitored with the inputs like frequency of eye blink and duration of eye closing. Template matching technic is used to match the open and close of eyes of the driver with the drowsy conditions. One of the important conditions of drowsiness is yawn. To find this condition, the mouth opening range and contour area of the mouth were tracked. Bhavya and Alice Josephine [3] used two-way approach for measuring changes of brain waves, eye blinking and heart rate by physiological signals. Using this method, the changes in driver's head position, sagging movement and state of the eyes were measured. Sontakke [4] used an algorithm called a modified ADA-Boost algorithm to detect the signs of driver's fatigue and symptoms of weariness. The detected symptoms were sent as a message to the control room by the image processing method. The symptoms were compared with the images in video and using human features. Bergasa [5] monitored the driver's vigilance where non-intrusive prototype computer system was used. It captured the image of the driver using IR illuminator, and software is used to monitor the visual behaviours of the driver's vigilance. Using this method, the duration of eye closing, percentage of eye close, the frequency of blinking, nodding frequency, fixed gaze and position of the face were calculated.

2 Part Description

The main components used in this paper are Arduino board, eye blink sensor, ultrasonic sensor, LCD display, buzzer, GSM device and pneumatic circuits. All the parts are connected with the Arduino board in order to receive and send signals.

2.1 *Eye Blink Sensor*

The eye is illuminated by an IR led, which is powered by the +5 V power supply, and the reflected light is recorded by an IR photodiode. This eye blink sensor is IR based; the variation across the eye will vary as per eye blink. The output mainly depends on the emitter and detectors positioning and aiming with respect to the eye. If the eye is closed, the output is high otherwise the output is low. This to know the eye is closing or opening position. This output signal is used as an input signal in the logic circuit to operate the alarm. This can be controlling the accident due to the unconsciousness of the driver.

2.2 *Buzzer*

It is connected with the Arduino board with 5 V DC supply. It operates under the current consumption of 9.0 mA maximum and having a sound frequency of 85 dB min.

2.3 Ultrasonic Sensor

This ultrasonic sensor is used to detect the obstacles and sends the signal to the Arduino board in order to actuate the pneumatic circuit for applying the break. The transmitter in the sensor emits an ultrasonic wave in one direction when there is no response from the driver. If any obstacles are found the receiver receives the signal which depends upon the distance of the obstacle.

2.4 GSM Device

GSM device used in this work is used to send a message to the stored mobile number about the driver's current position. The message will be sent once the break is applied using the pneumatic circuit.

2.5 LCD Display

LCD display used in this is to show the timing for the sensors to activate and the distance between the ultrasonic sensor and the obstacle. A 2 * 16 LCD display displays the required information.

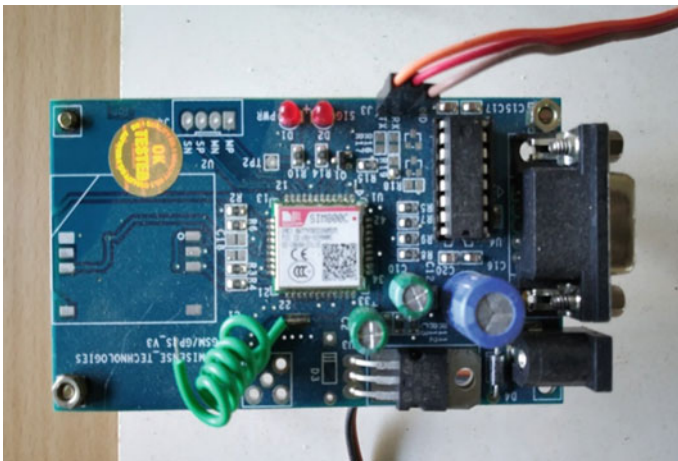


Fig. 1 Arduino board

2.6 Arduino Board

Arduino is used as open-source hardware, and it is used to design and manufacture kits like microcontrollers for digital projects and interactive objects that can sense and control objects in the physical world. It is a simple platform for beginners to do basic mechatronics-based projects. Arduino boards are available in an assembled form for commercial purpose (Fig. 1).

3 Working

When the driver is driving the vehicle, the eye blink sensor will sense the movement of the driver's eye. It sends a signal whenever the eye is closed for more than a specified time and starts the timer. If the eye blinking of the driver stops, the sensor sends a signal to the Arduino board and it activates the alarm and vibrator at the same time within the 2 s of signal received (Fig. 2).

If the driver does not wake up and is still in his fatigue condition, the ultrasonic sensor that is connected with the vehicle will be activated. It senses obstacles around the vehicle and gives a signal to the Arduino board. The signal from the ultrasonic sensor will contain data such as the distance of the obstacle from the vehicle. If there is an obstacle within a certain distance of the vehicle, a signal is sent to the solenoid

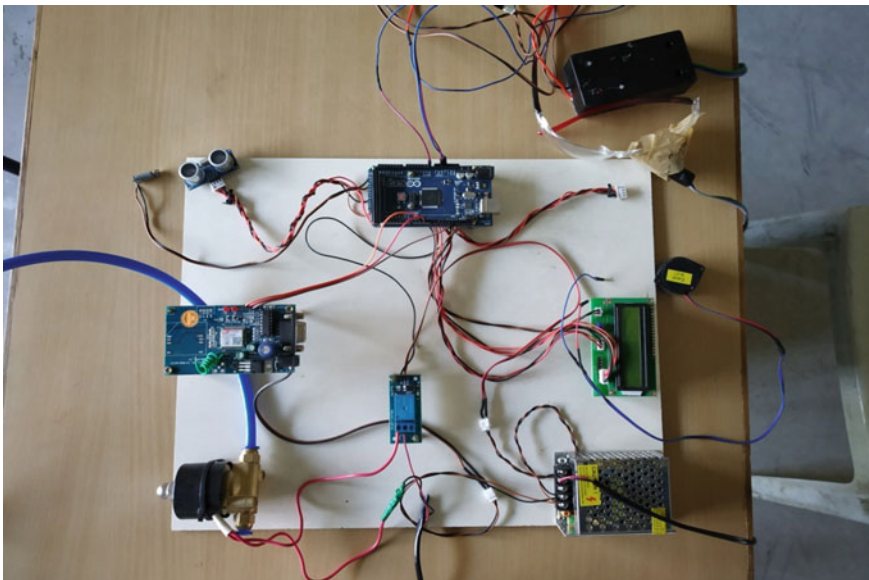


Fig. 2 Sleep detection device set-up

valve that actuates the pneumatic braking circuit. The pneumatic circuit contains a simple pneumatic cylinder coupled to the brake lever of the vehicle to actuate brake gradually in order to stop the vehicle. Once the vehicle is stopped, the signal from the Arduino board send to the GSM device which will send the message to the default stored mobile number containing the location of the vehicle where it is stopped.

4 Sample Coding

```
#include <SoftwareSerial.h>
void ShowSerialData();
SoftwareSerial mySerial(2, 3);
#include <LiquidCrystal.h> //includes the LiquidCrystal Library
LiquidCrystal lcd(9, 8, 7, 6, 5, 4);
const int trigPin = 31;
const int echoPin = 33;
const int trigPin1 = 35;
const int echoPin1 = 37;
long duration;
int distanceCm, distanceInch;
long duration1;
int distanceCm1, distanceInch1;
int outputValue0 = 0;
int outputValue1 = 0;
int k;
int sol = 13;
```

5 Conclusion

This project would have a bright future in the field where more safety enchantments are made electro-mechanically in the automotive sector. It could be successfully applicable to lorries, trucks and other vehicles that are being used to travel at night. Using this set-up, we can easily detect the fatigue of the driver and can prevent the accidents due to fatigue of the driver. Video camera can be replaced instead of the eye blink sensor for better results. For the demonstration of this work, the eye blink sensor is placed in front of the spectacles. A pneumatic circuit is used for applying brakes. Pneumatic circuits can be replaced by hydraulic one for smoother performance. Depending upon the category of the vehicle, we can change the components for better results. More concentrated research in this field could help upgrade technologies that could reduce the accidents caused by the ignorance of the drivers around 80%.

References

1. Kusuma Kumari BM (2014) A real time driver drowsiness detection system. *Int J Comput Appl* 32–34
2. Choudhary P, Sharma R, Singh G, Das S (2016) A survey paper on drowsiness detection & alarm system for drivers. *Int Res J Eng Technol* 1433–1437
3. Bhavya B, Alice Josephine R (2013) Intel-eye: an innovative system for accident detection (a two-way approach in eye gaze analysis). *Int J Comput Commun Eng* 2(2):189–193
4. Sontakke KM (2015) Efficient driver fatigue detection and alerting system. *Int J Sci Res Publ* 5(7):1–4
5. Bergasa LM (2006) Real time system for monitoring driver vigilance, *IEEE Trans Intell Transp Syst* 7(1):63–77
6. Ghimire D, Jeong S, Yoon S, Park S, Choi J (2015) Real-time sleepiness detection for driver state monitoring system. *Adv Sci Technol Lett* 120:1–8
7. Victoreia G, Yazhini D, Parameswari G, Gurumoorthi E, Vijayarathy G (2014) Driver fatigue monitoring system using eye closure. *Int J Mod Eng Res* 4(11):26–31
8. Fuletra JD, Bosamiya D (2014) A survey on driver's drowsiness detection techniques. *Int J Recent Innov Trends Comput Commun* 1(11):816–819
9. Garg EMVEA (2012) Detection and security system for drowsy driver by using artificial neural network techniques. *Int J Appl Sci Adv Technol* 1(1):39–43
10. Saini R, Saini V (2014) Driver drowsiness detection system and techniques: a review. *Int J Comput Sci Inf Technol* 5(3):4245–4249
11. Jayanthi D, Bommy M (2012) Vision-based real-time driver fatigue detection system for efficient vehicle control. *Int J Eng Adv Technol* 2(1):238–242
12. Malla AM, Davidson PR, Bones PJ, Green R, Jones RD (2010) Automated video based measurement of eye closure for detecting behavioural microsleep

Numerical Analysis and Design Optimization of Lip Seal Opening Pressure for Automotive Valves



T. Sukumar, B. R. Ramesh Babu, B. Durga Prasad and B. R. Vijay Prithiv

Abstract An approach for analyzing and optimizing seal opening pressure of a valve used in automotive application is presented. The seal is made up of Chloroprene rubber with hardness of 70 IRHD. Mooney–Rivlin hyperelastic material model is used to predict the behavior of the seal. The Chloroprene rubber is modeled as an incomparable hyperelasticity material under an assumption of isotropic flow. The behavior of the seal purely depends on the geometry, interference between the seal and housing and also hardness of the seal. The seal opening pressure is optimized by changing the geometry of the seal, and the interference between the seal and housing. In this paper, the existing seal is analyzed with the help of numerical analysis called finite element method. Finally, the optimized seal is manufactured and validated experimentally. The optimized seal met the required seal opening pressure of less than 0.125 MPa.

Keywords Hyperelastic material · Material models · Finite element analysis · Optimized seal · Opening pressure

Abbreviations

FEA Finite element analysis
IRHD International rubber hardness degrees

T. Sukumar (✉) · B. Durga Prasad
Department of Mechanical Engineering, JNT University, Anantapur, India
e-mail: thiru_sukumar@yahoo.com

B. R. Ramesh Babu
Department of Mechanical Engineering, Chennai Institute of Technology, Chennai, India

B. R. Vijay Prithiv
IntelliSense Software, Lynnfield, MA 01940, USA

© Springer Nature Singapore Pte Ltd. 2019
S. S. Hiremath et al. (eds.), *Advances in Manufacturing Technology*,
Lecture Notes in Mechanical Engineering,
https://doi.org/10.1007/978-981-13-6374-0_15

1 Introduction

Seals are playing a vital role in automotive applications to seal the pneumatic and hydraulic fluids. The seal has to open and release fluid whenever it is required. Another important requirement is that it should not leak during operating conditions to achieve the required performance of the system. Sukumar et al. [1–4] analyzed hyperelastic material numerically and experimentally for sealing elements like O-rings and seals with different hardness. Belforte et al. [5] investigated the performance of the pneumatic valves which depend on the type of rubber material, surface roughness, and geometry dimensions. Calvert et al. [6], Belforte et al. [7], and Lee et al. [8] re-designed and optimized the seal geometry using numerical analysis and verified experimentally. These studies are carried out in nominal mounting conditions and tolerances without considering the contact pressure.

The study is focused on designing a new seal from an existing one installed on automotive valve. In this particular application, the primary requirement of the seal is to open at minimum pressure, so as to avoid the back pressure inside the valve. If the pressure is tapped or increased, the system will not meet the automotive safety regulation. The seal design optimization process is divided into two stages. In the first stage, an existing seal is investigated to understand the elastic strain and contact pressure distribution on the seal. In the second stage, the cross section of seal is optimized to minimize the opening pressure. The seal design was analyzed and optimized using numerical method (finite element method).

2 Geometry and Function of the Seal

In commercial vehicle air braking system, the automotive valve shown in Fig. 1 is used to distribute the air from air dryer to front axle, rear axle brakes and to auxiliary applications like suspension system, door operating system, and clutch operation.

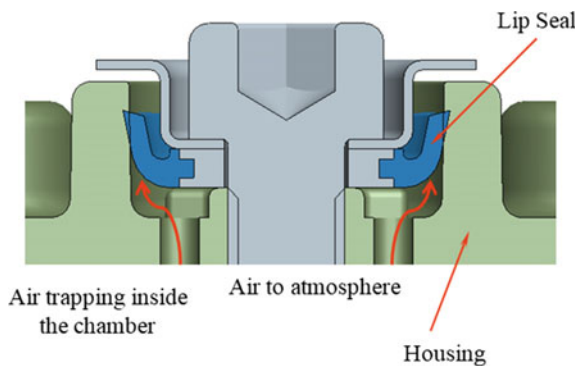


Fig. 1 Typical valve assembly with lip seal

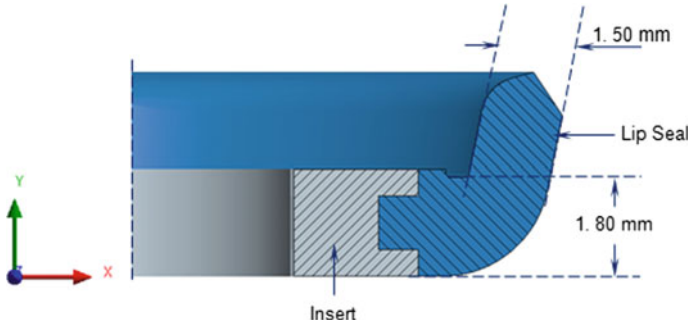


Fig. 2 Seal with existing design

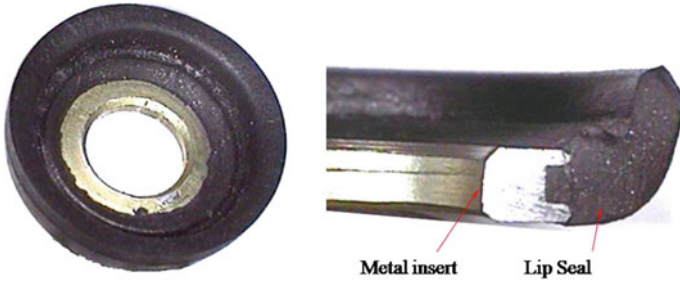


Fig. 3 Actual seal with initial design

Therefore, the valve is a safety device, whose functions should meet the regulatory requirements as per IS 11852 [9].

The seal studied in this research is a commercial seal designed for maintaining the opening pressure of <0.125 MPa. Figure 2 shows the cross-sectional 3D model of the assembly, and Fig. 3 shows the actual lip seal developed with cut section. In the assembly, the seal is clamped with a metal insert for an interference fit of 0.3 mm in tangential direction and 0.05 mm in axial (Y) direction.

3 Generation of Material Data

To study the behavior of seal using finite element analysis, exact material properties are required. The material properties of the Chloroprene rubber are obtained from the uniaxial tensile test machine. Dump-bell specimen was prepared for the Chloroprene rubber material as shown in Fig. 4 with hardness of 70 IRHD (International Rubber Degree Hardness), as per the ISO 37 specification [10]. An uniaxial tensile testing machine is used to generate the stress-strain data as per ASTM 412 D test standard and with strain rate of 500 mm/min. The generated data is input to the finite element

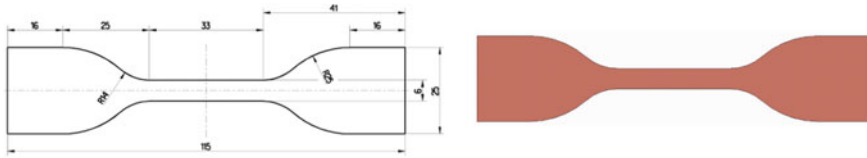


Fig. 4 Dumb-bell test specimen

analysis software to generate the material constants using Mooney–Rivlin material model.

The Chloroprene rubber can be well represented by the strain energy function according to the Mooney–Rivlin equation. In this analysis, Mooney–Rivlin two-parameter material model is used to predict the material constants C_{10} and C_{01} . The material model value is 0.18 and 0.66 MPa, respectively.

4 Finite Element Model

Finite element model of the seal and housing is shown in Fig. 5. The model was built using ANSYS in order to evaluate the seal performance under the operating conditions. The seal and housing arrangements are modeled using PLANE 182 four-node elements, TARGET 169 and CONTA 172 elements are used to simulate contact between the seal and the housing. The housing and metal insert are represented by rigid elements, indicating that there are no deformations compared with the initial shape. The analysis conditions are listed in Table 1.

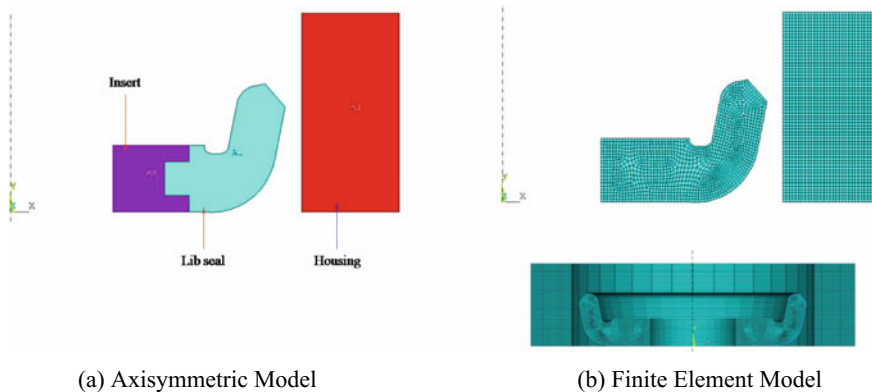


Fig. 5 Finite element model details

Table 1 Analysis conditions are divided into two kinds

Case A	Assembly of seal in housing: to study the effect of assembly interference between seal and housing
Case B	Study the effect of fluid pressure

Case A: It is achieved by movement of housing against the seal in the radial direction by a distance equal to 1.0 mm in order to establish the nominal condition with interference.

Case B: It is represented by a constant load per unit length on the outer edge of the seal. Loads are applied incrementally, which is helpful to converge the solution without much difficulty. Frictional contact is established between the seal and housing surface and the friction co-efficient (μ) of 0.15 considered for this analysis.

5 Seal Analysis Results

Finite element analysis is performed to study the behavior of seal at assembly and working conditions. The analysis results are plotted in Figs. 6 and 7 for case A. The mesh areas represent the un-deformed shape of seal before applying load conditions and solid planes indicate the new shape of seal after deformation.

Figure 7 demonstrates the contact pressure distribution at the seal and housing interface. It can be seen that the contact pressure at the central portion is very high but decreases very sharply at two sides of the seal. It clearly shows that the pressure distribution is highly non-homogenous. Also, the maximum contact pressure at the assembled condition is high when compared with the fluid pressure (0.265 MPa),

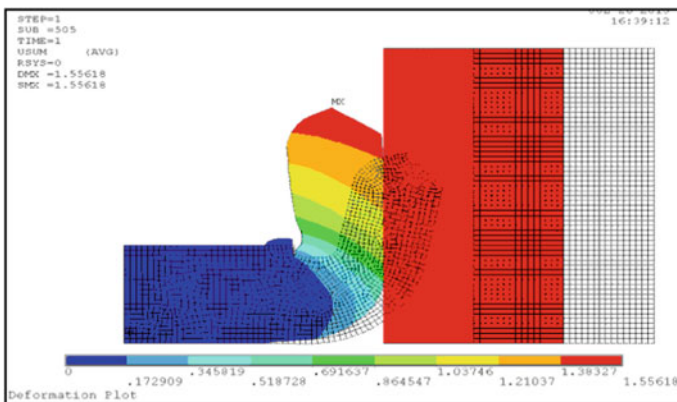


Fig. 6 Deformation due to assembly interference

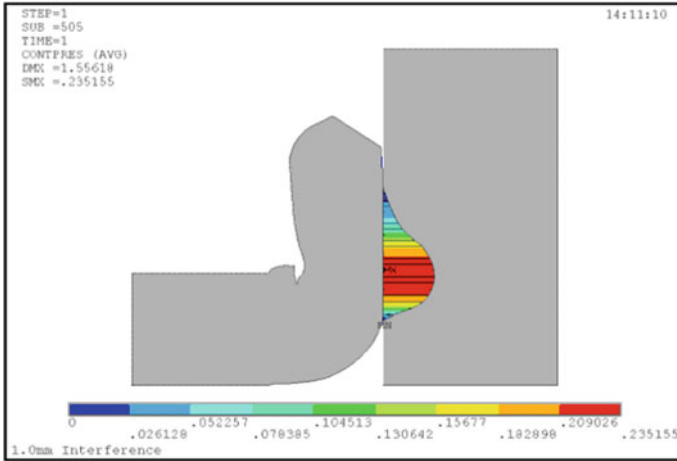


Fig. 7 Contact pressure for the assembly interference

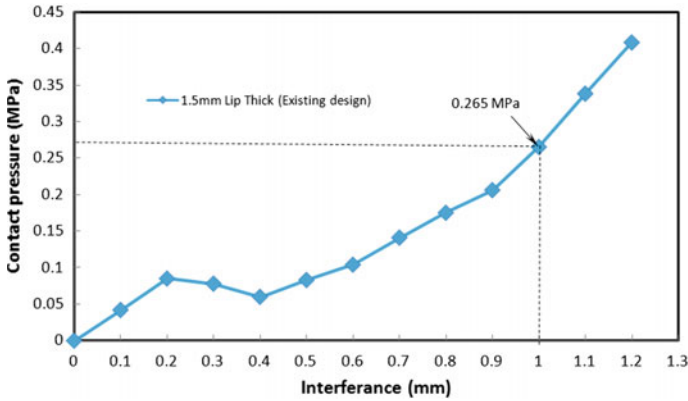


Fig. 8 Assembly interference corresponding to the contact pressure

which means that the pressure required to open the seal is very high and easily wears by means of friction.

Figure 8 shows the interference vs. contact pressure between the seal and housing. For 1.0 mm interference of the seal, contact pressure of 0.265 MPa is obtained. Hence, the pressure required to open the seal is >0.265 MPa which is very high when compared to the required opening pressure of 0.125 MPa.

6 Seal Design Optimization

In order to minimize the contact pressure to meet the design requirements, the lip seal design has to be optimized. In this regard, the existing seal analysis results are considered for reference. The analysis result demonstrates that the existing cross section has high stiffness and the pressure required to open the seal is 0.265 MPa, which is higher than the required specification of 0.125 MPa. Due to high stiffness of the seal, there is possibility for air pressure to get trapped inside. If the pressure is in valve spring chamber, the opposing force against the valve opening will increase. If the opening pressure of valve exceeds the governor cutout pressure, and when the driver releases the parking brake, there will be no air pressure for the brake, leading to accidents.

To meet the regulation, it is decided to optimize the seal design in terms of opening pressure and durability. Also, the contact pressure distribution at the seal interface with housing should be uniform to avoid the seal wear and damage. Hence, the new proposal should meet the two requirements.

- a. the maximum contact pressure should be <0.125 MPa
- b. the contact pressure should be uniform.

Two new seal designs are proposed for design optimization considering the interference and contact pressure. The difference between these two models and original (initial) model is that the seal profiles are different. A schematic view of them is depicted in Fig. 9, and Table 2 gives optimized seal parameters for the existing and the proposed designs. Parameter A represents the lip thickness, and parameter B represents root thickness of the lip seal.

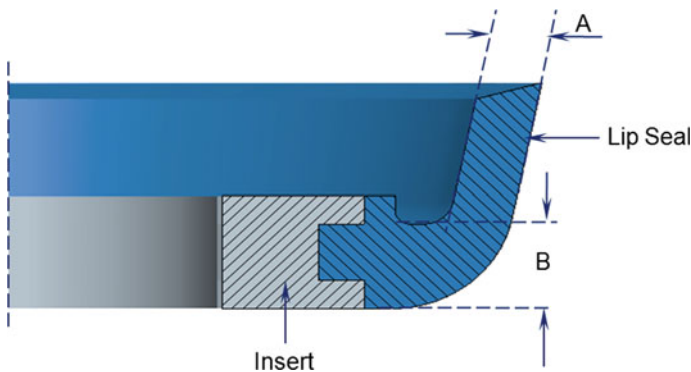


Fig. 9 Seal design parameters

Table 2 Optimization of seal parameters

Configuration	Parameter	Dimension (mm)
Initial design	A	1.50
	B	1.80
Proposal-1	A	1.25
	B	1.60
Proposal-2	A	1.00
	B	1.50

6.1 Optimization of Seal Parameters

Figure 10 shows the deflection of seal due to the interference of 1.0 mm between the lip and the housing. Figure 11 shows the contact pressure distribution between lip and housing. The contact pressure is maximum at the middle and gradually reduces toward the lip end.

Figure 12 shows the effect of seal profile and interference (between seal and the housing) due to contact pressure. The graph shows clearly that the increase in the lip thickness and interference will result in increase in the contact pressure. This is due to the reason that the stiffness of the existing lip seal is comparatively high. Hence, the pressure required to open the seal is higher than specification (0.125 MPa). Whereas, the optimized seal (proposal-2) has lower contact pressure with the interference of 1.0 mm. Hence, the proposal-2 design with interference of 1.0 mm is preferable.

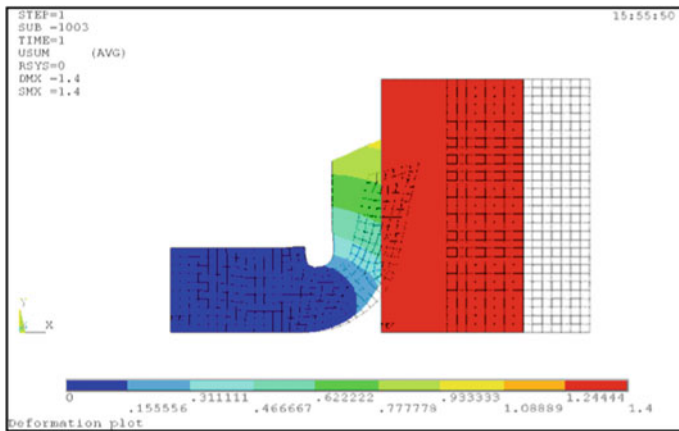


Fig. 10 Deformation plot

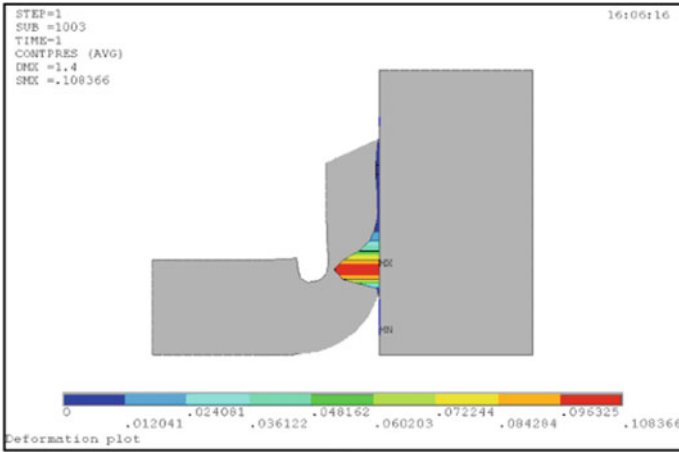


Fig. 11 Contact pressure

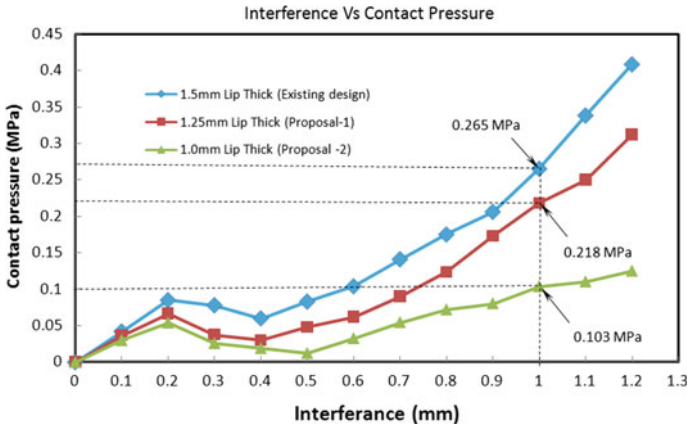


Fig. 12 Effect of seal profile and interference

7 Experimental Validation

The optimized lip seal has been developed with lip thickness of 1.0 m and root thickness of 1.5 mm as shown in Fig. 13. The results are verified experimentally and compared with the original seal design. Figure 14 shows the comparison between the existing (original) seal and optimized seal designs. For example, at twentieth actuation, the tapping pressure inside the system protection valve is very less (0.8 bar) when compared with the lip seal in original design (2.6 bar).

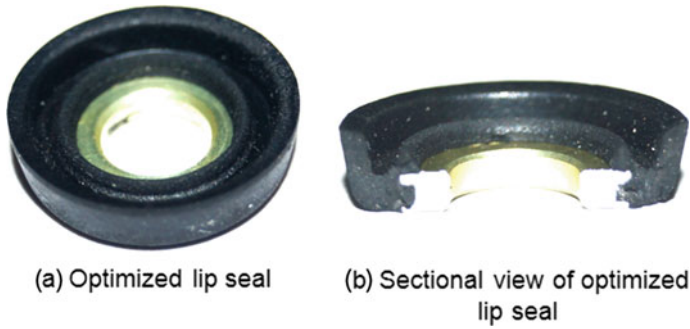


Fig. 13 Optimized lip seal

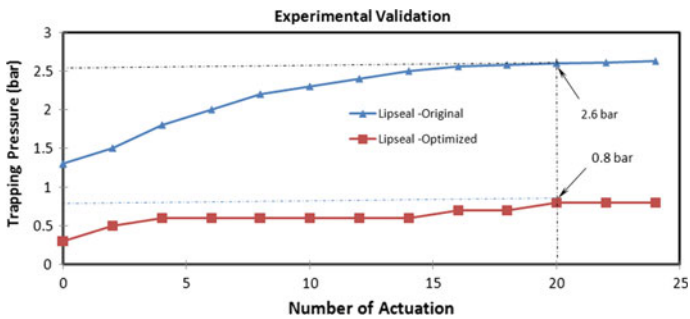


Fig. 14 Experimental result comparison

8 Conclusions

In this paper, the existing lip seal design was modeled and analyzed with help of finite element tool (ANSYS) and seal opening pressure was determined. Similarly, a new lip seal geometry was proposed by optimizing the seal parameters based on the existing seal analysis results. The optimized seal has two advantages when compared with initial design:

- First, the optimized seal design reduces the contact pressure while working under loading conditions, unlike the existing seal producing excessive pressure.
- Secondly, the optimized seal having uniform distribution of contact pressure.

The optimized seal design was validated experimentally and met the design requirements.

References

1. Sukumar T, Ramesh Babu BR, Durgaprasad B (2018) Determination of sealing pressure in hyperelastic O-ring with different hardness using numerical method. *J Elastomers Plast.* <https://doi.org/10.1177/0095244318817889>
2. Sukumar T, Ramesh Babu BR, Durgaprasad B (2018) Numerical and experimental evaluation of hyperelastic material parameters. *Advances in materials and metallurgy. Lecture notes in mechanical engineering.* Springer, Singapore. https://doi.org/10.1007/978-981-13-1780-4_47
3. Sukumar T, Ramesh Babu BR, Durgaprasad B (2018) An analysis of hyperelastic material models. *Int J Mech Prod Eng Res Dev (IJMPERD)* 8(7):1220–1229. ISSN (P): 2249–6890; ISSN (E): 2249-8001
4. Sukumar T, Subramanian M, Subramanian S, Subramanian N (2015) Design and optimization of lip seal for air braking system. SAE Technical paper 2015-26-0215. <https://doi.org/10.4271/2015-26-0215>
5. Belforte G, Conte M, Manuello A, Mazza L (2011) Performance and behavior of seals for pneumatic spool valves. *Tribol Trans* 54:237–246. Copyright: Society of Tribologist and Lubrication Engineers. ISSN: 1040-2004 Print/1547-397X online. <https://doi.org/10.1080/10402004.2010.538488>
6. Calvert C, Tirovic M, Solarski T (2002) Design and development of an elastomer-based pneumatic seal using finite element analysis. *Proc Inst Mech Engineers, Part J: J Eng Tribol* 26(3):127–138
7. Belforte G, Manuello A, Mazza L (2006) Optimization of the cross section of an elastomeric seal for pneumatic cylinders. *J Tribol* 128:406–413
8. Lee KO, Hur YM, Kang JH, Kang SS (2007) Performance estimation of dust wipers for hydraulic cylinders and optimization of geometric design variables. *J Mater Process Technol* 187–188:215–219
9. *Automotive Vehicles—Brakes and Braking system.* IS 11852, Part 3:2001
10. *Rubber, Vulcanized or Thermo plastics—Determination of Stress-Strain Properties.* ISO 37 Fifth Edition-2011

Mechanical and Microstructural Properties of Multi-Axially Forged LM6 Aluminium Alloy



Sudheer S. Sajjan, Mithun V. Kulkarni, S. Ramesh, P. C. Sharath, R. Rajesh and Vasantha Kumar

Abstract In the present investigation, commercially available light metal aluminium LM6 alloy was processed by Multi-axial forging (MAF) at ambient temperature. MAF was carried out to an equivalent strain in 0.83, 1.66 and 2.4 i.e., 6 passes, 12 passes and 18 passes, respectively. The mechanical properties like tensile test, compression test, hardness and microstructural characterization were studied in processed and unprocessed samples. Ultimate tensile strength (UTS) and ductility improved from 137 to 185 MPa and 3 to 6.2% for as-received to processed samples, respectively. After 18 passes of MAF, the compression strength (CS) has improved from 342 to 530 MPa. Hardness increased as the number of forging passes increases as compared to unprocessed samples. Optical microscopy images were used to study microstructure observations, the average grain size is reduced from 60 to 2 μm for as-received to processed samples, respectively. Strength and hardness increased because of the grain refinement for the processed samples and the introduction of the high amount of dislocation density into the material during the MAF process. Fracture study was conducted by utilizing scanning electron microscopy, dimples on tensile fracture surfaces revealed that ductile mode of fracture.

Keywords LM6 aluminium alloy · Multi-axial forging (MAF) · Microstructure

S. S. Sajjan (✉) · V. Kumar
Bearys Institute of Technology, Mangalore, India
e-mail: sudheersajjan1989@gmail.com

M. V. Kulkarni
Vijaya Vittala Institute of Technology, Bangalore, India

S. Ramesh
National Institute of Technology Karnataka, Surathkal, India

P. C. Sharath
Department of Metallurgical Engineering, Jain University, Bengaluru, India

R. Rajesh
Global Academy of Technology, Bangalore, India

1 Introduction

In the present days, attention will be focused on the fabrication of (UFG) metal through the severe plastic deformation (SPD) [1]. Different types of techniques will be available and the most encouraging methods will be the equal channel angular pressing in this process, the area will remain constant without introducing residual porosity (ECAP) [2–4], other techniques are high-pressure torsion (HPT) [5–7] and accumulative roll bonding (ARB) [8–10]. The restricted utility of the above strategies is because of design complexities and high tooling cost (ECAP), difficult to create bulk materials (HPT) and dreary handling techniques (ARB). In any case, these techniques are exceptionally famous as it empowers significant grain refinement in the system to deliver thermally stable ultrafine/nanostructured grain morphology with upgraded mechanical properties, which are not helpful in the traditional handling strategies [11, 12]. Among these above-mentioned processes, one of the SPD techniques is multi-axial forging also known as multi-directional forging (MDF) developed in the year 1990, aluminium, copper alloys have been converted so far to UFG material by using these techniques [13]. Refinement by SPD is based on the formation of dislocation cell or sub-grains during large plastic strains and evolution of these cells in an array of ultrafine grains separated by high-angle boundary [2]. Mg, Al-Mg, Al-6061, Al, Mg-7GD-5Y-1ND-0.5Zr alloy, Az61 Mg alloy have been processed by MAF to refine the microstructure and also to improve the mechanical properties like tensile strength, hardness [14–19]. In the current investigation, LM6 Aluminium alloys are choice of selection because this alloy exhibits high corrosion resistance and excellent castability. It is most appropriate for engine housing and substantial castings. Limited work is carried on the LM6 Aluminium alloys for MAF. The present work concentrates on mechanical properties and microstructural characterization of as-received and MAF processed alloy.

2 Experimental Procedure

The received LM6 aluminium alloy was in the form of ingot shape of $35 \times 500 \times 40 \text{ mm}^3$. The chemical composition of the alloy is Si—12.43 wt%, Fe—0.260 wt%, Cu—0.028 wt%, Mg—0.43 wt%, Ti—0.0058 wt%, remaining composition will be aluminium. Rectangular shapes with dimensions $30 \times 30 \times 25 \text{ mm}^3$ were cut from the as-received sample. Samples were MAF at ambient temperature for different number of passes utilizing a hydraulic press with capacity of 200 tonnages and with the pressing speed of 0.05 mm/s. The lubricant Molybdenum-di-sulphate (MoS_2) was used in between the die and specimen to reduce the friction. The process of MAF is shown in Fig. 1. In these techniques, material is processed by rotating the specimen in 90° for the every alternative passes like A-B-C, B-C-A and C-A-B with the configuration imposed the equivalent strain 0.18 during each pass [20]. The equivalent strain can be calculated by using the following equation $\ln(h_i/h_o)$

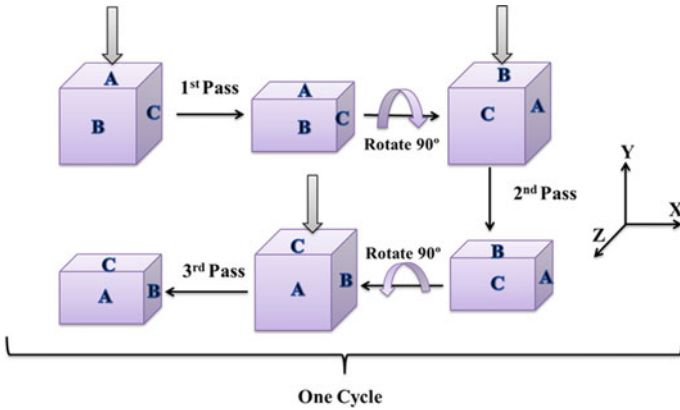


Fig. 1 Schematic representation of MAF process

where the h_i is the specimen initial height and h_o is the final height of the specimen respectively.

Vickers Hardness was measured with an average of seven measurements. Samples were cut and taken by perpendicular to the last forging axis. According to the ASTM E-8, standard tensile test specimen was prepared by considering dimensions as gauge length of 24 mm, gauge diameter of 6 mm and overall length as 55 mm. Tensile test was conducted utilizing the Shimadzu AG-X plusTM with a capacity of 100 kN at ambient temperature with strain rate of 0.5 mm/s. The ASTM E9-09 standard is used for preparing compression test specimen by fixing the length to diameter ratio of 1.25. Compression test was conducted using the Shimadzu AG-X plusTM with a capacity of 100 kN at ambient temperature at a strain rate of 0.5 mm/s. Optical microscopy will be used for investigating the microstructures of the samples and Nitol utilized as an etchant.

3 Results and Discussion

3.1 Microstructural Studies

The typical microstructure of the LM 6 Al alloy is shown in Fig. 2. The received alloy of a microstructure exhibits dendritic structure having an average grain size of 60 μm . It consists of Al-rich dendritic and Si particle distributed in the grain boundaries and interior. In the case of six passes processed sample, the grain size is decreased to about 15 μm , whereas the grain size is reduced to about 5 and 2 μm for the 12 passes and 18 passes sample, respectively. Si particle will be distributed on account of this process. After processing of six passes, the microstructure consists of quasi-equiaxed primary Al dendritic cells as shown in Fig. 2b. In case of higher

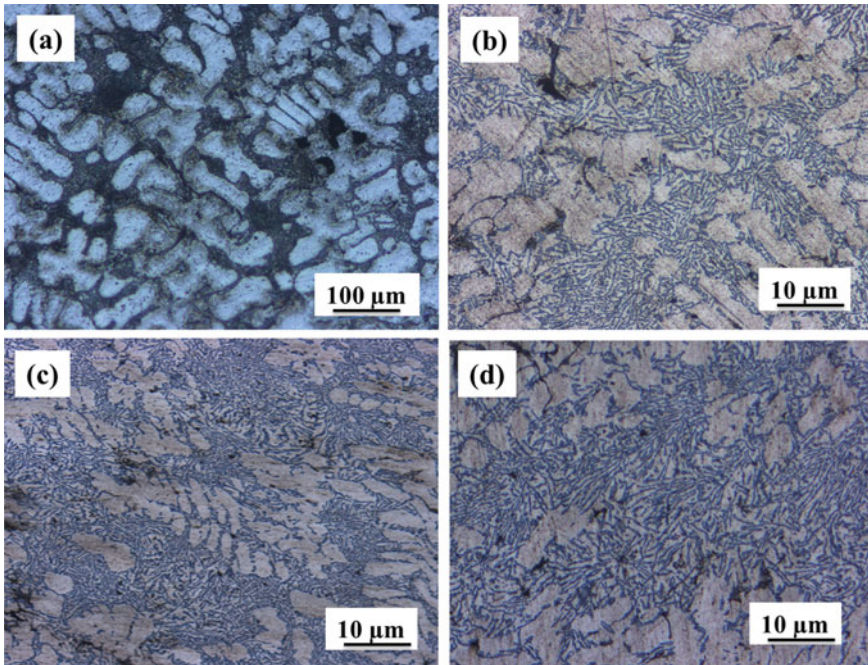


Fig. 2 Aspect of silicon particle in the Al-Si Specimen **a** received sample **b** MAF 6 pass **c** MAF 12 pass **d** MAF 18 pass

number of passes, the initial compression together with the progressive shearing of the primary Al dendrites and their size reduced continuously. It is apparent from the microstructure that particle size estimate and drops all together in the primary first pass of MAF. After that, there is just a minor decrease with extra pressings up to the greatest strain of 2.4. It was likewise finished up from the point-by-point assessment of the microstructure of Si which will be consistently distributed along the boundaries and within the matrix.

3.2 Mechanical Properties

(a) Tensile test

Figure 3 describes the typical engineering stress–strain curves for the received and processed alloy for different number of passes. Ultimate tensile strength 48 MPa and 3.2% of elongation increased significantly by comparing with as-received alloy. Initially received sample shown UTS of 137 MPa after processing it was increased to 185 MPa. Similarly, the percentage of elongation is also increased from 3% to the highest value of 6.2% for 18 passes for the processed sample. As-received sample

Fig. 3 Stress–strain curves for as-received and MAF processed tensile samples

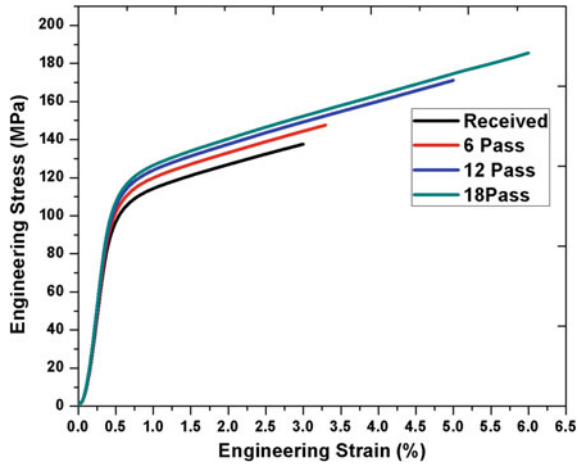


Table 1 Evaluation of grain size and mechanical properties for all the samples processed by MAF

No of MAF passes	UTS (MPa)	CS (MPa)	Hardness (VHN)	Avg. grain size (μm)
As-received	137	342	60	60
6 pass	147	413	72	15
12 pass	171	486	78	5
18 pass	185	530	86	2

shows tensile strength and ductility will be lower at room temperature because it consists of larger Al dendrites and large Si particles. Some of the casting defects like porosity or inter-dendritic micro-shrinkage may hinder the strength [21]. In case of processed sample, large Al dendrites were broken and casting defects were eliminated during the forging process. Grain size and morphology place an important role in materials properties. From Hall–Petch relation, it is shown that by diminishing the grain size, yield strength of the material can be improved [22]. MAF process reduces the grain size of the material also it is observed in the current study and presented in Fig. 2. It is the main reason for showing higher strength in the processed sample. Due to the morphological change of the Si particle made during the forging process ductility of the processed sample is improved.

(b) Vickers Hardness Test (VHN)

The hardness data are obtained based on the seven average measurements on the cross section of the samples. Hardness value has increased from 60 to 86 for unprocessed to processed sample for 18 numbers of passes as depicted in Table 1. The substantial increment in hardness can be credited to the impressive substructure of grain refinement which happens during intensive plastic deformation [23].

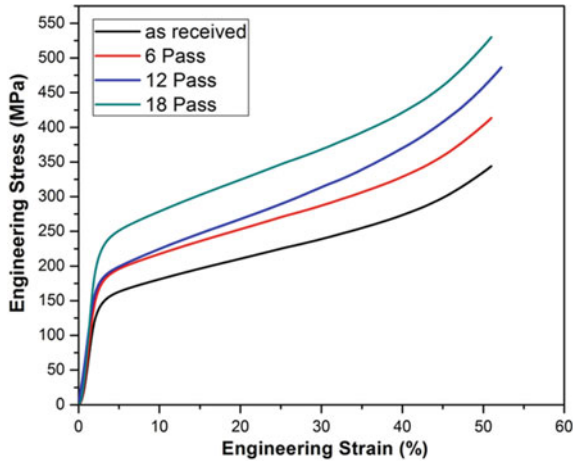


Fig. 4 Stress–strain curves for received and MAF processed compression samples

(c) Compression test

Compression testing was conducted for the samples taken through 6–18 passes of MAF. By examining, the compression strength of as-cast and the unpressed alloy was 342 MPa as shown in Fig. 4. It is obvious that the processing by MAF produces a huge increment in the strength of the alloy even after every alternative six passes. For $N = 6$ passes and strength 413 MPa and $N = 12$ passes and strength were 486 MPa for $N = 18$ passes and strength were 530 MPa with the strain rate of 0.5 mm/s. It is observed that for all the sample flow curves show work hardening. In this process, materials are subjected to MAF, which leads to the recovery during the initial stage. Those recovered material strain harden considerably during compression leading to higher compression strength values for MAF processed material similar type of behaviour has been observed for Zn-24Al Alloy [24].

(d) Fractography

The fracture surface of the tensile test specimens is shown in Fig. 5. To understand the specimen fracture surface area which was absorbed under the scanning electron microscope (SEM). Initially, the received tensile test specimen of the fracture surface was observed with large dimple size and the fractography is in typically ductile nature. As the number of passes increases from 6 passes to 18 passes, it is observed that dimple size keeps on reducing it. Dimple size occurring in the specimen during fracture due to the initiation of voids at the grain boundaries, it is reported in the literature by Padap et al. [25] in UFG pure titanium AIS 1016 STEEL.

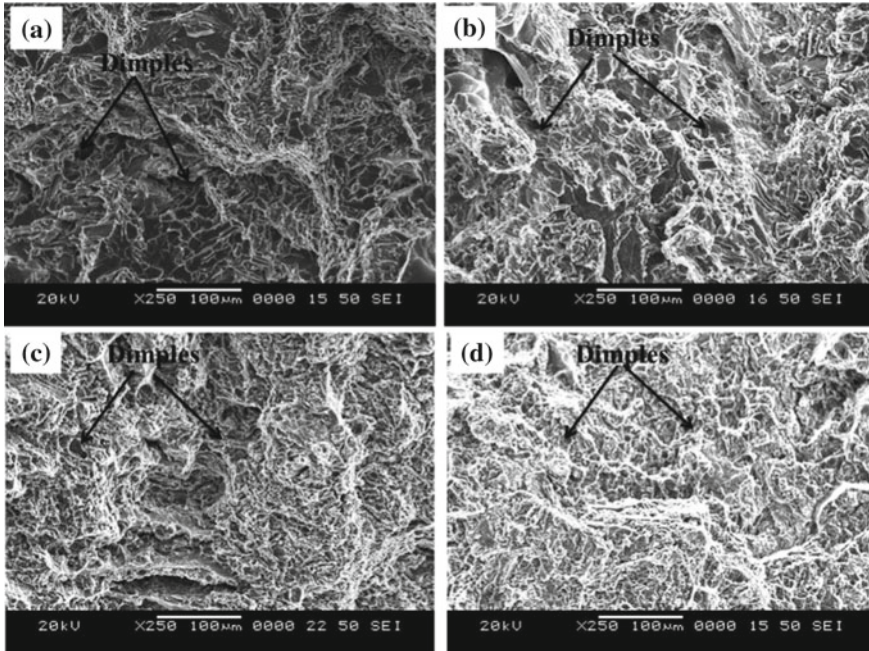


Fig. 5 SEM images of tensile fractured of as received and MAF processed **a** received **b** 6 pass **c** 12 pass **d** 18 pass

4 Conclusions

Multi-axial forging process on LM6 alloy at ambient temperature has been effectively done up to cumulative strain 0.83, 1.66 and 2.4. The following observations were recorded:

- Received material of the grain size is drastically reduced to 2 μm on the account of MAF processed sample for 18 passes from 60 μm .
- Increase in hardness value from 60 VHN to 86 VHN was observed for as-received materials to MAF processed sample for 18 passes, respectively. It is mainly due to the finer grain size and uniform distribution of secondary phase Si particles in the matrix.
- Increase in tensile strength and compression strength is due to breaking of Al-rich dendritic structure and elimination of casting defects. Flow curves exhibit a significant work hardening with further application of strain on the processed sample.
- Fractographic observation reveals many dimples in the processed sample which affects the ductility. Also, it is observed that dimple size is gradually decreased with increasing in imposing strain to the sample.

References

1. Venkateswarlu K, Das G, Pramanik AK, Xu C, Langdon TG (2006) Using ball-indentation to evaluate the properties of an ultra-fine grained Al–2% Si alloy processed by ECAP. *Mater Sci Eng A* 427(1–2):188–194. <https://doi.org/10.1016/j.msea.2006.04.053>
2. Raju KS, Krishna MG, Padmanabhan KA, Sarma VS, Gurao NP, Wilde G (2011) Microstructure evolution and hardness variation during annealing of equal channel angular pressed ultra-fine grained nickel subjected to 12 passes. *J Mater Sci* 46(8):2662–2671. <https://doi.org/10.1007/s10853-010-5122-Z>
3. Furukawa M, Horita Z, Nemoto M, Langdon TG (2002) The use of severe plastic deformation for microstructural control. *Mater Sci Eng A* 324(1–2):82–89. [https://doi.org/10.1016/s0921-5093\(01\)01288-6](https://doi.org/10.1016/s0921-5093(01)01288-6)
4. Vinogradov A, Ishida T, Kitagawa K, Kopylov VI (2005) Effect of strain path on structure and mechanical behavior of ultra-fine grain Cu–Cr alloy produced by ECAP. *Acta Mater* 53(8):2182–2192. <https://doi.org/10.1016/j.actamat.2005.01.046>
5. Liao XZ, Zhao YH, Zhu YT, Valiev RZ, Gunderov DV (2004) Grain-size effect on the deformation mechanisms of nanostructured copper processed by high-pressure torsion. *J Appl Phys* 96(1):636–640. <https://doi.org/10.1063/1.1757035>
6. Liao XZ, Zhao YH, Srinivasan SG, Zhu YT, Valiev RZ, Gunderov DV (2004) Deformation twinning in Nano crystalline copper at room temperature and low strain rate. *Appl Phys Lett* 84(4):592–594. <https://doi.org/10.1063/1.1644051>
7. Sabirov I, Pippin R (2005) Formation a nanostructure in a W-25% Cu during high pressure torsion. *Scripta Mater* 52:1293–1298
8. Kim HW, Kang SB, Tsuji N, Minamino Y (2005) Elongation increase in ultra-fine grained Al–Fe–Si alloy sheets. *Acta Mater* 53(6):1737–1749
9. Kamikawa N, Tsuji N, Huang X, Hansen N (2006) Quantification of annealed microstructures in ARB processed aluminum. *Acta Mater* 54(11):3055–3066
10. Roy S, Singh S, Suwas S, Kumar S, Chattopadhyay K (2011) Microstructure and texture evolution during accumulative roll bonding of aluminium alloy AA5086. *Mater Sci Eng* 528(29–30):8469–8478. <https://doi.org/10.1016/j.msea.2011.07.042>
11. Estrin Vinogradov A (2013) Extreme grain refinement by severe plastic deformation a wealth of challenging science. *Acta Mater* 61(3):782–817. <https://doi.org/10.1016/j.actamat.2012.10.38>
12. Lee SH, Saito Y, Sakai T, Utsunomiya H (2002) Microstructures and mechanical properties of 6061 aluminum alloy processed by accumulative roll-bonding. *Mater Sci Eng* 325(1–2):228–235. [https://doi.org/10.1016/s0921-5093\(01\)01416-2](https://doi.org/10.1016/s0921-5093(01)01416-2)
13. Sampath R, Nayaka HS, Gopi KR, Sahu S, Kuruveri UB (2018) Investigation of microstructure and mechanical properties of the Cu–3% Ti alloy processed by multiaxial cryo-forging. *J Mater Res* 1–11. <https://doi.org/10.1557/jmr.2018.253>
14. Zhao Z, Chen Q, Hu C, Shu D (2009) Microstructure and mechanical properties of SPD-processed an as-cast AZ91D+ Y magnesium alloy by equal channel angular extrusion and multi-axial forging. *Mater Des* 30(10):4557–4561. <https://doi.org/10.1016/j.matdes.2009.04.023>
15. Rao PN, Singh D, Jayaganthan R (2014) Mechanical properties and microstructural evolution of Al 6061 alloy processed by multi axial forging at liquid nitrogen temperature. *Mater Des* (1980–2015) 56:97–104. <https://doi.org/10.1016/j.matdes.2013.10.045>
16. Noda M, Hirohashi M, Funami K (2003) Low temperature super plasticity and its deformation mechanism in grain refinement of Al–Mg alloy by multi-axial alternative forging. *Mater Trans* 44(11):2288–2297. <https://doi.org/10.2320/matertrans.44.2288>
17. Kapoor R, Sarkar A, Yogi R, Shekhawat SK, Samajdar I, Chakravartty JK (2013) Softening of Al during multi-axial forging in a channel die. *Mater Sci Eng A* 560:404–412. <https://doi.org/10.1016/j.msea.2012.09.085>

18. Li T, Zhang K, Li X, Du Z, Li Y, Ma M, Shi G (2013) Dynamic precipitation during multi-axial forging of an Mg–7Gd–5Y–1Nd–0.5 Zr alloy. *J Mg Alloys* 1(1):47–53. <https://doi.org/10.1016/j.jma.2013.02.005>
19. Xia XS, Ming CHEN, Fan FY, Zhu CH, Huang J, Deng TQ, Zhu SF (2013) Microstructure and mechanical properties of isothermal Multi-Axial Forging formed AZ61 Mg alloy. *Trans Nonferrous Met Soc China* 23(11):3186–3192. [https://doi.org/10.1016/S10036326\(13\)62851-4](https://doi.org/10.1016/S10036326(13)62851-4)
20. Cherukuri B, Srinivasan R (2006) Properties of AA6061 processed by multi-axial compressions/forging (MAC/F). *Mater Manuf Processes* 21(5):519–525. <https://doi.org/10.1080/10426910500471649>
21. Venkateswarlu K, Das G, Pramanik AK, Xu C, Langdon TG (2006) Using ball-indentation to evaluate the properties of an ultrafine-grained Al-2% Si processed by ECAP. *Mater Sci Eng A* 427(1–2):188–194. <https://doi.org/10.1016/j.msea.2006.04.053>
22. Ma A, Saito N, Takagi M, Nishida Y, Iwata H, Suzuki K, Watazu A (2005) Effect of severe plastic deformation on tensile properties of a cast Al-11 mass% Si alloy. *Mater Sci Eng A* 395(1–2):70–76. <https://doi.org/10.1016/j.msea.2004.12.038>
23. Rezaee-Bazzaz A, Ahmadian S (2012) Modeling of mechanical behavior of ultra-fine grained aluminum produced by multiple compressions in a channel die. *Mater Des* 34:230–234. <https://doi.org/10.1016/j.matdes.2011.08.013>
24. Sharath PC, Udupa KR, Kumar GP (2017) Effect of multi axial forging on the microstructure and mechanical properties of Zn-24 wt% Al-2 wt% Cu alloy. *Trans Indian Inst Met* 70(1):89–96. <https://doi.org/10.1007/s12666-016-0863>
25. Padap AK, Chaudhari GP, Pancholi V, Nath SK (2010) Warm multi axial forging of AISI 1016 steel. *Mater Des* 31(8):3816–3824

Implementation of Lean Concepts Using Value Stream Mapping in Automotive Firm



Abhishek Deokar, S. Aravind Raj, K. Jayakrishna and H. Abdul Zubar

Abstract Lean manufacturing is the concept used to identify potential waste in industries to survive in competitive market. Lean concept was introduced by automotive firm known as Toyota Production System (TPS). The need of lean facilitates increase in productivity. Value stream mapping (VSM) is a lean tool to identify value-added and non-value-added activities in production line. This chapter focuses on studying the current state map of an automotive firm and to implement value stream mapping (VSM) to design future state map using appropriate lean tools to increase the productivity and eliminate non-value-added activities. The study was conducted on crankshaft line of an engine shop in an automotive firm. After conducting study, successful implementation of the VSM tools resulted in the reduction of cycle time by 56, 227, and 155 s of oil-hole drilling, induction hardening, and grinding, respectively. The productivity was improved by 24 units on an average after complete implementation of future state VSM.

Keywords Lean manufacturing · Value stream mapping (VSM) · Lead time · Quality improvement · Kaizen

1 Introduction

The concept of lean manufacturing was developed and implemented by Toyota Motors [1]. The main objective was to reduce manufacturing cost and deliver increase in value to the customer. Reduction in manufacturing cost can be done by considering non-value-added activities. VSM tools like Kaizen (continuous improvement), Muda

A. Deokar · S. Aravind Raj (✉) · K. Jayakrishna
Department of Manufacturing Engineering, School of Mechanical Engineering, Vellore Institute of Technology, Vellore 632014, Tamil Nadu, India
e-mail: aravindsakthivel@hotmail.com

H. Abdul Zubar
Department of Industrial Engineering, Faculty of Engineering, King Abdulaziz University, Jeddha, Kingdom of Saudi Arabia

© Springer Nature Singapore Pte Ltd. 2019
S. S. Hiremath et al. (eds.), *Advances in Manufacturing Technology*,
Lecture Notes in Mechanical Engineering,
https://doi.org/10.1007/978-981-13-6374-0_17

(waste reduction), Just-In-Time (JIT), VSM, Kanban, cellular manufacturing, and single minute of exchange die (SMED) were developed for optimal use of resources [2, 3]. Across the world, automobile sector has highly emerged demanding manufacturing unit. Due to huge customer population, there is constant increase in demand for automotive products. Globally automotive industry is facing huge competition in each and every aspect [1]. Lean manufacturing is the perfect solution to the various problems such as quality, work in progress (WIPs), bottlenecks, inventory, and processing time being faced by automotive sector. VSM tool of lean manufacturing is a process which monitors the existing manufacturing process with the help of current state map and recreates it with certain change known as future state map which helps to add value with respect to the customer. Numerous tools such as Kaizen, Muda, Gemba, 5S, TPM, and TQM enable the organization to reduce the wastes and change the current working structure of the organization and thereby increase the production [4]. Practically, it is impossible to achieve 100% output in process. However, with the help of lean concept and VSM tools, it can be minimized up to certain extent so that it can be beneficial to the organization in terms of productivity, cost reduction, quality, manpower, and less production lead time [5–7].

2 Case Study

This research was carried out in a leading automobile industry located in Pune, Maharashtra, India. There are various shops formed in the company such as transaxle shop, engine shop, paint shop, assembly shop, and research and development center. After analyzing and discussing with respective shop head, engine shop was selected for the research work. The company performs operations on four different engine parts of an engine in an engine shop, viz. (1) engine head, (2) block head, (3) crankshaft, and (4) camshaft. After collection of relevant data and discussing with the manager of an engine shop, the most critical product, i.e., crankshaft, has been selected for the value stream mapping. In this study, crankshaft of diesel engine has been studied, as the particular car was having huge demand in the market. As the target for crankshafts was 120 per shift, however on an average 80 per shift was achievable. Following is the information about working structure of the company.

- (1) Number of shifts—2
- (2) Target—120 jobs/shift
- (3) Available time—8 h/shift
- (4) Take time = $\frac{\text{Total available time per shift}}{\text{Total demand time per shift}}$
 $= \frac{8 \times 60 \times 60}{120}$
 $= 240 \text{ s}$

$$\begin{aligned}
 (5) \quad \text{Uptime} &= \frac{\text{Actual operating time}}{\text{Available time}} \\
 &= \frac{480 \text{ min}}{480 \text{ min}} = 100\%
 \end{aligned}$$

3 Literature Review

Belokar et al. [4] implemented VSM in the manufacturing unit of Malaysia. D54T from front disk assembly was selected, because it did not meet daily target. Future state map revealed the wastes and increased the productivity, thereby meeting daily production target. In Hines and Rich [5] VSM was developed to collect and use group of tools to help researchers and various organizations to find various wastes and find better ways to eliminate it. Aziziand Manoharan [8] studied PCB assembly line to implement lean techniques. The main objective of the paper was to reveal the factors which affect the smart tag production. The SMED technique was implemented at the insertion process that was bottleneck. SMED technique was successfully implemented as the machine setup time in the insertion process was reduced from 145 to 54 s. Tyagi et al. [9] explored about concept of VSM to the product development process (PDP) stresses on the importance of faster product development for the right edge on the market. Paper was narrowed down to the concept of development of product. Further research is to be done in the field of value stream mapping on other process of an organization. Rosa et al. [10] explored to change current working methods of the assembly line to avoid delays in future if the customer demand is increased. Various VSM tools such as 5S, TPM, and Kaizen were used to eliminate waste and other issues, which increased the productivity of the line by 41% [11–13].

4 Field Data Collection

4.1 Analysis of Current State Map

4.1.1 Bottleneck

In crankshaft production line bottleneck was found at the oil-hole drilling operation. The frequent breakdown of machine caused delay in the operation and subsequently more WIPs. Tool life of the drills was 60 jobs. Hence, operator had to change the drills twice in 1 shift, which approximately costs one hour in 1 shift.

4.1.2 Improper Sequence of Operation

It has been observed that improper sequence of operations has been affecting the productivity of crankshaft line. Many times due to unavailability of operator, deburring operation is done after oil-hole drilling which is to be done immediately after milling operations. Instead, it is done as milling—oil-hole drilling—deburring. Due to this issue, jobs had to travel to and fro causing more WIPs and inventory leading to more lead time and affecting the overall production of crankshaft line. Similar case was found at induction hardening.

4.1.3 WIP

Large amount of work in process (WIP) between the processes hinders the further operation resulting in delays. Operations such as induction hardening, grinding, and oil-hole drilling contribute large amount of WIPs as compared to other operations. This is mainly because unavailability of worker at workplace, breakdowns, issues with the manager, improper sequence of operations, and lack of planning.

4.1.4 Work Standards

Work ethics and culture of the production line have been affecting the production in terms productivity and lead time. It has been observed that operators of the various machines at crankshaft line do not follow certain work ethics such as tools which are not kept on assigned place. Many times cleaning of machinery before starting the operation is neglected by the operators.

4.2 Implementation of VSM Tools

Figure 1 shows the current state VSM of case company with seven operations and processing lead time as 2237 seconds.

4.2.1 Implementation of TPM

TPM was implemented on oil-hole drilling machine to avoid frequent breakdown due to various maintenance issues occurred.

5S: This VSM tool was implemented to improve work ethics among the operators and to follow certain rules imposed by management. 5S was essential to reduce the wastage of time occurred due to unavailability of certain tools, gloves, and helmets from their respective places.

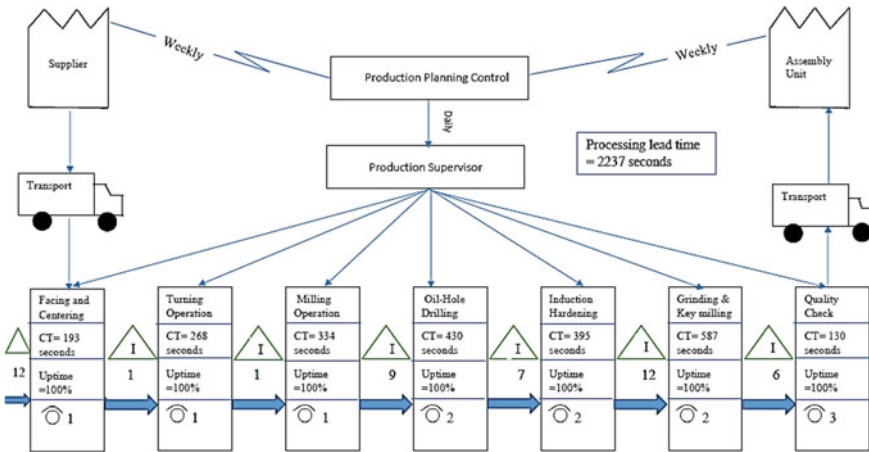


Fig. 1 Current state map

4.2.2 Implementation of the Modified Process by Elimination and Combination Operations

Induction hardening was done on two machines. Due to unavailability of the shank hardening coil at first machine, all jobs had to travel around 50 meters distance to get shank hardened at second machine. After discussing with the management, with the help of manager and line supervisor, they agree to shut down one induction hardening machine and to harden all parts of crankshaft on second machine. Hence, to reduce the processing lead time, immediately after oil-hole drilling deburring operation, all jobs were shifted to second machine (Alfing). As a result, the cycle time reduced from 395 to 168 s. However, certain changes had to made in the Alfing machine to harden all parts of crankshaft, which costs around 0.8 million to the company. Grinding and key way milling operations were leaned with the jigs and fixture tools (Fig. 1).

4.3 Results

Implementation of VSM tools on current state map had shown significant reduction in cycle time of operations such as drilling, induction hardening, and grinding. Eliminating bottleneck from the crankshaft line was major reason in the reduction of processing lead time. The prominent waste identified was bottleneck, due to bottleneck large amount of WIPs used to create in the process. In continuation to that idle time for following machines were reduced thereby lead time improvised by implementing VSM tools such as 5S, TPM which increases the productivity of crankshaft line. Results showed reduction in processing lead time of 438 s. Successful imple-

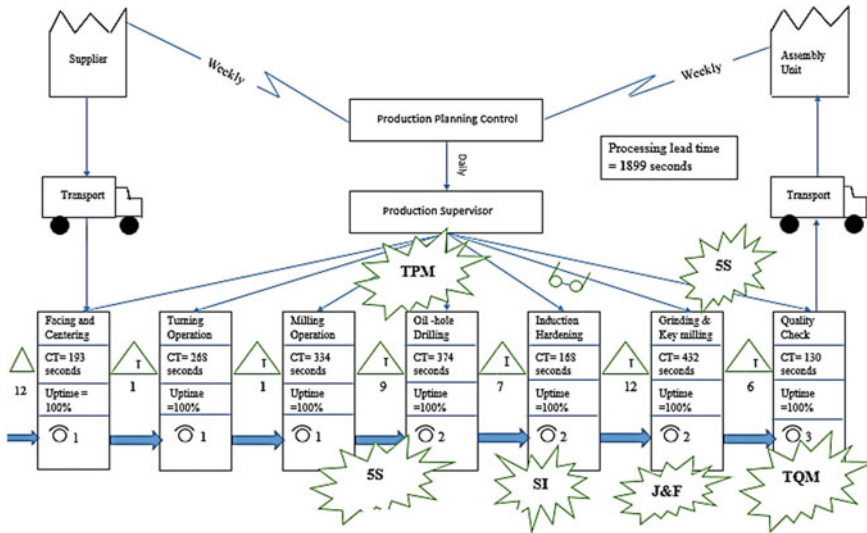


Fig. 2 Future state VSM

mentation of the VSM tools resulted in the reduction of cycle time by 56, 227, and 155 s of oil-hole drilling, induction hardening, and grinding, respectively. Finally, there was an increase in the productivity, on an average by 24 units. Figure 2 shows the future state VSM of case company with reduced processing lead time 1899 seconds.

5 Conclusion

Lean manufacturing is a technique which has become necessity in the manufacturing sector. Many researchers had proved that to overcome various constraints during production, lean manufacturing is been used. As a result, industries are keen to adopt lean concept in their industries. Current state map has been drawn after the selection of product family. And after analyzing and implementation of VSM tools, future state is drawn.

It can be concluded that implementation of VSM reduces cycle time and lead time and increases the productivity by eliminating various types of wastes and bottlenecks. As we cannot obtain 100% output in any process, similarly there are certain wastes which cannot be eliminated by using lean manufacturing too. After implementation of VSM on current state map, the results showed 15% reduction in cycle time of drilling operation, 57.46% reduction in induction hardening operation, and 26.4% in grinding operation. Hence, industrial organization which is facing problems in productivity, cycle time, and lead time should adopt lean manufacturing using VSM tools to overcome the issue up to certain extent.

References

1. Singh H, Singh A (2013) Application of lean manufacturing using value stream mapping in an auto-parts manufacturing unit. *J Adv Manage Res* 10(1):72–84. <https://doi.org/10.1108/09727981311327776>
2. Faulkner W, Badurdeen F (2014) Sustainable value stream mapping (Sus-VSM): methodology to visualize and assess manufacturing sustainability performance. *J Clean Prod* 85:8–18. <https://doi.org/10.1016/j.jclepro.2014.05.042>
3. Vinodh S, Selvaraj T, Chintha SK, Vimal KEK (2015) Development of value stream map for an Indian automotive components manufacturing organization. *J Eng Des Technol* 13(3):380–399. <https://doi.org/10.1108/jedt-08-2010-0054>
4. Belokar RM, Kumar V, Kharb SS (2012) An application of value stream mapping in automotive industry: a case study. *Int J Innov Technol Explor Eng* 1(2):152–157
5. Hines P, Rich N (1997) The seven value stream mapping tools. *Int J Oper Prod Manage* 17(1):46–64. <https://doi.org/10.1108/01443579710157989>
6. Haefner B, Kraemer A, Stauss T, Lanza G (2014) Quality value stream mapping. *Procedia CIRP* 17:254–259. <https://doi.org/10.1016/j.procir.2014.01.093>
7. Lacerda AP, Xambre AR, Alvelos HM (2016) Applying value stream mapping to eliminate waste: a case study of an original equipment manufacturer for the automotive industry. *Int J Prod Res* 54(6):1708–1720. <https://doi.org/10.1080/00207543.2015.1055349>
8. Azizi A, Manohanaran P (2015) Designing a future value stream mapping to reduce lead time using SMED—a case study. *Procedia Manuf* 2:153–158. <https://doi.org/10.1016/j.promfg.2015.07.027>
9. Tyagi S, Choudhary A, Cai X, Yang K (2015) Value stream mapping to reduce the lead-time of a product development process. *Int J Prod Econ* 160:202–212. <https://doi.org/10.1016/j.ijpe.2014.11.002>
10. Rosa C, Silva FJG, Ferreira LP (2017) Improving the quality and productivity of steel wire-ropes assembly lines for the automotive industry. *Procedia Manuf* 11:1035–1042. <https://doi.org/10.1016/j.promfg.2017.07.214>
11. Vamsi Krishna Jasti N, Sharma A (2014) Lean manufacturing implementation using value stream mapping as a tool: a case study from auto components industry. *Int J Lean Six Sigma* 5(1):89–116. <https://doi.org/10.1108/IJLSS-04-2012-0002>
12. Venkataraman K, Ramnath BV, Kumar VM, Elanchezhian C (2014) Application of value stream mapping for reduction of cycle time in a machining process. *Procedia Mater Sci* 6:1187–1196. <https://doi.org/10.1016/j.mspro.2014.07.192>
13. Verma N, Sharma V (2016) Energy value stream mapping a tool to develop green manufacturing. *Procedia Eng* 149:526–534. <https://doi.org/10.1016/j.proeng.2016.06.701>

Fabrication of Automated Scrap Collector Cum Scrubber for Production Industries



R. Bhoopathi, K. Karthikeyan, J. Balamurugan, S. Krishnakanth and T. Dharan Raj

Abstract The world is tremendously transforming toward automation that once stood in performing all the works by the manual method. Automation serves as a bridge that shows the path from inefficient work to efficient works. Traditionally, the cleaning processes are done by the manual method. Since the world is getting more technologically advanced, we discover new technology in our day-to-day life. Automation in the cleaning process is becoming more popular and is becoming a regular practice. The automatic cleaning process provides efficient and non-hazardous cleaning method. The main objective of this project is that we are cleaning the floor surfaces using a remote-controlled floor cleaner. It is primarily a tadpole design. Various load conditions are analyzed for designing the cleaner. The frame is made of Aluminum 6061. The wheels are made of Nylocast plastic using a lathe machine. The cleaner is driven using two 12 V 100 rpm DC motors. These two DC motors are controlled by the motor driver L293D. This cleaner is operated by mobile with the help of Wi-Fi module ESP8266. The Wi-Fi module is programmed using the Arduino Uno software. The brush which is used to clean the surfaces is made of Nylocast plastic and it is fixed in the frame using the bearings to clean the surface. The brush is controlled by a sewing machine motor. Batteries are used to power the motors and it can be recharged with solar panels. This machine finds its applications in the area of manufacturing, agriculture, and home utilities. This machine has other applications such as collecting the scrap materials in industries. It may be also used for collecting the dried grains in the field of agriculture. This machine can also be attached with blades to be used as a lawnmower. Since it is controlled by mobile, it reduces the efforts of human in the cleaning processes. It also promotes the mantra “SWACHH BHARAT” and creates awareness among people in making our country clean.

Keywords Tadpole · Remote control · Wi-Fi module · DC motor · Brush · Battery

R. Bhoopathi (✉) · K. Karthikeyan · J. Balamurugan · S. Krishnakanth · T. Dharan Raj
Department of Mechanical Engineering, Sri Sai Ram Engineering College, Chennai 600044, India
e-mail: bhoopathir.mech@gmail.com

© Springer Nature Singapore Pte Ltd. 2019
S. S. Hiremath et al. (eds.), *Advances in Manufacturing Technology*,
Lecture Notes in Mechanical Engineering,
https://doi.org/10.1007/978-981-13-6374-0_18

149

1 Introduction

The main disadvantage of manual cleaning is that the dust is not entirely removed; instead, some portions of it are moved to another place. The manual cleaning procedure causes pollution which also leads to respiratory problems. The efficiency of the cleaning procedure by manual work is low when compared to automatic cleaning [1]. Manual work is taken over the robot technology and many of the related robot appliances are being used extensively also. Here, the technology that proposed the working of a remote-controlled device for floor cleaning is represented. This floor cleaner robot can work in any of the two modes like automatic and manual [1–12]. Whenever a vacuum road sweeping machine operates on the road, dust clouds are formed [13]. If water is sprayed on the side brushes to tame the dust cloud, these filters get clogged up frequently. It has been seen recently that the end users are slowly shifting toward imported and good-quality road sweeping machines without any bag/cartridge filters [1]. However, these machines use a lot of good-quality water for taming the dust cloud and availability of drinking water is always a problem in Indian cities. Surprisingly, neighboring countries of India have realized the reason behind the under-performance of poorly designed sweeping machines and they have large numbers of good-quality and imported, properly designed sweeping machines on their roads. There are many papers regarding the automatic floor cleaning robots and other automatic floor cleaning systems. Most of the researchers have been studied about the social impact of these floor cleaners in the domestic environment. The automatic floor cleaning system is made with the help of infrared sensors to find obstacles and move accordingly [7]. Andrew Ziegler et al. have invented an autonomous floor cleaning robot for both dry and wet surfaces.

2 Components

2.1 Frame

The frame is base of the entire system. It holds the entire weight of the machine and has provisions to support the wheels, the collecting duct, and brush. The frame is made of aluminum 6061 material. The material is chosen based on the analysis test from the ANSYS software. Since the machine is to be used in the field of industrial cleaning and agriculture, it is made of lighter material. The analyzed frame assembly is shown in Fig. 1 [1–9].

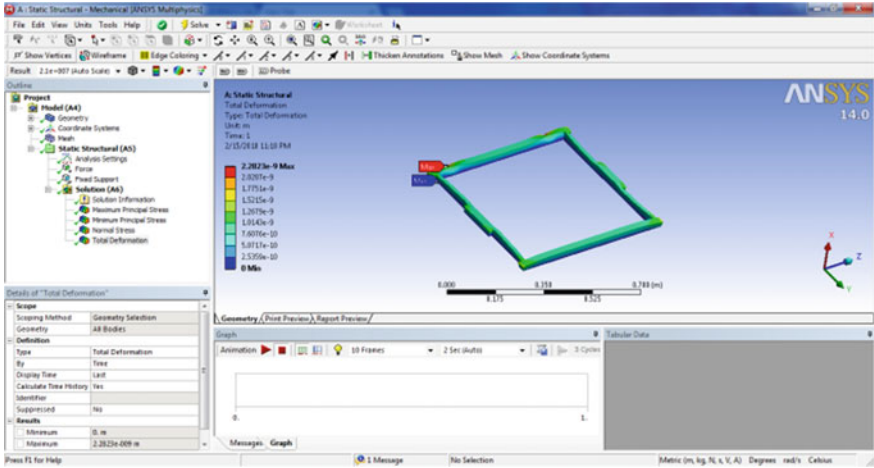


Fig. 1 Analysis of frame by ANSYS software

2.2 Wheels

The wheels are machined with the help of the lathe process. The rear wheels act as the driver, which are powered by 12 V 100 rpm DC motor [10]. The wheels are made of Nylocast plastic. The designed wheel by Pre-E software is shown in Fig. 2 and the fabricated wheel is assembled with DC Motor and frame units are shown in following Fig. 3 [1].

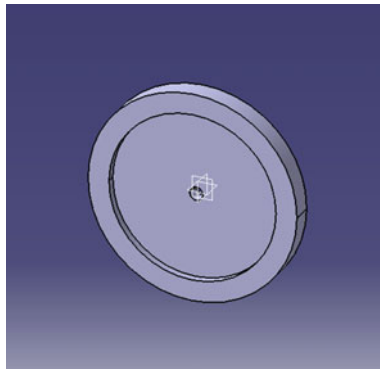


Fig. 2 Designed wheel assembly



Fig. 3 DC Motor and wheel assembly

2.3 *Brush*

The brush is used to collect the dirt particles from the ground. The brush is powered by a 6000 rpm motor [10]. The brush assemblies were designed by using Pro-E software and structural analysis was conducted to get the optimal design parameters under different speed and feed conditions with static loading. Figures 4 and 5 shows the designed and fabricated brush assembly unit with the frame of the automated floor cleaning machine.

2.4 *Collecting Duct*

The removable collecting duct/tray was designed and fabricated to collect the scraps and dust from the floor space during cleaning process [5–8]. The structural analysis was conducted on the designed duct under different weights and materials by using ANSYS software. Based on the obtained results, the optimal weight-carrying capac-

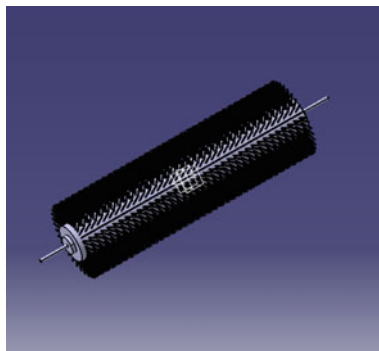


Fig. 4 Designed brush assembly



Fig. 5 Fabricated brush assembly

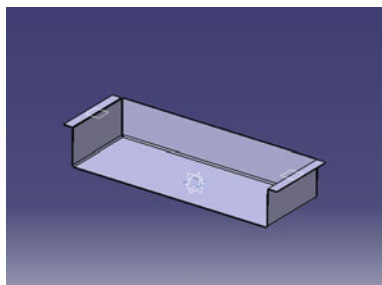


Fig. 6 Designed collecting duct by Pro-E software

ity and suitable material were selected. The collecting duct was made of GI sheets and fixed on frame at the bottom of the automated floor cleaner. The fabricated duct accumulates dust/scrap up to 3 kg in the form of dry and wet conditions. Figure 6 shows the designed dust-collecting duct by using Pro-E software.

2.5 Motor Driver: (L293D)

A motor controller is a device or group of devices that might include a manual or automatic means for starting and stopping the motor, selecting forward or reverse rotation, selecting and regulating the speed, regulating or limiting the torque, and protecting against overloads and faults. The L293 is an integrated circuit motor driver that can be used for simultaneous and bi-directional control of two small motors.

2.6 Wi-Fi Module

The ESP8266 Wi-Fi Module is a self-contained SOC with integrated TCP/IP protocol stack that can give any microcontroller access to your Wi-Fi network. The ESP8266 is capable of either hosting an application or off-loading all Wi-Fi networking functions from another application processor [8–12]. Each ESP8266 module comes pre-programmed with an AT command set firmware, meaning you can simply hook this up to your Arduino device and get about as much Wi-Fi-ability as a Wi-Fi shield offers (and that just out of the box). The ESP8266 module is an extremely cost-effective board with a huge, and ever-growing, community.

3 Fabrication Process

The main frame consists of four bars fastened together. It is fabricated by milling of aluminum 6061 [1]. The dimensions of the frame are 600 mm x 600 mm. The bars are fastened together with 5 mm Allen bolts. The collecting duct is machined using various sheet metal processes like cutting and bending processes. The wheels are made by turning and facing the Nylocast plastic in the lathe machine. The front wheel is 78 mm in diameter and 18 mm in thickness, and the rear wheels are 125 mm in diameter and 13 mm in thickness. The brush consists of two parts; one is the shaft and another part is the brush bristles. The shaft is supported by the end bearings. The completely designed and assembly of all devices are shown in Figs. 7 and 8 [9–13].

4 Working Principle

The floor cleaner cum scrap collector is made of tadpole design [1]. It is made of three wheels. The frame is made of aluminum 6061. The cleaner moves with the aid of wheels which is powered by 12 V DC motor. The DC motor is controlled by the motor drive L293D. The brush which is used to clean the surface is made of Nylocast plastic [6–10]. It is driven by the sewing machine motor. The high rpm of the motor enables

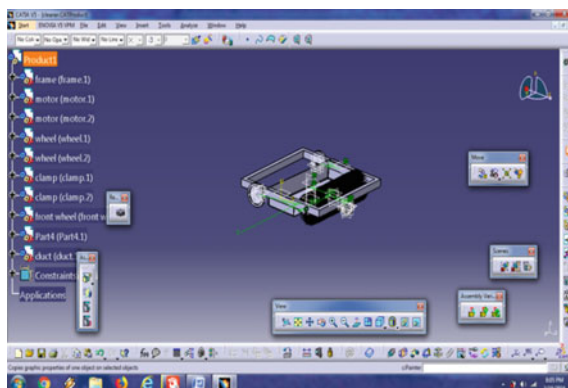


Fig. 7 Designed view of Automated dust collector



Fig. 8 Fabricated and assembled view of Automated dust collector

the brush to clean the dust or collect the scrap. The cleaned dust are then collecting duct. The collecting duct is made up of G.I sheets. The collecting duct is made such that the clearance between the brush and the collecting duct is very small so that the swept away dust or scrap settles in the collecting duct. The three motors are powered by the 12 V DC battery. The battery is rechargeable and it is recharged by a solar panel. The three motors are controlled by the mobile through the Wi-Fi module. The Wi-Fi module is programmed for this cleaning purpose using Arduino Uno software. This cleaner is suitable for different surface cleaning purpose. Depending upon the surface to be cleaned, the material of the brush is changed so that it collects fully and effectively. The cleaner can be moved in four directions with the help of the mobile. This enables the cleaner to completely remove the scrap effectively. The mobile controlling system makes the cleaner more efficient and reduces the manual effort to clean the surfaces.

5 Applications

This remote-controlled scrap collector finds its real-time application in industries and agricultural field. In industries, it is used to collect the small scraps and burs which are very difficult to clean. In the field of agriculture, it is used to collect the dried grains which is very to collect it by means of manual power. This machine is also used to remove the dust from the roadways which creates more air pollution and causes disturbances while driving. Since manual cleaning of the dust makes it circulate in the air, it causes invisibility to the human while driving. This leads to many accidents. This scrap collector collects all the dust in the surface and reduces air pollution.

6 Conclusion

This automated scrap collector is very much useful in industries for cleaning the floor surfaces. This cleaner also finds its application in the field of agriculture for collecting the dried grains. Since this machine is mobile-controlled, it makes a user-friendly environment. It also increases the efficiency of the cleaning process. The objective of this project is to create awareness about the importance of clean surrounding. Analysis of the machine reveals that this can be used in any loading conditions and also in sand terrains. This project has multipurpose applications. This machine can be used to clean the road surface and other floor surfaces such as in house and in industries. This automated scrap collectors can be used for all small-scale industries like fabrication/production industries, rice mill industries, and construction industries. This machine has also other applications such as collecting dried grains in the agricultural sector. This remote-controlled floor cleaner reduces the human's efforts in collecting dusts and grains and makes the process more efficient. It reduces land pollution and air pollution and makes the road surface cleaner. It also promotes the mantra "SWACHH BHARAT" and creates awareness among people in making our country cleaner. The inclusion of Wi-Fi-enabled controlling system makes the floor cleaner more efficiently and makes it work at a much faster rate. This project foreseen the improvement and effectiveness in a cleaning process.

References

1. Kalam S, Sekhri J, Bauddh T, Kumar S, Jha S, Rana PS, Kumar D, Singh A (2018) Road side dust collector machine. *Int Res J Eng Technol (IRJET)* 5(3):2688–2692
2. Jain M, Rawat PS, Morbale J (2017) Automatic floor cleaner. *Int Res J Eng Technol (IRJET)* 4(4):303–307
3. Taware RD, Hasure V, Ghule P, Shelke K (2017) Design and development of floor cleaner robot (automatic and manual mode). *Int J Res Trends Innov* 2(4):57–60
4. Sonali S, Sankpal, Swapnali D, Chavan, Sarika P, Valukar (2017) Floor cleaning robot. *Imp J Interdiscip Res (IJIR)* 3(4):1262–1264
5. Joshi NH, Ingale PH, Patil HS (2017) Android based automatic floor cleaning robot. *Int J Technol Res Eng* 4(8):1259–1260
6. Pradeep S, Sasikumar V, Sivaguru K, Yogaraj J, Yuvaraj R (2017) Electromagnetic metal collecting AGV. *Int Res J Adv Eng Sci* 2(2):179–182
7. Rathava S, Raval G, Solanki A, Rai S (2017) Scrap collecting vehicle. *Int J Adv Res Innov Ideas Educ* 3(2):1406–1411
8. Rewatkar V, Bagde ST (2015) A review on design of automated floor cleaning system. *Int J Recent Innov Trends Comput Commun* 3(2):120–122
9. Khalid U, Baloch MF, Haider H, Sardar MU, Khan MF, Zia1 AB, Qasuria TAK, Khan GI (2015) Smart floor cleaning robot (CLEAR). Institute of Engineering Sciences and Technology. www.standardsuniversity.org
10. Nurlansa O, Istiqomah DA, Pawitra MAS (2014) AGATOR (automatic garbage collector) as automatic garbage collector robot model. *Int J Futur Comput Commun* 3(5):367–371
11. Gutmann J-S, Culp K, Munich ME, Pirjanian P (2012) The social impact of a systematic floor cleaner. In: IEEE international workshop on advance robotics an its social impacts, Technische University munchen. <https://doi.org/10.1109/arso.2012.6213398>
12. Kaur M, Abrol P (2014) Design and development of floor cleaner robot (automatic and manual). *Int J Comput Appl* 97(19):32–38
13. Forlizzi J, DiSalvo D (2006) Service robots in the domestic environment. A study of the roomba vacuum in the home. In: International conference on human robot interaction (HRI), 258–265. <https://doi.org/10.1145/1121241.1121286>

Enhancement of Mechanical Properties Through Spheroidization Annealing for Low-Carbon Steel



D. Venkatesan and R. Chandramouli

Abstract EN353 is a low-carbon alloy steel, predominantly used for manufacturing heavy-duty gears, shaft and pinions, especially crown wheel and pinion. It is usually carburized, hardened and tempered to produce a hard ware-resistant case. Heat-treated EN353 steel exhibits enhancement in ductility, toughness, strength and hardness; internal stresses are relieved in the material. Grain sizes of the steel were found to be ranging from ASTM number 5 to ASTM number 8, i.e. average grain diameter of 0.022 to 0.062 mm. Spheroidizing of low-carbon steel is a method of prolonged heating at a temperature below the eutectoid temperature. By heating at this temperature, pearlite, which is the lowest energy arrangement of steel, gets converted to ferrite and cementite. The graphite content of steel assumes a spheroidal shape; and after prolonged heating, the pearlite layers are broken down and spherical lumps of cementite or spheroidite are found. The structures in spheroidite are 1000 times larger than those of pearlite and are spaced further apart. This means the spheroidite steel is extremely ductile. In this work, EN 353 billets are heat-treated to achieve spheroidization and the mechanical properties of the material were studied. After spheroidizing annealing, the hot-rolled EN353 low-carbon alloy steel became softer with an increase in ductility and toughness but at the expense of its yield and tensile strengths.

Keywords Spheroidization · EN 353 · Hot-rolled · Annealing

1 Introduction

EN353 is a low-carbon alloy steel, predominantly used for manufacturing heavy-duty gears, shaft and pinions, especially crown wheel and pinion. It is usually carburized, hardened and tempered to produce a hard ware-resistant case. Heat-treated EN353 steel exhibits enhancement in ductility, toughness, strength and hardness; internal

D. Venkatesan (✉) · R. Chandramouli
School of Mechanical Engineering, SASTRA Deemed University, Tanjore, India
e-mail: deevee@mech.sastra.edu

© Springer Nature Singapore Pte Ltd. 2019
S. S. Hiremath et al. (eds.), *Advances in Manufacturing Technology*,
Lecture Notes in Mechanical Engineering,
https://doi.org/10.1007/978-981-13-6374-0_19

stresses are relieved in the material. Spheroidizing of low-carbon steel is a method of prolonged heating at a temperature below the eutectoid temperature. By heating at this temperature, pearlite, which is the lowest energy arrangement of steel, gets converted to ferrite and cementite. The graphite content of steel assumes a spheroidal shape; and after prolonged heating, the pearlite layers are broken down and spherical lumps of cementite or spheroidite are found. The structures in spheroidite are 1000 times larger than those of pearlite and are spaced further apart. Several attempts have been made to achieve spheroidization annealing as the spheroidized steel is extremely ductile [1]. Ochi et al. [2] have studied the mechanism for spheroidizing medium carbon steel through annealing process. Dongsheng Qian et al. [3] investigated the effects of warm ring rolling for 52,100 bearing steel instead of the conventional cold rolling process with a view of reducing the high energy consumption due to long processing period required. G. Jha et al. [4] attempted spheroidized annealing for card clothing wire as the duplex ferrite and pearlitic structure of hypoeutectoid cold-drawn wires give high tensile strength and make them unsuitable for cold forming process. Y. G. Ko et al. [5] investigated the spheroidization behaviour of 10 wt% carbon steel and discussed the mechanism related to cementite dissolution. K. Z. Shepelyakovskii et al. [6] used induction heating method to achieve rapid spheroidizing annealing for roller bearings. K. Cvetkovski et al. [7] analysed the effect of thermal softening of fine pearlitic steel on its fatigue behaviour. Though the effect of softening caused by spheroidized annealing is universally known, the challenge is in achieving complete spheroidization. In this work, an attempt has been made to spheroidize EN 353, a low-carbon steel in two heat treatment cycles. The heat-treated specimens were subjected to mechanical testing and the properties were compared with hot-rolled specimens without heat treatment.

2 Experimental Work

Cylindrical specimens of 15 mm diameter and 300 mm length were cut from the hot-rolled EN 353 steel bars. The initial microstructure was obtained before the specimens were subjected to heat treatment. The composition of EN 353 material is given in Table 1.

2.1 Heat Treatment Procedure

To commence the heat treatment operation, the furnace was initially calibrated to determine the furnace operating temperature based on the pre-set furnace temperature. The specimen is heated to a temperature 850 °C and it is held at the temperature for a period of three hours. Then, it is cooled to a temperature of 680 °C and it is held for 4 h. Further, it is allowed to drop to room temperature slowly inside the furnace.

Table 1 Composition of EN 353 material

Element	Range	Actual
C	0.16–0.22	0.17
Mn	0.8–1.1	0.836
Si	0.1–0.33	0.205
Si	0–0.02	0.009
P	0–0.03	0.024
Cr	0.8–1.2	1.03
Ni	1.0–1.2	1.03
Mo	0.1–0.2	0.128
Al	0.02–0.05	0.029
Cu	0–0.25	0.1

Cycle time-I	Cycle time-II
Rising time: 5 h (to 850 °C)	Rising time: 6 h (to 850 °C)
Holding time: 3 h (at 850 °C)	Holding time: 6 h (at 850 °C)
Cooling time: 3 h (to 680 °C)	Cooling time: 4 h (to 680 °C)
Holding time: 4 h (at 680 °C)	Holding time: 6 h (at 680 °C)

Total cycle time: 15 h	Total cycle time: 22 h
Heating rate: 150 °C per hour (max)	150 °C per hour (max)
Cooling rate: 100 °C per hour (max)	100 °C per hour (max)

Microstructure Validation Microstructure evolution of the treated and untreated samples was carried out. Each sample was carefully grounded progressively on emery paper in decreasing coarseness, and were polished using Al₂O₃ carried on a microcloth. The crystalline structure of the specimens was made visible by etching using solution containing 5% HNO₃ and 95% Ethanol (5% NITAL) on the polished surfaces.

Microscopic examination of the etched surface of various specimens was undertaken using a metallurgical microscope with an in-built camera through which the resulting microstructure of the samples was all photographically recorded with magnification of 500X (Figs. 1 and 2).

Before heat treatment

Widmanstatten pattern (needle-like structures) in a matrix of ferrite and pearlite.

After heat treatment

Lamellar pearlite and spheroidized cementite in a matrix of ferrite.

From the two heat treatment cycles, it is observed that the concentration of spheroidized cementite is more (80%) in the specimen, annealed in cycle II.

Micro Structure Validation: Cycle I Magnification – 500X

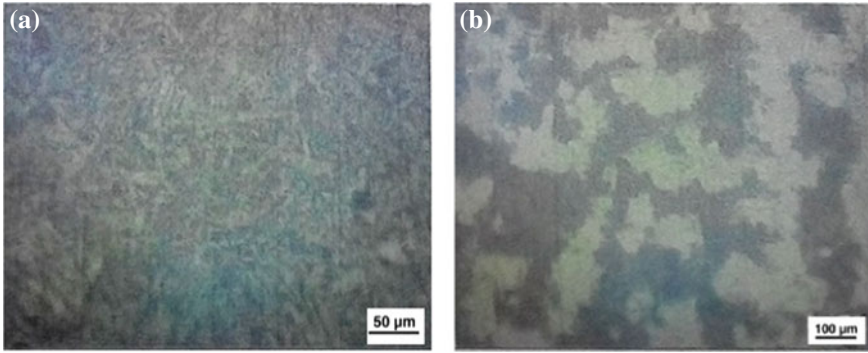


Fig. 1 a Before heat treatment. b After heat treatment

Micro Structure Validation: Cycle II Magnification – 500X

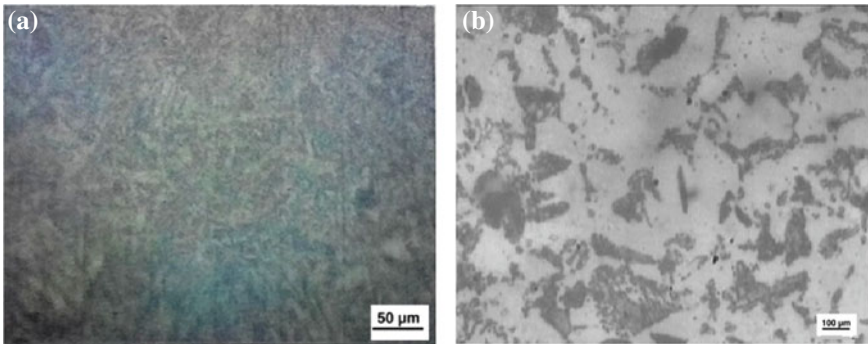


Fig. 2 a Before heat treatment. b After heat treatment

Table 2 Hardness values

Before heat treatment	After heat treatment	
	Cycle 1	Cycle 2
372HV/20/30	174HV/20/30	145HV/20/30

2.2 Mechanical Testing

The hardness values of both heat-treated and hot-rolled specimens were measured using Vickers hardness tester and the values were given in Table 2.

Uniaxial tensile test was performed on both hot-rolled and heat-treated specimens prepared as per ASTM standards and stress–strain curves as well as load–displacement curves were obtained for both specimens. Using these curves as reference, the

Fig. 3 ASTM standard for tensile test specimen preparation

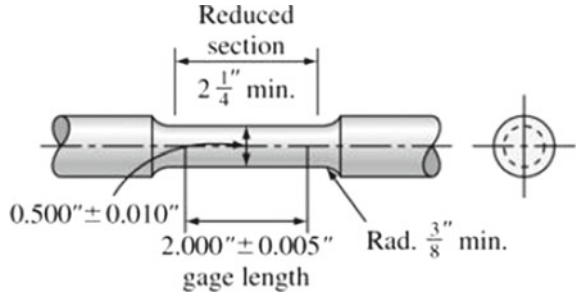


Table 3 Comparison of mechanical properties before and after heat treatment

Parameters	Before heat treatment	After heat treatment
% Elongation	37.7	47.12
% reduction in CS area	1	4.9
UTS kN/mm ²	0.874	0.620
Fracture strain, mm	18.85	23.56
Fracture strength, kN/mm ²	0.715	0.474
Yield strength, kN/mm ²	0.437	0.358
Tensile toughness, MJ/mm ²	214.4	222.2

mechanical properties of the initial hot-rolled and heat-treated materials are evaluated (Fig. 3).

2.3 Mechanical Properties Evaluation

From the stress–strain and load–displacement curves of both the initial hot-rolled and heat-treated materials, the following mechanical properties are evaluated (Table 3).

2.4 Toughness Evaluation Using MATLAB

Using MATLAB, the stress–strain curves for both the specimens made from initial hot-rolled and heat-treated materials are plotted. Toughness values are found out by calculating the area under the respective stress–strain curves (Fig. 4).

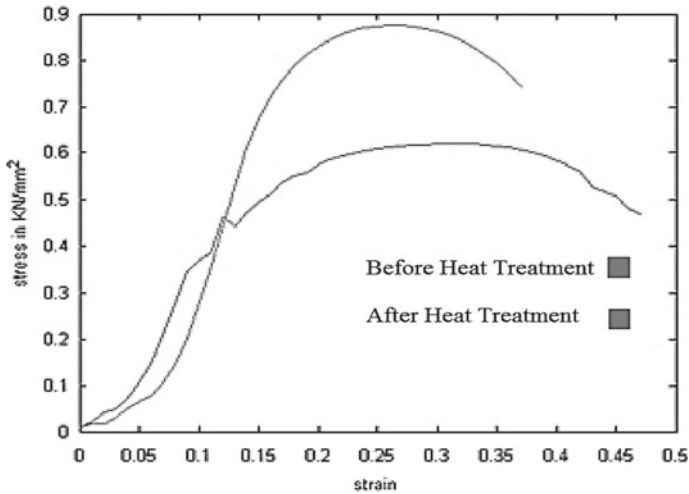


Fig. 4 Plots of stress—strain curves using MATLAB

3 Results and Discussion

The results obtained from the mechanical testing of both hot-rolled and spheroidized specimens were compared and shown in figure. From the figures shown below, spheroidized steel has reduced hardness and greater % elongation due to the improved ductility. The toughness value is increased significantly, but the material loses its strength. The extent of spheroidization has direct influence on the mechanical properties of the heat-treated specimen (Fig. 5).

4 Inferences and Conclusion

Because of the spheroidizing annealing heat treatment performed on the hot-rolled EN353 low-carbon alloy steel, its hardness decreases, i.e. the material became softer with an increase in its ductility and toughness, but at the expense of its yield and tensile strengths. Spheroidize annealing is successful for steels with more than 0.8% carbon. Upon complete spheroidization, cementite changes from a lamella formation to an alpha ferrite matrix with particles of spheroidal cementite (Fe_3C). In steel manufacturing, spheroidize annealing is preferred on components which have been strain hardened to facilitate further working. Thus, the resulting product has improved ductility and toughness with reduced hardness and strength. Since, there is an increase in its ductility and toughness, the material's ability to undergo plastic deformation is enhanced and its applicability in applications requiring high toughness is increased.

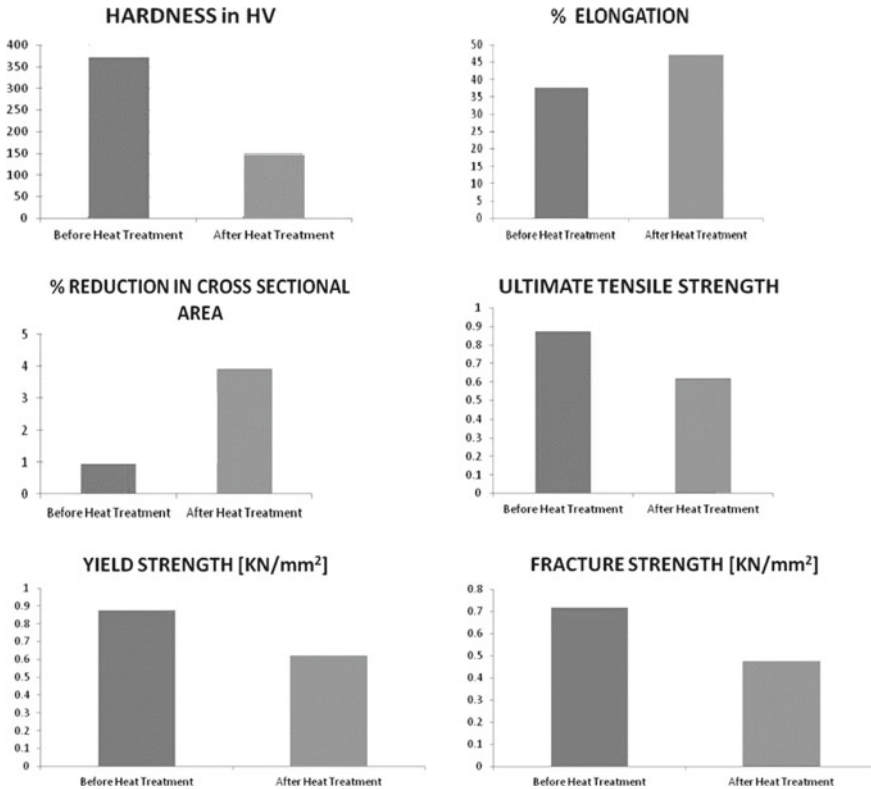


Fig. 5 Mechanical properties comparison for hot-rolled and spheroidized specimens

Acknowledgements The authors are grateful to Prof. R. Sethuraman, Vice Chancellor, SASTRA Deemed to be University for providing this opportunity to publish this work.

References

1. Robbins JL, Shepard OC, Sherby OD (1964) Accelerated spheroidization of eutectoid steels by concurrent deformation. *J Iron Steel Inst* 202:804–807
2. Ochi T, Koyasu Y (1992) A study of spheroidizing mechanism of cementite in annealing of medium carbon steel. *ISS Mechanical Working Steel Processing Conference Proceedings*, vol 29, pp 303–309
3. Qian D, Yang J, Mao H, Hua L (2017) Experiment Study on warm ring rolling of 52000 bearing steel coupling microstructure spheroidization. *Procedia Eng* 207:1224–1229
4. Jha G, Kumar K, Kundu S, Haldar A (2011) Institute of Materials, Minerals and Mining
5. Ko YG, Lee BW, Lee JS, Choi DY, Shin DH (2012) Institute of Materials, Minerals and Mining
6. Shepelyakovskii KZ, Spektor AG, Kuznetsov AN, Gubenko VT, Zdanovskii VS (1976) Rapid spheroidizing annealing of roller bearings with induction heating. *Met Sci Heat Treat* 18:78–80
7. Cvetkovski K, Ahlström J, Karlsson B (2010) Thermal softening of fine pearlitic steel and its effect on the fatigue behavior. *Procedia Eng* 2(2010):541–545

Effect of Rolling Reduction on Microstructure and Mechanical Properties Cu-3% Ti Alloy



Prabhjot Singh, S. Ramesh, Gajanan Anne and H. Shivananda Nayaka

Abstract Cu-3%Ti alloy is cold rolled with different reduction ratios and the microstructures and mechanical properties are compared with that of as-cast Cu-3%Ti alloy. Microstructure was analyzed using optical microscope and scanning electron microscope. Optical microscopy revealed significant grain refinement that occurred during the rolling process. Tensile test results indicate that the UTS is increased by a significant amount up to 80% rolling reduction. A significant amount of tensile strength increased up to 812 MPa is about 1.69 times that of the cast Cu-3%Ti alloy. Hardness of the rolled Cu-3%Ti increased as % reduction increased. Dimples were revealed on the fracture surface of the rolled Cu-3%Ti specimens indicating a ductile nature of the fracture.

Keywords Cu-3%ti alloy · Rolling · Grain refinement · Tensile strength

1 Introduction

Copper and its alloys have been extensively used in electrical applications because of their superior electrical, as well as, thermal conductivities, good strength, exceptional resistance to corrosion, good fatigue resistance as well as easy of fabrication [1, 2]. Among the family of copper alloys, copper beryllium (Cu–Be) alloys exhibit exceptional strength; but due to toxicity and high cost, nowadays, efforts have been concerted on the development of Cu–Ti alloys as a substitute for the Cu–Be alloys [3–5]. Cu–Ti alloys have comparable electrical and mechanical properties to Cu–Be alloys. Grain refinement has proved to be an important and useful technique for

P. Singh · S. Ramesh (✉) · H. Shivananda Nayaka
Department of Mechanical Engineering, National Institute of Technology Karnataka,
Surathkal, Mangalore 575025, India
e-mail: ramnitk2016@gmail.com

G. Anne
Department of Mechanical Engineering, Shri Madhwa Vadiraja Institute
of Technology & Management, Udupi 574115, Karnataka, India

© Springer Nature Singapore Pte Ltd. 2019
S. S. Hiremath et al. (eds.), *Advances in Manufacturing Technology*,
Lecture Notes in Mechanical Engineering,
https://doi.org/10.1007/978-981-13-6374-0_20

strengthening of non-ferrous metals and alloys which are backed by a Hall–Petch relation. Properties of Cu–Ti alloys result from the amount of titanium added, the size of matrix grain, the overall deformation as a result of cold working, and morphologies of dispersed precipitates of intermetallic phases that are formed between the alloy components. Cu–Ti alloys are getting an immense demand as ultra-high strength conductive materials for several applications such as interconnections, conductive springs etc. Numerous investigations on precipitation strengthening mechanism of copper–titanium alloys have been reported in the literature [6, 7]. Addition of 3% of Ti increases the mechanical strength, but electrical conductivity is compromised. Objective of the present work, the effects of Ti addition, and different reductions of cold rolling on the microstructure and mechanical properties of copper–titanium alloy were studied. The precipitation phases and microstructure were characterized using X-ray diffraction (XRD), and transmission electron microscopy (TEM), and the hardness, tensile tests were tested as well.

2 Experimental Procedure

2.1 Material Preparation

Cu-3% Ti alloy was casted with oxygen-free electronic copper in a vacuum induction melting furnace. Chemical composition of rolled Cu-3% Ti alloy was investigated using chemical spectroscopy as indicated in Table 1. Cast ingots were homogenized at 850 °C for 24 h and were then hot forged and rolled at 850 °C into 25 mm thick.

2.2 Rolling Process

Prepared cast ingot of Cu-3% Ti binary alloy with the dimension of 30 mm × 30 mm × 25 mm were cleaned thoroughly with acetone to remove any traces of contamination. Samples were then rolled in a laboratory rolling mill of 65 mm diameter with a reduction of 0.25 mm per pass at a roll speed of 30 revs/min. Schematic diagram of rolling process as shown in Fig. 1.

Strain (ε_i) accumulated during rolling is given by Eq. 1.

Table 1 Nominal composition of the Cu-3% Ti alloys

Elements	Ti	Mn	Zn	Sb	P	Pb	Ni	Cu
Percentage (%)	3	0.030	0.15	0.005	0.080	0.005	0.021	Balance

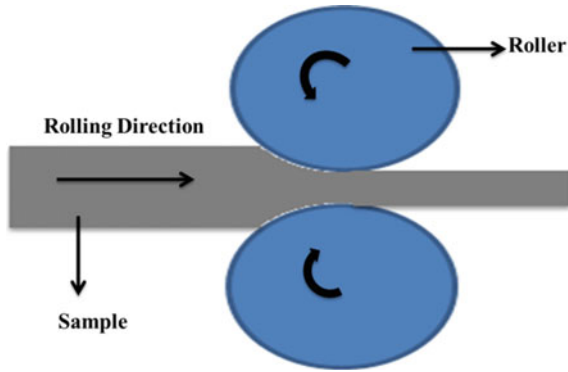


Fig. 1 Schematic diagram of rolling process

$$\varepsilon_i = \ln\left(\frac{t_i}{t_o}\right) \quad (1)$$

where

t_i = Samples initial thickness.

t_o = Samples final thickness

Cumulative strain after reduction of 90% (2.5–0.25 mm), 80% (2.5–0.5 mm), and 70% (2.5–0.75 mm) was found 2.3, 1.6, and 1, respectively.

2.3 Microstructure Analysis

Cu-3% Ti alloy (TD-RD plane) was polished by silicon carbide paper (up to 2000 grit) followed by diamond paste (0.25 μm). Then, a solution of 10 g potassium dichromate, 10 ml sulfuric acid and 10 drops of hydrochloric acid, and 90 ml of distilled water for 5 s were used to etch these metallographically polished samples. An optical microscope (image analyzer-BIOVIS materials plus) was used for microstructural characterization of the sample. X-ray diffraction (XRD) analysis was carried out for phase analysis, with Cu $K\alpha$ radiation at an angle of $20^\circ \leq 2\theta \leq 90^\circ$ and a scan rate of $2^\circ/\text{min}$, so as to identify the different phases present in Cu-3% Ti alloy.

2.4 Mechanical Properties

Tensile test was conducted using Tinius Olsen tensile machine, following the ASTM E8M standards. Vickers microhardness test (on RD-TD plane) was performed at a load of 100 g for 15 s (Omni-tech hardness machine). All the tested specimens were extracted from the middle of the sheet in the rolling direction. Following the standard,

the length, the radius of the fillet, width, and the gage length of the specimens were equal to 64, 7, 10, and 20 mm, respectively. Measurement of gauge length, width, and thickness of every specimen were taken before and after the tensile test. SEM was used for the analysis of fractured surface.

3 Results and Discussion

3.1 Microstructural Observations

Figure 2a shows as-cast Cu-3% Ti alloy consisting of primary α -Cu phase and Ti (β phase), mainly distributed along the grain boundaries. Figure 2b–d shows the microstructure of 70, 80, and 90% rolled samples, respectively, shear deformation bands can be noticed, and elongated grains in the rolling direction are observed. With the increasing number of rolling reductions, shear band density also increases. Elongated shear deformation bands were observed and with an increase in the number of rolling passes, the accumulation of dislocation occurs and it gets difficult to recognize the single grain in higher-reduction rolling samples [8].

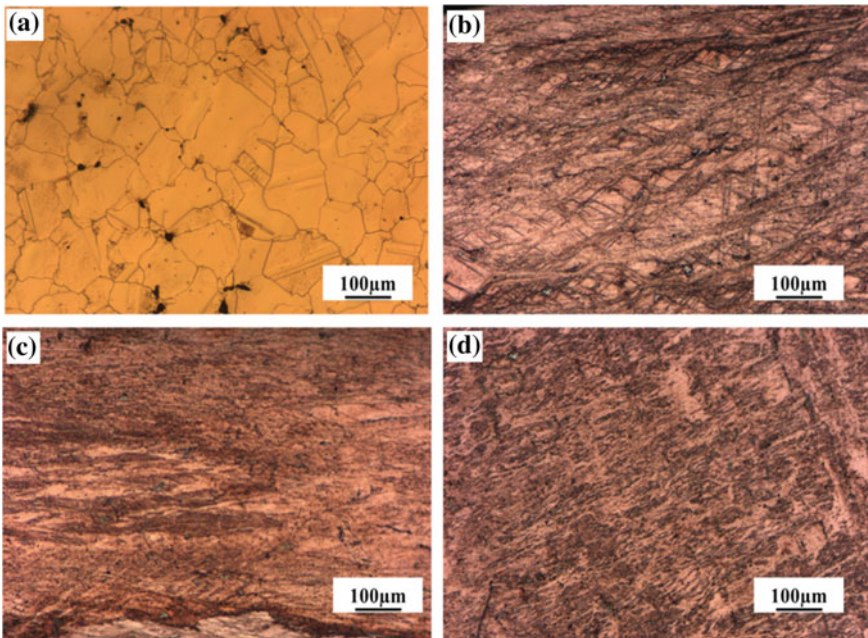


Fig. 2 Optical microstructure of **a** as-cast Cu-3% Ti alloy, **b** rolled 70% reduction Cu-3% Ti alloy, **c** rolled 80% reduction Cu-3% Ti alloy, and **d** rolled 90% reduction Cu-3% Ti alloy

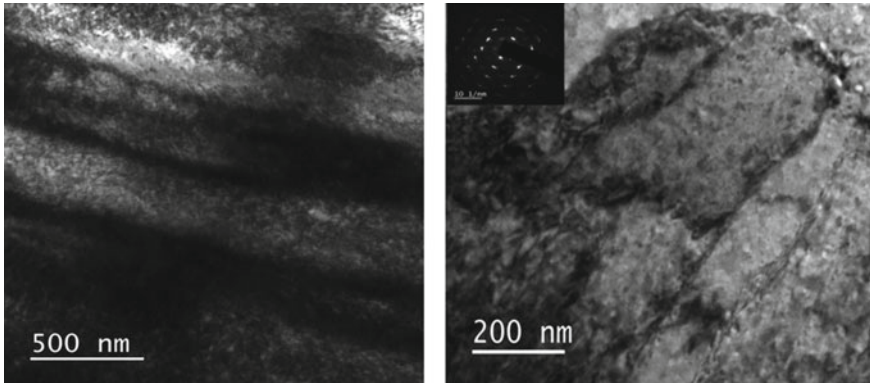


Fig. 3 TEM micrographs and SAED patterns of the rolled 90% reduction Cu-3% Ti alloy

3.2 TEM Analysis

Figure 3 shows TEM micrograph observed in rolling plane of the 90% reduction and corresponding selected area electron diffraction (SAED) in Cu-3% Ti alloy. Fine grains are clearly visible in the microstructure along with some regions showing dislocations, which indicates large misorientation. The sub-grain structure in the rolled 90% reduction sample of Cu-3% Ti alloy is confirmed from SAED patterns which are in the form of rings.

3.3 Microhardness

Figure 4 shows variations in microhardness of Cu-3% Ti alloy with respect to the different rolling reductions. It is observed that the microhardness of Cu-3% Ti alloy is increased with increase in rolling reductions. Microhardness value of as-received sample was found to be 203 Hv. Increase in microhardness can be observed in rolled samples as the rolling reduction increases. Microhardness is increased to 292 Hv (70% reduction), 310 Hv (80% reduction), and 322 Hv (90% reduction), respectively. 90% reduction rolled Cu-3% Ti alloy showed microhardness ~1.58 times higher as compared to counterpart as-received alloy. Increased microhardness of the rolled alloys is due to strain hardening and grain refinement.

3.4 Tensile Test

Figure 5 shows the stress–strain curves of Cu-3% Ti alloy of as-received and different reduction rolled samples. From stress–strain curves, it can be seen that with increase

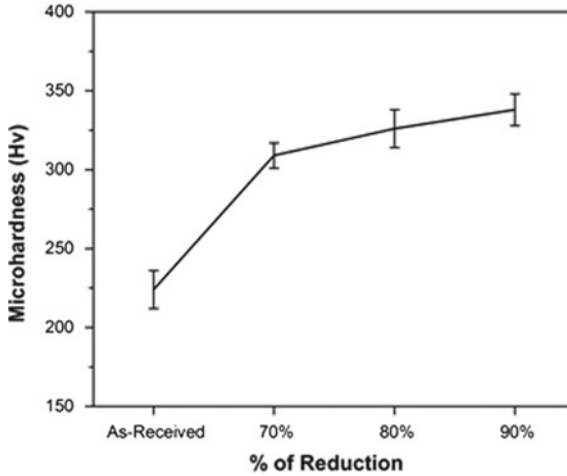


Fig. 4 Microhardness variation of Cu-3% Ti alloy with different rolling reduction

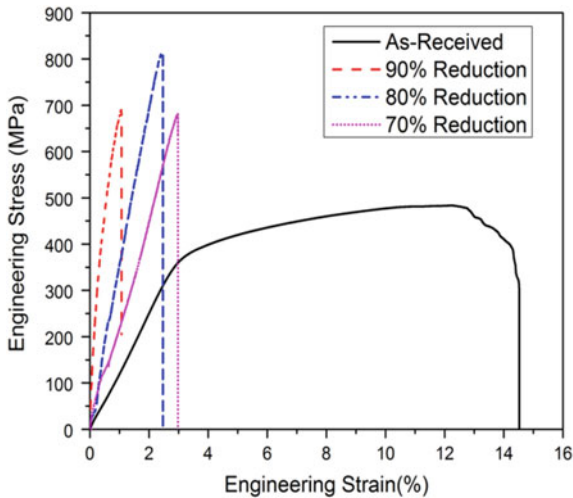


Fig. 5 Engineering stress–strain curves of as-received and different reduction rolled Cu-3% Ti alloy

in rolling reduction, UTS increases. As compared to counterpart as-cast Cu-3% Ti alloy, improvement in UTS is about 1.41, 1.69, and 1.43 times for reduction of 70, 80, and 90%, respectively. The grain boundary strengthening mechanism results in the increase of strength. Maximum UTS (812 MPa) was observed in 80% reduction Cu-3% Ti alloy; after further reduction, a noticeable decrease in ductility and strength is observed due to texture softening. However, obtained UTS values were still quite high in comparison to that of the as-received Cu-3% Ti alloy.

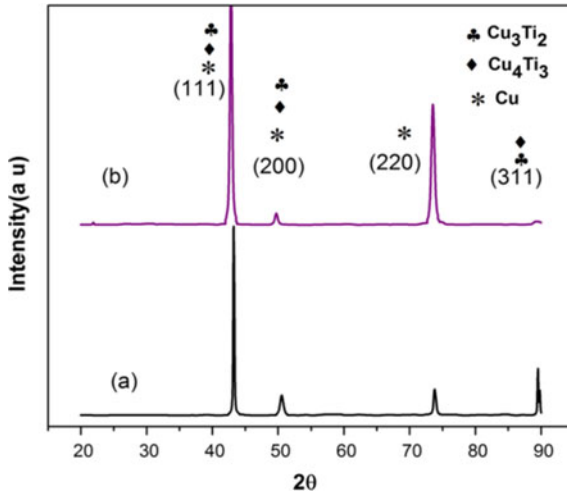


Fig. 6 XRD patterns along the cross section of the **a** as-cast and **b** rolled 80% reduction Cu-3% Ti alloy

3.5 X-ray Diffraction Analysis

Figure 6 depicts the XRD profile of Cu-3% Ti alloy (a) as-cast and (b) rolled 80% reduction. Both as-received and 80% reduction Cu-3% Ti alloy XRD profile peaks are indexed to Cu, $\text{Cu}_4\text{-Ti}_3$, and $\text{Cu}_3\text{-Ti}_2$. It can be observed that in case of rolled 80% reduction, Cu-3% Ti alloy peaks become broad due to the accumulation of strain during rolling process.

3.6 Fractography

Figure 7 illustrates the SEM micrographs of fracture surfaces of the as-cast and different reduction rolled samples obtained after tensile test. Figure 7a shows the fractured as-cast Cu-3% Ti alloy and depicts dimples and tear ridges in the structure, which indicates a ductile fracture. Figure 7b–d revealed that the elongated dimples which are being affected by the state of shear stress, which depicts shear ductile failure in the rolled Cu-3% Ti alloy. It can be seen from the fractographs that the failure is caused by dimple rupture and equiaxed dimples of varied size and depth were noticed in all cases. The large dimples contain ripple marks and tear ridges on their surfaces which are possible due to void growth by tearing.

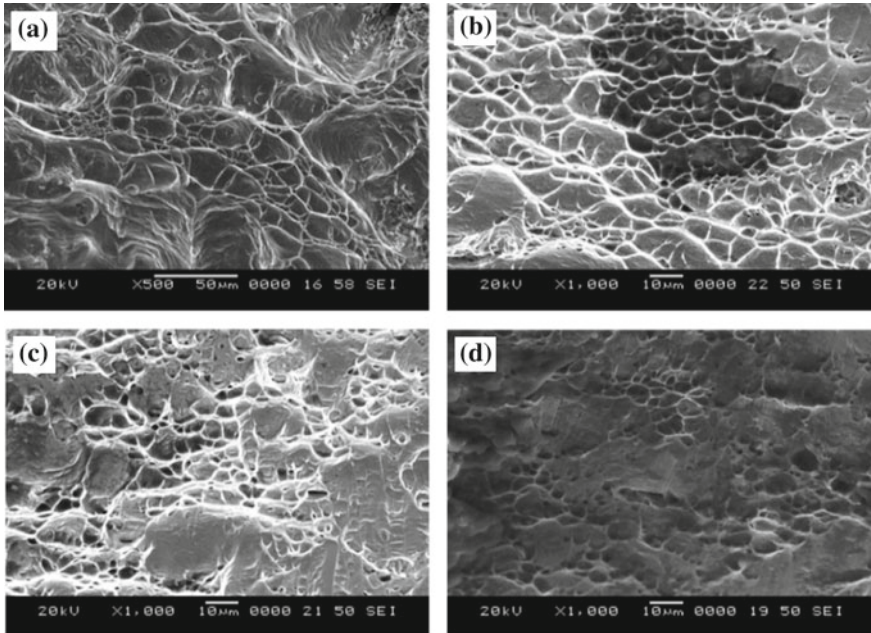


Fig. 7 SEM micrographs of the fractured surface of as-cast **a** Cu-3% Ti alloy, **b** rolled 70% reduction Cu-3% Ti alloy, **c** rolled 80% reduction Cu-3% Ti alloy, and **d** rolled 90% reduction Cu-3% Ti alloy

4 Conclusions

Rolling was successfully carried out at room temperature up to 90% reduction on Cu-3%Ti alloy and following points are concluded

- Elongated and shear deformation bands are observed in the optical and transmission electron microscope analysis. As the number of rolling pass increases, density of shear bands increased.
- Higher hardness was found in the rolled 90% reduction Cu-3%Ti alloy due to higher cumulative strain and high dislocation density.
- Rolled 80% reduction Cu-3%Ti alloy UTS was reached to 812 MPa which is 1.69 times higher than counterpart base alloy due to grain refinement.
- After 90% reduction fracture, surface reveals a combination of both ductile and brittle mode of fracture.

References

1. Xie GL, Wang QS, Mi XJ, Xiong BQ, Peng LJ (2012) The precipitation behavior and strengthening of a Cu-2.0 wt% Be alloy, *Mater Sci Eng A* 558:326
2. Soffa WA, Laughlin DE (2004) High-strength age hardening copper-titanium alloys: redivivus. *Prog Mater Sci* 49(3):347
3. Lebreton V, Pachoutinski D, Bienvenu Y (2009) An investigation of microstructure and mechanical properties in Cu-Ti-Sn alloys rich in copper. *Mater Sci Eng A* 508(1–2):83
4. Sobhani M, Mirhabibi A, Arbi H, Brydson RMD (2013) Effects of in situ formation of TiB_2 particles on age hardening behavior of Cu-1 wt% Ti-1 wt% TiB_2 , *Mater Sci Eng A* 7:16
5. Markandeya R, Nagarjuna S, Sarma DS (2005) Characterization of prior cold worked and age hardened Cu-3Ti-1Cd alloy. *Mater Charact* 54(4–5):360
6. Markandeya R, Nagarjuna S, Satyanarayana DVV, Sarma DS (2006) Correlation of structure and flow behavior of Cu-Ti-Cd alloys. *Mater Sci Eng A* 428(1–2):233
7. Bozic D, Dimcic O, Dimcic B, Cvijovic I, Rajkovic V (2008) The combination of precipitation and dispersion hardening in powder metallurgy produced Cu-Ti-Si alloy. *Mater Charact* 59(8):1122
8. Ramesh S, Nayaka HS, AnneG, Gopi KR (2018) Influence of cold rolling process on microstructure and mechanical properties of Cu-1.5% Ti alloy. *AIP Conference Proceedings*, vol 1943(1):020055

An Investigative Approach to Study the Corrosion Response of Copper–Brass TIG Welded Samples Using Nitric Acid as the Corroding Agent



Aparna Vinayan, Sourabh S. Nair, Raghuraman Srinivasan
and Sivachidambaram Pichumani

Abstract The work intends to study the behavior of a unique blend of the welded sample, joined through a couple of welding techniques, against corrosion attack initiated by an acid as the corroding agent with different exposure times and acid concentrations. The corrosion aspects of copper–brass weldments against nitric acid have been the focal point of our paper. The authors have extensively elaborated on the analysis factors used for the study through the introduction section. The literature review helped us to engage in the study covering the fundamental aspects. In this research article, we have attempted to study the response of a copper–brass alloy combination, welded with two different techniques of TIG welding—ATIG and PCTIG— against nitric acid as the corrosive agent. The corrosion rate is determined by the method of mass loss or weight loss method.

Keywords Copper · Brass · TIG welding · ATIG · PCTIG · Corrosion · Nitric acid

1 Introduction

Brass is a combination of copper, in a dominant proportion, usually coupled with zinc. Several combinations of brass with other elements tend to impart specific properties and thus are employed in several applications. Brass with 39% weight composition with 3% lead is used in components like switch terminals. A mixture of 24% zinc and 12% nickel is used in resistance wires, connectors etc. Gearbox components would invite brass in tandem with a series of elements like manganese, aluminum, lead, and silicon. Many applications of brass are driven by the economic factor like in the case of manufacturing valve chests which are costlier when done with steel. Copper (reddish-brown color atomic number 29), as we all know, has a wide range of applications [1]. The innumerable properties would encompass an FCC

A. Vinayan · S. S. Nair · R. Srinivasan (✉) · S. Pichumani
SASTRA Deemed University, Thanjavur 613401, Tamil Nadu, India
e-mail: raghu@mech.sastra.edu

© Springer Nature Singapore Pte Ltd. 2019
S. S. Hiremath et al. (eds.), *Advances in Manufacturing Technology*,
Lecture Notes in Mechanical Engineering,
https://doi.org/10.1007/978-981-13-6374-0_21

crystal structure, application-based qualities of conductivity, ductility, malleability, and also lower chemical reactivity. Copper, for example, finds major application in aquaculture to prevent biofouling. Easily shaped into pipes and drawn into wires, copper thus exhibits ductile nature. The toughness parameter establishes copper use in weaponry and other tools as they do not get fragmented upon impact or brittle under lower temperature conditions. Positives are aplenty and its non-magnetic behavior, attractive color, recyclable nature and not to forget its use as a catalyst in various chemical and biochemical reactions, etc. Thus, in view of the broad spectrum of utilization, copper has been perceived in this study as an opportunity for further analysis of its expansive functional domain [2].

1.1 Welding

Welding is one such mechanical operation which in simple terms is supposedly engaged in joining any two given metals or alloys or both. The materials, though, need to be tested for their response to such a mechanical process. Welding imparts a permanent joint aided by the application of heat or pressure as the materials to be joined are melted and allowed to solidify. Weldability is affected by factors like crack formation, oxidation, and hardness [3]. TIG welding, also referred to as gas tungsten arc welding (GTAW), has been found to be an appropriate welding method due to quality weld that promises improved resistance to faults and mechanical properties such as high strength and cleanliness and additional economic benefits. Though TIG is identified with certain positive attributes as just mentioned, other factors like coarse grain structure formation during welding of materials, say, for example in case of aluminum alloys and composites and intermetallic formation in the welded region tends to produce weak mechanical properties. Weld strength is assumed to be below par in case of arc welding. In order to overcome the grain structure challenge, the focus can be established on employing surface nucleation, with an agent like scandium, micro-cooler expansion, with silicon and titanium powders, circular segment swaying, and pulsing current that will, in turn, narrow down to a finer grain structure [4]. Dissimilar metal welding is a welding technique involved in fitting together two metals in possession of separate chemical and mechanical properties. Dissimilarity in nature of the materials is easily established due to the geological conditions under which they are formed. Factors to be taken note in order to maximize benefits: solubility, intermetallic compounds, weldability, thermal expansion, melting rates, and corrosion.

1.2 ATIG and PCTIG

ATIG welding promises better weld penetration with optimized flux coating thickness. SiO_2 seems to be highly cohesive to be used in ATIG for it gives the highest depth to width ratio with promising weld depth and width. Gas tungsten arc welding is

superseded by ATIG welding which promises a better process productivity, especially in welding of large components [5]. ATIG welding also promises better arc shape in comparison with TIG welding and is fruitful if the flux employed for welding is SiO_2 . Even though ATIG is promising compared to conventional TIG welding, it still has limitations and these forbid its usage in the industrial setups. Pulsed current TIG welding (PCTIG) can be employed in applications at the industrial scale as it requires minimal adjustments to available systems. There are several parameters to take into account which enhances the effectivity of PCTIG welding [6]. The parameters of PCTIG welding that were significant for its effective welding are supposedly influenced by factors like interaction effect, signal-to-noise ratio, and mean response. The parameters like pulse frequency, peak current, and base current have a direct effect on the microstructure and mechanical behavior on the heat subjected zone.

1.3 Corrosion

Corrosion can be simply defined as the erosion of any given material when subjected to certain environments that have been ascertained to be instrumental in aiding or initiating corrosion. This erosion of material, or corrosion, is common in metals and thus, it becomes one of the major parameters to establish the quality of a material. Since corrosion is a binding problem for any application, there exist several tools and mechanisms to deal with the harmful effects of the same [7]. Acidic corrosion is identified during the wear and damage of a metal under perilous acidic environments. The source of the acid could be from anywhere, for example, soil, industrial air or water, or subsequent reactions due to the contact of certain reactants. Nitric acid is corrosive in the sense it can initiate majorly general corrosion attacks, crevice attack, and intergranular attack. Materials like stainless steel, chromium-based alloys, and aluminum show good resistance to corrosion due to nitric acid while materials like carbon steel or copper-based alloys may not be as effective [8]. Thus, while preferring materials for a certain purpose would invite attention toward the application, equipment used concentration of the acid as well as its temperature. Though we have recognized several properties of copper and brass material, including their corrosion response, it is indeed a perceived fact that their action against corrosion due to an acidic medium is mild. Brasses especially are found to have excessive damage due to the presence of zinc as nitric acids tend to initiate dezincification process. Even though nitric acid is extremely reactive against these elements, certain surface complexation techniques have been evolved to successfully protect the materials against the perils of corrosion.

2 Methodologies

2.1 Welding

Welding has been carried out using ‘ADOR CHAMPTIG 300AD’ welding machine upon copper–brass weldment samples having a plate thickness of 6 mm (Figs. 1 and 2).

ATIG welding has been employed with help of flux powders of SiO_2 , Al_2O_3 , TiO_2 , etc., and both alternating and direct currents have been engaged during the process. A few of the weldments have been subjected to PCTIG welding as well. Standard for specimen preparation and testing—**ASTM G31**.

Fig. 1 TIG welding machine



Fig. 2 Rinsing apparatus after corrosion test A



2.2 Corrosion Test A

The samples so obtained after subjecting them to various welding techniques have been tested against nitric acid for their corrosion response. This test was carried out to map the possibilities of corrosion test B. Filing was then carried out to identify surface features of the weldments.

2.3 Corrosion Test B

The samples so obtained after subjecting them to initial corrosion test A against nitric acid for their corrosion response and filing were tested under another set of corrosion study as follows:

- (A) Initially, the samples are numbered 1–9 and stationed on a flat surface along with nine beaker samples of nitric acid and distilled water (observation Table 1).
- (B) The samples numbered 1–9 are weighed on the electronic weigh balance and their respective weights are noted down.
- (C) While beakers 1, 2, and 3 consist of purely nitric acid (50 ml, 70% conc.), beakers 4, 5, and 6 consist of nitric acid and distilled water taken in 1:1 ratio, respectively, (50 ml of 70% nitric acid + 50 ml of distilled water) and beakers 7, 8, and 9 consist of nitric acid and distilled water taken in 1:2 ratio, respectively, (50 ml of 70% conc. nitric acid + 100 ml of distilled water) (observation Table 1).
- (D) The sample 1–9 is dipped in beakers 1–9, respectively, taken in the same order as mentioned in point C.
- (E) The samples 1, 2, and 3 are exposed to nitric acid as per their corresponding beaker specifications for 60, 120, and 180 s, respectively (Fig. 3).



Fig. 3 Rinsing apparatus after corrosion test B

Table 1 Pictorial representation of samples before and after corrosion test A, filing and corrosion test B have been shown for three samples

Sample No.	Surface roughness value for copper (μm)	Surface roughness value for brass (μm)
1	2.02	2.51
2	1.85	1.92
3	1.64	1.27
4	2.55	1.89
5	2.95	1.40
6	3.46	1.02
7	2.17	1.53
8	2.09	1.68
9	2.10	1.58

Table 2 Tabulation showing rate of corrosion and percentage weight loss for the nine samples of corrosion test B

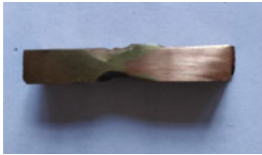

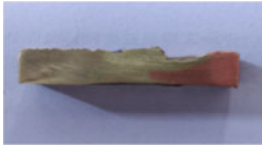

Sample No.	Time of exposure (s)	Change in weight ($I_A - F_A$) (g)	Rate of corrosion (gram/s)	Weight loss (%)
1	60	1.9860	0.0331	15.58
2	120	2.0516	0.01709	18.63
3	180	3.8392	0.0213	34.41
4	60	1.5370	0.0256	10.023
5	120	1.9270	0.1605	18.49
6	180	3.2340	0.01796	25.16
7	60	0.2251	0.00375	1.982
8	120	1.7980	0.01498	15.71
9	180	2.9415	0.01634	23.97

- (F) Similarly, samples 4, 5, 6, 7, 8, and 9 were exposed to nitric acid as per their corresponding beaker specifications for 60, 120, 180, 60, 120, and 180 s, respectively.
- (G) The samples are weighed again to note the loss in weight due to corrosion (observation Table 1).
- (H) The observations were tabulated (Table 2).

3 Results

See Table 3.

Table 3 Tabulation indicating the weight of the samples after filing and corrosion test B

Sample no.	Initial sample	Sample after corrosion
1		
2		

3.1 Surface Roughness

Several studies indicate that appropriate surface modification can lend remarkable resistance to corrosion attack. Especially, if the grain properties are known, it could impart significant insights into how to effectively deal with corrosion attacks. Henceforth, the surface roughness values have been tabulated as is below (Table 1 and 4).

4 Discussion

4.1 Rate of Corrosion and Percentage Weight Loss

Formulae:

$$\text{Corrosion rate} = \frac{\text{Initial weight} - \text{Final weight}}{\text{Time of reaction}} \tag{1}$$

$$\text{Percentage weight loss} = \frac{\text{Initial weight} - \text{Final weight}}{\text{Initial weight}} \times 100$$

Example 1: Consider sample 1 in corrosion test B

Initial weight = 12.7446 g

Final weight = 10.7586 g

Time of reaction = 60 s

Table 4 Surface hardness values for copper and brass after filing and corrosion test B

Sample No.	Time of exposure (s)	Concentration of nitric acid	Initial weight I_B (g)	Final weight F_B (g)
1	60	50 ml of 70% HNO ₃	12.7446	10.7586
2	120	50 ml of 70% HNO ₃	11.0104	8.9588
3	180	50 ml of 70% HNO ₃	11.1562	7.3170
4	60	50 ml of 70% HNO ₃ + 50 ml distilled water(1:1)	15.3333	13.7960
5	120	50 ml of 70% HNO ₃ + 50 ml distilled water(1:1)	10.4194	8.4924
6	180	50 ml of 70% HNO ₃ + 50 ml distilled water(1:1)	12.8532	9.6192
7	60	50 ml of 70% HNO ₃ + 100 ml distilled water(1:2)	11.3540	11.1289
8	120	50 ml of 70% HNO ₃ + 100 ml distilled water(1:2)	11.4229	9.6249
9	180	50 ml of 70% HNO ₃ + 100 ml distilled water (1:2)	12.2687	9.3272

Thus,

$$\text{Rate of corrosion} = \frac{12.7446 - 10.7586}{60} = 0.0331 \text{ gs}^{-1}$$

and

$$\text{Percentage weight loss} = \frac{(12.7446 - 10.7586)}{12.7446} \times 100 = 15.58\%$$

The study reveals the following extrapolations:

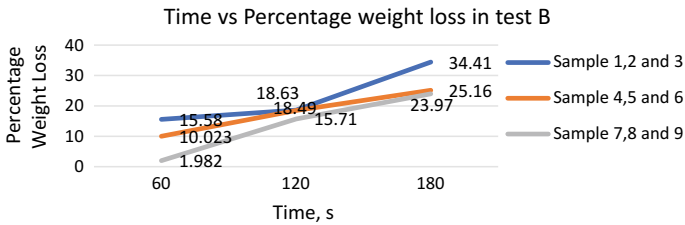


Fig. 4 Plot of exposure time and percentage loss of weight of samples in corrosion test B

1. The corrosion rate increases with an increase in exposure time and thus is directly proportional.
2. The corrosion rate is directly proportional to the concentration of the acid.
3. Points 1 and 2 need to be extensively experimented to decide the more dominating factor of the two.
4. A comparison between the type of TIG welding employed and the corrosion rate can produce substantial results.
5. Surface hardness can be evaluated in comparison with corrosion rate and an established relation between the two can help to devise techniques to tackle corrosion (Fig. 4 and Table 4).

5 Conclusion

The concluding points are:

1. The corrosion rate is dependent on the exposure time and concentration of the acid.
2. Maximum exposure and concentration yield maximum damage.
3. With an exposure time of 180 s and nitric acid, which is 70% in concentration, it is concluded that the corresponding sample has had maximum damage with maximum loss of weight in corrosion test B.
4. The minimum, as effectively, is a time of exposure of 60 s and consecutive nitric acid concentration of 70% taken with water in 1:2 ratio.

References

1. Mihit M, Belkhaouda M, Bazzi L, Salghi R, El Issami S, Ait Addia E (2007) Behaviour of brasses corrosion in nitric acid with and without PMT. *Portugaliae Electrochim Acta* 25(2007):471–480
2. Abeda Y, Kissi M, Hammoutia B, Taleb M, Kertit S (2004) Peptidic compound as a corrosion inhibitor for brass in nitric acid solution. *Progress Org Coat* 50:144–147

3. Mihit M, El Issami S, Bouklah M, Bazzi L, Hammouti B, Ait Addi E, Salghi R, Kertit S (2006) The inhibited effect of some tetrazolic compounds towards the corrosion of brass in nitric acid solution. *Appl Surf Sci* 252(2006):2389–2395
4. Ebrahimzadeha M, Gholamia M, Momenia M, Kosaria A, Moayeda MH, Davoodib A (2015) Theoretical and experimental investigations on corrosion control of 65Cu–35Zn brass in nitric acid by two thiophenol derivatives. *Appl Surf Sci* 332:384–392
5. Sarver E, Edwards M (2011) Effects of flow, brass location, tube materials and temperature on corrosion of brass plumbing devices. *Corros Sci* 53:1813–1824
6. Manam NS, Harun WSW, Shri DNA, Ghani SAC, Kurniawan T, Ismail MH, Ibrahim MHI (2017) Study of corrosion in biocompatible metals for implants: a review. *J Alloy Compd* 701:698–715
7. Asri RIM, Harun WSW, Samykano M, Lah NAC, Ghani SAC, Tarlochan F, Raza MR (2017) Corrosion and surface modification on biocompatible metals: a review. *Mater Sci Eng, C* 77:1261–1271
8. Modenesi Paulo J, ApolinaÂrio EustaÂquio R, Pereira Iaci M (2000) TIG welding with single-component fluxes. *J Mater Process Technol* 99:260–265

A Review on Mechanical Properties, Tribological, Corrosion, and Weldability Studies of Aluminium Composites Processed Using Stir Casting and ECAP Methods



Aravind Muralitharan, Krishna Madhavan, Raghuraman Srinivasan, Venkatraman Ramamoorthi and Sivachidambaram Pichumani

Abstract Equal-channel angular pressing (ECAP) is one of the idiosyncratic processes where the ultra-fine grain refinement takes place in an unsophisticated manner resulting in near-net shape products of good mechanical and metallurgical properties. A simple shear plastic deformation is generated as a result of which a shear strain that is large in magnitude is induced leading to homogeneity within the material which adds to the uniqueness of the ECAP method of processing apart from the benefit of strain hardening. The crux of this paper is to analyse the experimental studies such as fatigue behaviour, wear behaviour, and corrosion behaviour of various aluminium alloys based on ECAP parameters such as channel angle, number of passes, and route. This paper also focuses on the weldability study of aluminium material using pulsed current TIG welding and activated flux TIG welding.

Keywords ECAP · Stir casting · Fatigue · Wear · Corrosion · Welding

1 Introduction

In the present century, aluminium alloys have become more important due to the effects of the environment and the gradual reduction in the amount of available energy. Among the grain refinement processes, severe plastic deformation (SPD) process provided attractive and satisfactory results to researchers in improving the properties of the materials. Out of different SPD processes, ECAP potentially seems to be the most useful process. Welding of aluminium is important in today's world for various applications ranging from automobile to aerospace engineering. Welding of aluminium and its alloys using arc welding such as tungsten inert gas (TIG) welding is the conventional method adopted. This is because of the fact that welding is comparatively cheaper with conventional TIG welding process in comparison to pulsed current TIG welding. In the process of constant current TIG welding, the

A. Muralitharan · K. Madhavan · R. Srinivasan (✉) · V. Ramamoorthi · S. Pichumani
SASTRA Deemed University, Thanjavur 613401, Tamil Nadu, India
e-mail: raghu@mech.sastra.edu

© Springer Nature Singapore Pte Ltd. 2019
S. S. Hiremath et al. (eds.), *Advances in Manufacturing Technology*,
Lecture Notes in Mechanical Engineering,
https://doi.org/10.1007/978-981-13-6374-0_22

material exhibited coarse grains due to the presence of thermal stresses in the heat-affected zones at the time of welding. This results in reduced weld strength due to higher heat input and lesser rate of solidification. So, pulsed current TIG welding is adopted. Also, very less research works are being carried out on corrosion, wear, and fatigue of aluminium specimens after ECAP process.

1.1 Equal-Channel Angular Pressing (ECAP)

Severe plastic deformation (SPD) is a process which results in the reduction of grain size of the specimen, thereby increasing its strength. The processed material tends to show ultra-fine grained properties. Grain refinement/inoculation provides refined grains which can be used for cryogenic applications. ECAP is one of the SPD practices to impart severe strain through simple shear achieved by passing the material through an ECAP die with a diminishment in the cross-sectional territory of the sample and inducing homogeneity [1]. Large amount of shear strain is obtained without any change in the dimension of the specimen. The properties that are obtained through ECAP route are: (1) improved density, (2) high tensile strength and ductility, and (3) possibility of superplasticity at low temperatures [2]. The selection of the channel angle (Φ) and the corner angle (ψ) is very important while designing the equal-channel angular extrusion/pressing die.

1.2 Stir Casting Process

Stir casting is the most widely adopted process for metal matrix composites. The production through this route is more economical and also appropriate for large-scale manufacturing and, also its advantages lie in its simplicity and flexibility. The process involves the melting of matrix material first to get the molten metal and the addition of support material into the dissolve. Before the addition of reinforcement material, the molten matrix metal is susceptible to oxidation due to atmospheric effects. This is followed by the solidification of the melt. After the reinforcement is added, the stirrer is activated by means of a motor on top of stirrer. Stirring speed and stirring time are set properly in order to get the wanted conveyance of scattered stage in the cast framework. Preheating is additionally done at a wanted temperature to stay away from the warm mutilation of the composite material.

2 Mechanical Behaviour of Aluminium

Raghuraman S et al. performed an experiment on the influence of channel angle on deformation behaviour for AA6061-T6 through analysis in deform 3D for different

channel angles—90°, 110°, and 120°. The die models are considered to be rigid and homogenous. Isotropic, homogenous, and plastic frictionless conditions are considered for the material. It has been observed from the results that as the channel angle decreases, the load required for processing the specimen increases, and the effective strain developed due to induced stress increases. The maximum load is observed at 90° channel angle and the least at 120° channel angle [3].

3 Fatigue Studies on Aluminium

Hasan Kaya et al. performed an experiment on fatigue behaviour and mechanical properties of ECAP'ed and Thixoformed AA7075. In this experiment, high-cycle fatigue tests were performed on the five Aluminium 7075 samples. One sample was subjected to only thixoforming process. The ECAP experiment was carried out on four specimens for four different ECAP passes (1 pass, 2 passes, 3 passes, and 4 passes) through C route at a constant temperature of 483 K. The dimensions of the specimens were 20 mm in diameter and length equal to 55 mm. For the process of ECAP, the die had characteristic angles of $\phi = 90^\circ$ and $\psi = 0^\circ$. The stroke speed of the ram was $9 * 10^{-2}$ m/min. After performing ECAP process on the specimens, they were subjected to thixoforming process in order to enhance the properties of the materials. Fatigue experiment was conducted using a four-point bending fatigue machine according to ASTM standard E606/E606-12. It was observed that sudden fractures increase with the increase in the number of passes. The main reason for this observation was found to be related to the severe plastic deformation (SPD) rate created in the material. Another reason which accounts for this observation is the decrease in the recrystallization temperature due to increasing deformation of the material. This also leads to the decrease in the strength of the materials. From this table, it can be seen that the fatigue life cycles of thixoformed sample were better but when fatigue strength and hardness were taken as a whole, the ECAP 1 pass + thixoformed sample showed better results when compared to thixoformed samples and also other samples performed using different passes (2 passes, 3 passes, and 4 passes [4]) (Table 1).

Table 1 Obtained results showing life cycle values of the specimen

	Stress (Mpa)	Life cycles
Thixoformed	140	$5.5 * 10^7$
	120	$5.9 * 10^7$
	100	$6.2 * 10^7$
ECAP1 pass + thixoformed	140	$4.6 * 10^7$
	120	$4.8 * 10^7$
	100	$5.1 * 10^7$

C. S. Chung et al. performed an experiment on enhancement of microstructure of AA6061 alloys' process through equal-channel angular pressing (ECAP). They observed that the fatigue life was enhanced by 10 times when the number of pass is 1. But with the increase in the number of passes to 4, they observed a decrease in the fatigue life of the specimens. This was due to the fact that there was a significant increase in the number of high-angle grain boundaries [5].

4 Tribological Studies on Aluminium

Chegini et al. carried out a trial on the effect of equal-channel angular pressing (ECAP) on wear behaviour of Al-7075 Alloy. The investigations were led utilizing Al-7075 composite as the principle ECAP material. Before performing the ECAP process, the already extruded materials were subjected to annealing process for an hour at temperature of 415 °C. Al-7075 specimens were cut into tube shapes with breadth of 19.1 mm and stature of 140 mm and after that went through an ECAP process having a channel angle of 90° and corner angle of 20°. The number of passes subjected to the specimen is 4 with ram speed of 0.5 mm/s using processing route B_C. After the ECAP process, TEM was used for analysis of the microstructure of processed specimens. Then, wear test was performed on the ECAP'ed specimen. Dry sliding wear test was done on pin-on-disc machine at a relative dampness of 50–65% at room temperature against the counter face of a solidified and cleaned circle made of AISI 52100 steel with HRC 61–64 hardness. During the test, the nominal loads applied are 10, 20, and 30 N at a fixed sliding speed of 1.20 m/s. The outcome on the wear properties was that the wear mass was decreased extensively after 4 passes of ECAP process. Diminishment in the wear mass after ECAP process can be credited to the grain refinement and the expansion in the strength [6].

5 Corrosion Studies on Aluminium

Song et al. performed an experiment on corrosion behaviour of ultra-fine grained industrial pure Al fabricated by ECAP. They have investigated the corrosion behaviour of pure Al in a chloride ion medium after the processing of ECAP. They observed from the results that the resistance to pitting corrosion has been improved. The reason suggested for this observation was that due to larger number of grain boundaries, more stable passive film is formed on the surface of the specimen [7]. Gopala et al. carried their research work on localized corrosion of an ultra-fine grained Al-4Zn-2 Mg alloy produced by cryorolling and observed improved corrosion resistance [8].

6 Weldability Studies on Aluminium

During the TIG welding on aluminium alloys and aluminium composite, the materials show poor weld mechanical properties and also high susceptibility to stress corrosion cracking. This is due to higher heat input, and thereby, brittle intermetallic formations are observed. It causes the initiation site for the stress corrosion cracking [9]. To address this problem, new variants of TIG welding such PCTIG and ATIG welding are used on the welded materials so as to improve the stress corrosion cracking and wear properties. Pulsed current TIG (PCTIG) welding shows improved weld properties through grain refinement in weld zone, and the microstructure changes from coarse grain structure to fine grain structure [10]. PCTIG also reduces the width of the heat-affected zone and thermally induced stresses through increasing cooling rate of the weld zone and reducing the heat input in comparison to TIG welding leading to improvement in tensile properties and fatigue behaviour [11]. This pulsed current TIG welding reduces the formation of aluminium carbide which in turn increases the weld properties of Al-Sic composite. ATIG welding doubles the weld penetration than the normal TIG welding along with reduction in heat input and increased production rate.

7 Scope of Research

Aluminium alloys are often subjected to high temperatures in various applications. So, it is necessary to study its performance in those high-temperature deformations. Welding of aluminium plays a vital role because the right welding with the right parameters provides the material sufficient strength and adequate depth of penetration. Fewer research works are done on welding of aluminium alloys, and very less work has been carried out on the influence of ECAP on welding of aluminium alloys. So, this area needs to be focused for future purposes. Also, optimal channel angle and corner angle during the course of ECAP are necessary to achieve the desired properties of the specimens. So, this area also needs future focus. Also, research works are needed to be carried out on pulsed current and activated flux TIG welding on aluminium specimens and studied the factography of the specimens in order to get a deeper insight into its behaviour under high-temperature deformations.

8 Conclusion

Equal-channel angular pressing which induces severe plastic deformation (SPD) is capable of producing ultra-fine grain refinement of specimens. This increases the properties of the materials. The number of passes in ECAP plays a crucial role in deciding the performance of the specimens. Also, optimal channel angle and corner

angle of die are important. Because of the grain refinement after ECAP, they show improved resistance to corrosion, improved fatigue life cycle of the specimens and also resistance to wear. Stir casting plays a very crucial role in the production of metal matrix composites as they offer more advantages than other methods of production. Some of the advantages include mass production and also flexibility. In this process, parameters such as stirring speed, stirring time, and preheating temperature have a very important role. Pulsed current TIG welding and activated flux TIG welding have taken a very important positions because of their great advantages during the welding. Pulsed current TIG welding and activated flux TIG welding show better depth of penetration and fewer weld defects like porosity and high bead contour. So, welding of aluminium with these types of welding is necessary.

References

1. Raj Mohan R, Venkatraman R, Kabilan S, Raghuraman S (2012) A review of deformation studies of aluminium alloys processed through equal channel angular pressing. *Int J Mech Eng Robot Res* 1:72–80
2. Venkatakrishnan S, Shruthi S, Raghuraman S, Venkatraman R (2016) Experimental findings on the influence of back pressure on equal channel angular pressing of copper processed through powder metallurgy route. *Int J Innov Res Sci Eng Technol* (2016):3568–3574
3. Raghuraman S, Deepak, Kumar S, Vignesh B (2014) Modelling and analysis on deformation behaviour of AA6061 through equal channel angular extrusion (ECAE) die. *Int J Mech Eng Comput Appl* 2:37–41
4. Hasan K, Mehmet U (2013) Fatigue behaviour and mechanical properties of ecap and thixoformed AA7075. *High Temp Mater* 32:1–10
5. Chung CS, Kim JK, Kim HK, Kim WJ (2002) Improvement of high-cycle fatigue life in a 6061 Al alloy produced by equal channel angular pressing. *Mater Sci Eng A* 337:39–44
6. Chegini M, Fallahi A, Shaeri MH (2015) Effect of equal channel angular pressing (ECAP) on wear behavior of Al-7075 alloy. *Procedia Mater Sci* 11:95–100
7. Song D, Ma A, Jiang J, Lin P, Yang D (2009) Corrosion behaviour of ultra-fine grained industrial pure Al fabricated by ECAP. *Trans Nonferr Metals Soc China* 19:1065–1070
8. GopalaKrishna K, Sivaprasad K, Sankara Narayanan TSN, Hari Kumar KC (2012) Localized corrosion of an ultrafine grained Al-4Zn-2 Mg alloy produced by cryorolling. *Corros Sci* 60:82–89
9. Balasubramanian V, Ravisankar V, Madhusudhan Reddy G (2008) Effect of pulsed current welding on fatigue behaviour of high strength aluminium alloy joints. *Mater Des* 19:492–500
10. Balasubramanian V, Ravisankar V, Madhusudhan Reddy G (2007) Effect of pulsed current and post-weldageing treatment on tensile properties of argon arc welded high strength aluminium alloys. *Mater Sci Eng A* 459:19–34
11. Karunakaran K, Balasubramanian V (2011) Effect of pulsed current on temperature distribution, weld bead profiles and characteristics of gas tungsten arc welded aluminium alloy joints. *Trans Nonferr Metals Soc China* 21:278–286

Characterization and Comparison of Functionally Graded Al/Mg and Al/Al 7075 Metal Matrix Composites Manufactured by Die Casting



Goutam Mondal, Pradipta Kumar Rout, Gourab Mohanty and B. Surekha

Abstract The functionally graded materials (FGMs) are introduced to remove the sharp interface that has been present in the traditional composite materials. This sharp interface is replaced with the help of a gradually changing interface to produce continuously varying spatial composition profile. In the present research, an attempt is made to characterize the FGMs made with the combinations of Al/Mg and Al/Al 7075. In the present paper, authors have made an attempt to produce the FGMs by the gravity casting process. Once the FGMs are made, they are analyzed for their microstructure and mechanical properties. The microscopic observations and microhardness tests revealed a gradually changing interface of metal B in metal A and resulted in a continuous gradient FGM.

Keywords Metal matrix composite · Functionally graded materials · Aluminum 7075 · Gravity casting · Magnesium

1 Introduction

Metal matrix composites (MMCs) can be considered to be the future as it is replacing the monolithic materials at a very fast pace because of its lightweight and high strength-to-weight ratio [1]. This grade of materials has opened up new opportunities in the field of material science to explore for more desirable properties. One particular group from this large family is functionally graded materials (FGMs). Mechanical properties are found to change from one layer to another. A study by Galy et al. [2] focused on the characterization of functionally graded metal matrix composites (FGMMCs) which was based on pure aluminum reinforced with different percentages of SiC particles. Another experimental study of Udupa et al. revealed the relative changes in the properties of aluminum when CNT was added as a reinforcing material

G. Mondal · P. K. Rout · G. Mohanty · B. Surekha (✉)
School of Mechanical Engineering, KIIT Deemed to Be University, Bhubaneswar 751024,
Odisha, India
e-mail: surekhafme@kiit.ac.in

© Springer Nature Singapore Pte Ltd. 2019
S. S. Hiremath et al. (eds.), *Advances in Manufacturing Technology*,
Lecture Notes in Mechanical Engineering,
https://doi.org/10.1007/978-981-13-6374-0_23

in FGM [3]. Hadad et al. [4] proposed a reaction centrifugal-mixed powder method (RCMPM) through which FGM rings could be achieved with gradually distributed properties. Liu et al. [5] prepared a tungsten copper-based composite according to the concept of FGM and showed an excellent planetary and parallelism between the layers. Chumanoy et al. [6] introduced WC particles into liquid metal during filling of the mold in centrifugal casting machine. Red tape casting methodology was opted by Yeo et al. [7] to fabricate FGM using zirconia and stainless steel with the help of electrostatic repulsion. Furthermore, Kumar [8] developed the FGM using ultrasonic consolidation (UC) which demands the joining of different metallic foils together. Ulukoy et al. [9] investigated aluminum matrix FGM which contained aluminum and SiC. The specimen was prepared using centrifugal casting technique, and then, the aging treatment was carried out. This resulted in the production of varying hardness values and mechanical properties between SiC-rich and aluminum-rich region. Prakash et al. [10] studied the post-buckling behavior of FGM skew plates under thermal loads. Results showed bifurcation type of instability under thermal load.

2 Test and Analysis Techniques

2.1 *Fabrication of Pure Al/Mg and Pure Al/Al 7075 FGMs by Gravity Casting*

In the present experimental investigations, specimens are prepared with the help of gravity die casting. The die is made up of BS 970. The commercially available pure aluminum, aluminum 7075, and pure Mg are considered as the materials for making the FGMs.

The specimens A and B were prepared with Al/Mg and Al/Al7075 combinations, respectively, to analyze the distribution of metals Mg, Al7075 in metal Al, and their influence on the microstructure and microhardness. The FGM production process includes the following steps.

1. The specified volumes of metals Al, Al7075, and Mg have been separated from the stock and heated in a crucible by keeping them in separate crucibles.
2. The metals kept in separate crucibles are heated to their molten state and hold them there for a sufficient amount of time to achieve the desired degree of superheat.
3. Meanwhile, preheat the die to around 300 °C with the help of moving oxy-acetylene torch to avoid the casting defects related to the cold die.
4. When the metal completely transformed into molten state (700 °C), firstly Al is allowed to pour into the mold cavity followed by Mg. During this period also, the

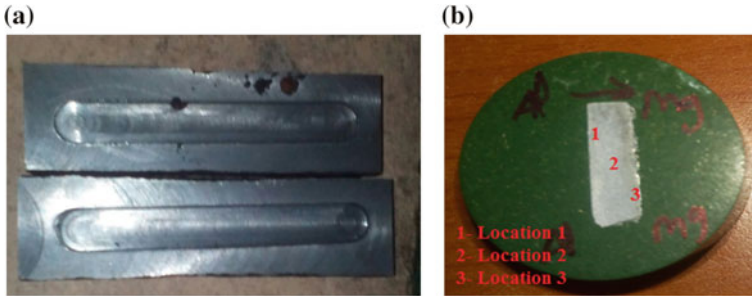


Fig. 1 Schematic diagram showing the **a** dies and **b** FGM specimen

preheating is continued. This will help the die to keep the metal Al in semi-molten state for establishing a proper interface with the metal Mg.

5. After the solidification, the casting is removed from the die cavity.
6. Same procedure will be repeated to produce the FGMs with pure Al and Al 7075.

2.2 Preparation of Samples

The sample for microscopic investigations has been sectioned from Al–Mg and Al–Al7075 cast FGMs. Once the required size of the specimen is removed from the casting, the samples were rough polished with the help of 600, 800, and 1000 graded sheets. Further, fine polishing is done with the help of 1/0, 2/0, 3/0, 4/0, and 5/0 sheets. Finally, the mirror surface is established by utilizing cloth polishing with aluminum oxide paste on disk polishing setup (Fig. 1a).

Then, the etching has been carried out on these properly polished surfaces with 0.5% diluted hydrochloric acid (HF). Microscopic examinations have been conducted using a metallurgical microscope shown in Fig. 2a. The difference in the distribution of Al7075 and Mg particles in the pure aluminum has been studied.

2.3 Evaluation of Mechanical Properties

The developed FGMs are characterized with the help of their mechanical properties also. The required size of the samples for microhardness test was cut with the help of wire-cut electric discharge machining (EDM) process. The Vickers microhardness testing machine shown in Fig. 2b has been used to test the hardness of the samples.

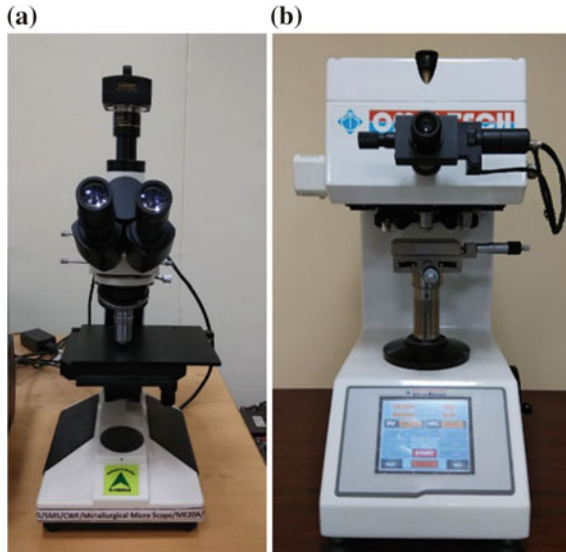


Fig. 2 Schematic diagram of **a** metallurgical microscope and **b** Vickers microhardness tester

3 Results and Discussions

3.1 Investigation of Microstructure

Metallographic samples were sectioned perpendicular to the ground after proper polishing and etching process to observe them under the microscope.

The microstructures at three different locations (that is, shown in Fig. 1b), namely location 1 (that is, Al-rich zone), location 2 (that is, interface zone), and location 3 (that is, Mg-rich zone), across the thickness of the specimen for Al–Mg FGM are recorded and are shown in Fig. 3a–c, respectively. The microstructure of Fig. 3a shows a microstructure rich in Al and very less percentage of Mg, which shows the penetration of Mg into Al. Figure 3b represents almost equal fractions of Al and Mg. Further, Fig. 3c represents the microstructure dominated by Mg. The above microstructures have revealed the evidence of the formation of continuous gradient FGMs across the thickness. A similar result has also been observed for the Al–Al7075 FGM and revealed the formation of FGM.

3.2 Effect Reinforcement on Hardness

In addition to the above study, the microhardness of the as-cast Al–Mg and Al–Al7075 FGMs has also been tested with the help of the microhardness tester with a load of

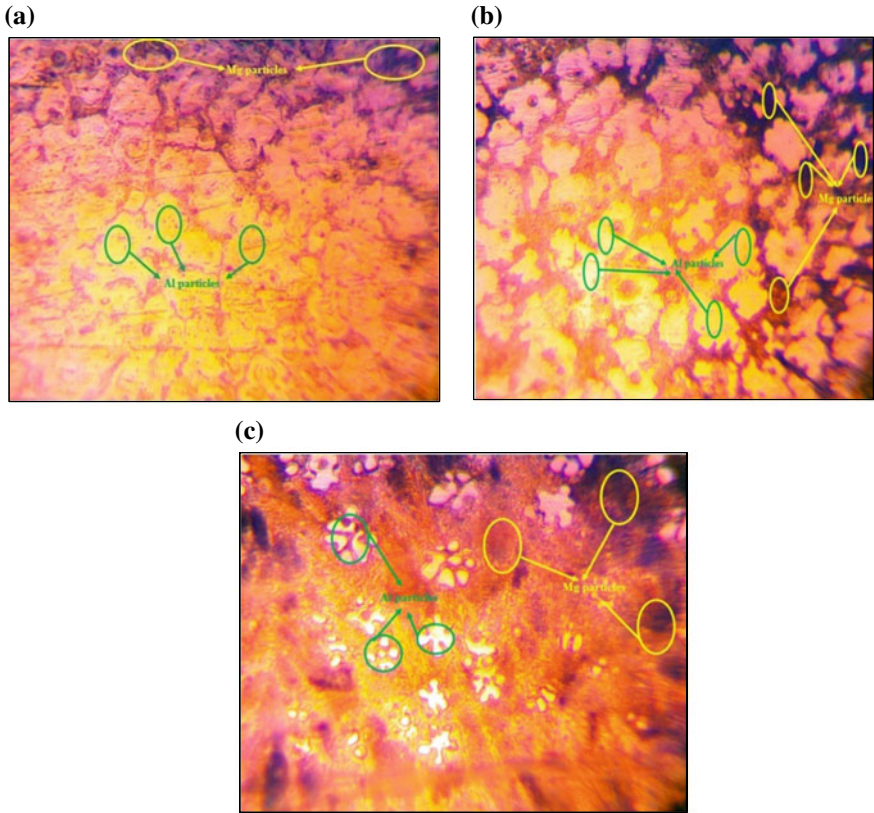
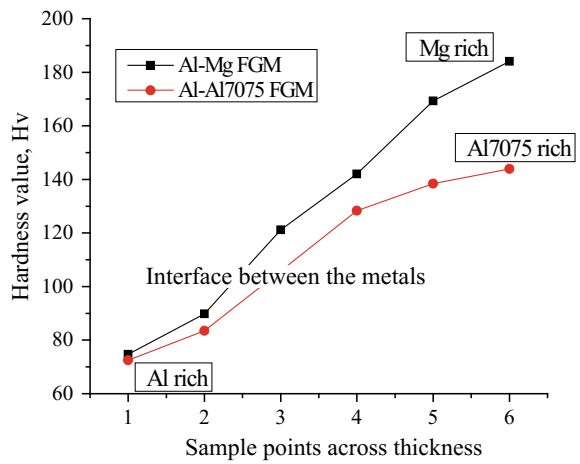


Fig. 3 Schematic diagram showing the microstructures of Al–Mg FGMs, **a** bottom layer, **b** interface layer, and **c** top layer

Fig. 4 Showing the microhardness values for the Al–Mg FGM measured across the thickness



500 g and a steel ball indenter of 1/16 mm diameter. Figure 4 shows the variation of hardness values across the thickness from Al-rich side to Mg-rich and Al7075-rich sides of the two FGM compositions. It has been observed that the hardness values are seen to increase from Al-rich side to the Mg-rich side and Al7075-rich side, respectively, for both the FGMs. This result has also confirmed the formation of FGMs.

4 Conclusions

The fabrication of Al–Mg and Al–Al7075 functionally graded materials is carried out successfully through gravity casting process. Two sets of specimens are separated from the workpiece to carry out the microstructural studies and to evaluate the Vickers microhardness values. After, thorough cleaning and polishing of the two samples microscopic study are conducted using a metallurgical microscope. From the result of hardness and microscopic study, it is concluded that the metal B (Mg or Al7075) is distributed over metal A and resulted in the formation of functionally graded materials.

References

1. Ashish S, Prayag G, Avdresh K, Yamini K, Kanu KV (2014) A review on fabrication and characterization of hybrid aluminium metal matrix composite. *Int J Adv Res Innov* 2:242–246
2. El-Galy IM, Ahmed MH, Bassiouny BI (2017) Characterization of functionally graded Al–SiCp metal matrix composites manufactured by centrifugal casting. *Alex Eng J* 56:371–381
3. Gururaja U, Shrikantha Rao S, Gangadharan KV (2014) Functionally graded composite materials: an overview. *Procedia Mater Sci* 5:1291–1299
4. Shima EH, Hisashi S, Eri MF, Yoshimi W (2010) Fabrication of Al–Al3Ti/Ti3Al functionally graded materials under a centrifugal force. *Materials* 3:4639–4656
5. Liu S, Shen Q, Luo G, Li M, Zhang L (2013) Fabrication of W/Cu FGM By aqueous tape casting. *J Phys Conf Ser* 419
6. Chumanov IV, Anikeev AN, Chumanov VI. Fabrication of functionally graded materials by introducing wolframium carbide dispersed particles during centrifugal casting and examination of FGM's structure. *Procedia Eng* 129:816–820
7. Yeo J-G, Jung Y-G, Choi S-C (1998) Zirconia-stainless steel functionally graded material by tape casting. *J Eur Ceram Soc* 18:1281–1285
8. Kumar S (2010) Development of functionally graded materials by ultrasonic consolidation. *CIRP J Manuf Sci Technol* 3:85–89
9. Ulukoy A, Topcu M, Tasgetiren S (2015) Experimental investigation of aluminum matrix functionally graded material: Microstructural and hardness analyses, fretting, fatigue, and mechanical properties. *J Eng Tribol* 230:143–155
10. Prakash T, Singha MK, Ganapathi M (2008) Thermal postbuckling analysis of FGM skew plates. *Eng Struct* 30:22–32

Statistical Quality Control of Torque Wrenches Used in Automotive Assembly Department



Soham Kulkarni, Chaitanya Kulkarni, K. E. K. Vimal and K. Jayakrishna

Abstract For automobile organizations to stay in business, it is crucial that its products conform to specifications. For adherence to required part specifications, correct application of torque is necessary for achieving the right amount of clamping force that prevents the fasteners from loosening or the joints from failing due to their relative motion. This study reports the application of statistical process control techniques to ensure the quality of torque wrenches used at workstations that deliver the right torque and other countermeasures required, considering the economic constraints. The processes at each and every workstation were checked for their process capability to reduce the dependence on inspection.

Keywords Statistical process control (SPC) · Process capability · Total quality management (TQM)

1 Introduction

To thrive in the competitive global market, every business must work toward the goal of productivity improvement. Productivity mainly has four dimensions: quality, cost, time, and flexibility [1]. This paper aims at improving the productivity of a two-wheeler manufacturer ABC focusing on these quality dimensions. SPC aims to improve the functionality of a product or process by means of various statistical tools [2, 3].

S. Kulkarni · C. Kulkarni · K. E. K. Vimal · K. Jayakrishna (✉)
School of Mechanical Engineering, VIT University, Vellore 632014, Tamil Nadu, India
e-mail: mail2jaikrish@gmail.com

© Springer Nature Singapore Pte Ltd. 2019
S. S. Hiremath et al. (eds.), *Advances in Manufacturing Technology*,
Lecture Notes in Mechanical Engineering,
https://doi.org/10.1007/978-981-13-6374-0_24

2 Literature Review

Patil [4] used statistical process control (SPC) for evaluating the quality of the tightening of bolted connections and verified if the process is stable. Dr. T. V. U. Kiran Kumar used LVDT setup for the collection of data, Minitab software for performing SPC using X-bar charts and process capability histograms for calculating bottom wobble, bottom lift, top wobble and top lift of a wheel producing unit [2]. Sultana et al. [5] used Minitab software for plotting control charts for two machines of a cigarette producing unit and performed Pareto analysis to identify the major causes of machine breakdowns. Momin et al. [6] performed SPC in a pipe manufacturing industry using the control obtained from Minitab software. Avakh Darestani and Aminpour [7] used the short-run control charts in an automotive parts supplier industry for the batch production where limited data (less than 25 observations of each sample) is accessible. Wooluru et al. [8] performed process capability studies in an automotive and evaluated c_p , c_{pk} , c_{pm} , and c_{pmk} indices for analyzing the processes involved. Bendre et al. [9] discussed the process capability indices and the five MT techniques to boost the productivity of a manufacturing industry. S. Mondal et al. performed process capability studies on a multi-stage locomotive wheel manufacturing plant [10]. O. Adeoye Akeem et al. performed process capability studies in Dr. Vamis Oral Rehydration Salt (ORS) production and concluded that the machines were producing the drug with a significant amount of variation in the weight and recommended required solutions [11]. Eramah et al. [12] performed process capability studies on an AJL180-325VS Gap Bed Lathes machine installed for student training for purpose of the industrial application. The X-bar and R-bar charts were also plotted, and C_P and C_{PK} values were evaluated. Shri. Bhushan et al. performed process capability studies on an automotive component supplier manufacturing cylinder head by analyzing 25 specimens and evaluating c_p and c_{pk} values.

3 Methodology

Pertaining to the literature review, the use of SPC methods for quality improvements seems effective and applicable in this case; hence, SPC methods are adopted for process analysis. Initially, theoretical studies on bolted connections, fasteners, advanced pneumatic tools were carried out, followed by workstation-wise observation of the assembly line to find out the types of tools used in each station. Then, training was undertaken offline in the repair zone on the use of dial torque wrench. The torque values were collected in the form of 50 samples per station from all the general stations. If the variation was found to be high, countermeasures were suggested to bring them under control. The data was collected post-implementation of countermeasures.

Following this step, the analysis of the newly collected data was performed. If the variation was found to be under control, the results were documented for future ISO audits or else new countermeasures were suggested, and the process of data collection and analysis was repeated.

3.1 Case Study

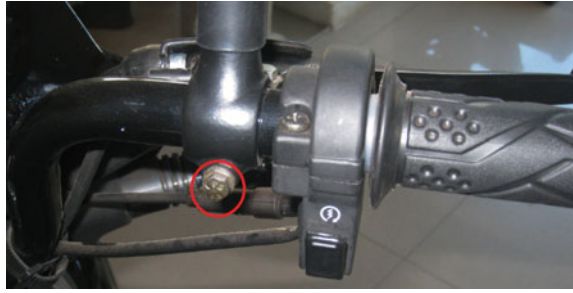
The case study was carried out in a two-wheeler manufacturing unit located in Narsapura, Karnataka, India (hereafter designated as ABC) that requires all its processes to be free of variation. As the current torquing process generates significant variations, the SCP analysis is needed to eliminate those variations. Two types of torque wrenches are used for assembling various parts through fasteners on the assembly line. First is the impact wrench that operates on a hammering mechanism, and another is the oil pulse tool which uses oil as a medium to transfer torque to the fasteners. The former being cheap, it is preferred by the management. However, the impact wrench does not offer a precise control on the torque value unlike the oil pulse tool which has an auto shut-off feature that shuts down the tool when the set torque is achieved. The variation levels in this case become difficult to control as the majority of the guns on the assembly line are impact wrenches. Hence, those guns must be replaced where the torquing process has rendered ineffective.

The data was collected for 50 scooter stations and 49 motorcycle stations. Out of these 50 scooter stations, 10 were found out of control, and out of 49 motorcycle stations, 11 were found out of control based on the analyzed data. For the motorcycle stations, the out-of-control stations are as follows:

1. Bracket R/L handle lever
2. Winker switch assembly
3. Start switch assembly
4. Speedometer assembly
5. Front cushion assembly
6. Number plate stay assembly
7. Wind screen assembly
8. RR unit bolt
9. Chain case assembly lower bolt
10. Chain case assembly upper bolt
11. Side cover screw RH

Similarly, for the scooter model the out-of-control stations are as follows:

1. Throttle housing
2. RHC matching
3. Rear fender
4. Key set
5. Battery box

Fig. 1 Bracket handle lever

6. Air suction valve (ASV) stay tightening
7. Under cover assembly
8. Front cover right side
9. Seat assembly
10. Inner cover screw tightening.

These stations have been brought under control with the help of SPC and control charts improving repeatability of torque values achieved and reducing gun upon substitution of the impact wrenches with the oil pulse tools.

3.2 Sample Station Results and Calculations

After performing SPC analysis on the data collected from the Bracket R/L Handle Lever station, the variations in torque achieved were reduced. The red circle in Fig. 1 highlights the Bracket Handle Lever which is clamped to the handlebar with the help of an M6 bolt and needs torque in the specification range of 8–12 N-m to be tightened.

3.3 Situation Before Use of Oil Pulse Tool

The torque data was collected for 50 samples for subgroup size of 5. The control charts were plotted using the collected data.

Equation (1) shows the formula to calculate the mean (μ) (Fig. 2).

$$\mu = \frac{\sum X}{N} \quad (1)$$

where μ is the mean value, $\sum X$ represents the sum of all observations, and N is the total number of operations. For example, the first subgroup has five observations 15, 14, 13, 12, and 14. Therefore,

Sample size(N)	X̄Chart		σ	R-Chart constants		S-Chart constants	
	A ₂	A ₃		LCL	UPL	LCL	UCL
2	1.88	2.690	1.128	0	3.367	0	3.267
3	1.023	1.954	1.693	0	2.574	0	2.568
4	0.729	1.628	2.059	0	2.282	0	2.266
5	0.577	1.427	0.326	0	2.114	0	2.089
6	0.483	1.287	2.534	0	2.004	0.030	1.970
7	0.419	1.182	2.704	0.076	1.924	0.118	1.882
8	0.373	1.099	2.817	0.136	1.864	0.185	1.815
9	0.337	1.032	2.970	0.184	1.816	0.239	1.761
10	0.308	0.975	3.078	0.223	1.777	0.284	1.716
11	0.285	0.927	3.173	0.256	1.744	0.321	1.679
12	0.266	0.886	3.258	0.283	1.717	0.254	1.646
13	0.249	0.850	3.336	0.307	1.693	0.382	1.618
14	0.235	0.817	3.407	0.328	1.672	0.406	1.594
15	0.233	0.789	3.472	0.347	1.653	0.428	1.572
16	0.212	0.763	3.532	0.363	1.637	0.448	1.552
17	0.203	0.739	3.588	0.378	1.622	0.466	1.534
18	0.194	0.718	3.640	0.391	1.608	0.482	1.518
19	0.187	0.698	3.689	0.403	1.597	0.497	1.503
20	0.180	0.680	3.735	0.415	1.585	0.510	1.490
21	0.173	0.663	3.778	0.425	1.575	0.523	1.477
22	0.167	0.647	3.819	0.434	1.566	0.534	1.466
23	0.162	0.633	3.858	0.443	1.557	0.545	1.455
24	0.157	0.619	3.895	0.451	1.548	0.555	1.445
25	0.153	0.606	3.931	0.459	1.541	0.566	1.435

Fig. 2 X̄ chart constants

$$\mu = (15 + 14 + 13 + 12 + 14)/15 = 13.6$$

For plotting, the X-bar chart control limits are required which are as follows:

$$UCL = \bar{X} + A_2 \times \bar{R} \tag{2}$$

$$LCL = \bar{X} - A_2 \times \bar{R} \tag{3}$$

where $\bar{X} = \sum \bar{X}/N$, $\bar{R} = \sum \bar{R}/N$ for all the subgroups, A_2 is a constant depending on subgroup size which in this case is 5 highlighted in Fig. 4 with green color as 0.577 for subgroup size 5.

$$\bar{X} = \frac{(13.6 + 14.4 + 12.4 + 13 + 13.8 + 14.8 + 13 + 13.2 + 12.4 + 13.4)}{10} = 13.4$$

$$\bar{R} = \frac{(3 + 4 + 2 + 2 + 2 + 4 + 3 + 3 + 3 + 5)}{10} = 3.10$$

Therefore, $UCL = 13.4 + 0.577 \times 3.10$, $LCL = 13.4 - 0.577 \times 3.10 = 11.611$.

From Fig. 3, it can be seen that all the subgroups have their respective means within the control limits.

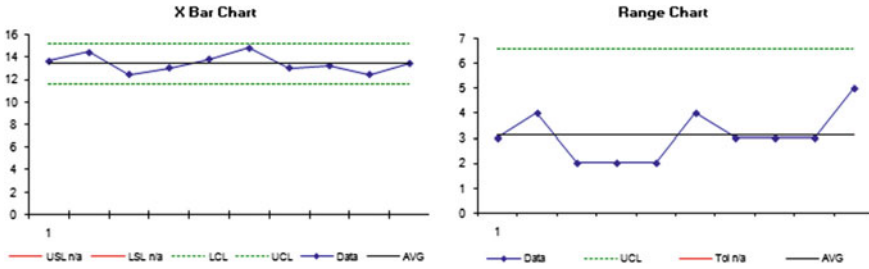


Fig. 3 \bar{X} and \bar{R} charts before change

The R-bar chart plots the ranges of the various subgroups. The formula for calculating the range is shown in Eq. (4).

$$\text{Range} = 15 - 12 = 3$$

$$\bar{R} = \frac{\sum \bar{R}}{N} = \frac{(3 + 4 + 2 + 2 + 2 + 4 + 3 + 3 + 3 + 5)}{10} = 3.10 \tag{4}$$

For plotting, the R-bar chart control limits are required which are as follows:

$$\text{UCL} = D_4 \times \bar{R} \tag{5}$$

$$\text{LCL} = D_3 \times \bar{R} \tag{6}$$

wherefor all the subgroups, D_4 and D_3 are constants depending on subgroup size (here, $D_4 = 0$ and $D_3 = 2.114$).

Therefore,

$$\text{UCL} = 0 \times 3.10 = 0$$

$$\text{LCL} = 2.114 \times 3.10 = 6.5565$$

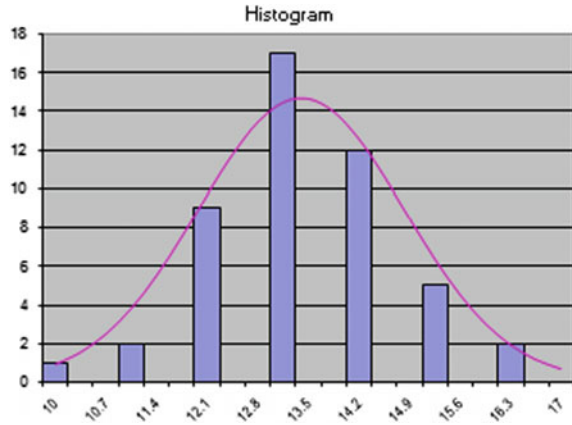
The range for each subgroup is plotted on the R-bar chart with the control limits LCL and UCL as shown in Fig. 3.

It can be seen that all the points are within the control limits. The process capability studies were carried out which give detail about the variation and whether the data is centered to the mean value or not.

The formulae for calculating the process capability index are shown in Eqs. (7)–(10).

$$C_p = \frac{(\text{USL} - \text{LSL})}{6\sigma} \tag{7}$$

Fig. 4 Histogram before change



$$C_{pU} = \frac{(USL - \bar{X})}{3\sigma} \tag{8}$$

$$C_{pL} = \frac{(\bar{X} - LSL)}{3\sigma} \tag{9}$$

$$C_pK = \text{Min}(C_{pU}, C_{pL}) \tag{10}$$

But for the process capability index to be calculated, we need to first calculate the standard deviation or sigma as shown in Eq. (7).

$$\sigma = \sqrt{\frac{1}{N} \sum_{i=0}^N (x_i - \mu)^2} \tag{11}$$

The c_p was found out to be 0.5, meaning the process is barely capable and the c_{pk} was found out to be -0.35 , which means that the process is not centered as $c_p \neq c_{pk}$.

After this, the oil pulse gun was used for the torquing process. The results are shown below. Figure 4 shows the histogram.

4 Situation After Use of Oil Pulse Tool

After the oil pulse tool was implemented, data was collected for the Phase-2 trials with 25 samples. The same control charts were plotted. The $\bar{\bar{X}}$ and 6 were calculated as in the earlier case:

$$\bar{\bar{X}} = \frac{(9.8 + 9.8 + 9.8 + 9.5 + 9.8)}{5} = 9.74$$

$$\bar{R} = \frac{(0.5 + 1 + 1 + 1 + 1)}{5} = 0.9$$

$$\therefore \text{UCL} = 9.74 + 0.577 \times 3.10 = 10.259$$

$$\therefore \text{LCL} = 9.74 - 0.577 \times 3.10 = 9.2207$$

The X-bar chart in Fig. 5 shows that all the subgroups have their means within the control limits and close to the target mean of 10. This clearly indicates that the use of oil pulse tools will yield better results and improve accuracy of the process. Similarly, for the R-bar chart, the control limits were calculated using Eqs. (5) and (6) as follows:

$$\text{UCL} = 2.114 \times 0.9 = 1.9035$$

$$\text{LCL} = 0 \times 0.9 = 0$$

The R-bar chart was plotted using these control limits as shown in Fig. 6.

Here, all the points are within the control limits. Thereafter, the process capability studies were carried out to record the variation details to find out whether the data

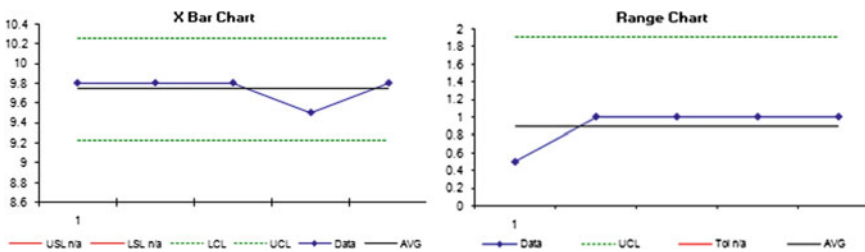


Fig. 5 X-bar chart after change

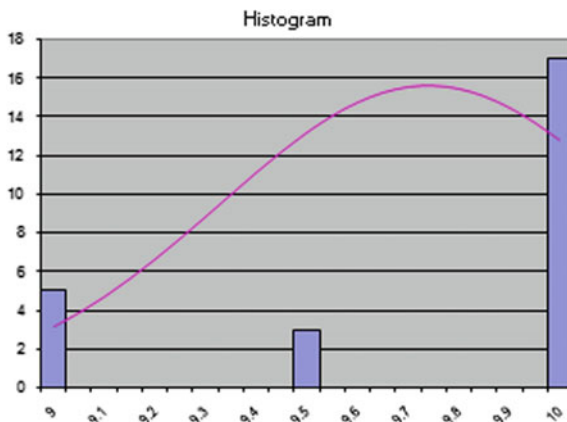


Fig. 6 Histogram after change

is centered on the mean value or not. After the implementation of oil pulse tool, the repeatability has been improved for the mean value of 10 as shown in the histogram below.

The c_p was found out to be 1.72, meaning the process has now become capable and the c_{pk} was found out to be 1.5. Both the values are greater than 1.33 which means the process now delivers accurate results with good repeatability. But still, the process is not centered as $c_p \neq c_{pk}$. The trial and error method could be used to make the process perfect with $c_p = c_{pk}$.

5 Results and Conclusion

This project improved the accuracy of the assembly process at ABC industry by means of statistical process control (SPC), control charts, and process capability indices and further reduced defective assemblies at 10 scooter stations and 11 motor-cycle stations. The dial-type torque wrench was used for the torque data collection in Phase-1 of both the assembly lines. At the end of Phase-1, the stations where variation was found to be more were issued oil pulse tools which have a higher accuracy than the impact wrenches due to the presence of torque setting and auto shut-off feature. The torque was set, and data was collected on a trial and error basis in the Phase-2 to find the best set value for the oil pulse tool which gave repeatable results nearer to the mean value of the specification limit. This eliminated the operator dependence and improved repeatability of the torque values achieved after considering the joint conditions. On the basis of the data collected and analyzed, the management will procure the necessary amount of oil pulse tools or impact wrenches from different vendors like IEC, Yakota, and Atlas Copco considering gun suitability for various stations. With the help of SPC, the line executives and managers can reduce the number of defective assemblies due to joint failures and hence reduce product recalls.

References

1. Jansen-Vullers MH, Kleingeld P, Looschilder MWNC, Reijers H (2007) Performance measures to evaluate the impact of best practices. In: Proc Work Dr Consort 19th international conference on advance information systems and engineering, pp 359–368
2. I. Engineering (2013) SPC tools in automobile component to analyze inspection process, vol 2(1), pp 624–630
3. Deshmukh S, Thampi GT, Deshmukh P (2015) Identification of cost and quality benefits on implementation of ICT based practices in Indian SMEs. *Int J Mech Prod Eng Res Dev* 5(4):115–122
4. Patil P (2016) Torque measurement and statistical process control of bolted connections, vol 3, no. 2, pp 37–40
5. Sultana F, Razive NI, Azeem A (2009) Implementation of statistical process control (SPC) for manufacturing performance improvement. *J Mech Eng ME*.40(1):15–21

6. Momin SA, Kader G, Rahaman M (2016) Study on quality control charts in a pipe manufacturing industry study on quality control charts in a pipe manufacturing industry, 3:359–364
7. Avakh Darestani S, Aminpour N (2014) Short-run control chart for multiproducts with multi-items based on unequal means and variances. *J Qual Reliab Eng* 2014
8. Wooluru Y, Swamy D, Nagesh P (2014) The process capability analysis-a tool for process performance measures and metrics-a case study. *Int J Qual Res* 8(3):399–416
9. Bendre S, Pawar S, Lohar A, Shirke S (2015) *R s p c*, vol 8(2), pp 211–218
10. I. Scienceand (2014) Application of process capability indices to measure performance of a multistage manufacturing process. *Aimtdr*, pp 1–6
11. Federal S, Offa P, Federal S (2013) Process capability analysis as a means of decision making in manufacturing company, vol 1(1), pp 15–18
12. Eramah AA, Raji NA, Durojaye RO, Yussouff AA (2016) Process capability analysis of a centre lathe turning process, *March*, pp 79–85

Optimal Sequence Identification in Parallel Flow Line Environment Using Heuristics



N. Rajeswari and K. Balasubramanian

Abstract In manufacturing environment, it is necessary to find the sequence of jobs on different machines; so that technological constraints are satisfied and the performance criteria are optimized. This paper explores parallel flow line scheduling environment where similar set of machines with varying capabilities exist. The jobs are required to be processed by every machine available in the assigned line and the processing time of similar machines differs between lines. The complexity increases in parallel flow line scheduling because it combines both the flow shop and parallel machine arrangement. This work concentrates on the considered objective, i.e., minimization of makespan in a large parallel flow line machine setup using three metaheuristics, namely Genetic Algorithm (GA), Simulated Annealing (SA), and Bee Colony Algorithm (ABC). To perform computations, a code with Visual Basic language was developed and run on a personal computer. From the test conducted on a set of randomly generated problems demonstrates that GA outperforms SA for the given objective. Secondly, the solutions of GA are compared with ABC Algorithm and inferred that GA outperforms in all instances. Thirdly, the solutions of SA and ABC algorithm are compared. On comparing the results of various algorithms on the same set of problems considered, it is revealed that GA outperforms other algorithms for the chosen conditions of random samples. To measure the efficiency of algorithms apart from the fitness function, computational time taken to achieve the near optimal sequence in the instances is also considered.

Keywords Parallel flow line setup · Optimal sequences · Metaheuristics

N. Rajeswari
St. Peter's College of Engineering & Technology, Chennai, Tamil Nadu, India

K. Balasubramanian (✉)
Bharath Institute of Higher Education and Research, Chennai, Tamil Nadu, India
e-mail: balaraji1974@gmail.com

© Springer Nature Singapore Pte Ltd. 2019
S. S. Hiremath et al. (eds.), *Advances in Manufacturing Technology*,
Lecture Notes in Mechanical Engineering,
https://doi.org/10.1007/978-981-13-6374-0_25

1 Introduction

Scheduling and Sequencing are the methods play a vital role in production environment to find optimal sequences of jobs and machines to carry out a finite set of operations within the constraints. Sequencing refers to the order in which the jobs are processed, whereas Scheduling is a timetable of when the job enters a machine and when it exits and its sequence. One important attribute of a good schedule is minimum work-in-process time. Enumerative algorithm increases the computational time exponentially with problem size while aiming to find the best optimal solution to NP-hard, scheduling problems. Due to dynamic nature of manufacturing system, the complication of scheduling manifolds and therefore the scheduling problems have become the subject of extensive research in the past few decades. Agent-based technology offers a new way of thinking about many complex systems and overcoming the complexity problem. Due to the complexity in scheduling problems, nowadays, conventional complete enumeration techniques are getting replaced by some of the efficient approximation methods or heuristic approaches like Genetic Algorithm, Simulated Annealing, and Tabu Search [1], though it is still a topic of debate. In the manufacturing systems, scheduling is used to meet an objective or a set of objectives. Though there are a number of objectives, some of the most frequently needed non-regular performance measures commonly used in machine scheduling, viz minimize the makespan, minimize the tardiness, and minimize both the makespan and tardiness. Minimization of makespan, an important scheduling criterion, denotes the completion time of last scheduled job as it reflects on production costs, and this criterion causes better usage of the resources specially machinery and manpower. Hence, the most obvious objective is minimization of job completion time, i.e., makespan. Because of the NP-hard nature of the problem, approximation algorithms are preferred to achieve the near optimal solutions to parallel flow line scheduling problem.

2 Parallel Flow Line Scheduling

The various production scheduling environments can be briefly characterized by (i) ' n ' number of jobs on a single machine, i.e., single machine scheduling, (ii) ' m ' number of machines in the same order to process different ' n ' number of jobs, i.e., Flow shop scheduling, (iii) Sequencing and scheduling of number of jobs on number of machines, i.e., Job Shop Scheduling, (iv) Single parallel machine system, i.e., parallel machine scheduling, and (v) Assigning number of jobs on number of machines available in number of performing lines, i.e., parallel flow line scheduling such that certain performance demands like time or cost effectiveness can be fulfilled. Several researchers have studied the above type of scheduling problems, and it has been solved by numerous heuristics. Very few have attempted on parallel flow line

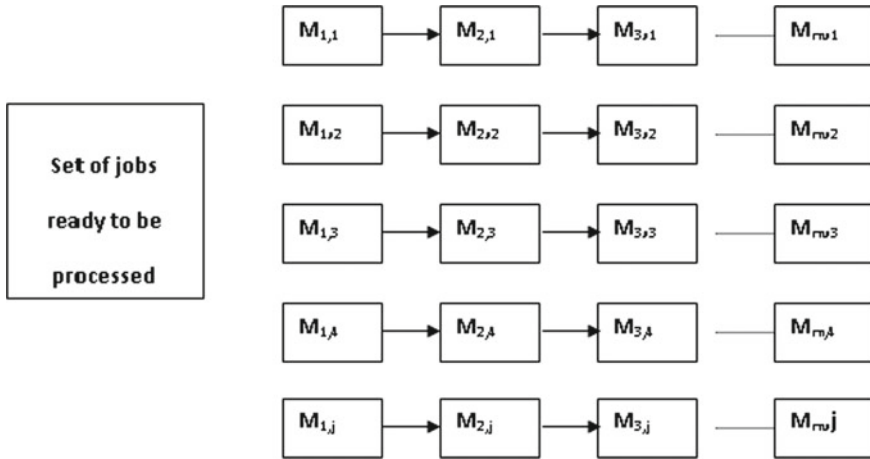


Fig. 1 Comprehensive parallel flow line setup

scheduling problems, and there is no known comparison found in respect of the work presented here (Fig. 1).

The parallel flow line scheduling is characterized by the combination of both parallel machine and flow shop setup. In flow shop, different machines are arranged in line sequence whereas in parallel machine setup, the similar machines but varying capacities are arranged in more than one processing line for the jobs to be processed. Hence, the parallel flow line is characterized by a number of parallel lines, each consisting of 'n' number of machines. The corresponding machines in any two given parallel lines are considered as identical and have equal number of machines on the lines. The essential consideration of conditions in a parallel flow line is that the jobs are not moved from one line to other during phase of processing. Even though the processing time of a job is not same for each machine, once the job is assigned to one particular line and all operations are to be completed in that line only. The selection of a particular algorithm for resolving this situation is not an easy one as there are multiple options to consider. Based on the literature surveys, in order to achieve near global optimal solution to the considered problem in a least time and also to study the pattern of time taken to accomplish the complex problems, metaheuristic algorithms using GA, SA and ABC have been identified. The objective of minimization of makespan in parallel flow line environment is presented in this paper.

3 Literature Survey

In Literature, arriving at optimal sequences is guaranteed in optimization approaches, whereas heuristic approaches confirm delivering near optimal sequences. Heuristics are further observed as twofold: constructive and improvement. Mostly, in construc-

tive category, the methods have been devised by following Johnson's algorithm [2]. Chen and Bulfin [3] studied the complexity of various single machines, bicriteria problems and derived the results largely based on the behavior of the single criterion problem on single machine. Mosheiov [4] handled makespan minimization at various scheduling problem environments like flow shop, open shop, and job shop problems. Chen and Lee [5] considered a two-machine cross-docking flow shop scheduling problem in which a job at the second machine can be processed only after the processing of some jobs at the first machine are completed with the objective of minimization of makespan.

Karaboga and Akay [6] handled ABC algorithm for optimizing large set of unconstrained numerical test functions and analyzed the performances of proposed algorithm with Genetic Algorithm, Particle Swarm Optimization, Differential Evolution Algorithm, and Evolution Strategies. They concluded from the results that ABC is superior to the other population-based algorithms and the proposed algorithm can be used to handle multidimensional optimization problems. Czapinski [7] presented a parallelizable simulated annealing with genetic enhancement (SAwGE) algorithm. Chettha and Kanchana [8] focused on the minimization of makespan in hybrid flow shop with time windows constraint. Three heuristics which include one basic heuristic and two improved heuristics were developed to solve several problem sets of permutation flow shop scheduling problem (PFSSP) with total flow time criterion.

Younes et al. [9] investigated and compared the SA technique and pure flow shop heuristics to generate improved makespan schedules for the flow shop with multiple processors. Yang [10] addressed the objective of minimization of makespan in wire bonding scheduling problem, which is an identical parallel machine scheduling setup. Simulated annealing is so named because of its analogy to the process of physical annealing with solids, in which a material is heated and then allowed to cool very slowly until it achieves its most regular possible crystalline state, with corresponding minimum energy. Metropolis et al. [11] were the first to publish an algorithm that simulates the physical annealing process. Their simulation operates by generating a state perturbation and calculating the resulting energy change. Ever since its introduction, based on the joint efforts of Kirkpatrick et al. [12], simulated annealing algorithm has been considered as one of the promising techniques to produce good results for large combinatorial optimization problems, particularly in scheduling problems.

Ruiz [13] reviewed several variants of hybrid flow shop (HFS) environment with different assumptions, constraints and objective functions, and exact heuristic and metaheuristic methods that have been proposed for its solution. Edis et al. [14] reviewed the parallel machine scheduling problems with five main categories of machine environment, additional resource, objective functions, complexity results and solution methods, and other important issues. Finally, extensions of integer programming models for two main classes of related problems were given and conclusions were drawn based on computational studies. Joo [15] derived a mixed integer programming model for the unrelated parallel machine scheduling with setup and production availability. Besides, hybrid genetic algorithm (HGA) with three differ-

ent dispatching rules has been developed and their performances were evaluated on randomly generated examples.

4 Problem Description and Solution Methodology

There exist extensive research works on various types of scheduling methods. The parallel flow line scheduling is one area which has potential requirement in Beverage, Textile, Plastics Industry, Electrical Equipment Assembly Lines, etc. but sufficient proven options still elude the researches. This work is aimed at one such desired combination of parallel line and flow shop leading to a definition of parallel flow line scheduling. The chosen problem is proposed to be handled by several heuristic methods. By considering the NP-hardness of parallel flow line scheduling problem, it is proposed to explore and compare the sequences that generate near optimal sequences using a computationally efficient and successful heuristic method which includes approaches based on Genetic Algorithm (GA), Simulated Annealing (SA), and Artificial Bee Colony Algorithm (ABC).

In order to define the objectives of the problem of static parallel flow line scheduling (PFLS), some assumptions are taken as given below.

- There are set of ‘*n*’ independent jobs $J_1, J_2, J_3, \dots J_n$ simultaneously available, and the machine group consists of *m* independent machines $M_1, M_2 \dots M_m$, each performs a different function.
- Jobs have deterministic operation times on readily available machines *m*, $m = 1 \dots M$.
- Each job consists of ‘*m*’ number of different operations whose precedence structure is a strict ordering of the operations, where, for each job, the first operation requires machine M_1 , the second operation requires M_2 , and so on.
- Jobs are independent and setup time is based on the sequence and is included in the processing time.
- Job processing on the subsequent machines must be carried out with no delays between any two machines and one operation at a time without splitting.

Here, the objective is to determine which job is to be allocated in which line and in what sequence so as to **minimize makespan**.

The objective function is:

$$\text{Min } Z(X) = \text{MAX } [T_{i1}, T_{i2}, T_{i3} \dots T_{il}] \tag{1}$$

where

$$T_{il} = \sum_{i=1}^n \sum_{l=1}^j \sum_{k=1}^m t_{ilk} + (q_{i-1})\text{max}(t_{ilk}) + S_{i-i} \tag{2}$$

- T_{il} total processing time of job i in line l
 i Jobs identifier $\{i = 1, 2, 3 \dots n\}$
 l Lines identifier $\{l = 1, 2, 3, \dots j\}$
 k Machines identifier $\{k = 1, 2, 3 \dots m\}$
 t_{ilk} Processing time of job i at line l in machine k
 q Quantity of jobs.

5 Results and Discussion

A number of problems have been randomly generated with different combination of number of jobs, machines, lines, and processing times. The processing times of different jobs are randomly generated using random number generator in Microsoft Visual Basic with processing time range between 1 and 10. The three solution methods were tested on a set of same 100 randomly generated problems through a series of computational experiments. A program was written in Microsoft Visual Basic integrated environment to apply the solution methods (GA, SA and ABC) on the generated problems.

It is emphasized that all the experiments were implemented in the same computation environment. A Microsoft vb5.0 code is developed to solve the randomly generated parallel flow line scheduling problems using nature-inspired, population-based, memory usage algorithm, i.e., GA, and non-nature-inspired, single-point search and memoryless algorithm, i.e., SA and ABC and the obtained results, i.e., makespan are compared.

6 Comparison of Metaheuristics Performance

i. GA versus SA

The schedules obtained by the proposed metaheuristic procedure are compared, and from the experimental problems the sequence obtained by GA gives the minimum makespan time as shown in Fig. 2. From the results, the proposed GA outperforms SA algorithm and both GA and SA generate more or less same value to the small-size problems in terms of number of lines and machines employed and that improvement exhibited by GA is significant as the problem size increases.

ii. SA versus ABC

The computational results of SA and ABC algorithm are shown in Fig. 3. From the results, Artificial Bee Colony technique is superior over Simulated Annealing Algorithm and the SA-based scheduling procedure is able to produce the makespan for the small-size problems similar that of ABC.

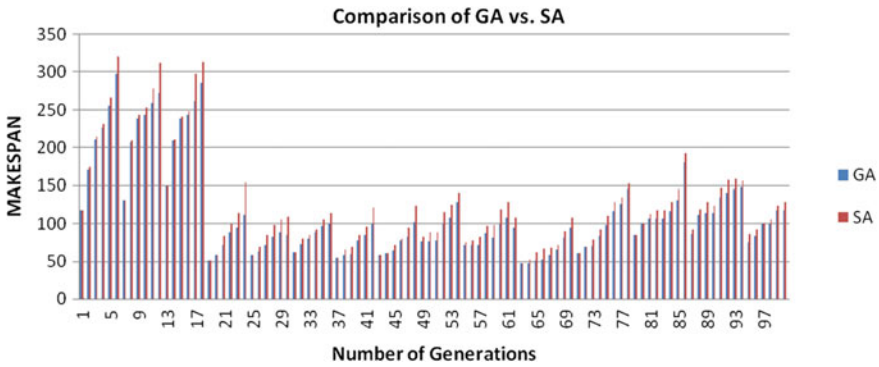


Fig. 2 Performance comparison between GA and SA

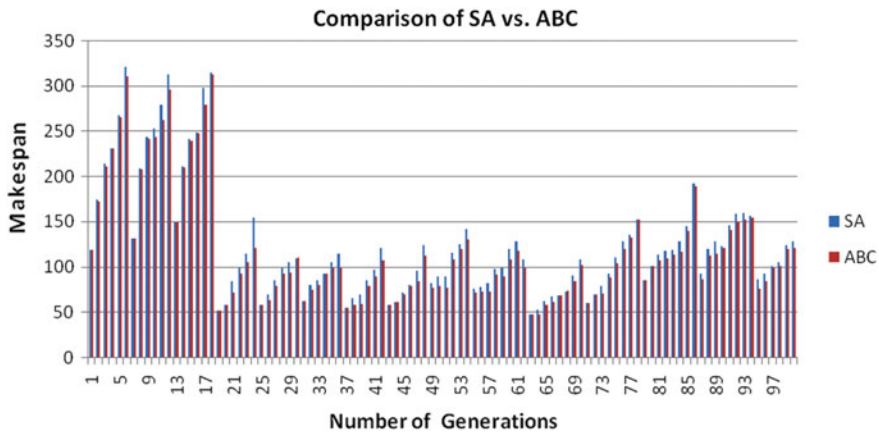


Fig. 3 Performance comparison between SA and ABC

iii. GA versus ABC

The computational results of GA and ABC as exhibited in Fig. 4, the GA based algorithm produce optimal solutions than ABC algorithm in all cases.

iv. GA versus SA versus ABC

Figures 2, 3, 4, and 5 show the results of different metaheuristics used for minimizing makespan in the considered parallel flow line scenario, and it is evident from the figure and statistical analysis that the population-based Genetic Algorithm can give better result in comparison with the other algorithms Simulated Annealing and Artificial Bee Colony Algorithm in terms of effectiveness.

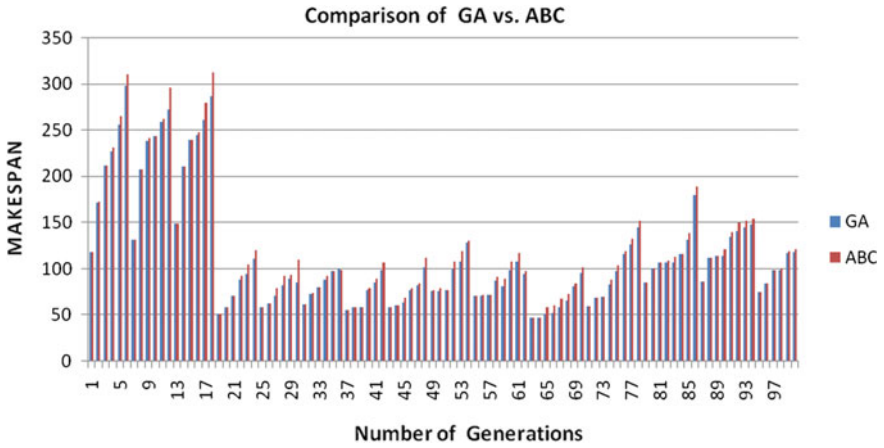


Fig. 4 Performance comparison between GA and ABC

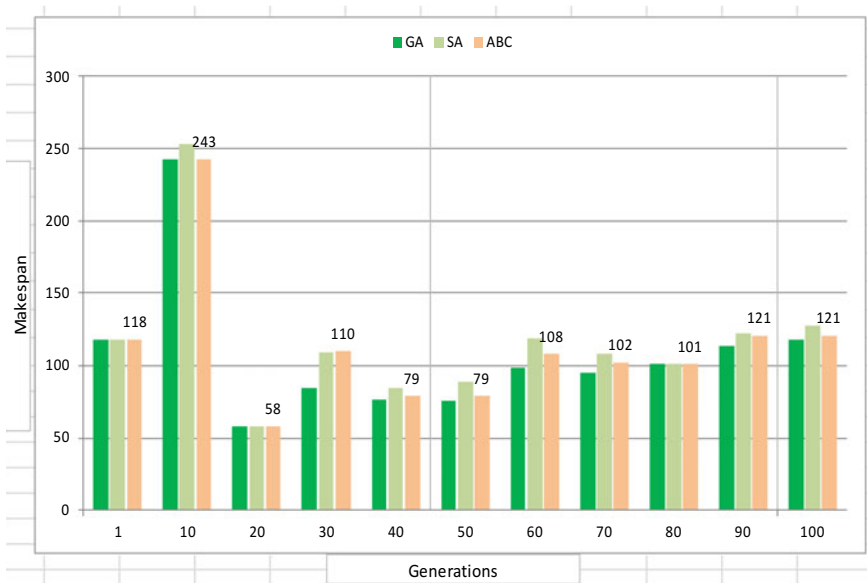


Fig. 5 Performance comparison of GA, SA, and ABC

7 Conclusion

The computation time (sec.) of each metaheuristics to derive an optimal solution to an instance of a problem has been taken into consideration and also been computed to measure the efficiency of solution methods. The mean computation time of various metaheuristics over hundred problem instances shows that the computation time for small-size problems is similar for all the three algorithms. When the problem size increases, it is observed that the computation time of algorithms also increases and varies exponentially. From the experiments, it is inferred that the GA is fastest followed by ABC and SA takes the more computational time. From this, in overall, it is construed that Genetic Algorithm is showing better results than both SA- and ABC-based algorithms.

References

1. Aldulaimi BF, Ali HA (2008) A novel genetic algorithm approach for solving flow shop problem. *Int J Comput Sci Netw Secur* 8(9):229–235
2. Johnson SM (1954) Optimal two- and three-stage production schedules with setup times included. *J Naval Res Logistics Q* 1(1):61–68
3. Chen CL, Bulfin RL (1993) Complexity of single machine, multi-criteria scheduling problems. *Eur J Oper Res* 70(1):115–125
4. Mosheiov G (2002) Complexity analysis of job-shop scheduling with deteriorating jobs. *Discrete Appl Mathematics* 117(1):195–209
5. Chen F, Lee CY (2009) Minimizing the makespan in a two-machine cross-docking flow shop problem. *Eur J Oper Res* 193(1), 59–72
6. Karaboga D, Akay B (2009) A comparative study of artificial bee colony algorithm. *Appl Math Comput* 214(1):108–132
7. Czapinski M (2010) Parallel simulated annealing with genetic enhancement for flow shop problem with C_{sum} . *Comput Ind Eng* 59(4):778–785
8. Chettha C, Kanchana S (2013) Heuristics for scheduling hybrid flow shop with time windows. *Int J Eng Technol* 5(1):41–44
9. Younes N, Santo DL, Maria A (1998) A simulated annealing approach to scheduling in a flow shop with multiple processors. In: *Industrial engineering research conference proceedings, Banff, Canada*, pp 1–8
10. Yang T (2009) An evolutionary simulation optimization approach in solving parallel machine scheduling problems—a case study. *J Comput Indus Eng* 56(3):1126–1136
11. Metropolis N, Rosenbluth A, Rosenbluth M, Teller A, Teller E (1953) Numerical simulation of annealing—equation of state calculations by fast computing machines. *J Chem Phys* 21(5):1087–1092
12. Kirkpatrick S, Gellat CD, Vecchi MP (1983) Optimization by simulated annealing. *J Sci* 220(4598):671–680
13. Ruiz R, Vázquez-Rodríguez JA (2010) The hybrid flow shop scheduling problem. *Eur J Oper Res* 205(1):1–18
14. Edis EB, Oguz C, Ozkarahan I (2013) Parallel machine scheduling with additional resources: notation, classification, models and solution methods. *Eur J Oper Res* 230(3):449–463
15. Joo CM, Kim BS (2015) Hybrid genetic algorithms with dispatching rules for unrelated parallel machine scheduling with setup time and production availability. *Comput Ind Eng* 85:102–109

Design and Analysis of Stringer on the Chassis Frame in Load Carrying Vehicle



B. Stalin, M. Ravichandran, C. Ramesh Kannan and K. Sathiya Moorthi

Abstract In this paper, design and analysis of stringer for the chassis frame in load carrying vehicles is reported. In order to resist the shock, twist, and other stresses, the chassis must be a very hard one. In addition to the strength, the chassis should withstand adequate bending and torsional stiffness. Here, the work performed towards the analysis of stringer in chassis with the constraints of stiffness and strength by using finite element analysis software. Results show that hat stringer is stronger than C-stringer when the stringer is in bending conditions.

Keywords Stringer · Design · Mechanical properties · Finite element analysis

1 Introduction

Patel et al. [1] have analysed the existing heavy vehicle chassis of TATA 2518 TC for different materials. The model of the chassis is drawn by using CAD packages and analysed by using finite element analysis software. After analysis, the results are compared between the existing structures in steel chassis. The geometrically and materially nonlinear analysis is carried out to the pre-stressed compression members on the building boundary conditions.

The stress analysis is carried out on the Pro-Mechanica software and calculated the max stress generated on the chassis. The displacement analysis is also done, and

B. Stalin (✉) · K. Sathiya Moorthi
Department of Mechanical Engineering, Anna University, Regional Campus
Madurai, Madurai 625019, Tamilnadu, India
e-mail: stalin1312@gmail.com

M. Ravichandran
Department of Mechanical Engineering, K. Ramakrishnan College of Engineering,
Samayapuram, Trichy 621112, Tamilnadu, India

C. Ramesh Kannan
Department of Mechanical Engineering, Karpagam Academy of Higher Education,
Coimbatore 641021, Tamilnadu, India

the calculated deformation value is in safe condition. The maximum strain value is also found in the analysis. Finally, the shear stress developed on the TC 2516 chassis is also retrieved from the analysis [2]. Patel et al. [3] have evaluated the optimization of weight on the chassis of truck 2516TC by varying the sections used on the frame of the chassis. The sections used on the chassis are C-stringer, I-stringer, rectangular stringer, and modified C-stringer. Mat et al. [4] have designed and analysed the space frame-type, pressed aluminium-type, and monocoque-type designs of the eco car. The analysis of stress distribution and displacement is done on three characterized conditions. Nor et al. [5] have studied the analysis of an actual low loader structure of I-beam design application of 35 tonne trailer schemed in the house. For the various safety factors, the defection and stress analysis is carried out in FEA 3D and is compared with the 2D numerical analysis. In the C-shaped beam, the circular holes are added to the face to create the cellular beams. It is inspected in the FEM analysis and testing by comparison. For FEM analysis, the ABAQUS software is used. The analysis is carried out for all the specimens, and the failure load results are tabulated in graphical representations drawn between the groups [6]. Ellobody [7] has analysed the castellated steel beams which means that the C-shaped beam is holed on the face as hexagonal shape. Firat [8] has investigated the computerized analysis of four-point bending fatigue of a rear axle assembly. Then, the equivalent von Mises stress analysis is carried out and the fatigue life distribution is calculated. By using FEM analysis, the stress distribution is found on the longitudinal stringer. The original stringer is tested, and the results are found that are having high stress, but in reinforced model, a stringer is giving the better results on stress distribution and displacement of 5.9 mm at 90 KN [9].

2 Methodology

A stringer is a supportive component which is a longitudinal structural part of the framework. Here, the cross member of the chassis frame is going to be analysed in the vehicle TATA 2516 TC truck. The component used in the chassis is C-shaped cross member. Now, we replace the C-shaped cross member by hat-shaped cross members. The hat stringers with 9.53-, 20-, 30-, 40-mm fillet are modelled by using CAD packages and analysed by using FEA software.

The exact C-stringer cross section is 262 mm \times 65 mm. The length of the stringer is 2440 mm. The fillet between the edges is 9.53 mm from Fig. 1. The material of the component is 9345 standard S37 steels. The properties of the S37 steel material are attained from the literature by Patel et al. [1]. The Young's modulus, ultimate tensile strength, and Poisson's ratio are 2.1×10^5 Mpa, 370–490 Mpa, and 0.29, respectively. The hat stringer model developed by the cross section dimensions is 262 mm height, 132 mm in top phase, and 65 mm inside edge. The length of the hat stringer is 2440 mm. The fillet on the edges is 9.53, 20, 30, and 40 mm. The truck capacity is 25 tons, and model no is TATA 2516TC. The weight to be applied on

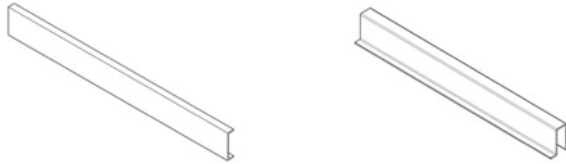


Fig. 1 C-stringer and hat-shaped stringer

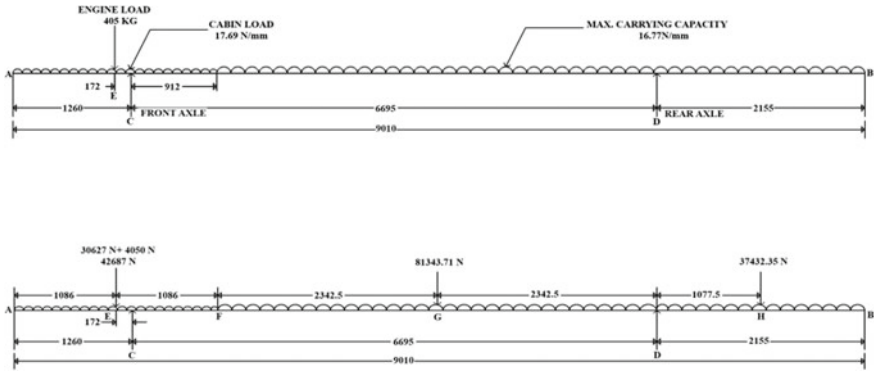


Fig. 2 Load conditions on chassis

the chassis is 245250 N. The capacity factor is 1.25, and then, the weight will be 306562 N. These load characteristics are obtained from the paper (Fig. 2) done by Patel et al. [2].

3 Results and Discussion

In bending analysis, the three-point bending action is carried out by the loading conditions of cabin load, carrying capacity, and engine load. The load values are applied on the category of pressure as well as point load. The pressure load value is 17.69 Mpa due to the carrying capacity and cabin load. The point load value is 4050 N due to the engine load. The three-point bending test is carried out to calculate the deformation of the stringer and the reaction force exerted from the support. The pressure load is due to the total weight of the truck body (cabin and loading carriage). The point load is due to the engine load in the bottom of the cabin.

Deformation of stringer. While applying the loading conditions, the stringer will get deformation in the applied load direction. Here, the load applied direction is the Z-direction. The five models are being analysed for the bending analysis, and the results are given below in Fig. 3.

Stress distribution. Due to the applied load condition, the stress will be created on the stringer. The von Mises analysis is carried out for all the five models to obtain

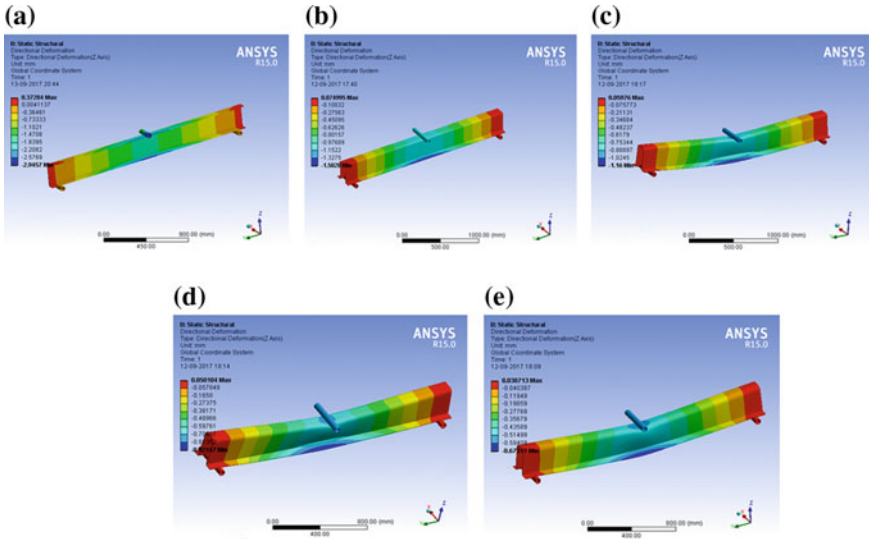


Fig. 3 Deformation of five structures: **a** C-stringer, **b** hat stringer with 9.53-mm fillet, **c** hat stringer with 20-mm fillet, **d** hat stringer with 30-mm fillet, and **e** hat stringer with 40-mm fillet

the stress in maximum and to find its location. The stress distribution of the C-stringer is 1178.5 Mpa which is obtained from Fig. 4a. Figure 4b shows the stress result of 788.9 Mpa on hat stringer with 9.53-mm fillet. The hat stringer with 20-mm fillet is attaining the stress distribution of 659.3 MPa from Fig. 4c. On hat stringer with 30-mm fillet, the stress is circulated over the structure of 502.3 MPa which is got from Fig. 4d. From Fig. 4e, the stress distribution on the hat stringer with 40-mm fillet is 379.2 MPa.

Strain Energy. While applying the given load condition, the energy which is in the form of elastic deformation is called as strain energy of the structure. Here, the strain energy for the five models is obtained from the analysis. The strain energy value for the C-stringer is 903 mJ which is obtained from Fig. 5a. Due to the load application, the hat stringer with 9.53-mm fillet is storing the strain energy of 46.05 mJ which is shown in Fig. 5b. From Fig. 5c, the strain energy value for the hat stringer with 20-mm fillet is 38.4 mJ. Figure 5d displays the strain energy value of 39.5 mJ for the hat stringer with 30-mm fillet. The hat stringer with 40-mm fillet is showing the strain energy value of 33.4 mJ from Fig. 5e.

Reaction force exerted from the support. The reaction force is getting from the bottom two fixed points. The reaction force is calculated by the probe option in the Ansys Workbench. For all models, the reaction forces are gathered. With that, the graphical representation is given and compared. From Fig. 6, the maximum reaction forces are exerted on the model second, third, and fourth models as compared to the first model. Among the three models, the second model is giving the maximum reaction force from Fig. 6. The reaction force exerted from the support is minimum

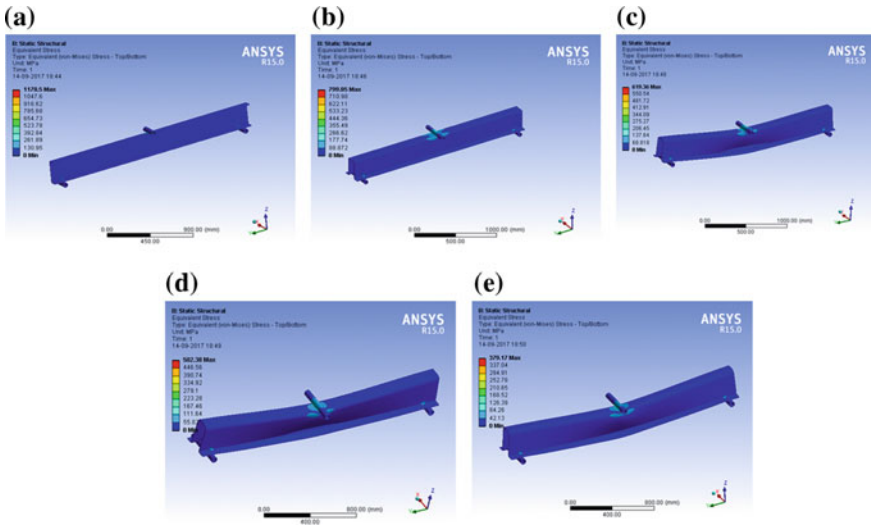


Fig. 4 Stress distribution of five structures: **a** C-stringer, **b** hat stringer with 9.53-mm fillet, **c** hat stringer with 20-mm fillet, **d** hat stringer with 30-mm fillet, and **e** hat stringer with 40-mm fillet

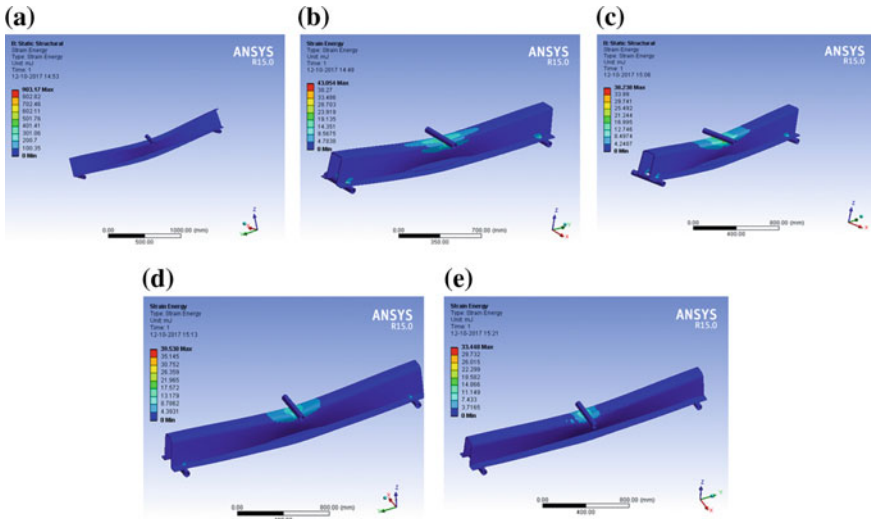


Fig. 5 Strain energy of five structures. **a** C-stringer, **b** hat stringer with 9.53-mm fillet, **c** hat stringer with 20-mm fillet, **d** hat stringer with 30-mm fillet, and **e** hat stringer with 40-mm fillet

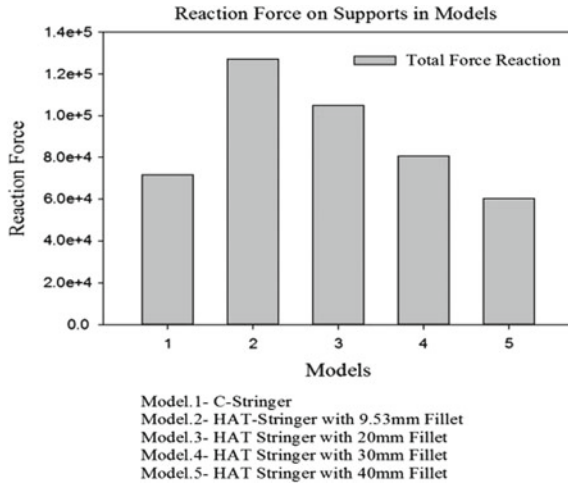


Fig. 6 Reaction force exerted from support

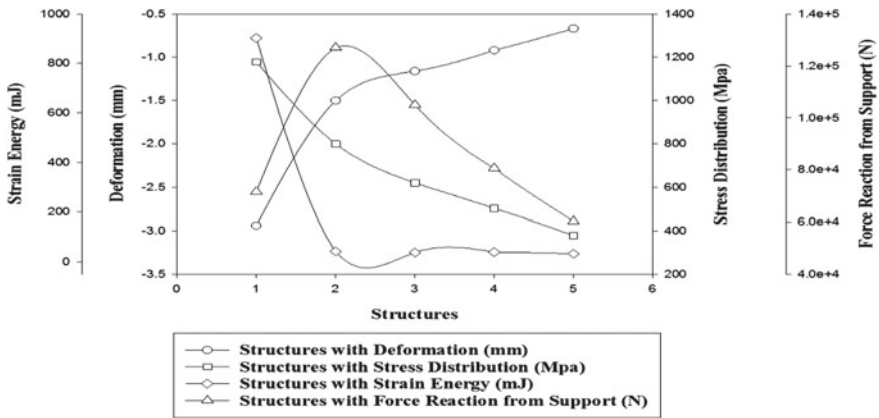


Fig. 7 Comparison of bending parameters

in hat stringer with 40-mm fillet as compared to other hat stringer but maximum in the C-stringer. These are referred from Fig. 7.

4 Conclusion

This paper summarizes the design and analysis of stringer on the chassis frame on load carrying vehicles in bending conditions. Here, hat stringer with 50-mm fillet is not taken for analysis because the top contact area will be reduced due to the increment of

fillet which leads to the decrement of percentage of improvement between C-stringer and hat stringer. In bending, the deformation values are decreased between C-stringer and hat stringer. Among the various stringers studied, very less deformation was observed for the hat stringer with 40-mm fillet. The stress concentration for hat stringer with 40-mm fillet is very less as compared to other structures. Hence, the best model for the substitution of the C-stringer on the chassis on TATA-2516 TC truck is a hat stringer with 40-mm fillet.

References

1. Patel AS, Srivastava A (2016) Modeling, analysis & optimization of TATA 2518 TC truck chassis frame using CAE tools. *Int J Eng Res Technol* 5:10
2. Patel RL, Gawande KR, Morabiya DB (2014) Design and analysis of chassis frame of TATA 2516TC. *Int J Res Appl Sci Eng Technol* 2:III
3. Patel RL, Divyesh Morabiya B, Anil Rathour N (2014) Weight optimization of chassis frame using Pro-Mechanica. *SSRG Int J Mech Eng (SSRG-IJME)* 1:8
4. Mat MH, Ghani ARA (2012) Design and analysis of 'Eco' car chassis. *Procedia Eng* 41:1756–1760
5. Nor MA, Rashid H, Mahyuddin WM, Azlan MA, Mahmud J (2012) Stress analysis of a low loader chassis. *Procedia Eng* 41:995–1001
6. Ellobody E (2012) Nonlinear analysis of cellular steel beams under combined buckling modes. *Thin-Walled Struct* 52(1):66–79
7. Ellobody E (2011) Interaction of buckling modes in castellated steel beams. *J Constr Steel Res* 67(5):814–825
8. Firat M (2011) A computer simulation of four-point bending fatigue of a rear axle assembly. *Eng Fail Anal* 18(8):2137–2148
9. Veloso V, Magalhaes HS, Bicalho GI, Palma ES (2009) Failure investigation and stress analysis of a longitudinal stringer of an automobile chassis. *Eng Fail Anal* 16(5):1696–1702

Design and Analysis of Active Controlled Prosthetic Hand



E. Vijayaragavan, Nikhar Khandelwal and Pathan Aftab Altaf

Abstract Prosthetic hands are artificial hands used by the people who are born with disabilities, who have developed some disease, or who have met with an accident, which has made them incapable to use their hand and hence must rely on artificial hand. Use of prosthetic hand is not a new practice; it rather is the matter of technology which is being used. This chapter details the designing, analysis, and manufacturing of suitable active controlled prosthetic hand, which can perform some complicated hand gestures. Four fingers, thumb, and a palm were designed, and the analysis was made in SolidWorks 2016 by applying necessary boundary conditions. The finite element analysis predicts the safe design under desired conditions. A mobile application with Bluetooth connectivity is developed for the voice-controlled feature for the better implementation. The MIT's 'App Inventor' platform is used for app development, and Google's 'speech-to-text converter' is used for voice recognition. This mechanical prosthetic hand with voice control mechanisms was found feasible for performing regular task of the subjects of interest.

Keywords Prosthetic hand · App Inventor · Voice control

1 Introduction

Current prosthetic hands are fundamentally straightforward grippers which may be a couple degrees of flexibility, which scarcely reestablish the capacity of the thumb-index pinch or some other confused hand signal. This study aims to design and fabricate a suitable multi-finger prosthetic hand which could take place of real hand or at least come closer to it in terms of functionality with tendon control. Although tendon-driven hands are complex and difficult to implement, they have many advantages. A tendon-driven manipulator allows for a much lighter and streamlined design

E. Vijayaragavan (✉) · N. Khandelwal · P. A. Altaf
Department of Mechanical Engineering, SRM Institute of Science and Technology,
Kattankulathur 603203, Tamil Nadu, India
e-mail: vijayaragavan.e@ktr.srmuniv.ac.in

© Springer Nature Singapore Pte Ltd. 2019
S. S. Hiremath et al. (eds.), *Advances in Manufacturing Technology*,
Lecture Notes in Mechanical Engineering,
https://doi.org/10.1007/978-981-13-6374-0_27

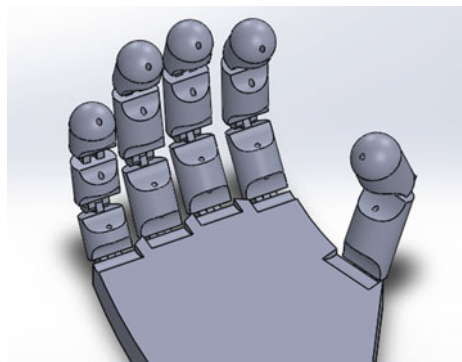
along with cheaper components and maintenance cost. Figure 1 shows the bones and articulation of the hand. Every finger has 4 degrees of freedom, 3 for flexion and extension and 1 for abduction and adduction [1]. The thumb is the most intricate structure, having a total of 5 degrees of freedom.

Currently, many researchers are working in the design and development of robotic arms based on its requirement. Several actuation methods have been employed in different designs been used. The tendons in the human hands are replicated by cables passing through the fingers, and these cables are controlled by motors positioned at the joints [2]. Some prosthetic hands use gears for power transmission from the forearm to the fingers, while others have actuators that can directly transmit power at the required locations [3]. Pneumatic muscles were used by Anthroform Arm, and shape memory alloy wires were employed as tendons which can extend and contract based on temperature gradient [4–6]. This work attempts to lay the foundation of a prosthetic hand that can mimic the human hand in terms of functionality with ease of controls.

2 Design of Prosthetic Hand

The main scope of this work includes complete design of a mechanical hand system that can imitate human hand motions and constraints. The tendons and muscles are the actuators of the human hand. Understanding of their capability, interdependencies, and constraints is immensely important before designing any mechanical system. The designed mechanical hand has a total of 14 degrees of freedom, with thumb has only 2 degrees of freedom instead of 4. The design contains four fingers, a thumb, and a palm module as shown in Fig. 1.

Fig. 1 Assembled hand model



3 Control Mechanisms

3.1 Voice Control

A voice-based control mechanism was designed to overcome some of the control limitations in FSR controlled mechanism. Figure 2 represents the operational cycle of voice control mechanism. A mobile application for android was developed on MIT’s ‘App Inventor’ platform so that anyone can use the hand just by using a mobile application. For the connectivity, the user is just needed to connect the mobile’s Bluetooth to the hand’s Bluetooth receiver and tap on the microphone button followed by giving it a voice command. Google’s ‘speech-to-text recognizer engine’ was used to accurately convert voice command to text [6], and then, the mobile app’s functionality is used to send that text to the Bluetooth module for the Arduino to read from.

3.2 Mobile Application

The mobile application is supported in all versions of android devices. It uses speech-to-text convertor engine to convert speech command to text command; then, by using Bluetooth serial, it sends that command to receiver Bluetooth module. Before giving any command, one has to first click on the Bluetooth image to set up a connection with the desired Bluetooth module. When this is done, red colored ‘Not Connected’ text will change to green colored ‘Connected’ text and the application is ready to send the commands. After this, user needs to tap the microphone button and give voice commands, which then the app converts to text command and sends to connected Bluetooth module. Figure 3 can be referred for mobile application program to convert speech to text.

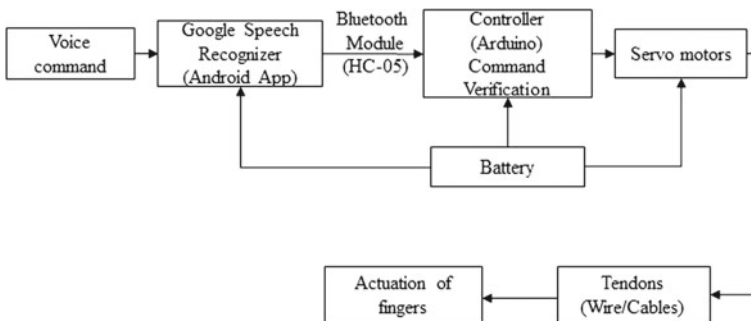


Fig. 2 Operational cycle of voice-controlled mechanism

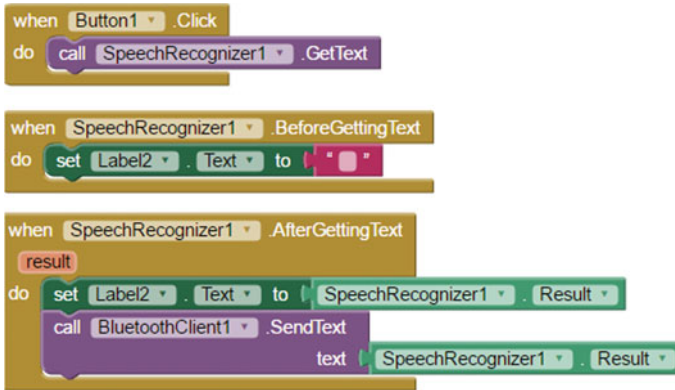


Fig. 3 Mobile application program to convert speech to text

3.3 Servomotors

They are rotatory actuators with precise angular orientation, velocity, and acceleration. Their purpose is to pull the tendons, which in turns pull the fingers and align them into a suitable orientation based on ones need. The specifications of the servomotor are as follows:

Rotational range	0°–180°
Operating voltage	4.6–6 V
Operating speed	10/60 s/deg
Stall torque	18–2.4 kg cm.

4 Forces in Finger

When an object is grasped by frictionless point contact, there is a provision that the contact force should always act in the normal direction; otherwise, grasping is not possible. In the case of the object being grasped and manipulated as in force closure conditions, there is always some friction between the grasped object and the hand. To estimate the effect of friction during grasping of the object, a set of codes is developed using MATLAB platform. The coding is done in MATLAB for analyzing the effect of incident angle on the applied force.

5 Results and Discussion

The grasping power of the prosthetic hand is determined by performing finite element analysis. Hence, mathematical models were developed for different shaped objects subjected to force closure condition. Using these mathematical expressions, the force exerted on each fingertip with its position/orientation is determined.

5.1 Stress Analysis of Finger Joint

The analysis (stress, strain, and displacement) of finger and hand assembly is done in SolidWorks 2016. Figure 4 shows the stress analysis of finger joint, as 20, 40, 60, and 80 N of centrifugal loadings were applied.

5.2 Stress Analysis of Hand Assembly

For the analysis purpose of a hand assembly, various initial parameters had to be defined, which include: **Connectors**—Pin connectors were used for the purpose of restricting the individual links from translating and only allowing rotation about it. **Material Assignment**—The material ‘Nylon 101’ is used for the analysis purposes. **Fixtures**—The lowest link of the finger assembly was fixed so as to run the analysis. Bearing fixtures were applied on each of the finger joints. **Loads**—Various loads were assigned to different parts of the assembly so as to get the FOS. Force includes

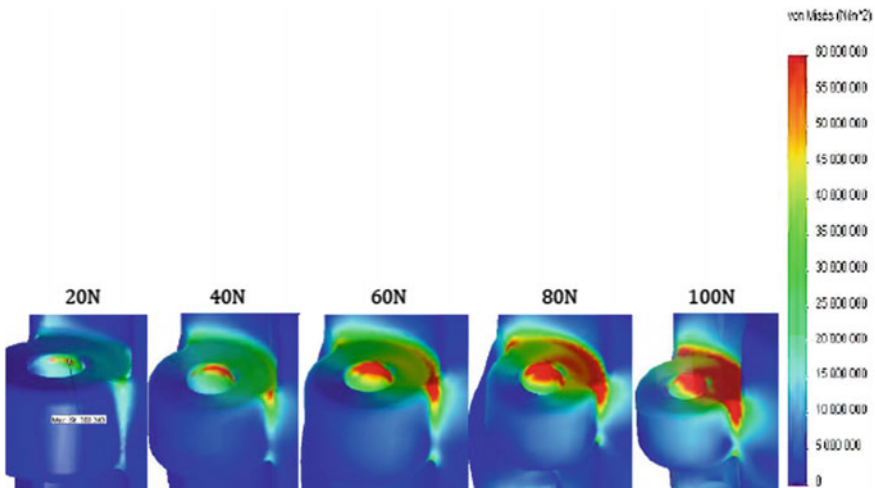


Fig. 4 Stress analysis of finger hinge at various centrifugal loadings

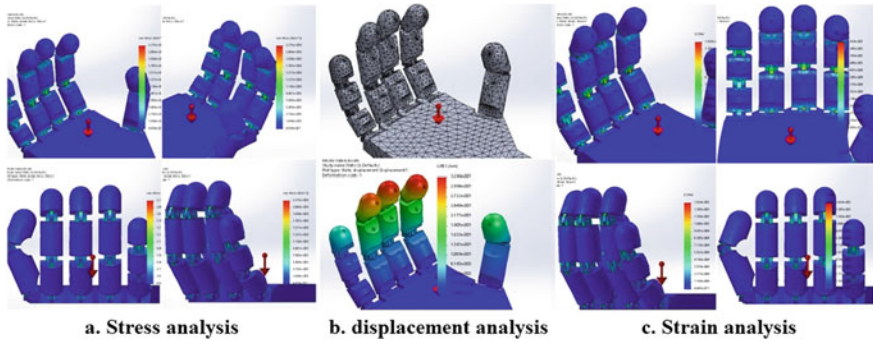


Fig. 5 Finite element analysis of hand assembly

vertical gravity vector, 40 N normal force, and 1 Nm torque at each joint.

Figure 5 shows the analysis study (stress, displacement, and strain, respectively) of fully assembled hand model.

6 Conclusion

An active mechanical prosthetic hand with voice control mechanism was developed. The design was found feasible and stable by performing the finite element analysis in SolidWorks 2016. The displacement, stress, and strain analysis was performed for individual fingers and the assembled hand. Considering the cost-effectiveness, nylon was selected to manufacture the initial prototype of the prosthetic hand. Manufacturing in terms design of prosthetic hand is found both feasible and stable in terms of stress and strain analysis. The voice control mechanism supported with a mobile app plays a vital role in controlling the prosthetic hand to perform various actions including complicated hand gestures. This work can be further continued for providing better retraction of fingers and to provide a cosmetic appeal to the users.

References

1. Susan JH (2012) Basic biomechanics, 6th edn. McGraw-Hill
2. Chen WJ, Xie M (2009) On the design of a novel dexterous hand. *Int J Rob Res* 127:55–76
3. Kato I, Sadamoto K (1967) Mechanical hands illustrated. *Am J Physiol* 213:1560–1564
4. Klute GK, Czerniecki JM, Hannaford B (1998) McKibben artificial muscles: pneumatic actuators with biomechanical intelligence. *J Dyn Syst Measure Control* 27:210–232
5. Banks JL (1986) Anthropomorphic robotic finger platform based on shape memory alloy. *J Biomech* 19:887–898
6. DeLaurentis KJ, Mavroidis C, Pfeiffer C (2003) Development of a shape memory alloy activated robotic hand. *Eng Technol* 25:125–141

Biodegradable Composites from Leaf Wastes for Packing Applications



S. Renold Elsen, R. Bharanidaran and S. Surendarnath

Abstract The present analysis gives an insight to understand the preparation of composite materials using biodegradable wastes. In the current scenario, disposal of non-degradable materials like electronic waste, construction waste, biomedical waste, radioactive waste and industrial waste are main problems to the human society. In the organic waste, the major portion of waste is fallen from trees as dry leaves. Those leaf wastes are not handled appropriately and due to human ignorance, they are not disposed properly. The pollutants that are generated from the burning leaves enter into the atmosphere which results in greenhouse gas effect as a whole, as well as the formation of particulate matter. The composite can be easily manufactured from the dry leaves at desired shape through casting process by using the raw sources available from the plant waste. The composite developed without any additives, chemical treatments and synthetic fillers was a biodegradable and eco-friendly material.

1 Introduction

Waste is a class of substance that no longer serves any purpose and is generally thrown away. Biodegradable waste, construction waste, electronic waste, food waste, industrial waste, biomedical waste, municipal solid waste, radioactive waste and scrap metal are the various categories of waste [1]. All wastes are particularly hazardous if not carefully disposed off and will have an impact on the environment. Especially, organic waste occupies about 50% of total solid waste. Worldwide, it is estimated that three billion metric tons of biomass such as wood, leaves, trees, grass and trash are being burned [2]. This is estimated to be the largest source of air pollution in the

S. Renold Elsen (✉) · R. Bharanidaran
Department of Design and Automation, School of Mechanical Engineering, VIT
Vellore, Vellore, India
e-mail: renoldelsen@gmail.com

S. Surendarnath
Department of Mechanical Engineering, Nalla Narasimha Reddy Education Society's
Group of Institutions, Hyderabad, India

© Springer Nature Singapore Pte Ltd. 2019
S. S. Hiremath et al. (eds.), *Advances in Manufacturing Technology*,
Lecture Notes in Mechanical Engineering,
https://doi.org/10.1007/978-981-13-6374-0_28

developing countries. Organic wastes play a major role in causing pollution due to the human activities like landfill, fermentation, etc. In the organic waste, the major portion of waste is fallen dry leaves from trees. These leaf wastes are not handled properly, and due to human ignorance, they are not disposed properly. The pollutants that are generated from the burning leaves enter into the atmosphere which results in greenhouse gas effect as a whole, as well as the formation of particulate matter [3]. In addition to the chemical pollutants released, mould spores are distributed in the plume of the fire. These particulates can reach deep into lung tissue and cause coughing, wheezing, chest pain and sometimes long-term respiratory problems.

To address the above problem, the current work aims to develop a composite by utilizing the dry leaves from various trees as filler material and the natural pine resins as a binder. The composite of pad shape can be easily manufactured at desired shape through casting process by using the raw sources available from the plant waste [4]. The composite developed without any additives, chemical treatments and synthetic fillers will be a biodegradable material. Ultimately, the proposed composite will be an economic and eco-friendly material than the conventional composite products used for packing, namely thermocol (polystyrene).

2 Materials and Methods

The procedure for the fabrication of the composite is given in Fig. 1. The dry leaves of different trees were pulverized and sieved to the grain size range from 1000 μm to be used as a filler material as shown in Figs. 2, 3, 4 and 5 (Figs. 6, 7 and 8).

The collected resins from pine tree were cleaned without any dusts, and foreign matters then crushed manually to reduce its size. The dry leaf pine resin composite was developed from casting process by varying the dry leaves' content from 1:1 wt% of pine resin. After that 50 g of sieved leaves' powder was gently added to a separated 50 g of warm resins' mixture and simultaneously stirred it as to reach a molten state. A die (Fig. 9) was prepared with MS plate and fabricated as per standards using water jet machining process. Finally, the prepared molten mixture is carefully poured into the die and placed in sunlight for 2 days to cure the composite in Fig. 10. Then the dried composite was removed gently from the die and sized if needed. Figure 11 shows the specimen prepared for tensile test and Fig. 12 shows the specimen prepared for flexural test.

The mechanical properties such as tensile and flexural tests were found by experiments as per ASTM standards. The tensile and flexural properties were carried out in Tinius Olsen (H-50kN capacity) machine according to ASTM D 3039 [5, 6] and ASTM D 790 [7] with a feed rate of 0.5 mm/min. For tensile test, composite fabricated with specifications of gauge length, width, and thickness was $70 \times 10 \times 5$ mm, respectively. The composite fabricated for flexural with specifications of gauge length, width and thickness was $140 \times 14 \times 5$ mm, respectively.

Fig. 1 Composite preparation method

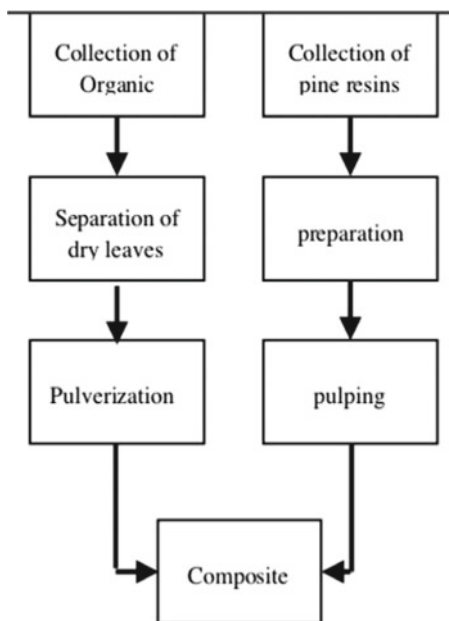


Fig. 2 Collected dry leaves



Fig. 3 Pulverized leaves**Fig. 4** Sieving**Fig. 5** Weighing the grounded leaves

Fig. 6 Resin heating**Fig. 7** Molten resin mixture

3 Results and Discussions

From the tensile test (Fig. 13), the parameters such as ultimate tensile stress and % elongation both were determined and given in Table 1. The tensile strength and flexural strength of the fabricated composite were found to be close to that of polystyrene with 0.332 MPa.



Fig. 8 Paste of composite



Fig. 9 Die for the preparation of the composite

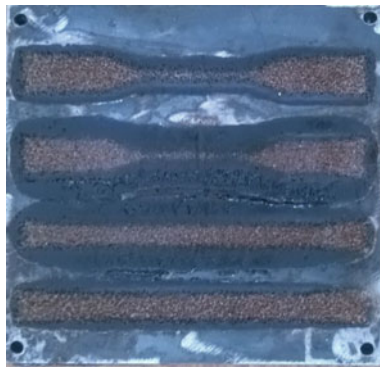


Fig. 10 Cast leaf composite in die



Fig. 11 Tensile test specimen



Fig. 12 Flexural test specimen



Fig. 13 Tensile testing on the composite

Table 1 Tensile test results of the composite

Width (mm)	Thickness (mm)	Ultimate force (N)	Ultimate stress (MPa)	Break distance (mm)	Total elongation (%)	Yield stress (MPa)	Yield strain %
20.0	5.00	33.2	0.332	1.92	2.74	N/F	N/F

The flexural strength of composite material was conducted using 3-point bend test and it is illustrated in Fig. 14. The flexural test results were listed in Table 2. The yield stress of 0.149 and ultimate stress of 0.71 MPa were obtained.

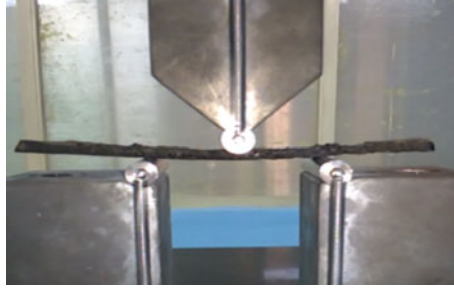


Fig. 14 Flexural testing on the composite property

Table 2 Flexural test results of the composite materials

Width (mm)	Thickness (mm)	Area (mm ²)	Support span (mm)	Yield force (N)	Yield stress (MPa)	Yield strain %	Ultimate force (N)	Ultimate stress (MPa)
14	05	70	50	0.696	0.149	0.438	3.33	0.71

4 Conclusion

The proposed composite products need waste materials when compared to the conventional composite products which can be an added advantage. The biodegradable composite leads to sustain the resources as it has a potential to serve as packing material and also can be extended to false ceiling applications. The various natural resins available in southern parts of India can be used to develop a high-strength composite. Also, natural reinforcement can be done to strengthen the final composite.

By successful development of the proposed composite, this accumulation of degradable wastes can be reduced. The composite can be manufactured with ease for any desired shape by casting process by using the resources available in the surroundings.

- The people from rural background in India can easily develop the composite without any machinery.
- Many microscale industries can benefit with low investment and maximum gain if the composite of desired properties can be obtained from the successful completion of the work.

References

1. Reddy PJ (2012) Municipal solid waste management. CRC Press/Balkema, The Netherlands. Retrieved 9 October 2012
2. Sharholly M, Ahmad K, Mahmood G, Trivedi RC (2008) Municipal solid waste management in Indian cities—a review. *Waste Manag* 28(2):459–467

3. Joshi R, Ahmed S (2016) Status and challenges of municipal solid waste management in India: a review. *Cogent Environ Sci* 2(1):1139434
4. Aseer JJRR, Sankaranarayanan K, Jayabalan P, Natarajan R, Dasan KP (2015) Morphological and mechanical properties of chemically treated municipal solid waste (MSW)/banana fiber and their reinforcement in polymer composites. *Sci Eng Compos Mater* 22(4):353–363
5. Aseer JR, Sankaranarayanan K, Jayabalan P (2013) Morphological, physico-mechanical and thermal properties of banana plant fibers (*Musa Sapientum*). *Appl Polym Compos* 1(3):197–207
6. ASTM D (2000) Standard test method for tensile properties of polymer matrix composite materials 10:3039
7. ASTM D (2003) Standard test methods for flexural properties of unreinforced and reinforced plastics and electrical insulating materials 11:790-03

A Comparative Study of Flow Characteristics of BMW M6 and AUDI R8 Commercial Sports Car Using Flow Design Software



S. Renold Elsen, K. Jegadeesan and J. Ronald Aseer

Abstract The aerodynamic characteristics of the vehicular profiles have grown more concentration as it has influence on fuel consumption, comfort, and driving characteristics. The objective of the current work is to study the aerodynamic characteristics investigations of BMW M6 and AUDI R8 using both experimental and computational approaches. The computation analysis was done using the models developed using FREE FORM SCULPT module in AUTODESK FUSION 360. The airflow around a model is analyzed by AUTODESK FLOW DESIGN-VIRTUAL WIND TUNNEL software to assess the drag force, drag co-efficient and interacting flow fields. The drag force is also calculated analytically for the two cars and was found to be in good agreement with the computational results. The prediction of experimental aerodynamic characteristics is done by conventional wind tunnel approach. The experimental investigations were done on an open-loop suction-type wind tunnel having a 30 cm × 30 cm × 100 cm test section. The 3D prototype of reduced scale (1:15) of the two car models was developed using the 3D printing machining from generated software models. The computation results were found to be validated by the experimental results by the wind tunnel method.

1 Introduction

The improvement in highway connectivity has led to mounting pressure in faster commutation but in the same time demands superior stability of vehicle with lower energy consumption. To satisfy all the above requirements, the design of vehicle

S. Renold Elsen (✉)

Department of Design and Automation, School of Mechanical Engineering,
VIT, Vellore, Tamilnadu, India
e-mail: renoldelsen@gmail.com

K. Jegadeesan

School of Mechanical Engineering, SRMIST, Chennai, Tamilnadu, India

J. Ronald Aseer

School of Mechanical Engineering, Galgotias University, Greater Noida,
Uttar Pradesh, India

© Springer Nature Singapore Pte Ltd. 2019

S. S. Hiremath et al. (eds.), *Advances in Manufacturing Technology*,

Lecture Notes in Mechanical Engineering,

https://doi.org/10.1007/978-981-13-6374-0_29

body profile should focus on the reduction of total weight and on the improvement of aerodynamic characteristics [1]. Aerodynamic designing along with the styling of an automobile is an essential aspect, and it encompasses the integration of engineering and aesthetics [2]. An aerodynamically designed automobile requires minimal power to overcome the air resistance or drag exerted on the car and therefore unveils greater performance [3]. Further, it helps in higher stability of vehicle which in turn aids the comfort of the passengers. Accordingly, in the current epoch of extremely escalating prices of fuels with swiftly draining natural resources, optimization of car aerodynamics has become more important [4]. More specifically, the decrease in drag coefficient (CD) and the analysis of aerodynamic forces and moments are of key attention predominantly for automotive industries. The reduction of drag has been focused in the design of car and CFD techniques [5] were used by many investigators to accomplish numerical simulations. The minimizations of CD were primarily influenced by the car's peripheral contour. In this work, a comparative study of the aerodynamic characteristics of the commercial sports car of two world renowned automobile brand, namely BMW and AUDI, is taken.

2 Evaluation of Vehicle Drag Analysis

2.1 Modeling of the Design and Aerodynamic Simulation

The three dimensional geometrical modeling values of the BMW M6 and AUDI R8 are given in Table 1. Further, the other dimensions were obtained using the 3D tracing of the car profile using the FREE FORM MODULE AUTODESK FUSION 360 as shown in Fig. 1. The models of BMW M6 and AUDI R8 were created as shown in Figs. 2 and 3, and aerodynamic characteristics are analyzed and compared using computational fluid dynamics (CFD) [6]. CFD can be effectively employed to identify the phenomena evolved in the aerodynamic design and furnish a background to improve the performance. It was exported to AUTODESK FLOW DESIGN [7, 8] module in IGES, a neutral standard format used to exchange three-dimensional models among any standard CAE systems [9, 10].

Aerodynamic behavior of a design is assessed using computational fluid dynamics (CFD) and is used for the product development process in the field automotive and aerospace application. CFD helps engineers to recognize the physical phenomena developed in the design and provides a background to improve the performance with respect to focused design criteria. The wind speeds of 100, 150, and 200 kmph were taken, respectively, and the analysis was done. The outlet boundary conditions are given in Table 1.

Table 1 BMW M6 and AUDI R8 car specifications

BMW M6 car		AUDI R8 car	
Specifications	Details (mm)	Specifications	Details (mm)
Overall length	5011	Length	4426
Overall width	1899	Width	2037
Overall height	1395	Height	1240
Wheel base	2964	Ground clearance	110
Front headroom	1030	Wheel base	2650
Rear headroom	941	Front tread	1599
Front shoulder room	1517	Rear shoulder room	1454

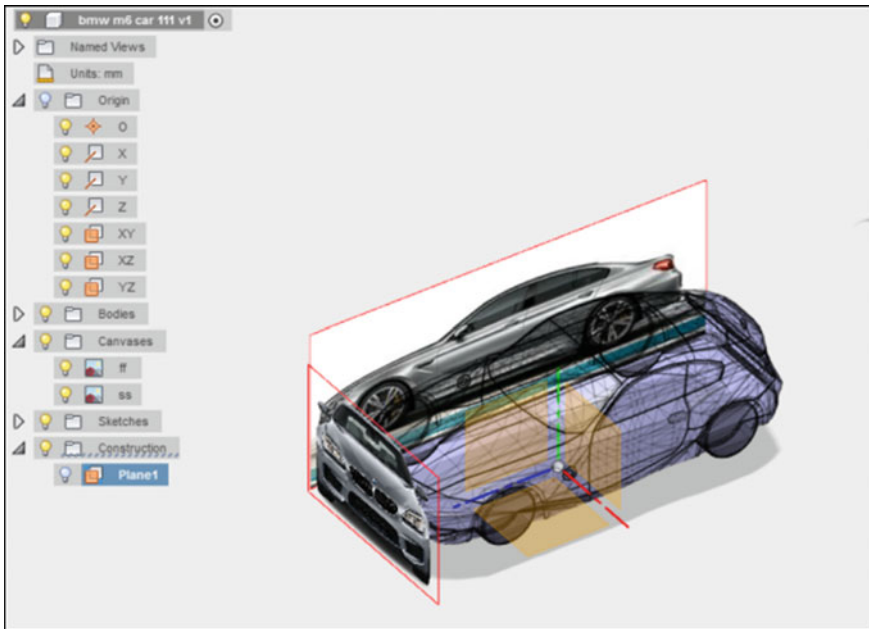


Fig. 1 Modeling of exact profile using Fusion 360

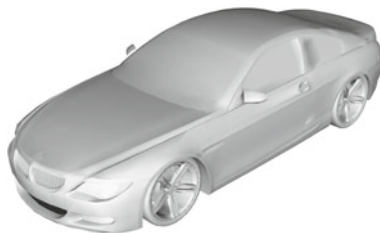
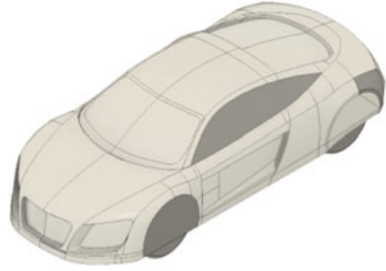


Fig. 2 3D model of the BMW M6 car

Fig. 3 3D model of the AUDI R8



2.2 Mathematical Modeling of Flow Analysis

The drag force is the opposing force to lift force and is the element of the fluid-dynamic force parallel to the flow direction. Drag force developed in a profile due to airflow is influenced by the density of medium, the square of the velocity, the air's viscosity, and its compressibility. The size and profile of the body along with the body's orientation to the direction of airflow has an impact on drag force.

$$\text{The drag force is } F = \frac{1}{2} C_p \rho A V^2 \quad (1)$$

The “ F ” is drag force, “ C_p ” drag coefficient, “ ρ ” fluid mass density, “ A ” projected area, and “ V ” relative velocity. For BMW M6, the density of the working fluid (air) is taken as $1.22 \text{ (kg/m}^3\text{)}$ with the drag coefficient and projected area (A) of 0.4 and 0.81 m^2 respectively. For AUDI R8, the drag coefficient and projected area are selected as 0.39 and 1.93 m^2 respectively. The projected area of the two car models was calculated from the cad package.

2.3 Wind Tunnel, Model Details, and Instrumentation

The complete car proto-models of the BMW M6 and AUDI R8 were developed by means of the 3D printing method from the developed 3D model using AUTODESK FUSION 360 shown in Figs. 4 and 5, respectively. The 3D prototype of reduced scale (1:15) of the two car models was developed.

Fig. 4 3D model of the BMW M6 car





Fig. 5 3D model of the AUDI R8



Fig. 6 Wind tunnel setup to test at subsonic speed

Table 2 Wind tunnel specification

Details	Specifications
Wind tunnel testing chamber cross section	1 m × 1 m
Wind tunnel length	2.5 m long
Maximum range	50 m/s
Working range	35 m/s
Angle of attack	140

The experiments were conducted to assess the aerodynamic characteristics of the aircraft design in a subsonic wind tunnel at MAM Engineering College–Trichy, as shown in Fig. 6. The specifications of the wind tunnel are given in Table 2.

The estimation of air density in the laboratory atmosphere is carried out by measuring the ambient pressure, temperature, and humidity recorded using barometer, thermometer, and hygrometer correspondingly. The wind tunnel tests were carried out with free-stream velocity of 100 kmph (27.77 m/s), 150 kmph (41.66 m/s), and 200 kmph (55.56 m/s), respectively.

3 Result and Discussion

3.1 Computational Studies of the Car Models

The computational studies of the two models were done, and the results were further analyzed. Figures 7, 8, and 9 gives the aerodynamic characteristics, namely drag force, coefficient of drag, velocity, and pressure of the BMW M6 at three different velocities.

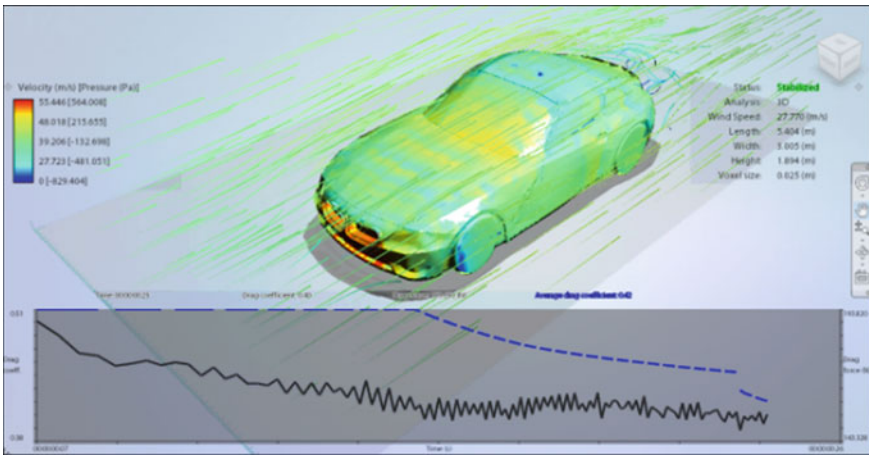


Fig. 7 BMW M6 aerodynamic characteristics at 27.770 m/s

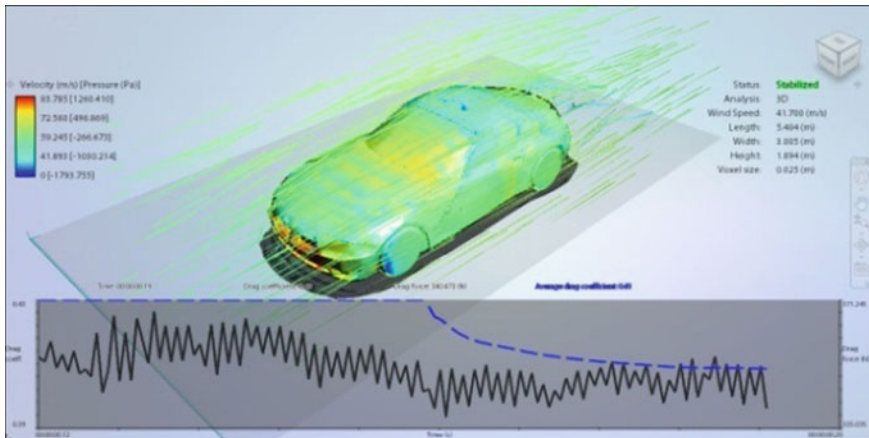


Fig. 8 BMW M6 aerodynamic characteristics at 41.7 m/s

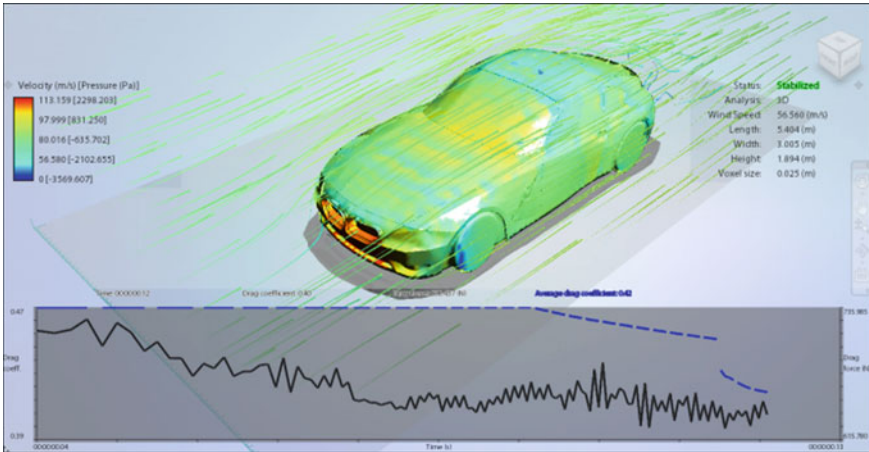


Fig. 9 BMW M6 aerodynamic characteristics at 55.56 m/s

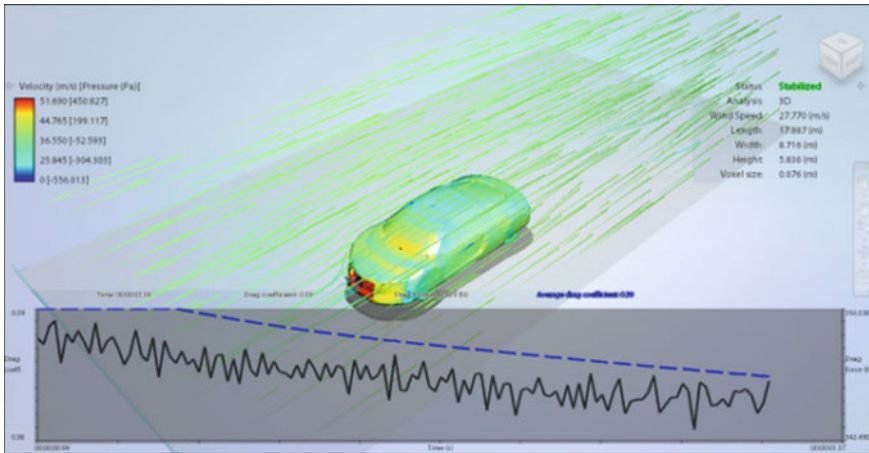


Fig. 10 AUDI R8 aerodynamic characteristics at 27.70 m/s

Figures 10, 11, and 12 give the AUDI R8's aerodynamic characteristics at three different velocities, namely drag force, coefficient of drag, velocity, and pressure. From Fig. 13 it can be concluded that the BMW M6 has higher velocity compared to AUDI R8 at various wind speeds, and also the velocity increases with increase in wind speed. The range of maximum, minimum, and intermediate velocities is found to be in close at different wind speeds. From Fig. 14, it can be concluded that the BMW M6 has higher pressure level compared to AUDI R8 at various wind speeds, and also the pressure increases with increase in wind speed. The range of maximum, minimum, and intermediate pressures is found to be more at different wind speeds.

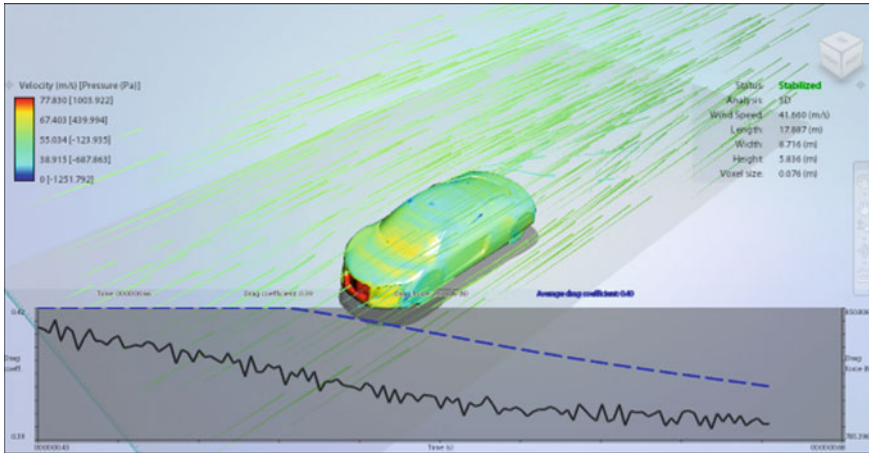


Fig. 11 AUDI R8 aerodynamic characteristics at 41.6 m/s

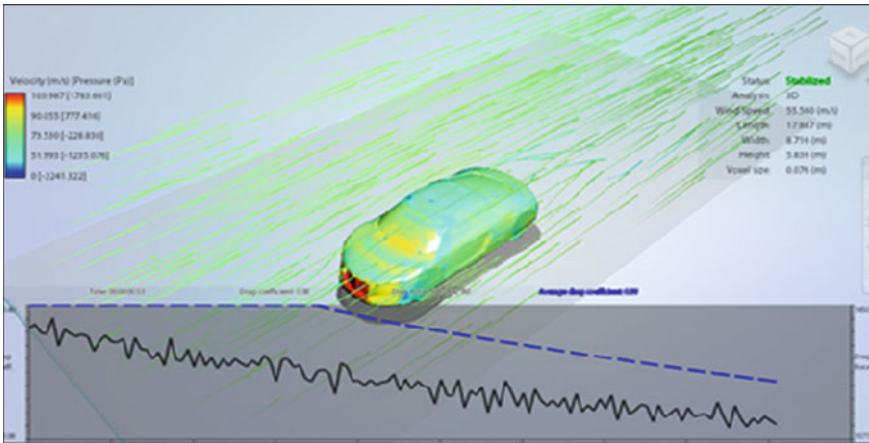


Fig. 12 AUDI R8 aerodynamic characteristics at 55.56 m/s

From Fig. 15, it can be concluded that the BMW M6 has lower drag force compared to AUDI R8 at various wind speeds, and also the drag increases with increase in wind speed. The range of maximum, minimum, and intermediate pressures is found to be more at different wind speeds. The drag forces of the car models from both the computation and analytical charts were compared for BMW M6 in Fig. 16 and AUDI R8 in Fig. 17.

From both the charts, it can be observed that the drag force increases with the increases in the velocity of the vehicle and the prediction is very similar for both the CFD and analytical values. The flow pattern of the BMW M6 and AUDI R8 in the

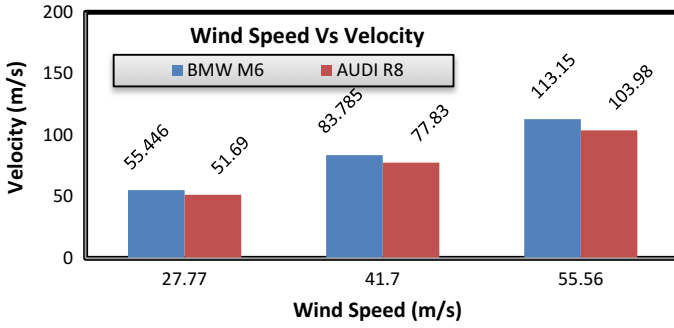


Fig. 13 Wind speed versus velocity

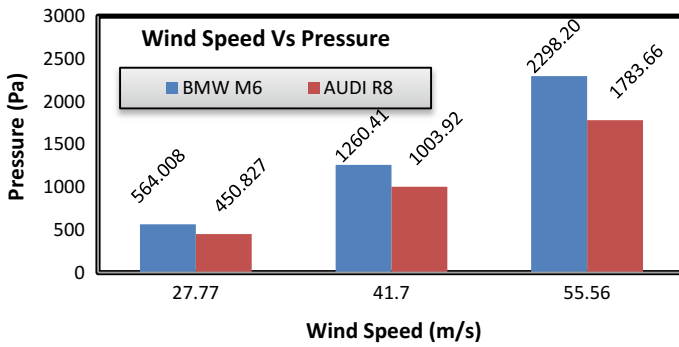


Fig. 14 Wind speed versus pressure

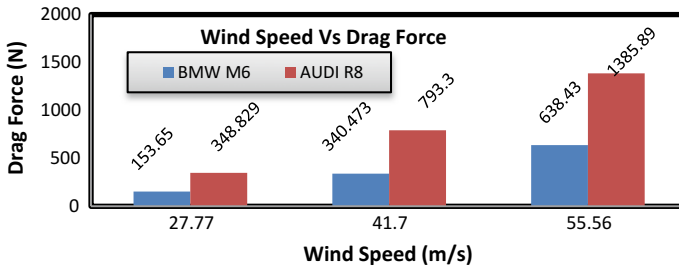


Fig. 15 Wind speed versus drag force

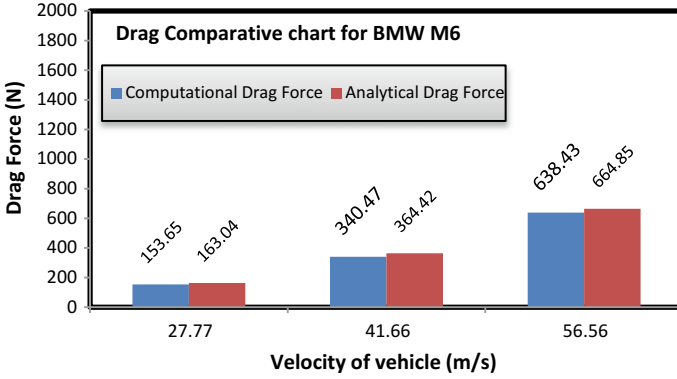


Fig. 16 Computation and analytical comparison chart for BMW M6

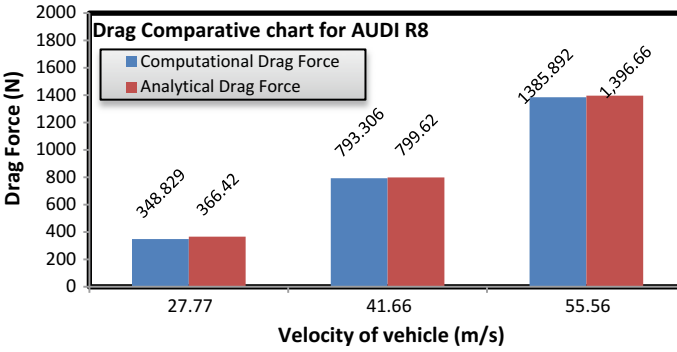


Fig. 17 Computation and analytical comparison chart for AUDI R8

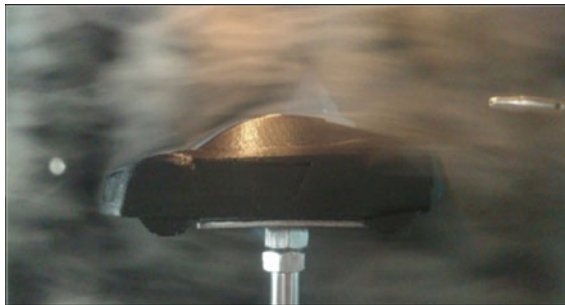


Fig. 18 Flow characteristics study of AUDI R8 in wind tunnel

wind tunnel was found to be in close acceptance of the computational flow pattern as shown in Fig. 18.

4 Conclusion

The aerodynamic characteristics of BMW M6 and AUDI R8 were investigated using computational, analytical, and experimental approaches. The computation analysis was done using the models developed using AUTODESK FUSION 360. The computational airflow around a model, namely drag force, drag coefficient, and interacting flow fields, is assessed using AUTODESK FLOW DESIGN, a virtual wind tunnel software. The drag force was also calculated analytically for the two cars and was found to be in good agreement with the computational results. The pressure and velocity at different wind velocities were found to more, but the drag force was found to be minimal for BMW M6 when compared to AUDI R8. The flow patterns were found to be similar in both the wind tunnel and computational methods.

References

1. Gilhaus RH, Hoffmann R (1998) Directional stability, aerodynamics of road vehicles. SAE International, Warrendale, PA
2. Braess HH, Seiffert UW (2005) Handbook of automotive engineering, Vol. 312. SAE Technical Paper
3. Hucho WH, Sovran Gino (1993) Aerodynamics of road vehicles. *Annu Rev Fluid Mech* 25(1):485–537
4. Katz J (2006) Race car aerodynamics: designing for speed. R. Bentley
5. Han T et al (1996) Flow-field simulations of three simplified vehicle shapes and comparisons with experimental measurements, No. 960678. SAE Technical Paper
6. Ratzel Marc, Ludescher Thomas (2013) Streamlining aerodynamic CFD analyses. Altair Engineering Inc., USA
7. Renold Elsen S et al (2018) Limbs related handicap drivable non commercial electric shuttle vehicle. SAE Technical Paper
8. Vivekananthan et al (2018) Bike with modified steering system to assist people with forearm disability. SAE Technical Paper
9. Renold Elsen S et al (2014) Design of composite fixture for machining ceramic materials using abrasive water jet machining (AWJM). *ARPN J Eng Appl Sci* 9(4):388–392
10. Renold Elsen S et al (2016) Empirical and finite element prediction and validation of weld bead profile generated during TIG welding process. *Glob J Pure Appl Math (GJPAM)* 12(4):15–20

Mechanical Characterization of Glass Fiber-Strengthened Balsa–Depron Composite



Nallusamy Tamilselvam, S. Varsha, D. S. Seema and B. Indhumathy

Abstract The present day records the greatest usage of unmanned aerial vehicles (UAVs) in civil and military fields. UAVs are experimenting materials with respect to physical and mechanical properties which should have more strength to weight ratio, resistance to buckling, high ultimate tensile strength, less inflammable, low thermal gradient, high resistance to noise, high resistance to vibration, resistant against deteriorative fuels and chemicals, low corrosion, low oxidation, and high fatigue. This paper presents an experimental investigation of mechanical properties of balsawood–glass fiber, depron–balsa wood, and depron–glass fiber–balsa wood composites. Tensile, hardness, flexural, and thermal tests of different samples are conducted as per ASTM standards. Depron–glass fiber–balsa wood showed 6 times greater tensile strength and 66% hardness than plain balsa wood. Depron–glass fiber–balsa wood showed 34% greater flexural strength than plain balsa wood.

Keywords Balsawood · Depron · Glass fiber · Composite · Stiffness · Hardness

1 Introduction

Since the early beginning of aviation, researchers are working on the development of unmanned aerial vehicle to carry out a military operation without the risk of human life and for civilian use such as agriculture field, and image capturing. While designing a UAVs, it is all about finding the optimal proportion weight of the vehicle and payload. The material needs to be strong and stiff enough to withstand the exceptional circumstances in which it has to operate. Durability is an important factor. In addition, if a part fails, it does not necessarily result in the failure of the whole UAV. In order to improve the stiffness and to reduce weight of UAV, one

N. Tamilselvam (✉) · S. Varsha · D. S. Seema · B. Indhumathy
Department of Aeronautical Engineering, Mangalore Institute of Technology and Engineering,
Moodabidri, Mangalore 574225, Karnataka, India
e-mail: selva.gte.research@gmail.com

© Springer Nature Singapore Pte Ltd. 2019
S. S. Hiremath et al. (eds.), *Advances in Manufacturing Technology*,
Lecture Notes in Mechanical Engineering,
https://doi.org/10.1007/978-981-13-6374-0_30

255

cannot use material like aluminum 6061-T6. As a result, composite materials takes an important role in design and manufacturing of drones.

Carbon fiber, balsa wood, depron and rubber are presently used as the material in UAV. A recent study confirmed that balsa wood has higher toughness compared to other low-density materials used as core materials such as foams. LVL balsa wood can potentially improve the toughness of a core material compared to solid balsa. The improvement, however, depends on the adhesive used in the lamination. The polyurethane adhesive (G39) would be the suitable adhesive for good bonding [1]. In most of the earlier researches, balsa wood was used as a core material in sandwiched beam [2–5]. To overcome the disadvantage of sandwiched balsa wood material and to get better strength to weight ratio, a new composite material is fabricated by combining depron, glass fiber and balsa wood. This paper presents the fabrication of three different lightweight composite materials using balsa wood, depron and glass fiber. The properties like tensile strength, flexural strength, shore D hardness and temperature resistance are also presented.

Fabrication plays an important role on mechanical properties of composites. In fabrication, the final product is made from raw or semi-finished materials instead of assembled from the ready-made component or parts. Since the composite processed here is polymer matrix composite and it is a combination of natural and synthetic material, hand lay-up method is preferred for fabrication.

1.1 Fabrication of Balsawood–Depron Composite (B-D Composite)

B-D composite is a combination of balsa wood and depron laminates arranged one above the other by hand lay-up process. Balsa wood was compressed and was prior wetted in the water and then dried in the sun to have better compression. Then, the wetted balsa wood is compressed by hydraulic compression press with the pressure of 5 tonne for 2 h. Balsa wood strip thickness is reduced to 0.7 mm from 1 mm. Then, depron is compressed by the same hydraulic compression molding press with the pressure of 5 tonne each time, nearly three times for better compression and left for 2 h. Depron sheet thickness is reduced to 0.5 mm from 1 mm. After compression, the actual process is started. Clean mold plate was taken since it was open molding process, and then, wax poll autopolish was applied on to it. Above that, layer of depron sheet is placed according to the dimension and mixture of epoxy resin-hardener (10:1 ratio) is applied. Next layer on the resin-hardener mixture 2 and a half strip of balsa wood placed according to the dimension vertically on depron sheet and another layer of resin applied. Followed by balsa wood strips and resin, another layer of depron foam sheet is placed. Above that, resin layer is applied and followed by three strips and another strip of 27 mm length of balsa wood is placed horizontally. Above the balsa wood, the resin is applied and the last layer of depron sheet is placed. Same way, the laminates ware arranged one above the other. The epoxy resin bonds the

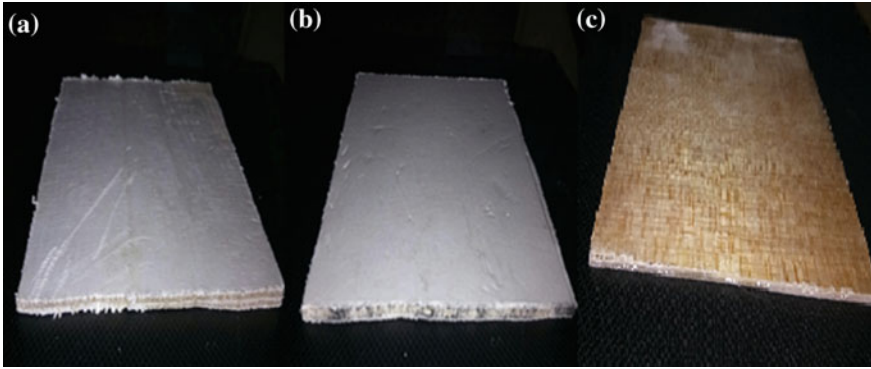


Fig. 1 **a** Balsawood–depron composite, **b** balsawood–glass fiber–depron, **c** balsawood–glass fiber

three layers of depron and two layers of balsa wood strips. Finally, the composite is placed in hydraulic press under 7 tonne and is left 72 h for curing. Figure 1a shows the B-D composite fabricated through hand lay-up method.

1.2 Fabrication of Balsawood–Glass Fiber–Depron Composite (B-G-D Composite)

B-G-D composite is a combination of balsa wood, glass fiber, and depron laminates arranged one above the other by hand lay-up process. Balsa wood is compressed after wetting in water and then dried in the sunlight. Then, it is compressed by hydraulic press with the pressure of 5 tonne for 2 h. Balsa wood strip thickness is reduced to 0.7 mm from 1 mm. Depron is compressed by the same hydraulic compression press with the pressure of 5 tonne each time. This process is repeated nearly 3 times for better compression and left it for 2 h. Depron sheet thickness is reduced to 0.5 mm from 3 mm. Initially, the resin was applied on open mold plate on which polyvinyl releasing agent was placed. On top of that, first layer of depron foam sheet of measured dimension is placed. Above the depron sheet, epoxy resin, and hardener, mixture (100:10 g) is applied and then glass fiber mat of measured dimension is placed on the applied resin. Since the glass fiber mat has pores, there is no need to apply resin once again. Same resin comes out of pores and acts as the next layer. Next layer consists of three balsa wood strips placed next to each other to fit glass fiber and depron according to dimensions. Finally, the laminar composite with middle layer of balsa wood strip and adjacent two layers of glass fiber mats and followed by two outer layers of depron foam is fabricated. Then, the composite is placed in a hydraulic press, compressed up to 5 tonne, and cured for 72 h in sunlight.

1.3 Fabrication of Balsawood–Glass Fiber Composite (B-G Composite)

B-G composite is a combination of balsa wood and glass fiber laminates arranged one above the other by hand lay-up process. Balsa wood is wetted in water, compressed, and dried in the sunlight. Again the hydraulic compression press with the pressure of 5 tonne compressed it for 2 h. Balsa wood strip thickness is reduced to 0.7 mm from 1 mm. The open mold plate is placed, and wax poll autopolish is applied. Above that, polyvinyl releasing assassinate agent (P.V.A) is placed. Initially, a layer of epoxy resin is applied. On top, glass fiber mat is placed and the resin is pulled through the fiber pores and followed by balsa wood single strip according to the dimension placed. Next layer of epoxy resin is applied, and at the top of glass, fiber mat is placed according to the same dimension. Finally, the composite is placed in hydraulic press under 5 tons and cured in sunlight for 72 h.

2 Result and Discussion

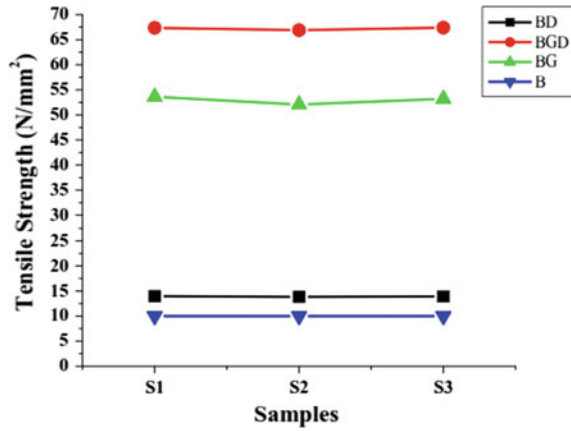
2.1 Tensile Properties

Three different samples of B-D, B-G-D, and B-G composites are prepared and tested in universal testing machine under various loading conditions. The results of the tensile test for different samples are presented in Table 1. The dimensions of B-G composite samples are as follows: width—17.68 mm, thickness—2.0 mm, area—35.36 mm²; the dimensions of the B-G-D composite samples are as follows: width—23.40 mm, thickness—4.3 mm, area—100.62 mm²; the dimensions of the B-D composite samples are as follows: width—22.87 mm, thickness—3.77 mm, area—86.22 mm².

Table 1 Tensile test result of B-D, B-G-D, and B-G composites

Sample ID	Sample number	Tensile strength (N/mm ² or Mpa)
B-D composite	S1	13.97
	S2	13.84
	S3	13.91
B-G-D composite	S1	67.36
	S2	66.90
	S3	67.40
B-G Composite	S1	53.60
	S2	52.08
	S3	53.21

Fig. 2 Tensile strength of various test specimens



The ultimate tensile strength possessed by B-D, B-G-D, and B-G composites is 13.97, 66.90, and 53.60 N/mm², respectively. When compared, B-D composites showed 0.5 times greater tensile strength than that of plain balsawood [6]. Similarly, B-G-D and B-G composites expelled greater improvement in tensile strength than that of plain balsawood. Balsawood is like a fibrous composite, which is having cellulose fibers in a lignin matrix. The cellulose fibers have a high tensile strength and are very flexible. The addition of glass fiber and depron increased tensile strength tremendously by filling the band gap between the cellulose fibers and lignin matrix [6]. Figure 2 explains the variation of tensile strength of B-D, B-G-D, and B-G composites.

2.2 Temperature Resistant

In the present day, UAVs are used in fire and rescue applications. Most of the UAV materials have to withstand a high temperature. Therefore, the balsawood–glass fiber composite is subjected to temperature-resistant test, and the results are listed in Table 2. The composite sample is resized as a square with a dimension of 28 mm length and width of 28 mm. B-G composite showed good result than plain balsawood in temperature-resistant test, and up to 200 °C, there is no sign of blister or pores. The other two composites such as balsawood–glass fiber–depron composite and balsawood–depron composite cannot undergo temperature-resistant test, as the depron in the composite burnt easily.

Table 2 Temperature-resistant test results of B-G composites

Sample ID	Units	Temperature-resistant results
B-G composite	100 °C for 30 min	No sign of blister or pores
	200 °C for 30 min	No sign of blister or pores

2.3 Shore D Hardness

Measuring hardness using shore A and D is a new method of measuring hardness of soft elastomers (rubbers) and other soft polymers materials, which follow DIN ISO 7619-1 standard. In shore D, the point of steel rod penetrates into the material. The depth of penetration is measured on a scale of 0–100. A schematic diagram, which explains durometer measurement (shore D hardness test), is presented in Fig. 3. Different specimens of B-D, B-G-D, and B-G composites are prepared and tested

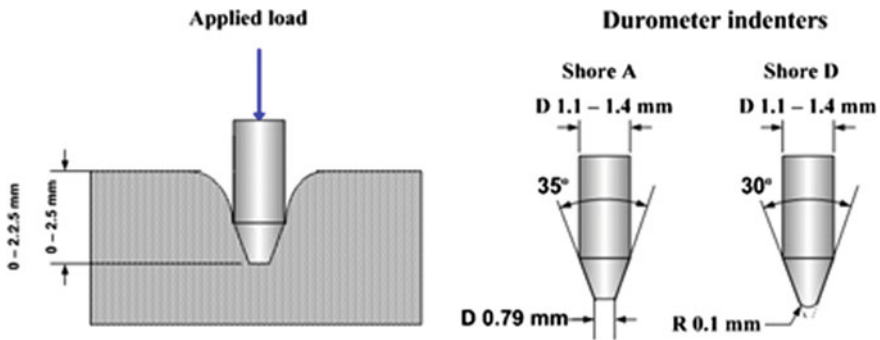
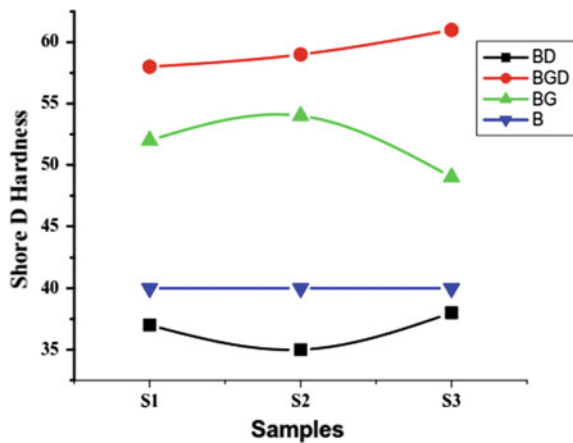


Fig. 3 Durometer testing—shore D hardness [7]

Fig. 4 Shore hardness test results



in durometer. B-D composites are having maximum hardness number 38, which is almost equal to the hardness value of plain balsa wood. The addition of glass fiber with B-D composite increased the hardness (Fig. 4).

Numerically obtained maximum hardness value of B-G-D composite (glass fiber-strengthened B-D composite) was 61, which is considerably bigger than the hardness value of plain balsa wood composite. Glass fibers are used as a strengthening agent here, which decreases the gap between the molecules. Glass fibers provide good bonding strength. Similarly, the addition of glass fiber increased the hardness value of 54. When compared to plain balsa wood, B-D, B-G-D, and B-G composites are showing 5, 52, and 35% increment in hardness, respectively.

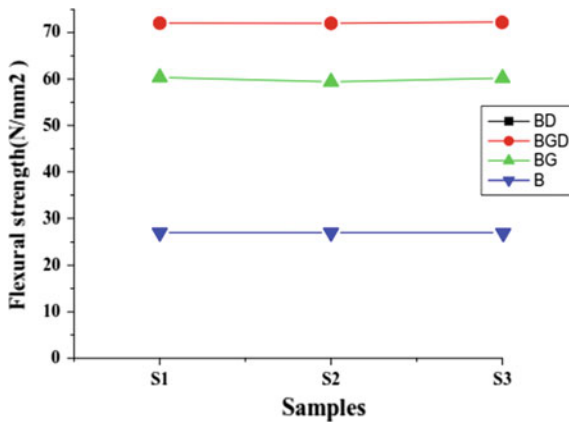


Fig. 5 Three-point bending test results

Table 3 Three-point bending test result of B-D, B-G-D, and B-G composites

Sample ID	Sample number	Flexural strength (N/mm ²)
B-D composite	S1	5.98
	S2	5.40
	S3	6.01
B-G-D composite	S1	72.06
	S2	72.01
	S3	72.30
B-G composite	S1	60.36
	S2	59.40
	S3	60.20

2.4 Flexural Test

The specimens of B-D composite are prepared with the following dimensions: width—17.47 mm, thickness—1.85 mm, length—50 mm; the maximum flexural strength possessed by the B-D composite is 6.01 N/mm², which is comparatively less than the flexural strength of balsa wood (Fig. 5 and Table 3).

3 Conclusion

Materials are most important in the construction of any UAVs. It should meet the necessary requirement to satisfy the needs of the application of the UAVs. Balsa wood is widely used for making lightweight UAVs and glides. In the present research, strengthening of balsa wood is done by adding glass fiber and depron sheet as a strengthening agent. The three composites B-D, B-G-D, and B-G were fabricated by hand lay-up method and tested for tensile, flexural, shore D hardness, and fire resistance. The addition of glass fiber increases the mechanical as well as thermal withstanding capability of the plain balsa wood. The average tensile strength possessed by B-D, B-G-D, and B-G composites is 13.90, 67.22, and 52 N/mm², respectively. Average shore D hardness of the B-D, B-G-D, and B-G composites is 37, 60, and 52, respectively. Similarly, the average flexural strength of all three materials is as follows: 5.79, 72.12, and 60 N/mm². Out of the three composites, B-G composite is having higher fire resistance. From the test results, it is concluded that the addition of glass fiber strengthens the balsa wood. These glass fiber-strengthened composites are most suitable for lightweight unmanned aerial vehicle construction. This material will replace the future balsa wood applications.

References

1. Mohammadi MS, Nairn JA (2017) Balsa sandwich composite fracture study: comparison of laminated to solid balsa core materials and deboning from thick balsa core materials. *Compos Part B Eng (Elsevier)* 122:165–172. <https://doi.org/10.1016/j.compositesb.2017.04.018>
2. Jover N, Shafiq B, Vaidya U (2014) Ballistic impact analysis of balsa core sandwich composites. *Compos Part B Eng (Elsevier)* 67:160–169. <https://doi.org/10.1016/j.compositesb.2014.07.002>
3. Osei-Antwi M, Castro J, Vassilopoulos AP, Keller T (2013) Shear mechanical characterization of balsa wood as core material of composite sandwich panels. *Construct Build Mater (Elsevier)* 41:231–238. <https://doi.org/10.1016/j.conbuildmat.2012.11.009>
4. Atas C, Sevim C (2010) On the impact response of sandwich composites with cores of balsa wood and PVC foam. *Compos Struct (Elsevier)*, 93(1):40–48. <https://doi.org/10.1016/j.compstruct.2010.06.018>
5. Kepler JA (2011) Simple stiffness tailoring of balsa sandwich core material. *Compos Sci Technol* 71(1):46–51. <https://doi.org/10.1016/j.compscitech.2010.10.002>

6. Newaz G, Mayeed M, Rasul A (2016) Characterization of balsa wood mechanical properties required for continuum damage mechanics analysis. *J Mater Des Appl* 230(1):206–218. <https://doi.org/10.1177/1464420714564711>
7. Mix W, Giacomini AJ (2011) Standardized polymer durometry. *J Test Eval* 39(4):1–10

Milling Cutter Flank Wear Prediction Using Ensemble of PSO-Optimized SVM and GLM Regression Models



B. Stalin, M. Ravichandran, S. Marichamy and C. Anandavel Murugan

Abstract The main aim of this research is to build an accurate wear prediction model for predicting flank wear in milling cutters. Flank wear is predicted based on vibration and acoustic emission signals in the table and spindle of the machining center. The flank wear prediction model is built using regression ensembles that contains support vector regression and generalized linear regression models. The individual regression model in the ensemble is fine-tuned using particle swarm optimization (PSO). Generally, to fine-tune the models, hyper-parameters of the model need to be adjusted. A grid search is commonly used to find the optimum values for the hyper-parameters. Since grid search does not guarantee optimal values, particle swarm optimization is used to find the optimum values. Optimal values for the hyper-parameters results in individual optimal regression models. Then, by stacking the optimal regression models, highly accurate flank wear prediction model is built. The accuracy of the model is demonstrated using a high determination coefficient.

Keywords Milling · Particle swarm optimization · Tool wear

1 Introduction

Milling is a machining process used to remove material from a workpiece using a rotating multi-point cutting tool called milling cutter. Because of its ubiquitous application and high profile uses, milling has been researched over the years. One

B. Stalin (✉) · C. Anandavel Murugan
Department of Mechanical Engineering, Anna University, Regional Campus
Madurai, Madurai 625019, Tamilnadu, India
e-mail: stalin1312@gmail.com

M. Ravichandran
Department of Mechanical Engineering, K. Ramakrishnan College of Engineering,
Samayapuram, Trichy 621112, Tamilnadu, India

S. Marichamy
Department of Mechanical Engineering, CMR Institute of Technology, Hyderabad 501401,
Telangana, India

of the main areas of research includes analysis of milling cutter wear. Since cutter wear and failure are inevitable, researchers have been studying options, either to reduce the wear by optimizing machining parameters or to predict the wear before it occurs. The second area is a recent one, and the focus is mainly on finding RUL (remaining useful life) in advance so that disruption in the machining process can be avoided by proactively replacing the tool. Most of the recent research in this area has been focused on applying algorithms like artificial neural networks (ANN), support vector machines (SVM), decision trees, and genetic algorithm to predict the cutter wear. Shi et al. [1] illustrated tool wear prediction model using least square support vector machines. Benkedjough et al. [2] demonstrated health assessment and life prediction of tool using support vector regression. Palanisamy et al. [3] demonstrated the application of artificial neural networks and regression to predict the tool wear in end milling. But very less research has been done in the application of ensemble algorithms for tool wear prediction.

In this research, ensemble learning has been studied to build a prediction model for cutter flank wear. The stacking ensemble technique is studied to improve the accuracy of cutter wear prediction model. To aid in building better ensembles, individual models are tuned using particle swarm optimization. Very high accuracy is demonstrated by ensembling PSO-optimized models.

2 Regression Ensembles

Ensemble learning is a technique in machine learning which uses multiple diverse machine learning models called base learners and combines them in a variety of ways to provide better predictions. Many times base learners are not weak and may provide better accuracy too. But ensembling results in better learners than the individual learners. Ensemble learning has been studied over years by multiple researchers. Caruana et al. [4] proposed a method of building ensembles from thousands of models that use same algorithm but different parameters. Liu et al. [5] studied neural network ensembles and suggested that using different neural networks to learn different aspects or parts of data and ensembling them together would provide better results.

3 Particle Swarm Optimization

PSO is a metaheuristic optimization algorithm which mimics the social behavior of a flock of birds searching the food. PSO optimizes a problem by initializing of the population of candidate solutions called particles which move around the search space in multiple iterations. In each iteration, position and velocity of the particle are updated based on local best position and global best position. In this way, with each passing iteration, swarm of particles moves toward the best position resulting in convergence. Researchers have used PSO in multiple diverse optimization fields. But

in recent years, researchers have started using PSO to tune another algorithm. Hayder et al. [6] proposed a hybrid genetic algorithm (GA) and PSO to tune convolutional neural network (CNN). Hadavandi et al. [7] used PSO for parameter estimation of a time series model used in forecasting gold price.

4 Materials and Methods

This research is done using a milling cutter wear experimental dataset collected by Agogino et al. [8]. This dataset contains measurements made in experimental runs on a Matsuura machining center under various operating conditions.

4.1 Experimental Conditions

During measurement, cutting speed was set to 200 m/min. Two different depths of cut, i.e., 1.5 and 0.75 mm, respectively, were chosen, and feed values were fixed at 0.5 and 0.25 mm/rev. Cast iron and stainless steel J45 were used as workpiece material. The size of the workpiece was chosen as $483 \times 178 \times 51$ mm. To avoid any bias, measurements were made second time with the same set of parameters with another set of inserts. Flank wear measurements were done at irregular intervals based on the cutter wear condition. Other parameters measured were feed, depth of cut, spindle current, table vibration, spindle vibration, acoustic emission in the table, and spindle.

5 Cutter Flank Wear Prediction

In this research, it is decided to build the flank wear prediction model as it is the key health indicator of the tool. Table vibration, spindle vibration, table acoustic emission, and spindle acoustic emission data are used as independent variables for the model. Multiple researchers have applied various transformation techniques for vibration and acoustic emission. Dornfeld et al. [9] developed a relationship between cutting parameters and root-mean-square (RMS) voltage of the acoustic emission signal. Kamarthi et al. [10] demonstrated flank wear estimation model using wavelet transformed acoustic emission signals. Jianming et al. [11] demonstrated that the application of time and frequency analysis of vibration and acoustic emission signal is useful in finding tool wear. Orhan et al. [12] analyzed vibration signals and found that the first three multiples of the tooth passing frequency gave more information about tool wear. In this research, for keeping the model simple, statistical features extracted from vibration and acoustic emission signals listed in Table 1 are used.

Table 1 Statistical features

Feature	Description	Applicable signal
Root-mean-square (RMS)	The square root of the arithmetic mean of the square of a set of values	Table vibration
Skewness	Skewness indicates the symmetry of the probability density function (PDF) of the amplitude of the signal	Spindle vibration
Kurtosis	Kurtosis measures the peakedness of the PDF of a signal	Acoustic emission in table
Variance	The variance of a signal measures the dispersion of the time series data samples around the mean value	Acoustic emission in spindle

Table 2 SVM model tuning results

Model	Kernel	Cost	Epsilon	Gamma	R^2
SVM_1	Linear	1	0.1	NA	0.29
SVM_2	Radial	1	0.1	0.0833	0.76
SVM_3	Radial	10	0.5	0.01	0.88
SVM_4	Radial	687.7	0.189	0.005	0.92

Out of these features, after pairwise correlation check, collinear variables are dropped. Records with no measurements for flank wear are dropped. To improve accuracy, it is decided to build separate models for different workpiece material. Each of the predictor variables used for building the model is centered and scaled.

After all preprocessing, two diverse regression models are built. The first model is built using support vector machines. This regression model is tuned using particle swarm optimization. For tuning the model, parameters like cost and epsilon need to be tuned. Generally, grid search is used to identify the optimal values for these tuning parameters. Using particle swarm optimization, global optimal values for cost and epsilon are found. Root-mean-square error (RMSE) is used as the objective function in this optimization, and optimal values for cost and epsilon were found. PSO iterations were stopped when the variance of the last 20 iterations were less than 0.001.

Table 2 demonstrates the improvement in SVM performance using PSO. Four SVM models were built to find the best model. The linear kernel provided low accuracy model, and hence, it was replaced with a radial kernel. Grid search for tuning parameters improved the model, but PSO outsmarted grid search in terms of yielding model with best determination coefficient. So PSO-optimized SVM_4 model is chosen as the best model.

```
> summary(glm_caret_model)

Call:
NULL

Deviance Residuals:
    Min       1Q   Median       3Q      Max
-0.19926  -0.05516  -0.01490   0.05389   0.29495

Coefficients:
            Estimate Std. Error t value Pr(>|t|)
(Intercept)  7.978e-01  2.696e-01   2.959  0.00434 **
kurtsmcac    1.230e+00  2.463e-01   4.995  4.94e-06 ***
kurtsmcdc   -1.329e-01  5.150e-02  -2.581  0.01220 *
kurtvbt     1.437e-01  4.485e-02   3.204  0.00213 **
kurtvbs     1.460e-05  7.587e-05   0.192  0.84802
kurtaet     -9.847e-04  4.677e-02  -0.021  0.98327
kurtaes     3.076e-02  3.136e-02   0.981  0.33031
skwsmcac    -9.241e-01  2.055e+00  -0.450  0.65442
skwsmcdc    -6.893e-01  2.094e-01  -3.291  0.00164 **
skwvbt      3.296e-01  7.287e-02   4.523  2.76e-05 ***
skwvbs      4.293e-03  3.844e-03   1.117  0.26835
skwaet     -3.013e-01  5.924e-02  -5.086  3.53e-06 ***
skwaes      7.501e-02  4.724e-02   1.588  0.11731
---
signif. codes:  0 '***' 0.001 '**' 0.01 '*' 0.05 '.' 0.1 ' ' 1

(Dispersion parameter for gaussian family taken to be 0.01267784)

Null deviance: 3.0102 on 75 degrees of freedom
Residual deviance: 0.7987 on 63 degrees of freedom
AIC: -102.54

Number of Fisher Scoring iterations: 2
```

Fig. 1 Summary of generalized linear regression model

Since diverse base learners result in better ensembles, generalized linear regression has been chosen as the next model in the ensemble. Repeated fivefold cross-validation is used to train this model. Irrespective of cross-validation, this model has less determination coefficient 0.46 because of the limitations of this algorithm. Figure 1 shows the summary of the generalized linear model.

Next, ensemble stack is created using the SVM and GLM model, and they are ordered by their root-mean-square error (RMSE). Both these models are ensembled using generalized linear regression, and to improve the robustness of the model, tenfold cross-validation is utilized. The best model from the ensemble is chosen, and it has a determination coefficient 0.96 which is higher than both the individual models. The accuracy of the model is validated using the held-out data.

Table 3 shows the comparison between measured and predicted wear. Figure 2 shows a residual plot of flank wear.

Table 3 Comparison between predicted and actual wear

Case	Run	Depth of cut	Feed	Life	Predicted wear	Measured wear	Absolute error
1	1	1.5	0.5	7	0.005	0.0	0.005
3	6	0.75	0.25	75	0.437	0.44	0.002
4	6	1.5	0.25	34	0.384	0.4	0.016
11	3	0.75	0.25	10	0.076	0.07	0.006
11	6	0.75	0.25	17	0.094	0.09	0.004
12	7	0.75	0.5	3	0.019	0.02	0.001
12	11	0.75	0.5	11	0.384	0.4	0.015

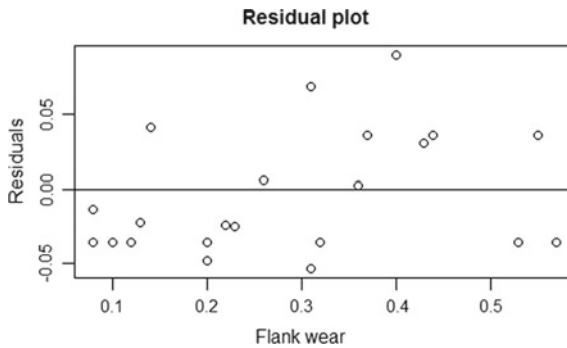


Fig. 2 Residual plot of flank wear

6 Conclusion

This study has presented flank wear prediction model for milling process using stacking regression ensembles having PSO-optimized individual models. This study has established a flank wear prediction model using temporal statistical features of vibration and acoustic emission. Model built in this approach has the least root-mean-square error (RMSE) and the highest determination coefficient. This proves that PSO can be used to tune the regression model and ensemble learning can improve the accuracy of the model further.

References

1. Shi D, Gindy NN (2007) Tool wear predictive model based on least squares support vector machines. *Mech Syst Signal Process* 21(4):1799–1814
2. Benkedjouh T, Medjaher K, Zerhouni N, Rechak S (2015) Health assessment and life prediction of cutting tools based on support vector regression. *J Intell Manuf* 26(2):213–223

3. Palanisamy P, Rajendran I, Shanmugasundaram S (2008) Prediction of tool wear using regression and ANN models in end-milling operation. *Int J Adv Manuf Technol* 37:29–41
4. Caruana R, Niculescu-Mozil A, Crew G, Ksikes A (2004) Ensemble selection from libraries of models. In: Proceedings of the twenty-first international conference on machine learning, p 18. Banff, Canada
5. Liu Y, Yao X, Higuchi T (2000) Evolutionary ensembles with negative correlation learning. *IEEE Trans Evol Comput* 4:380–387
6. Albeahdili HM, Han T, Islam NE (2015) Hybrid algorithm for the optimization of training convolutional neural networks. *Int J Adv Comput Sci Appl* 6(10):79–85
7. Hadavandi E, Ghanbari A, Abbasian-Naghneh S (2010) Developing a time series model based on particle swarm optimization for gold price forecasting. In: Proceedings of the third international conference on business intelligence and engineering (BIFE), pp 337–340. IEEE Computer Society, Hong Kong, China
8. Agogino A, Goebel K (2007) BEST lab. In: UC Berkeley, milling data set. NASA Ames prognostics data repository. <http://ti.arc.nasa.gov/project/prognostic-data-repository>, NASA Ames Research Center, Moffett Field, CA
9. Dornfeld D, Kannatey Asibu E (1980) Acoustic emission during orthogonal metal cutting. *Int J Mech Sci* 22(5):285–296
10. Kamarthi S, Kumara S, Cohen P (2000) Flank wear estimation in turning through wavelet representation of acoustic emission signals. *ASME J Manuf Sci Eng* 122(1):12–19
11. Jianming S, Yongxiang L, Gong W, Mengying Z (2016) Milling tool wear monitoring through time-frequency analysis of sensory signals. In: IEEE international conference on prognostics and health management (ICPHM)
12. Orhan S, Osman Er A, Camuşcu N, Aslan E (2007) Tool wear evaluation by vibration analysis during end milling of AISI D3 cold work tool steel with 35 HRC hardness. *NDT E Int* 40:121–126

Investigation on the Corrosion Resistance Characteristics of Automobile Lug Nuts



K. Sridharan, B. Muthuselvan, R. Gopinath and M. Umamaheswari

Abstract The present work investigates the corrosion resistance characteristics of automobile lug nuts under accelerated and normal conditions for determining the mass loss and surface properties. The study has been performed on different samples made of brass, steel and coated steel samples coated with zinc and copper. The experiments were carried out on the different samples in the standard salt bath for a specific time, and mass loss has been calculated as per the ASTM standards. The resistance of coated steel lug nut for corrosion has been studied, and the influence of surface treatments has been assessed for the economic and their survival. From the experiments conducted, the coated samples have shown better corrosion resistance properties than the steel and their survival was comparatively better than the steel samples. Even though samples made of brass shown better corrosion resistance, their cost is being high. From the investigation, it has been inferred that the heat-treated samples with zinc coating would reasonably show better performance with respect to cost and service conditions.

Keywords Corrosion · Coating · Resistance · Economic · Surfaces

1 Introduction

The global trend forces the automotive industry to use more environmentally friendly, safer and cheaper materials. Automobile manufacturing companies have made the most of research and development on materials and its alloys. In addition to technical, ecological and economic requirements, some basic requirements have to be met to achieve their goals with respect to material selection for particular applications. Lug nuts are typically used to secure a wheel to threaded wheel studs and thereby to a vehicle's axles in automobiles. The lug nuts have been exposed to severe environ-

K. Sridharan (✉) · B. Muthuselvan · R. Gopinath · M. Umamaheswari
Department of Mechanical Engineering, Madha Engineering College,
Anna University, Chennai, India
e-mail: sridharankad@gmail.com

© Springer Nature Singapore Pte Ltd. 2019
S. S. Hiremath et al. (eds.), *Advances in Manufacturing Technology*,
Lecture Notes in Mechanical Engineering,
https://doi.org/10.1007/978-981-13-6374-0_32

mental conditions during their lifetime in the wheel assembly. The wheel lug nuts may have different shapes and profiles based on the desire of automotive manufacturers. The fasteners are made using by different materials, and selection of the material should be based on such considerations such as environment (corrosive or temperature extremes), weight, magnetic properties, stresses, reusability and expected life. To keep costs down, the usage of standard materials must be a good practice. Thus specifying a fastener material with a specific chemical analysis adds time and cost. Often, a standard fastener can be altered by heat treating, cold working or coating to meet special needs.

The present work concentrates on analysing different materials for lug nuts such as steel, copper and coated materials. Generally, most fasteners are made from steel as their specifications cover a broad range of mechanical properties that are indicated by a bolt head marking system that identifies the fastener by grade. The properties of stainless steel had been studied under different ageing conditions for corrosion resistivity [1]. The limitation towards corrosion resistance property of the steel makes the designer choice to turn over on other materials. Stress corrosion cracking is a term used to describe service failures in engineering materials that occur by slow, environmentally induced crack propagation [2]. One of the most malleable of all metals is copper which has good corrosion resistance and the highest conductivity of all the non-precious metals. At present, many research works report the progress of steel corrosion protection for automobile applications, and also more and more steel corrosion protection technologies have been reported, such as hot galvanizing, inorganic coating and addition of corrosion inhibitors [3]. Recent developments in coating have shown the improved creep and corrosion resistance properties of the components under their services. The results of the studies concluded that a reasonable price and improved properties when compared to alternative materials such as Magnesium and its alloys for the applications in automotive industry [1].

The corrosion of metals can produce a premature failure of metallic components, resulting in financial losses, environmental contamination [4]. The understanding of corrosion behaviour possesses a critical challenge for the alloys under service conditions [5]. There are different techniques for preventing the corrosion of metals. One is the coating of a metal surface with an anti-corrosive layer to provide a barrier between the metal surface and the corrosive environment [6]. From many research conducted at the past, it has been inferred that contact between the corrosive solution and the metal/coating interface will corrode the metal surface [7]. Besides the wear resistance requirements of an engineering component during its service, it is additionally desirable that the coating should provide substrate with an improved corrosion resistance [8].

2 Experimental Studies

The experiments were conducted on brass and steel-coated lug nuts, respectively, for finding out the superior material among those by saltwater immersion test method. ASTM B895 is the standard test method specifically meant to the test under



Fig. 1 Lug nut samples

hood condition. The present study utilized the above-said standard methods that reasonably simulated the corrosive environment, except that conditions were made severe enough to produce results in a relatively short time. In service, it is common for automotive components to be alternately wetted and dried as the vehicle is driven and parked. The test method sought to duplicate that environment under controlled but accelerated conditions.

The steel, brass and coated lug nut samples were used for the experimental studies and the images of the samples have been presented in Fig. 1. Similarly, the other samples made of brass, coated with zinc along with dichromate and copper, has been used for the study. The most common plating system electro-galvanizing is used for coating the steel samples, which consists of a layer of pure zinc and copper, with an average thickness of about 0.004 mm.

2.1 Test Procedure

In this experimental study, the specimens are alternately dipped in an electrolyte solution for 10 min and then allowed to drain/dry for 50 min. The wet–dry cycle is repeated several times for all the coated and uncoated samples evenly, or until visual examination reveals the onset of corrosion. The brass and steel samples were exposed in separate tanks in the present study. The alternate immersion test was performed to measure the chloride stress corrosion cracking resistance of brass and steels. The procedure followed the test temperature of $33 \pm 1^\circ\text{C}$ and relative humidity of $45 \pm 6\%$. The above conditions were maintained in the tests for entire set of coated and uncoated samples. The corrosive medium is a solution of ordinary rock salt which is the most common, de-icing compound. In addition to chloride, the tests corrosion environment contained some sulphate, calcium and lesser amounts of magnesium. The initial solution pH was adjusted to 7.1. The parts during the immersion test were visually examined after roughly 24, 48, 72, 96 and 120 h of accumulated immersion. The continued exposure of the testing is used to monitor the extent of corrosion as a function of time.

2.2 Mass Loss

The weight loss calculation of the samples has been carried out precisely using electronic weighing machine with higher accuracy. The loss in weight of each set of coated and uncoated samples has been recorded along with physical change in their appearance as per the standard testing conditions. The percentage of total mass loss has been calculated for the suggestion of the most appropriate material for lug nut.

3 Results and Discussion

It is commonly accepted that extreme care needs to be taken to obtain good corrosion resistance for steel parts as they exhibit a wide range of corrosion behaviour. From the experiment conducted on the steel samples, the salt in the solution makes the protective layer to corrode and completely break down the coating, allowing the underlying steel to rust. Figures 2 and 3 depict the mass loss behaviour of the copper-coated samples and steel nuts. The coated samples shown some good resistance to corrosion and the mass loss were comparatively less than the steel samples. Exposure to accelerated corrosion conditions in salt spray and alternate immersion environments clearly affects both the steel samples and coated steel samples. After 120 h of salt spray exposure, the copper coating appears to perform at least as well; this begins to tarnish quite rapidly. Though steel is the cheapest, it has the highest corrosion rate compared to all the other materials. The steel nuts coated with coatings like zinc along with dichromate and copper are good, as its corrosion resistivity increases at some point of its life.

From the test conducted on the steel samples, all coatings eventually break down, and the physical condition of the products degrades significantly. Figure 4 depicts

Fig. 2 Mass loss in copper-coated nut

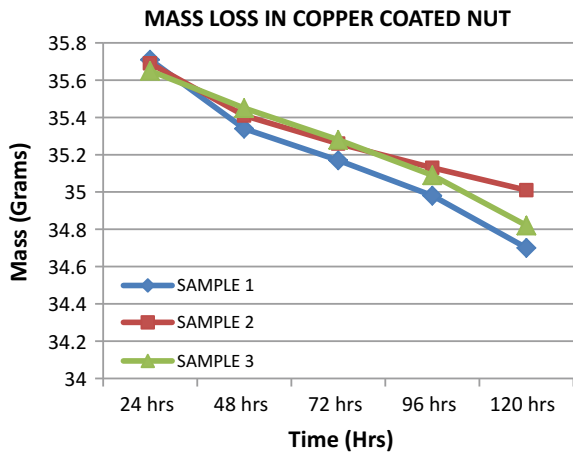


Fig. 3 Mass loss in steel nut

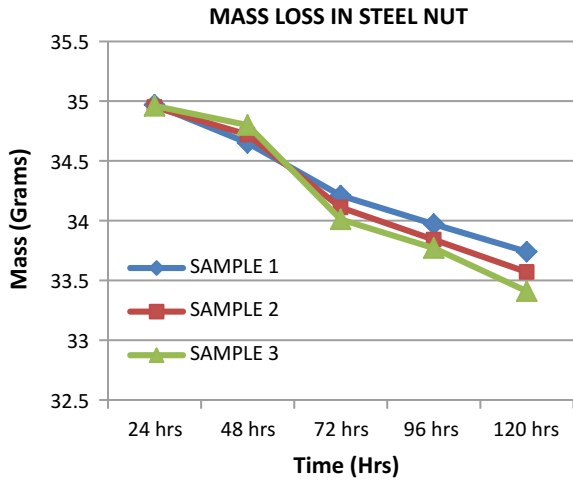
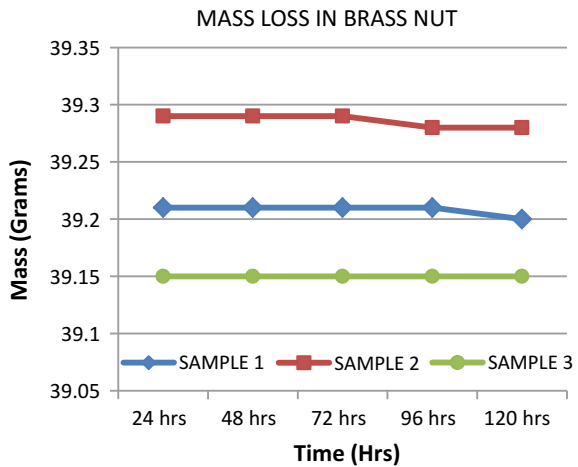


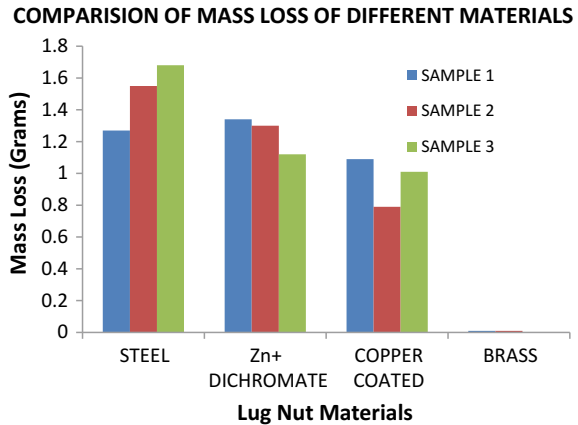
Fig. 4 Mass loss in brass nut



the mass loss behaviour of the brass nuts. However, the inherent corrosion resistance of brass becomes more and more evident. Brass samples lasting quality ensure that products not only retain their appearance, they also continue to do the job they desired for. From the experiments conducted, it has been inferred that the brass samples do not require extra corrosion protection because the material inherently resists corrosive environments.

By referring to the mass loss and cost analysis of each component, we may conclude the following factors; the corrosion resistance of brass is far greater than the other materials which when compared to others. On the contrary, brass has the highest material cost when compared to other materials. In the steel samples, corrosion products build up in unsightly patches, and the parts are left far from their original

Fig. 5 Comparison of mass loss for different materials for lug nut



appearance. Threads corrode, possibly to the point where unfastening connections might prove difficult. Appearance is certainly important in today's quality-conscious market, but the mass loss data measured in this brief study prove that brass corrosion resistance property is comparably high.

Figure 5 presents the comparison of mass loss for different materials for lug nut. Appearance is certainly important in today's quality-conscious market, but the mass loss data measured in this brief study prove that brass corrosion resistance is more than other materials. The brass lasting quality ensures that products not only retain their appearance, they also continue to do the job they have been proposed. On the contrary, brass has the highest material cost. Though steel is the cheapest, it has the highest corrosion rate compared to all the materials. The coated lug nut samples are clearly tarnished and contain numerous areas covered by a gray-green corrosion product. The corrosion product appears to be thin and adherent, even in threaded regions. The zinc plate plus yellow (thick) chromate coating contains only small patches of visible corrosion product but is otherwise unaffected. The bare zinc part and bare steel both show evidence of complete coating failure with corrosion product and distinct areas of red rusting. From the comparison graph shown in Fig. 5, it is clear that the zinc-coated samples have comparatively less mass loss than the other samples. By considering the cost aspects even though the brass samples show negligible mass loss due to their high cost, the zinc-coated samples would be good for corrosive environments.

4 Conclusion

From the experiments conducted on the coated and uncoated lug nut samples with respect to mass loss and cost consideration of the materials. The investigation reveals that, the corrosion resistance of brass is far greater than the other materials, but it

costs high. Though steel is the cheapest, it has the highest corrosion rate compared to all the materials compared. Thus the steel nuts coated with coatings such as zinc with dichromate and copper its corrosion resistivity increased and in turn decreases the cost of the lug nuts. As testing proceeds, however, the inherent corrosion resistance of brass becomes more and more evident. Brass lasting quality ensures that products not only retain their appearance, they also continue to do the job they were intended for.

References

1. Raja KS, Prasad Rao K (1993) On the hardness criterion for stress corrosion cracking resistance of 17-4 PH stainless steel 12:963–966
2. Jones RH, Ricker RE (1992) Mechanisms of stress-corrosion cracking. *ASM Int* 1–40
3. Claire L, Marie G, Julien G, Jean-Michel S, Jean R, Marie-Joelle M, Stefano R, Michele F (2016) New architected hybrid sol-gel coatings for wear and corrosion protection of low-carbon steel. *Prog Org Coat* 99:337–345
4. Wang D, Bierwagen GP (2009) Sol-gel coatings on metals for corrosion protection. *Prog Org Coat* 64(4):327–338
5. Umamaheshwerrao AC, Vasu V Govindaraju M, Saisrinadh KV (2016) Stress corrosion cracking behaviour of 7xxx aluminum alloys: a literature review. *Trans Nonferrous Metals Soc China* 26(6):1447–1471
6. Wang P, Zhang D, Lu Z (2015) Advantage of super-hydrophobic surface as a barrier against atmospheric corrosion induced by salt deliquescence. *Corros Sci* 90:23–32
7. Feng L (2014) Super hydrophobic aluminum alloy surface: fabrication, structure, and corrosion resistance. *Colloids Surf Physicochem Eng Asp* 441:319–325
8. Bouzida K, Beliardouhb NE, Nouveauc C (2015) Wear and corrosion resistance of CrN-based coatings deposited by R.F magnetron sputtering. *Tribol Indus* 37(1):60–65

Optimization of Process Parameters of Electrochemical Machining of TiC-Reinforced AA6063 Composites



S. Saravanan, M. Ravichandran, B. Stalin, S. Saravanel and S. Sukumar

Abstract The paper focused on the electrochemical machining behavior of AA6063 reinforced with various weight percentages of TiC particles fabricated using stir casting method. The experiments are conducted by using an ECM tester. The machining performance was investigated based on Taguchi L_{16} array. Maximum MRR is get for medium quantity of TiC strengthening and superior values of voltage and electrolyte concentration. Scratches in the worn surfaces were also analyzed using scanning electron microscopy.

Keywords Machining · Composite · ECM · MRR · Taguchi

1 Introduction

Recently, the developed technologies in manufacturing industry required the production of much more accurate and proficient parts [1]. The non-conventional machining of particulate reinforced MMCs is relatively new. Electrochemical machining (ECM) is mainly used as advanced non-conventional machining processes introduced by Gussef in which the samples and tool is anode and cathode respectively [2]. The electrolyte is a NaCl solution and used to reduce heat generation and to remove the reaction products. ECM generates no stress, no burrs, and it has high material removal rate, and surface quality with longer tool life [3]. Therefore, ECM has been utilized

S. Saravanan (✉) · M. Ravichandran · S. Saravanel
Department of Mechanical Engineering, K. Ramakrishnan College of Engineering,
Trichy 621112, India
e-mail: nanosaran007@gmail.com

B. Stalin
Department of Mechanical Engineering, Anna University, Regional Campus
Madurai, Madurai 625019, India

S. Sukumar
Department of Mechanical Engineering, University College of Engineering,
Pattukkotai, Rajamadam 614701, India

© Springer Nature Singapore Pte Ltd. 2019
S. S. Hiremath et al. (eds.), *Advances in Manufacturing Technology*,
Lecture Notes in Mechanical Engineering,
https://doi.org/10.1007/978-981-13-6374-0_33

in many industrial applications such as defense, aerospace, surgical implants, and automotive including gears, turbine blades, and engine casings [4, 5]. An investigation of the liberation method in ECM of a MMC was undertaken, and a model to disclose the exciting field performing on a hydrogen bubble in the process has been established by Liu et al. [6]. A variety of process parameters, e.g., applied voltage, current, frequency, electrolyte concentration, feed rate, electrolyte flow rate, greatly influences the metal removal rate (MRR), surface roughness (Ra), and overcut (OC) characteristics on ECM processes. Optimization methods are requisite to recognize the optimal mixture of factors for capitalize on the optimized MRR and minimizing the Ra in electrochemical machining processes [7]. Goswami et al. [8] have optimized for different output characteristics including MRR and Ra for ECM of mild steel and aluminum material by Taguchi technique. Many investigators made an attempt the process parameters optimization in electrochemical machining processes [9–18].

From the above literature, in this paper reinforcement percentage has been taken one of the input factors along with voltage and electrolyte concentration, and the effect of these factors on MRR was studied.

2 Experimental Details

In this work, AA6063 is used as matrix and TiC particles as reinforcements. The production of AA6063-TiC composites, 3, 6 and 9% of TiC by weight, was carried out by stir casting method [17, 18]. Figure 1 shows the produced composites of the image of the machined part size of 20 mm diameter and 5 mm thickness. The machining was carried out on ECM setup having a power supply of 415 V, 3-phase AC, 50 Hz, and it consists of three major subunits: the machining cell, the control panel, and the electrolyte circulation tank. The copper tool and NaCl solution were used as an electrolyte. Inter-electrode gap of 0.1 mm was kept during the machining. The effects of intervening parameters on the output response of during the ECM process of AA6063-TiC composites were studied. Four levels of each parameter were determined, and the related OA L_{16} is shown in Table 1. Minitab statistical software was used to designs plots and the weight loss method to find the MRR.

3 Results and Discussions

Table 1 shows the calculated S/N ratios. An ANOVA is used to recognize the importance of the factors on the MRR at 95% confidence level. “Larger is better” objective function is chosen for the main effect plot lines. The weight percentage of TiC particles and voltage is the much influenced parameter for controlling the MRR of the composites. The main effect plot for MRR, the reasonably high weight percentage of TiC particles, highest voltage, and electrolyte concentration which generates supe-



Fig. 1 Casted samples

Table 1 Experimental results for MRR with calculated S/N ratios

Expt. No.	Reinforcement (wt%)	Voltage (V)	Electrolyte concentration (g/lit)	MRR (mm ³ /m)	S/N ratio
1	0	11	10	0.164	-15.70
2	0	14	20	0.242	-12.32
3	0	17	30	0.284	-10.93
4	0	20	40	0.392	-8.13
5	3	11	20	0.276	-11.18
6	3	14	10	0.295	-10.60
7	3	17	40	0.454	-6.86
8	3	20	30	0.498	-6.06
9	6	11	30	0.428	-7.37
10	6	14	40	0.484	-6.30
11	6	17	10	0.501	-6.00
12	6	20	20	0.578	-4.76
13	9	11	40	0.251	-12.01
14	9	14	30	0.284	-10.93
15	9	17	20	0.384	-8.31
16	9	20	10	0.445	-7.03

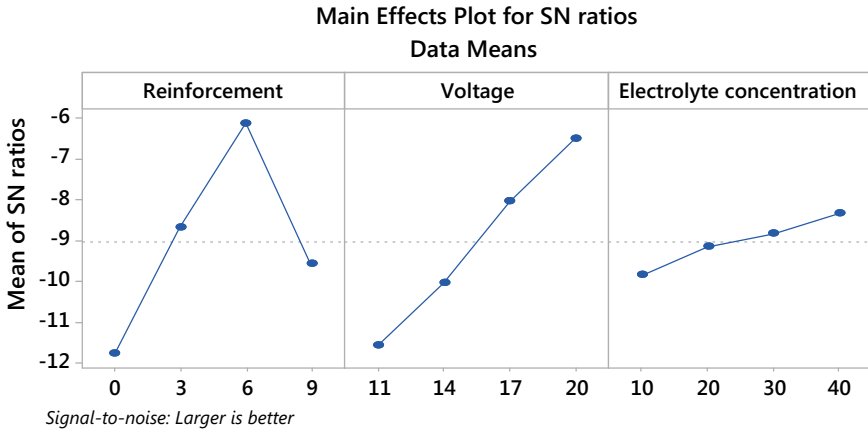


Fig. 2 Main effect plots for MRR

Table 2 ANOVA for S/N ratios of MRR

Source	DF ^a	Adj SS ^b	Adj MS ^c	F	p ^d	Remarks
Reinforcement	3	0.108608	0.036202	53.90	0.000	Significant
Voltage	3	0.092121	0.030707	45.72	0.001	Significant
Electrolyte concentration	3	0.003906	0.001302	1.94	0.225	Insignificant
Error	6	0.004030	0.000672	–	–	Insignificant
Total	15	0.208664	–	–	–	–

rior MRR is shown in Fig. 2. The MRR is increased up to 6 wt% and then decreased. The adding of reinforcement material decreases the machinability of the composites.

Table 2 shows the ANOVA and SN ratio, wt% of TiC particles and voltage are originate to be major scheming parameters on MRR and electrolyte concentration is found to have minor effect on MRR. Figure 3a–c shows that increasing MRR while the high voltage leads to high machining current. The percentage of TiC particles present in the samples does not affect the MRR, because TiC is an inert particle; it is not affected by an electrolytic reaction. But its neighboring aluminum metal is dissolved when the current is supplied to the inter-electrode gap. The decrease in electrolyte concentration increases MRR. It is attributed to the rise in the conductance of the electrolyte with the rise of attention. But attention above certain limit scares the mobility of ions which in return decreases MRR.

Figure 3d shows residuals are distributed along the straight and the model is adequate. The four samples of AA6063-TiC composite specimens machined under the different condition of voltage and electrolyte concentration were chosen for scanning electron microscopy studies. Figure 4a–d shows SEM images of different weight per-

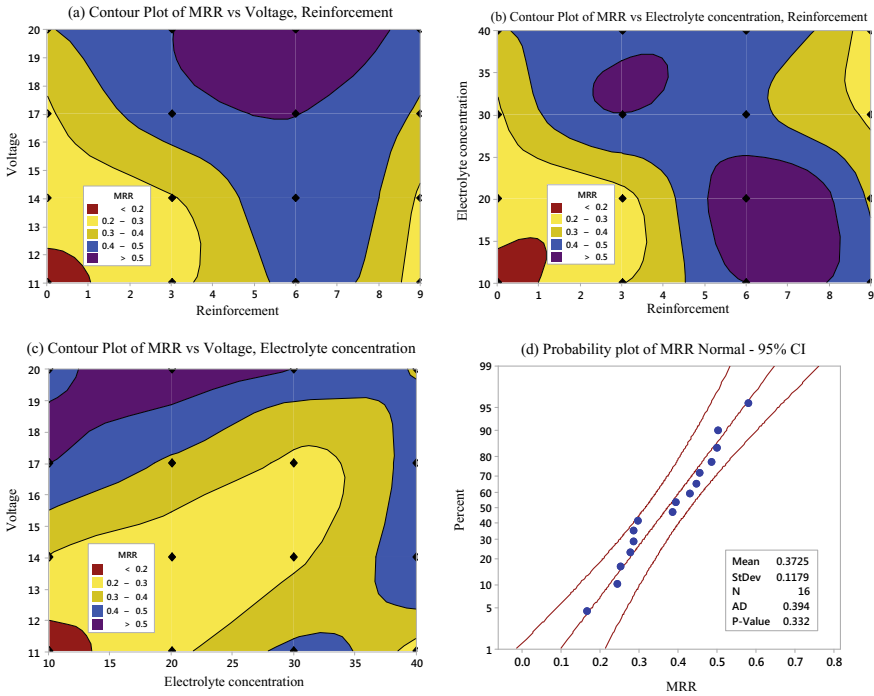


Fig. 3 a–c Contour plots for MRR. **d** Probability plot of MRR

centage of AA6063-TiC composites’ machined surface by ECM. The percentage of TiC increases, and MRR also increases. As increase in both voltage and electrolyte concentration increases the MRR moderately. Superior erosive can be seen in the images of Fig. 4b–c because of high voltage and medium electrolyte concentration.

4 Conclusion

AA6063-TiC composites were produced by stir casting process, and its ECM behavior has the following conclusions which are drawn:

- The raise of TiC decreases the MRR.
- In 0.578 g/min MRR at voltage of 20 V and electrolyte concentration of 20 g/lit of 6 wt% of TiC composites.
- Maximum MRR is achieved for medium wt% TiC and higher values of voltage and electrolyte concentration.
- SEM morphology shows that an erosive structure at 9 wt% TiC at V = 20 V and EC = 10 g/lit.

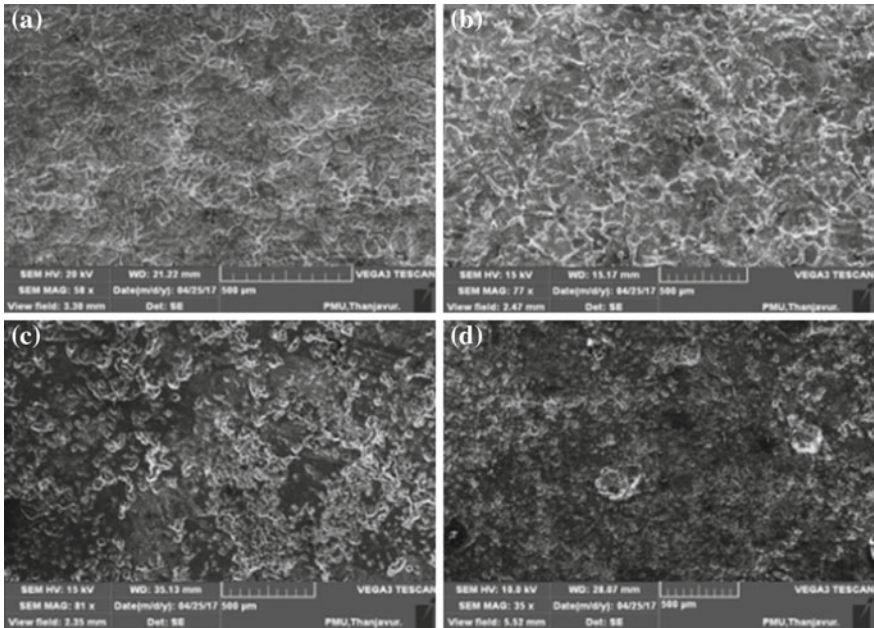


Fig. 4 SEM images of ECM-machined surface

References

1. Pramanik A, Zhang LC (2006) Prediction of cutting forces in machining of metal matrix composites. *Int J Mach Tools Manuf* 46(14):1795–1803
2. Kozak J (1998) Mathematical models for computer simulation of electrochemical machining process. *J Mater Process Technol* 76:170–175
3. Senthilkumar C, Ganesan G (2009) Study of electrochemical machining characteristics of Al/SiCp composites. *Int J Adv Manuf Technol* 43(3–4):256–263
4. Rajukar KP, Zhu D, McGeough JA, Kotak J, De Silva A (1999) New developments in electrochemical machining. *Ann CIRP* 48(2):567–579
5. Ebeid SJ, Hewidy MS, El-Towell TA, Youssef AH (2004) Towards higher accuracy for ECM hybridized with low frequency vibrations using the response surface methodology. *J Mater Proc Technol* 149:432–438
6. Liu JW, Yue TM, Guo ZN (2010) An analysis of the discharge mechanism in electrochemical discharge machining of particulate reinforced metal matrix composites. *Int J Mach Tools Manuf* 50:86–96
7. Asokan P, Ravikumar R, Jeyapaul R, Santhi M (2008) Development of multi-objective optimization models for electrochemical machining process. *Int J Adv Manuf Technol* 39:55–63
8. Goswami R, Chaturvedi V, Chouhan R (2013) Optimization of electrochemical machining process parameters using Taguchi approach. *Int J Eng Sci Technol* 5:999–1006
9. Senthilkumar C, Ganesan G, Karthikeyan R (2009) Study of electrochemical machining characteristics of Al/SiCp composites. *Int J Adv Manuf Technol* 43:256–263
10. Jawalkar CS, Sharma AK, Kumar P (2012) Micromachining with ECDM: research potentials and experimental investigations. *World Acad Sci Eng Technol* 61:90–95
11. Chigal G, Saini G, Singh D (2013) A study on machining of Al 6061/SiC (10%) composite by electrochemical discharge machining (ECDM) process. *Int J Eng Res Technol* 2

12. Solaiyappan A, Mani K, Gopalan V (2014) Multi-objective optimization of process parameters for electrochemical machining of 6061Al/10%Wt Al₂O₃/5%Wt SiC composite using hybrid Fuzzy-Artificial Bee Colony algorithm. *Jordan J Mech Ind Eng* 8(5):323–331
13. Rao SR, Padmanabham G (2014) Optimization of multiple machining in electrochemical machining of aluminium composites using design of experiments. *J Sci Ind Res* 73:251–257
14. Florence T, Dharmalingam S, Natarajan N, Babu B, Padmanaban G (2015) Experimental investigations on Al/Sic/ B4c composites using electro chemical micro machining. *J Appl Sci Res* 11(14):151–156
15. Babu B, Raja K, Dharmalingam S, Udhayaraj S, Vairamani V (2015) Electrochemical micro machining on hybrid metal matrix composites. *Int J ChemTech Res* 8(2):508–518
16. Sankar M, Gnanavelbabu A, Rajkumar M, Mariyappan M (2016) Electro chemical machining of aluminum-boron carbide-nanographite composites. *Appl Mech Mater* 852:136–141
17. Saravanan S, Senthilkumar P, Ravichandran M, Anandakrishnan V (2017) Mechanical, electrical and corrosion behavior of AA6063/TiC composites synthesized via stir casting route. *J Mater Res* 32(3):606–614
18. Dinesh Kumar S, Ravichandran M (2016) Experimental investigations of Al-TiO₂-Gr hybrid composites fabricated by stir casting. *Mater Test* 58(03):211–217

Performance Analysis of SS304 Steel Hat Stringer on the Chassis Frame



C. Ramesh Kannan, B. Stalin, M. Ravichandran and K. Sathiya Moorthi

Abstract This investigation concentrates on the analysis of ‘C’ and hat stringer on chassis frame. The C-stringer is a component which is supporting the chassis frame to resist the load applying on it. This component should have high strength and high stiffness. The different materials of C-stringer, and hat stringer are designed with their mechanical properties are analyzed. The selected materials for analysis are SS304 steel, duplex 2101, aluminium 7075 and glass/epoxy composite, respectively. The parameters analysed in the software are von Mises stress, elastic strain, total deformation and strain energy, respectively. As the result, the SS304 steel hat stringer is selected to conduct the experiment due to high strength and stiffness.

Keywords Stringer · SS304 steel · Duplex 2101 · Aluminium 7075 · Glass/epoxy composite

1 Introduction

The total load of the vehicle is fully supported by the chassis of the vehicle, and the strength of the vehicle is to be very high in bending. The chassis frame is attached in between by the stringers in the shape of ‘C’, ‘hat’, ‘I’, ‘L’, and ‘T’, respectively. The strength of the stringer can be improved by different design structures or changing

C. Ramesh Kannan

Department of Mechanical Engineering, Karpagam Academy of Higher Education,
Coimbatore 641021, Tamilnadu, India

B. Stalin (✉) · K. Sathiya Moorthi

Department of Mechanical Engineering, Anna University, Regional Campus
Madurai, Madurai 625019, Tamilnadu, India
e-mail: stalin1312@gmail.com

M. Ravichandran

Department of Mechanical Engineering, K. Ramakrishnan College of Engineering,
Trichy, Samayapuram 621112, Tamilnadu, India

© Springer Nature Singapore Pte Ltd. 2019

S. S. Hiremath et al. (eds.), *Advances in Manufacturing Technology*,

Lecture Notes in Mechanical Engineering,

https://doi.org/10.1007/978-981-13-6374-0_34

the material. Santos et al. [1] have designed the lightweight structures by using the different aluminium materials and cast steel material in the truck industry. This investigation focused on air suspension bracket, X-links on MAN truck and spring hanger brackets are designed by using the cast steel material and tested. Patel and Srivastava [2] have studied the obtainable chassis of TATA 2518 tc model for various materials. The results are associated with the existing part of the chassis. Chai and kangas [3] have conducted research on the structure, design and application of the duplex material for obtaining high strength, corrosion resistance and good fatigue properties. Pichal et al. [4] stated that materially nonlinear investigation is conceded out to the prestressed compression members on the building boundary conditions. By using software, the analysis is performed on 3D critical buckling loads of stayed columns. A simple modelling of sliding stays needs the shell elements and promotion of friction at the saddle stay interface. Mo et al. [5] have estimated the buckling and post-buckling response of the hat stringer subjected to axial compression. The stability analysis and deformation of the stiffened panel and the hat stringer are checked with experimental data. Purohit et al. [6] have fabricated the glass/epoxy composite by some additional material of fly ash and analysed the properties of the composite. The analysis of stress is done on the chassis. Patel et al. [7] examined the displacement analysis, and the deformation was controlled. The peak value of strain is also found in the investigation. Finally, the shear stress created on the TC 2516 chassis is also recovered from the examination.

Very few researches have studied the analysis of stringers. Veloso et al. [8] studied the stress distribution on the longitudinal stringer. The stringer is examined and found the results that are having high stress, but in reinforced model, a stringer is giving the better results on stress distribution and displacement of 5.9 mm at 90 KN. Karaoglu et al. [9] have investigated the stress analysis of truck chassis with riveted joints which is carried out in Ansys; it found the von Mises stress distribution along the side member is measured for the suggested design structures. From that results, the side member thickness increases with the stress on the joint area decreases.

The present study aims to analysis the effect of hat stringer on different materials and the mechanical properties of SS304 steel were reported. This analysis has two sections. The first one deals with the selection of materials, which occupy the identification of material and their properties. The second section comprises results and analysis of different material using Ansys finite element analysis software.

2 Selection of Materials

The materials selected for the analysis are aluminium 7075, SS304, duplex 2101 and glass/epoxy composite, respectively. The parameters chosen for the investigation are von Mises stress, elastic strain, strain energy and deformation. The dimension of the

Table 1 Properties of the materials

Material	Young’s modulus (Gpa)	Poisson’s ratio	Yield strength (Mpa)	Ultimate tensile strength (Mpa)
Aluminium 7075	71.7	0.3	503	572
Duplex 2101	210	0.3	450	650
Glass/epoxy composite	2.62	0.3	97.6	97.6
SS304 steel	193	0.4	205	515

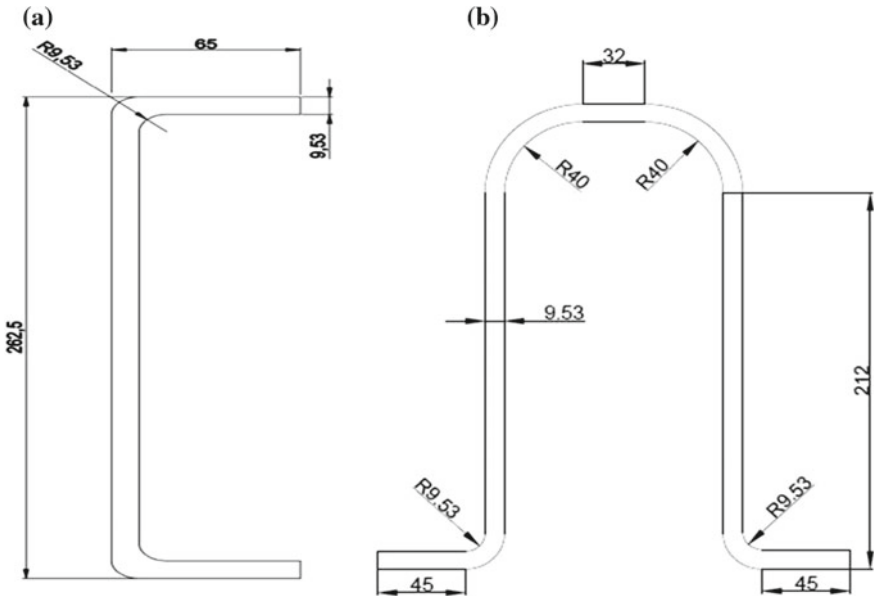


Fig. 1 Cross section of stringer **a** C-stringer, and **b** hat stringer

C-stringer is 262 mm of height, 65 mm of a bent edge on top and bottom, 2440 mm of length and 9.53 mm of thickness, respectively. The materials selected for the analysis are aluminium 7075, duplex 2101, SS304 steel and glass/epoxy composite, respectively. The properties of the above materials are given below in Table 1. The properties of the glass/epoxy composite and duplex material are obtained from the reference by SS304 material properties which are observed by Azzi et al. [10]. The cross sections of the C and hat stringer are represented in Fig. 1, which is drawn in AutoCAD.

3 Results and Analysis

The analysis is carried out with the load of 100 KN on the top face of the stringer. The maximum load applied on the chassis stringer is 81.3 KN. The parameters to be analysed on the application of the above load are von Mises stress, elastic strain, strain energy and deformation, respectively.

4 Analysis of C-Stringer

The stress analysis with all four materials and the stress distribution of all materials are 320.75 Mpa for aluminium 7075, 324.04 Mpa for duplex 2101, 323.57 Mpa for glass/epoxy composite and 219.47 Mpa for SS304 steel, respectively. The elastic strain analysis value of the C-stringer for different materials is achieved as 0.0045 for aluminium 7075, 0.0015 for duplex 2101, 0.12 for glass/epoxy composite and 0.0011 for SS304 steel, respectively. In Fig. 2, the analysis of the total deformation is achieved for all materials. The deformation of all four materials is recovered from the analyses. The values are 20.39 for aluminium 7075, 6.92 for duplex 2101, 570.2 for glass/epoxy composite and 7.69 for SS304 steel, respectively.

The analysis results of strain energy for C-stringer under four different materials are 668.55 for aluminium 7075, 227.83 for duplex 2101, 18755 for glass/epoxy composite and 283.75 for SS304 steel, respectively.

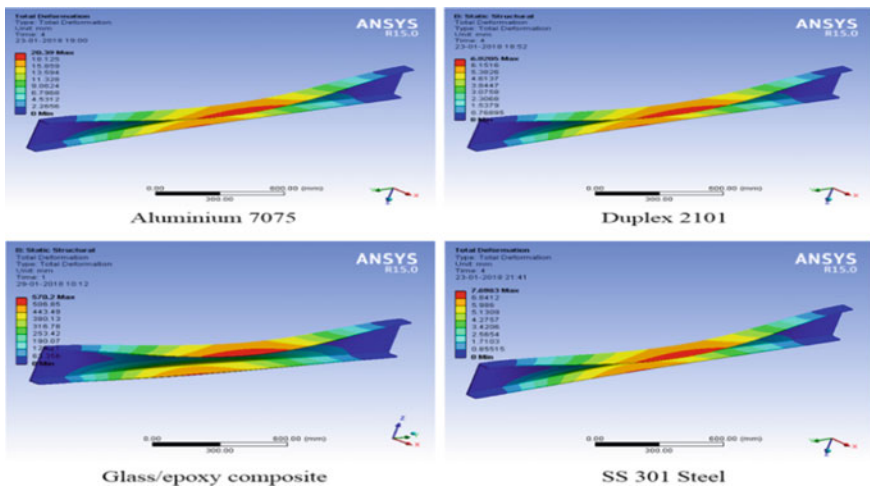


Fig. 2 Total deformation of aluminium 7075, duplex 2101, glass/epoxy composite and SS304 steel (C-Stringer)

5 Hat Stringer

The stress analysis with all four materials is done, and the strain analyses of the selected materials are discussed; the analysis of the total deformation is derived from all the four materials. The stress distribution of all materials is 68.925 Mpa for aluminium 7075, 78.673 Mpa for duplex 2101, 78.473 Mpa for glass/epoxy composite and 64.535 Mpa for SS304 steel, respectively.

The strain values of the hat stringer for different materials are achieved as 0.00096 for aluminium 7075, 0.000336 for duplex 2101, 0.027 for glass/epoxy composite and 0.000334 for SS304 steel, respectively. The deformation of all four materials is recovered from Fig. 3. The values are 1.45 for aluminium 7075, 0.497 for duplex 2101, 41.05 for glass/epoxy composite and 0.53 for SS304 steel, respectively.

The analysis results of strain energy for hat stringer under four different materials are 36.388 for aluminium 7075, 12.609 for duplex 2101, 1039.2 for glass/epoxy composite and 13.019 for SS304 steel, respectively.

The results of all parameters for all materials are shown in Table 2. From Table 2, we can say that duplex material is good because the deformation and strain energy of the duplex material structure are very low as compared to other three material structures. The stress value of duplex material is high as compared to other materials, but it is very safe while considering the yield strength of the duplex material.

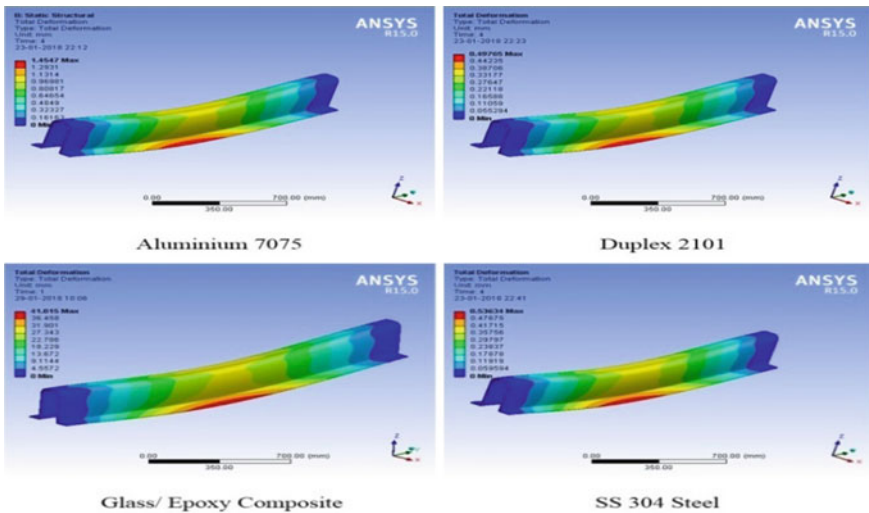


Fig. 3 Total deformations of aluminium 7075, duplex 2101, glass/epoxy composite and SS304 steel (hat Stringer)

Table 2 Results obtained in analysis

Description	Aluminium 7075		Duplex steel 2101		Glass/epoxy composite		SS304 steel	
	C-stringer	Hat stringer	C-stringer	Hat stringer	C-stringer	Hat stringer	C-stringer	Hat stringer
Von Mises stress (Mpa)	320.75	68.92	324.04	70.473	323.57	70.47	219.47	64.53
Total deformation (mm)	20.39	1.45	6.92	0.49	570.21	41.01	7.69	0.53
Elastic strain (mm/mm)	0.0045	0.0009	0.0015	0.0003	0.1269	0.0271	0.0011	0.0003
Strain energy (mJ)	668.55	36.38	227.83	12.60	1875.51	1039.21	283.05	13.01

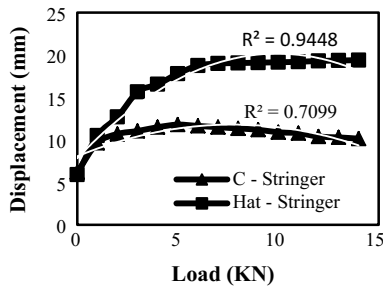


Fig. 4 Load with displacement for C and hat stringer

6 Experimental Results Graph

From Fig. 4, the load values are plotted against the displacement; then, stress versus strain graph is plotted in Fig. 5 by using the reading of the C-stringer. From Fig. 6, the load values are plotted against the displacement; then, stress versus strain graph is plotted.

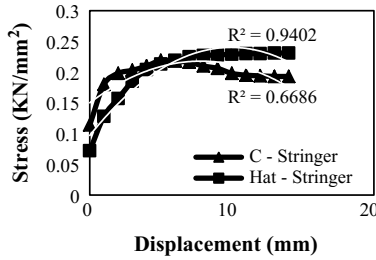


Fig. 5 Displacement with stress for C and hat stringer

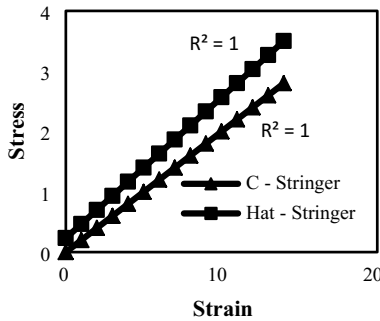


Fig. 6 Stress versus strain graph for C-stringer and hat stringer

7 Conclusion

Finally, the high strength and high stiffness of giving material for the structure are observed by the analysis of C-stringer and hat stringer with the properties of all four materials. The best material for fabrication is duplex 2101 steel, but when we take the cost as a parameter, SS304 steel material is less cost. The SS304 steel material is widely used in automobile industries. From the materials analysis, the best material for the fabrication is found out; then; the experimental analysis is carried out by testing the fabricated components in UTM machine. The paper summarizes that the hat stringer is having more strength when compared to C-Stringer. There is also a scope to study the stringer design of different structures with different advanced materials to attain the maximum strength in the chassis framework. Further studies could be performed on the microstructural properties of composite materials for stringer design with different material compositions.

References

1. Santos J, Gouveia RM, Silva FJG (2017) Designing a new sustainable approach to the change for lightweight materials in structural components used in truck industry. *J Cleaner Prod* 164:115–123
2. Patel AS, Srivastava A (2016) Modeling, analysis and optimization of TATA 2518 TC truck chassis frame using CAE tools. *Int J Eng Res Technol* 5(10)
3. Chai G, Kangas P (2016) Super and hyper duplex stainless steels: structures properties and applications. *Procedia Struct Integrity* 2:1755–1762
4. Pichal R, Machacek J (2017) Buckling and post-buckling of prestressed stainless steel stayed columns. *Eng Struct Technol* 9(2):63–69
5. Mo Y, Ge D, He B (2016) Experiment and optimization of the hat-stringer-stiffened composite panels under axial compression. *Compos Eng Part B* 84:285–293
6. Purohit R, Sahu P, Ranaa RS, Parashar V, Sharma S (2017) Analysis of mechanical properties of fibre glass-epoxy-fly ash composites. *Mater Today Proc* 4(2):3102–3109
7. Patel RL, Gawande KR, Morabiya DB (2014) Design and analysis of chassis frame of TATA 2516TC. *Int J Res Appl Sci Eng Technol* 2(III)
8. Veloso V, Magalhaes HS, Bicalho GI, Palma ES (2009) Failure investigation and stress analysis of a longitudinal stringer of an automobile chassis. *Eng Fail Anal* 16(5):1696–1702
9. Karaoglu C, Kuralay NS (2002) Stress analysis of a truck chassis with riveted joints. *Finite Elem Anal Des* 38(12):1115–1130
10. Azzi M, Benkahoul M, Klemberg-Sapieha JE, Martinu L (2010) Corrosion and mechanical properties of duplex-treated 304 stainless steel. *Surf Coat Technol* 205(5):1557–1563

Finite Element Modeling of Single Spark Material Removal and Heat Flux Distribution in Micro-Electro Discharge Machining Process



Ishwar Bhiradi, Leera Raju and Somashekhar S. Hiremath

Abstract Micro-Electro Discharge Machining (Micro-EDM) is a prominent non-conventional machining process. In this process, material removal takes place due to the melting and evaporation of electrode materials. The process gained a lot of research interest due to its ample potential in machining metallic materials and simple construction. In this paper, a thermal model has been developed to study the single spark material removal in Micro-EDM process. Single spark material removal study provides the significant information about optimization of the input parameters such as pulsed DC voltage, input current, spark duration, material removal rate of the electrodes, and area of heat distribution on the workpiece. ANSYS multiphysics is used to study the thermal analysis to determine the temperature and heat flux distribution on the workpiece. Silver material is used for both the electrodes. To validate the model, experiments were designed and conducted on tailor-made Micro-EDM setup. From the simulation study, it was found that for the pulse-on time (spark duration) of 40 μ s, the material removed for single per spark was 7.53 ng per spark and the maximum heat flux obtained was 2614.2×10^8 W/m². Simulation results were compared with the actual machined results. Crater profile was analyzed by Veeco Wyko NT1100 non-contact surface profilometer. The material removed by the single spark is obtained up to 8.16 ng. There was 8% error variation between simulation and experimental study. This may be due to assumptions made during simulation study and the presence of elemental impurities.

Keywords Micro-EDM · ANSYS · Single spark · Material removal · Surface profilometry

1 Introduction

Miniaturization of the components is the need of every industry. Many engineering, medical, telecommunication components such as biosensors, pacemakers, micropumps, and microchips are increasingly gaining the importance in various fields [1–3].

I. Bhiradi · L. Raju · S. S. Hiremath (✉)
Indian Institute of Technology, Madras, Chennai 600036, India
e-mail: somashekhar@iitm.ac.in

© Springer Nature Singapore Pte Ltd. 2019
S. S. Hiremath et al. (eds.), *Advances in Manufacturing Technology*,
Lecture Notes in Mechanical Engineering,
https://doi.org/10.1007/978-981-13-6374-0_35

The rapid growth of such requirements needs various micromachining methods for production. Micro-EDM is one such process extensively used in generating microfeatures smaller than 100- μm dimensions on difficult to machine conducting materials. It is a contactless process in which tool (cathode) and workpiece (anode) are separated by less than 10- μm electrode gap, immersed in a dielectric fluid. The potential difference between the electrodes ionization of dielectric medium results in extremely high temperature up to 12,000 $^{\circ}\text{C}$, which causes melting and vaporization of electrode materials. Even though working principle is the same as conventional EDM process [4], Micro-EDM differs in specific energy, tool size, inter-electrode gap, pulse-on time, and open circuit voltage [5]. Commercial as well as developed setups are widely used nowadays in the field of research. Developed setup focuses on improving the process performance by appending certain critical modules such as tool feed, pulsed power supply, and dielectric supply. Some of the setups were developed to control tool feed mechanisms like piezoactuator type [6], inchworm type [7], and servo feed mechanisms. The type of power supply used in Micro-EDM affects the quality of features produced. Jahan et al. [8] compared the effect of transistor type and RC-type power supplies on the quality of micro-holes produced. Several researchers have explored this process for generating various microfeatures. Yu et al. [9] has reported the generation of blind holes on stainless steel with square, rectangle, and pentagonal shapes. Likewise, Hiremath et al. [10] has reported the generation of micro-holes on the copper plate using NiP-coated hollow copper tool. Micro-EDM can be used for super finishing operations. Surface defects like non-homogeneity, cracks, arc spots, and black spots are reduced up to $R_a < 0.1 \mu\text{m}$ [11]. Deburring of microfeatures is necessary for assembly and inspection. Jeong et al. [12] demonstrated successful removal of burrs on aluminum, stainless steel, and copper workpieces using low specific energy and low diameter tool. Sahu et al. [13, 14] innovatively used Micro-EDM for the generation of nanoparticles and nanofluids. In their research work, they have studied the dispersion stability and thermal conductivity of copper nanofluid. In the setup, both the electrodes were copper and the dielectric medium was DI water. Particle size up to 2 nm has been reported by the authors. In their recent work on the generation of aluminum nanoparticles in a polyethylene glycol stabilizer medium with DI water as a dielectric medium, they have achieved average 196-nm particle sizes [15].

Working at low specific energy and low dimensions, optimization of input parameters turn out to be much important in reducing the machining time and increasing the machining quality. Simulations studies are essential in such conditions, and diverse studies have been reported in optimizing the parameters. Finite element modeling was proposed by many researchers to map the relationship between the input and output performance parameters under single discharge and multiple discharge conditions. Katz et al. [16] proposed a numerical simulation model in which Micro-EDM parameters were converted to dimensionless groups to optimize material removal rate. Theoretical formulation studies [17] use of soft computing techniques [18] and analytical modeling of electro-thermal effects on electrodes [19, 20], in which the model incorporates voltage, current, and pulse-on time during material removal to predict the temperature distribution on the workpiece as a result of single discharge

in the Micro-EDM process. An ANSYS model was developed by Lijo et al. [21] for electrochemical discharge machining process. They have reported the effect of DC and pulsed current on temperature distribution. Numerical simulation of multi-spark discharge in Micro-EDM was developed. It was done with the two-dimensional heat equation along with appropriate boundary conditions. The model equation was solved using the finite volume method [22]. Dibitonto et al. [23, 24] developed the cathode and anode erosion models for EDM setup, and they considered power as the boundary condition instead of temperature to produce a Gaussian distributed heat flux on the surface electrode material. Even though a considerable amount of research has been done in this field, the simulation studies for the input power supply and heat flux distribution on the workpiece can be explored. In this paper, ANSYS multiphysics is used for the demonstration of a single spark effect on material removal and the heat flux distribution on the workpiece in the Micro-EDM process. The results obtained from the analysis are used for calculating and comparing material removed with the experimental results.

2 Single Spark Simulation Study Using Finite Element Modeling

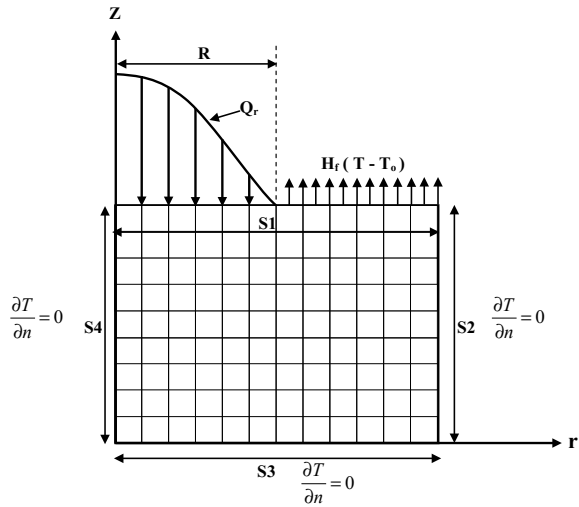
Finite elemental analysis (FEA) is a method to analyze the responses of loading conditions. The input parameters and boundary conditions act as loading conditions on a work sample. The whole sample will be divided into discrete blocks called as elements. On each element, loading will be distributed based on exact governing equations. The sum of each elemental solution gives rise to overall solution of the model. ANSYS is one such FEA software package well known for structural, thermal, electromagnetic, and fluidics study.

2.1 Thermal Modeling of Micro-EDM Process

In this study, thermal analysis is used to determine temperature and heat flux distribution on the workpiece. In the Micro-EDM process, material is removed due to melting and vaporization (thermal erosion) caused by repetitive sparks between tool and workpiece. The process can be modeled as the heating of the electrode by the incident plasma channel. Some assumptions are made for modeling [19].

Governing Equation. For the modeling of heat loading on the workpiece, the domain is considered to be axisymmetric to save the computational time. In such domain, number of elements will be less which leads to early convergence with lesser errors. The governing heat transfer equation in cylindrical coordinate system of an axisymmetric thermal model can be written as Eq. 1. In this equation, the heating

Fig. 1 Schematic representation of load distribution on workpiece



of workpiece is due to the discharge of single spark and governed by transient heat conduction with no heat generation.

$$\frac{1}{r} \frac{\partial}{\partial r} \left(kr \frac{\partial T}{\partial r} \right) + \frac{\partial}{\partial z} \left(k \frac{\partial T}{\partial z} \right) = \rho C_p \frac{\partial T}{\partial t} \tag{1}$$

where ρ is density, k is thermal conductivity, C_p is specific heat capacity of workpiece material in solid state, T is temperature, t is time, and r and z are cylindrical coordinate axes.

Heat Source and Heat Distribution. The heat source, heat input, and thermo-mechanical properties of the material are the most important parameters to be considered while thermal modeling of the process. The plasma channel breakdown causes the high energy discharge which increases temperature on the electrodes. Several researchers have considered point source or uniform distribution of heat flux. But in reality, neither is practical. Hence, recent researches considered Gaussian heat distribution for the modeling [21, 25, 26]. The load distribution is shown in Fig. 1. The figure shows that the model comprises of four boundaries S_1 , S_2 , S_3 , and S_4 . Top surface S_1 of workpiece will be experiencing heat flux up to plasma radius R as per Gaussian distribution.

The heat flux equation for a single spark is given by Eq. 2 [26].

$$Q_r = \frac{4.57 P V_c I_c}{\pi R^2} \exp \left[-4.5 \left(\frac{r}{R} \right)^2 \right] \tag{2}$$

where P is the fraction of energy transferred to the workpiece, V_c , I_c , and R are voltage, current, and plasma radius, respectively. Q_r is the heat flux entered into the workpiece having flux radius r . Beyond ‘ R ’ surface, heat loss happens on S_1

by convective heat transfer H_f . In the direction n being normal to the surface, heat transfer across S_2 and S_3 are zero due to far distance spark location. The surface S_4 is axisymmetric, hence assumed there is a zero net heat transfer. At the beginning when time $t = 0$, workpiece is immersed in dielectric medium therefore the domain is in room temperature T_0 .

Plasma Radius (R). To find out the heat flux radius, it is necessary to obtain the plasma radius. But it is practically difficult to measure the plasma radius. Many researchers have adopted many theories to calculate the plasma radius. In this modeling, authors have considered discharge current (I) and discharge time (T_{on}) for the calculations of plasma radius as per Eq. 3 [27].

$$R = 2040 I^{0.43} T_{on}^{0.44} \tag{3}$$

2.2 FE Modeling of Single Spark Discharge

For solving the model, commercially available ANSYS 18.0 software is used. There are three stages in this modeling and simulation study. The first stage is the pre-processing stage in which geometric and thermal details will be entered and meshing is done. The second stage is the solution stage, and loads are applied on each node based on governing equations. The third stage is post-processing in which results are analyzed and graphs are plotted for the study. The geometry of workpiece is taken as $50 \mu\text{m} \times 50 \mu\text{m}$ in 2D axisymmetric model, with a mesh size of $1 \mu\text{m}$. ANSYS thermal transient analysis is selected for the simulation study. The properties considered for the simulation are mentioned in Table 1. As per the requirements, heat flux from the Eq. 2 is reduced to Eq. 4 which is used for loading the nodes in the simulation study. Here, Q_r is the function of flux radius r in Gaussian distribution.

$$Q_r = 2.6142 \times 10^{12} \times \exp[-7.2 \times 10^{11} \times r^2] \tag{4}$$

Table 1 Thermal properties of the material used for FEM modeling

Property	Values
Material	Silver
Thermal conductivity	406 W/m K
Specific heat	238.64 J/Kg K
Density	10490 kg/m ³
Melting point	1235 K
Room temperature	298 K

2.3 Material Removal Modeling for Single Spark Discharge

Single spark discharge removes the material and leaves a crater impression on the workpiece. The generated crater is hemispherical with a radius r and volume V as determined using Eq. 5.

$$V = \frac{2}{3}\pi r^3 \tag{5}$$

Material removed per spark M_s is given by Eq. 6.

$$M_s = \rho V \tag{6}$$

where ρ is the density of the workpiece material.

2.4 Single Spark Discharge FE Modeling

The domain is divided into 2601 elements, and the load is applied on each node. As the loading condition is Gaussian distribution in nature, up to $2.5 \mu\text{m}$ length of heat flux distribution is found. Maximum temperature of 7425 K reached on node nos. 302 and 301. From the nodal solution, heat flux plasma radius was taken by considering nodes till melting temperature. Figure 2 shows the nodal solution of the simulation results using ANSYS, and Fig. 3 plot shows the heat flux distribution concerning flux radius. From the nature of the graph, Gaussian distribution of the heat flux can be seen.

The maximum temperature reached at the spark occurrence ($0 \mu\text{m}$), and it is distributed by convection as per the assumptions made. The gradual decrease in

Fig. 2 Nodal solution of the simulation

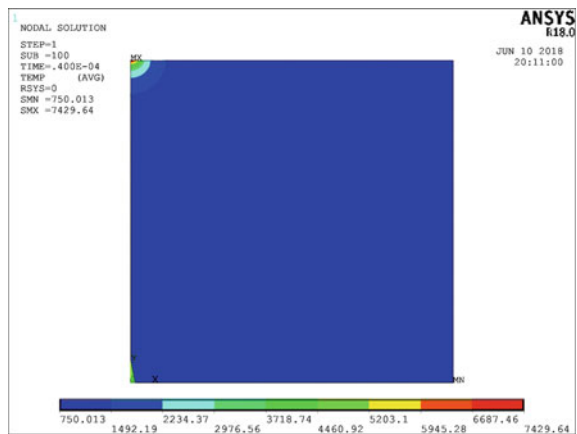


Fig. 3 Heat flux distribution chart

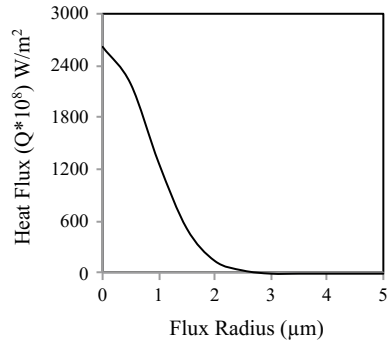
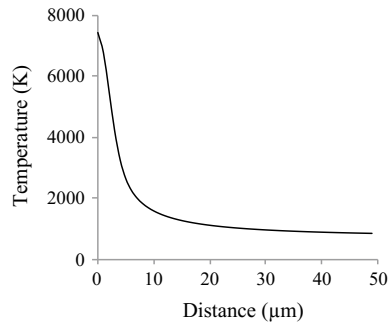


Fig. 4 Temperature distribution chart



temperature from spark zone is shown in Fig. 4. It is observed that up to the plasma radius, temperature is very high above the boiling temperature of silver (2435 K) and then the workpiece is exposed to the dielectric medium. Hence, the temperature decreases away from the spark zone. The obtained heat flux distribution (Fig. 3) and temperature distribution (Fig. 4) can be correlated with the theory described in Fig. 1.

From the graphs, the crater radius is considered up to 7 μm which includes the nodes up to boiling temperature. From Eq. 5 and Eq. 6, material removal from simulation study is found out to be 7.53 ng.

To validate the obtained FE results, experimentation has been carried out using the in-house developed Micro-EDM setup, which has been detailed in Sect. 3.

3 Experimentation

The experimental study has been conducted on developed Micro-EDM setup as shown in Fig. 5. It consists of two electrodes, workpiece as anode and tool as cathode, separated by inter-electrode gap of 10 μm. This arrangement is submerged in a dielectric medium (de-ionized water), and when the potential difference is applied between two electrodes, the dielectric medium breaks down generating high energy

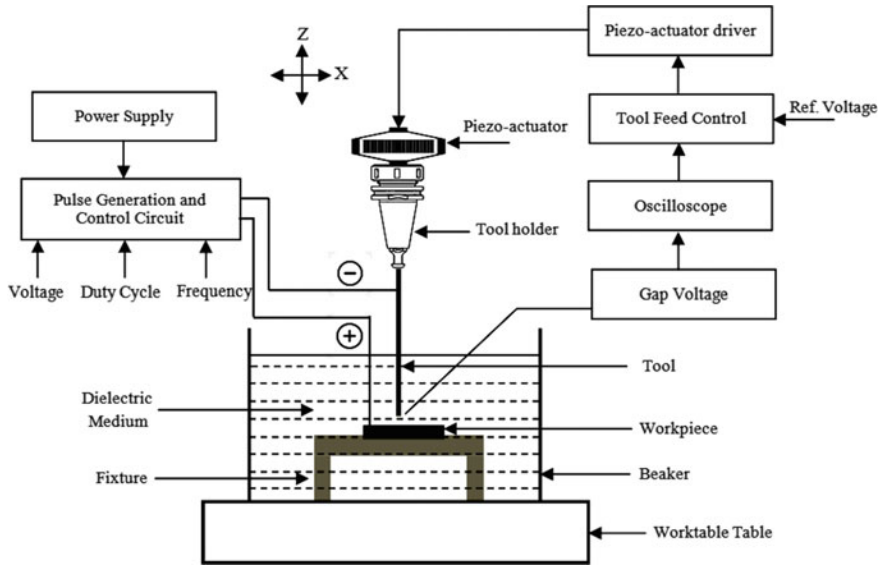


Fig. 5 Schematic diagram of Micro-EDM setup with the tool feed mechanism

Table 2 Machining parameters used for experiments

Parameters	Specifications
Workpiece material	Silver (anode)
Tool material	Silver (cathode)
Dielectric fluid	De-ionized water
Voltage	24 V
Current	1 A
Capacitance	220 μ F
Pulse-on time	40 μ s
Frequency	5 kHz

plasma channel. This allows the discharge to take place that causes melting and vaporization of electrode material, and as a result a small crater will be formed on the electrode.

In this setup, tool feeding mechanism is controlled by a piezoactuator. Every discharge removes some of the material from the electrodes, increasing the inter-electrode gap distance making the circuit open. The feedback circuit senses the change in average voltage and sends the signal to the amplifier to change the input voltage accordingly. The amplified signal is sent to piezoactuator, which then feeds the tool to maintain the required interelectrode gap. Transistor-type pulse generator is used to maintain uniform discharge energy and for high material rate [13]. The potentiometer is used to vary the frequency and the duty cycle of the discharge.

The processing parameters for generating microfeatures on silver plate are summarized in Table 2.

3.1 Single Spark Material Removal from Experimental Results

Experiments are conducted using the parameters mentioned in Table 2. The results are studied from Veeco Wyko NT1100 surface profiler. It is a non-contact-type optical profiler to study the height variations on the work surface with great precision. Optical interference and the wavelength of the light as a ruler are the main features of this instrument to plot the surface profile. It compares the optical path difference

Fig. 6 2D display of the crater

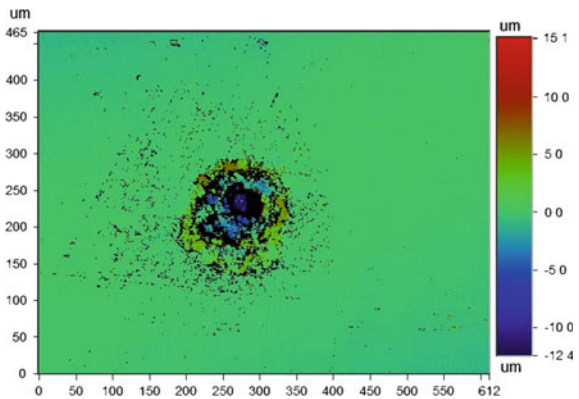
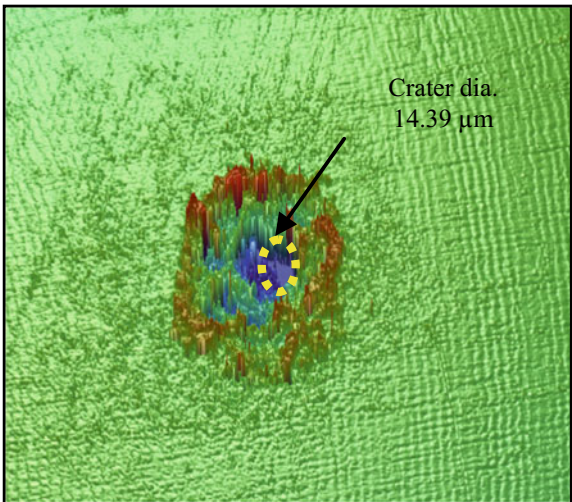


Fig. 7 3D display of the crater



between the surface and the reference plane. The 2D and 3D displays of the crater generated by a single spark are shown in Figs. 6 and 7. A recast layer can be observed in the 3D display; hence the highlighted area in Fig. 7 is only considered for the material removal study. It is generated from the vision software used for processing the profilometer-generated data. Red color indicates the highest surface and the blue color indicates lowest surface on the machined surface.

Applying the diameter obtained from surface profiler in Eqs. 5 and 6, material removed for single spark is found to be 6.16 ng. This shows the difference of nearly 8% from the simulated results.

4 Conclusions

In this paper, a thermo-mechanical model has been developed in ANSYS to study the single spark effect material removal by Micro-EDM process. The silver material is used as anode and cathode materials; hence, only silver properties were considered for the modeling. The simulation results were then compared with the actual machining. The conducted study can be concluded as follows:

- A single spark can create a crater on the workpiece which is in a hemispherical shape. The material removed from the simulation study is obtained up to 7.53 ng.
- Actual machined surface was analyzed using optical profiler which shows recast layer surrounding the crater. The depth of the crater was 23.20 μm , and Ra value was found to be 366.55 nm.
- Material removal obtained from experimentation is about 8.16 ng. There is 8% difference from the simulation value. This is due to assumptions made during modeling and may be a change in actual material properties because of elemental impurities present.

References

1. Masuzawa T (2000) State of the art of micromachining. *CIRP Ann Manuf Technol* 49(2):473–488
2. Alting L, Kimura F, Hansen HN, Bissacco G (2003) Micro engineering. *CIRP Ann Manuf Technol* 52(2):635–657
3. Rajurkar KP, Levy G, Malshe A, Sundaram MM, McGeough J, Hu X, DeSilva A (2006) Micro and nano machining by electro-physical and chemical processes. *CIRP Ann Manuf Technol* 55(2):643–666
4. Lee SH, Li XP (2001) Study of the effect of machining parameters on the machining characteristics in electrical discharge machining of tungsten carbide. *J Mater Process Technol* 115(3):344–358
5. Raju L, Hiremath SS (2016) A State-of-the-art review on micro electro-discharge machining. *Procedia Technol* 25:1281–1288
6. Venugopal TR, Rao R (2014) Development of micro-EDM incorporating in-situ measurement system. *Procedia Mater Sci* 5:1897–1905

7. Li Y, Guo M, Zhou Z, Hu M (2002) Micro electro discharge machine with an inchworm type of micro feed mechanism. *Precis Eng* 26(1):7–14
8. Jahan MP, Wong YS, Rahman M (2009) A study on the quality micro-hole machining of tungsten carbide by micro-EDM process using transistor and RC-type pulse generator. *J Mater Process Technol* 209(4):1706–1716
9. Yu ZY, Rajurkar KP, Shen H (2002) High aspect ratio and complex shaped blind micro holes by micro EDM. *CIRP Ann Manuf Technol* 51(1):359–362
10. Hiremath SS, Raju L (2017) Investigation on machining copper plates with NiP coated tools using tailor-made micro-electro discharge machine. *Adv Mater Process Technol* 3(4):522–538
11. Maradia U, Scuderi M, Knaak R, Boccadoro M, Beltrami I, Stirnimann J, Wegener K (2013) Super-finished surfaces using meso-micro EDM. *Procedia CIRP* 6:157–162
12. Jeong YH, HanYoo B, Lee HU, Min BK, Cho DW, Lee SJ (2009) Deburring microfeatures using micro-EDM. *J Mater Process Technol* 209(14):5399–5406
13. Sahu RK, Hiremath SS, Manivannan PV, Singaperumal M (2014) Generation and characterization of copper nanoparticles using micro-electrical discharge machining. *Mater Manuf Process* 29(4):477–486
14. Sahu RK, Hiremath SS, Manivannan PV (2015) Ultrasonic technique for concentration characterization of copper nanofluids synthesized using μ -EDM: a novel experimental approach. *Powder Technol* 284:429–436
15. Sahu RK, Hiremath SS (2017) Synthesis of aluminium nanoparticles in a water/polyethylene glycol mixed solvent using μ -EDM. In: IOP conference series: materials science and engineering, vol 225, No 1, p 012257. IOP Publishing
16. Katz Z, Tibbles CJ (2005) Analysis of micro-scale EDM process. *The Int J Adv Manuf Technol* 25(9–10):923–928
17. Shankar P, Jain VK, Sundararajan T (1997) Analysis of spark profiles during EDM process. *Mach Sci Technol* 1(2):195–217
18. Mandal D, Pal SK, Saha P (2007) Modeling of electrical discharge machining process using back propagation neural network and multi-objective optimization using non-dominating sorting genetic algorithm-II. *J Mater Process Technol* 186(1–3):154–162
19. Yeo SH, Kurnia W, Tan PC (2007) Electro-thermal modelling of anode and cathode in micro-EDM. *J Phys D Appl Phys* 40(8):2513
20. Mitra S, Vasa NJ, Singaperumal M (2010) Investigation on particle generation by micro-electro discharge machining. In: *Micromachining and microfabrication process technology, XV, Vol 7590, p 75900*. International Society for Optics and Photonics
21. Paul L, Korah LV (2016) Effect of power source in ECDM Process with FEM modeling. *Procedia Technol* 25:1175–1181
22. Somashekhar KP, Panda S, Mathew J, Ramachandran N (2015) Numerical simulation of micro-EDM model with multi-spark. *Int J Adv Manuf Technol* 76(1–4):83–90
23. Patel MR, Barrufet MA, Eubank PT, DiBitonto DD (1989) Theoretical models of the electrical discharge machining process. II. The anode erosion model. *J Appl Phys* 66(9):4104–4111
24. DiBitonto, DD, Eubank PT, Patel MR, Barrufet MA (1989) Theoretical models of the electrical discharge machining process I. A simple cathode erosion model. *J Appl Phys* 66(9):4095–4103
25. Kuriachen B, Varghese A, Somashekhar KP, Panda S, Mathew J (2015) Three-dimensional numerical simulation of microelectric discharge machining of Ti-6Al-4V. *Int J Adv Manuf Technol* 79(1–4):147–160
26. Giridharan A, Samuel GL (2015) Modeling and analysis of crater formation during wire electrical discharge turning (WEDT) process. *Int J Adv Manuf Technol* 77(5–8):1229–1247
27. Salonitis K, Stournaras A, Stavropoulos P, Chryssolouris G (2009) Thermal modeling of the material removal rate and surface roughness for die-sinking EDM. *Int J Adv Manuf Technol* 40(3–4):316–323

Electrochemical Micromachining of Aluminium Alloy Composite



S. Ramesh and V. Subburam

Abstract Electrochemical micromachining (EMM) is in the forefront among the non-traditional machining processes that are brought into micromachining domain. The major influencing factors of EMM process are more sensitive at the micro-level machining, and for achieving precision the right combination of parameters is essential. Continuous research works are required to study and analyse every new possible set of variables that can be applied to carry out this machining process. The objective of the present research work is to generate micro-holes using an aluminium composite workpiece through EMM and study the capability of the process to machine such non-homogenous materials. An EMM set-up developed with pulse power facility for experimental purposes was used to carry out the experiments. The experimentation included an aluminium composite containing ceramic reinforcement as work specimen (anode), a hollow brass electrode as the machining tool and the solution of NaCl (sodium chloride) as the ion-conducting medium (electrolyte) to facilitate the process. The effect of input factors like voltage, current and pulse-on time on response parameters such as machining rate (MR) and overcut (RC) was studied from experimental observations. It was a general observation that speeding up the machining rate with higher level input of parameters affects the accuracy of the process outcome. Generally, the response of the EMM process is slow and requires time to produce machining accuracy.

Keywords Electrochemical micromachining · Aluminium composite · NaCl · Machining rate · Overcut

S. Ramesh (✉)

Department of Mechanical Engineering, KCG College of Technology,
Chennai 600097, India
e-mail: ramesh_1968in@yahoo.com

V. Subburam

Department of Mechanical Engineering, Paavai Engineering College,
Namakkal 637018, India

© Springer Nature Singapore Pte Ltd. 2019

S. S. Hiremath et al. (eds.), *Advances in Manufacturing Technology*,
Lecture Notes in Mechanical Engineering,
https://doi.org/10.1007/978-981-13-6374-0_36

309

1 Introduction

Electrochemical micromachining is required to cater new demands that arise with new materials of different compositions and varied operating conditions. Schuster et al. [1] applied ultra-short pulses and reduced electrode machining gap to show the capability of the EMM process in the micromachining range. Machines for experimental works were developed by many researchers to enhance the performance of the EMM process [2–4]. A stir-cast hybrid aluminium metal matrix composite specimen containing alumina, silicon carbide and carbon particulates was micro-holed through electrochemical micromachining to study the performance characteristics such as material removal rate (MRR), surface roughness (SR), over cut (OC), taper cut (TC), micro-spark affected zone (MSAZ) and electrode wear rate (EWR). The report indicates the values of 1.5 A machining current, 13 V machining voltage, 15 g/l electrolyte concentration, 10 ms pulse-on time, 10 ms pulse-off time and 0.2 l/min electrolyte flow rate as the optimal combination for ideal results [5]. The role of electrolyte as a transferring medium for material stock is very crucial in the EMM process. Acidified electrolytes are used for machining hard materials in the EMM process and composite electrolytes are used for special metal combinations [6, 7]. The input variables like supply voltage, electrolyte pressure, temperature and tool feed were investigated for their influence on material removal rate, electrode gap and surface quality in the EMM process of aero-engine material. The impact of the electrode feed rate was found to be dominant by Liu et al. [8]. The contaminants are one of the important factors that affect the accuracy of EMM process. Schulze et al. [9] studied the effect of contaminants on the performance of electrochemical process. The contaminants include particles of conductive and non-conductive nature, gas bubbles which tend to reduce electrode gap, and change the distribution of current that leads to stray machining and affects the process quality. The present work involves EMM of a composite to produce micro-holes for performance study.

2 Experimentation

2.1 EMM Set-up

The experimental set-up used for EMM experimentation is given in Fig. 1. The machine is an integrated set-up with all the sub-systems for various requirements such as framework for supporting components, tool-feeding arrangement, work-holding mechanism, electrolyte supplying and filtering components, a stepper motor for micro-feeding and the pulse generator for producing pulsed power. The set-up has the tool-feeding facility only in the vertical direction.

Fig. 1 EMM set-up

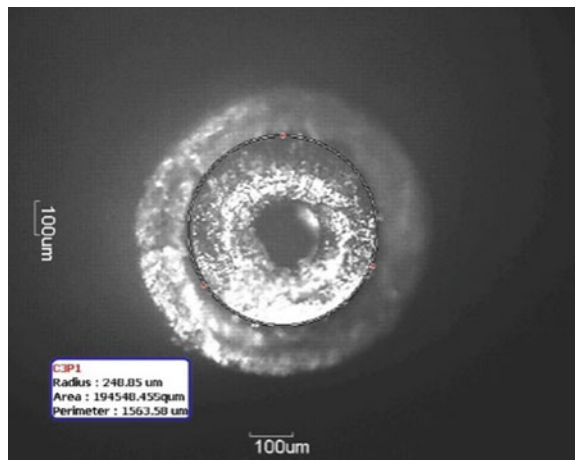


2.2 Details of Experimental Conditions

The work material is an aluminium composite having a composition of Aluminium7075 (87%) + Al₂O₃ (6%) + Borosilicate glass powder (7%). The external and internal diameters of a hollow brass electrode are 0.480 mm and 0.178 mm, respectively, used as the cathode tool. The cross-sectional image of the microtool is shown in Fig. 2, where the outermost portion shows the coating on the tool. The electrolyte used was NaCl solution.

The input factors that were kept constant for all the experiments are the electrolyte concentration at 20 g/l, inter-electrode gap at 40 μm and the frequency at 50 Hz. The input variables selected for study were three levels of each for machining: voltage, current and pulse-on time. The performance characteristics investigated were machining rate of the process and radial overcut of the generated hole. The total number of pulses is decided by frequency from which pulse-on and pulse-off times

Fig. 2 Cross-sectional view of micro-tool



are calculated. Fifty pulses per second are used with pulse duration of 20 ms, and in one of the combinations, the pulses on time and off times are 10 ms each.

Since the work specimen used is new composite material, preliminary experiments have been conducted to set the initial values of the input variables to begin the micro-drilling process. It was also observed that the machining process got delayed inordinately if the values were kept lesser than these initial values.

3 Results and Discussion

3.1 Experimental Results

The results obtained from the experiments with a selected level of input parameters and the observed readings along with the calculated values of the response parameters are given in Table 1.

3.2 Effect of Input Parameters

The experimental results have been represented in the graphs below, and the effects of the input parameters on the output performance indicators are discussed.

Table 1 Experimental results with levels of input parameters

Sl. No	Process parameters			Results recorded		Performance indicators (calculated)	
	Current (ampere)	Machining voltage	Pulse-on time (ms)	Machining time (in sec)	Radius of hole (μm)	Machining rate ($\mu\text{m/s}$)	Radial overcut (μm)
1	1.2	10	12	2016	251.18	0.198	150.33
2	1.2	11	12	1943	479.10	0.205	230.25
3	1.2	12	12	1722	516.31	0.232	267.46
4	1.2	12	12	1774	490.72	0.225	241.87
5	1.1	12	12	1786	430.26	0.223	181.41
6	1.0	12	12	2580	476.77	0.155	227.92
7	1.2	12	12	1560	555.84	0.256	306.99
8	1.2	12	11	1250	416.30	0.320	167.45
9	1.2	12	10	660	281.41	0.660	32.56

Fig. 3 Effect of voltage on machining rate

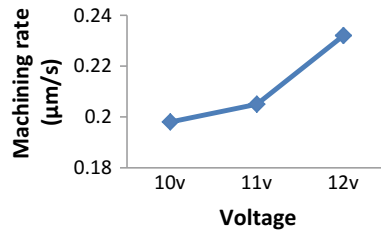
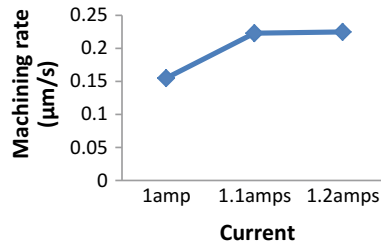


Fig. 4 Effect of current on machining rate



3.2.1 Effect of Voltage on Machining Rate

The effect of machining voltage on machining rate of the electrochemical micromachining process for drilling micro-holes on the composite work specimen is plotted as a graph in Fig. 3.

The machining rate shows an increasing trend with an increase in machining voltage. When the voltage level is increased, the electrons on the surface of the work material are de-bonded forcibly and tend to travel in the electrolyte medium getting attracted towards the cathode area. But the flushing electrolyte pushes them away from the machining site. As the increase in voltage provides more energy to the surface ions of the work material, they get evicted in a fast manner from the anode material increasing the dissolution rate (machining rate).

3.2.2 Effect of Current on Machining Rate

The effect of supply current on machining rate of the electrochemical micromachining process for drilling micro-holes on the composite work specimen is plotted as a graph in Fig. 4.

The machining rate shows an increasing trend to the first increment of current level from 1 to 1.1 A, and for the next increment the machining rate is found to provide a constant pattern. When the current is increased, the available electrons/ions in the medium for electrolysis increases and the machining rate also increases. But at certain levels of ampere current, the increase in the electron/ion level in the medium tends to clog the inter-electrode gap and hinder machining. This process of clogging the electrode gap reduces the machining rate.

Fig. 5 Effect of pulse-on time on machining rate

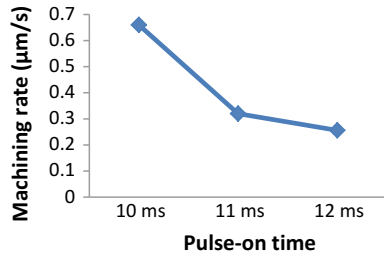
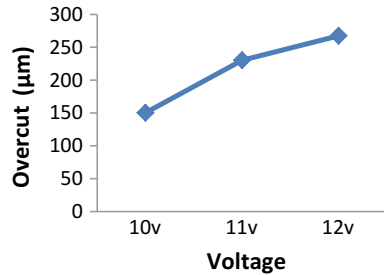


Fig. 6 Effect of voltage on overcut



3.2.3 Effect of Pulse-on Time on Machining Rate

The effect of pulse-on time on machining rate of the electrochemical micromachining process for drilling micro-holes on the composite work specimen is plotted as a graph in Fig. 5.

It can be observed from the graph that the machining rate decreases with the rise in the pulse-on time values. When the pulse-on time is increased, the pulse-off time available for cleaning the sledges from the inter-electrode gap is reduced. Hence, the sledges deposited at the machining site slow down the machining rate though comparatively more machining time is available.

3.2.4 Effect of Voltage on Overcut

The effect of supply voltage on overcut of the electrochemical micromachining process for drilling micro-holes on the composite work specimen is plotted as a graph in Fig. 6.

The plot of supply voltage versus overcut shows that an increase in the machining voltage causes an increase in the overcut of holes. As the increase in voltage speeds up the machining rate in the overall system, the localisation effect gets affected and forcible energy available for electrolysis tends to eject ions from regions away from the machining site leading to stray machining and hence the result.

Fig. 7 Effect of current on overcut

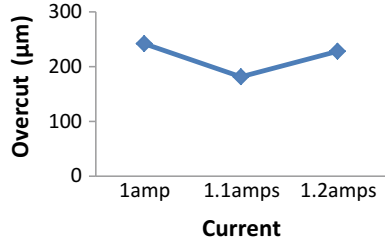
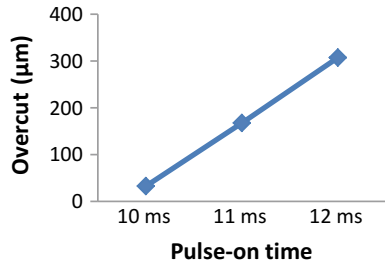


Fig. 8 Effect of pulse-on time on overcut



3.2.5 Effect of Current on Overcut

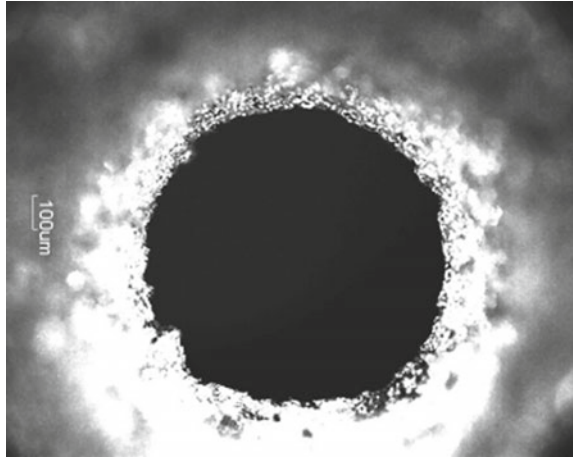
The effect of ampere current on overcut of the electrochemical micromachining process for drilling micro-holes on the composite work specimen is plotted as graph in Fig. 7.

It can be observed from the plot that overcut shows decreasing trend for the first increment of current from 1 A to 1.1 A, and then from 1.1 A to 1.2 A, it shows incremental trend. The change in trend is due to the production of surplus ions at the higher level current of 1.2 A that accumulate and spread around the machining site causing removal of ions from the adjacent area, resulting in the extension of overcut.

3.2.6 Effect of Pulse-On Time on Overcut

The effect of pulse-on time on overcut of the electrochemical micromachining process for drilling micro-holes on the composite work specimen is plotted as a graph in Fig. 8.

The pulse-on time is a dominant factor in the EMM process which affects the precision of the machining. When pulse-on time is increased, more time is available for machining, but the process produces more sledges which obstruct the machining process itself as the electrode gap gets reduced creating a risk of sparks and stray cut machining. Moreover, the increase in pulse-on time reduces the period of pulse-off time which further aggravates the situation as less time is left in each cycle to remove the sledges from the machining gap. The combined effect of these factors tends to increase the overcut in the machining process.

Fig. 9 Micro-hole image

3.2.7 Micro-Hole Image

The optical microscope image of the micro-hole produced on the composite specimen through electrochemical micromachining is shown in Fig. 9. The micro-hole is generated at the parametric combination of 10 V, 1.2 A and 12 ms pulse-on time. The composition of the aluminium composite includes ceramic materials such as alumina and borosilicate which remain inert during electrochemical reactions. The inhomogeneous nature and the presence of ceramic compounds in the work material that affect the uniform dissolution of the workpiece are the reasons for the jagged edges found at the circumference of the micro-hole.

4 Conclusions

Composite materials are not paid much attention in the electrochemical micromachining domain. This work is an attempt to apply electrochemical micromachining on aluminium composite containing alumina and borosilicate glass powder to analyse the performance.

The EMM set-up was used to generate micro-holes on the composite work material. The influence of input parameters such as voltage, current and pulse-on time on the performance indicators such as machining rate and radial overcut are studied.

The experimental observations show that the machining rate increases with an increase in voltage level, but for the rise in supply current and pulse-on time the machining rate shows varying trends which means they are crossing the optimum levels for these parameters. It is clear from the trend that 10 ms is the optimum pulse-on time value among the three levels used, and above this level machining rate

shows only decreasing values as the amount of sledges clogging the inter-electrode gap begins to increase due to the availability of lesser pulse-off time for cleaning.

In the case of overcut, the observations show that the input parameters are to be kept at lower levels to achieve good accuracy.

The sodium chloride solution used is an aggressive electrolyte and caused erosion all around the machining area making the specimen brittle. Hence to check the influence of a soft electrolyte, few experiments were conducted with sodium nitrate solution (NaNO_3) and such problems of erosion around the machining site did not occur.

References

1. Schuster R, Kirchner V, Allongue P, Ertl G (2000) Electrochemical micromachining. *Science* 289:98–101
2. Bhattacharya B, Doloian B, Sridhar PS (2001) Electrochemical micro-machining: new possibilities for micro-manufacturing. *J Mater Process Technol* 113:301–305
3. Ramarao S, Padmanabhan G (2012) Effect of process variables on metal removal rate in electrochemical machining of Al-B4C composites. *Arch Appl Sci Res* 1844–1849
4. Hackert-Oschätzchen M, Lehnert N, Martin A, Schubert A (2016) Jet-electrochemical machining of particle reinforced aluminum matrix composites with different neutral electrolytes. *IOP Conf Ser Mater Sci Eng* 118:012036
5. Kalra I CS, Kumar V, Manna A (2015) Analysis of electrochemical behavior on micro-drilling of cast hybrid Al/(Al₂O₃p/SiCp) MMC using micro-ECM process. *Proc Inst Mech Eng Part L J Mater Des Appl* 232(1):67–79
6. Subburam V, Ramesh S, Arunachalam RM, Thanigaivelan R (2013) Effect of acidified electrolyte on the performance of electrochemical micromachining. In: *Proceedings of the second international conference on advances in materials processing and characterisation (AMPC 2013)*, vol II, pp 799–806
7. Tang L, Yang S (2013) Experimental investigation on the electrochemical machining of 00Cr₁₂Ni₉Mo₄Cu₂ material and multi-objective parameters optimization. *Int J Adv Manuf Technol* 67:2909–2916
8. Liu J, Zhu D, Zhao L, Xu Z (2015) Experimental investigation on electrochemical machining of γ -TiAl intermetallic, 15th machining innovations conference for aerospace industry. *Procedia CIRP* 35:20–24
9. Schulze HP, Schatzing W (2013) Influences of different contaminations on the electro-erosive and the electrochemical micro-machining. *The Seventeenth CIRP Conference on Electro Physical and Chemical Machining (ISEM)*. *Procedia CIRP* 6:58–63

Analysis on Mechanical Behaviour of Binary and Hybrid Al2014 Metal Matrix Composites



S. Arivukkarasan, B. Stalin, A. Suresh Babu and M. Pandiyarajan

Abstract Aluminium matrix composites have improved mechanical and tribological properties due to the addition of reinforcements into the metallic matrix. The reinforcements improve tensile and yield strengths, elastic modulus, wear, fatigue and creep properties compared to the other monolithic materials. This class of material has a greater potential and finds vast applications in automotive, aircraft, defence and other industries. The objective of this work is to investigate the mechanical behaviour of aluminium alloy 2014 reinforced with aluminium oxide (Al_2O_3) and silicon carbides (SiC) particulates. The combinations planned for the study include binary which consists of aluminium2014-5% aluminium oxide and aluminium2014-5% silicon carbide particles. Also, hybrid reinforcement with composite has 5% each of aluminium oxide and silicon carbide particles in order to analyse the combined effect. Composite specimens were prepared using a liquid metallurgy technique, i.e. Stir casting. The specimens were prepared and tests were conducted as per ASTM standard. The result shows an increasing property with the introduction of reinforcement and hybrid arrangement. The tested samples were investigated utilising a scanning electron microscope (SEM) for the characterisation and correlated with the test results.

Keywords Aluminium alloy · Hybrid composites · MMC · SEM · ASTM

S. Arivukkarasan · M. Pandiyarajan
Department of Mechanical Engineering, SACS MAVMM Engineering College,
Madurai, Tamilnadu, India

B. Stalin (✉)
Department of Mechanical Engineering, Anna University, Regional Campus
Madurai, Madurai 625019, Tamilnadu, India
e-mail: stalin1312@gmail.com

A. Suresh Babu
Department of Manufacturing Engineering, College of Engineering Guindy, Anna University,
Chennai 600025, Tamilnadu, India

1 Introduction

Composite materials are designed to meet the industrial requirements such as higher specific strength, higher strength-to-weight ratio, corrosion and wear resistance and environmental friendliness. Aluminium metal matrix composites (AMCs) have been of interest as engineering materials because of the ever-increasing demands of modern technology. The reinforcement in aluminium matrix composites could be in the form of fibre with different orientation, whiskers or particulates. Nowadays, aluminium matrix composites (AMCs) are synthesised with various reinforcements such as graphite, aluminium oxide, boron carbide, silicon carbide, titanium carbide and silicon nitrate. A wide range of AMCs is generally manufactured either by solid state or by liquid state process effectively. Among the various manufacturing technologies, stir casting is one of the most advantageous techniques to fabricate composite with isotropic distribution of particles in matrix with satisfactory dimensional accuracy and lightweight components with cost effectiveness.

Ozden et al. [1] studied the impact behaviour of Al reinforced with SiC under different temperature conditions. Particle clustering, particle cracking and weak interface bonding affect the impact behaviour of composites. Ozben et al. [2] investigated the mechanical and machinability properties for various SiC particle reinforcement ratios of composites. Tensile strength, density and hardness of AMC material were found to be increased while decreasing the impact toughness. Singla et al. [3] related with various weight percentages of aluminium combination with SiC particulates from 5 to 30 by utilising a two-stage blending strategy for stir casting system and investigated that enhancement in weight fraction of SiC improved the hardness and impact strength. Park et al. [4] explored the impact of Al_2O_3 in aluminium reinforced with 5–30% volume fraction. They established that the increase in volume fraction of Al_2O_3 results in a decrease of the fracture toughness of the MMC which is attributed to the decrease in space between microvoids nucleated during processing. Sujan et al. [5] studied the physical and mechanical properties, namely low coefficient of thermal expansion (as low as $4.6 \times 10^{-6}/^\circ\text{C}$), high ultimate tensile strength (up to 23.68%), high hardness and impact strength were achieved through stir cast SiC and Al_2O_3 reinforced metal matrix composite material. Miyajima and Iwai [6] investigated the AMCs fabricated by powder metallurgy technique for their mechanical properties. They comprehend the influence of Al_2O_3 fibre, SiC particulates and whisker. Ling et al. [7] assessed the mechanical properties and porosity in AMC strengthened with SiC fabricated by the powder metallurgy technique. He also illustrated the existence of a solid evidence on the effects of percentage of volume and various classes of reinforcement. It additionally showed that the mechanical properties of AMCs were remarkably affected by reinforcement particles. Further, Karnezis et al. [8] and Suresh Babu and Jeyabalan [9, 10] stated that in Al/SiC or Al/ Al_2O_3 composites with a maximum of 10% reinforcement bringing about the uniform distribution of reinforcement within the matrix was the main influence which affect the final structure and reliability of composite material. The composite materials have the potential to be applied as low density and lightweight materials in automotive parts. Exper-

imentally, it is found that lower wear rate is achieved with the addition of Al–SiC reinforcement particles, as compared to Al–Al₂O₃ composites.

From the literature review, it is found that extensive research work is carried out on pure aluminium and aluminium alloy with various reinforcements. Only very few works are carried out on aluminium alloy 2014 metal matrix composites to study the effect of reinforcement particles on mechanical properties like tensile strength, yield strength, percentage of elongation and hardness. As there is a need for detailed study, the different weight fractions of silicon carbide (SiC), Aluminium oxide (Al₂O₃) and both particulates (SiC and Al₂O₃) added to aluminium 2014 matrix are considered to fabricate the binary composites and hybrid aluminium metal matrix composites.

2 Experimental Procedure

2.1 Materials

Aluminium 2014 is used as matrix material with reinforcements of aluminium oxide and silicon carbide. The Composition of Al2014 alloy is presented in Table 1.

2.2 Fabrication

Among the variety of manufacturing processes achievable for aluminium matrix composites, the stir casting process is generally acknowledged as a particular promising route, currently practiced commercially. Aluminium Alloy 2014 is melted at 850 °C in a graphite crucible using resistance furnace. The melt was agitated with the help of stirrer to form a fine vortex. At the temperature of 800 °C, aluminium oxide particles and silicon carbide particles were added individually and combined into the vortex with mechanical stirring at 350 rpm for 7 min. The cover flux (40%KCl + 45%NaCl + 10%NaF) is added during the process to reduce the atmospheric contamination. The molten metal at a temperature of 850 °C was then poured into the mould and allowed to solidify. The composites were prepared as detailed in Table 2.

Table 1 Composition of Al2014 alloy

Al	Cr%	Cu%	Mg%	Mn%	Si%	Ti%	Ti + Zn%	Zn%	Fe%
Remaining	0.1	3.9–5	0.2–0.8	0.4–1.2	0.5–1.2	0.15	0.2	0.25	0.7

Table 2 Weight% of specimens

Specimen code	Aluminium2014 (%)	Aluminium oxide	Silicon carbide
S_0	100	–	–
S_1	95	–	5%
S_2	95	5%	–
S_3	90	5%	5%

3 Testing

The tensile specimens were prepared as per ASTM E8M standard. The ultimate tensile stress was estimated using computerised mini-axial tensile testing machine. The micro-hardness of the specimen was measured at different locations using Zwick Vickers hardness tester at a load of 0.5 kgf for 10 s.

4 Results and Discussion

The tensile and yield strengths of binary and hybrid Al2014 composites are shown in Table 3. The tests were conducted for homogeneous Al2014 alloy specimen (S_0), two binary specimens (S_1 and S_2) and hybrid specimen (S_3). The specimen (S_3) is having higher tensile and yield strength than that of S_0 , S_1 , and S_2 specimens. However, with the same percentage, but different reinforcements, the specimen (S_2) has a marginally higher strength than that of the specimen (S_1). The tensile and yield strength values are plotted in Fig. 1.

Table 3 Tensile and yield strengths binary and hybrid Al2014 composites

Test	S_0	S_1	S_2	S_3
Tensile strength (MPa)	62.15	149	191.65	240.67
Yield strength (MPa)	56.43	114.93	157	182.93

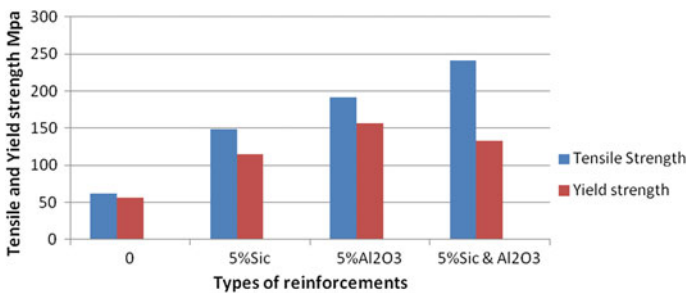


Fig. 1 Tensile and yield strengths of binary and hybrid Al2014 composites

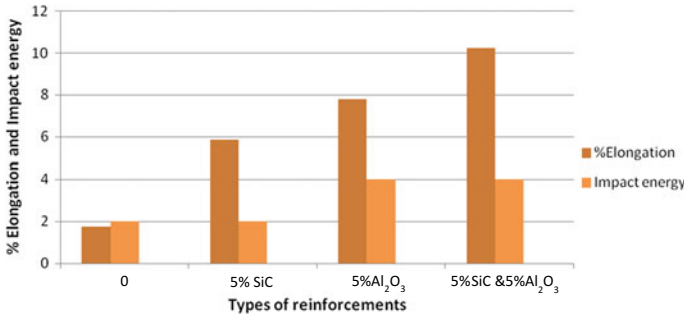


Fig. 2 Percentage elongation and impact energy of binary and hybrid Al2014 composites

Table 4 Hardness of binary and hybrid Al2014 composites

Specimen	S ₀	S ₁	S ₂	S ₃
Hardness (HV)	82	104	108	116

The percentage elongation and impact energy results are presented in Fig. 2. The percentage elongation of the specimens is marginally increased for all specimens. However, with the same percentage, but different reinforcements, the specimen S₁ (5.88%) has a lower percentage elongation than that of the specimen S₂ (7.8%). The impact energy of specimens S₂ and S₃ (4J) is the same, which is greater than that of the specimens S₀ and S₁. The specimens S₀ and S₁ (2J) are also having same impact energy.

The hardness test results are shown in Table 4. The hardness of specimen is increasing gradually for all specimens. However, with the same percentage, but different reinforcements, specimen (S₂) has marginally greater hardness than (S₁).

The morphological analysis was done using SEM. The specimens were cut and prepared according to standard metallographic procedure. The specimens were polished using grit paper (600–1000 mesh) and velvet cloth followed by etching using Keller’s reagent (HNO₃ + HCl + HF). Then, microstructure was observed after drying and the SEM images of composite prepared by adding 5% SiC particulates, 5% Al₂O₃ particulates and 5% SiC and 5% Al₂O₃ are presented in Fig. 3a–c. Figure 3a shows an SEM image of Al2014 alloy with 5% SiC. The microstructure of the 5% SiC composite reveals that irregularly shaped and randomly dispersed silicon carbide particles in the Al2014 alloy matrix. Clustering of the particles was also observed, resulting in the formation of a particle-rich region surrounded by particle-depleted region, making the distribution of SiC particles in the matrix non-uniform. The accumulation of SiC particles may be harmful to the mechanical properties.

Figure 3b shows Al2014 alloy with 5% Al₂O₃. It is observed that the addition of aluminium oxide particles improves the tensile and yield strength. The aluminium oxide particles refine the grain size of aluminium-casting composites by nucleating small grains and hence increase the amount of grain boundary during the solidification process. Figure 3c shows the SEM image of Al2014 alloy with 5% SiC and 5% Al₂O₃.

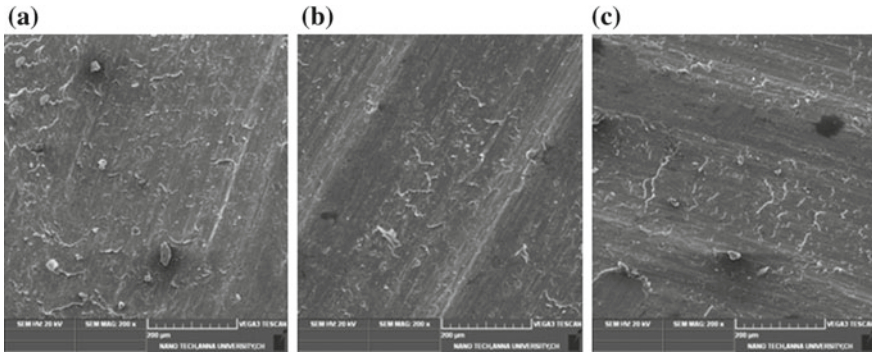


Fig. 3 SEM images **a** Al2014 alloy + 5% SiC **b** Al2014 alloy + 5% Al₂O₃ **c** Al2014 alloy + 5% SiC +5% Al₂O₃

It is understood that the addition of both reinforcements (SiC and Al₂O₃) in the homogeneous Al2014 alloy illustrates a notable improvement in the distribution of reinforcements. It also reveals a very strong interface between the Al matrix and reinforcements which improves the mechanical properties due to the absence of crack and pores throughout the matrix.

5 Conclusion

The homogeneous Al2014 is reinforced with different reinforcements such as SiC, Al₂O₃ and both which improves the mechanical properties. The strength of the composite is increased for all the reinforcements. The tensile and yield strength of aluminium matrix composite was found to be maximum (240.67 and 182.93 MPa, respectively) for the hybrid (5% SiC and 5% Al₂O₃) composites. The maximum percentage of elongation is obtained to be 10, and the maximum impact energy is obtained to be 4J for the hybrid composites. The hardness of the composites increases for all the binary and hybrid composites. The maximum hardness is obtained to be 116 HV for the hybrid composites. Thus, the SEM analysis reveals that the presence of SiC, Al₂O₃ and hybrid (Al₂O₃ and SiC) particles in this composite, and there is a good particulate interface bonding in the hybrid composites than the binary composites because of reasonable distribution of both the reinforcement particles in the metal matrix.

References

1. Ozden S, Ekici R, Nair F (2007) Investigation of impact behavior of aluminium based SiC particle reinforced metal–matrix composites. *Compos Part A* 38(2):484–494
2. Ozben Tamer, Kilickap Erol, Cakir Orhan (2008) Investigation of mechanical and machinability properties of SiC particle reinforced Al-MMC. *Mater Process Technol* 198(1–3):220–225
3. Singla M, Dwivedi DD, Singh L, Chawla V (2009) Development of aluminium based silicon carbide particulate metal matrix composite. *J Miner Mater Charact Eng* 8:455–467
4. Park BG, Crosky AG, Hellier AK (2008) Fracture toughness of microsphere Al₂O₃–Al particulate metal matrix composites. *Compos Part B* 39(7–8):1270–1279
5. Sujan D, Oo Z, Rahman ME, Maleque MA, Tan CK (2012) Physio-mechanical properties of Aluminium metal matrix composites reinforced with Al₂O₃ and SiC. *Int J Eng Appl Sci* 6:288–291
6. Miyajima T, Iwai Y (2003) Effects of reinforcements on sliding wear behavior of aluminium matrix composites. *Wear* 255(1–6):606–616
7. Ling CP, Bush MB, Perera DS (1995) The effect of fabrication techniques on the properties of Al–SiC composites. *J Mater Process Technol* 48:325–331
8. Karnezis PA, Durrant G, Cantor B (1998) Characterization of reinforcement distribution in cast Al–Alloy/SiCp composites—effect of particle type and size on mechanical properties. *Mater Charact* 40:97–109
9. Suresh Babu A, Jayabalan V (2009) Weibull probability model for fracture strength of aluminium (1101)-alumina particle reinforced metal matrix composite. *J Mater Sci Technol* 25(3):341–343
10. Suresh Babu A, Jayabalan V (2010) Statistical analysis of the fracture strengths of aluminum alloy-alumina (AlO) particulate composites. *J Mater Sci* 45(24):6586–6592

Study of Forces, Surface Finish, and Tool Life on Machining of Inconel 718



K. Venkatesan, S. Devendiran, Biplav Bijoy Goswami, Prafful Kumar and Shakya Rishabh Singh Tejpalsinng

Abstract Inconel 718 is a family of nickel-based superalloy. Dry experiments are carried out based on L_{16} orthogonal array using advanced coated cutting tool. The factor effects on turning forces, surface roughness, and flank wear are studied using response surface 3D plots. It reveals that higher cutting speed, low feed rate along cutting depth resulted in lower cutting force and surface roughness but low cutting speed for tool wear. Using desirability function approach, the optimal parameter is determined as feed rate of 0.1 mm/rev, cutting speed of 70 m/min, and 0.5 mm depth of cut. Using SEM, abrasive wear along with welding of workpiece material is found on the wedge of cutting insert. At the end of tool life, the obtained surface is about 0.479 μm at 4 min.

Keywords Turning responses · Carbide inserts · Dry machining

1 Introduction

Superalloys are well matched for high-temperature environments. About 50% of the gas-turbine engine components in aerospace industries are made up of superalloys [1]. Inconel 718, a nickel–chromium-based superalloy, is noticed as difficult machine materials due to its superior characteristics [2]. In manufacturing sector, superalloys are particularly found to be more due to their supreme properties at high temperature that of titanium alloys [3]. In spite of these advantages associated with Inconel 718, it is very important to select the appropriate machining parameters in order to combat this problem. Surface quality gets deteriorated on continuous use of same tool at high speed due to rapid tool wear rate while conducting trials with cutting speed varies as follows 60, 90, 190, and 255 m/min using CVD tool [4]. On the other hand, use of solid lubricant on turning Inconel 718 increases in tool life by 17 and 4% by oil mixed with graphite than oil mixed MoS_2 and pure oil at speed (50 m/min),

K. Venkatesan (✉) · S. Devendiran · B. B. Goswami · P. Kumar · S. Rishabh Singh Tejpalsinng
School of Mechanical Engineering, Vellore Institute of Technology, Vellore, India
e-mail: venkatesan.kannan@vit.ac.in

feed (0.1 mm/rev), and turning depth (0.5 mm) [5]. The tensile residual stresses found to decline for lesser and higher magnitude of tool wear; whereas compressive residual stress increases with the tool wear under the tested trials with uncoated tool [6]. The author emphasized PCBN tool with lower CBN content and its TiN-based ceramic binder high-speed machining of alloy 718 shows outstanding wear resistance at operating speed of 300 m/min [7]. PCBN tool produces compressive stress at 200 m/min that tensile stress produced with ceramic tool on turning of alloy 718 in the subsurface region [8]. The wear mechanisms of CBN tool in high-speed machining of Inconel 718 at speed ranges from 20 to 300 m/min were studied. The smoothening of tool surface (rake face) is effective in reducing wear and increasing tool life [9]. On the other side, CBN with textured tool increases the tool life and suppresses the cutting edge chipping at operating speed of 300 m/min on turning of 718 alloy [10]. Cryogenic machining produces less tensile stresses on the surface/subsurface of turned workpiece than that of dry machining on turning of Inconel 718 are studied [11]. The productivity-dependend surface integrity characteristic has investigated on turning of Inconel 718 and concluded that water vapor machining increases the product sustainability index of 82.92% at medium material removal rate that of dry, flood coolant [12]. A study reveals that PVD-coated tool with smaller nose radius (0.4 mm) at cutting speed (60 m/min), feed rate (0.1 mm/rev), and depth of cut (1 mm) resulted in higher compressive residual stress and lower tensile residual stress [13]. Based on the above fact, CBN, PCBN, and ceramic tool are investigated to note the turning behavior on 718 alloy. Further, it is found that no note is reported on PVD (AlTiN) to determine the current attainable limits toward the optimizing the turning parameters of Inconel 718. In this context, the present study aims to fulfill the objective to study and determine the current attainable optimal factors on turning of 718 alloy with advanced coated tool. At the determined factors, tool life and its wear mechanism are studied.

2 Experimental Section

The current study employs Inconel 718 alloy as workpiece materials with 32 diameter and 300 mm length. The chemical composition of workpart is 51.10% Ni, 20.633% Fe, 18.1% Cr, 4.81% NB + TA, 2.88% Mo, 0.89% Ti, 0.65% Co, 0.41% Al, 0.18% Si, 0.17% Mn, 0.11% Cu, 0.03% C, 0.004% S, 0.003% P [1, 2]. Dry turning test is performed on high-speed lathe. PVD-coated (AlTiN) carbide inserts labeled ISO (KCU 25 CNMG 120408-MP) that is rigidly mounted on a tool holder labeled ISO (PCLNR 2020 K12) are used for turning trials. Each trial in the design matrix of L_{16} orthogonal array is conducted over a length of 20 mm of the workpiece. A fresh tool is used for all the turning trials. During cutting trial, cutting force: F_z is measured with 9257B-type piezoelectric dynamometer.

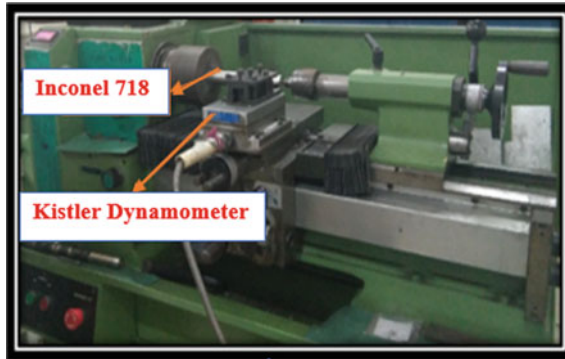


Fig. 1 Experimental steps

Table 1 Cutting parameters and experimental results for PVD inserts

Trial No.	Control factors			Mean response values		
	V_c : cutting velocity m/min	f : feed rate mm/rev	A_p : cutting depth mm	F_z : cutting force (N)	R_a : surface roughness (μm)	V_{ba} : flank wear (μm)
S1	70	0.1	0.3	69.69	0.375	58.32
2	70	0.15	0.4	95.75	0.685	68.93
3	70	0.2	0.5	310.3	1.596	129.11
4	70	0.25	0.6	217	1.550	82.18
5	120	0.1	0.4	89.66	0.690	111.4
6	120	0.15	0.3	93	0.592	124.60
7	120	0.2	0.6	155.1	1.494	76.90
8	120	0.25	0.5	194.9	1.371	123.31
9	170	0.1	0.5	93.82	0.659	92.793
10	170	0.15	0.6	105.9	0.994	150.38
11	170	0.2	0.3	87.21	2.151	129.92
12	170	0.25	0.4	147.4	2.193	133.95
13	220	0.1	0.6	69.97	4.159	133.82
14	220	0.15	0.5	120.6	0.730	60.97
15	220	0.2	0.4	121.8	1.832	103.53
16	220	0.25	0.3	113.4	3.124	90.20

Two values of surface roughness are measured for each trial which is then averaged to get the mean surface roughness value (R_a) with Mahr surf test. The tool wear (V_{ba}) width is measured for each trial using the optical microscope Fig. 1 shows the research methodology adopted for the present study. Table 1 shows the cutting parameters and experimental results obtained based on Taguchi L_{16} parameter design.

3 Results and Discussion

3.1 3D Surface Plots for Cutting Forces

Figure 2 shows the interaction effects of the process parameters with the cutting forces using 3D surface plots at V_c : 145 m/min, F : 0.175 mm/rev, and A_p : 0.45 mm, respectively. It is from plot 1 that a minimum cutting force around 80–110 N is observed for high velocity (150–200 m/min) and low feed rate (0.1 mm/rev). From plot 1 and 2, it is seen that speeding up the velocity decreases the value of cutting force but at higher velocities >200 m/min, it starts to increase slowly. From plot 1, a high cutting force >250 N is obtained for low velocity (60–80 m/min) and high feed rate (0.25 mm/rev). The lowest force of 80–100 N is noticed for a velocity around 170–200 m/min. The maximum force of 200–230 N is observed for depth of cut about 0.45 mm and for low velocity (60–80 m/min). From plot 3, a minimum cutting force around 30–50 N is visible for a low f : 0.1 mm/rev and low a_p : 0.3 mm. With the increment in the feed rate, cutting force increases. It reaches a maximum around 150–180 N for maximum feed rate (0.25 mm/rev). This shows that to reducing cutting force the V_c : 150 m/min, f : 0.1 mm/rev and a_p : 0.3 mm.

3.2 3D Surface Plots for Surface Roughness

Figure 3 in plot 1 shows that up to velocity around 150 m/min, with an escalation in feed surface roughness increases but with higher velocities higher feed rates have better surface finish. A low surface roughness (0.4–0.8 μm) is obtained for low feed rate (0.1 mm/rev) and low velocity (60–80 m/min). And a maximum roughness about 2.5–3 μm is observed for low velocity (60–80 m/min) and high feed (0.25 mm/rev). From plot 2, lowest surface roughness about 0.3–0.8 μm for V_c : 140–180 m/min and a_p : 0.45 mm. It decreases initially with increases in velocity, but later surface finish decreases as velocity goes higher. Similar trend is visible while varying the depth of cut. Highest surface roughness about 2–2.5 μm is obtained for low a_p : 0.3 mm and low velocity (60–80 m/min). It is observed in plot 3 that for lower depth of cut, roughness increased with increment feed. However, decreases when

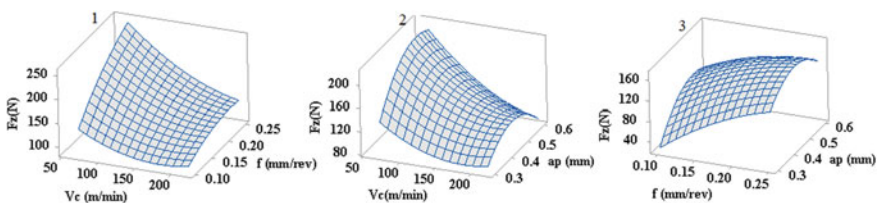


Fig. 2 Response surface plot for cutting force

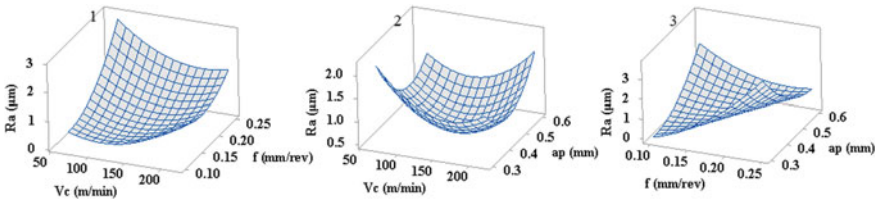


Fig. 3 Response surface plot for surface roughness

turning depth is high (>0.5 mm). Lowest value of roughness is detected for low f : 0.1 mm/rev and low a_p : 0.3 mm. A_{tap} : 0.3 mm and f : 0.25 mm/rev, roughness measured is highest (3.5–4 μm). This shows that to reducing cutting force the V_c : 120 m/min, f : 0.1 mm/rev and a_p : 0.35 mm. The minimum surface roughness obtained by using 16 trials is 0.375 μm .

3.3 3D Surface Plots Tool Wear

It is observed from Fig. 4 in plot 1 that minimum tool wear occurs at low f : 0.1 mm/rev and low V_c : 60–80 m/min. Highest tool wear value about 130–150 μm is noticed for high f : 0.25 mm/min and V_c ranging between 80–160 m/min. From plot 1, it shows that tool wear increases with increasing velocity but decreases after a certain point as velocity value goes higher. From plot 2, minimum tool wear about 60–80 μm is noticed for higher V_c (>200 m/min) and low a_p : 0.3 mm. Plot 3 shows that up to a feed rate around 0.15–0.17 mm/rev, tool wear upsurges with an increment of turning depth. As the feed becomes higher (>0.17 mm/rev), with increasing turning depth tool wear decreases. This shows that to reducing tool wear the V_c : 220 m/min, f : 0.1 mm/rev, and a_p : 0.3 mm. Therefore, the best condition of turning parameters is obtained at f : 0.1 mm/rev, V_c : 70 m/min, and a_p : 0.5 mm using response surface multi-response optimization. At this condition, optimal factor produces $F_z = 58.64$ N, $R_a = 0.37$ μm , and $V_{ba} = 56.82$ μm . At this determined optimized cutting conditions, the tool life and its wear mechanism study have been analyzed.

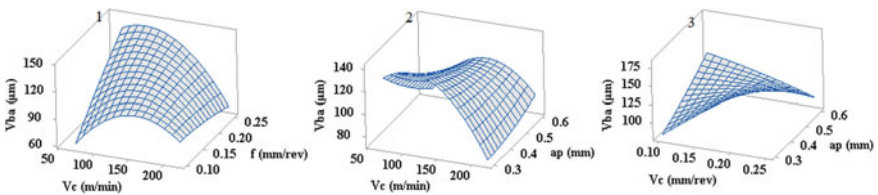


Fig. 4 Response surface plot for tool wear

3.4 Tool Life Study

Figure 5a shows the graph plotted between surface roughness and tool wear obtained at optimal factors. Increase in tool wear at 250 μm , the surface roughness found to decrease and then increased. This attributed to difference in the thermal conductivity of tool (4.92 W/mK) and work material (11.5 W/m K). At 250 μm , the value of $R_a = 0.3242 \mu\text{m}$ is obtained then increased to is 0.479 μm at 332 μm . Compared to Trial 1, at optimal factor, the value of R_a is lessened with dull tool due to the protective layer of Al in TiN structure. From Fig. 5b, the tool wear reached the flank wear criteria (as per of ISO 3685 standards of 300 μm) of 332 μm after 4 min. From optical image of Fig. 6a, abrasive wear (Image 1), adhesion (Image 1 and 2), and chipping (Image 4) are observed as tool wear mechanism. Abrasive is due to frictional rubbing, adhesion is due to high temperature, and mechanical breakage/edge chipping is due to thermo-mechanical shocks on the cutting edge. Similar observations are reported in previous note [13]. Figure 6b shows the SEM image at 4 min. Image 1 of Fig. 6b clearly depicts the crater wear, abrasive or chipping wear at rake face of the tool insert. This mainly due to the friction between the hot chips and the rake surface, which forces or pushes the rake surface and cause the sliding friction. It has been observed that the rake side of the tool insert is more prone to crater wear. The reason for this is the chemical reaction takes place between workpiece and the cutting tool materials. Moreover, the reaction is amplified by the cutting speed. The cutting edges weaken and can lead to fracture with excessive crater wear. Image 3 depicts the constituents of the elements and their atomic and weight percentages of the wear surface of the tool insert. The tool is titanium coated, so there is 4.42% Ti present in the observed surface of the tool insert. Since the tool insert is a carbide tool, which is depicted by constituent of iron, Fe that is 12.81% and carbon, C which is 18.67%. The major constituent of the workpiece, i.e., Inconel 718 rod is Ni (51.1% in the alloy) and Cr (18.1% in the alloy) tends to affect the constituent of the tool insert as well. While machining with the same tool edge for the four trials on the workpiece, Ni constitutes around 29.56 wt% and Cr constitutes around 15.11% in the observed part of the tool insert.

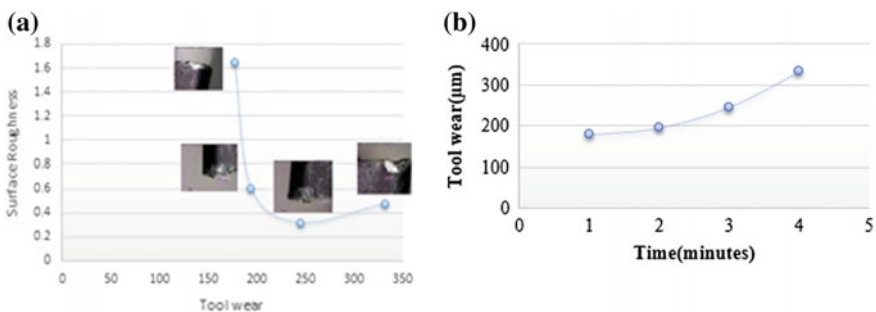


Fig. 5 a Tool wear versus surface roughness, b Tool wear versus time

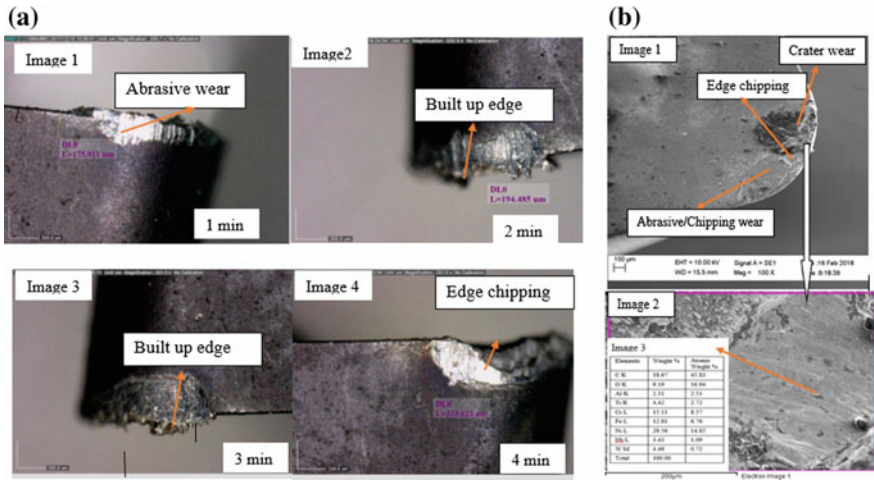


Fig. 6 a Optical micrograph, b SEM micrograph of tool wear at 0.3 mm criteria

4 Conclusion

In this work, the dry turning experiments on 718 alloy using PVD (AlTiN) are conducted based on L_{16} orthogonal array. From surface plots, increase of feed and cutting depth lead to increase the force, roughness, and tool wear while decreases with an increment of feed. At V_c : 70 m/min, f : 0.1 mm/rev, and a_p : 0.4 mm, determined by desirability function analysis, the surface roughness is obtained as 0.3242 μ m at flank wear rate of 250 μ m. Using SEM, crater, abrasive, adhesion, and mechanical breakage are the tool wear mechanisms observed at both flank and rack faces of cutting insert after using the same tool tip for 4 min at optimal parameters. The constituents in the wear region indicate presence of Ni (29.56 wt%) and Cr (15.11 wt%), which gets into the workpiece due to the interaction of workpiece and tool during machining.

References

1. Venkatesan K (2017) The study on force, surface integrity, tool life and chip on laser assisted machining of Inconel 718 using Nd: YAG laser source. J Adv Res 8(4):407–423
2. Venkatesan K, Ramanujam R, Kuppan P (2014) Laser assisted machining of difficult to cut materials: research opportunities and future directions-A comprehensive review. Proc Eng 97:1626–1636
3. Ulutan D, Ozel T (2011) Machining induced surface integrity in titanium and nickel alloys: a review. Int J Mach Tools Manuf 51(3):250–280
4. D’Addona DM, Raykar SJ, Narke MM (2017) High speed machining of Inconel 718: tool wear and surface roughness analysis. Proc CIRP 62:269–274

5. Marques A, Guimarães C, da Silva RB, Fonseca MDPC, Sales WF, Machado ÁR (2016) Surface integrity analysis of Inconel 718 after turning with different solid lubricants dispersed in neat oil delivered by MQL. *Proc Manuf* 5:609–620
6. Madariaga A, Kortabarria A, Hormaetxe E, Garay A, Arrazola PJ (2016) Influence of tool wear on residual stresses when turning Inconel 718. *Proc CIRP* 45:267–270
7. Tanaka H, Sugihara T, Enomoto T (2016) High speed machining of Inconel 718 focusing on wear behaviors of PCBN cutting tool. *Proc CIRP* 46:545–548
8. Zhou J, Bushlya V, Peng RL, Chen Z, Johansson S, Stahl JE (2014) Analysis of subsurface microstructure and residual stresses in machined Inconel 718 with PCBN and Al₂O₃-SiCw tools. *Proc CIRP* 13:150–155
9. Sugihara T, Enomoto T (2015) High speed machining of Inconel 718 focusing on tool surface topography of CBN tool. *Proc Manuf* 1:675–682
10. Sugihara T, Nishimoto Y, Enomoto T (2017) Development of a novel cubic boron nitride cutting tool with a textured flank face for high-speed machining of Inconel 718. *Precision Eng* 48:75–82
11. He ZH, Zhang XM, Ding H (2016) Comparison of residual stresses in cryogenic and dry machining of Inconel 718. *Proc CIRP* 46:19–22
12. Kadam GS, Pawade RS (2017) Surface integrity and sustainability assessment in high-speed machining of Inconel 718—an eco-friendly green approach. *J Cleaner Prod* 147:273–283
13. Niaki FA, Mears L (2017) A comprehensive study on the effects of tool wear on surface roughness, dimensional integrity and residual stress in turning IN718 hard-to-machine alloy. *J Manuf Proc* 30:268–280

Investigations on Corrosion Behaviour of AA 8011-ZrB₂ in Situ Metal Matrix Composites



B. M. Muthamizh Selvan and V. Anandakrishnan

Abstract The composite system of AA 8011-ZrB₂ (0, 4 and 8 wt%) was synthesized by using economical and efficient fabrication method of in situ stir casting technique and the corrosion behaviour was investigated. The fabricated samples were exposed to X-ray diffraction and scanning electron microscope to confirm the existence of ZrB₂ and for the study of the morphology of ZrB₂ particles in aluminium composites, respectively, and also the ZrB₂ particles were clearly located by using energy dispersive spectroscopy. The corrosion behaviour of the synthesized composite system was investigated in NaCl solution and the inclusion of in situ formed ZrB₂ in AA 8011 improved the corrosion resistance, it was evidently proved through scanning electron microscope images.

Keywords Aluminium · Metal matrix composites · In situ stir casting · Corrosion behaviour · Potentiodynamic polarization

1 Introduction

Aluminium matrix composites lead the race among the metal matrix composites in current research and utilization due to its low cost, ease of production and other attractive properties such as high specific strength, high specific stiffness, the low thermal coefficient of expansion, improved tribological and corrosion resistance. Due to such incredible properties, aluminium matrix composites have attracted great scientific attention as the promising candidate which is used in wide range of applications includes recreation, sports, packaging, precision instruments, biotechnology, automotive, aerospace, military, nuclear, electronic thermal management and marine industries [1–4]. In the fabrication of corrosive and cryogenic environment application products like Arctic chemical processing equipment, Moss- and SPB-type tanks

B. M. Muthamizh Selvan (✉) · V. Anandakrishnan
Department of Production Engineering, National Institute of Technology,
Tiruchirappalli 620015, India
e-mail: muthamizh.bm@gmail.com

© Springer Nature Singapore Pte Ltd. 2019
S. S. Hiremath et al. (eds.), *Advances in Manufacturing Technology*,
Lecture Notes in Mechanical Engineering,
https://doi.org/10.1007/978-981-13-6374-0_39

335

(LNG carrier insulation systems), subsea pipelines, pressure vessels and drill pipes (offshore structures) aluminium metal matrix composite play a vital role [5]. Aluminium composites are fabricated through various techniques such as centrifugal casting, squeeze casting, powder metallurgy, stir casting (ex situ) and reactive processing (in situ) [6]. Fabrication of the aluminium metal matrix composites through in situ route provides several advantages such as ease of production, economical, grain refinement, thermodynamic stability, uniform distribution of reinforcements, the excellent bonding strength between matrix and reinforcement. ZrB_2 owns fabulous properties such as high melting temperature, good thermal conductivity, excellent mechanical properties, oxidation resistance, elastic modulus and resistance to chemical attack [7]. In situ formed ZrB_2 was fabricated in aluminium alloy through reaction of K_2ZrF_6 and KBF_4 with molten aluminium alloy. The fine and homogeneous distribution of ZrB_2 particles in aluminium alloy was confirmed through micro-structural studies and due to the incorporation of the in situ ZrB_2 particles, the mechanical properties of the aluminium alloy were amplified [8]. The AA 2618 matrix was reinforced with AlN, Si_3N_4 , and ZrB_2 (0, 2, 4, 6, and 8), and the ZrB_2 has been synthesized in AA 2618 matrix through in situ stir casting technique by mixing K_2ZrF_6 and KBF_4 in molten AA 2618 alloy. Increase in the percentage of ZrB_2 enhanced the corrosion resistance in aluminium composite [9].

From the above literature survey, it is clear that the aluminium matrix composites are used in real-time application which requires corrosion resistance and the addition of reinforcements in aluminium matrix had cemented the route for the enrichment of corrosion resistance. The in situ stir casting technique offers the fine and homogeneous distribution of reinforcements in aluminium matrix economical approach. In this paper, AA 8011- ZrB_2 (0, 4 and 8 wt%) is synthesized through in situ stir casting technique and the synthesized materials are involved in X-ray diffraction and scanning electron microscope (SEM) to study the presence and distribution of the ZrB_2 particles. Corrosion behaviour of the samples was investigated through the potentiodynamic polarization technique.

2 Experimental Procedure

2.1 Fabrication of Materials

AA 8011 was tested to confirm the material compositions as per the ASTM-B-209 M, given in Table 1. The composite system of AA 8011- ZrB_2 (0, 4 and 8 wt%) was fabricated by using an in situ stir casting technique. AA 8011 rods were heated in the graphite crucible at the temperature of 860° . Stoichiometrically, calculated halide salts (K_2ZrF_6 and KBF_4) as given in Table 2 were added to the molten form of aluminium which was preheated at the temperature of $250^\circ C$ for the removal of moisture. Stirring was carried out for every 5 min by using graphite rod to distribute the halide salts homogeneously and the time allowed for completion of the reaction is

Table 1 Chemical composition of AA 8011 alloy (%)

Si	Fe	Cu	Mn	Mg	Cr	Zn	Ti	Al
0.6	0.7	0.25	0.15	0.9	0.2	0.25	0.15	Remaining

Table 2 Quantity of halide salts added for obtaining various compositions of materials

Salts in gm	AA 8011-0 wt% ZrB ₂	AA 8011-4 wt% ZrB ₂	AA 8011-8 wt% ZrB ₂
K ₂ ZrF ₆	0	100.45	200.91
KBF ₄	0	89.25	178.51

30 min. During these processes, exothermic reactions take place between the halide salts and aluminium matrix is shown (1), (2) and (3)



After the completion of the in situ reaction, elements other than ZrB₂ were evaporated or removed as slag and the process parameters were decided through literature reviews of [8].

2.2 Corrosion Study

The electrochemical corrosion behaviour of AA 8011-ZrB₂ (0, 4 and 8 wt%) was investigated by potentiodynamic polarization (PDP) technique in 3 wt% of sodium chloride solution using IVIUM electrochemical workstation with the three electrode system. The calomel electrode as reference, graphite as counter electrode and the sample under test acted as the working electrode. The PDP curves were obtained in the potential range of -500 to +500 mV with reference to OCP with the scan rate of 1 mV/s. The Tafel extrapolation was used to calculate the E-Corr and i-Corr values from the PDP curves which is helpful to evaluate the corrosion resistance of the synthesized aluminium materials.

3 Results and Discussion

3.1 X-Ray Diffraction (XRD) Analysis

Figure 1 shows the X-ray diffractogram of AA 8011-0 wt% ZrB_2 , AA 8011-4 wt% ZrB_2 and AA 8011-8 wt% ZrB_2 which were performed in RINGKU X-ray diffraction machine. The peak intensities of (002), (022), (113) aluminium rise with the increasing addition of ZrB_2 . This denotes that ZrB_2 acts as a pinning particle to arrest the grain growth of aluminium which leads to smaller crystallite size. The ZrB_2 appears at the vicinity of 2θ positions (24.99), (32.39), (41.45), (73.90) which confirms the presence of reinforced ZrB_2 .

3.2 Micro-Structural Analysis

The microstructure of the fabricated composite system was studied through HITACHI SU 3000 SEM machine and the SEM images are shown in Fig. 2a–e. Figure 2a clearly indicates the absence of ZrB_2 particles along the grain boundaries, but the presence of ZrB_2 along the grain boundaries of the aluminium matrix is observed in Fig. 2b–c some particles were observed along the grain boundaries of AA 8011-4 wt% ZrB_2 and AA 8011-8 wt% ZrB_2 . The magnified SEM image of the particles of Fig. 2c was

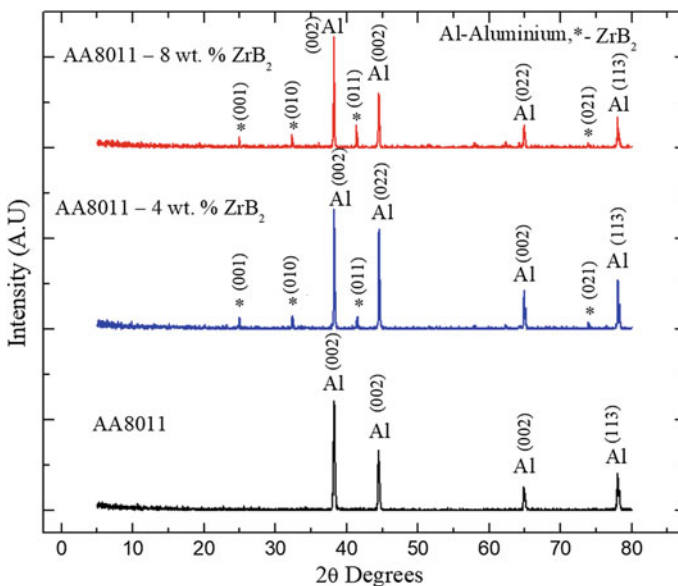


Fig. 1 X-Ray diffraction results of as casted AA-8011 and composites

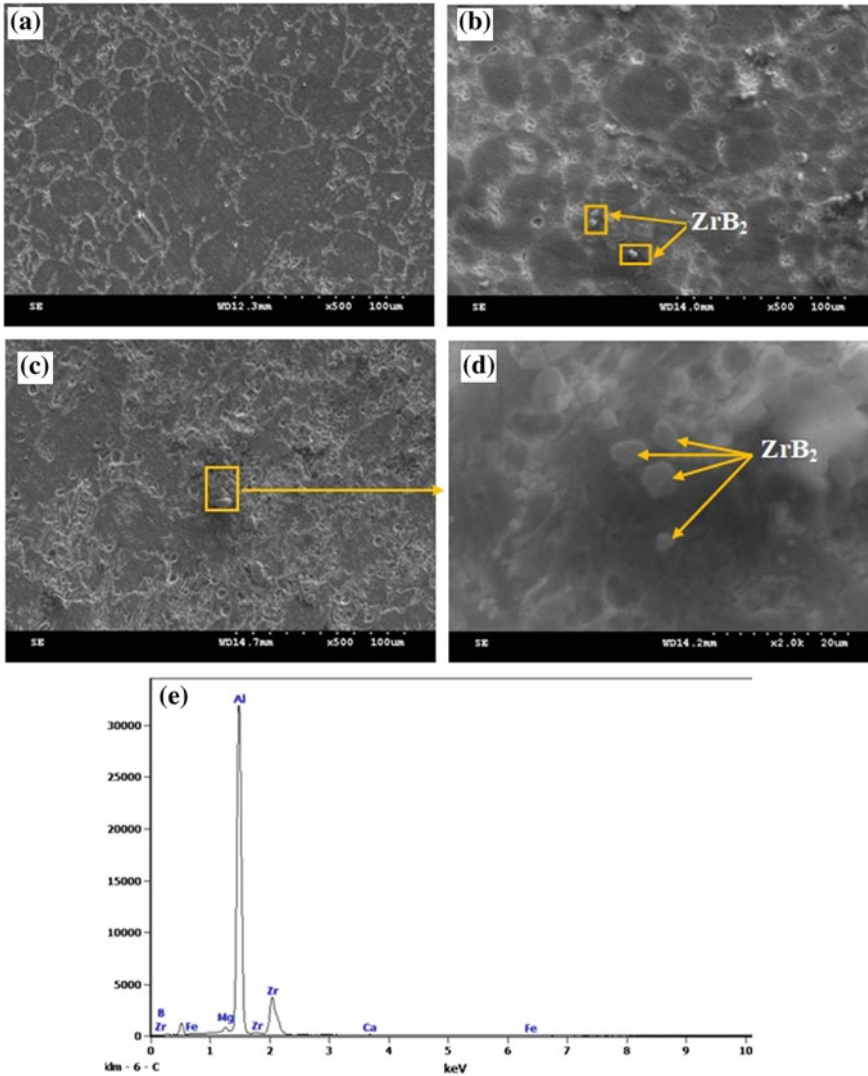


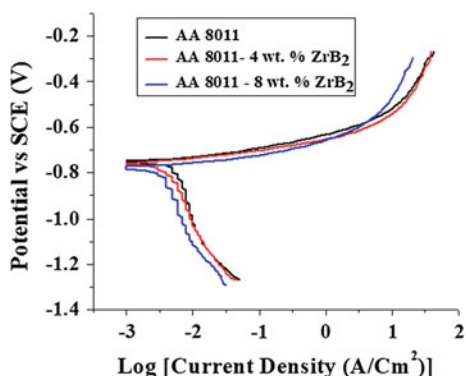
Fig. 2 SEM images of **a** AA8011, **b** AA8011- 4 wt% ZrB₂, **c** AA8011-8 wt% ZrB₂, **d** magnified SEM image of ZrB₂, **e** energy dispersive spectroscopy of Fig. 2d

captured and the magnified view is shown in Fig. 2d which evidently proved as ZrB₂ particles by the spectrum (Fig. 2e) and it shows the peaks of Al, Zr and B which were obtained from energy dispersive can be observed clearly and their percentages are given in Table 3. The distribution of the ZrB₂ is uniform and homogeneous along the grain boundaries of aluminium matrix and both AA 8011-4 wt% ZrB₂ and AA 8011-8 wt% ZrB₂ which is evidently visible Fig. 2b–c. The uniform distribution of the ceramic particles in aluminium matrix is significantly influenced by the density

Table 3 Elemental analysis of energy dispersive spectroscopy

Element	Weight (%)	Atomic (%)
Al K	73.85	90.09
Zr L	25.67	9.26
Mg K	0.48	0.64
Total	100.00	100.00

Fig. 3 Potentiodynamic polarization curves of the samples, **a** AA8011-0 wt% ZrB₂, **b** AA8011-4 wt% ZrB₂ and **c** AA8011-8 wt% ZrB₂



difference between the ceramic particles and aluminium particles. When the density difference between the ceramic particle and aluminium matrix is greater than 2 g/cm^3 during solidification, this makes ceramic particles to sink easily in molten aluminium and to be suspended for a long time. The density difference between the molten AA 8011 matrix and in situ formed ZrB₂ is more than 2 g/cm^3 which paves the way for the uniform distribution of ZrB₂ along the grain boundaries. Also, the wetting property between the ceramic particles and molten aluminium matrix arrests the movement of ZrB₂ particles which leading to the long-time suspension of ZrB₂ particles in molten aluminium matrix during solidification for better distribution of ceramic particles [10].

3.3 Electrochemical Studies

3.3.1 Potentiodynamic Polarization

The corrosion behaviour was studied by potentiodynamic polarization (PDP) test conducted by exposing the surface area of 0.5 mm^2 in sodium chloride solution. The PDP curves for aluminium samples are shown in Fig. 3a–c it clearly says that the curve is shifting right side to left side with the addition in the percentage of

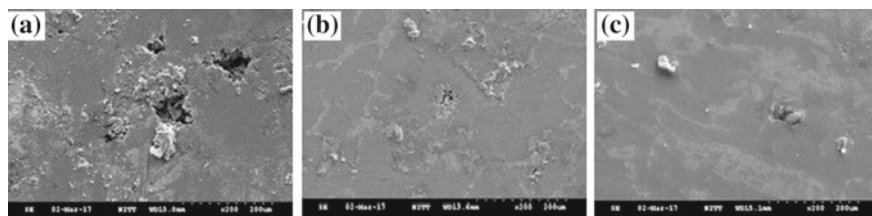


Fig. 4 SEM image of corroded surfaces of AA8011 matrix composites with ZrB₂ reinforcement, **a** 0 wt%, **b** 4 wt%, and **c** 8 wt%

Table 4 Experimental results obtained from potentiodynamic polarization curves

Name of the material	E-Corr (V)	i-Corr (A)	Corrosion rate (mm/year)
AA8011-0 wt% ZrB ₂	-0.7505	2.15×10^{-7}	1.1560
AA8011-4 wt% ZrB ₂	-0.7594	1.73×10^{-7}	0.9304
AA8011-8 wt% ZrB ₂	-0.7746	1.61×10^{-7}	0.8672

reinforcement and this demonstrates the decrement in i-corr value. The corrosion current density or i-Corr values reveal the flow of current in open circuit potential as a result of the reduction reaction. The i-Corr values are inversely proportional to the corrosion resistance. Corrosion potential (E-Corr) values demonstrate the ionization tendency of a material in NaCl solution [11, 12]. The E-Corr and i-Corr values are tabulated in Table 4 which undoubtedly establishes that the increase in the percentage of ZrB₂ is inversely proportional to the i-corr value. Also, the corrosion rate in AA 8011 alloy is reduced from 1.156 to 0.8672 by reinforcing it with the ceramic of ZrB₂ is evident that addition of ZrB₂ will enhance the corrosion resistance [9]. Because the ZrB₂ possess the excellent chemical inertness which provides excellent resistance to chemical attack, oxidation and corrosion [8].

Figure 1 confirms the presence of ZrB₂ and the SEM images that were captured as shown in Fig. 2b–c that the reinforcement is unvaryingly distributed along the grain of AA 8011 alloy which is essential for improving corrosion resistance. The SEM images that captured in the corrosion surfaces are shown in Fig. 4a–c supports the previous statement depicts that addition of ZrB₂ in aluminium alloy has clearly arrested the corrosion. Figure 4a displays that AA 8011 had been severely corroded in the NaCl solution but Fig. 4b–c reveals that AA 8011-4 wt% ZrB₂ and AA 8011-8 wt% ZrB₂ had shown resistance to corrosion in NaCl solution.

4 Conclusion

1. The AA 8011-ZrB₂ (0, 4 and 8 wt%) was successfully fabricated through in situ stir casting technique.

2. Corrosion behaviour of fabricated aluminium samples AA 8011-ZrB₂ (0, 4 and 8 wt%) was investigated in sodium chloride environment and evaluated by using potentiodynamic polarization technique with reference to open circuit potential by using three electrochemical cell system.
3. The presence of ZrB₂ was confirmed by XRD analysis and energy dispersive spectroscopy.
4. The homogeneous distribution of ZrB₂ along the grain boundaries of aluminium was confirmed through SEM images.
5. The corrosion resistance was improved in AA 8011 by the inclusion of ZrB₂ and the AA8011-8 wt% ZrB₂ exhibits the superiority in corrosion resistance.

References

1. Oladijo OP, Bodunrin MO, Sobiyi K, Maledi NB, Alaneme KK (2016) Investigating the self-healing behaviour of under-aged and 60Sn–40Pb alloy reinforced aluminium hybrid composites. *Thin Solid Films* 620:201–205
2. Kaushik NC, Rao RN (2016) Effect of grit size on two body abrasive wear of Al 6082 hybrid composites produced by stir casting method. *Tribol Int* 102:52–60
3. Natarajan N, Vijayarangan S, Rajendran I (2006) Wear behaviour of A356/25SiCp aluminium matrix composites sliding against automobile friction material. *Wear* 261(7–8):812–822
4. Kumar S, Panwar RS, Pandey OP (2013) Effect of dual reinforced ceramic particles on high temperature tribological properties of aluminum composites. *Ceram Int* 39(6):6333–6342
5. Kumar PSR, Smart DR, Alexis SJ (2017) Corrosion behaviour of aluminium metal matrix reinforced with multi-wall carbon nanotube. *J Asian Ceram Soc* 5(1):71–75
6. Baskaran S, Anandakrishnan V, Duraiselvam M (2014) Investigations on dry sliding wear behavior of in situ casted AA7075–TiC metal matrix composites by using Taguchi technique. *Mater Des* 60:184–192
7. Gaurav G, Anitha M (2015) Effect of ZrB₂ particles on the microstructure and mechanical properties of hybrid (ZrB₂+Al₃Zr)/AA5052 insitucomposites. *J Alloy Compd* 649:174–183
8. Kumar N, Gautam RK, Mohan S (2015) In-situ development of ZrB₂ particles and their effect on microstructure and mechanical properties of AA5052 metal-matrix composites. *Mater Des* 80:129–136
9. Kumar NM, Kumaran SS, Kumaraswamidhas LA (2015) An investigation of mechanical properties and corrosion resistance of Al2618 alloy reinforced with Si₃N₄, AlN and ZrB₂ composites. *J Alloy Compd* 652:244–249
10. Dinaharan I, Murugan N, Parameswaran S (2011) Influence of in situ formed ZrB₂ particles on microstructure and mechanical properties of AA6061 metal matrix composites. *Mater Sci Eng, A* 528(18):5733–5740
11. Sathiyar P, Ramesh T (2017) Experimental investigation and characterization of laser welded NiTiInol shape memory alloys. *J Manufact Process* 25:253–261
12. Kannan TDB, Ramesh T, Sathiyar P (2016) A review of similar and dissimilar micro-joining of nitinol. *JOM* 68(4):1227–1245

Introducing Various Image Processing Techniques to Improve Topology Optimization Process to Develop Compliant Mechanism-Based Microgripper



S. P. Banu Murthy, R. Bharanidaran, T. Ramesh and S. Renoldelsen

Abstract In recent development in engineering, researchers and scientists are more interested in precision manufacturing, assembly and manipulation of small parts. For manipulation and assembly of small parts, microgripper is the key component to handle micro-sized objects with precision at the micron level. The design of microgripper is required to consider many aspects of microphysics. Microgripper is functionally divided into two divisions such as mechanism part and gripping jaw segment. This research paper mainly focuses on devising the mechanism segment of a microgripper which basically transfers the motion in precise and controlled manner and is generally complicated to design. Topology optimization is utilized to design a compliant mechanism for a microgripper since it is the best choice for microlevel actuators. Topological optimized design is required for performing post-processing and removing the staircase effect and node-to-node connectivity developed during design. Various filtering and interpolation methods are adopted to minimize the limitations of topology optimization and also to generate mesh independence and perfect boundary. Finite element method (FEM) is used to analyze the microgripper developed through topology optimization technique, and the results are compared with a rigid body model which is equivalent of the mechanism. Graphical position analysis is also carried out to find the output displacement of an equivalent rigid body model of microgripper mechanism.

Keywords FEM · Filtering · GPA · Interpolation · Microgripper · Topology optimization

S. P. Banu Murthy · R. Bharanidaran (✉) · S. Renoldelsen
Vellore Institute of Technology, Vellore, India
e-mail: bharanidaran123@gmail.com

T. Ramesh
National Institute of Technology, Trichy, India

© Springer Nature Singapore Pte Ltd. 2019
S. S. Hiremath et al. (eds.), *Advances in Manufacturing Technology*,
Lecture Notes in Mechanical Engineering,
https://doi.org/10.1007/978-981-13-6374-0_40

1 Introduction

Manipulating precision of micro-sized objects is assured in the engineering such as assembly of micro-objects, drug delivery, electronic applications, optical measures, microrobotics, manipulation of tissues and surgeries which are minimally invasive [1–5]. Components such as microgrippers are essential to manipulate microparts precisely. The microgripping device which is used for holding the micro-objects has two jaws to transfer the motion from the actuator. Two divisions of the microgripping structure are important to manipulate micro-object precisely [6]. Mechanism design is the most significant part in microgripping system and to actuate the jaws of the gripper input force which is essential is transferred precisely. Conventional joints found in mechanism designs cannot be used in avoiding errors which are related to assembly and manufacturing and to reduce friction and wear to confirm the precision motion between the assembled components. The friction and wear and error factors demand the designer to design an appropriate mechanism which is joint-less in structure and is named monolithic design. Various procedural approaches are involved in designing a mechanism which is compliant such as synthesis of mechanisms [7, 8], pseudo-rigid body model [9] and optimization technique [10]. The most common and competent technique among the above approaches is structural optimization which has been with its results. Finite element method-based topology optimization has received more attention and is found to be more efficient. The power law model [10] is used in solid isotropic material with penalization (SIMP), in which the design variation is assumed as material density. The power law approach has been accepted extensively because of its computational efficiency and conceptual simplicity; however, the SIMP method has restrictions that it cannot solve nonexistence of solutions and thus it leads to numerical instabilities in solution. Checkerboard pattern, dependency of mesh and local minima are the most important numerical instabilities. Filtering technique was recommended by Sigmund [11, 12] to resolve the problem of checkerboard pattern. Filtering is one of the image processing techniques to improve the image quality and to remove the noise [15, 16]. Filtering the sensitivity of the design variations also provides a mesh-dependent solution.

2 Design of Compliant Mechanism

Designing a microgripper with controlled and precision motion demands a compliant-based monolithic structure to overcome the limitations of conventional joints such as wear, friction between the parts and assembly error. The most efficient and logical technique which is recommended to design a mechanism of compliant structure is topology optimization.

Post-processing of optimized topology in the perspective of manufacturing is done for the final design of the microgripper [13]. To minimize the effect of post-processing, various interpolation and filtering methods are used. The compliant

model microgripper has gripping force and geometrical advantage (GA) as key parameters, and the influence of these parameters in the design is studied according to variation of critical parameters in flexure design.

2.1 Topology Optimization

The efficient and logical method to obtain conceptual design of compliant mechanism is topology optimization. Initial domain derivation in this method is shown in Fig. 1 [14]. In this research work, objective function of optimization problem is to maximize the mutual potential energy (MPE) of the mechanism. Young’s modulus ‘ E_0 ’ is assumed as 1 and uses penalization ‘ p ’ to make intermediate densities ‘ ρ ’ in SIMP method.

$$E_i = \rho_i^p E_0 \tag{1}$$

forces exerted by Jaws of the gripper f_{1out} and f_{2out} during application of f_{in} at input port.

Optimization problem formulation and the objective function of the topology are given in Eq. (2).

$$\begin{aligned} \text{Maximize : } & -\text{MPE} = U_1^T K U_2 = \sum_{e=1}^N (x_e)^p (u_{e2}^T k_0 u_{e1} - u_{e3}^T k_0 u_{e1}) \\ \text{Subject to : } & V(x)/V_0 = f \\ & : KU = F \\ & : 0 < x_{\min} \leq x \leq 1 \end{aligned} \tag{2}$$

where U is the global displacement vector (global); F is the force vector (global); K is the stiffness matrix (global); u_{e1} is the displacement vector of element due to input

Fig. 1 Initial domain [14]



port; k_e is the stiffness matrix (element); u_{e2} is the displacement vector (element) due to f_{1out} output port; u_{e3} is the displacement vector (element) due to f_{2out} output port; x -vector (design variables); x_{min} is the relative density (minimum) (to avoid singularity nonzero value has been assumed in MATLAB program); N is the element number; p is the power of penalization (typically $p = 3$); $V(x)$ is the volume of material; V_0 is the volume of design domain; and F is the volume fraction (volfrac).

Objective function of sensitivity is represented in Eq. (3)

$$\frac{\partial u_{out}}{\partial x_e} = -p(x_e)^{p-1}(u_{e2}^T k_0 u_{e1}) + p(x_e)^{p-1}(u_{e3}^T k_0 u_{e1}) \tag{3}$$

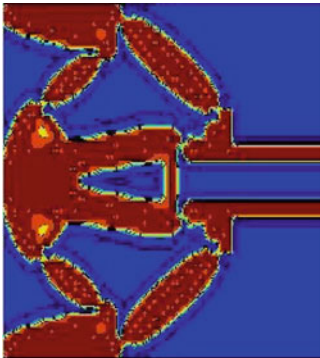
Equation for mesh-independency filter by changing the element sensitivities is given in (4)

$$\frac{\hat{\partial}c}{\partial x_e} = \frac{1}{x_e \sum_{f=1}^N \hat{H}_f} \sum_{f=1}^N \hat{H}_f x_f \frac{\partial c}{\partial x_f} \tag{4}$$

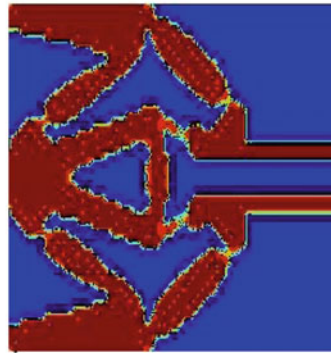
Weight factor of convolution operator is given in Eq. (5)

$$\hat{H}_f = r_{min} - \text{dist}(e, f), \{f \in N | \text{dist}(e, f) \leq r_{min}\}, \text{ where } e = 1, \dots, \tag{5}$$

where $\text{dist}(e, f)$ is the distance between the element centers ('e', 'f').



Cubic Interpolation



Gaussian Filter

3 Structural Analysis

Figure 2 shows the von Mises stresses induced at various reaction forces.

Various input displacements from 2 to 5 μm are applied to calculate the output displacement. For the maximum input displacement of 1.6 μm applied for this design, the stress developed in the hinges is found to be 168 MPa which is below the yield limit. Theory of Gerber is used in calculation of fatigue life.

Where S_{ca} = stresses due to correction of alternating (based on zero mean) and S_y = yield stresses (Fig. 3)

$$S_{ca} = \frac{S_a}{1 - \left(\frac{S_{mean}}{S_u}\right)^2} \tag{6}$$

S_u = ultimate strength, S_a = stress due to alternating = $(S_{max} - S_{min})/2$, S_{mean} = mean stress = $(S_{max} + S_{min})/2$.

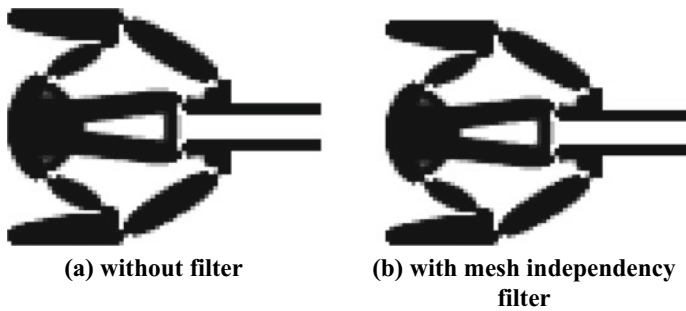


Fig. 2 Topology optimized mechanism design

Fig. 3 Von Mises stresses induced at various reaction forces

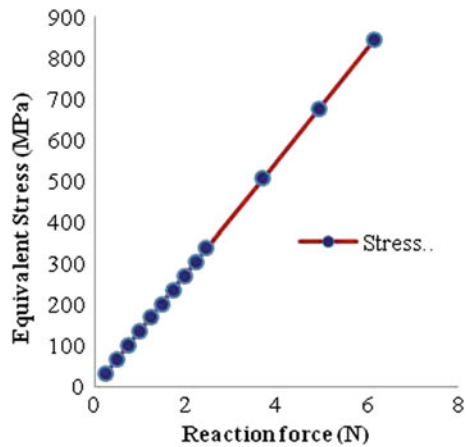


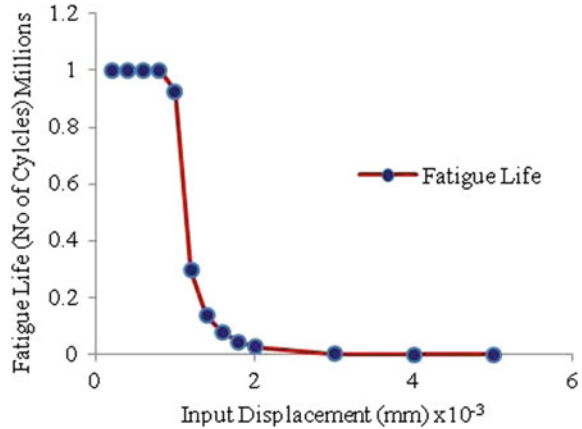
Fig. 4 Fatigue life behavior

Figure 4 illustrates fatigue life behavior of the gripper due to input displacement. It shows that the fatigue life of the components is better for the applied input displacement of 0.8 μm .

4 Conclusion and Future Work

In this investigation, image processing techniques are efficiently used to refine the topology optimization process. Interpolation technique shows a promising level of improvement in the topology of the gripper and confirms in this research. Various filtering techniques are also used to compare the effectiveness of the mesh-dependency filter. Hence, the mesh-dependency filter itself found ahead of others. The geometrical advantage of the designed microgripper is found at 4.95 through FE analysis. The fatigue life of the model also found more than one million cycles for input displacement of 0.8 μm .

Acknowledgements Science and Engineering Research Board (SERB), India (Grant Number ECR/2016/001938), has supported this work.

References

1. Nah SK, Zhong ZW (2007) A microgripper using piezoelectric actuation for micro-object manipulation. *Sens Actuators A Phys* 133:218–224
2. Dario P, Carrozza MC, Benvenuto A, Menciassi A (2000) Micro-systems in biomedical applications. *J Micromech Microeng* 10:235–244
3. Zhong ZW, Zheng Z (2003) Flying height deviations in glide height tests. *Sens Actuators A Phys* 105(3):255–260

4. Sun J, Zhong Z (2002) Finite element analysis of a new PZT actuator for hard disk drives. *Sens Actuators A Phys* 100:257–263
5. Zhong ZW, Gee SH (2004) Failure analysis of ultrasonic pitting and carbon voids on magnetic recording disks. *Ceram Int* 30(7):1619–1622
6. Fearing RS (1995) Survey of sticking effects for micro parts handling, intelligent robots and systems 95. In: *IEEE/RSJ international conference on 'human robot interaction and cooperative robots'*, proceedings, vol 2, pp 212–217
7. Saggere L, Kota S (2001) Synthesis of planar, compliant four-bar mechanisms for compliant segment motion generation. *J Mech Des-T Asme* 123:535–541
8. Albanesi A, Fachinotti V, Pucheta M, Cardona A (2007) Synthesis of compliant mechanisms for segment-motion generation tasks. *Asociación Argentina de Mecánica Computacional*, vol 26, pp 2919–2930
9. Howell LL (2001) *Compliant mechanisms*. Wiley
10. Bendsoe MP, Sigmund O (2004) *Topology optimization: theory, methods and applications*. Springer, Berlin
11. Bourdin B (2001) Filters in topology optimization. *Int J Numer Methods Eng* 50:2143–2158
12. Anthony Parker J, Kenyon RV, Troxel DE (1983) Comparison of interpolating methods for image resampling. *IEEE Trans Med Imaging* M1-2(1)
13. Shih CJ, Lin CF (2006) A two-stage topological optimum design for monolithic compliant microgripper integrated with flexure hinges. In: *International MEMS conference 2006. Journal of physics: conference series*, vol 34, pp 840–846
14. Bharanidaran R, Ramesh T (2014) Numerical simulation and experimental investigation of a topologically optimized compliant microgripper. *Sens Actuators A* 205:156–163
15. Bharanidaran R, Ramesh T (2017) A modified post-processing technique to design a compliant based microgripper with a plunger using topological optimization. *Int J Adv Manuf Technol* 93(1–4):103–112
16. Srikanth SA, Bharanidaran R (2017) Design and development of compliant mechanisms using parameterization technique. *Mater Today Proc* 4(8):7388–7396

Study on Tensile Strength of GFRP Nanocomposites by VARTM



A. Thiagarajan, K. Jagadish Chandra Bose, K. Velmurugan
and V. S. K. Venkatachalapathy

Abstract Present state of the art aims to enhance the mechanical properties of GFRP by incorporating nanofillers with different weight percentages into the resin matrix. Zinc oxide (ZnO) nanoparticles are used as the filler material and infused into the epoxy resin (diglycidyl ether of bisphenol A). In this work, woven roving mat (WRM) of glass fiber is used as reinforcement material. Nanocomposite specimen was prepared by VARTM process by varying the percentages of zinc oxide weight as 0, 1, 3 and 5 wt% respectively. The surface morphology was detected by scanning electron microscope (SEM). The effect of ZnO nanoparticles on mechanical properties of GFRP was determined by conducting tensile test. From the results obtained, it is evident that the infusion of 1 wt% zinc oxide (ZnO) nanoparticles in epoxy resin showed 20% increment in tensile strength compared with neat epoxy composite.

Keywords Glass fiber-reinforced polymer (GFRP) · Zinc oxide (ZnO) · VARTM · Tensile strength · SEM

1 Introduction

Fiber-reinforced polymer stands for its better mechanical strength and became better choice where corrosion resistance would be the major requirement. Generally, FRP stands for low mass object with splendid temperature-resistant properties and provides thermal insulation. They can be fabricated in complex shapes easily. FRP products are simple to fix repairs and require least maintenance.

GFRP is one of the varieties of plastic composites that particularly use glass fiber materials to enhance mechanical properties like high strength and modulus of polymers [1]. The resin stood up for extra protection to the fiber by causing perfect bonding between two materials [2]. Requisitions of glass fiber-reinforced plastics

A. Thiagarajan (✉) · K. Jagadish Chandra Bose · K. Velmurugan · V. S. K. Venkatachalapathy
Department of Mechanical Engineering, Sri Manakula Vinayagar Engineering College,
Puducherry 605107, India
e-mail: thiagusmvec@gmail.com

© Springer Nature Singapore Pte Ltd. 2019
S. S. Hiremath et al. (eds.), *Advances in Manufacturing Technology*,
Lecture Notes in Mechanical Engineering,
https://doi.org/10.1007/978-981-13-6374-0_41

351

have been continuously increasing since few decades, because of getting popularity in most of the applications like aircraft industries, transportation industries, fiberglass construction and supporting materials [3]. The combination of less weight materials reduces the production cost that advances the fabrication of parts, resulting in the production of polymer products at low cost which could be used in fields like automobile industries and railcar.

Additionally, glass fiber-reinforced polymers are very flexible in designing complex shapes. Due to its outrageous benefit of susceptibility, more endurance of the structure brings enhanced structural strength by its weight [4]. Superior properties like excellent corrosion resistance reduced overall weight and increased mechanical properties enable glass fibers and its product finds many applications especially in railways and construction industries [5].

Glass fibers are generally employed by considering resin or vinyl esters and isophthalic polyester resin [6] to deal with drawbacks in the applications of polymers, for example reduced stiffness and strength; ceramic particles are frequently used to meliorate the tribological, thermal and mechanical behavior [7].

Infusing nano or micro fillers into the polymer composites improves the overall performance of the material and also reduce the cost of the material [8]. Agglomeration is one of the main criteria for nanofillers or particles that can reduce the physical properties of the polymer composites when infused into its polymer matrix. Such agglomeration problem was solved by mechanical agitation through particle stabilization and proper dispersion [9]. Zinc oxide is an artificial filler media and also a semiconducting material that is available in variety of structures. The applications of ZnO include photocatalytic, optoelectronics and antibacterial, especially as dermatological barriers [10]. Enhanced physical as well as thermal response of polymeric materials can be experienced by infusing ZnO in addition to polymer composite materials [11]. Hong et al. investigated the effect of ZnO-filled LDPE composites for dielectric properties. In this study, a comparison was made between infused particle attentiveness and conventionally entrained miniaturized ZnO fillers for the dielectric constants of polymer composites [12].

Sound research work exhibited the considerable enhancements in service life and physical characteristics of fiber-reinforced composites in which variety of filler mediums are mixed. Madugu et al. [13] found that by increasing the amount of infusing miniaturized particles into polymer composites, a remarkable advancement was noticed in hardness, porosity and density values, respectively, and at the same situation some physical properties like impact energy and linear shrinkage were observed. Garay et al. [14] concluded from their research that the tensile modulus and surface hardness seemed to be increased and still mechanical properties of polymer nanocomposite get decreased. Moorthy and Manonmani [15] explained from the research that by increasing the wt% of TiO₂, noticeable increase in mechanical and chemical resistance was observed. Even though inquiry toward effect of ZnO fillers on the physical properties of plastic composites is however ongoing research, it is still in advance stage.

The current research focused on influence of ZnO nanofillers on GFRP composite specimen by evaluating its tensile strength. The surface morphology and

fractured composites were analyzed and characterized by incorporating scanning electron microscopy.

2 Experimental Details

2.1 Materials Used

The entire experimentation was performed by following the testimonials furnished by American Society for Testing and Materials code for test methods of composite structures. The epoxy system was made with diglycidyl ether of bisphenol A (DGEBA) in the trade of LY 556, and it is in the form of liquid wax. The curing agent/hardener used was tri-ethylene tetra amine of HY-951. The woven roving mat (WRM) of glass fiber with density of 610 g/m^2 was used as reinforcement as shown in Fig. 1.

The zinc oxide (ZnO) was procured from Sigma-Aldrich from USA, and the zinc oxide image is shown in Fig. 2. The amount of zinc oxide (ZnO) into the epoxy system was facilitated with weight percentages of 0, 1, 3 and 5 wt%, respectively. Polyvinyl alcohol (PVA) was used to act as releasing agent, and it helps to remove the laminates from the molding. Mechanical stirrer was used for mixing epoxy resin with ZnO nanoparticles.

Processing of nanocomposite laminates:

ZnO particles are dispersed into the epoxy resin with different compositions by using mechanical stirrer at constant speed of 750 rpm for 2 h as shown in Fig. 3.

Fig. 1 Woven roving mat (WRM)

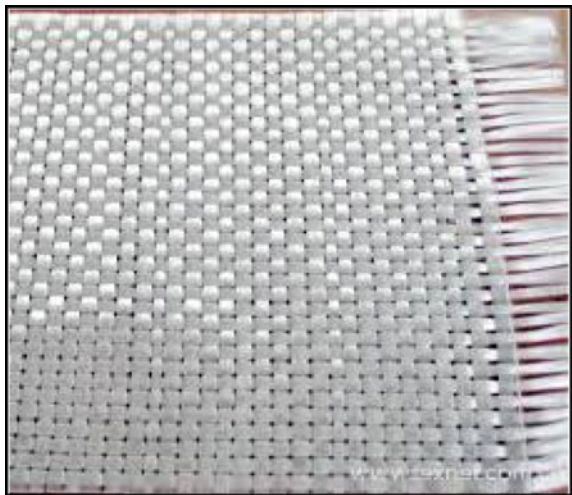


Fig. 2 Zinc oxide (ZnO) nanofiller



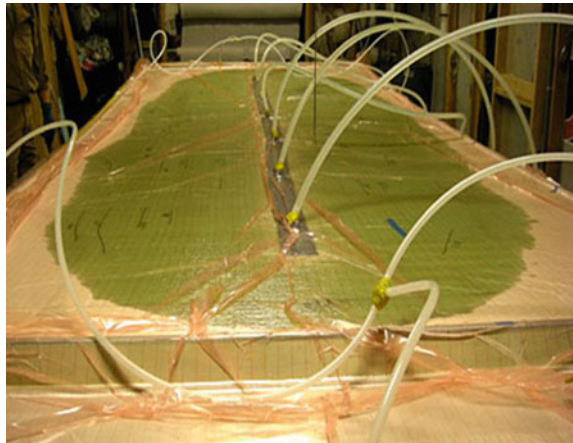
This will make the filler particles to uniform distribution into matrix of the epoxy [12]. A special type of fabrication method called vacuum-assisted resin transfer molding (VARTM) method was used for fabricating the nanocomposite materials. This method has proved as efficient and economical in large part of fabrication perspective, and it employs vacuum to infuse the liquid resin into the laminated fiber stack in the mold and thereby heat hardening. Due to fore-mentioned benefits, VARTM method was selected for fabrication of composite laminates. The schematic diagram of VARTM process is illustrated in Fig. 4. Initially, 1 wt% ZnO was added to the epoxy resin LY 556 and allowed to stir for two hours for mixing proportionately and it was followed by addition of hardener HY-951 to begin the hardening epoxy resin before reinforcement. Then, the mixed solution was allowed to flow through mold using hoses with help of vacuum; afterward, the sheet was allowed to dry for 24 h. Likewise, entire process was repeated for 3 and 5 wt% nanocomposites, respectively.

Many researchers carried out investigations by considering different weight percentages of the nanoparticles in order to enhance the properties but at the percentages with little variations and with different sizes of the nanoparticles [9, 11]. In present state of the art, three different weight percentages were used to find the optimized filler weight percentage. For current work, results showed that at the addition range of 1 wt% of ZnO nanoparticles, composite specimen experienced the best tensile strength compared to other weight percentages. Six layers of laminates were placed inside the mold and enclosed with vacuum bag. Then, nano-filled epoxy resin with hardener mixture was allowed to flow into the mold, and vacuum facilitates the nano-filled epoxy resin to flow into fiber layup contained with a mold tool covered by a vacuum bag as shown in Fig. 4. After the occurrence of impregnation, composite specimen was allowed to cure for 24 h at ambient temperature with optional post-cure as shown in Fig. 5 [10]. Post-cured composite specimen was removed from the

Fig. 3 Mechanical stirring (epoxy + ZnO particle)



Fig. 4 Laminate preparation through VARTM



mold, and the final specimen is shown in Fig. 6. Current work uses the composite specimen size of 300 mm × 300 mm.

Tensile strength:

Ultimate tensile strength (UTS) is frequently called as tensile strength. In the present work, tensile test was conducted as per the ASTM testing procedure of composite materials. The tensile behavior of nano-filled composite polymer specimen was tested in accordance with ASTM D638 of composite materials [12]. Test specimen has the dimensions of 165 mm × 15 mm × 3.5 mm [7]. The specimen is then loaded between two manually alterable grips of computerized universal testing machine. Each trial was iterated for thrice, and their mean value was calculated as tensile strength of the GFRP nanocomposite specimen. The schematic diagram of servo-controlled universal testing machine is shown in Fig. 7a, and the experimental setup is illustrated in Fig. 7b.

Fig. 5 Curing process of composite laminate



Fig. 6 Fabricated nanocomposite laminate



3 Characterization

It is necessary to characterize the composite specimens to empathize the influence of nanoparticulates clearly on physical properties of specimen. For characterizing the post-tested nanocomposite specimens, scanning electron microscopy was employed. The post-tested specimen characterized results were given in the results and discussion sections with graphical images.

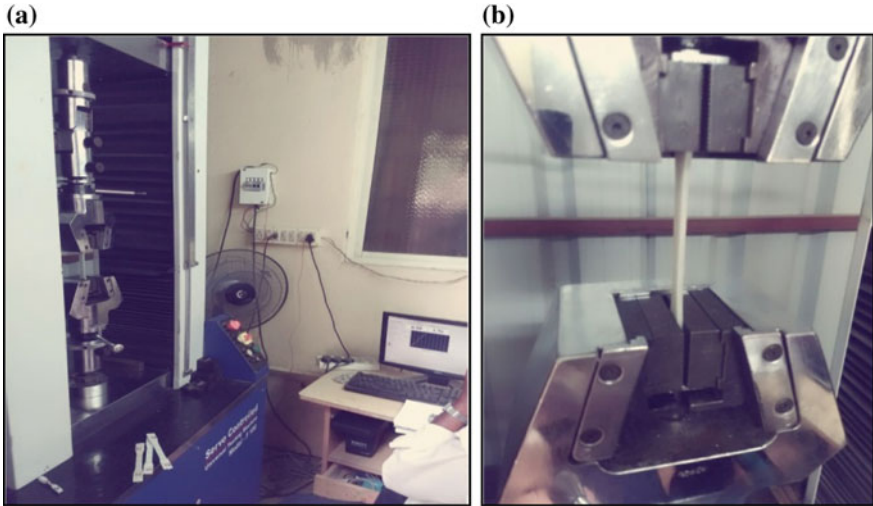


Fig. 7 a Universal testing machine and b experimental setup

4 Results and Discussion

4.1 Tensile Testing

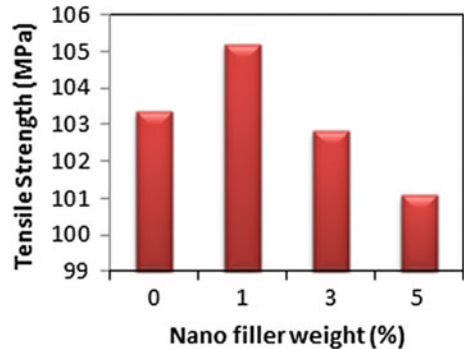
The tensile attributes of nanoparticulate-infused glass fiber-reinforced polymer composite were ascertained as per the ASTM D638 testing standards. The sample specimens for tensile test are shown in Fig. 8. The tensile tests were performed on computer-controlled screw-driven universal testing machine with the capacity of 100 KN and with a constant crosshead velocity of 1 mm/min [10]. Averaged tensile strength of each loading of fillers was reckoned by five tests, and the same is given as shown in Table 1.



Fig. 8 Prepared specimens for tensile testing

Table 1 Tensile strength for polymer nanocomposites

Nanofiller (wt%)	Tensile strength in MPa
0	103.38
1	105.21
3	102.84
5	101.09

Fig. 9 Tensile strength of the nanocomposites

The addition of zinc oxide particles in tensile strength of the specimen is shown in Fig. 9. The addition of nanoparticles increases interfacial adhesion of the elements in the composite system and heightens trivial ratio of area to the volume which shows positive results in the improvement of performance of the imbedded elements. From the tensile test results, it is reasoned that, with addition of ZnO, enhanced the tensile strength up to a certain limit that is optimum loading limit of nanofillers.

The enhanced tensile strength was ascribed to the unequaled morphology of interface and better phase properties between the epoxy matrix and the fiber materials. The interfacial bonding between the fiber and the matrix was attributed to be one of the most significant factors that influence the tensile strength of glass fiber-reinforced and particulate-filled polymer epoxy nanocomposites. From the experimental observation, higher content of nanoparticles did not present with respect to mechanical properties regarding tensile strength.

Surface Morphology using SEM

The scanning electron microscopic micrographs were obtained toward 1 wt% of ZnO nano-filled specimen and 3 wt% ZnO nanoparticle-infused specimen, and the same is shown in Fig. 10a, b respectively. Morphological observations for 1 wt% ZnO nanoparticle-infused polymer nanocomposite specimen explained that perfect distribution of ZnO nanofillers in the epoxy matrix was detected and glass fibers are in adhered stipulation with the matrix.

Strong attractive Van der Waals forces seed ZnO to heap that minimizes the enduringness of the nanocomposite through stress concentration phenomena. Agglomerations causing from the ZnO nanoparticles are little bit hard to carve up and penetrate

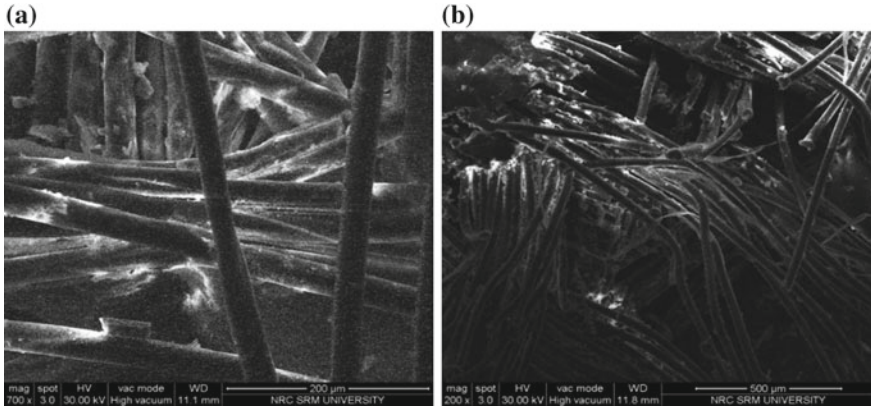


Fig. 10 a ZnO 1 wt% filled specimen and b ZnO 3 wt% filled specimen

with matrix as they get stuck and develop unnecessary irregular structures because of their high aspect ratios. Two physical processes called disaggregation and scattering in the epoxy resin depend on van der Waals forces between them and on the respective surface tension of the ZnO particles. Nevertheless, optimum diluting and undifferentiated dispersion of ZnO nanofillers in matrix are key parameters to promote better ZnO-filled polymer matrix phase properties to accomplish effective infusion dispersion among the two components of polymer nanocomposite specimen.

5 Conclusion

The nanocomposite laminates were successfully processed and fabricated by VARTM method, and tensile strength was studied using universal testing machine (UTM). From the results obtained during testing, tensile strength was enhanced at 1 wt% of ZnO filler loading of composite laminate and then decreased beyond 1 wt% concentration due to agglomeration. SEM results from the post-tested specimens showed that, at 1 wt% ZnO-filled specimen have got maximum adhesion bonding between the particles and the matrix of the fiber materials. As well it is witnessed that reduction of tensile strength because of concentrations of 3 and 5 wt% ZnO-filled samples was on account of agglomeration and weak interfacial adhesion.

References

1. Callister WD (2007) Materials science and engineering: an introduction, 7th edn. Wiley, New Jersey
2. Staab GH (1999) Laminar composites. Butter Worth-Heinemann, London

3. Daniel I, Ishai O (1994) Engineering mechanics of composite materials. Oxford University Press, New York
4. Bank LC (2006) Composites for construction: structural design with FRP materials. Wiley, New Jersey
5. Lopez FA, Martin MI, Alguacil FJ, Rincon JM, Centeno TA, Romero M (2012) Thermolysis of fiber glass polyester composite and reutilization of the glass fiber residue to obtain a glass ceramic material. *J Anal Appl Pyrol* 93:104–112
6. Sahu H, Rout A, Kumar A (2012) Development and characterization of particulate filled glass fiber reinforced hybrid composites. *Indian J Mech Eng Technol* 2(3):89–93
7. Raja RS, Manisekar K, Manikandan V (2014) Study on mechanical properties of fly ash impregnated glass fiber reinforced polymer composites using mixture design analysis. *Mater Design* 55:499–508
8. Sathiyamurthy S, Thaheer ASA, Jayabal S (2013) Prediction and optimization of mechanical properties of particles filled coir–polyester composites using ANN and RSM algorithms. *Indian J Fiber Text Res* 38:81–86
9. Fu S-Y, Feng X-Q, Lauke B, Mai Y-W (2008) Effects of particle size, particle/matrix interface adhesion and particle loading on mechanical properties of particulate–polymer composites. *Compos Part-B* 39:933–961
10. Hossain MK, Hossain ME, Hosur MV, Jeelani S (2011) Flexural and compression response of woven e-glass/polyester–CNF nano phased composites. *Compos Part-A* 42:1774–1782
11. Yahya N, Puspitasari P, Latiff NRA (2013) Hardness improvement of dental amalgam using zinc oxide and aluminum oxide nanoparticles. In: *Characterization and development of biosystems and biomaterials. Advanced structural materials*, vol 29, pp 9–32
12. Hong JI, Winberg P, Schadler LS, Siegel RW (2005) Dielectric properties of zinc oxide/low density polyethylene nanocomposites. *Mater Lett* 59:473–476
13. Madugu IA, Abdulwahab M, Aigbodion VS (2009) Effect of iron fillings on the properties and microstructure of cast fiber–polyester/iron filings particulate composite. *J Alloys Compd* 11(13); 476:807
14. Garay AC, Heck V, Zattera AJ, Souza JA, Amico SC (2011) Influence of calcium carbonate on RTM and RTM light processing and properties of molded composites. *J Reinf Plast Compos* 30(14):1213–1221
15. Moorthy SS, Manonmani K (2013) Fabrication and characterization of TiO₂ particulate filled glass fiber reinforced polymer composite. *Mater Phys Mech* 18:28–34

Investigations on Wire Spark Erosion Machining of Aluminum-Based Metal Matrix Composites



N. Manikandan, J. S. Binoj, K. C. Varaprasad, S. Sree Sabari and Ramesh Raju

Abstract Wire EDM is an advanced approach of machining which is developed from the concept of electrical discharge machining and primarily employed to remove material from difficult to machine materials. Also, this advanced machining process has been exclusively employed to produce intricate shapes on the electrically conductive work materials. Composite materials provide enhanced mechanical properties which depend upon the constituents. Graphene is identified as an excellent reinforcing element which supports to enhance the desired properties of aluminum metal matrix composites in a significant manner. In the present investigation, an experimental analysis has been performed on Wire electrical discharge machining (WEDM) of Al-GNP composites. Pulse-on-time, pulse-off-time, and servo voltage are deemed as input process variables. Material removal and surface roughness are deemed as the desired performance characteristics in this exploration. Taguchi's design of experiment method has been employed for devising the experimental runs, and an L_9 orthogonal array was adopted to conduct the experimental runs. The impact of process variables was analyzed by Taguchi's single response analysis and ANOVA. Multiple regression analysis has been performed to develop an empirical relationship among the selected input and output characteristics. The best possible combination of process parameters was determined to attain improved machining performance.

Keywords WEDM · Al-GNP composites · Taguchi's approach · Orthogonal array · Response and regression analysis · ANOVA · Optimization

N. Manikandan · J. S. Binoj (✉) · K. C. Varaprasad · S. Sree Sabari
Micromachining Research Centre, Department of Mechanical Engineering, Sree Vidyanikethan Engineering College (Autonomous), Tirupati 517102, Andhra Pradesh, India
e-mail: binjloxman@gmail.com

Ramesh Raju
Department of Mechanical Engineering, Santhiram Engineering College, Nandyal 518501, Andhra Pradesh, India

1 Introduction

Metal matrix nano-composites deemed as one of the advanced metal matrix composites (MMCs) which are having a wide range of structural applications. Graphene is the reinforcing element that possesses considerable mechanical, thermal, and optical properties, and because of this point, the graphene has been extensively used for making multi-functional composites [1, 2]. Among the various metal-graphene-based composites, Al-GNP MMC has more attraction because of its low weight amalgamated with high strength and better ductility [3]. Addition of graphene improves the fracture strength and hardness of the fabricated composites [4, 5]. The possible application of WEDM method has been identified as expeditiously grown material removal process nowadays because of the needs in various manufacturing applications and especially employed in cutting tool and die-manufacturing applications, automobiles, aerospace, and nuclear industries. The removal of material happens because due to consecutive sparks occurred between the wire electrode and the workpiece material in the existence of dielectric medium. The machining occurred irrespective of the hardness of the material [6, 7]. The outline of WEDM setup is shown in Fig. 1.

Nowadays Taguchi's approach is considered as an influential tool for increasing the rate of production by means of proper experimental planning and determining the better process parameters for single-objective optimization which helps the manufacturer to produce parts with a better quality and minimum cost [8]. Sahoo and Pradhan [9] presented a study on the machining of aluminum composites using Taguchi's approach. Mathematical models were evolved for determining roughness and flank wear. It is perceived from the study that the developed mathematical models are found to be statistically significant for predicting the process parameters. Various researchers employed Taguchi's method of planning the experiments and also single aspects optimization for Wire EDM of various work materials [10–14].

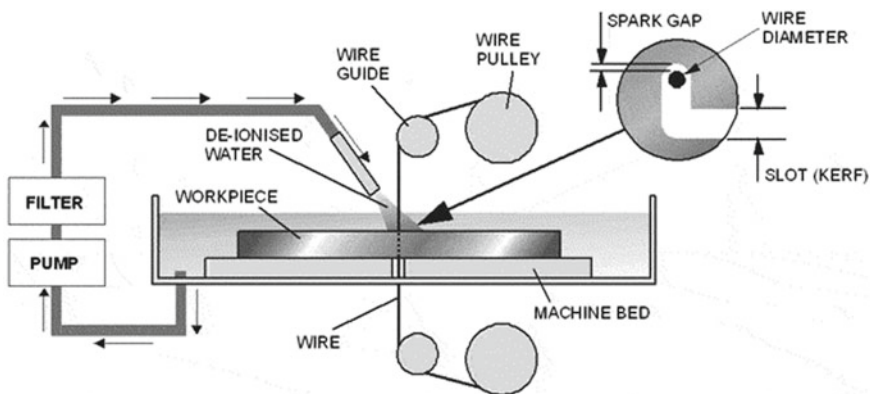


Fig. 1 Schematic of Wire EDM setup

Table 1 Parameters and their levels for WEDM of Al-GNP composite

Factor	Process parameters	Levels		
		1	2	3
A	Pulse-on-time (μs)	105	108	111
B	Pulse-off-time (μs)	54	57	60
C	Servo voltage (V)	20	25	30

It is observed from the available literature that there is a deficiency in the literature on WEDM of Al-GNP metal matrix composite to analyze the process parameters. In the present investigation, an endeavor has been taken to establish the significance of process variables for the rate of material removal and roughness during the Wire EDM process. Taguchi's single response analysis method is used to optimize the rate of material removal and roughness of the machined surface in WEDM process.

2 Materials and Methods

Taguchi's experimental design approach is adopted to plan the experiments. A total of three machining parameters, namely pulse-on-time, pulse-off-time, and servo voltage, were considered as input process variables. The WEDM process variables and levels are given in Table 1. The WEDM setup comprises of machining chamber, control panel, and dielectric fluid circulation system. Al-GNP is selected as the workpiece material, and the composite is prepared by a stir casting method. The work sample is fixed in the vice provided inside of the machining chamber. The independent process variables, namely pulse-on-time and pulse-off-time, and servo voltage, were varied. Experiments were conducted on ELEKTRA make Wire EDM (Model: ULTRACUT 843). Brass is the tool materials which is used as a wire electrode and connected between the rollers. An L_9 orthogonal array has been selected for conducting the experiments. The deionized water has been chosen as a dielectric fluid for conducting experiments, and it is circulated between the tool and workpiece. The machining was performed to make a through hole, and MRR was measured using the weight loss method. The surface roughness has been measured with the aid of Mitutoyo surface roughness testing device (SJ-210). The results obtained from the experimentation in WEDM are evaluated.

3 Results and Discussion

The planned experiments were performed as per L_9 orthogonal array to examine the importance of input process variables on the rate of material removal and roughness of the machined surface. An attempt was taken to determine the best possible

process parameters for attaining the effective and competent machining process. In the WEDM process, the rate of material removal is considered as higher the better, and surface roughness is considered as lower the better criteria which will be considered as better machining performance.

3.1 Analysis of Process Parameters on Material Removal Rate

Figure 2 shows the main effects plot for the material removal rate during the WEDM process. From the illustration, it is clear that the rate of material removal increases with an escalation in pulse-on-time, and it reduces with an increase in pulse-off-time. Also, pulse-on-time is the most significant process parameter for the rate of material removal rate during the Wire EDM process. With increment in pulse-on-time, the discharge energy offered at the machining zone will be higher which results in a powerful explosion, leading to an increase in the rate of material removal. Increasing the pulse-on-time has the possibility of increasing the number of electrons forcing on the work material surface, thus eroding the more amount of material from the surface of the workpiece per discharge.

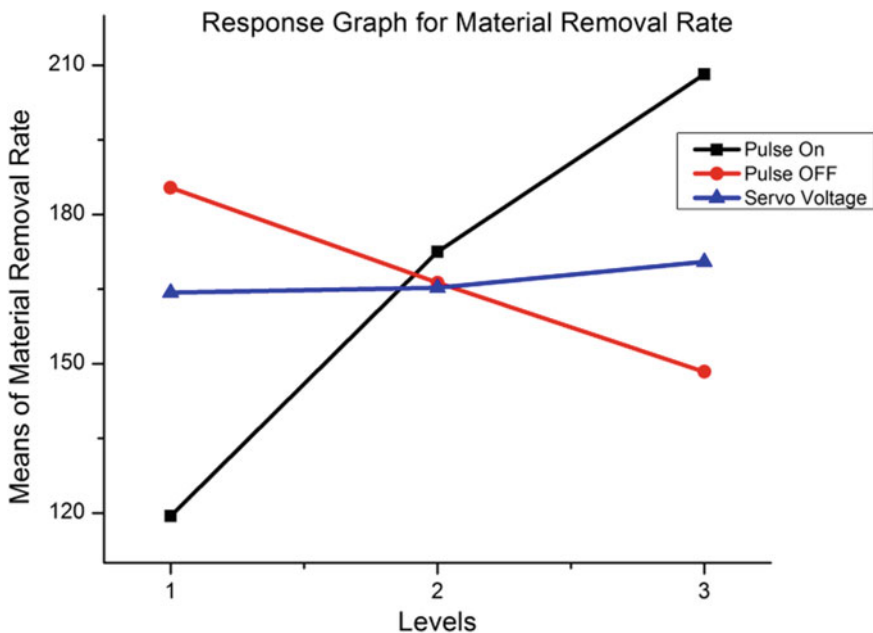


Fig. 2 Response graph for material removal rate

Table 2 Taguchi analysis—response table for MRR

Levels	Means			S/N ratio		
	A	B	C	A	B	C
1	119.4	185.4	164.3	41.49	45.18	44.18
2	172.5	166.3	165.3	44.69	44.17	44.14
3	208.2	148.4	170.5	46.35	43.18	44.2
Delta	88.8	37	6.3	4.86	2	0.06
Rank	1	2	3	1	2	3

A—Pon (μ s), B—Poff (μ s), C—Servo voltage (V)

Table 2 gives the results of Taguchi’s response analysis for material removal rate, and the results are depicted. In summary, the best possible combinations of machining parameters for obtaining an improved rate of material removal are $A_3B_1C_3$. This means the optimum level for material removal rate is: Pon—111 μ s, Poff—54 μ s, and servo voltage—30 V. Pon is the most contributing parameter, and then, it is followed by Poff time and servo voltage.

3.2 Analysis of Process Parameters on Surface Roughness

Figure 3 graphically shows the plot for the main effects for surface roughness during the WEDM process. From the illustration, it is perceived that the roughness value gets increased with an escalation in Pon, and it gets decreased with an increment in Poff. Also, Pon is the influential process parameter for surface roughness during the Wire EDM process. The superior discharge energy offered crater in a larger manner which causes more roughness on the machine surface.

Taguchi’s single response analysis has been performed, and the results are given in Table 3. In summary, the best possible combination of machining parameters to attain lower surface roughness is $A_1B_3C_3$. This means the optimum level for surface roughness is: Pon—105 μ s, Poff—60 μ s, and servo voltage—30 V. Pon is the predominant process parameter, and then, it is followed by Poff and servo voltage.

3.3 ANOVA for Desired Performance Measures

A statistical tool ANOVA has been adopted to ascertain the impact of input process parameters on the selected performance characteristics at a 95% confidence level, and it is evaluated by statistical analysis software Minitab 16.0.

The ANOVA analysis for the rate of material removal, roughness of WEDMed surface in WEDM of Al-GNP is presented in Table 4. From the ‘P’ values, it is

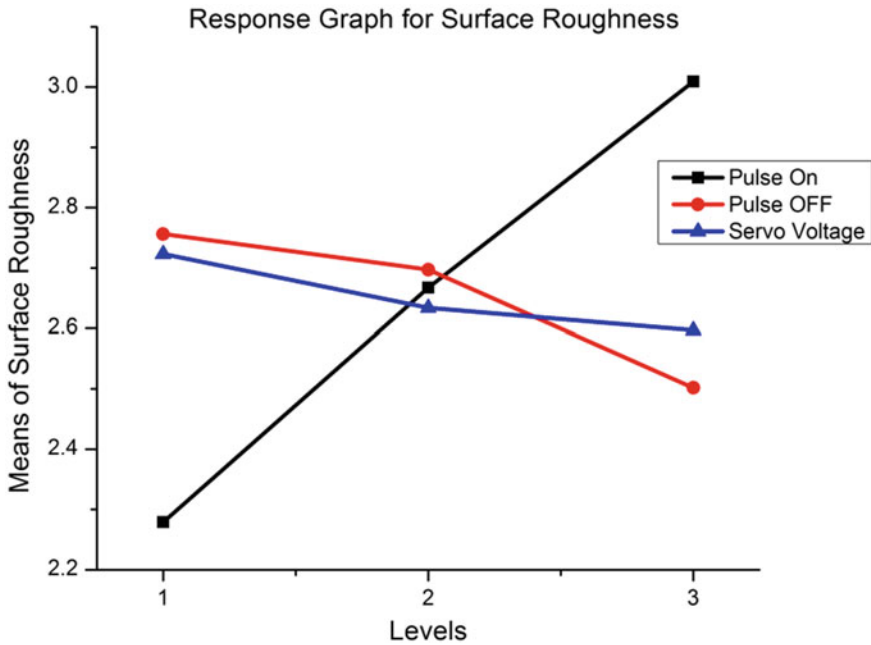


Fig. 3 Response graph for surface roughness

Table 3 Taguchi analysis—response table for surface roughness

Levels	Means			S/N ratio		
	A	B	C	A	B	C
1	2.279	2.756	2.723	-7.124	-8.769	-8.666
2	2.667	2.697	2.634	-8.519	-8.564	-8.38
3	3.009	2.502	2.597	-9.563	-7.871	-8.159
Delta	0.729	0.254	0.126	2.439	0.898	0.507
Rank	1	2	3	1	2	3

A—Pulse-on-time (μ s), B—Pulse-off-time (μ s), C—Servo voltage (V)

perceived from the investigation that the ‘Pon’ is the predominant process variable for the rate of material removal and roughness of the machined surface in WEDM of Al-GNP composites.

3.4 Development of Multiple Regression Models

Multiple regressions technique is employed to ascertain the relationship among the process variables. Regression equations have various models such as linear, quadratic,

Table 4 ANOVA for WEDM of Al-GNP composites

Source	DF	Seq SS	Adj SS	Adj MS	F	P
<i>Material removal rate (g/min)</i>						
Pulse-on (μs)	2	10060.7	10060.7	5030.3	8.55	0.105
Pulse-off (μs)	2	1248.8	1248.8	624.4	1.06	0.485
Servo voltage (V)	2	1630.1	1630.1	815	1.38	0.419
Error	2	1177.3	1177.3	588.7	–	–
Total	8	14116.9	–	–	–	–
<i>Surface roughness (Ra) (μ)</i>						
Pulse-on (μs)	2	0.79892	0.79892	0.39946	58.22	0.017
Pulse-off (μs)	2	0.1062	0.1062	0.0531	7.74	0.114
Servo voltage (V)	2	0.0252	0.0252	0.0126	1.84	0.353
Error	2	0.01372	0.01372	0.00686	–	–
Total	8	0.94405	–	–	–	–

interaction, and full model and are as shown in Eqs. (1)–(4) (for three input parameters):

Linear equation:

$$y = \beta_0 + \beta_1 X_1 + \beta_2 X_2 + \beta_3 X_3 \tag{1}$$

Quadratic equation:

$$y = \beta_0 + \beta_1 X_1 + \beta_2 X_2 + \beta_3 X_3 + \beta_4 (X_1)^2 + \beta_5 (X_2)^2 + \beta_6 (X_3)^2 \tag{2}$$

Interaction equation:

$$y = \beta_0 + \beta_1 X_1 + \beta_2 X_2 + \beta_3 X_3 + \beta_4 X_1 X_2 + \beta_5 X_1 X_3 + \beta_6 X_2 X_3 \tag{3}$$

Second-order equation (full model):

$$y = \beta_0 + \beta_1 X_1 + \beta_2 X_2 + \beta_3 X_3 + \beta_4 (X_1)^2 + \beta_5 (X_2)^2 + \beta_6 (X_3)^2 + \beta_7 X_1 X_2 + \beta_8 X_1 X_3 + \beta_9 X_2 X_3 \tag{4}$$

where ‘y’ is criterion variable and ‘X₁,’ ‘X₂,’ and ‘X₃’ are predictor variables. ‘β₁,’ ‘β₂,’ ‘β₃’ ... ‘β_n’ are regression coefficients.

3.4.1 Regression Model for MRR

The empirical equations for associating the relationship among the desired performance measure and the considered process variables have been obtained, and the desired regression equation for MRR is shown in Eq. (5)

$$\text{MRR (mm}^3/\text{min)} = -921.806 + 11.7153 P_{\text{on}} (\mu\text{s}) - 4.27778 P_{\text{off}} (\mu\text{s}) + 2.68333 \text{ Servo voltage (V)}. \quad (5)$$

3.4.2 Regression Model for Surface Roughness

The mathematical relationship which is attained to examine the significance of the predominant machining variables on the surface roughness is given in Eq. 6.

$$\text{Surface roughness } (\mu\text{m}) = -7.74844 + 0.121556 P_{\text{on}} (\mu\text{s}) - 0.0423333 P_{\text{off}} (\mu\text{s}) - 0.0126 \text{ Servo voltage (V)}. \quad (6)$$

4 Conclusions

The present article describes a single-objective optimization of WEDM of Al-GNP composite using Taguchi Analysis. The rate of material removal and roughness of the WEDMed surface are the performance measures considered in this investigation. Following are conclusion obtained from this exploration:

- Taguchi's single response analysis helps to optimize the input process parameter under this study as a single-objective optimization. Best possible set of process parameter for the desired performance characteristics was determined by Taguchi's signal-to-noise ratio analysis.
- The predominance of considered input process parameters on the performance characteristics was divulged by response analysis. P_{on} is the significant process variable for the output measures in the present exploration.
- From the statistical tool known as ANOVA, it is made known that the pulse-on-time (μs) is the most significant parameter for desired performance characteristics.
- The empirical equations were developed using multiple regression analysis for correlating the connection among the independent and dependent process variables and the based on the R^2 values, the developed equations are used for further predictions.
- The discussed Taguchi's methodology in the present investigation is a most appropriate for establishing the best combination of the process parameter to attain improved machining performance.

- The results and discussions from the present exploration will be providing an exclusive.
- The outcome of the present investigation will be comprehensive support manufacturers to enhance the productivity and quality of products in making various products with the aid of WEDM process.

References

1. Lee C, Wei XD, Kysar JW, Hone J (2008) Measurement of the elastic properties and intrinsic strength of monolayer Graphene. *Science* 321:385–388
2. Georgiou T, Britnell L, Blake P, Gorbachev RV, Gholinia A, Geim AK et al (2011) Graphene bubbles with Controllable curvature. *Appl Phys Lett* 99:093–103
3. Konakov VG, Kurapova OY, Lomakin IV, Archakov IY, Solovyeva EN, Ovidko IA (2016) Fabrication of Aluminum-graphene and metal-ceramic nanocomposites. A selective review. *Rev Adv Mater Sci* 44(4):361–369
4. Li Z, Fan G, Tan Z, Guo Q, Xiong D, Su Y, Zhang D (2014) Uniform dispersion of graphene oxide in aluminum powder by direct electrostatic adsorption for fabrication of graphene/aluminum composites. *Nanotechnology* 25(32):325–601
5. Wang J, Li Z, Fan G, Pan H, Chen Z, Zhang D (2012) Reinforcement with graphene nanosheets in aluminum matrix composites. *Scripta Mater* 66(8):594–597
6. Ho KH, Newman ST, Rahimifard S, Allen RD (2004) State of the art in wire electrical discharge machining (WEDM). *Int J Mach Tools Manuf* 44(12–13):1247–1259
7. Ross PJ (2005) Taguchi techniques for quality engineering, Chap. 7. McGraw-Hill, New York, USA
8. Baburaja K, Subbaiah KV, Vanaja T, Ramesh NN (2017) Resultant surface roughness aluminium and haste alloy C-276 using wire electro discharge machining. *Mater Today Proc* 4(2):1013–1018
9. Sahoo AK, Pradhan S (2013) Modeling and optimization of Al/SiCp MMC machining using Taguchi approach. *Measurement* 46:3064–3072
10. Chiang KT, Chang FP (2006) Optimization of the WEDM process of particle-reinforced material with multiple performance characteristics using grey relational analysis. *J Mater Process Technol* 180(1–3):96–101
11. Huang JT, Liao YS (2003) Optimization of machining parameters of wire-EDM based on grey relational and statistical analyses. *Int J Prod Res* 41(8):1707–1720
12. Kanlayasiri K, Boonmung S (2007) Effects of wire-EDM machining variables on surface roughness of newly developed DC 53 die steel: Design of experiments and regression model. *J Mater Process Technol* 192:459–464
13. Ramakrishnan R, Karunamoorthy L (2006) Multi response optimization of wire EDM operations using robust design of experiments. *Int J Adv Manuf Technol* 29(1–2):105–112
14. Yang RT, Tzeng CJ, Yang YK, Hsieh MH (2012) Optimization of wire electrical discharge machining process parameters for cutting tungsten. *Int J Adv Manuf Technol* 60(1–4):135–147

Optimization of Coefficient of Friction for Direct Metal Laser Sintered Inconel 718



S. Sathish, V. Anandakrishnan, V. Dillibabu, Duraiselvam Muthukannan and N. Balamuralikrishnan

Abstract Direct metal laser sintering is one of the rapid prototyping techniques, which has the ability to fabricate the components with a wide range of materials and with varying geometries. With this technique, the Inconel 718 material was fabricated in three different build orientations (horizontal, vertical, and angular). Further, the fabricated samples subjected to a heat treatment process as per the standards. Samples from the fabricated material were analyzed through the X-ray diffraction technique and scanning electron microscope analysis. Dry sliding wear test was conducted with Taguchi's orthogonal design, and the coefficient of friction was considered as the response. Best parameter combination to obtain the minimum coefficient of friction was identified with the main effect plot. The significant parameter which affects the response was identified through the analysis of variance.

Keywords Additive manufacturing · Direct metal laser sintering · Inconel 718 · Taguchi technique

1 Introduction

Nickel alloys are the furthestmost extensively usable material in the aerospace industries due to their excellent properties even at higher temperatures. Inconel 718 is one among the nickel-based alloy which has its applications in aircraft turbine engines which subject to higher temperatures [1]. The higher strength of the Inconel 718 material made the material difficult to machine, which directly creates an impact on the production. Along with the difficulties, the complexities in the design of the components will also tie together and create more complex in machining conventionally. Direct metal laser sintering is one of the rapid prototyping techniques [2]

S. Sathish · V. Anandakrishnan (✉) · D. Muthukannan
Department of Production Engineering, National Institute of Technology,
Tiruchirappalli 620015, India
e-mail: krishna@nitt.edu

V. Dillibabu · N. Balamuralikrishnan
Gas Turbine Research Establishment, Defence Research and Development Organization,
Bangalore 560093, India

© Springer Nature Singapore Pte Ltd. 2019
S. S. Hiremath et al. (eds.), *Advances in Manufacturing Technology*,
Lecture Notes in Mechanical Engineering,
https://doi.org/10.1007/978-981-13-6374-0_43

under the roof of powder bed system [3], which made an alternative to handle the production of difficult materials with greater flexibility in different materials [4], creating complex profiles, with better dimensional accuracy [5] and surface finish [6]. Peng et al. [7] fabricated the nickel alloy samples by direct metal laser sintering technique to optimize the system process parameters and found that the direct laser fabrication process of nickel alloy components is feasible under open loop control. Inconel 718 was fabricated with the powder bed fusion process and its microstructure and thermal behavior were examined along with the numerical modeling, and the results were found to be good with the actual behavior [8]. Bertol et al. [9] studied the various process parameters such as support structures, inclination and orientation of the model, and its internal structure on direct metal laser sintering of Ti-6Al-4V, and the results proved that it is feasible to laser sinter Ti-6Al-4V with better dimensional accuracy. Tang et al. [10] synthesized copper-based alloy with direct laser sintering process and found the density of the component increases when the laser power increases, and the scan speed and scan spacing decrease. Experimental studies on direct metal laser sintered Inconel 718 were done to investigate the effect of laser power and scan speed on densification and properties and found that the densification was directly controlled by the energy density of the laser [11]. The tribological behavior of the direct laser sintered Inconel 600 alloy was investigated by Vaishal et al. using the Taguchi technique and created a mathematical model using the regression analysis [12]. The high-temperature wear test was conducted on the Inconel 617 alloys, and it was compared with the X32CrMoV33 steel and the experimental results showed a better wear resistance in Inconel 617 alloys when compared to steel [13]. The tribological behavior of direct metal laser sintered Fe-Ni-Cr alloy was tested after the hot isostatic pressing and high ultrasonic frequency peening and found minimum amount wear and coefficient of friction in the peened material [14]. The literature review summarizes the different materials which were synthesized through the additive manufacturing process and further the need for extensive study on the metallurgical, mechanical, and tribological properties. The literature review clearly presented that the direct metal laser fabrication is technically proven one, and hence, an attempt was made to develop the Inconel 718 material with direct metal laser sintering technique. The coefficient of friction significantly influences the vibration of the components when it is subjected to relative motion, and hence, identifying the minimum coefficient of friction is more vital. Further, the tribological behavior of the direct metal laser sintered Inconel 718 is planned with the dry sliding wear test, and the present paper focusses on the minimization of the coefficient of friction through the Taguchi analysis.

2 Experimental Details

To fabricate the additive product, Inconel 718 was preferred as the raw material, and the suitability of the Inconel 718 powders was tested with the mill test as per EN10204 standard. Additive samples were realized in the three orientations like

Table 1 Experimental design with coefficient of friction

S. No.	Build orientation (angle)	Load (N)	Sliding velocity (m/s)	Coefficient of friction
1	0	9.81	1	1.204382
2	45	9.81	2	0.519907
3	90	9.81	3	0.152144
4	0	19.62	2	0.839946
5	45	19.62	3	0.382127
6	90	19.62	1	0.831922
7	0	29.43	3	1.279798
8	45	29.43	1	1.602125
9	90	29.43	2	0.918882

horizontal, vertical, and angular. Samples were printed in the form of cylinders of 9 mm diameter and height 52 mm, and further, the samples were subjected to the heat treatment process as per AMS 5662 standard. From the direct metal laser sintered cylinders, samples were sectioned, grounded, polished, and etched as per the standard procedures to reveal the metallurgical features through the X-ray diffraction analysis and scanning electron microscope analysis. Wear pins were sectioned from the laser sintered samples with the help of wire electric discharge machining, and its ends were polished. The dry sliding wear test was conducted in the pin on disk setup by considering the parameters build orientation, load, and sliding velocity. Taguchi's L_9 design was utilized to do the experiments, and the response coefficient of friction was calculated using Eq. (1) from the obtained wear data collected with the data acquisition system as given in Table 1.

$$\text{Coefficient of friction} = \text{Shear force/Normal force} \quad (1)$$

3 Results and Discussion

3.1 Metallurgical Analysis

The results of the X-ray diffraction of laser sintered Inconel 718 were analyzed, and it is shown in Fig. 1. The analysis showed the development of nickel chromium, nickel titanium, and nickel aluminum precipitates with the hkl plane of (111), (022), and (111), respectively.

The results of the scanning electron microscopic image (Fig. 2) show the existence of γ' , δ , and carbides.

3.2 Wear Analysis

With the obtained coefficient of friction from the experiments, statistical analysis was performed with smaller the better quality characteristics. The response table was obtained from the analysis as given in Table 2, and load was identified as the highly endowing factor with the higher delta value of 0.6415 followed by sliding velocity and build orientation with the delta values of 0.6081 and 0.4737, respectively. The optimum parameter combination to minimize the coefficient of friction was identified as 90° of build orientation, 10 N of load, and 3 m/s of sliding velocity from Fig. 3.

The analysis of variance is used to identify the significance among the means. The significance of the parameters was identified with the values of probability. From Table 3, it was observed that all the three parameters load, build orientation, and sliding velocity were lesser than 0.05 value, which shows that all the parameters are significantly affecting the coefficient of friction. It was noted that the maximum

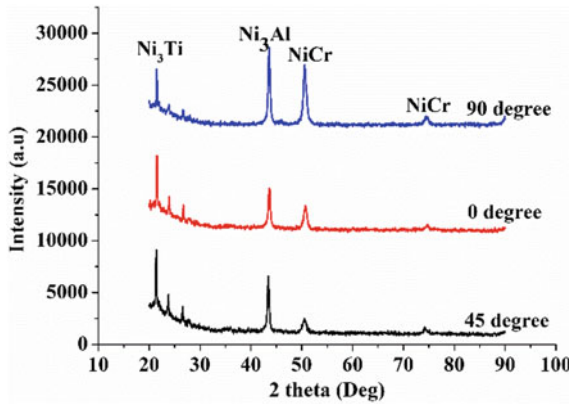


Fig. 1 X-ray diffraction analysis

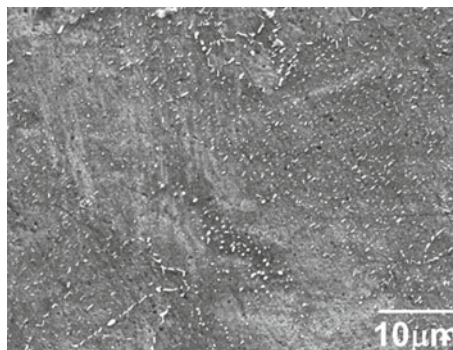


Fig. 2 SEM image of angular build Inconel 718

Table 2 Response table (smaller is better)

Level	Build orientation	Load	Sliding velocity
1	1.108	0.6255	1.2128
2	0.8347	0.6847	0.7596
3	0.6343	1.2669	0.6047
Delta	0.4737	0.6415	0.6081
Rank	3	1	2

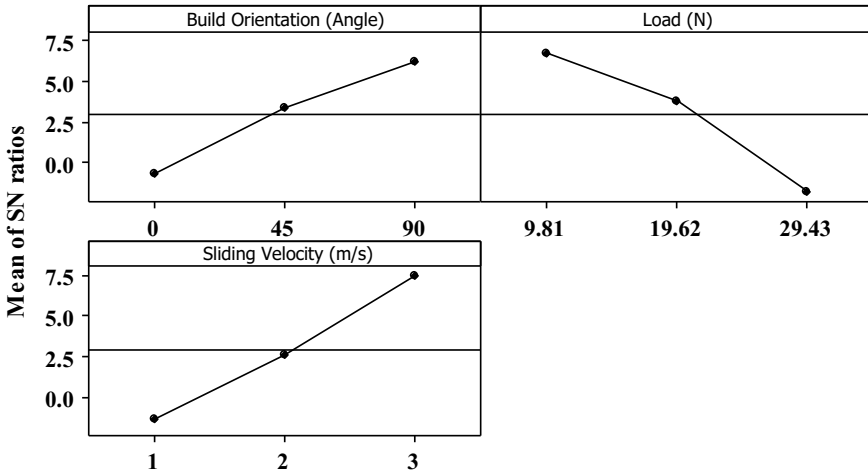


Fig. 3 Main effect plot for coefficient of friction

Table 3 Analysis of variance for coefficient of friction

Source	DF ^a	Seq SS ^b	Adj SS ^c	Adj MS ^d	F	P ^e	P (%)
Build orientation	2	0.33928	0.33928	0.16964	121.05	0.008	20.01
Load	2	0.75401	0.75401	0.377	269.03	0.004	44.48
Sliding velocity	2	0.59922	0.59922	0.29961	213.8	0.005	35.35
Error	2	0.0028	0.0028	0.0014			0.17
Total	8	1.69531					

S = 0.0374348, R-Sq = 99.83%, R-Sq (adj) = 99.34%

^aDegrees of freedom

^bSequential sums of squares

^cAdjusted sums of squares

^dAdjusted mean squares

^eProbability

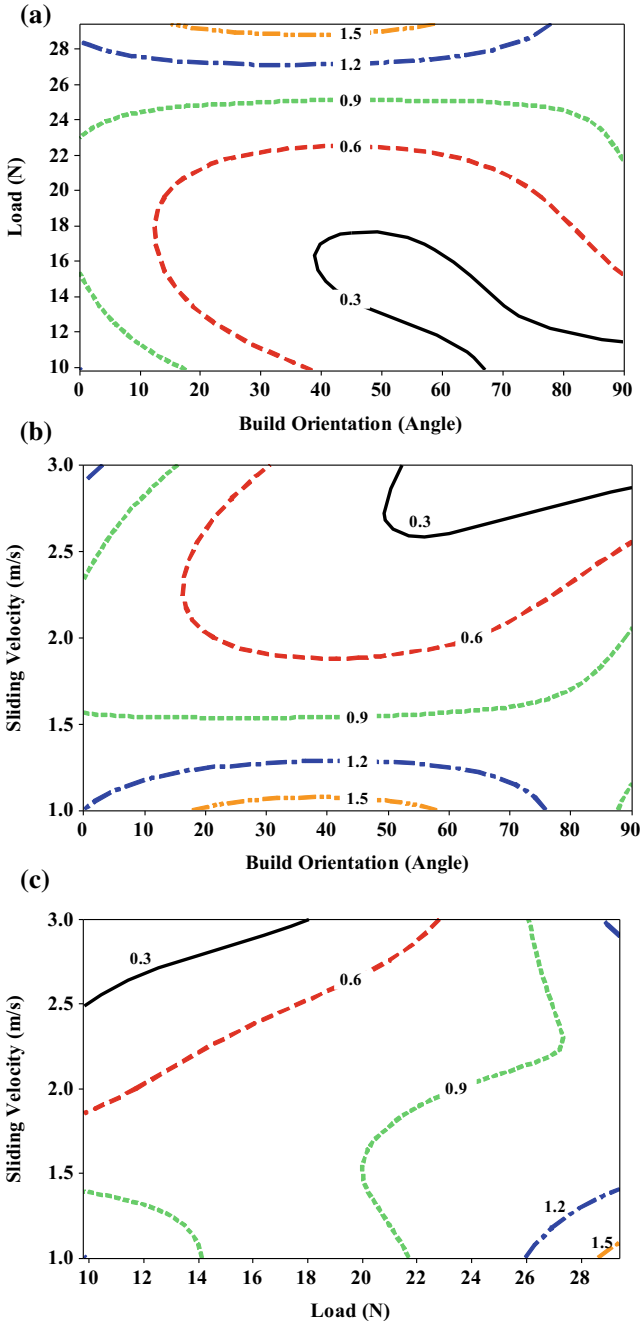


Fig. 4 Contour plot for coefficient of friction

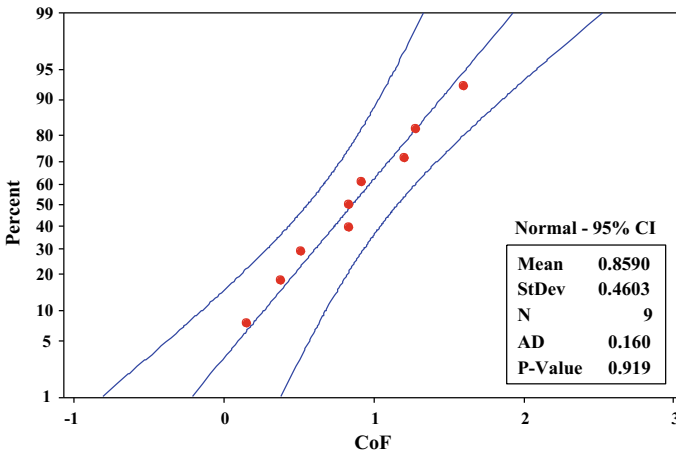


Fig. 5 Normal probability plot for coefficient of friction

percentage of probability was 44.48 for load followed by 35.35 and 20.01 for sliding velocity and build orientation, respectively. Though all the parameters were significant, load has the highest stimulus over the coefficient of friction.

Contour plots are used to represent the response variables graphically with respect to the corresponding input factors. Contour plots for the coefficient of friction in a combination with build orientation and load, build orientation and sliding velocity, and load and sliding velocity are shown in Fig. 4a–c. Lesser values of coefficient of friction of 0.3 are observed in combination with the lower loads and higher build orientation, whereas larger values of coefficient of friction of 1.5 are observed in combination with the higher loads and lower build orientation from Fig. 4a. Likewise, lesser values of coefficient of friction of 0.3 are observed in combination with higher build orientation and higher sliding velocity, whereas larger values of coefficient of friction of 1.5 are observed in combination with medium build orientation and lower sliding velocity from Fig. 4b. Figure 4c shows the lesser values of coefficient of friction of 0.3 are at higher sliding velocity and lower load, whereas larger values of coefficient of friction of 1.5 are observed at higher load and lower sliding velocity.

The experimental runs were validated using the confirmation test and normal probability plot. The predicted value of the coefficient of friction with the optimum parameter combination obtained through the main effect plot is 0.146431, and the experimental value of the coefficient of friction is 0.152144. The percentage error of the predicted value and experimented value is found to be 3.90%. Further, with the normal probability plot as shown in Fig. 5, the experimental data were assessed and found that the experimental data were laid within limits and fitted along the straight line.

4 Conclusion

With the direct metal laser sintering technique, Inconel 718 material was fabricated in three different build orientations of horizontal, vertical, and angular. Subsequently, the metallurgical analysis was performed, and the existence of gamma, gamma prime and precipitates was identified. Based on the Taguchi's design, wear tests were performed, and the response coefficient of friction was calculated and analyzed statistically. The optimum parameter combination to obtain the minimized coefficient of friction was identified as 90° of build orientation, 10 N of load, and 3 m/s of sliding velocity. Load was identified as the most contributing factor on the coefficient of friction through analysis of variance and response table. Further, the corrosion behavior of the direct metal laser sintered Inconel 718 material may be carried out as the future work.

References

1. Davis JR (2000) Nickel, cobalt, and their alloys. ASM International, USA. <https://doi.org/10.1361/ncta2000p013>
2. Khaing MW, Fuh JYH, Lu L (2001) Direct metal laser sintering for rapid tooling: processing and characterisation of EOS parts. *J Mater Process Technol* 113:269–272. [https://doi.org/10.1016/S0924-0136\(01\)00584-2](https://doi.org/10.1016/S0924-0136(01)00584-2)
3. Frazier WE (2014) Metal additive manufacturing: a review. *J Mater Eng Perform* 23:1917–1928. <https://doi.org/10.1007/s11665-014-0958-z>
4. Wong KV, Hernandez A (2012) A review of additive manufacturing. *ISRN Mech Eng* 1–10. <https://doi.org/10.5402/2012/208760>
5. Vayre B, Vignat F, Villeneuve F (2012) Metallic additive manufacturing: state-of-the-art review and prospects. *Mech Ind* 13:89–96. <https://doi.org/10.1051/meca/2012003>
6. Sateesh NH, Kumar GCM, Prasad K, Srinivasa CK, Vinod AR (2014) Microstructure and mechanical characterization of laser sintered Inconel-625 superalloy. *Procedia Mater Sci* 5:772–779. <https://doi.org/10.1016/j.mspro.2014.07.327>
7. Peng L, Taiping Y, Sheng L, Dongsheng L, Qianwu H, Weihao X et al (2005) Direct laser fabrication of nickel alloy samples. *Int J Mach Tools Manuf* 45:1288–1294. <https://doi.org/10.1016/j.ijmachtools.2005.01.014>
8. Promoppatum P, Yao S-C, Pistorius PC, Rollett AD, Coutts PJ, Lia F et al (2018) Numerical modeling and experimental validation of thermal history and microstructure for additive manufacturing of an Inconel 718 product. *Prog Addit Manuf*. <https://doi.org/10.1007/s40964-018-0039-1>
9. Bertol LS, Júnior WK, da Silva FP, Aumund-Kopp C (2010) Medical design: direct metal laser sintering of Ti-6Al-4V. *Mater Des* 31:3982–3988. <https://doi.org/10.1016/j.matdes.2010.02.050>
10. Tang Y, Loh HT, Wong YS, Fuh JYH, Lu L, Wang X (2003) Direct laser sintering of a copper-based alloy for creating three-dimensional metal parts. *J Mater Process Technol* 140:368–372. [https://doi.org/10.1016/S0924-0136\(03\)00766-0](https://doi.org/10.1016/S0924-0136(03)00766-0)
11. Jia Q, Gu D (2014) Selective laser melting additive manufacturing of Inconel 718 superalloy parts: densification, microstructure and properties. *J Alloy Compd* 585:713–721. <https://doi.org/10.1016/j.jallcom.2013.09.171>
12. Banker VJ, Mistry JM, Thakor MR, Upadhyay BH (2016) Wear behavior in dry sliding of Inconel 600 alloy using Taguchi method and regression analysis. *Procedia Technol* 23:383–390. <https://doi.org/10.1016/j.protcy.2016.03.041>

13. Birol Y (2010) High temperature sliding wear behaviour of Inconel 617 and Stellite 6 alloys. *Wear* 269:664–671. <https://doi.org/10.1016/j.wear.2010.07.005>
14. Amanov A, Sasaki S, Cho IS, Suzuki Y, Kim HJ, Kim DE (2013) An investigation of the tribological and nano-scratch behaviors of Fe-Ni-Cr alloy sintered by direct metal laser sintering. *Mater Des* 47:386–394. <https://doi.org/10.1016/j.matdes.2012.11.062>

Experimental and Numerical Investigation on Incremental Forming of IS513Cr3



M. D. Vijayakumar and G. Gopalaramasubramaniyan

Abstract The incremental sheet forming (ISF), also known as die-less forming, has the potential to form complex three-dimensional objects. It has a higher formability limit than the conventional forming. ISF is the method of producing complex sheet metal components with enhanced productivity and improved quality. Further, the ISF can also be applied in various levels of manufacturing. Major advancements in the ISF have proved the manufacturing flexibility of the process. The present research work discusses important findings on various factors like wall angle, tool material, step depth, spindle speed, and feed corresponding to the response which is related to wall thickness, roughness, geometry, and forming angle. Such features are found to be the characteristic formability feature in the ISF. The entire process has been investigated by using numerical analysis software. The final fabrication includes designing the fixtures for clamping sheet metals, and suitable programming inputs have been given to the CNC machine. In addition to the analytical results, various iterations in the ISF of IS513Cr3 have been conducted by changing the wall angle correspondingly. The computational results of the ISF are compared with the actual values obtained from the experimentation, and various process parameters have been investigated and studied.

Keywords Incremental sheet forming · Die-less forming · Formability limit · Manufacturing flexibility · Computational results

M. D. Vijayakumar (✉)

Department of Mechanical Engineering, St. Peter's Institute of Higher Education and Research, Avadi, Chennai, Tamil Nadu 600054, India

e-mail: vijayakumar.md@gmail.com

G. Gopalaramasubramaniyan

Department of Mechanical Engineering, Saveetha Engineering College, Saveetha Nagar, Thandalam, Chennai, Tamil Nadu 602105, India

© Springer Nature Singapore Pte Ltd. 2019

S. S. Hiremath et al. (eds.), *Advances in Manufacturing Technology*,

Lecture Notes in Mechanical Engineering,

https://doi.org/10.1007/978-981-13-6374-0_44

1 Introduction

The sheet metal has a wide variety of application in the engineering stream. Everyday contemporary manufacturing operations have been exploited for the formation of sheet metals to required shapes. Various forming operations have been currently used to produce complex profiles on the basis of the application. In such a case, the incremental sheet metal forming is an emerging technology that focuses on the production of complex structures. Unlike using the conventional method of die forming, the IF is a customized method of manufacturing. This type of forming is highly specialized, expensive, and time-consuming in producing parts. Various studies have been done to understand the current technological developments in the incremental sheet metal forming. Numerous research works in the field have been carried out to investigate the influence of process parameters on surface quality, geometric accuracy, forming forces, thinning, and sustainability. Ambrogio et al. [1] investigated the influence of process parameters on accuracy through the statistical analysis. Durante et al. [2] studied the influence of tool rotation on an incremental forming (IF). He explained the relationship between the tool rotations evaluated at different speeds and also revealed the influence of tool rotation in terms of forming forces, temperature reached, and surface roughness. Hussain et al. [3] has done the work by utilizing varying wall angle conical frustum (VWACF) test. He has attempted to find out the effect of variation in curvature of the part on formability. In order to quantify the formability, it has been defined as the maximum wall angle (θ_{max}) that a sheet would endure without fracturing. Thus, the formability limit gives the tolerance of the sheet during fracturing. The influencing factors affecting single point IF were found to be material type, material thickness, formed shape, tool size, and incremental step size. Experimental work, carried by Ham and Jeswiet [4], presented the graphical response surface that shows the formability limit and its dependent factors. Further, forming limits are presented in terms of forming limit diagrams. The novel idea of producing symmetric parts by a so-called die-less forming method applying a single point tool was patented by Leszak in the USA in 1967. There was significant interest in processes where sheet metal deformed plastically in a small zone enabling really flexible production of complex parts. The accuracy of the sine law for prediction of wall thickness in SPIF or TPIF has been found to be variable across the profile of a formed product. Thus, the various research outcomes have analyzed in detail, and detailed work layout has been used.

2 Experimental Details

Initially, the necessary parameters for the frustum model such as wall angle, the shape of the final form, raw material properties, sheet thickness, feed and speed of operation, machine to be used, and coolant to be applied are studied in detail for better process optimization in IS513Cr3.

The model is kowtowed to be produced from CAD files rehabilitated into 3D CAM files. CNC is applied to direct the tool conduit. More recent studies [5–8] show the operation of IF in polymers. Inferences obtained from the usage of three axes CNC machines evidenced the effectiveness of IFP [9–12].

Particularly on the SPIF modality, [13, 14] the process is defined as a flat metal sheet, adjoined on a mobile device, and it slides matching to Z-axis. CNC with ball nose tools glides on the sheet and progressively during upright augmentation (ΔZ). The outline of the end part is found by the displacement of the tool in three axes.

The sheets are set to imaginative holdup which preserves steady height virtual to the bottom. Hussain et al. [15] mentioned that closures avert the movement through the process and finish the plastic deformation. The wall angles play a major role in the sheet metal deformations. Studies have revealed that the changes in wall angles have a profound effect on the manufacturing flexibility and failure of sheet metal forming.

If there are maximum wall angle values, that allow the plastic forming which does not cause the material fracture due to increase in resistance, leading a little resistance [16]. Be considered to a wall angle, it is formed between the horizontal plane and the wall of the shaped part. For calculating the final thickness (S1) of the sheet after forming and wall thickness after forming (t1) are used to sine Law as reported elsewhere [12–16]. The experimental set up of incremental forming is shown in Fig. 1.

3 Results and Discussions

Based on experimental studied reported on the literature, IS513Cr3 prototyping and customization of final product was carried out in this research work. Pro-E® software was used to design the blank. Master CAM® software was used for program

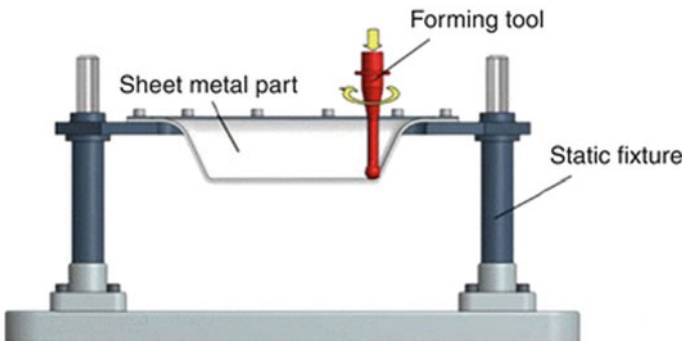


Fig. 1 Incremental forming setup. Source Author

generation. To analyze the true strains (ϕ_1 and ϕ_2), the experiments analyzed were with the wall angle (\emptyset) reached a maximum of 66° .

Initially, the wall angle of 60° was taken for the sheet metal forming, and it is solved by using Hypermesh[®] software. The input parameters include increasing the step depth of 0.2, 0.3, and 0.4, respectively. The experiment is carried out by an increase in the spindle speed in the range of 100, 200, and 300. Further, feed is given as 500, 1000, and 1500. The tool is made up of high speed steel (HSS). Figure 2 shows the stress variation in the sheet metal with a wall thickness of 63° . From the result, it is inferred that there is a maximum concentration of stress in the bottom most point of the frustum element. From Fig. 3, the % thinning of the sheet metal with respect to the feed is identified. Figure 4 shows the plastic strain in the sheet metal after deformation. Further, Fig. 5 shows the forming limit diagram from which the forming of sheet

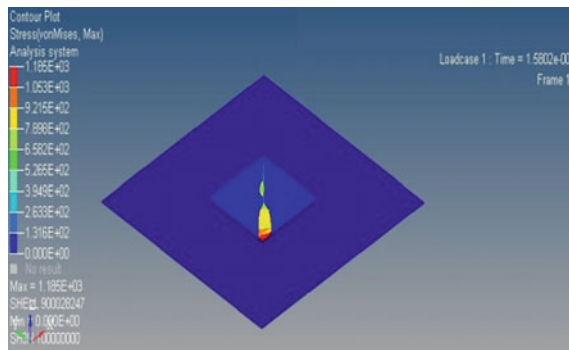


Fig. 2 Stress variation in 60° wall angle

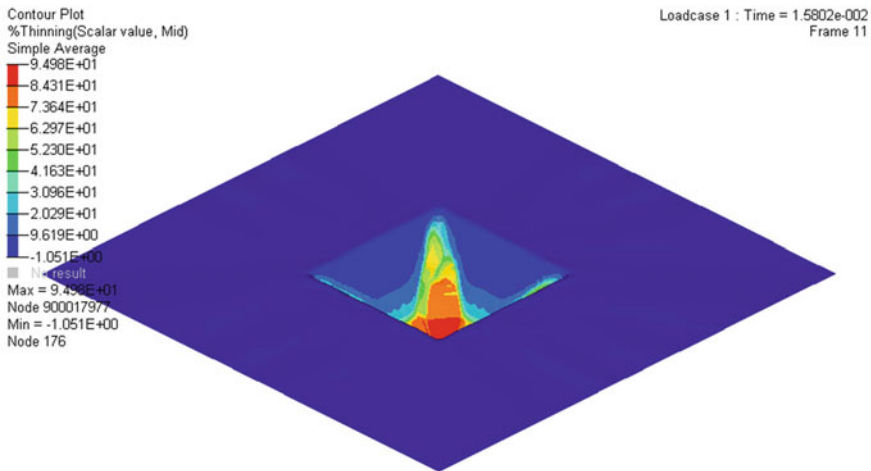


Fig. 3 Percentage of thinning in 60° wall angle

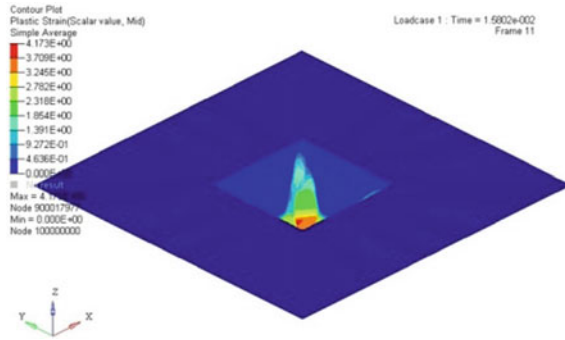


Fig. 4 Plastic strain in 60° wall angle

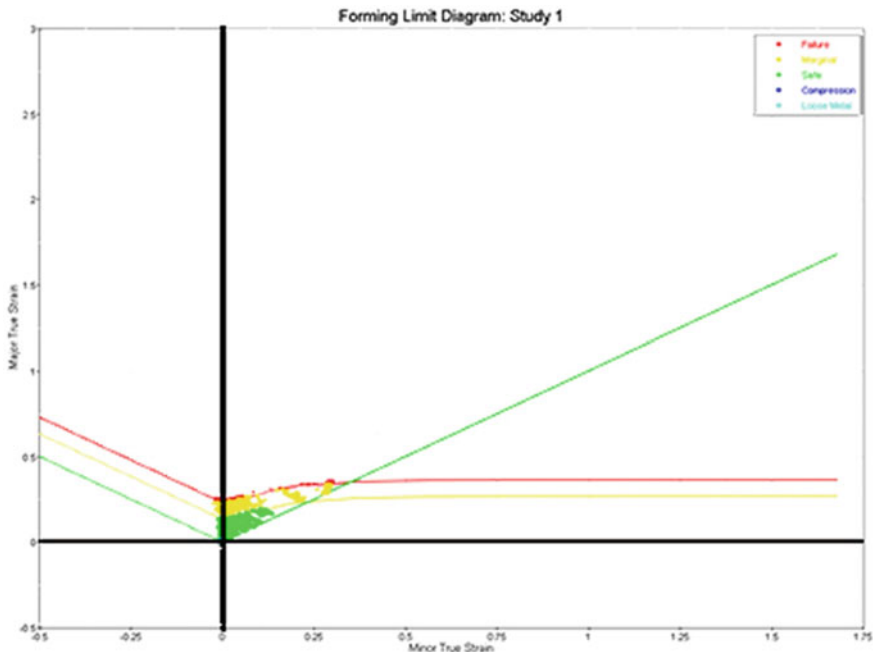


Fig. 5 Forming limit diagram for 60° wall angle

metal is evaluated, and the variation of forming limit with the variation in the depth is studied. After the experimentation of the SIF process with the wall angle of 60°, the prototype model is tested and is compared with the analysis results. It is found that there is a variation in the wall thickness with increasing depth of the frustum. The hardness is also measured at random points along the wall of the component, and the results are tabulated. It is also found that the geometry and forming angle remain constant throughout the sheet metal forming (Figs. 6, 7, 8, and 9).

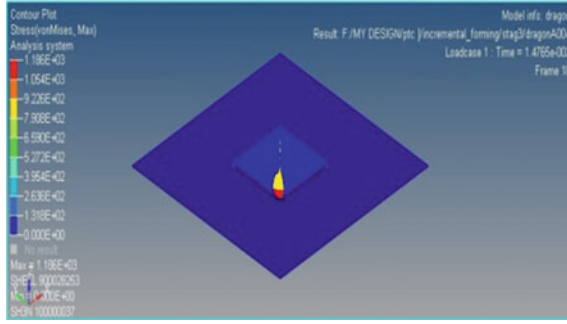


Fig. 6 Stress variation in 63° wall angle

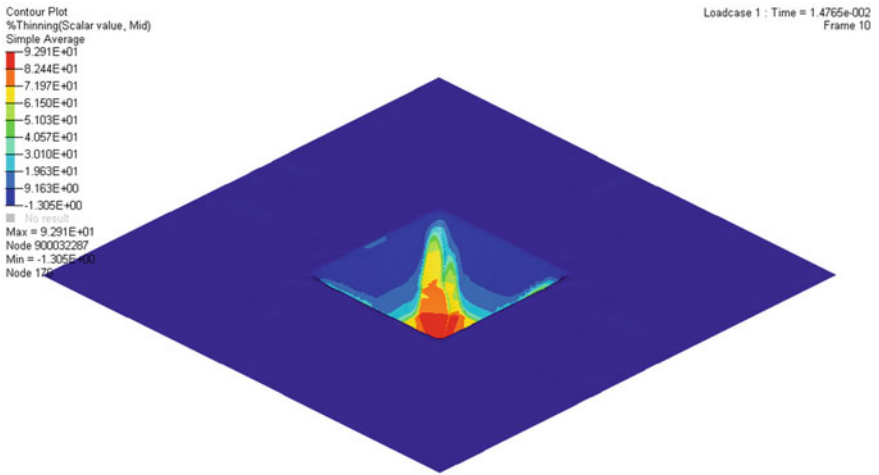


Fig. 7 Percentage of thinning in 63° wall angle

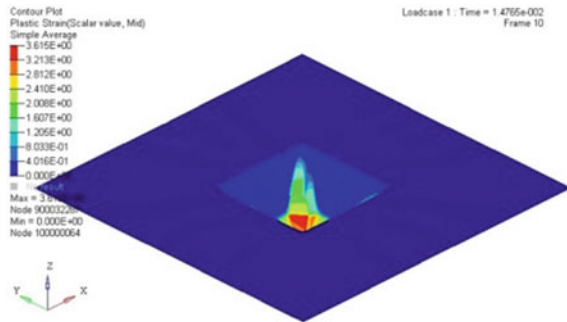


Fig. 8 Plastic strain in 63° wall angle

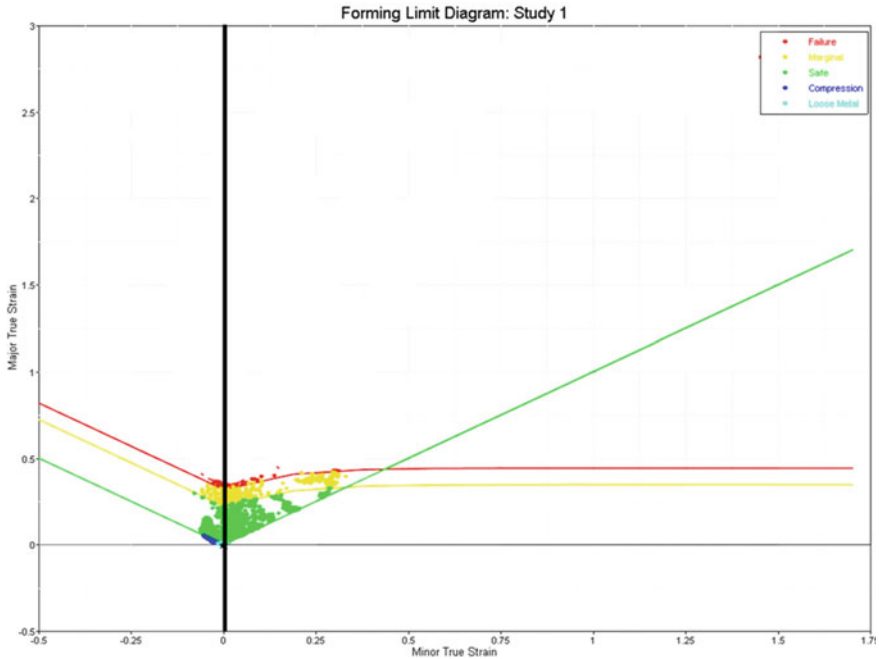


Fig. 9 Forming limit diagram for 63° wall angle

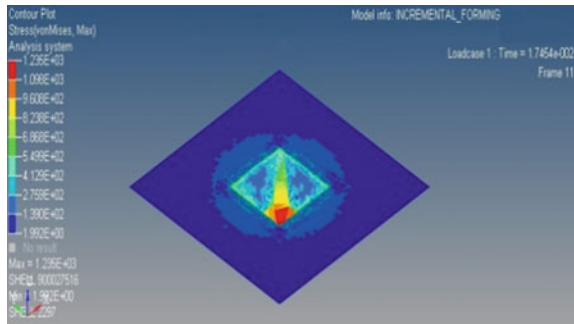


Fig. 10 Stress variations in 66° wall angle

Finally, the experiment was conducted by assigning the wall angle of 66° for the sheet metal forming. It is numerically analyzed by using Hypermesh® software. The input parameters include increasing the step depth of 0.2, 0.3, and 0.4, respectively. Increase in the spindle speed is in the range of 100, 200, and 300. Further, feed is given as 500, 1000, and 1500. The tool is made up of high speed steel (HSS). Figure 10 shows the stress variation in the sheet metal with the wall thickness of 66°. From the result, it is inferred that there is a maximum concentration of stress in the bottom most point of the frustum element. From Figure 11, the % thinning

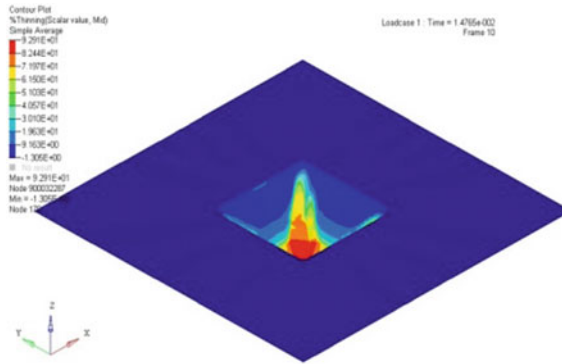


Fig. 11 Percentage of thinning in 66° wall angle

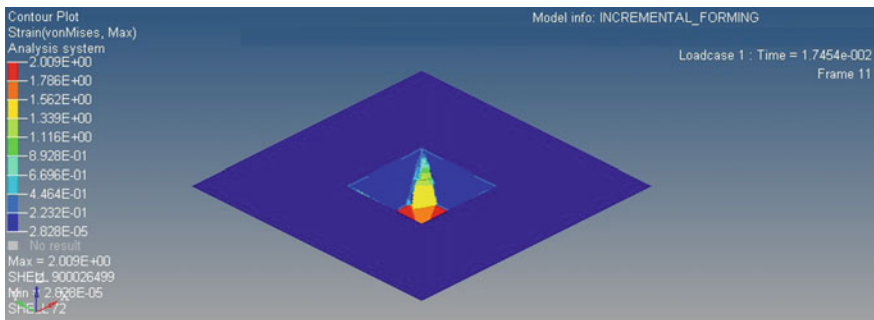


Fig. 12 Plastic strain in 66° wall angle

of the sheet metal with respect to the feed is identified. Figure 12 shows the plastic strain in the sheet metal after deformation. Further, Fig. 13 shows the forming limit diagram from which the forming of sheet metal is evaluated, and the variation of forming limit with the variation in the depth is studied. After the experimentation of the SIF process with the wall angle of 66°, the prototype model is tested and is compared with the analysis results. It is found that there is a variation in the wall thickness with increasing depth of the frustum. The hardness is also measured at random points along the wall of the component, and the results are tabulated. It is also found that the geometry and forming angle remain constant throughout the sheet metal component.

The setup to perform the ISF is a fixture to hold the sheet metal, single point forming tool, computer numerical controlled machinery that controls the motion of tools. Among which the integral component is a single point forming tool. One of the complex processes in the ISF is the design of the fixture for the process that would meet the requirements of the forming. The fixture has been designed according to the size and shape of the sheet metal to be formed. Solid hemispherical tool is used when plastically deforming sheet metal incrementally. Since it is of asymmetric IF,

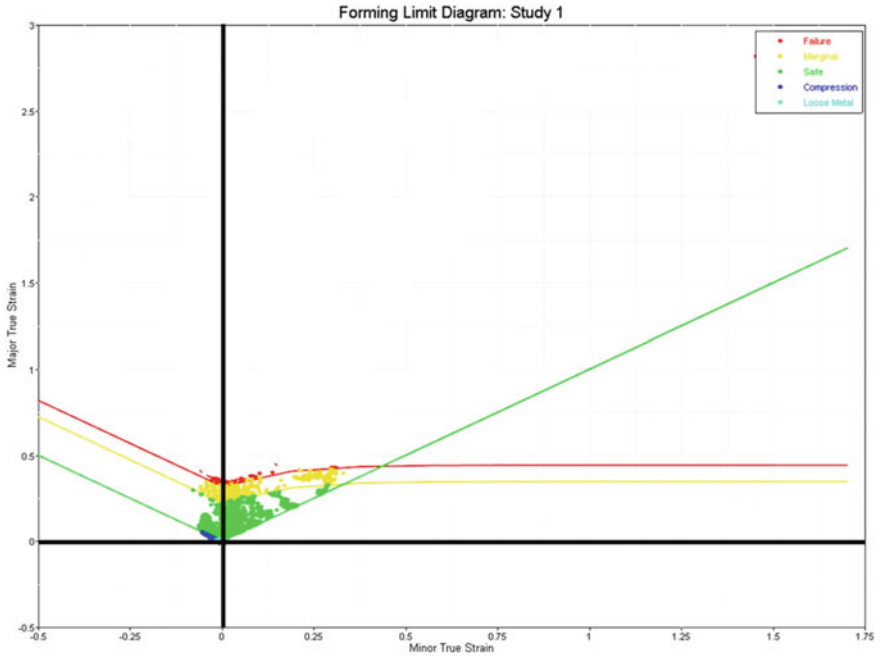


Fig. 13 Forming limit diagram for 66° wall angle

the solid hemispherical tool is used. High speed steel (HSS) tool has been chosen to reduce friction. The tool has been selected depending on the properties of sheet metal and its wear properties. Further, adequate lubrication has been given to the tool. Also, the diameter of the ball head has been chosen. Semi-spherical tool of 8 mm diameter has been chosen for the IF process. It consumes more power during operation since a large contact angle is involved. The tool diameter has also influenced on the surface quality of the product as well as the manufacturing time. The small tools can reach their loading limit while forming materials like stainless steel or titanium. The total length of the tool is found to be 110 mm. The fixture is made up of mild steel plate with the dimensions as shown in the figure. The raw material is a square-shaped sheet made up of IS513Cr3 with the dimension of 200 mm. The manufacturing is supported by the CNC machine with the programs evolved out from the Master CAM software.

4 Conclusion

By practical experiments, it was proved the good applicability of software CAD/CAM and CNC machining center as from IS513Cr3 sheet with 0.5 mm thickness using

the ISF process and SPIF modality. Further, it can be surely stated that ISF is, probably, the answer to the challenge of increasing flexibility in the field of sheet forming. Majority of the last researches, focused on improving the accuracy of the part, were successful, and new strategies of processing occurred, solving one of the weak points—the uncontrolled spring back of the material. The present work also proved the reliability and accuracy of sheet metal IF when compared with other forming operations. Further, developments must optimize the design of the CAM module which controls the tool movement, able to assure the suitable forming strategy according to any kind of hollow shape. A superior deformation of IS513Cr3 sheet metal is potential in SPIF. Small tool size is the favorite to get the obligatory shape at a quicker rate, but the possibilities of breakdown due to localized stress are larger.

References

1. Ambrogio G, Cozza V, Filice L, Micari F (2007) An analytical model for improving precision in single point incremental forming. *J Mater Process Technol* 191:92–95
2. Durante M, Formisano A, Langella A, Minutolo FMC (2009) The influence of tool rotation on an incremental forming process. *J Mater Process Technol* 209:4621–4626
3. Hussain G, Gao L, Hayat N, Qijian L (2007) The effect of variation in the curvature of part on the formability in incremental forming: an experimental investigation. *Int J Mach Tools Manuf* 47:2177–2181
4. Ham M, Jeswiet J (2006) Single point incremental forming and the forming criteria for AA3003. *Ann CIRP* 55(1)
5. Fratini L, Ambrogio G, Lorenzo RD, Filice L, Micari F (2004) Influence of mechanical properties of the sheet material of formability in single point incremental forming. *Ann CIRP* 53(1):207–210
6. Franzen V et al (2009) Single point incremental forming of PVC. *J Mater Process Technol* 462–469 (Dortmund, Germany)
7. Marques TAF (2010) Estampagem Incremental de Polímeros. UniversidadeTécnica de Lisboa, Lisboa, p 109
8. Martins PAF et al (2009) Single point incremental forming of polymers. *CIRP Ann Manuf Technol* 229–232
9. Jeswiet J et al (2005) Asymmetric single point incremental forming of sheet metal. *5Katholieke Universiteit Leuven*, p 27
10. Hirt G et al (2005) Flexible CNC incremental sheet forming: process evaluation and simulation. Institute of Materials Technology/Precision Forming (LWP), Saarland University, Germany, p 12
11. Hussain G, Gao L (2007) A novel method to test the thinning limits of sheet metals in negative incremental forming. *Int J Mach Tools Manuf* 419–435
12. Ambrogio G et al (2005) Application of Incremental Forming process for high customised medical product manufacturing. *J Mater Process Technol* 156–162
13. Hussain G et al (2009) A new formability indicator in single point incremental forming. *J Mater Process Technol* 4237–4242
14. Dufloy JR et al (2008) Process window enhancement for single point incremental forming through multi-step tool paths. *CIRP Ann Manuf Technol* 253–256
15. Hussain G et al (2007) A comparative study on the forming limits of an aluminum sheet-metal in negative incremental forming. *J Mater Process Technol* 94–98
16. Kopac J, Kampus Z (2005) Incremental sheet metal forming on CNC milling machine-tool. *J Mater Process Technol* 622–628 (University of Ljubljana, Slovenia)

Modeling of Support Vector Mechanism for Green Manufacturability Quantification of Production



T. Sathish

Abstract Awareness of consumers toward the environment as well as sustainability is increasing, which is forcing the industry to face the challenge of balancing economic and fiscal needs against ecological and social accountabilities. New strategies and procedures are being created to provide food these difficulties in a productive way. This work aims to develop a roadmap to convert a unit manufacturing process more 'green' by minimizing resource utilization. Various control strategies using SVM algorithm have evaluated, implemented in a numerical simulation mode. The experimental data suggested significant improvement on the Green Index of the process.

Keywords Green manufacturing · Simulation · SVM algorithm · Surface grinding

1 Introduction

Consideration regarding manageability is developing in today's industry. Green generation is utilized to address a supportable point of view, and lean goes about as a wellspring of achieving manageability. Lean and green generation frameworks require green use of assets and effective creation.

In today's world, organizations from different fields are managing ecological commitments. In the previous decades un-went before development in economy, population and industrialization expand the utilization of common assets. Since the most recent decade, corporate organizations are getting inspired by natural insurance and clients are requesting condition neighborly items (Noah, V. also, Bradley, W). Businesses attempt to diminish the usage of asset to counteract condition. The results of creation squander on the atmosphere were depicted in a report by the Intergovernmental Panel on Climate Change (IPCC) as:

T. Sathish (✉)
Vesta Research Institute, Aranthangi, Tamil Nadu, India
e-mail: sathish.sailer@gmail.com

© Springer Nature Singapore Pte Ltd. 2019
S. S. Hiremath et al. (eds.), *Advances in Manufacturing Technology*,
Lecture Notes in Mechanical Engineering,
https://doi.org/10.1007/978-981-13-6374-0_45

391

The effect on situations including mechanical and business is more extreme and distinctive. Key Performance Indicator (KPI) have been actualized generally with business forms; anyway little has been done in the territory of creation process administration. Chosen KPI can recognize wanted region to improve the execution. Despite the fact that green generation procedure is picking up notoriety in assembling ventures, the vast majority of the pros in the industry do not have real information of what is green creation and its structures are—the manner by which to recognize the accepted procedures of a green generation strategy.

2 Quantifying Green Manufacturability of a Unit Production Process Based on SVM

Assembling is the motor that drives industrialized progression, and supportability is a standout among the most imperative late assembling contemplations. Specialists and industry consider manageability of assembling forms as indispensable test monetarily practical, sheltered and sound routes for representatives, networks, and shoppers and which are socially and inventively remunerating for all partners for the short and long haul future.

Green manufacturing is among the key components that fall under the all-encompassing umbrella of maintainability. Green assembling manages to keep up ecological, financial, and social goals of manageability in the assembling space. A few cases of reasonable green assembling exercises are decreasing dangerous discharges, killing inefficient assets utilization, and reusing. Assembling is the real section for modern vitality utilization and mechanical contamination. It is responsible for 84% of vitality-related industry CO₂ emanations and furthermore devours 90% of industry vitality.

From frameworks' perspective of assembling, fabricating exercises are considered being made out of different levels, from an essential level (unit process) to that of the whole endeavor, including each and every one of the exercises in the assembling framework. Dufrou et al. characterize single-machine instruments as the smallest unit, of which creation frameworks are made of every unit procedure interfaces with other unit forms and the ecosphere through its limits.

2.1 Green Manufacturing in Grinding Process

As of late, there has been an extensive research in green assembling in the field of granulating forms.

Among the machining forms, crushing requires amazingly higher energies to expel a particular material volume when contrasted with other ordinary machining forms like turning, processing, and so on. The primary purpose behind this is the high measure of rubbing and furrowing activities happening as a result of an extensive number of bleeding edges, or rough cornmeal. Hashimoto, by concentrating the vitality utilization for pounding utilizing distinctive chip thicknesses, and for hard turning a similar sort of work pieces, found that grating procedures like crushing outcome in higher vitality utilization.

Moreover, water-based crushing liquid is generally utilized for grease to enhance granulating proficiency, cooling, and cleaning. Constituents of regular crushing liquid are bases of chlorine, sulfur, and phosphorus, which are harmful and furthermore cause ecological contamination. Additionally, usage of crushing liquids results in high expenses. For instance, in a few vehicle creations, 15–30% of the machining that costs for a car fabricate is identified with the utilization of crushing liquid. Additionally, the conveyance and cleaning of liquids need a high measure of vitality. It has been watched that in specific situations, up to 32% of the aggregate vitality utilization of an assembling plant has been ascribed to cutting liquids, and it is considerably higher when cooling-related assistants, for example, fog authorities, are incorporated. Scientists have chipped away at elective (naturally considerate) cutting liquid, for instance, Winter et al. built up an approach which was connected in a pounding case proposing water miscible polymer weakening as a better option over non-miscible mixable granulating oil. Winter et al. have characterized producing forms as a unit procedure.

We chose pounding as unit fabricating forms for this examination and accentuated on the previously mentioned features of greenness utilizing the unit procedure.

Least amount grease is a method that uses a shower of little oil droplets in a packed air fly. The grease is splashed straightforwardly into the cutting zone, as a trade for the colossal streams of traditional surge coolant. Since the air fly conveys the oil beads straightforwardly in the cutting zone, it gives proficient oil. Anyway, extraordinary setup and courses of action are required when customary surge coolant is utilized as a part of request to enable the liquid to enter the cutting zone productively. Scientists have exhibited MQL as one of the noticeable systems for green assembling. For example, Sadeghi and Haddad dissected utilizing the trial information that in pounding of Ti6Al4V, better crushing execution is given by MQL strategy when contrasted with traditional oil techniques.

MQL liquid application technique is contrasted MQL has different strategies in this work.4.4. Reproduction in assembling numerous systems that utilization recreation emphases have been grown for finding ideal answers for mind-boggling, and troublesome improvement issues that developed in the field of building, and administration.

The SVM has considered a machine learning algorithm for the classification of two-class problems. The training of support vector machines with the positive and negative types of data is known as one-against-all or one-against-rest. The two-class type SVM is combined for creating a multi-class support vector machine. The classification by this algorithm is represented as in Eq. (2) [16].

$$F(\theta) = \text{sgn} \left[\left(\sum_{j=1}^n \gamma_j x_j \tau(\theta, \theta_j) + b \right) \right] \quad (1)$$

In (1), γ_j is the Lagrange multiplier, θ_j and x_j are the dimensional vectors of the two associated classes, and $\tau(\theta, \theta_j)$ is the Kernel function. The numerical difficulties of this method are eliminated using Kernel function.

In this SVM, we utilize the vector for Pr—the training process in which the spam reviews are identified. This vector contains the optimally selected feature subset. The following equation is the SVM's objective function which may identify the support vector for the classification.

$$\text{Out} = \sum_i \omega_i * K(s_i, \text{Pr}) + b_i \quad (2)$$

where s_i is the support vectors; ω is the weight; b is the bias value; Pr is the vector for classification; and K is the Kernel function.

In our proposed system, the SVM output value 'out' for a review will arise between 0 and 2, in which if these values are below or equal to 1 (≤ 1) it is considered as harm review otherwise spam review, i.e., above 1 (> 1).

After evaluating SVM, it may make some error which is reduced by using the formulas given below.

$$\arg \min \text{Pt} \sum_{x=0}^{n'_s-1} \nu_x + 0.5\lambda^T \cdot \lambda \text{ if, } \text{cl}_x(\lambda^T k(\hat{\text{pr}}_x) + c) \geq 1 - \nu_x \text{ else } \nu_x \geq 0 \quad (3)$$

where 'pt' is penalty constant, ' ν ' is a parameter that handles the data, ' λ ' is a matrix of coefficients, cl_x is the class label of the x th dataset, c is the constant, and k is the kernel that transforms the input data to the feature space. Hence, by minimizing the error function, the SVM learns the training dataset $\hat{\text{pr}}$ well and so that it can classify the vector that is similar to the training set. Once the errors are minimized to a minimum value, we obtain the spam review separately.

3 Results and Discussion

Green manufacturing is among the key components that fall under the all-encompassing umbrella of supportability. Green assembling manages to keep up ecological, monetary, and social targets of maintainability in the assembling space. A few cases of practical green assembling exercises are lessening risky emanations, taking out inefficient assets utilization, and reusing. Assembling is the significant portion for mechanical vitality utilization and modern contamination. It is respon-

sible for 84% of vitality-related industry CO₂ discharges and furthermore expands 90% of industry vitality.

Unit fabricating process chose here is surface granulating. Info factors chosen are depth of cut (DOC) and table speed (V_w) under three diverse cooling mediums, viz. dry, surge, and MQL. Yield factors estimated are distracting power (F_t), typical power (F_n), and surface unpleasantness (R_a). The estimations of F_t , and F_n are estimated by Web-based observing framework, and surface unpleasantness (R_a) is estimated utilizing Surtronic surface profiler after each trial. Workpiece utilized for the experimentation is titanium amalgam (Ti6Al4V) that has wide application in producing airships. Workpiece of the measurement 160 mm × 25 mm × 5 mm is mounted over MS plate estimating 179 mm × 60 mm × 16 mm is mounted specifically on to the dynamometer with the assistance of screws. MS plate is utilized to dodge warm mutilation of the dynamometer. Aluminum rough crushing wheel with particulars A46J5V10 is utilized. The crushing powers were estimated with the assistance of KISTLER Piezo-electric dynamometer, type 9257A, and the information

Table 1 Unit manufacturing cutting conditions

Parameter	Value
Grinding wheel speed	20 m/s
Depth of cut (DOC)	6, 10, and 14 μm
Table speed (V_m)	5, 10, and 15 m/min
Grinding wheel	A46J5V10
Coolant flow rate	4.5 l/min
MQL flow rate	80 ml/h

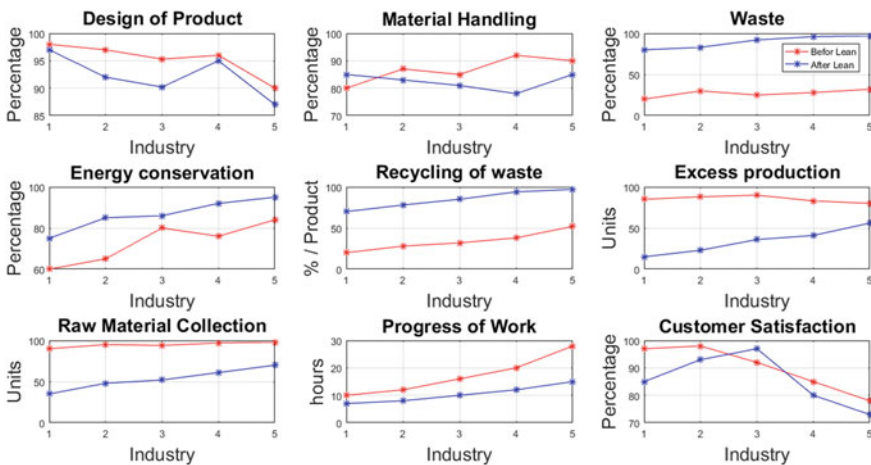


Fig. 1 Performance comparison

is put away and displayed by utilizing MATLAB programming, according to the application prerequisite.

The full factorial test plan for all blend of parameters esteems is considered for the present case, with 3 levels of profundity of cut and 3 levels of table speed under 3 different ways (dry, surge, and MQL) of liquid application. Altogether, there are 27 ($3 \times 3 \times 3$) arrangements of examinations. Cutting conditions chose for this unit-producing process are given in Table 1.

Granulating wheel mounting, adjusting, and arrangement, spouts stream rates, dynamometer yield, surface unpleasantness profiler were altogether aligned before beginning the tests (Fig. 1).

4 Conclusion

Consumer mindfulness toward condition and manageability is on the ascent, which is constraining the industry to confront the test of adjusting financial and fiscal needs against natural and social accountabilities. New strategies and systems are being created to cook these difficulties in a proficient way. This work plans to build up a guide to change over a unit-producing process more 'green' by limiting asset use. Live research center examinations were directed to demonstrate different variables affecting the 'greenness' of the unit procedure which was surface pounding. We assessed different control methodologies (factor settings) utilizing SVM calculation, executed in a numerical reproduction mode. The trial information proposed a noteworthy change on the Green Index of the procedure.

References

1. Anon. (2007a) IT performance management group (ITPMG). Developing an IT Performance Management Program. Bethel, Connecticut
2. Anon. (2007b) IT performance management group (ITPMG). Initiating an IT Performance Management Program. Bethel, Connecticut
3. Anon. (2009) Permalink. Why use key performance indicators (KPI)?
4. Balan K (2008) Introduction to green manufacturing. *Shot Peener* 22(3):4–6
5. Bryman A (2001) *Social research methods*, 2 edn. Oxford University Press, Oxford
6. Bryman A (2007) *Business research methods*, 2 edn. Oxford University Press, Oxford
7. Creswell using mixed-methods sequential explanatory design: from theory to practice field methods (Feb 2006)
8. Dornfeld. Green issues in manufacturing—greening processes, systems and products. Laboratory for Manufacturing and Sustainability
9. Environmental Management System (EMS). International Institute for Environment and Development (IIED)
10. Environmental Protection Agency. The U.S. environmental protection agency's design for the environment program: partnerships for a cleaner future (4 Mar 2011)
11. Environmental Protection Agency. Design for the environment projects (4 Mar 2011)
12. Environmental Protection Agency. Environmental management system tools: a reference guide

13. Friend G (2009) *The truth about green business*. Ft Press, Upper Saddle River, New Jersey
14. Gummesson E (2000) *Qualitative method in management research*. SAGE Publications Inc, Thousand Oaks
15. Hosseini A (2007) Identification of green management system's factors—a conceptualized model 2
16. Karthick S (2017) Semi supervised hierarchy forest clustering and KNN based metric learning technique for machine learning system. *J Adv Res Dyn Control Syst* 9(1):2679–2690
17. Revelle C (2000) Research challenges in environmental management: a invited review. *Eur J Oper Res*

Experimental Study on Surface Roughness and Optimization of Process Parameters Using ANN-GA in Milling of Super-Duplex Stainless Steel Under Dry and Wet Conditions



Soumya Sambhedana, N. Subhash, P. Nithin Raj and T. Jagadeesha

Abstract Duplex stainless steel (DSS) 2507, also called super-duplex stainless steel (SDSS), is one of the newest members of the modern duplex family. Owing to the high levels of its various constituent alloying elements, DSS SAF 2507 exhibits an exceptional combination of high mechanical strength, high toughness, high corrosion resistance and superior resistance to chloride pitting. However, the high levels of alloying render it a very poor machinability. This study discusses machinability of SDSS SAF 2507 for milling operation under a range of machining parameters. The temperature generated during milling is studied for both dry and wet conditions. Area surface roughness of the milled surface is also measured under varying cutting speeds and feed rates. Predictive models are developed using two approaches that are Response Surface Methodology (RSM) and Artificial Neural Networks (ANNs). Optimization of the cutting parameters to obtain maximum surface finish is done using Genetic Algorithm (GA). From the analysis, it is observed that feed rate has the most significant effect.

Keywords Super-duplex stainless steel · Milling · Temperature · Surface roughness · Optimization

1 Introduction

In search of more corrosion-resistant and mechanically superior materials for highly aggressive environments such as hot chlorinated sea water and highly acidic, chloride-containing media, DSSs have emerged as the best-suited materials. DSS 2507 (ASME Standard A240—UNS S32750) is a highly alloyed super-duplex stainless steel having high tensile strength, high fatigue strength, high toughness, high critical pitting temperature, corrosion resistance which sets it apart from other gen-

S. Sambhedana · N. Subhash · P. Nithin Raj · T. Jagadeesha (✉)
Department of Mechanical Engineering, National Institute of Technology Calicut, Calicut
673601, India
e-mail: jagdishsg@nitc.ac.in

© Springer Nature Singapore Pte Ltd. 2019
S. S. Hiremath et al. (eds.), *Advances in Manufacturing Technology*,
Lecture Notes in Mechanical Engineering,
https://doi.org/10.1007/978-981-13-6374-0_46

erations of DSSs. Hence, it is used in high-end applications such as desalination equipment, chemical industries, pressure vessels, piping and heat exchangers, tropical marine usages, offshore oil and gas exploration and petrochemical processing.

Due to the dual-phase microstructure, DSSs showcase a combination of both austenitic and ferritic properties. The superior chemical and mechanical properties are due to high amounts of alloying elements in DSS 2507. But the increased alloying also results in the worst machinability amongst all high-performing materials, and consequently results in a shorter tool life. Also, sulphur content is kept low in the material composition to aid in corrosion resistance, which further impairs the machinability.

Since milling is one of the most important operations when it comes to applications of DSS 2507, there is a need to study the effects of various machining conditions in the milling operation. Sai et al. [1] analysed microstructure, microhardness and surface roughness in relation to different parameters. They noted that a high value of cutting speed combined with small value of feed improves the machined surface quality. To minimize the surface roughness and cutting force in turning of DSS 2205, Thiyagu et al. [2] used Box–Behnken design (BBD) and RSM for design of experiments and optimization and found that feed rate and cutting speed influenced the roughness the most. Selvaraj et al. [3] conducted dry end milling experiments on DSS with three spindle speeds, feeds and depth of cut and used BBD and RSM to study their effects on surface roughness. They verified the developed model using analysis of variance (ANOVA). It was found from the prediction equation that feed rate has the highest influence on surface finish. To find the optimal measuring strategy that will minimize the pollution generated due to the use of cutting fluids, Krolczyk et al. [4] carried out turning experiments in dry and wet conditions and measured roughness, force and tool life. The results demonstrated that dry conditions yielded much better tool life than cooling conditions. In their dry turning experiments on two different grades of nitrogen-alloyed DSS, Selvaraj et al. [5] optimized the cutting parameters using signal-to-noise ratio (SNR) and ANOVA. They studied the effect of speed and feed on roughness, cutting force and tool wear by conducting turning operations and concluded that cutting speed influenced the tool wear the most. To obtain long tool life, high productivity and low surface roughness, Gamarra and Diniz [6] carried out turning experiments of SDSS 2507. For developing the best combination of machining strategies, tool geometries and feeds, they tested and deduced that while longitudinal machining at a low feed rate with the use of conventional insert resulted in longest tool life and low surface roughness, taper turning did not improve the tool life.

Temperature plays a very important role in machining of DSSs, since exposure to elevated temperatures induces the formation of some intermetallic phases like sigma phase and gamma phase that are detrimental to the material properties. Along with this, exposure to high temperatures also decreases the corrosion resistance and toughness of DSSs. It is observed from the literature review that not much studies have been conducted earlier on cutting temperature generated during milling of DSS 2507 and its effect on the surface properties and tool life. In the present work, an attempt has been made to investigate the influence of various cutting conditions such as cutting speed, feed rate and use of coolants on the temperature generated and

its effect on surface properties. Along with temperature, the area surface roughness is also measured under a range of cutting parameters. This paper also presents an approach to determine optimum values of machining parameters in order to obtain maximum surface finish by Genetic Algorithm. Predictive models are developed using Artificial Neural Networks approach as well as Response Surface Methodology and the results from both the models are compared with the experimental results.

2 Experimental Procedure

This section presents the material properties of DSS SAF 2507, the course of plan to carry out the milling tests for measuring temperature and measurement and optimization of surface roughness.

2.1 Material Properties of DSS SAF 2507

Super-duplex stainless steel 2507 is highly alloyed to improve both mechanical and metallurgical properties. Table 1 clearly shows that the levels of alloying elements such as Ni, Cr and Mo are quite high, sulphur content is low, and there is a small trace of nitrogen in the material composition, whose combined result is the poor machinability of DSSs. Table 2 shows the mechanical properties of the material.

2.2 Milling Experiments

The milling experiments were conducted on a CNC 4-axis vertical machining centre (Agni BMV45 TC24) having maximum spindle speed of 6000 rpm and control system FANUC OiMC. A DSS 2507 block of dimensions 140 mm × 60 mm × 10 mm is used as the workpiece. Milling was carried out for a range of different cutting parameters for both wet and dry conditions using a WIDIA-made milling

Table 1 Chemical composition of DSS SAF 2507 [5]

Alloy	Cr	Ni	Mo	Mn	C	Si	S	N
Percentage by weight	25.1	6.77	3.68	0.74	0.02	0.23	0.01	0.3

Table 2 Mechanical properties of DSS SAF 2507 [5]

UTS (MPa)	Yield (MPa)	Hardness HV _{100 g}
866	570	285

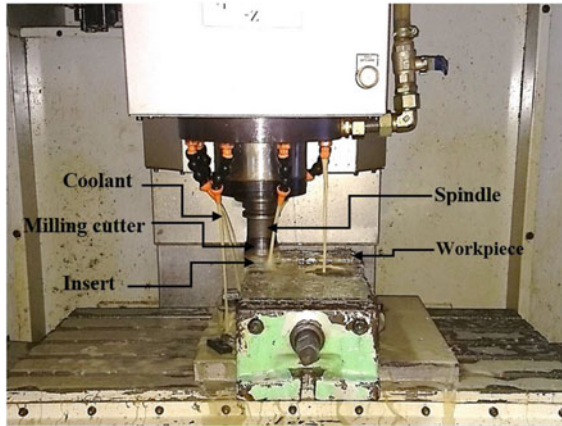


Fig. 1 Experimental set-up

carbide insert of ISO SDMT 1204PDRML WS40PM grade (PVD coating on an advanced alloyed substrate). The cutter used is WIDAX M690 having a diameter of 63 mm, which holds five cutting inserts. All the experiments were planned with a constant depth of cut of 0.5 mm and three levels of cutting speed that are 60, 80 and 100 m/min and three levels of feed rate that are 0.05, 0.1 and 0.15 mm/tooth ($3^2 = 9$ experiments each for wet and dry conditions). During wet machining conditions, cutting fluid used was SAVO-Cut soluble cutting oil (SCO). The experimental set-up for the milling experiments is shown in Fig. 1.

3 Results and Discussions

3.1 Temperature Measurement

The temperature measurement was done using thermal imaging Fluke Ti400 infrared camera (as shown in Fig. 2) by taking an emissivity of 0.7.

It is observed that for a particular feed and depth of cut, as the cutting speed is increased, the temperature generated increased significantly (Fig. 3). Apart from that, it is seen that the temperature also increases with increasing feed rate at a given cutting speed and depth of cut. It can be seen that the increase is not so pronounced at lower cutting speeds but it is significant at higher cutting speeds. Also, with the use of cutting fluid, there was a noticeable reduction in the temperature.

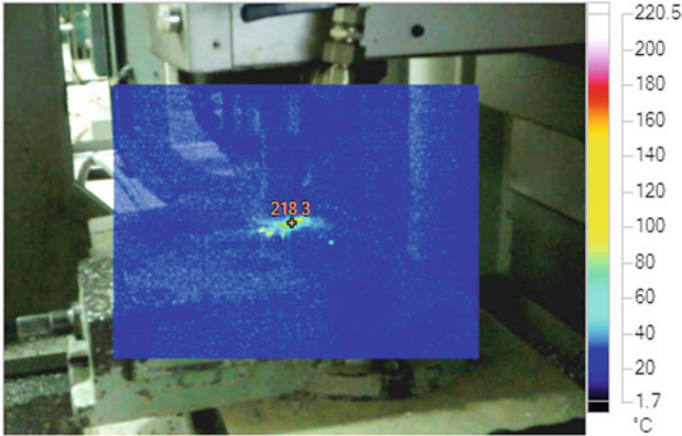


Fig. 2 Developed thermal image from Fluke Ti400 software for cutting speed 100 m/min, feed rate 0.15 mm/tooth and depth of cut 0.5 mm under wet condition

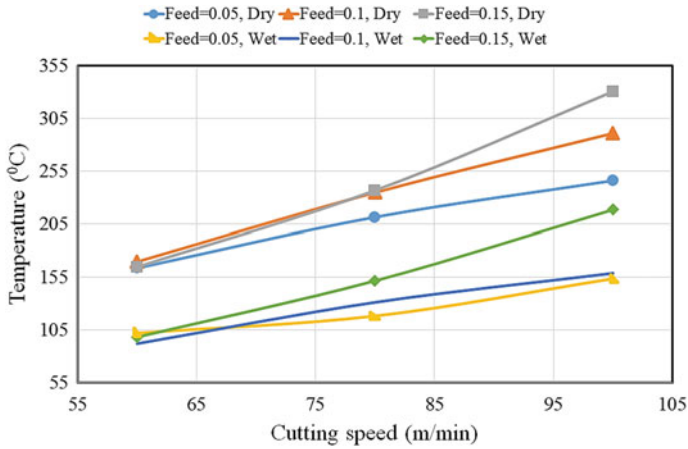


Fig. 3 Variation of cutting temperature with respect to cutting speed and feed rate for a constant depth of cut of 0.5 mm

3.2 Measurement of Surface Roughness

The area surface roughness (S_a) was measured using Alicona InfiniteFocus non-contact optical 3D surface roughness measurement machine (focus variation-based measurement principle), and 3D area roughness profiles obtained under various magnifications are shown (Fig. 4).

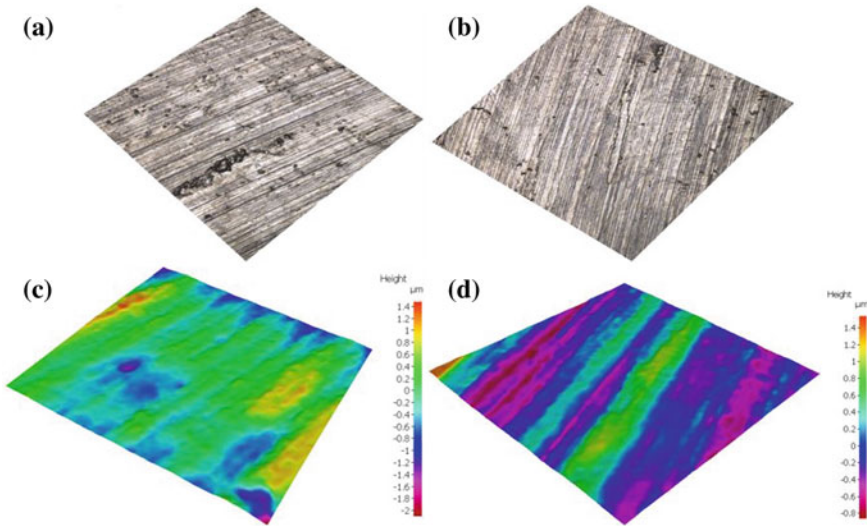


Fig. 4 3D Alicona surface roughness images for cutting speed 60 m/min, feed rate 0.15 mm/tooth and depth of cut 0.5 mm for **a** dry condition 10×, **b** wet condition 10×, **c** dry condition 100×, **d** wet condition 100×

3.3 Optimization of Cutting Parameters

Two approaches to develop the predictive models have been used to analyse the results of the surface roughness. The first predictive model is RSM done using Minitab software. Prediction equations are generated for both wet and dry conditions. The second approach for development of the prediction model is ANN. An evolutionary technique of GA is used to obtain the optimum values of the cutting speed and feed.

Response Surface Methodology

RSM technique, one of the popular statistical approaches, is used in developing the predictive model to fit the corresponding surface response design [7]. The regression equations are generated for both dry and wet conditions which give the relation between the independent variables (cutting speed and feed rate) and the dependent variable (surface roughness).

$$\begin{aligned}
 Sa_{dry} = & -0.18 + (0.0217 * \text{Cutting speed}) + (6.89 * \text{Feed}) \\
 & -(0.000144 * \text{Cutting Speed} * \text{Cutting Speed}) \\
 & -(15.2 * \text{Feed} * \text{Feed}) - (0.0217 * \text{Cutting speed} * \text{Feed}) \quad (1)
 \end{aligned}$$

$$\begin{aligned}
 Sa_{wet} = & -0.501 + (0.03584 * \text{Cutting speed}) + (3.20 * \text{Feed}) \\
 & -(0.000232 * \text{Cutting speed} * \text{Cutting speed}) \\
 & -(16.07 * \text{Feed} * \text{Feed}) - (0.0125 * \text{Cutting speed} * \text{Feed}) \quad (2)
 \end{aligned}$$

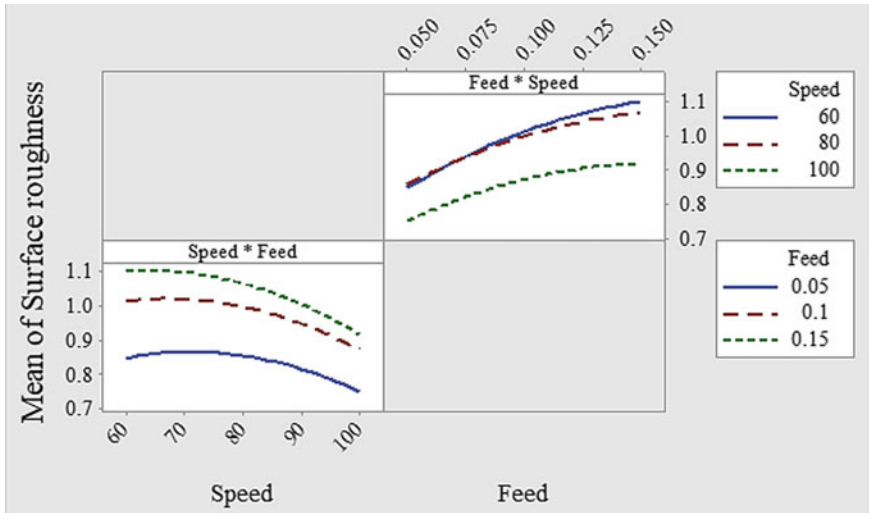


Fig. 5 Interaction plot for dry machining

It can be observed from the above two equations that coefficient of square of the feed rate (16.07) is the largest compared to all other coefficients, which means Sa value is affected the most by feed rate. Also, coefficient of cutting speed is almost approaching to zero which shows that surface roughness is not much affected by cutting speed.

The interaction plot given in Figs. 5 and 6 shows the variation in area surface roughness with respect to cutting speed at various feed rates and the variation with respect to feed rate at various cutting speeds for dry and wet machining conditions, respectively.

It is observed that in both dry and wet machining, surface finish is better at high cutting speeds combined with low feed rates. From the surface plots (Fig. 7), it is observed that the Sa value increases with increase in feed rate at a constant cutting speed and depth of cut. The reason for this effect maybe that, as the feed rate increases, the contact area between the insert and the material increases, which in turn increases the force and hence there is an increase in the area surface roughness [8]. It is also observed that for a constant feed rate, there is a slight increase in the Sa value up to a certain cutting speed and then it decreases, which may be due to the formation of built-up edge up to a particular speed. However, there is no built-up edge formation at higher speeds because of faster chip removal. From the graphs, it is also seen that there is reduction in Sa values in wet machining when compared to dry machining because the entry of cutting fluid particles in the chip–tool interface prevents abrasion wear as well as built-up edge formation.

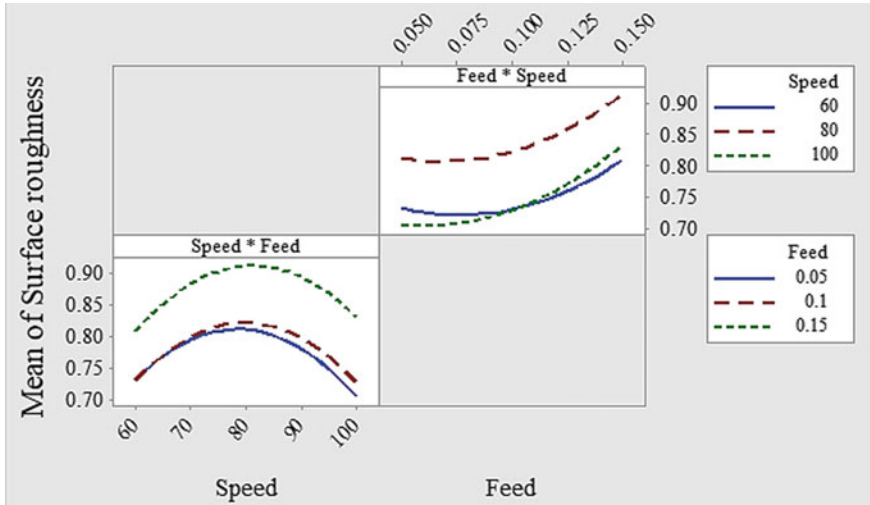


Fig. 6 Interaction plot for wet machining

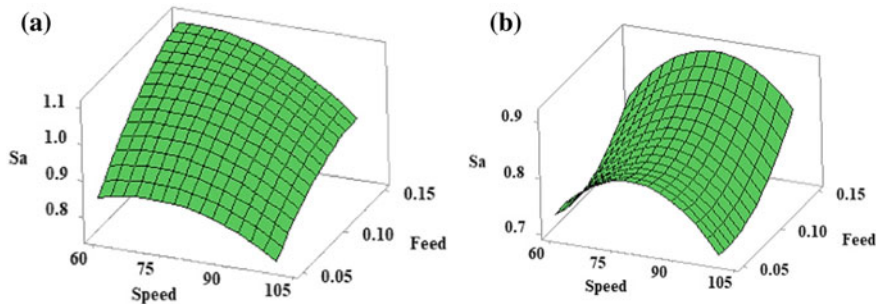


Fig. 7 Surface plot for a dry and b wet machining

Artificial Neural Network

ANNs are one of the most well-known computing systems that are inspired by the biological neural networks. The neural networks toolbox in MATLAB is used to formulate the ANN. A number of models were designed and tested to obtain the optimal architecture, best-suited activation function and training algorithm. For prediction and selection of the regression coefficient (R) values of the trained models, the mean squared error (MSE) criterion was used. The Levenberg–Marquardt (LM) algorithms which are one of the fast and less memory consuming algorithms were used as the training function to train the algorithm. The tansig (hyperbolic tangent sigmoid) transfer function is used in both hidden and output layers. LEARNNGDM function was used as the learning function which minimizes the total mean square error of the computed output by gradient descent with momentum weight and bias

method [9]. A feed-forward neural network with single hidden layer consisting of eight neurons was found to be the best.

The results showed a regression coefficient of 0.9983 and 0.9962 for dry and wet conditions, respectively. Both values are close to 1 which indicates that network outputs are strongly correlated with experimental values. The network is tested for all values from experiment.

Comparison Between RSM and ANN

After the development of the prediction models using both ANN and RSM techniques, the predicted responses of both the approaches are compared and validated with experimental values. The absolute prediction errors between the experimental and predicted values are also calculated by using the given formula.

$$\text{Error}(\%) = [(\text{Practical value} - \text{Fitted value}) / \text{Practical value}] \times 100 \quad (3)$$

It was found from the validation and comparison results that for both RSM and ANN approaches, the absolute prediction errors are quite low. But when compared to RSM, the error percentages in ANN technique are much lower, which proves that ANN is a better prediction model.

The validation of the two models and their capabilities can also be seen in the comparative plots shown in Figs. 8 and 9. The close proximity between all the three curves for most of the experimental data set shows that the predicted values obtained

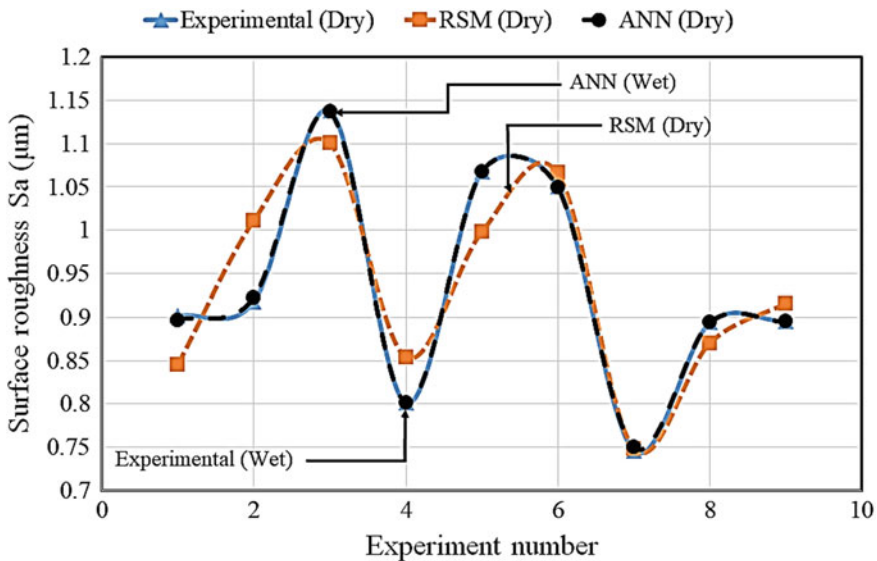


Fig. 8 Comparative plot showing the closeness of the experimental values with the values predicted by RMS and ANN models for dry machining

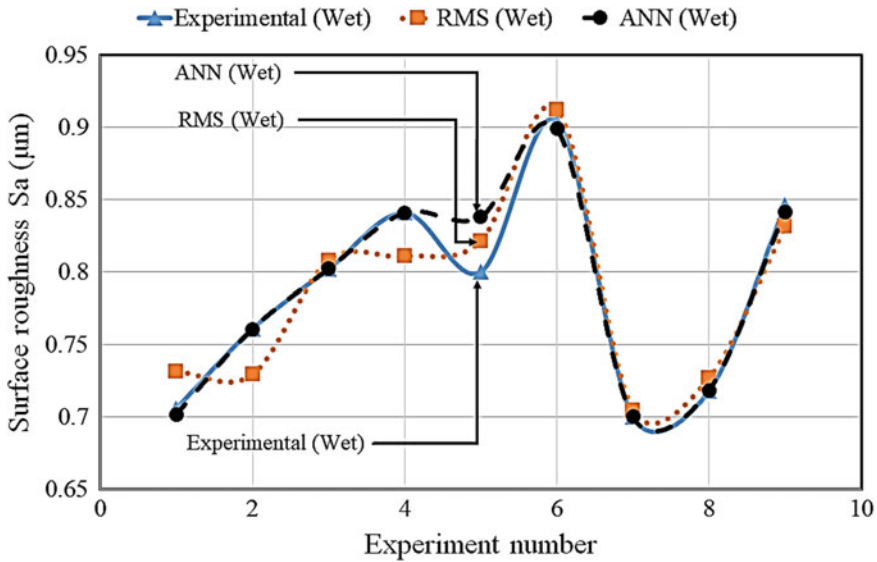


Fig. 9 Comparative plot showing the closeness of the experimental values with the values predicted by RMS and ANN models for wet machining

from the models agree nicely with the experimental values. However, the ANN curve shows a much greater agreement with the experimental curve.

Optimization Using Genetic Algorithm

Of all the optimization algorithms, GA is one of the very popular evolutionary optimizing approaches. In the present study, the optimization problem is to minimize the area surface roughness. The final optimization results generated in GA give the optimum value of objective function (S_a) as $0.748 \mu\text{m}$ in dry and $0.703 \mu\text{m}$ in wet machining. The corresponding optimized values of the constraints are as follows: cutting speed 100 m/min for both dry and wet machining and feed rate 0.05 mm/tooth and 0.06 mm/tooth for dry and wet conditions, respectively. Hence, it can be deduced from the modelling and optimization procedure that a higher cutting speed combined with lower feed rate yields the best surface finish. And the use of coolant (wet condition) shows a significant decrease in the area surface roughness.

4 Conclusions

Milling experiments were carried out on DSS SAF 2507 under both dry and wet machining conditions for a range of cutting parameters. Some of the conclusions which can be drawn from this study are:

- Feed rate showed the most significant effect on area surface finish.
- ANN technique showed more efficiency in predicting the roughness values as compared to RSM.
- Optimization results showed that the combination of high cutting speed and low feed rate yielded a better surface finish.
- With increase in cutting speed, there was a significant increase in the temperature generated.

Acknowledgements We would like to thank Department of Science and Technology (DST), Govt. of India, and Centre for Precision Measurements and Nanomechanical Testing, Department of Mechanical Engineering, National Institute of Technology Calicut, for providing us the facility purchased under the scheme FIST—No. SR/FST/ETI-388/2015.

References

1. Sai WB, Salah NB, Lebrun JL (2001) Influence of machining by finishing milling on surface characteristics. *Int J Mach Tool Manuf* 41:443–450
2. Thiyagu M, Karunamoorthy L, Arunkumar N (2014) Experimental studies in machining duplex stainless steel using response surface methodology. *Int J Mech Mechatron Eng IJMME-IJENS* 14:48–61
3. Selvaraj DP, Chandramohan P, Rajesh PK (2015) Prediction of surface roughness in end milling operation of duplex stainless steel using response surface methodology. *J Eng Sci Technol* 10(3):340–352
4. Krolczyk GM, Nieslony P, Maruda RW, Wojciechowski S (2017) Dry cutting effect in turning of duplex stainless steel as a key factor in clean production. *J Clean Prod* 142:3343–3354
5. Selvaraj DP, Chandramohan P, Mohanraj M (2014) Optimization of surface roughness, cutting force and tool wear of nitrogen alloyed duplex stainless steel in a dry turning process using Taguchi method. *Measurement* 49:205–221
6. Gamarra JR, Diniz AE (2018) Taper turning of super duplex stainless steel: tool life, tool wear and workpiece surface roughness. *J Braz Soc Mech Sci Eng* 40:39
7. Sahoo AK, Sahoo B (2013) Performance studies of multilayer hard surface coatings (TiN/TiCN/Al₂O₃/TiN) of indexable carbide inserts in hard machining: part-II (RSM, grey relational and techno economical approach). *Measurement* 46:2368–2884
8. Airao J, Chaudhary B, Bajpai V, Khanna N (2018) An experimental study of surface roughness variation in end milling of super duplex 2507 stainless steel. *Mater Today Proc* 5:3682–3689
9. Sangwan KS, Saxena S, Kant G (2015) Optimization of machining parameters to minimize surface roughness using integrated ANN-GA approach. *Procedia CIRP* 29:305–310

Experimental Study on Tool Wear and Optimization of Process Parameters Using ANN-GA in Turning of Super-Duplex Stainless Steel Under Dry and Wet Conditions



N. Subhash, Soumya Sambedana, P. Nithin Raj and T. Jagadeesha

Abstract Super-duplex stainless steels (SDSSs), the second generation duplex stainless steels (DSSs), provide an excellent combination of high mechanical strength, high toughness, and good corrosion resistance. However, due to high levels of various alloying elements, machinability of SDSSs is very poor. In this study, machinability of SDSS SAF 2507 is discussed for turning operation under varying machining conditions. Temperature is measured for a range of cutting speeds under both dry and wet conditions. The techniques of response surface methodology (RSM) and artificial neural network (ANN) are used to obtain and compare predictive models for surface roughness. Optimization of cutting parameters is done using Genetic Algorithm (GA) to obtain maximum surface finish. From the results obtained, feed rate was found to be the most significant factor for surface roughness. Flank wear is studied after a fixed time of turning for various cutting speeds, and it was seen that it increased significantly with increase in cutting speed.

Keywords Super-duplex stainless steel · Turning · Surface roughness · Temperature · Optimization

1 Introduction

As the offshore oil and gas industry is moving further deeper into the waters, there is a growing need for stronger, lighter, and more corrosion-resistant materials. Super-duplex stainless steels are one of the newest groups of austenitic ferritic steels which provide an excellent combination of good corrosion resistance, high mechanical strength, high toughness, and ease of fabrication. Owing to such superior properties, they claim to be an attractive alternative to other high-performing materials such as super-austenitic stainless steels and nickel-based alloys. Hence, their implementation

N. Subhash · S. Sambedana · P. Nithin Raj · T. Jagadeesha (✉)
Department of Mechanical Engineering, National Institute of Technology Calicut, Calicut
673601, India
e-mail: jagdishsg@nitc.ac.in

© Springer Nature Singapore Pte Ltd. 2019
S. S. Hiremath et al. (eds.), *Advances in Manufacturing Technology*,
Lecture Notes in Mechanical Engineering,
https://doi.org/10.1007/978-981-13-6374-0_47

varies from refineries, chemical industries, oil and gas industries, marine applications to architecture and civil engineering industries.

The term duplex denotes the two-phase microstructure of DSSs with nearly equal proportions of ferrite and austenite. Due to high level of chromium, nickel, and molybdenum, they showcase high corrosion resistance and pitting resistance equivalent (PRE). However, increasing the content of these alloying elements (particularly nitrogen) correspondingly decreases the machinability. To preserve the corrosion resistance, the sulfur content is kept very low which further reduces the machinability. Also higher is the PRE, lower is the alloy's machinability. Therefore, faster tool wear and higher cutting temperatures are typically seen in machining super-duplex stainless steels. In addition to this, properties like high mechanical strength, high fracture toughness, high ductility, high hardening rate, and low thermal conductivity also impair the machinability.

The problem of poor machinability and shorter tool life necessitates the need of finding the best combination of cutting strategies carried out with the most suitable cutting tool insert. Gamarra and Diniz [1] adopted two types of machining (longitudinal and taper cutting) with two indexable insert geometries (conventional and wiper) and different feeds for turning of SDSS SAF 2507. Use of conventional insert in longitudinal cutting with low feed rate showed the longest tool life with low roughness value. In their comparative machinability tests conducted on duplex alloys SAF 2205 and SAF 2507, Nomani et al. [2] found both the duplex alloys displayed poorer machinability responses, with 2507 being worst. DSS 2507 yielded higher cutting force and poorer surface finish. Selvaraj et al. [3] tried to optimize the dry turning parameters of DSS 2507 grade 5A and grade 4A by using Taguchi method. The experiments were conducted using TiC- and TiCN-coated carbide cutting tool inserts. It was found that feed rate influenced the surface roughness and cutting force the most. Cutting speed was the more significant parameter influencing the tool wear. While investigating chip formation mechanism and machinability of wrought DSS alloys, SAF 2205 and SAF 2507, Nomani et al. [4] observed that the tool wear (TiAlN + TiN-coated solid carbide twist drill) was dominantly due to the adhesion process developed from BUE formation. To determine the tool life and the tool point surface topology of Al₂O₃-coated carbide tools, Krolczyk et al. [5] identified the wear mechanisms occurring on the rake face and major flank. Longer tool life and a greater resistance to abrasive wear were observed without the use of cooling lubricant. Application of cutting fluids is a must in machining of DSS, which also leads to negative environmental and health impacts. Hence, yet in another attempt, Krolczyk et al. [6] have identified the optimal machining strategy and condition to reduce pollution caused by coolants and emulsions.

In the studies conducted earlier, not much work has been done on cutting temperature generated during machining of DSS 2507 and its effect on the surface properties and tool life. Temperature plays quite an important role in machining of DSSs, as high temperatures have chances of inducing the creation of some intermetallic elements that degrade the chemical and mechanical properties of the material. In the present work, the main objective is to investigate the influence of cutting speed on the temperature generated and its effect on surface properties and tool life for both

dry and wet machining conditions. Apart from temperature, surface finish is also studied under a range of cutting speeds and feed rates and the cutting conditions are optimized using GA technique to minimize surface roughness. Tool flank wear is also measured at different cutting speeds for wet and dry turning.

2 Experimental Procedure

In this section, the details of material DSS SAF 2507, the course of plan to carry out the turning experiments for temperature measurement, flank wear study, and measurement and optimization of surface roughness are discussed.

2.1 Properties of DSS SAF 2507

Duplex stainless steel 2507 is highly alloyed in order to improve properties like corrosion resistance, mechanical strength, and toughness. It can be seen from Table 1 that the levels of alloying elements such as Ni, Cr, and Mo are high as well as levels of sulfur are low, resulting in poor machinability of the material. The mechanical properties of the material are given in Table 2.

2.2 Turning Experiments

The turning experiments were carried out on a CNC lathe (Jobber LM—Maximum spindle speed 4000 rpm and spindle motor power 5.5 kW). The workpiece used was a DSS 2507 round bar of 45 mm diameter and 250 mm length. Machining was done for different values of cutting parameters under both dry and wet conditions using an ISCAR-made carbide tool insert of ISO CNMG 120408TF IC6015 grade (coating-type CVD with coating layers TiCN + Al₂O₃ + TiN) which has a very hard substrate with cobalt-enriched outer layer and alpha-Al₂O₃ coating. The tool holder used for

Table 1 Chemical composition of DSS SAF 2507 [3]

Alloy	Cr	Ni	Mo	Mn	C	Si	S	N
Percentage by weight	25.1	6.77	3.68	0.74	0.02	0.23	0.01	0.3

Table 2 Mechanical properties of DSS SAF 2507 [3]

UTS (MPa)	Yield (MPa)	Hardness HV _{100g}
866	570	285

machining is DCLNL2525M12. The experiments for temperature measurement were performed with a constant feed rate and depth of cut which are 0.1 mm/rev and 1 mm, respectively, and five levels of cutting speed that are 40, 60, 80, 100, and 120 m/min. The surface roughness (R_a) was measured using Mitutoyo Profilometer SJ-410, and tests were carried out at three levels of cutting speed (60, 80, and 100 m/min) and three levels of feed rate (0.05, 0.1, and 0.15 mm/rev) at a constant depth of cut of 0.5 mm ($3^2 = 9$ experiments each for dry and wet machining). Tool flank wear was measured for machining tests done under a constant depth of cut of 0.5 mm and feed rate of 0.1 mm/rev and four levels of cutting speed (40, 60, 80, and 100 m/min). During the wet machining conditions, cutting fluid was applied on the cutting zone using a nozzle. The cutting fluid used was SAVO-Cut soluble cutting oil (SCO).

3 Results and Discussion

3.1 Temperature Measurement

The temperature was measured using thermal imaging Fluke Ti400 infrared camera (taking emissivity of 0.7). The thermal images and maximum temperature are obtained from Fluke software (Fig. 1), and it is observed that, as the cutting speed is increased for a particular feed and depth of cut, the temperature generated increased significantly, which is represented in the graph shown in Fig. 2. Also, with the use of cutting fluid, there was a noticeable reduction in temperature.

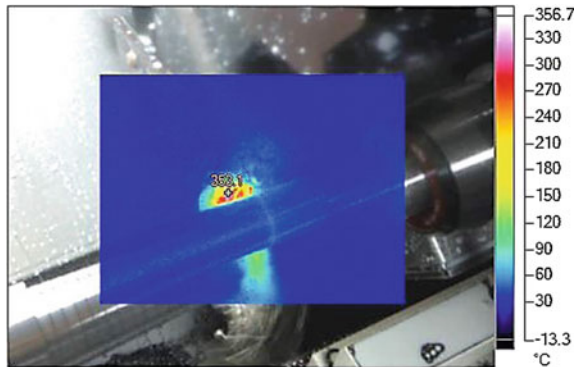


Fig. 1 Developed thermal images from Fluke Ti400 software for cutting speed 40 m/min, feed rate 0.1 mm/rev, and depth of cut 1 mm under dry condition

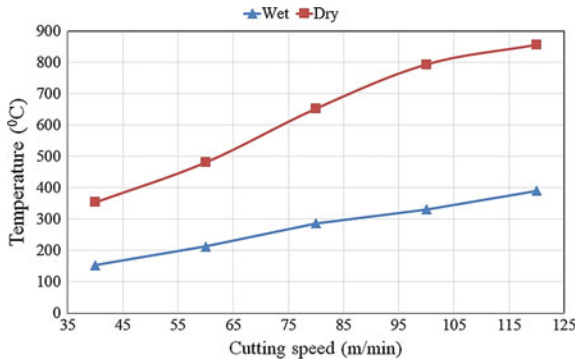


Fig. 2 Variation of cutting temperature with respect to cutting speed for a constant feed rate of 0.1 mm/rev and a depth of cut of 1 mm

3.2 Surface Roughness

Response Surface Methodology

Response surface modeling is one of the popular techniques for predicting the responses. The results of the surface roughness are analyzed using Minitab. From the results of the analysis, it was found that feed rate is the significant factor for both dry and wet machining. After developing a predicted model at 95% confidence level to fit the surface response design, the following regression equations for dry and wet machining were obtained, which show the relation between the independent variables (cutting speed and feed rate) and the dependent variable (surface roughness).

$$\begin{aligned}
 Ra_{dry} = & -2.62 - (0.0501 * \text{Cutting speed}) + (38.0 * \text{Feed}) \\
 & - (0.000293 * \text{Cutting Speed} * \text{Cutting Speed}) \\
 & - (94.1 * \text{Feed} * \text{Feed}) + (0.151 * \text{Cutting speed} * \text{Feed}) \quad (1)
 \end{aligned}$$

$$\begin{aligned}
 Ra_{wet} = & -0.043 - (0.0096 * \text{Cutting speed}) + (27.52 * \text{Feed}) \\
 & - (0.000023 * \text{Cutting speed} * \text{Cutting speed}) \\
 & - (123.9 * \text{Feed} * \text{Feed}) + (0.0290 * \text{Cutting speed} * \text{Feed}) \quad (2)
 \end{aligned}$$

From the above two equations, it is observed that coefficient of cutting speed is almost approaching to zero, which shows that surface roughness is not much affected by cutting speed. However, the coefficient of square of the feed rate is the largest compared to all other coefficients, which means Ra value is affected the most by feed rate.

The surface plot for dry and wet machining has been shown in Fig. 3. From both the graphs, it is observed that at a constant cutting speed, the Ra value increases for increase in feed rate. This effect occurs because the contact area between the insert and the workpiece increases as the feed is increased, which in turn increases the

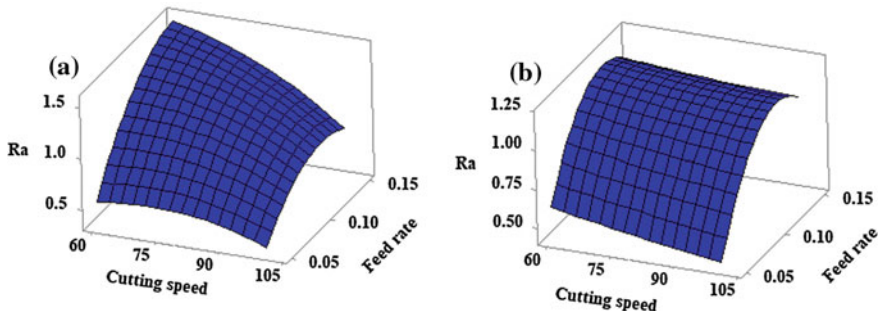


Fig. 3 Surface plot for **a** dry and **b** wet machining

force and hence the surface roughness also. For dry machining, it is observed that Ra value first increases up to a certain cutting speed and then decreases for a constant feed rate. Reason for this phenomenon may be the formation of built-up edge up to a particular speed that increases the surface roughness, but at higher speeds there is no built-up edge formation as chip is removed rapidly and heat is dissipated faster. It is also seen from the graph that Ra value decreases in wet machining when compared to dry machining because a thin layer of cutting fluid particles enters the chip–tool interface and prevents abrasion wear as well as built-up edge formation.

Figure 4 shows the variation of surface roughness with respect to increasing cutting speed at various feed rates and variation of surface roughness with respect to increasing feed rate at various cutting speeds for both dry and wet conditions. It is observed that in both dry and wet machining, surface finish is better at high cutting speeds combined with low feed rates.

Artificial Neural Network

Artificial neural network is one of the efficient computing techniques, whose central theme is borrowed from the analogy of biological neural networks and is the most widely used predictive model [7]. In this study, artificial neural network formulation is done using the MATLAB with the neural networks toolbox. For obtaining the optimal activation function, training algorithm, and the best-suited architecture, various models were designed and validated. The R (regression coefficient) values of the trained models were selected and optimized by the mean squared error (MSE) criterion. The Levenberg–Marquardt (LM) was used to train the algorithm which is one of the fastest algorithms. The feed-forward neural network with single hidden layer consisting of eight neurons was found the best.

In the modeling process of each responses, tolerance in error and number of epoch are adopted as 0.001 and 1000, respectively. After training, the data has been simulated and compared with input data and this process was repeated for number of cycles. Similar procedure has been followed in the earlier works [8, 9]. After developing the prediction model using ANN and RSM techniques, the predicted responses of both techniques are compared with experimental values and error between the experimental and predicted value has been found from the formula given below.

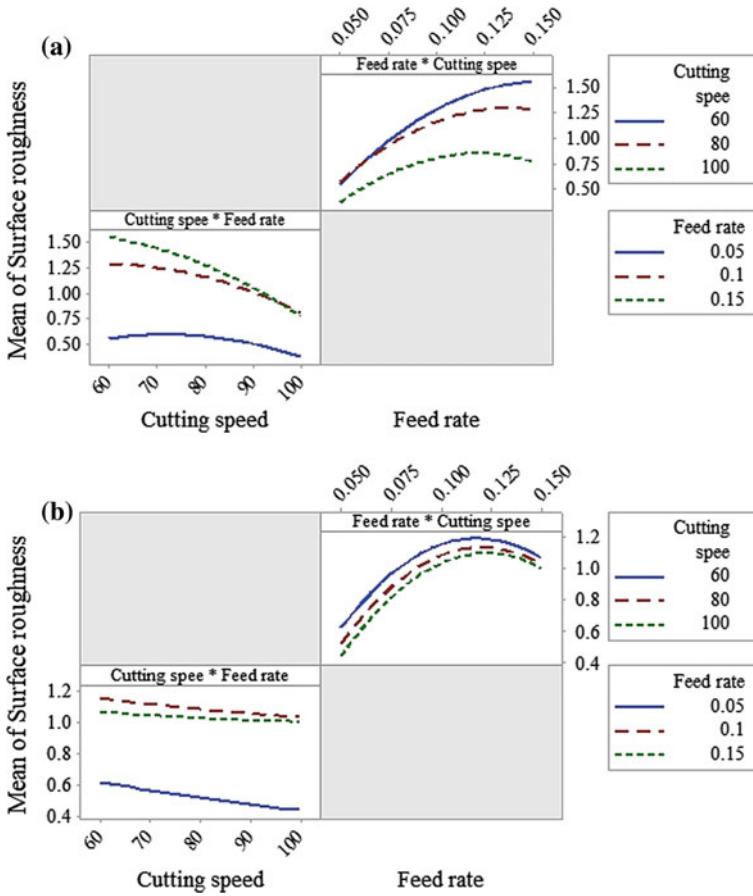


Fig. 4 Interaction plot for a dry and b wet machining

$$\text{Error}(\%) = \frac{(\text{Practical value} - \text{Fitted value})}{\text{Practical value}} \times 100 \quad (3)$$

It was observed that absolute percentage error is more for the values predicted by RSM; hence, it is clear that model developed by ANN better suits the prediction of surface roughness. The comparison graphs (Figs. 5 and 6) show the validation of the models with the values obtained from the experiment. All the three curves show closeness with each other, signifying that the models closely agree with the experimental values in both wet and dry machining conditions.

Optimization Using Genetic Algorithm

Genetic Algorithm (GA) has been used in this study to solve the optimization problem, which is minimization of the Ra value. GA is a technique that is used to solve constrained and unconstrained optimization problems. The solution approach is based on a natural selection process mimicking biological evolution. Here cutting speed

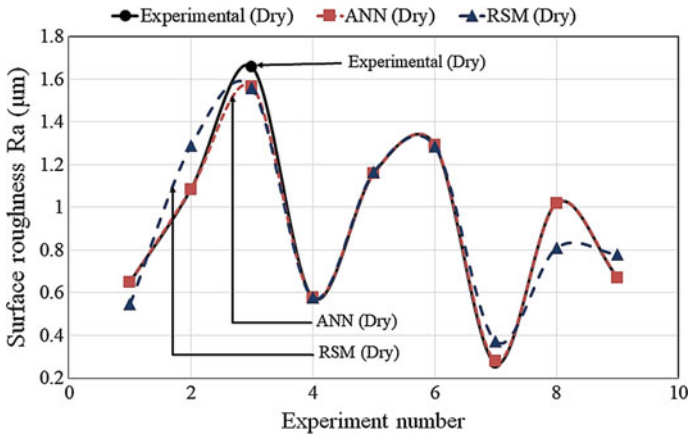


Fig. 5 Comparison between experimental values and values from prediction models for dry machining

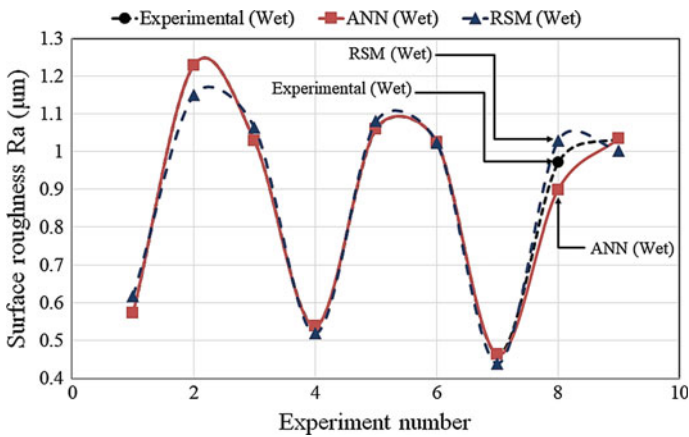


Fig. 6 Comparison between experimental values and values from prediction models for wet machining

(from 60 to 100 m/min) and feed rate (0.05 to 0.15 mm/rev) have to be optimized. MATLAB R2017a optimization tool is used to carry out the optimization. The final optimized values of the cutting parameters given by GA are cutting speed 100 m/min and feed rate 0.05 mm/rev for both dry and wet conditions, and the corresponding Ra values are 0.438 µm in dry and 0.693 µm in wet condition.

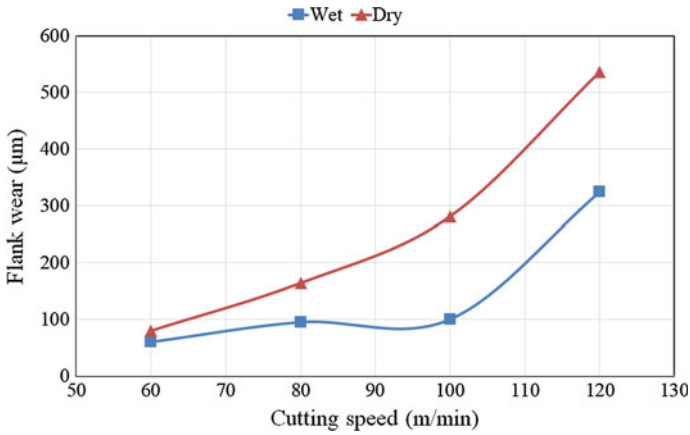


Fig. 7 Variation of flank wear with respect to cutting speed at 0.1 mm/rev feed and 0.5 mm depth of cut

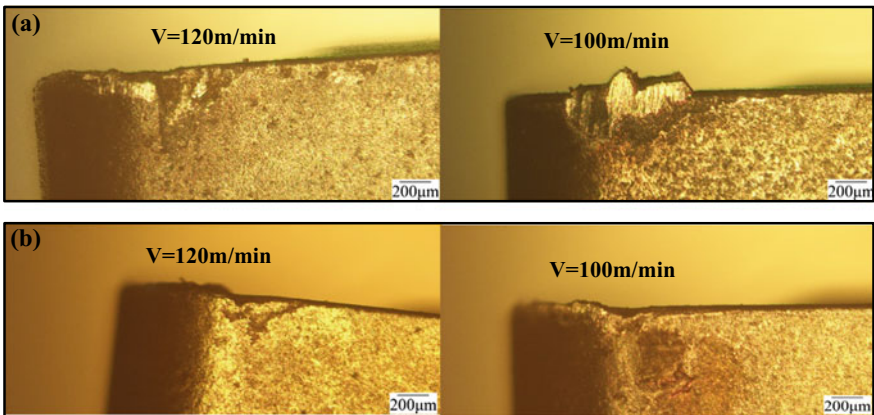


Fig. 8 Microscope images of the cutting insert for **a** dry machining and **b** wet machining

3.3 Tool Wear

Flank wear is the most important tool wear in any machining operation. Its occurrence is attributed to the rubbing action between the tool and the workpiece surface [10]. The tool flank wear was studied using optical microscope. The variation of the tool flank wear with the cutting speed is shown in Fig. 7. It was observed that the tool flank wear increased rapidly with increase in cutting speed both in dry and wet conditions. However, the increase was much more pronounced in case of dry machining as compared to wet machining. Also in few cases of dry machining, formation of built-up edge was found. Figure 8 shows the microscope images of the flank wear after 5 min of machining for both dry and wet conditions.

4 Conclusions

Experiments were carried out on DSS SAF 2507 under both dry and wet machining conditions for a range of cutting parameters. Some of the conclusions which can be drawn from this study are:

- Prediction results of both ANN and RSM are compared with experimental results for surface roughness. Prediction carried out by ANN is more favorable compared to that given by RSM.
- Feed rate showed the most significant effect on surface finish.
- GA was used as the optimization algorithm to obtain the optimum values of the cutting parameters.
- No built-up edge formation was observed at higher cutting speeds, which resulted in the better surface finish. The combination of high cutting speed and low feed rate yielded a better surface finish. Wet machining conditions resulted in better surface properties.
- There was significant increase in temperature with increase in the cutting speed.
- Tool flank wear was observed more in case of dry machining, and the values increased with increasing cutting speed.

References

1. Gamarra JR, Diniz AE (2018) Taper turning of super duplex stainless steel: tool life, tool wear and workpiece surface roughness. *J Braz Soc Mech Sci Eng* 40:39
2. Nomani J, Pramanik A, Hilditch T, Littlefair G (2013) Machinability study of first generation duplex (2205), second generation duplex (2507) and austenite stainless steel during drilling process. *Wear* 304:20–28
3. Selvaraj DP, Chandramohan P, Mohanraj M (2014) Optimization of surface roughness, cutting force and tool wear of nitrogen alloyed duplex stainless steel in a dry turning process using Taguchi method. *Measurement* 49:205–215
4. Nomani J, Pramanik A, Hilditch T, Littlefair G (2015) Chip formation mechanism and machinability of wrought duplex stainless steel alloys. *Int J Adv Manuf Technol* 80:1127–1135
5. Krolczyk GM, Nieslony P, Legutko S (2015) Determination of tool life and research wear during duplex stainless steel turning. *Arch Civil Mech Eng* 15:347–354
6. Krolczyk GM, Nieslony P, Maruda RW, Wojciechowski S (2017) Dry cutting effect in turning of duplex stainless steel as a key factor in clean production. *J Clean Prod* 142:3343–3354
7. Sangwan KS, Saxena S, Kant G (2015) Optimization of machining parameters to minimize surface roughness using integrated ANN-GA approach. *Procedia CIRP* 29:305–310
8. Beatrice BA, Kirubakaran E, Thangaiah PRJ, Wins KLD (2014) Surface roughness prediction using artificial neural network in hard turning of AISI H13 steel with minimal cutting fluid application. *Procedia Eng* 97:205–211
9. Senthilkumar N, Tamizharasan T (2015) Flank wear and surface roughness prediction in hard turning via artificial neural network and multiple regressions. *Aust J Mech Eng* 13(1):31–45
10. Kumar R, Sahoo AK, Das RK, Panda A, Mishra PC (2018) Modelling of flank wear, surface roughness and cutting temperature in sustainable hard turning of AISI D2 steel. *Procedia Manuf* 20:406–413

Multi-Response Optimization Using Grey Relation Analysis in Mechanical Micro Drilling (MMD) of Titanium Alloy—(CP-Ti) Grade II



P. Prashanth and Somashekhar S. Hiremath

Abstract Mechanical Micro Drilling (MMD) process is a conventional micro-machining process used to produce micro-holes on various engineering materials. This paper investigates the optimal machining parameters required in MMD Titanium alloy—(CP-Ti) grade II. Grey relation analysis (GRA) is used for optimizing the process parameters such as spindle speed and feed for responses such as thrust force, diameter variation in entry and exit (DVEE), and exit burr height. Full factorial design with three levels of spindle speed (8000, 11,000, 14,000) rpm and feed (5, 7.5, 10) $\mu\text{m}/\text{rev}$ was considered for experimentation. Solid carbide drill bit of $\phi 300 \mu\text{m}$ was used to machine a hole in dry condition on 1 mm Titanium alloy—(CP-Ti) grade II sheet. The grey relation grades (GRG) was calculated for all the experiments, and responses were recorded. From the response table, the optimal parameters for multiple responses were obtained at a spindle speed of 11,000 rpm (Level-2) and at a feed 5 $\mu\text{m}/\text{rev}$ (Level-1), respectively. Analysis of variance (ANOVA) on GRG was carried out, and it is observed that both spindle speed and feed are significant on multiple responses.

Keywords Micro-drilling · Grey relation analysis · Burr height · ANOVA

1 Introduction

Today's rapidly changing manufacturing scenario has compelled to develop miniaturized products with micro-features of 500 μm size or less. Micro-holes are features that are essential in biomedical, automobiles, optical, aerospace, and electronic products, and they need to be machined economically and accurately in different materials. Micro-holes are usually machined in printed circuit boards (PCBs), fuel injection nozzles, vents in turbine blades, and many micro-fluidic applications to create source and sinks. Many micro-machining processes have been developed in

P. Prashanth · S. S. Hiremath (✉)
Indian Institute of Technology, Madras, Chennai 600036, India
e-mail: somashekhar@iitm.ac.in

© Springer Nature Singapore Pte Ltd. 2019
S. S. Hiremath et al. (eds.), *Advances in Manufacturing Technology*,
Lecture Notes in Mechanical Engineering,
https://doi.org/10.1007/978-981-13-6374-0_48

past decades to machine micro-holes; these can be broadly divided as contact and non-contact type depending on workpiece and tool interaction during machining. MMD is a contact type process in which a micro-drill rotating at high speeds is made to pass through a stationary workpiece to generate micro-holes. MMD process used to machine large number of holes in short duration with better roundness, surface finish, and straightness as compared to other micro-machining processes due to the direct tool and workpiece contact [1, 2].

In MMD process, the aspect ratios are higher compared to conventional drilling. Moreover, the micro-drills are slender having low stiffness which causes an increase in thrust forces, resulting in drill breakage due to bending stresses during machining [3]. Peck drilling is found to be more suitable over continuous drilling in MMD as it reduces the thrust forces and also sudden drill breakages [4].

Titanium and titanium alloys are widely used in biomedical and aerospace applications. Titanium alloy—(CP-Ti) grade II has high corrosion resistance and remains passive in most of the aqueous solutions which makes it a popular choice in biomedical applications like dental implants, artificial hips and joints, surgical equipment, heart valves, and pacemakers [5, 6]. Titanium alloy—(CP-Ti) grade II is also preferred in aerospace applications for its high strength-to-weight ratio for airframe and engine parts. High toughness and thermal stability make it suitable for use as fuel tanks for liquid H₂ storage in space vehicles [6]. Other applications of Titanium alloy—(CP-Ti) grade II include condenser tubing, heat exchangers, and marine chemical parts. In spite of wide range of applications titanium and its alloys are usually considered hard to cut materials due to its properties like poor thermal conductivity, affinity with tool materials at higher temperatures, and ability to maintain high mechanical strength even at elevated temperatures making machining difficult due to increased resistance [7, 8].

Many studies were carried out in the past on drilling titanium and titanium alloys. Carbide drills were found very effective in reducing thrust force and burr height in drilling of Ti-6Al-4V alloy compared to HSS drills [9]. Titanium alloy—(CP-Ti) grade II was machined using MMD and $\phi 500 \mu\text{m}$ holes were drilled using HSS drill coated with Al₂O₃ using atomic layer deposition method. Tool life and hole roundness error were analyzed, and it was observed that roundness was not affected by the coating whereas tool life increased [10]. The effect of spindle speed and feed rate on burr height was analyzed by drilling 700 μm holes in titanium alloy Ti-6Al-4V using uncoated carbide drill 3D profiling, which was used for measuring burr height, increase in feed rate and decrease in spindle speeds resulted in a rise in exit and entry burr height [11]. Hole of $\phi 300 \mu\text{m}$ was drilled in Ti-6Al-4V alloy at spindle speeds (60,000, 80,000, and 100,000 rpm) and feed (0.0167, 0.025, and 0.03 $\mu\text{m}/\text{rev}$). Mechanistic model for prediction of drilling forces and burr height was developed [12].

From the literature review, it was evident that very less work is carried out in mechanical micro-drilling of Titanium alloy—(CP-Ti) grade II material in the optimization of process parameters. In the present work, spindle speed and feed are selected as process parameters. Thrust force, diameter variation in entry and exit (DVEE), and exit burr height are considered as responses. Multi-response optimiza-

tion is carried out using the grey relation analysis (GRA) to establish levels of process parameters to minimize all the three responses.

2 Experimental Work

2.1 Material and Tools

The Titanium alloy—(CP-Ti) grade II material with a thickness of 1 mm was chosen as the workpiece with an average micro-hardness of 166.20 H_v. The chemical composition of major constituents by weight percentage is given in Table 1. Solid carbide drill was used in machining with specifications given in Table 2

2.2 Experimental Setup

Experiments were carried out on KMi118 of JYOTHI CNC three axes high-speed machining center. Multi-component dynamometer 9257B of Kistler make was used to measure cutting forces in *X*, *Y*, and *Z* directions. Charge amplifier was used to amplify the signals. Data acquisition system was used to acquire the cutting force data from the charge amplifier. The experimental setup used for experimentation is shown in Fig. 1.

Table 1 Chemical composition of Titanium alloy—(CP-Ti) grade II

Element	Ti	C	C _r	O	Fe
Titanium alloy—(CP-Ti) grade II	99.70	0.031	0.02	0.010	0.13

Table 2 Micro-drill specifications

S. No.	Parameter	Specification
1	Diameter	φ0.3 mm
2	Total length	38.1 mm
3	Cutting edge length	6 mm
4	Shank diameter	φ3.157 mm
5	Helix angle	30°
6	Point angle	128°

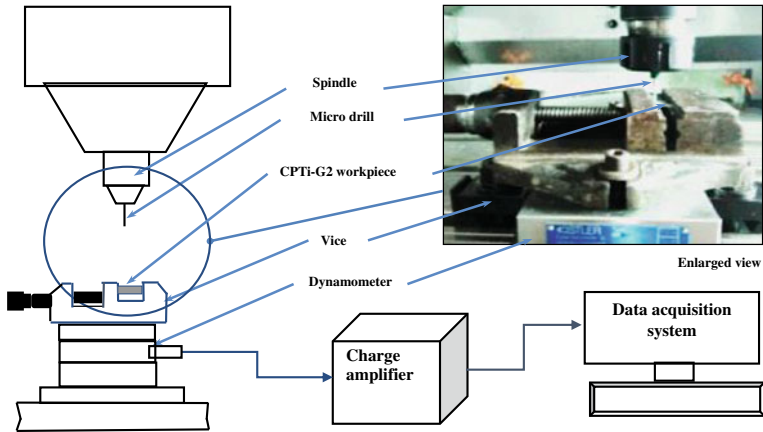


Fig. 1 Schematic of experimental setup

Table 3 Experimental design

Parameters	Levels		
	1	2	3
Spindle speed (rpm)	8000	11,000	14,000
Feed ($\mu\text{m}/\text{rev}$)	5	7.5	10

2.3 Design of Experiments and Experimentation

Full factorial design with two parameters—spindle speed and feed and three levels—speed: (8000, 11,000, 14,000) rpm and feed: (5, 7.5, 10) $\mu\text{m}/\text{rev}$ are selected for experimentation and the experimental design is presented in Table 3.

Experiments are repeated three times for repeatability and $\phi 300 \mu\text{m}$ holes are machined in dry condition using solid carbide drill using peck drilling with a pecking depth of $50 \mu\text{m}$.

2.4 Measurements

Three responses such as thrust force, exit burr height and diameter variation in entry and exit (DVEE) are considered for analysis. Lower values of these responses indicate the better performance.

Thrust force

Thrust force was measured along z-direction in each trial of all three experiments. The maximum thrust force value was considered in each trial, and an average of three trials was calculated for analysis. The data were acquired at a sampling rate of 1400

Fig. 2 Thrust force variation with time: **a** at spindle speed: 8000 rpm and feed: 5 $\mu\text{m}/\text{rev}$, **b** at spindle speed: 14,000 rpm and feed: 7.5 $\mu\text{m}/\text{rev}$

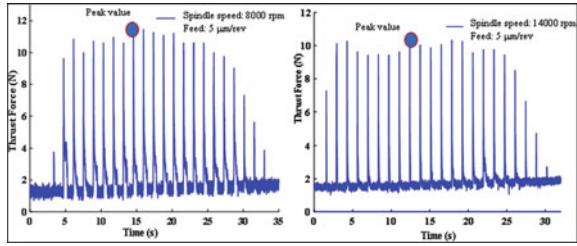
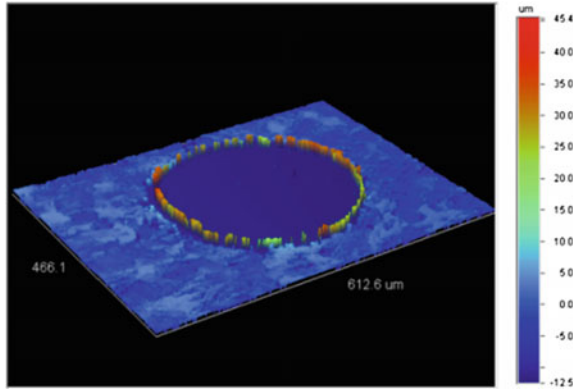


Fig. 3 Three-dimensional profiler image of hole exit burr at spindle speed: 11,000 rpm and feed: 7.5 $\mu\text{m}/\text{rev}$



samples per second using *Dynoware* software. The variation of thrust force “ F_z ” in newton (N) with time is shown in Fig. 2.

Exit burr height

In micro-drilling, burrs are formed at the exit surface because of deformation of material caused due to the point angle of micro-drill [11]. Burr formation on the exit surface of the hole are characterized by burr height, measured by using non-contact 3D profiling by Veeco 3D profile meter. Maximum value of burr height was considered for each trial, and the average of three trials is determined for analysis. The 3D profile meter image of burr height measurement is shown in Fig. 3.

Diameter variation in entry and exit (DVEE)

In micro-drilling, it has been observed that the diameter of the hole at the entry side of the drill will be more than the hole diameter at exit side, and this is called as the diameter variation in entry and exit (DVEE) [13]. The main reason for DVEE is due to the wandering motion of micro-drill, and the other reason is the dynamic imbalance during the initial entry stage of micro-drill [14, 15]. The DVEE was calculated as the difference of measured diameters on hole entry and exit sides using an optical microscope. The DVEE is given as

$$DVEE(\mu\text{m}) = \text{hole entry diameter} - \text{hole exit diameter} \tag{1}$$

2.5 Grey Relation Analysis (GRA)

In the present work, three responses are to be minimized by selecting suitable process parameters. Grey relation analysis is applied for multi-response optimization. The grey relation analysis was carried out using the following steps.

Data preprocessing

In the first step of GRA, the mean data values for each response were normalized by data preprocessing. Normalization is done to transform raw data in original sequence to a comparable sequence for further analysis. Let $x_o(k)$ and $x_i(k)$ represent original and comparable sequences, respectively. In which $i = 1, 2, 3, \dots m, k = 1, 2, 3, \dots n$ where m represents the number of experiments carried out, and n is the total number of observed responses. As responses considered are to be minimized, smaller the better criteria are selected for data preprocessing, and the original data sequence is normalized by using Eq. 2.

$$x_i^*(k) = \frac{\text{Max} \cdot x_i^{(o)}(k) - x_i^{(o)}(k)}{\text{Max} \cdot x_i^{(o)}(k) - \text{Min} \cdot x_i^{(o)}(k)} \tag{2}$$

where $x_i^*(k)$ = normalized mean value after data preprocessing

$x_i^{(o)}(k)$ = original sequence

Max. $x_i^{(o)}(k)$ = largest value of the original sequence

Min. $x_i^{(o)}(k)$ = smallest value of the original sequence

Deviation sequences determination

The deviation sequence $\Delta_{oi}(k)$ is calculated as the absolute difference of reference sequence $x_o^*(k)$, and comparable sequence $x_i^*(k)$ after normalization is given as

$$\Delta_{oi}(k) = |x_o^*(k) - x_i^*(k)| \tag{3}$$

Grey relational coefficients (GRC)

GRC values were computed to normalized mean values in the second step, which is given as

$$\gamma(x_i^{(o)}(k), x_i^{(*)}(k)) = \frac{\Delta_{\text{Min}} + \lambda \Delta_{\text{Max}}}{\Delta_{oi}(k) + \lambda \Delta_{\text{Max}}} \tag{4}$$

where $\text{GRC} = \gamma(x_i^{(o)}(k), x_i^{(*)}(k))$

λ = distinguishing coefficient, $\lambda \in (0, 1)$

Grey relation grade is a weighted sum of grey relation coefficients and is given as

$$\gamma(x_o^{(*)}, x_i^{(*)}) = \sum_{k=1}^n \beta_k \gamma(x_i^{(o)}(k), x_i^{(*)}(k)) \sum_{i=1}^n \beta_k = 1 \tag{5}$$

3 Results and Discussions

The average values of three trials of output responses thrust force, diameter variation at entry and exit (DVEE), and exit burr height were calculated and given in Table 4. Using optical microscope, the images of machined holes are acquired for each experiment and shown in Fig. 4.

The best response is the minimum of all the three responses: thrust forces, DVEE, and exit burr height. Thus, the smaller the better characteristic was selected, and output response values were preprocessed using equation number 2. The original reference sequence and comparable sequence after preprocessing are given in Table 5.

The grey relation coefficients (GRC) computed after normalization for all output responses, and grey relation grade (GRG) was computed considering an equal

Table 4 Average output responses

Experiment number	Spindle speed (rpm)	Feed ($\mu\text{m/s}$)	Average thrust force (N)	Average DVEE (μm)	Average burr height (μm)
1	8000	5	11.841	31.037	28.650
2	8000	7.5	12.166	36.837	43.000
3	8000	10	12.940	30.895	30.640
4	11,000	5	11.312	25.879	18.260
5	11,000	7.5	11.271	21.825	38.780
6	11,000	10	12.166	20.316	22.780
7	14,000	5	10.498	22.347	27.400
8	14,000	7.5	11.922	24.549	33.830
9	14,000	10	13.062	23.279	19.820

Table 5 Sequences after data preprocessing: thrust force, DVEE, and exit burr height

Reference/comparable sequence	Thrust force	DVEE	Exit burr height
Reference sequence	1.00	1.00	1.00
Comparable sequence			
Experiment number 1	0.476	0.351	0.580
Experiment number 2	0.349	0.000	0.000
Experiment number 3	0.048	0.360	0.499
Experiment number 4	0.683	0.663	1.000
Experiment number 5	0.698	0.909	0.171
Experiment number 6	0.349	1.000	0.817
Experiment number 7	1.000	0.877	0.630
Experiment number 8	0.444	0.744	0.370
Experiment number 9	0.000	0.821	0.937

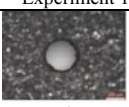
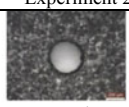
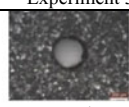



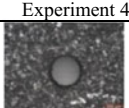

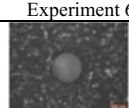

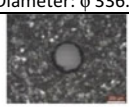
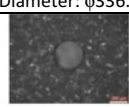

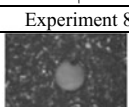
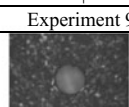
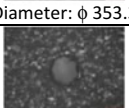
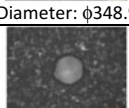
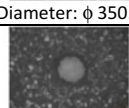
 Entry Diameter: $\phi 329.89\mu\text{m}$	 Entry Diameter: $\phi 348.86\mu\text{m}$	 Entry Diameter: $\phi 349.77\mu\text{m}$
 Exit Diameter: $\phi 306.49\mu\text{m}$	 Exit Diameter: $\phi 315.81\mu\text{m}$	 Exit Diameter: $\phi 307.32\mu\text{m}$
 Entry Diameter: $\phi 342.53\mu\text{m}$	 Entry Diameter: $\phi 336.89\mu\text{m}$	 Entry Diameter: $\phi 336.36\mu\text{m}$
 Exit Diameter: $\phi 314.04\mu\text{m}$	 Exit Diameter: $\phi 313.12\mu\text{m}$	 Exit Diameter: $\phi 314.30\mu\text{m}$
 Entry Diameter: $\phi 353.37\mu\text{m}$	 Entry Diameter: $\phi 348.96\mu\text{m}$	 Entry Diameter: $\phi 350.93\mu\text{m}$
 Exit Diameter: $\phi 312.29\mu\text{m}$	 Exit Diameter: $\phi 310.37\mu\text{m}$	 Exit Diameter: $\phi 312.278\mu\text{m}$

Fig. 4 Images of machined holes

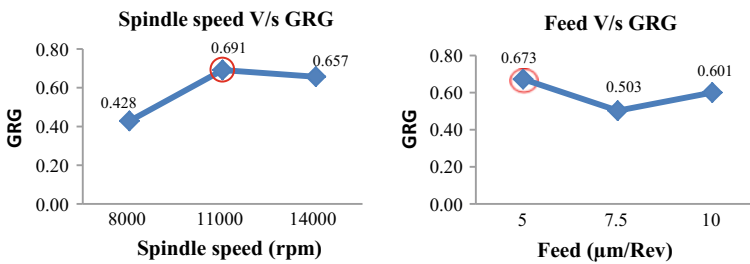


Fig. 5 Average GRG for spindle speed and feed

weightage for each factor. The GRC and GRG values for each experiment are given in Table 6.

Response table was constructed based on the grey relation grades by computing the average of process parameters at each level and is given in Table 7. The values of the response table were plotted as shown in Fig. 5

Table 6 Grey relation coefficient and grey relation grades

Experiment number	Spindle speed (rpm)	Feed ($\mu\text{m}/\text{rev}$)	GRC thrust force	GRC DVEE	GRC burr height	GRG	Ranking
1	8000	5	0.488	0.435	0.544	0.489	7
2	8000	7.5	0.434	0.333	0.333	0.367	9
3	8000	10	0.344	0.438	0.500	0.427	8
4	11,000	5	0.612	0.598	1.000	0.736	2
5	11,000	7.5	0.624	0.845	0.376	0.615	5
6	11,000	10	0.434	1.000	0.732	0.722	3
7	14,000	5	1.000	0.803	0.575	0.793	1
8	14,000	7.5	0.474	0.661	0.443	0.526	6
9	14,000	10	0.333	0.736	0.888	0.652	4

Table 7 Response table

Parameter	Levels			Delta (max-min)	Rank
	1	2	3		
Spindle speed (rpm)	0.428	0.691	0.657	0.263	1
Feed ($\mu\text{m}/\text{rev}$)	0.673	0.503	0.601	0.170	2

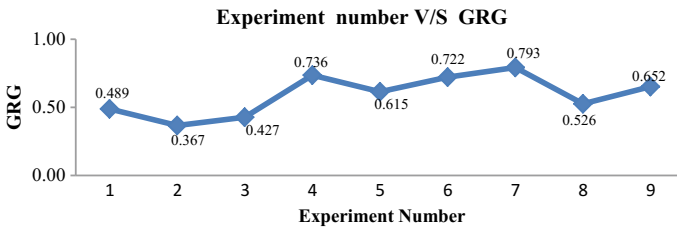


Fig. 6 Experiment number versus GRG

Optimal parameters for multiple responses were obtained at 11,000 rpm (Level-2) spindle speed and 5 $\mu\text{m}/\text{rev}$ (Level-1) feed based on maximum GRG. The GRG values for each experiment are plotted and shown in Fig. 6.

The analysis of variance (ANOVA) was done by considering GRG as a response, spindle speed and feed as process parameters. The ANOVA results are given in Table 8.

From the ANOVA table, it is clear that spindle speed was highly significant factor with p value of 0.004 followed by feed with p value of 0.025.

Table 8 Analysis of variance (ANOVA)

Source	DF	Adj SS	Adj MS	F value	p value
Spindle speed	2	0.1230	0.0615	30.19	0.004
Feed	2	0.0436	0.0218	10.72	0.025
Error	4	0.0081	0.0020	–	–
Total	8	0.1748	–	–	–

4 Conclusions

Mechanical Micro Drilling (MMD) process has been used successfully to machine holes on Titanium alloy—(CP-Ti) grade II sheet with solid carbide tool of $\phi 300 \mu\text{m}$. Some of the findings of the study are presented as follows:

- The grey relation analysis was carried out, and optimal level of spindle speed and feed was obtained responses: thrust forces, exit burr height and diameter variation at entry and exit (DVEE).
- ANOVA was done by considering GRG as output response with spindle speed and feed as process parameters.
- From ANOVA, it was evident that the spindle speed was the most significant parameter followed by feed toward GRG.

References

1. Kim DW, Lee YS, Park MS, Chu CN (2009) Tool Life Improvement by Peck drilling and thrust force monitoring during deep-micro-hole drilling of steel. *Int J Mach Tools Manuf* 49:246–255
2. Leo Kumar SP, Jerald J, Kumanan S, Prabakaran R (2014) A review on current research aspects in tool-based micromachining processes. *Mater Manuf Process* 29:1291–1337
3. Yong Chen P, Qing chang T, Zhaojun Y (2006) A study of dynamic stresses in micro-drills under high-speed machining. *Int J Mach Tools Manuf* 46(14):1892–1900
4. Kim DW, Lee YS, Park MS (2009) Tool life improvement by peck drilling and thrust force monitoring during deep-micro-hole drilling of steel. *Int J Mach Tools Manuf* 49(3–4):246–255
5. Ramsden JJ (2007) The design and manufacture of biomedical surfaces. *CIRP Ann Manuf Technol* 56–2:687–711
6. Singha Paramjit, Pungotrab Harish, Kalsib Nirmal S (2017) On the characteristics of titanium alloys for the aircraft applications. *Mater Today: Proc* 4:8971–8982
7. Hong SY, Ding Y (2001) Cooling approaches and cutting temperatures in cryogenic machining of Ti-6Al-4V. *Int J Mach Tools Manuf* 41:1417–1437
8. Khan Akhtar, Maity Kalipada (2018) Influence of cutting speed and cooling method on the machinability of commercially pure titanium (CP-Ti) grade II. *J Manuf Process* 31:650–661
9. Li Rui, Hegde Parag, Shih Albert J (2007) High-throughput drilling of titanium alloys. *Int J Mach Tools Manuf* 47:63–74
10. Giorleo L, Ceretti E, Giardini C (2011) ALD coated tools in micro drilling of Ti sheet. *CIRP Ann—Manuf Technol* 60:595–598
11. Percin M, Aslantas K, Uzun I (2016) Micro-drilling of Ti-6Al-4V alloy, the effects of cooling/lubricating. *Precis Eng* 45:450–462

12. Mittal RK, Yadav S, Singh RK (2017) Mechanistic force and burr modeling in high-speed micro drilling of Ti6Al4V. *Procedia CIRP* 58:329–334
13. Swain N, Kumar P, Srinivas G (2017) Mechanical micro-drilling of nimonic 80A super alloy using uncoated and Ti Al N-coated micro-drills. *Mater Manuf Process* 32(13):1537
14. Chae J, Park SS, Freiheit T (2006) Investigation of micro-cutting operations. *Int J Mach Tools Manuf* 46:313–332
15. Mohammed TH (2001) Hole quality in deep hole drilling. *Mater Manuf Process* 16:147–164

A Glance Through History of Automobile Industry and Current Market Study of Some of the Legendary Models in India



Muthu Ajay, Sridhar Kannan, P. Prem Narayan
and R. Deepak Suresh Kumar

Abstract India is one of the biggest automobile manufacturers in the world. The automobile industry in India accounts for 7.1% of country's gross domestic product (GDP). The two-wheeler segment with 81% market share is the leader of the Indian automobile industry. Indian automobile history began from 1897–1898. Now we can see almost all world brand vehicles in Indian market along with its own products. But major portion of customers still love the oldest models especially two-wheelers like Yamaha RX 100, Yezdi Roadking, Samurai, Bajaj Chetak, Rajadoot, etc. And they believe some of the brands are symbol of legacy and status. This is analyzed by conducting a literature survey, market study and successful market of manufacturers who preserve older design, appearance, etc. The journal concludes with an eye on future of some legendary models when regenerated incorporating latest technologies and scope of a company to find market if considered models are regenerated.

Keywords Indian automobile industry · Legendry models · Vintage vehicles · Market study · Market survey

1 Introduction

The automotive industry in India is one of the largest in the world with an annual production of 23.96 million vehicles (2015–2016). In addition, India is the biggest auto exporter with an expectation to top the world market by 2020 with the help of several initiatives by the Government of India and the major automobile players in the Indian market [1]. The automobile industry in India accounts for 7.1% of country's gross domestic product (GDP). The two-wheeler segment with 81% market share is the leader of the Indian automobile industry. This fact is clearly shown by the graph in Fig. 1 constructed based on SIAM data (Society of Indian Automobile Manufacturers) about Indian automobile sector.

M. Ajay · S. Kannan · P. Prem Narayan (✉) · R. Deepak Suresh Kumar
Chennai Institute of Technology, Kundrathur, Chennai, India
e-mail: researchppn@gmail.com

© Springer Nature Singapore Pte Ltd. 2019
S. S. Hiremath et al. (eds.), *Advances in Manufacturing Technology*,
Lecture Notes in Mechanical Engineering,
https://doi.org/10.1007/978-981-13-6374-0_49

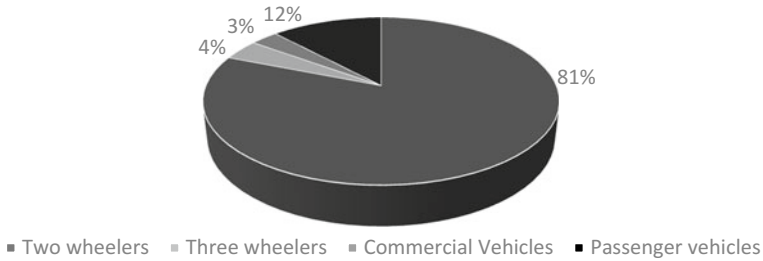


Fig. 1 Domestic market share for 2015–2016

2 History

The history of Indian automobile industries is said to be started during the time period 1897–98 [2]. Simpson & co. were the one to manufacture steam cars and buses, petrol-driven passenger services and import chassis from USA at first. Variety of vehicles was introduced for military services after World War I. Later many manufacturers with series of automobile products came to existence of which few were shut down; other continued to grow in the market. Certain of them collaborated while few departed to form independent manufacturer. Table 1 shows the list of manufacturers, the year of establishment, and few of their finest products of the period.

After 1991, automobile industry began to expand at a faster rate. In 1997, many multinational companies like Daewoo, Peugeot, General Motors, Mercedes Benz, Honda, Hyundai, Toyota, Mitsubishi, Suzuki, Ford, Fiat, and Volvo entered the Indian auto sector. At present, we can see almost all world-class manufactures in the Indian automobile market. These are just some of the main milestones of Indian automobile sector.

In this rich history, there were large numbers of models in both two- and four-wheelers sector. Today major portion of the market is controlled by Hero, Honda, Bajaj Auto Ltd., TVS, Yamaha, Royal Enfield, Piaggio, Triumph, Harley-Davidson (two-wheeler) and Hyundai, Toyota, Honda, Ford, Volkswagen, Nissan, fiat, Renault, Skoda, Chevrolet, Tata Motors, Audi, BMW, Mercedes Benz, General

Table 1 List of manufacturers and their products with year of establishment

S. No.	Manufacturer	Established year	Place	Product
1	Hindustan Motors	1942	Kolkata	Ambassador
2	Premier Automobile Ltd.	1944	Pune	Padmini
3	TELCO	1961	Pune	Tata Sumo
4	Ashok Leyland	1948	Chennai	Leyland Bus
5	Bajaj Ltd.	1945	Pune	Bajaj Scooter

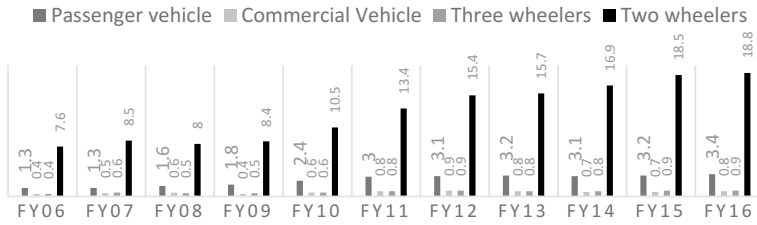


Fig. 2 Total production of automobiles in India (2015–16) in million units

Motors (four-wheeler), etc. By accepting varying technologies, needs, features in the market better products are manufactured by companies and Indian automobile sector achieves a continuous growth [3]. It is found that production of automobiles increased at a compound annual growth rate of 9.4% over 2015–16 from the data’s of SIAM and is plotted below in Fig. 2.

3 Relevance of Vintage Models

Even in this changing environment, there are many who consider some legendary models for their status and power as once they were symbol of wealth and legacy. Some of such two-wheeler models were Rajadoot (Yamaha RD 350), Yezdi Roadking, Yamaha RX100, Kawasaki Triple, Z1, Honda CB750, Kawasaki Eliminator, Royal Enfield bullets. Few four-wheeler models were Ambassador, Contessa, Padmini, Sigma, Armada, Voyager, Opel etc. [4].

Vintage and Classic car club of India, Team BHP, Bullet clubs, Yezdi clubs are strong evidence for the relevance of old models in the current market. Nowadays the growing trends in owing such vehicles have increased. Participation of peoples in various rallies and camps conducted by different teams are proof for the current trend among people. The increase in status of woman has also let to change in the attitude toward riding which can be explained by the Bullet rally conducted by Thrissur Woman’s club on January 16, 2017.

Some companies have understood the trends and are producing earlier model vehicles with the support of modern technologies [5]. The customers accept these concepts and ready to pay for these models. These models to find spaces in the competitive market and the manufacturers earn profit. While some other world-class companies still continues with their basic model of the vehicle by just incorporating the relevant latest technologies. These companies are able to maintain the standard in the market at constant level. Some of which are; Rols Royce, Harley Davidson, Royal Enfield, Volkswagen etc. Following are some comparisons of such historic models which have found certain place in the current market as well as some models which the above-listed companies have maintained.

3.1 *LML Vespa Versus Piaggio Vespa*

Vespa is a legendary scooter brand that is a part of the Italian conglomerate, Piaggio [6] which is founded in 1946 in Florence and is one of the oldest two-wheeler brands in the world. The Vespa scooters are known for their design, simplicity, and its ability to catch an eye at any time on road. The company's Indian stint began in the 1960s when it gave the license to Bajaj for producing Vespa scooters. After Bajaj, the Italian scooter brand tied up with LML Motors, Kanpur to manufacture and sell its scooters in 1983. The NV two-stroke series scooters of LML were an instant success in Indian market. "LML Vespa NV" this brand models of LML gave a tough competition to that times market leader Bajaj Chetak, Super models. By 1998, LML was the second largest scooter manufactures in India with a market share of 28%. But the joint venture between LML and Piaggio did not last long. In 1999, the joint venture was called off and LML decided to go alone with the scooter. Entry of motorcycles to the market was a disaster for them. LML's first bike FREEDOM was a failure. The LML Company fell into severe financial crisis, also labor unrest in plants leads to end of the company.

Piaggio has a presence in Indian market in the three-wheeler segment and the resurgence of scooter market has inspired by the company to re-enter the Indian market with the Vespa brand. Piaggio launched the Vespa brand of scooters in India officially at the 2012 auto Expo. Since then, the company has not looked back. It sells six models in India—the SXL 150, VXL 150, SLX125, VXL 125, Elegance and the Vespa LX125. These models are sold through two-type dealerships—regular Vespa showrooms and Motorplux-Piaggio's premium showrooms that also sell Aprilla and MotoGuzzi range of bikes. The Vespa models are successfully sold now in Indian market with some new features;

- It has a monocoque body which gives more rigidity, balance, improved handling, etc.
- It is the first scooter with monocoque chassis in the world.
- CVT automatic power transmission.
- Mileage of 60 km/L.

3.2 *Kawasaki Eliminator Versus Bajaj Avenger*

The Kawasaki Eliminator is a cruiser type motorcycle that has been produced in several variants. Since its introduction in 1985 was with 900 Eliminator. But the first model was produced only for two years. At that time, ZL900 was only the bike in its segment using an inline four power plant instead of V4 configuration. These bikes were produced by Kawasaki in American market. Kawasaki collaborates with Bajaj Auto in India. The Eliminator 175 was manufactured and sold as the Kawasaki Bajaj Eliminator. The last model was Eliminator 125, powered by 125 cc, air cooled, four strokes, single-cylinder engine. It had some styling features which include a stepped

seat with laid back riding comfort, straight flow exhaust, and chrome-plated single headlight. The production period of Eliminator was 1985–2007.

Bajaj Auto designed and manufactured a new cruiser style motorcycle named Bajaj Avenger in India. It draws the styling and other design cues from the Kawasaki Eliminator. The Avenger 180 was the first cruiser developed by an Indian company. Now there are several models of Avenger ranging from 180 cc to 220 cc. Avenger 220 is a successful cruiser in India when compared to other with reliability, price tag, performance, maintenance cost, power, and glamor. This model is now replaced by its own new featured models like Avenger Street 150, Avenger Street 220, Avenger cruise 220.

3.3 Roles-Royce

Roles-Royce motor cars Ltd. is a luxury car company who engineers, manufactures, distributes automobiles and parts world widely. It is a wholly owned subsidiary of BMW established in 1998 after BMW won licensed the rights to the Roles-Royce brand name and logo from Roles-Royce PLC and acquired the rights to the spirit of Ecstasy and from the Volkswagen AG the Roles-Royce grill shape. Roles-Royce motor cars Ltd. operates from England, UK. The Roles-Royce “PHANTOM” four-door sedan was the first product from the company in 2003—present. But they are not willing to change the name of “PHANTOM” for that particular series of car, i.e., the names of models as Phantom Coupe, Phantom Drophead coupe. All of them have comparable body language like longer bonnets, full-size luxury, front engine rear-wheel-drive layout, and V-12 engine. The changes are only in roof setup, improved audio, connectivity systems, gearbox, etc.

3.4 Harley-Davidson

It is an American motorcycle manufacturer founded in 1903. It has a rich heritage of 114 years also an iconic brand widely known for its loyal following with owners clubs, rallies, and events. Harley-Davidson traditionally marketed heavyweight, air cooled, and cruiser model motorcycles with engine displacements greater than 700 cm³. And still they are one of the best competitors in the market.

3.5 Royal Enfield

The motorcycle manufacturer Royal Enfield introduced first in market in 1931 in UK. The product name was “Royal Enfield Bullet” in 350 cc, 500 cc options. The first launching of Bullet bikes in India was on 1955 for military purposes. On that

time, 350 cc bullets were imported as parts. But Enfield India Ltd. manufactures bullets completely under license. The product design was almost the same with earlier models. But the company failed to introduce time to time improvements to their products.

In the 1990s, they get collaborates with Eicher Group, India and they introduced Royal Enfield 350 cc, 500 cc standard, classic, Electra, Machismo 500 models of this new venture. There are still models of classic; standard under 350 cc and 500 cc options in the market they have almost same structure of previous models. They are willing to introduce changes in spark ignition systems, electric start switch, fuel injection systems in their models keeping the same muzzle body of earlier models. Himalayan, continental GT are new models of Royal Enfield in different platform.

3.6 Volkswagen Beetle

The Volkswagen Beetle is a two door, four passengers, rear engine economy car which manufactured and marketed by German automaker Volkswagen from 1938. The need for this car and its features was first formulated by Adolf Hitler, leader of Nazi Germany. He wanted a cheapest, simple car. Hitler signed a deal with Ferdinand Porsche in 1934 to design and build the Beetle. They finalize the design in 1938. The Beetle is the longest running and most manufactured car of a single platform ever made.

But in 1977, the last Beetle was sold in the USA with some convertibles available through 1979. It was in 1985 when all the countries except Mexico stopped manufacturing and buying of Beetles. But in early 1991, Volkswagen engineers in California were working on modernized Beetles that would leverage nostalgia of the brand and it is charged with better features, design, performance that consumers wanted in the 1990s. And new Beetles debuted in 1994 Detroit Auto show and the new Beetle was manufactured in 1998 to the present day. They are also sold well and earn profit to the company.

4 Market Survey

From the study on relevance of few models did above, we can conclude that earlier models which was once popular are still live in the dreams of every bike lovers & also the market. That is why the customers buy these type models with comparatively more price than current models. Due to these reasons, one thing we can say, if we introduce older hit models in with a support of newer technologies, features, marketing methods, comparable prices of current models then there should be success in the market. Some of the historic legendary models that people want to back in market are mainly;

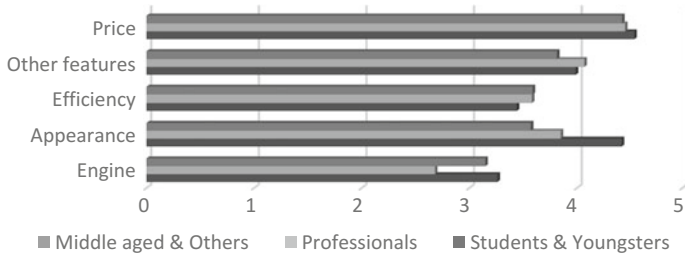


Fig. 3 Graph displaying the market survey of road king

1. Rajdoot (Yamaha RD 350)
2. Yezdi Road king
3. Yamaha RX100
4. Bajaj Chetak.

In order to justify the above conclusions from the literature survey, a market survey is conducted and for purpose we cannot consider whole of the models due to time limit. So we select “Yezdi Road king” [7, 8] which is one of the finest engines ever made in the history of Indian motorcycle. There were also numbers of reason to choose this model;

- In 1974, Yezdi Roadking accomplished the runner-up spot in the motocross world championship.
- The bike won several Indian bike rallies and races.
- The bike was produced completely in India.
- At that time, it was the bike having minimum time to attain a speed of 120 km/h.
- Yezdi Company was the first introducer of separating oil lube system via an oil pump and moves away the older premixed fuel system in India.
- The logo “ForEver Bike ForEver Value” very aptly signifies the ideology behind the product. This motive remains unchanged to this day, even in the stiff competition.

In this survey, opinion of almost 150 persons among deferent categories such as students and youngsters, professionals and middle-aged, and others in five aspects of the vehicle Yezdi “Road King” is taken. The aspects such as engine efficiency, appearance, drive comfort, other features, and price are rated under a mark of 5 and tabulated below in Fig. 3.

From this data, an average percentage of each criterion was discussed and presented in a bar format as shown in Fig. 4. The figure below indicates the percentage acceptance of our market for the criticized features of the considered product.

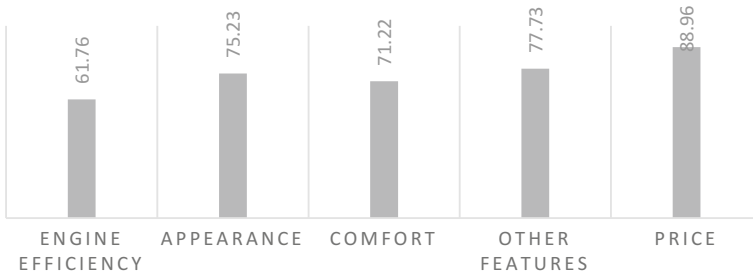


Fig. 4 Percentage acceptance of considered features

5 Conclusion

From the above literature review market survey and the plotted graph, it can be concluded that the legendary models in vintage vehicles have still live markets and which can be fully flourished by modulating some relevant changes as per the latest technologies. By the market survey done under specified criterion for road, King shows that improvement in engine efficiency and few other aspects considered such as disk break, self-starting system, universal gear system can much more improve the acceptance rate and reducing the market price would sure make a promising market. The production unit for such vehicle under Make in India scheme would be of great opportunities for employment among youngsters as well. Conclude this wright up by putting an eye on future of this survey as a design project on full flourished manufacturing sector for considered vehicle after empowering the required changes would be of fine quality to estimate plant lay out cost, production cost, etc., so that a satisfactory price can be fixed for the product still expecting a profit within a short mature period.

References

1. Krishnaveni M, Vidya R (2015) Growth of Indian automobile industry. *IJCRAR*—ISSN 3(2):2347–3215
2. George S, Jha R, Nagarajan HK (2002) The evolution and structure of the two-wheeler industry in India. *JEL Classification: D2, L1, L6*
3. Statistics—Society of Indian Automobile Manufactures. www.siamindia.com/statistics.aspx?mpgid=8&pgidtrail=9
4. Most Iconic Motorcycles in History—Gear Patrol. <https://gearpatrol.com/2013/08/27/50-most-iconic-motorcycles>
5. Anthony PD (1995) Costa: the restructuring of the Indian automobile industry: Indian state and Japanese capital. *World Dev* 23(3):485–502
6. VESPA—INDIA. www.vespa.in
7. Ideal Jawa Open Access Articles. research.omicsgroup.org/index.php/Ideal_Jawa
8. JAWA Motorcycles in India. <https://bikeadvice.in/>

9. Sing Kavitha (2007) Predicting organizational commitment through organization culture: a study of automobile industry in India. *J Bus Econ Manag* 8(1):29–37
10. Husain Z, Sushil RD (2001) Pathak: a technology management perspective on collaborations in the Indian automobile industry: a case study. *J Eng Technol Manag* 19:167–201
11. Jain P (2015) A study of customer satisfaction of two wheelers on Yamaha. *IOSR J Bus Manag* 17(8Ver. II):08–19
12. Automobile Industry in India, Indian Automobile Industry <https://www.ibef.org/industry/india-automobiles.aspx>

Effect of Twist Angle and RPM on the Natural Vibration of Composite Beams Made up of Hybrid Laminates



Rakesh Potluri, V. Diwakar, K. Venkatesh and R. Sravani

Abstract Rotating beams are crucial components that have a wide range of application in the aerospace and mechanical engineering fields. Some of the applications of the rotating composite beams include the helicopter blades, wind turbine blades, and propellers but rather than having a straight beam they are generally twisted which gives some added advantage to them. Having a good understanding of their behaviour, especially the natural frequencies of the structure, is crucial for designing a very good structure. In this paper, the effect of the pre-twist angle, rotation speed on the natural vibration behaviour of the rotating composite beams made up of a hybrid laminate was studied. A comparison between the natural frequencies and mode shapes of the composite beam with and without rotation and pre-twist effects was performed. The hybrid laminate was designed and properties of the laminate were found using the CLT theory, executed in the MATLAB software. Finite element analysis (FEA) was used for performing this work using the ANSYS Workbench software.

Keywords Rotating beams · Modal frequencies · Hybrid laminate · Twist angle · RPM (revolutions per Minute) · FEA (finite element analysis)

1 Introduction

In modern times, the metal beams used for the structural purpose are being replaced by the composite ones due to their inherent benefits offered by the composite materials. Rotating beams are usually found in applications such as wind turbines, turbomachinery, robotic sensors, and helicopter blades. Usually, the beams can be classified

R. Potluri (✉)

DVR & Dr HS MIC College of Technology, Kanchikacherla, Krishna Dt., Andhra Pradesh, India
e-mail: y09me042@gmail.com

V. Diwakar

Department of Mechanical Engineering, DIET, Krishna Dt., India

K. Venkatesh · R. Sravani

Department of Mechanical Engineering, GCET, Hyderabad, Telangana, India

© Springer Nature Singapore Pte Ltd. 2019

S. S. Hiremath et al. (eds.), *Advances in Manufacturing Technology*,

Lecture Notes in Mechanical Engineering,

https://doi.org/10.1007/978-981-13-6374-0_50

into different categories based upon different characteristics such as their thickness, their geometric shape, their way of being attached to the structure, and material used for the beams. According to their thickness characteristic, they can be classified as thin or thick beams. According to their material of manufacture, they can be called as either isotropic or composite beams. According to their geometric shape, they can be classified as circular, curved, tapered, twisted, or straight beams. According to the attachment type, they can be classified to be stationary or rotating beams with end condition like clamped, free, and simply supported. The usage of the composite materials in the different structures is on the rise due to the benefits such high strength to weight and high stiffness to weight ratios, their fatigue, and corrosion resistance. Rotating beams and plates are the best examples of the applications of the beams at the industrial level.

Sandwich structures are a special class of composite materials which are usually manufactured by attaching a soft material in between two thin but stiff sheets using an adhesive material. The soft material is referred to as the core, and this core can be made in the form of either foam or honeycomb-like structure. Both isotropic and composite materials can be used for preparing the honeycomb core, and usually, an isotropic material is used for the foam core. The stiff and thin material attached above and below the core material is known as the skin or the face sheet. The best example for such type of constructions is used in the helicopter blades where the skin material is made up of composite layers and the middle portion of the blades is made from a combination of both types of cores. These helicopter blades can also be taken as the great example for rotating beams with one fixed to the hub and another end free.

A lot of engineering applications have used the rotating beams and a good amount of studies on the vibration behaviour of the stationary and rotating beams have been conducted using different theories and FEM as well. Even studies on the mode shapes and natural frequencies of the composite beams made up of composite laminates were performed. But, these studies haven't included the beams made of sandwich structures and hybrid laminates. But if practically analysed, these types of beams may provide a better or more suitable distribution of mass and strength than uniform beams and therefore can meet special functional requirements in architecture, aeronautics, robotics, and other innovative engineering applications.

Rao et al. [1] studied the vibration of the twisted isotropic beams with rotation boundary condition. They concluded that the natural frequencies of the beams were majorly affected by the twist angle of the beam rather than the rotation of the beam. Giurgiutiu and Stafford et al. [2] developed a theoretical model using the motion equations which also took shear and rotary inertia into account for producing the vibration behaviour of the isotropic blades subjected to a constant angular velocity condition. Varadaraja et al. [3] studied the vibration characteristics of a pre-twisted rotating thin-walled beam using the higher shear deformation theory (HSDT) made up with composite laminate for application to actuators and sensor. Patel et al. [4] studied the vibration characteristics of composite beam using the technique of finite element method (FEM). Yoo et al. [5] investigated the vibration behaviour of the rotating beam made out of composite laminates using the Timoshenko beam theory. Kim et al. [6] used the Hamilton principles to derive the chord-wise, axial-

and flap-wise vibrations of a rotating beam. Lee et al. [7] investigated the vibration behaviour of the rotating composite beams with cantilever boundary conditions. Many other people studied the vibration behaviour of the rotating beams using different energy methods, theories, and FEM which were also referred [8–10]. Rakesh et al. [13] studied the effect of the core thickness and face sheet thickness on the bending phenomena of foam cored sandwich structures. In another study, Rakesh et al. [16] performed analytical and FEM analysis on finding out the properties of the honeycomb-cored sandwich structures. Rakesh et al. [11–21] studied the effect of different hybridizations on the mechanical properties of the composite materials, creating and analysing different composites using FEM, experimental and analytical methods. Other references on the FEM, hybrid composites laminates and sandwich structures were also referred from various papers [11–21].

2 Finite Element Analysis

2.1 Objective and Methodology

The primary motive of this work is to study the effect of rotational speed and the angle of twist variation on the fundamental natural frequencies of a rotating cantilever beam. The beam is made up of a sandwich structure which has hybrid composite laminate skin and a thick foam core. First, the properties of the foam core material were found out using the analytical models developed by the Gibson and Ashby [13, 16]. The properties of the composite laminates were found using the classical laminate theory. Analytical calculations for both of the face sheets and the core were performed using the MATLAB software. Surface model of the rotating beam with pre-defined twist angles were created using the SOLIDWORKS software. The surface models and the material models have been used for modelling of the rotating beam made up of sandwich structure and FEA study was performed using the ANSYS Workbench software.

2.2 Geometry

The geometry of the rotating beam consists of the shell surface model for the blade or the beam on which our sandwich structure layup will be modeled. Figure 1 shows the rotating of the beam configuration of the beam. Different beam configurations with different pre-twist angles starting from 0° up to 90° angles with an interval of 15° are designed in SOLIDWORKS and then imported into the ANSYS Workbench software. Figure 2 shows the rotating beam geometries with 0° , 45° , 90° pre-twist angles. The length of the beam is 160 mm and width of the beam is 50 mm. The total thickness of the beam after modelling the layup will be 18 mm in which each face sheet is of 4 mm thickness and the core is of 10 mm thickness.

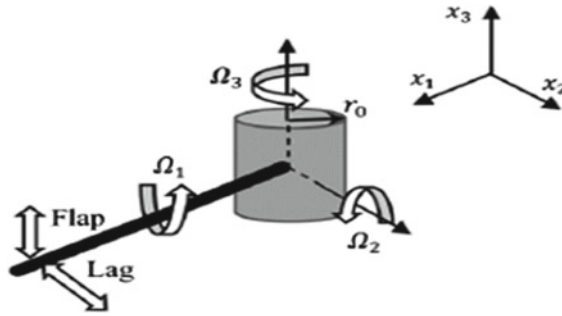


Fig. 1 Rotating beam configuration

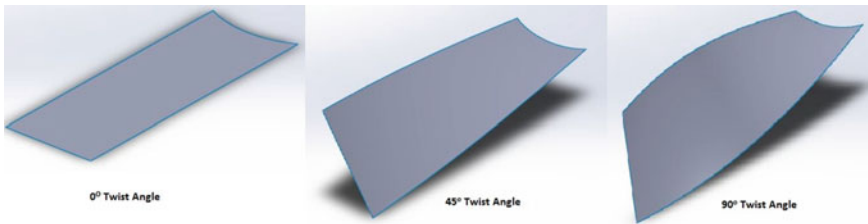


Fig. 2 Rotating beam geometries with different twist angles

2.3 Materials

The skin material is made up of an angle-ply hybrid composite laminate containing S-glass and carbon fibre laminas stacked in the form of an interlaced hybrid layup configuration. Figure 3 shows the layup taken for the face sheets. The properties of the individual laminas are taken from the reference [14]. Analytical calculations using MATLAB for the SAN foam were performed to ensure that the SAN foam material model is available within the ANSYS composite materials database is the one with the same cellular structure and properties that are needed for the study. This is because the structure of the cell inside the foam changes the properties of the foam even if they are made from the similar material. The major reason for selecting this particular foam is its impact resistance and toughness. This type of foam with closed-cell structure is widely being applied to the defence and marine, wind energy, and aerospace structures. Figure 4 shows the layup taken for the sandwich structure.

2.4 Meshing

Shell 281 Element was used for meshing the surface model of the beam in ANSYS Workbench. Figure 5 shows the element type used for the meshing of the shell



Fig. 3 Hybrid composite Laminate layup

Fig. 4 Representation of sandwich structure

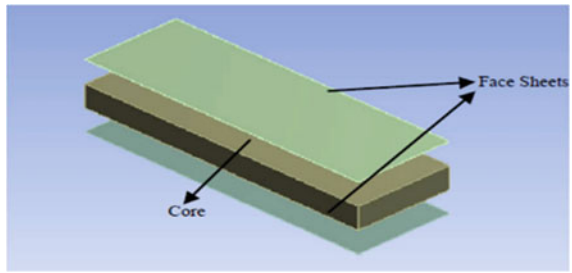
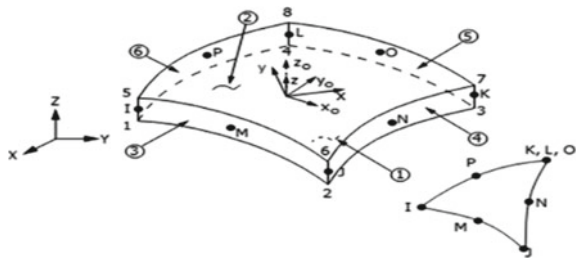


Fig. 5 Shell 281 element



geometry. It contains eight nodes with six degrees of freedom at each node. It is very efficient in modelling thin to moderately thick shell structures. The modelling of the composite structures using this element is mainly dependent on the Mindlin–Reissner shell theory.

2.5 Boundary Conditions

Cantilever boundary condition was considered for the rotating beam. The circular end of the beam is kept fixed and the other end of the beam is left free. The rotational

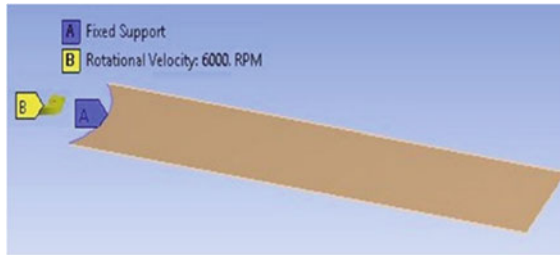


Fig. 6 Boundary conditions applied for the rotating beam FEM model

velocity is also applied at the circular end of the rotational axis in the global y -direction. Figure 6 shows the boundary conditions applied to the rotating beam.

2.6 FEM Validation

The FEM model that is to be used for this study was first validated against the theoretical values obtained from the existing literature. Model consisting of the composite material laminas were created and then the values obtained from the FEA of this model was validated against the theoretical results [10]. From this process, the FEA procedure and model were validated. Then this particular model was further extended to be used for the current study. Figure 7 shows the error percentages between the theoretical and FEM models.

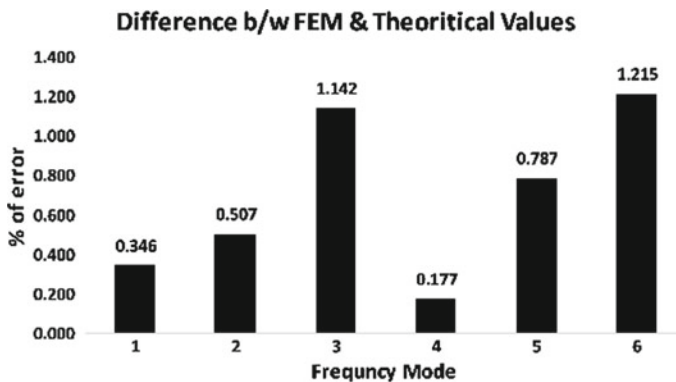


Fig. 7 % of error between FEM and theoretical values in different modes

3 Results

The effect of the twist angle of the beam on different modes of natural frequencies at 0 rpm is shown in Fig. 8. The first six natural frequency modes are taken into account for this study. Flap-wise bending was observed the modes 1, 3, 5, and Lag-wise bending was observed in the modes 4, 6, and twisting was observed in the mode 2 of vibration of the beam. The same modes were observed even when the twist angle was introduced on to the beam. The first natural frequency tends to decrease with the increase in the twist angle of the beam which can be observed from Fig. 8. The second natural frequency also tends to decrease with the increase in the twist angle of the beam which can be observed from Fig. 8.

The third natural frequency tends decreases at first and then it is also seen to be increasing with the twist angle as indicated by Fig. 8. Mode 4th natural frequency tends to decrease with the increase in the twist angle of the beam as indicated in Fig. 8. The 5th and 6th mode natural frequencies tend to increase as with the increase in the twist angle of the beam which is indicated by Fig. 8.

The rate of change in the natural frequencies with respect to the twist angle remains similar at all the different rotational velocities taken for analysis of the rotating beam. From Fig. 9, it can be clearly observed that there is no effect of RPM on the trends shown by the change of natural frequencies with respect to the twist angle. At 15° twist angle, the beam slightly acted in the opposite manner in comparison with the other twist angles in every mode except for the 1st and 2nd modes. The twist angle had a greater effect on the flap-wise and torsional vibration of the beam when compared to that of the lag-wise vibrations.

As the rotational velocity (given in RPM) is increasing, the natural frequencies in all the modes are increasing. The effect of velocity on the first six natural frequencies of the rotating beam is shown in Fig. 10. The rate of change and the trend in the change of the natural frequency values with respect to that of the RPM are analysed at 0°

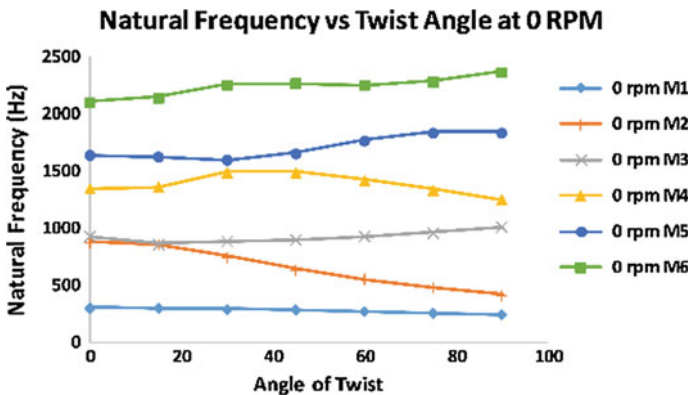


Fig. 8 Mode-1 vibration frequency versus twist angle

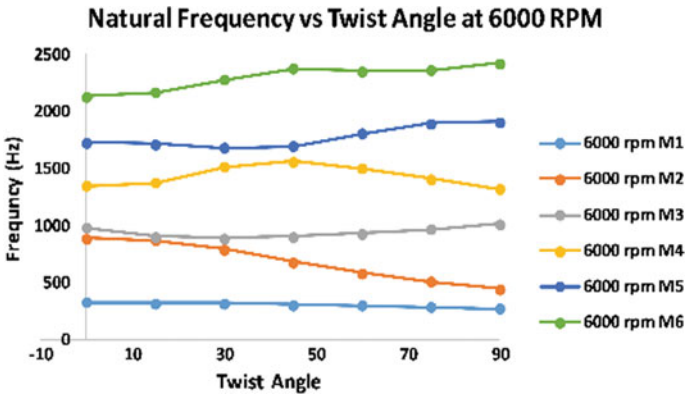


Fig. 9 Natural frequency versus twist angle at 6000 rpm

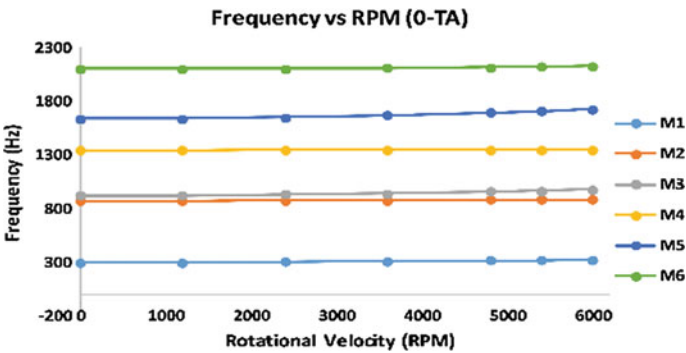


Fig. 10 Variation of natural frequency w.r.to RPM at 0° twist angle

twist angle is shown in Fig. 11. The rate of change in the natural frequencies with respect to the rotational velocity is similar at all the different twist angles taken for the rotating beam. The vibration in the mode 4 and 6 which is the lag-wise vibration has seen a very slight increase in the natural frequency, with respect to the change in the rotational velocity of the beam. The similar trends were observed for all the twist angles. There was no twist angle effect on the general natural vibration behaviour of the rotating beam when the behaviour of the natural frequencies is tested against the rotational velocity. The rotational velocity had a greater impact on the flap-wise and torsional vibration of the rotating composite beam.

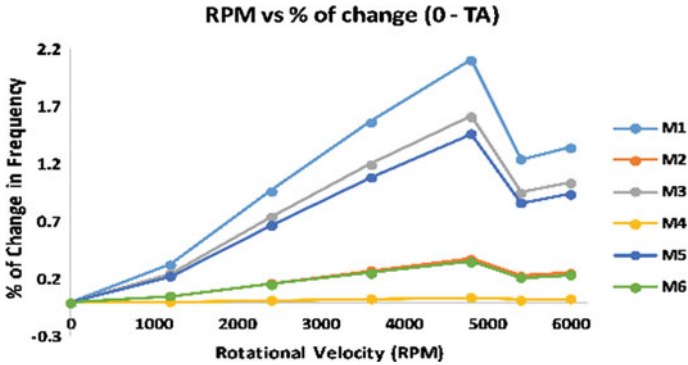


Fig. 11 % of change in the natural frequency w.r.to change in RPM

4 Conclusions

FEM modelling of the rotating beams with sandwich-type hybrid constructions was successfully conducted and the effect of the twist angle and the rotational velocity (given in RPM) on the natural vibration behaviour was studied. All the natural frequencies tend to increase with the increase in the rotational velocity of the beam. The vibrational frequencies of the rotational beam in the modes of 3, 5, 6 are increasing and in the modes, 1, 2, 4 are decreasing with the increase in the twist angle.

References

1. Rao SS, Gupta RS (2001) Finite element vibration analysis of rotating Timoshenko beams. *J Sound Vibr* 242:103–124
2. Giurgiutiu V, Stafford RO (1977) Semi analytic methods for frequencies and mode shapes of rotor blades. *Vertica* 1:291–306
3. Vadiraja DN, Sahasrabudhe AD (2009) Vibration analysis and optimal control of rotating pre-twisted thin-walled beams using MFC actuators and sensors. *Thin-Walled Struct* 47:555–567
4. Patel BP, Ganapathi M (1999) Free vibration analysis of laminated composite rotating beam using C shear flexible element. *Defence Sci J* 49(1):3–8
5. Yoo HH, Lee SH, Shin SH (2005) Flap wise bending vibration analysis of a rotating multi-layered composite beams. *J Sound Vib* 286:745–761
6. Kim H, Yoo HH, Chung J (2013) Dynamic model for free vibration and response analysis of rotating beams. *J Sound Vib* 332:5917–5928
7. Lee SH, Shin SH, Yoo HH (2004) Flapwise bending vibration analysis of rotating composite cantilever beams. *KSME Int J* 18(2):240–245
8. Southwell R, Gough F (1921) The free transverse vibration of air screw blades. *British A.R.C. Reports and Memoranda No: 766* (1921)
9. Bath RB (1986) Transverse vibrations of a rotating uniform cantilever beam with tip mass as predicted by using beam characteristic orthogonal polynomials in the Rayleigh Ritz methods. *J Sound Vib* 105(2):199–210
10. Aksencer T, Aydogdu M (2015) Flapwise vibration of rotating composite beams. *Compos Struct* 134:672–679

11. Potluri R (2017) Mechanical properties of pineapple leaf fiber reinforced epoxy infused with silicon carbide micro particles. *J Nat Fibers* 00:1–15
12. Potluri R, Dheeraj RS, Vital GVVNG (2018) Effect of stacking sequence on the mechanical and thermal properties of hybrid laminates. *Mater Today Proc* 5:5876–5885
13. Potluri R, Eswara A, Raju MN, Prakash KR (2017) Finite element analysis of cellular foam core sandwich structures. *Mater Today Proc* 4:2501–2510
14. Potluri R, Eswara Kumar A, Navuri K, Nagaraju M, Rao DM (2016) Buckling analysis of a ring stiffened hybrid composite cylinder. In: *IOP Conference Series: Materials Science and Engineering*
15. Potluri R, Diwakar V, Venkatesh K, Reddy BS (2018) Analytical model application for prediction of mechanical properties of natural fiber reinforced composites. *Mater Today Proc* 5:5809–5818
16. Potluri R, Rao UK (2017) Determination of elastic properties of reverted hexagonal honeycomb core: FEM approach. *Mater Today Proc* 4:8645–8653
17. Potluri R, Paul KJ, Babu BM (2018) Effect of silicon carbide particles embedment on the properties of Kevlar fiber reinforced polymer composites. *Mater Today Proc* 5:6098–6108
18. Potluri R, Paul KJ, Abdul S, Prasanthi P (2017) Mechanical properties characterization of okra fiber based green composites and hybrid laminates. *Mater Today Proc* 4:2893–2902
19. Potluri R (2018) Mechanical properties evaluation of T800 carbon fiber reinforced hybrid composite embedded with silicon carbide microparticles: a micromechanical approach. *Multidiscip Model Mater. Struct*
20. Potluri R (2015) Comparative study of pressure vessels made from laminated composite material (COPV) with the pressure vessels made with sandwich core composite material. *J Mater Sci Mech Eng* 2:203–207
21. Potluri R, Ketha KK (2015) Comparison between GFRP and CFRP composite power take-off shaft in helicopters for prescribed torque and geometrical constraints. *J Mater Sci Mech Eng* 2:214–219

Tribological Behavior of AZ91–Al₂O₃ Composites by Powder Metallurgy



N. Keerthivasan, S. Selvaraj, V. Anandakrishnan and E. Thayumanvan

Abstract An economic system of magnesium matrix composites was prepared through powder metallurgy technique by varying the reinforcement weight percentage. The developed composite is prepared for the metallographic studies as per the standards and subjected X-ray diffraction (XRD), optical microscopy, and scanning electron microscopy (SEM) analysis to visualize the microstructure, presence and distribution of reinforcement. The tribological study has been conducted with the L9 design and statistically analyzed for the significance of the parameters like reinforcement, load, and sliding velocity using pin-on-disk apparatus. Based on the statistical analysis, the highly influencing parameters are identified as reinforcement percentage followed by sliding velocity and load. Also, using the main effect plot, optimal parameters are identified as high reinforcement percentage, least level load, and maximum level sliding velocity.

Keywords Magnesium matrix composite · Wear rate · Taguchi technique

1 Introduction

Magnesium is the much-sought structural metal, after iron and aluminum in recent years. It is the lightest metal which makes it imperative to develop lightweight and high-strength materials which in turn helps in improving the energy efficiency in plenty of engineering applications. Metal matrix composites (MMCs) based on magnesium alloys are notable for engineering light structures and have tremendous capability in automotive, defense, and aerospace applications. The most commonly using magnesium alloy is AZ91D due to its strength, good atmospheric stability, and outstanding corrosion resistance [1]. The property of the material may be enhanced

N. Keerthivasan (✉) · S. Selvaraj · V. Anandakrishnan · E. Thayumanvan
National Institute of Technology, Tiruchirappalli, Tamil Nadu, India
e-mail: keerthinavaneethan@gmail.com

V. Anandakrishnan
e-mail: krishna@nitt.edu

© Springer Nature Singapore Pte Ltd. 2019
S. S. Hiremath et al. (eds.), *Advances in Manufacturing Technology*,
Lecture Notes in Mechanical Engineering,
https://doi.org/10.1007/978-981-13-6374-0_51

with the help of reinforcements either it may be in the form of oxides, carbides, or borides. Among the reinforcements, Al_2O_3 is the one who used widely due to its thermal and chemical stability [2]. Several research findings were made on the composites through castings and powder metallurgy techniques. In the synthesis processes, the powder metallurgy seems to be most suitable and effective process for the development of metal alloys and the metal matrix composites. Especially, metal matrix composite synthesized using the powder metallurgy route has extended applications in the marine, automobile, aeronautical, and space sectors [3]. Several composites were developed with AZ91 as a matrix with the reinforcements SiC, TiC, ZrB_2 , etc., as (one or in combination) and its metallurgical, mechanical, corrosion, and tribological studies on the produced composites were analyzed as it has more application in the wear, corrosion, and high-temperature environment [3–8]. From the literature, it is understood that there was a much need for the newer magnesium composites and its tribological studies on the magnesium composites. So, this work was proposed to develop AZ91/ Al_2O_3 composite using powder metallurgy technique and further to study its tribological behavior.

2 Experimental Procedure

The powders AZ91 and Al_2O_3 required for the development of the composite are procured from Nextgen Pvt. Ltd, Mumbai. To develop the composite with 0, 1, and 2 wt%, Al_2O_3 reinforcement powder mixture is measured and mixed in such way that 0, 1, and 2 g of Al_2O_3 for every 100 g of AZ91, respectively. Further for uniform distribution and blending of reinforcement, each mixture is ball milled using high-energy ball mill. Subsequently, blended mixture is compacted in cylindrical die using universal testing machine and the compacted preforms are sintered using the furnace at 440 ± 10 °C [9] for two hours and then it is allowed to cool in furnace itself. The developed composite is prepared for the metallographic studies as per the standards and subjected X-ray diffraction (XRD), optical microscopy, and scanning electron microscopy (SEM) analysis to visualize the microstructure, presence, and distribution of reinforcement. The tribological behavior of the developed composites has been studied. For that, the samples from the sintered composites and D3 steel counter disk are prepared as per the requirement of the pin-on-disk wear testing machine. ASTM:G99 standard has been used to conduct the pin-on-disk wear test. The wear rate is taken as the output response has been calculated by measuring the before and after weight of the samples and substitute in the standard equation as given by Baskaran et al. [10] for the wear rate. The reinforcement percentage, load, and sliding velocity are varied to in nine different combinations as per the L9 orthogonal array of Taguchi and corresponding wear rate is obtained as shown in Table 1 and analyzed to find the significance of each variable.

Table 1 L₉ orthogonal array with the wear rate

Reinforcement (wt%)	Load (N)	Sliding velocity (m/s)	Wear rate (mm ³ /min)
0	9.81	1	0.026721
0	19.62	2	0.020848
0	29.43	3	0.020882
1	9.81	2	0.014314
1	19.62	3	0.012088
1	29.43	1	0.023546
2	9.81	3	0.006403
2	19.62	1	0.013605
2	29.43	2	0.012406

3 Result and Discussion

3.1 X-Ray Diffraction Analysis

X-ray diffraction (XRD) is a technique that can be used to analyze the given material both qualitatively and quantitatively. The XRD analysis of the AZ91, AZ91–1 vol.% Al₂O₃, and AZ91–2 vol.% Al₂O₃ is shown in Fig. 1. The first X-ray diffraction pattern is the base metal of AZ91 while the second and third X-ray diffraction patterns show the peaks of composites developed which confirms the presence of Al₂O₃.

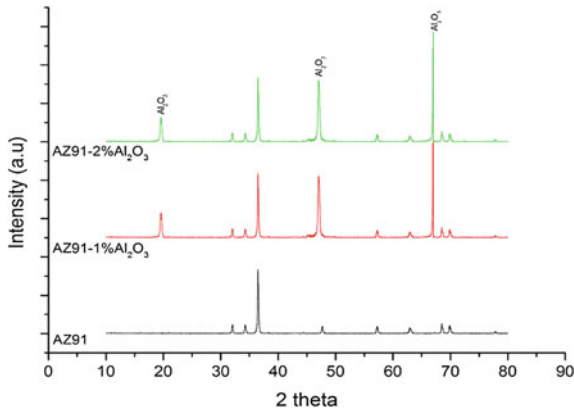
**Fig. 1** XRD pattern showing AZ91, AZ91–1vol.% Al₂O₃ and AZ91–2vol.% Al₂O₃

Table 2 Signal-to-noise ratios for the responses

Level	Reinforcement (wt%)	Load	Sliding velocity
1	32.90	37.41	33.78
2	35.93	36.43	36.21
3	39.78	34.76	38.61
Delta	6.88	2.64	4.83
Rank	1	3	2

3.2 Optical and Scanning Electron Microscope Analysis

The optical microscopy (OM) images of AZ91, the base alloy, are shown in Fig. 2a, and it shows the formation of grain boundaries. The SEM images in Fig. 2b, c of AZ91–1 wt% Al₂O₃ and AZ91–2 wt% of Al₂O₃ confirm the uniform distribution of Al₂O₃ particles in the AZ91 matrix and percentage difference of Al₂O₃.

3.3 Wear Analysis

To attain the required objective of minimum wear rate, Taguchi's "lower the better" quality characteristics are used. A statistical analysis is performed to identify the influence of the variables on the wear rate. From Table 2, the response table for wear rate, it is identified that the reinforcement percentage is the most influencing factor further in the sequence of sliding velocity and load.

The minimum wear rate is obtained for the parameter combination of 2 wt% Al₂O₃, least load of 9.81N, and maximum velocity of 3 m/s, which is identified from the main effect plot as shown in Fig. 3. From the interaction plot, we can identify the significance of the parameter interactions. Figure 4 shows interactions between wt.% of Al₂O₃, load and sliding velocity, in which interactions of load and sliding velocity at lower and medium levels of wt.% are found to be insignificant. When looking at the interaction between load and sliding velocity, it shows significance for lower and medium levels of the load for higher sliding velocity.

The contour plot for a load with sliding velocity infers the least wear rate of 0.010 mm³/min low load and high sliding velocity more than 2.5 m/s as shown in Fig. 5a. Figure 5b illustrates the contour plot for the reinforcement wt%, and sliding velocity infers the low wear rate of 0.010 mm³/min at high sliding velocity above 2.5 m/s and high reinforcement wt% more than 1.5 wt%. Figure 5c expressing contour plot of reinforcement wt.% with load, infers low wear rate at load less than 1.4m/s and reinforcement more than 1.5 wt.% [10].

From the ANOVA, as shown in Table 3, it is identified that the reinforcement percentage of Al₂O₃ is the most significant factor having lesser probability value followed by sliding velocity and load with 99.68% R-sq value. Figure 6 shows

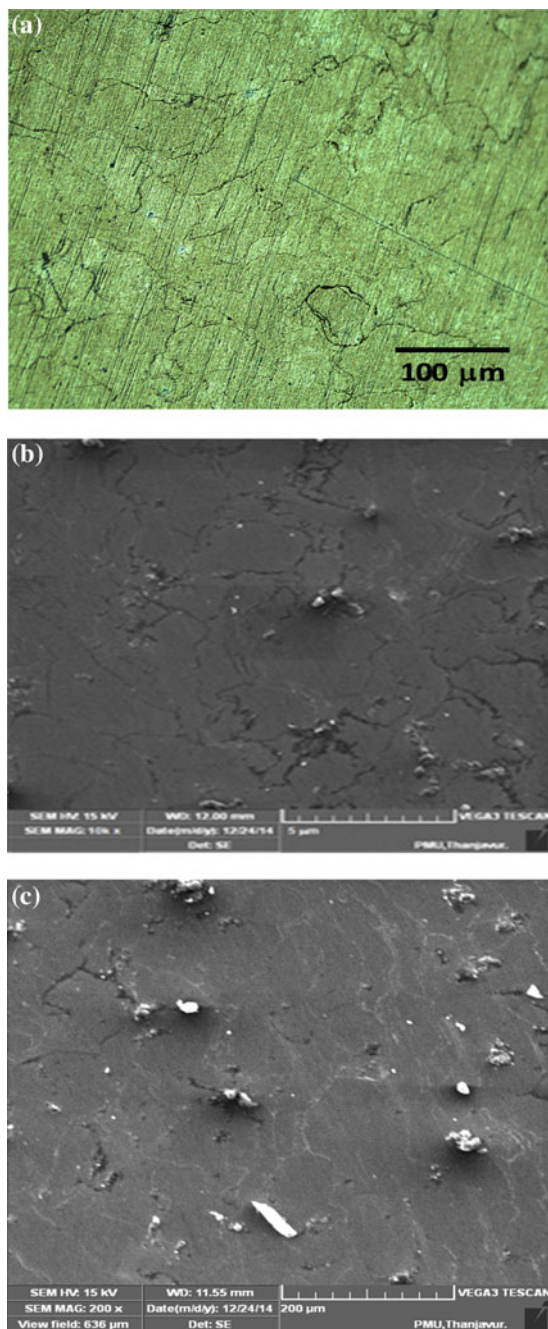


Fig. 2 a Optical microscopy of AZ91, b scanning electron microscopy of AZ91–1 wt% Al₂O₃ composite, c scanning electron microscopy of AZ91–2 wt% Al₂O₃ composite

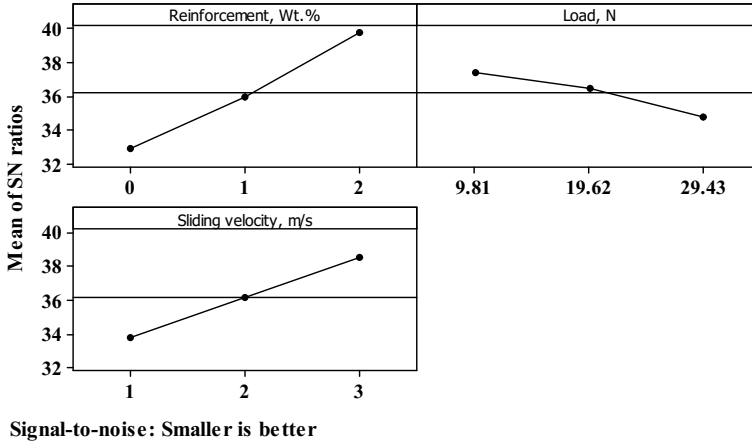


Fig. 3 Wear rate—main effect plot for a mean of SN ratio

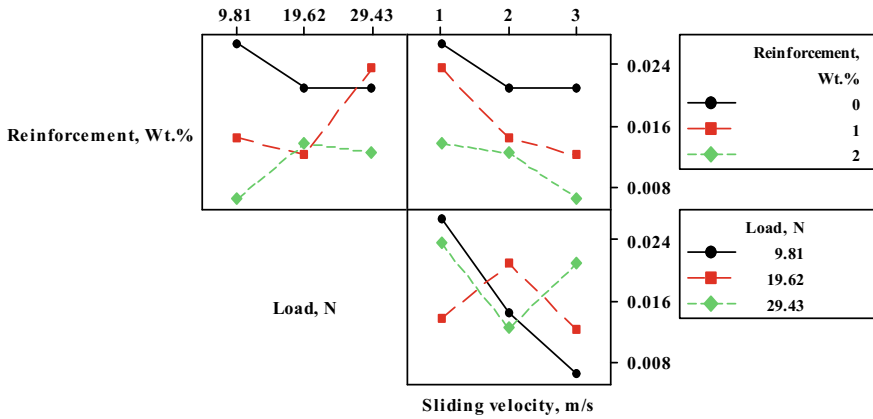


Fig. 4 Wear rate—interaction plot

a normal probability plot in which residues are distributed within the range by following the straight line. The predicted value of wear rate from the analysis is 0.0062280 mm³/min for the run 2 wt% of Al₂O₃, 9.81N load, and 3 m/s sliding velocity which is confirmed with experimental results with least error percentage of 2.81.

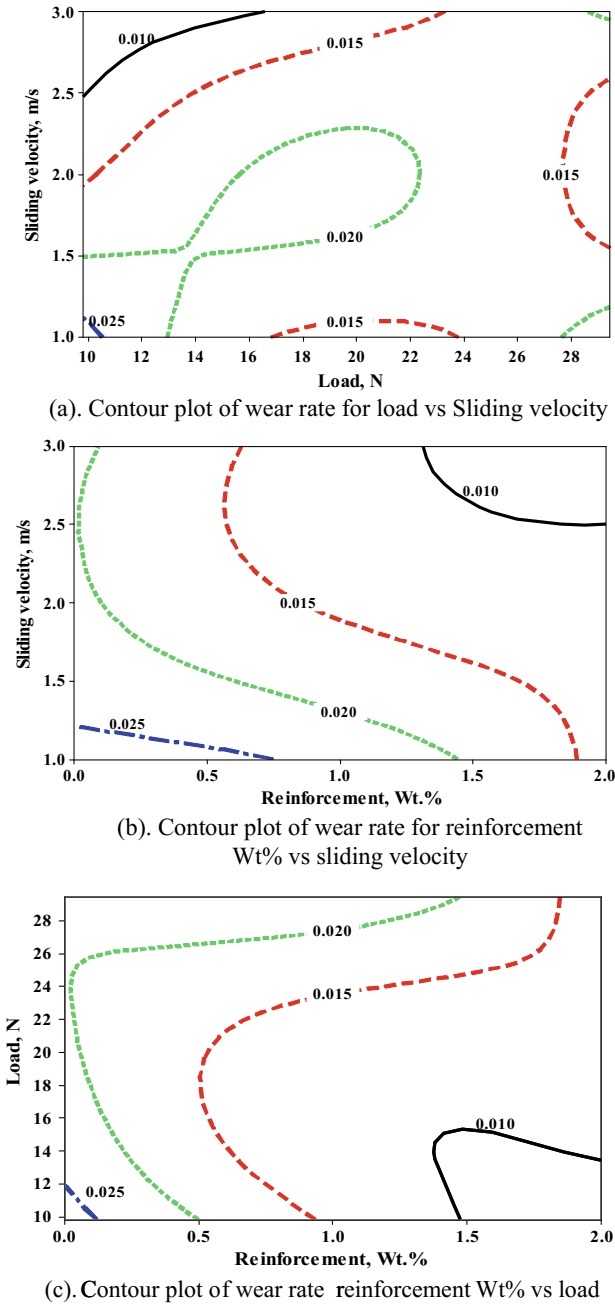


Fig. 5 Wear rate—contour plot of **a** load versus sliding velocity, **b** reinforcement wt% versus sliding velocity, and **c** reinforcement wt% versus load

Table 3 Analysis of variance for the signal-to-noise ratios

Source	DF	Seq SS	Adj SS	Adj MS	F	P ^e
Reinforcement (wt%)	2	0.0002165	0.0002165	0.0001082	195.08	0.005
Load (N)	2	0.0000217	0.0000217	0.0000108	19.53	0.049
Sliding velocity (m/s)	2	0.0001037	0.0001037	0.0000518	93.43	0.011
Error	2	0.0000011	0.0000011	0.0000006		
Total	8	0.0003430				

S = 0.000744892, R-Sq = 99.68%, R-Sq(adj) = 98.71%

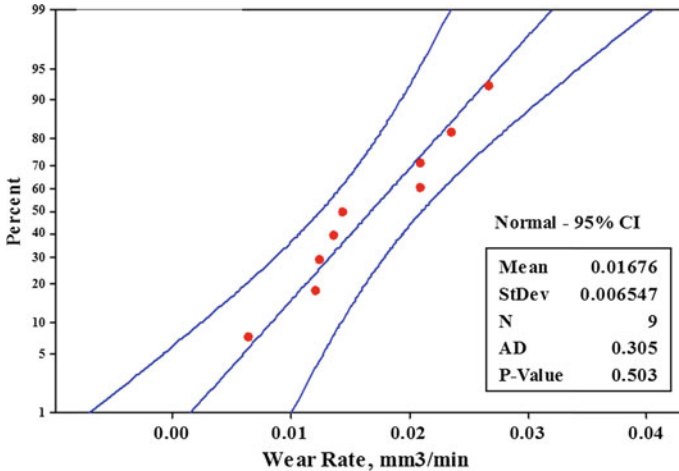


Fig. 6 Wear rate—normal probability plot

4 Conclusion

The metal matrix composite made of AZ91 (matrix) and 0, 1, 2 wt% Al₂O₃ (reinforcement) using powder metallurgy route has been synthesized. The Al₂O₃ presence and uniform distribution have been visualized using the XRD results and SEM images. The tribological study has been conducted with the L9 design and statistically analyzed for the significance of the parameters like reinforcement, load, and sliding velocity. The optimal parameters for obtaining least wear rate as maximum reinforcement of two percentage, low load of 9.81N, and maximum velocity of 3 m/s are identified from the wear rate main effect plot. From the response table, ANOVA, the interaction, and the contour plot, the weight percentage of reinforcement found to be most influencing parameter in obtaining minimum wear rate. The confirmation test was conducted for optimum parameters and obtained very least error.

References

1. Housh S, Mikucki B (1992) Properties and selection: nonferrous alloys and special-purpose materials, vol 2, 10th edn. ASM Handbook
2. Kok M (2005) Production and mechanical properties of Al₂O₃ particle-reinforced 2024 aluminium alloy composites. *J Mater Process Technol* 161:381–387
3. James WB, West GT (2002) Powder metal technologies and applications, vol 7. ASM Handbook
4. Zafari A, Ghasemi HM, Mahmudi R (2014) An investigation on the tribological behaviour of AZ91 and AZ91+3 wt% RE magnesium alloys at elevated temperatures. *Mater Design* 54:544–552
5. Muley SV, Singh SP, Sinha P, Bhingole PP, Chaudhari GP (2014) Microstructural evolution in ultrasonically processed in situ AZ91 matrix composites and their mechanical and wear behaviour. *Mater Design* 53:475–481
6. Ajith Kumar KK, Pillai UTS, Pai BC, Chakraborty M (2016) Dry sliding wear behaviour of Mg–Si alloys. *Wear* 303:56–64
7. Arora HS, Singh H, Dhindaw BK (2013) Wear behaviour of an Mg alloy subjected to friction stir processing. *Wear* 303:65–77
8. Nami H, Halvae A, Adgi H (2011) Transient liquid phase diffusion bonding of Al/Mg₂Si metal matrix composite. *Mater Des* 32:3957–3965
9. Narayanasamy R, Anandakrishnan V, Pandey KS (2008) Effect of carbon content on the workability of powder metallurgy steels. *Mater Sci Eng, A* 494(1–2):337–342
10. Baskaran S, Anandakrishnan V, Duraiselvam M (2014) Investigations on dry sliding wear behaviour of in situ casted AA7075—TiC metal matrix composites by using Taguchi technique. *J Mater Des* 60:184–192

Annealing and ZnO Doping Effects on Hydrophilicity and Mechanical Strength of PVDF Nanocomposite Thin Films



Mani Satthiyaraju, T. Ramesh and Kumarasamy Jagatheswaran

Abstract Polyvinylidene fluoride (PVDF)-based nanocomposite thin films for water filtration devices, sensors and actuators, and biomedical applications were prepared using phase inversion technique. The main aim of this research work is to analyze the effects of annealing temperatures on hydrophilicity, mechanical strength, and elongation at break of the zinc oxide (ZnO) modified PVDF nanocomposite thin films. Thermal treatment of annealing across broad ranges is the responsible for the molecular structure orientation and formation of beta phase in the PVDF nanocomposites. Also crosslinking between the polymer molecules is occurred due to the effect of thermal conditioning. Finally, this recrystallization of the polymer molecules is shown the enhancement in the hydrophilic nature (53.7°) for 4 wt% ZnO at 160 °C, tensile strength (3.42 MPa), and elongation at break (105.46%) for 1 wt% ZnO at 130 °C condition conditioned PVDF nanocomposite thin films.

Keywords Thin films · PVDF · Annealing · Nanocomposite · Mechanical strength · Hydrophilicity

1 Introduction

Recent development of polymer nanocomposite thin films is more attracted in the field of sensors and actuators [1], energy harvesting [2], piezoelectric devices [3], filtration devices [4], nanogenerators [5], and biomedical [6] applications. Among the polymer thin films preparation methods of electrospinning, phase inversion and melt blending, the phase inversion is simple and easy to manufacture and low cost.

M. Satthiyaraju · T. Ramesh
Department of Mechanical Engineering, National Institute of Technology,
Trichy 620015, India

K. Jagatheswaran (✉)
Department of Mechanical Engineering, Erode Sengunthar Engineering College,
Perundurai 638057, India
e-mail: jagatheswaran3@gmail.com

© Springer Nature Singapore Pte Ltd. 2019
S. S. Hiremath et al. (eds.), *Advances in Manufacturing Technology*,
Lecture Notes in Mechanical Engineering,
https://doi.org/10.1007/978-981-13-6374-0_52

The addition of inorganic nanofillers with polymer is one of the keys to identify the novel functions in the wide range of applications.

Moreover, blending with other polymers, thermal treatment, organic fillers, inorganic fillers, and methods of preparations are considered as key parameters. Mainly, the polymer nanocomposite membranes are treated with heat for the reason of improving membrane firmness, mechanical stability, and chemical stability. Hence, the molecular chains of the polymer have been rearranged and cause the property variations. Based on the two preparation methods, we have used top-down way as nanofillers and polymer blended directly.

PVDF is semi-crystalline, easy formable into thin membranes, good mechanical and chemical stability, and it possesses high-level ferroelectric behavior. To our best part of the literature review, there is no much evidence on mechanical strength and hydrophilicity of PVDF nanocomposite membranes. The breaking strength of the nanocomposite thin films may be enhanced by heat treatment process. The influence of thermal degradation on the morphological and mechanical conditions of PVDF has been investigated to find the crystallization phase of the PVDF thin films. They also revealed that higher heat-treated temperature would affect the crystalline phase of the PVDF membranes. Consequently, mechanical strength of the PVDF polymer depends on the annealing conditions and treatments [7]. Moreover, it should be appropriate to understand optimized annealing treatments for improving the mechanical strength and morphological effects on the PVDF due to interfusion between the molecular chains. The cooling conditions of the PVDF thin films also important aspect to be considered but here that has not been accounted to know the crystallization kinetics of the polymer.

In this work, ZnO-modified PVDF thin films were prepared using phase inversion technique. Different ranges about 0, 1, 2, and 3 wt% ZnO nanoparticles doped PVDF polymer thin films were treated with different temperatures such as 100, 130, and 160 °C. Hydrophilic nature and mechanical stability of annealed PVDF nanocomposite thin films were using water contact angle test and uniaxial tensile test. Interfusion between the bonds of PVDF molecules has shown the greater role in pore size and superior mechanical strength.

2 Experimental Methods

2.1 Materials and Methods

Polyvinylidene fluoride (PVDF), Zinc oxide (ZnO) nanoparticles, Dimethylacetamide (DMAc) as a solvent were purchased from Sigma-Aldrich. All the materials and chemicals were processed as received without any further purification. PVDF membrane was prepared using the phase inversion method and the composition details of the solution is given in Table 1.

Table 1 Compositions of the Heat-treated and ZnO-doped thin films

Thin film code	PVDF (wt%)	ZnO (wt%)	Solvent (DMAc) (wt%)
M1	20	0	80
M2	20	1	79
M3	20	2	78
M4	20	3	77

The polymer solution was magnetically stirred for 3 h and then sonicated for 30 min to avoid the agglomeration problems of nanoparticles with polymer chains. After processing the polymer solution, the thin films were cast on the glass substrate using the knife. Finally, they were dried in vacuum condition. Then, all the thin films were annealed at 100, 130, and 160 °C about 6 h in vacuum oven.

2.2 Contact Angle Measurement

The distinct static water contact angles of the thin films were examined at atmospheric conditions using goniometer (ACamD3, Apex Instruments, India). A 4 μ L droplet of deionized water was placed on the surface of the thin films and the angle between the thin film and water droplet was captured by using high-speed camera. The static WCA measurement was noted again and again as nearly threefold to fivefold and stated as the mean value. The hydrophilicity, hydrophobicity adhesion property, and surface free energy were determined by measuring the static and dynamic water contact angles [8].

2.3 Mechanical Testing

The mechanical strength and elongation at break of the nanocomposite thin films were determined using a miniature version of tensile testing machine (Tinius Olsen, H50KL/150). The thin films were stretched in a unidirectional way as clamps moved away from them at 0.5 mm/min strain rate. By dividing the final length and initial length of the thin film after and before stretching, the stretching ratio was calculated. After conditioning of the thin films in the dry oven, the samples were cut into shape of rectangular (10 mm \times 30 mm). All the test samples of thin films were conducted in atmospheric condition. As per the ASTM, D882 M has been followed for the samples tensile testing of the nanocomposite thin films.

3 Results and Discussion

3.1 Contact Angle Results

Water contact angle was accounted to estimate the morphological behavior of the thin film surface that has shown an important role in the permeability performance of the nanocomposite surfaces. The hydrophilic nature of the PVDF nanocomposite and heat-treated thin film was examined by the water contact angle results. Figure 1a–d shows the water contact angles for the untreated and nanocomposite membranes. Different wt% of ZnO nanoparticles reveal the effect on the water contact angles that metal oxides like ZnO nanofillers have attraction toward the water particles. Hence, increment of nanofillers has been resulted the decreasing order of the water contact angle. Additionally, the thermally treated thin films also show the hydrophilic nature. PVDF is a hydrophobic natured material. Here, additional conditions on the membranes totally agree with the hydrophilic nature of the PVDF polymer nanocomposite membranes. The water contact angle values of the films were listed in Table 2.

The pure PVDF (M1) and untreated thin film have shown the greater contact angle of 78.7°, signifying that it was in hydrophobic nature. After introducing the ZnO nanoparticles as 0, 1, 2, and 3 wt%, the contact angles were decreased to 76.7°, 73.1°, and 68.8° (Fig. 2), suggesting greater hydrophilic nature of PVDF/ZnO due to the presence of hydroxyl groups on the surface of the ZnO nanofillers. This effect from the ZnO nanoparticles reveals the high affinity of water molecules of nanocomposite thin films.

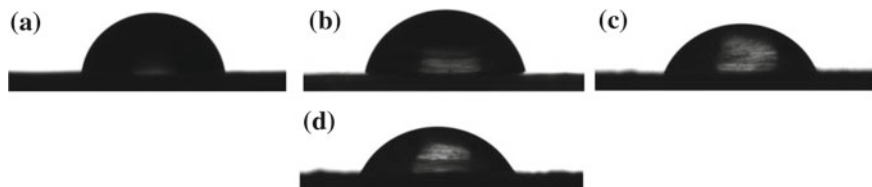


Fig. 1 Water contact angle images of PVDF nanocomposite membranes for **a** M1_UT, **b** M2_100 °C, **c** M3_130 °C, **d** M4_160 °C

Table 2 Contact angle values for various thermal annealing temperatures and doping effects

Sample code	Temperature conditions											
	Untreated			100 °C			130 °C			160 °C		
	<i>L</i>	<i>R</i>	Mean	<i>L</i>	<i>R</i>	Mean	<i>L</i>	<i>R</i>	Mean	<i>L</i>	<i>R</i>	Mean
M1	79.1	78.4	78.7	77.3	75.4	76.3	70.1	67.6	68.9	60.7	58.5	59.6
M2	77.4	76.1	76.7	73.6	72.7	73.2	68.1	67.4	67.7	58.1	57.4	57.8
M3	73.8	72.5	73.1	71.9	70.6	71.2	65.5	64.3	64.9	55.8	54.4	55.1
M4	69.4	68.1	68.8	68.1	67.5	67.8	63.2	62.9	63.0	54.1	53.3	53.7

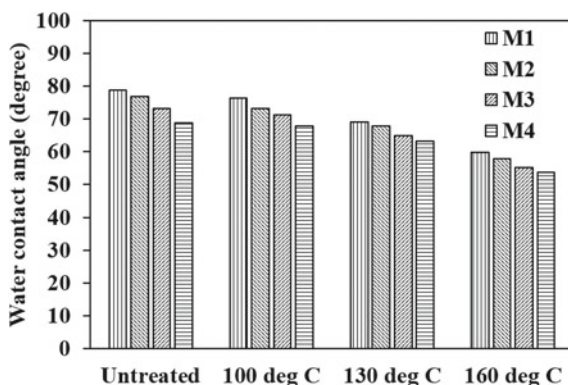


Fig. 2 Water contact angle bar chart for thin films treated with various annealing temperatures and ZnO doping effects

When sustained to add the ZnO wt%, the water contact angle of M4 was similarly decreased with compared to M1 as pure PVDF thin film. It could be attributed to the chance of agglomeration of ZnO nanoparticles in excess addition, motivated to the weakening of the surface and hydrophilic nature of PVDF. Moreover, the additional concentration of ZnO particles has seen as susceptible to measure the surface morphology. Finally, the more addition toward higher percentage, it leads to hydrophobic again due to the excess of ZnO nanofillers.

Moreover, the heat treatment has shown that the water contact angle is decreased as hydrophobic to hydrophilic nature due to the reason of pore size of the PVDF nanocomposite thin films has been minimized. Compare than untreated pure PVDF, 100, 130, and 160 °C annealed thin films has resulted with 76.3°, 68.9°, and 59.6°, respectively. Also, the water contact angle decreased for annealed PVDF nanocomposite thin films due to the combined effect of annealing and nanoparticles concentration.

Conclusively, the water contact angle declined to 53.7° for the thin film code M4 at 160 °C annealed nanocomposite membranes. Therefore, the combined effect of nanofillers and thermal treatment resulted in the hydrophilic nature compare than untreated pure PVDF nanocomposite thin films.

3.2 Mechanical Testing Results

The heat treatment and nanoparticles doping have affected physical bonding between the macromolecules of PVDF polymer [9]. The thin films were treated with various ranges of temperatures to evaluate the optimized temperature which possess good mechanical strength and elongation. Here, the temperature range of 100, 130, and

160 °C was selected to examine the influence of annealing temperature of PVDF/ZnO nanocomposite thin films.

Hence, the addition of ZnO nanoparticles has revealed the enhancement in the ultimate strength of the PVDF nanocomposite thin films. As shown in Fig. 3, addition of ZnO nanofillers increased the mechanical stability up to 1 wt% after that it has been decreased for the reason of excessive addition of the nanoparticles with the presence of the agglomeration. Moreover, the heat treatment and doping effects show the interesting results that the enhancement of mechanical strength of 1 wt% of ZnO with 130 °C annealed thin film. Then, the result of elongation at break reveals that there is a decreasing nature of elongation at 130 and 160 °C due to the interdiffusion of the PVDF molecular chains.

Though the temperature effect of 160 from 100 °C for the pure PVDF/ZnO nanocomposite thin films, the elongation at break declined to 118.25–84.56%. Based on these results, it shows that after 130 °C, thin films are stiffer than the films treated with 160 °C. However, the mechanical performance of the treated thin films is significantly influenced by PVDF/1 wt% ZnO at 130 °C with respect to stress–strain curves of the annealed nanocomposite thin films. The porosity and pore sizes are decreased with the temperatures from 100 to 160 °C due to the internal molecular physical bonding of chains. Finally, the thin film PVDF/ZnO 1 wt% treated at 130 °C revealed the greater tensile strength (3.42 MPa) and elongation at break (105.46%). Conclusively, as per the aforesaid wide-ranging results, the mechanical stability and hydrophilicity could be regulated by modifying the ZnO wt% doping and annealing temperature.

Figure 3 shows the thin film treated with 130 °C and 1 wt% ZnO doping results the maximum mechanical tensile strength (3.42 MPa) compared to all other treated and doping conditions due to the physical bonding chains.

Though, the compaction of PVDF/ZnO molecular chains has the direct relation to the enhancement of the mechanical strength and decrement in elongation at break after the processing with thermal treatment. The elongation at break has been decreased from 107 to 84.58% for the pure PVDF thin films. Then, the thermal treatment has shown the further decrement in the elongation at break for the nanocomposite thin films as 96–63.82% over the wide ranges of the temperature effects.

Though, the agglomeration of excessive addition of ZnO nanoparticles could weaken the mechanical strength and elongation at break of the PVDF/ZnO nanocomposite thin films [10]. Thermal treatment over the 110 °C, the viscosity of the PVDF/ZnO nanocomposite thin films declines more to permit the molecular chain movements and molecular chain rearrangements in the crystalline phase [11].

Finally, the breaking strength of the PVDF nanocomposite membranes could be enhanced through the annealing process, and it is highly promising to the applications of sensors and actuators, water purification systems, piezoelectric energy harvesting, and biomedical systems.

Fig. 3 a–d Stress–strain curves and e–h tensile strength and Elongation bar charts for M1, M2, M3, and M4 treated with various annealing temperatures and ZnO doping effects

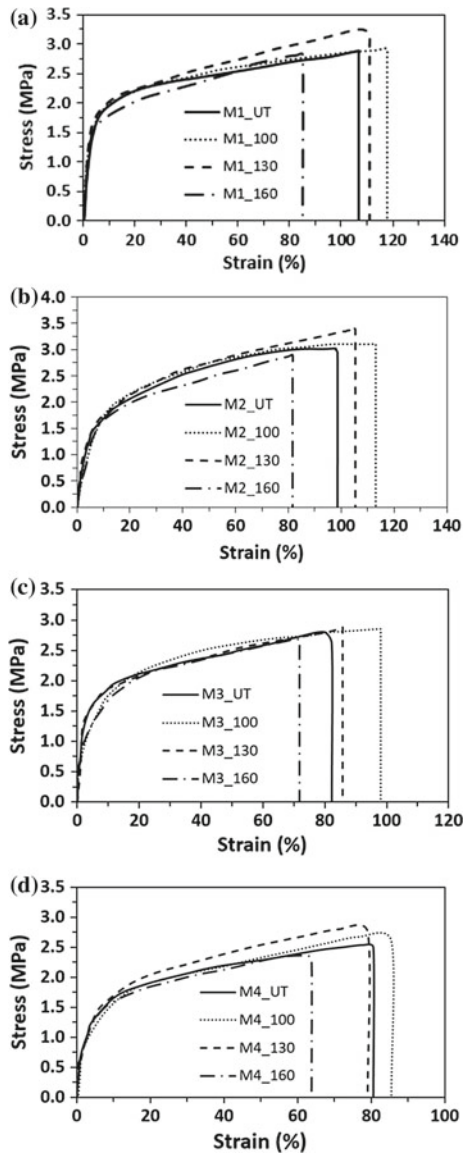
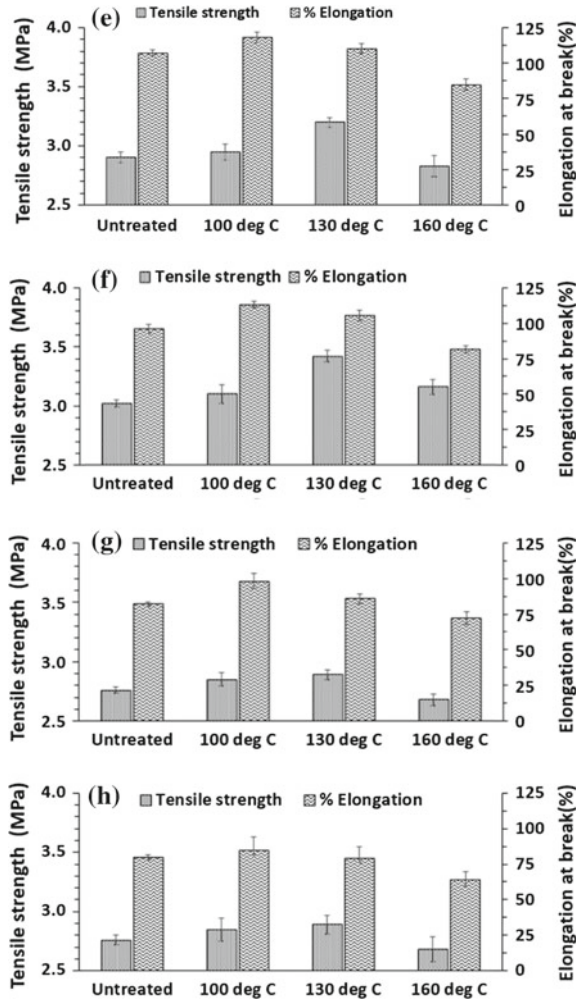


Fig. 3 (continued)



4 Conclusion

In conclusion, the nanocomposite PVDF thin films modified with ZnO were prepared using the phase inversion technique. The broad ranges of the temperature effects on the water contact angle, mechanical strength, and elongation at break of the nanocomposite thin films are observed. The WCA indicates that hydrophobic nature of the PVDF turns to the hydrophilic nature and stress–strain curves show the mechanical responses of the recrystallized polymer nanocomposites. Finally, the crosslinking of polymer molecules due to the thermal treatment is the main reason for the enhancement of mechanical properties as tensile strength (3.54 MPa) and elongation at break (105.46%) 1 wt% ZnO at 130 °C condition. It is promising that

annealed and enhanced mechanical properties of the PVDF nanocomposite membranes could be used in water filtration devices, sensing and actuating platforms, and purification systems.

References

1. Lopes AC, Gutierrez J, Barandiaran JM (2018) Direct fabrication of a 3D-shape film of polyvinylidene fluoride (PVDF) in the piezoelectric β -phase for sensor and actuator applications. *Eur Polymer J* 99:111–116
2. Si SK, Karan SK, Paria S, Maitra A, Das AK, Bera R, Bera A, Halder L, BKhatua B (2018) A strategy to develop an efficient piezoelectric nanogenerator through ZTO assisted γ -phase nucleation of PVDF in ZTO/PVDF nanocomposite for harvesting bio-mechanical energy and energy storage application. *Mater Chem Phys* 213:525–537
3. Huang L, Lu C, Wang F, Dong X (2016) Piezoelectric property of PVDF/graphene composite films using 1H, 1H, 2H, 2H-Perfluorooctyltriethoxysilane as a modifying agent. *J Alloy Compd* 688:885–892
4. Zhang X, Shen L, Lang W, Wang Y (2017) Improved performance of thin-film composite membrane with PVDF/PFSA substrate for forward osmosis process. *J Membr Sci* 535:188–199
5. Thakur P, Kool A, Hoque NA, Bagchi B, Khatun F, Biswas P, Brahma D, Roy S, Banerjee S, Das S (2018) Superior performances of in situ synthesized ZnO/PVDF thin film based self-poled piezoelectric nanogenerator and self-charged photo-power bank with high durability. *Nano Energy* 44:456–467
6. Shin KY, Lee JS, Jang J (2016) Highly sensitive, wearable and wireless pressure sensor using free-standing ZnO nanoneedle/PVDF hybrid thin film for heart rate monitoring. *Nano Energy* 22:95–104
7. Liu J, Lu X, Wu C (2013) Effect of annealing conditions on crystallization behavior and mechanical properties of NIPS poly(vinylidene fluoride) hollow fiber membranes. *J Appl Polym Sci* 129:1417–1425
8. Al-Gharabli S, Kujawa J, Mavukkandy MO, Arafat HA (2017) Functional groups docking on PVDF membranes: Novel Piranha approach. *Eur Polym J* 96:414–424
9. Arribas P, Khayet M, García-Payo MC, Gil L (2014) Self-sustained electro-spun polysulfonenano-fibrous membranes and their surface modification by interfacial polymerization for micro- and ultra-filtration. *Sep Purif Technol* 138:118
10. Bai H, Wang X, Zhou Y, Zhang L (2012) Preparation and characterization of poly(vinylidene fluoride) composite membranes blended with nano-crystalline cellulose. *Progr Nat Sci: Mater Int* 22(3):250–257
11. Satapathy S, Pawar S, Gupta PK, Varma KBR (2011) Effect of annealing on phase transition in poly(vinylidene fluoride) films prepared using polar solvent. *Bull Mater Sci* 34(4):727–733

Optimization of Transient State Temperature Distribution Analysis on Diffusion-Bonded Joints of Ti–6Al–4V With SS304L Stainless Steel Alloy



K. Muthukumar, R. B. Durairaj, G. Mageshwaran, J. Jayajeevahan, V. Sriram and Vikram Naidu

Abstract The Experimental study of transient solid state diffusion bonding was created with dissimilar material such as Ti–6Al–4V and SS304L stainless steel for the parameters such as temperature (1023, 1073, and 1123 K), pressure (50, 100, and 150 bar), and holding time (1, 1.5, and 2 h). The maximum tensile strength and maximum hardness were gained experimentally and theoretically for the corresponding conditions of temperature, pressure, and holding time. Among the analysis from the results relations to the chosen parameters were studied and mentioned. Also maximum and minimum temperature distributions and maximum and minimum stress intensities of diffusion-bonded joints were mentioned through ANSYS diagrams.

Keywords Diffusion bonding · Tensile strength · Hardness · Temperature distribution · Stress intensity

1 Introduction

Orhan et al. [1] explained about the basics of diffusion bonding. They mentioned that the highly developed bonding development of two same or different materials bonded in solid state by diffusion bonding. Balasubramanian et al. [2] studied about the solid state diffusion bonding of Ti–6Al–4V with AISI 304 stainless steel joints and they concluded that the greatest lap shear strength obtained at 800 °C, 60 min, and 5 MPa, and after 800 °C with increase in holding time, the shear strength will be reduced. Kurt et al. [3] experimentally studied about diffusion bonds of gray cast iron and AISI 4140 steel boundary microstructure and shear strength by the effect

K. Muthukumar (✉)

Chendhuran College of Engineering and Technology, Pudukkottai, India
e-mail: mkmuthuind@gmail.com

R. B. Durairaj · G. Mageshwaran · J. Jayajeevahan · V. Sriram · V. Naidu
Sathyabama Institute of Science and Technology, Chennai, India

© Springer Nature Singapore Pte Ltd. 2019
S. S. Hiremath et al. (eds.), *Advances in Manufacturing Technology*,
Lecture Notes in Mechanical Engineering,
https://doi.org/10.1007/978-981-13-6374-0_53

of temperature. They mentioned that the corresponding materials' maximum shear strength reached at 1000 °C.

Bulent Kurta et al. [4] concluded that ferrite stabilization on the AISI 4140 side owing to Cr diffusion from the SS was the most important feature of the microstructures. Orhan et al. [5] experimentally investigated about a micro-duplex SS to Ti-6Al-4V diffusion bonding and they concluded with the help of SEM tests and EDS analyzes that high-quality bonding was created with 30 min and 800 °C. Islam and Ridley [6] explained for the variety of bonding circumstances of the compressive lap shear strength of bonds in Avesta 2205 as a function of pressure and time. Elrefaey et al. [7] obviously investigated about the diffusion-bonded joints that were studied through SEM, micro-hardness measurement, shear strength test, and XRD. They concluded that the diffusion joints could not be bonded even at holding time of 3 h at inferior than the temperature of 800 °C.

Ghosh et al. [8] clearly provided optical micrographs and SEM-BSE images of the transition joints bonded at 850 °C for 30–150 min. Fielding et al. [9] mentioned that the enough holding time is necessary for diffusion bonding temperature and pressure to achieve near contact between the faying surfaces. Yuan et al. [10] completely mentioned about TA17 to 0Cr18Ni9Ti diffusion bonding by the impulse pressure and the associations between the bonding parameters and the tensile strength of the bonded joints with the help of SEM fractographs of gray region and dark block region. He et al. [11] clearly discussed about diffusion bonding with the help of the SEM, EPMA, and XRD for the effect of the crossing-point structures.

2 Materials

The most important properties related to this investigation were listed in Table 1 [12].

For diffusion bonding, the specimen's sizes were mentioned in Table 2. The mating surfaces of Ti-6Al-4V and AISI 304 stainless steel material pieces were refined in a disk polishing unit with 0.6 μm diamond paste and also the mating surfaces of the both material pieces were ground to obtain flat surface with the help of surface grinder (Table 3).

3 Experimental Method

The full factorial design of the diffusion-bonded joints of Ti-6Al-4V—SS304L stainless steel were clearly given in Table 4. By using the diffusion bonding unit, the prepared sample specimens were placed into the heating chamber along with the spacers to adjust the height. Spacers were used to restrict 2–3 mm bellows movement;

Table 1 Properties of Ti-6Al-4V and SS304L stainless steel

No.	Properties	Unit	Ti-6Al-4V	SS304L
1	Melting point	(°C)	1550–1650	1400–1450
2	Density	(Kg/m ³)	4420	1073
3	Thermal conductivity	W/m k)	5.8	16.2
4	Specific heat	(J/Kg/K)	620	480
5	Thermal diffusivity	(m ² /s)	8×10^{-6}	3.91×10^{-6}
6	Hardness	(HV)	305–340	125–140
7	Elastic modulus	(GPa)	106	190
8	Ultimate tensile strength	(MPa)	985–1090	519
9	Yield strength	(MPa)	830–930	170
10	Elongation	(%)	14	40

Table 2 Specimen sizes

No.	Parameters	Dimension (mm)
1	Diameter (<i>d</i>)	40
2	Length (<i>l</i>)	20

Table 3 Design of experiments

Level	Temperature (°C)	Pressure (bar)	Time (h)
1	1023	50	1
2	1073	100	1.5
3	1123	150	2

then, the heating chamber and the chiller unit of the vacuum system were switched on and also the required temperature was positioned. After the require temperature was reached, the press was switched on and the load indicator was checked to read 0000. Then, the required load was applied by lowering the ram of the hydraulic press; the bellows movement is minimum ensured. Starting time and ending time were noted. The temperature in hours and the load in bar were maintained for the fixed process time. Then the heating chamber was switched off and the press was unloaded. But, the vacuum system and chiller unit of the heating chamber was running. When the temperature of chamber reaches to surrounding temperature then the vacuum system would be switched off. Finally, the chamber was opened and the diffusion-bonded sample piece was taken out. This process was repeated for our various requirement conditions.

Table 4 Full factorial design for diffusion bonding of Ti–6Al–4V—SS304L stainless steel

Experiment No.	Temperature (K)	Pressure (bar)	Time (h)
1	1023	50	1
2	1023	50	1.5
3	1023	50	2
4	1023	100	1
5	1023	100	1.5
6	1023	100	2
7	1023	150	1
8	1023	150	1.5
9	1023	150	1
10	1073	50	1.5
11	1073	50	2
12	1073	50	1
13	1073	100	1
14	1073	100	1.5
15	1073	100	2
16	1073	150	1
17	1073	150	1.5
18	1073	150	2
19	1123	50	1
20	1123	50	1.5
21	1123	50	2
22	1123	100	1
23	1123	100	1.5
24	1123	100	2
25	1123	150	1
26	1123	150	1.5
27	1123	150	2

$$\text{DOE} = (\text{Level})^{\text{Factors}} = 3^3 = 27$$

4 Result and Discussion

4.1 Transient Analysis in ANSYS of Ti–6Al–4V—SS304L Stainless Steel

Temperature distribution and stress intensity of diffusion-bonded joint of Ti–6Al–4V—SS304L stainless steel at temperature of 1023 K, pressure 50 bar, and 1 h holding time was shown in Fig. 1; similarly, Fig. 2 showed for 1023 K temperature,

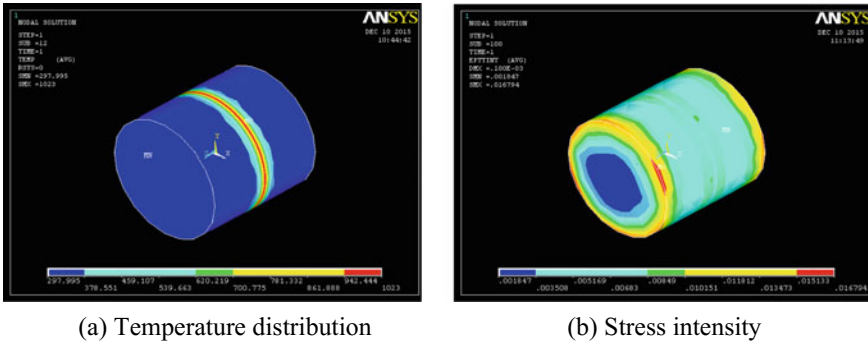


Fig. 1 Diffusion-bonded joint of Ti–6Al–4V—SS304L stainless steel (1023 K, 50 bar, and 1 h)

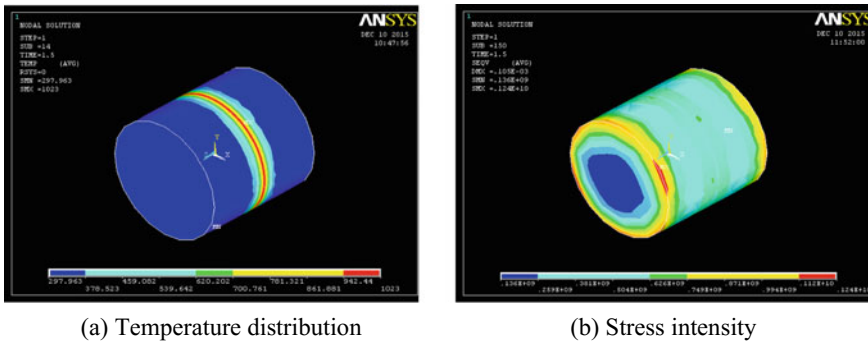
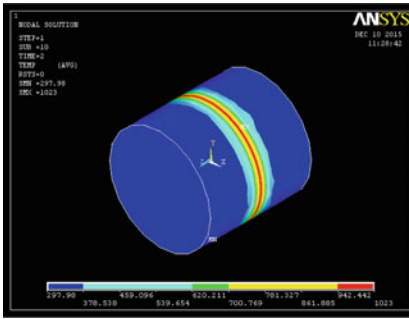


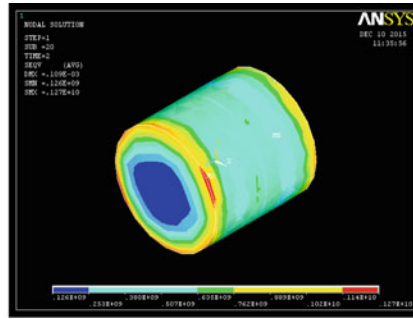
Fig. 2 Diffusion-bonded joint of Ti–6Al–4V—SS304L stainless steel (1023 K, 100 bar, and 1.5 h)

100 bar pressure, and 1.5 h holding time; Fig. 3 indicated for 1023 K temperature, 150 bar pressure, and holding time 2 h; Fig. 4 mentioned for 1073 K temperature, 50 bar pressure, and holding time 1 h; Fig. 5 illustrated for temperature 1073 K, 100 bar pressure, and holding time 1.5 h; Fig. 6 specified for 1073 K temperature, 150 bar pressure, and holding time 2 h, Fig. 7 demonstrated for 1123 K temperature, 50 bar pressure, and holding time 1 h; Fig. 8 declared for 1123 K temperature, 100 bar pressure, and holding time 1.5 h; and finally, Fig. 9 also demonstrated for 1123 K temperature, 150 bar pressure, and holding time 2 h (Fig. 7).

The maximum temperature on joint was represented by red color and minimum temperature was represented by blue color in the temperature distribution diagram. For all the joints in center portion reached the maximum temperature. The stress intensity is a fracture mechanics to predict the state near the tip of crack caused by isolated load or residual stress which is measured by stress intensity factor (SIF). Maximum stress intensity was represented by red color and minimum stress intensity was represented by blue color in all ANSYS diagrams. The tensile stress and hardness results of various diffusion-bonded joints, with respect to chosen temperature, time, and pressure were tabulated in Table 5. The regression analysis for tensile stress

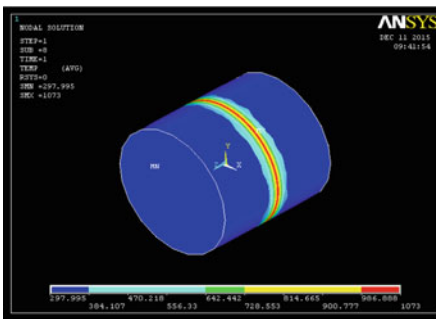


(a) Temperature distribution

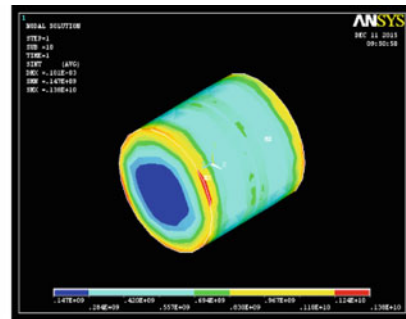


(b) Stress intensity

Fig. 3 Diffusion-bonded joint of Ti-6Al-4V—SS304L stainless steel (1023 K, 150 bar, and 2 h)

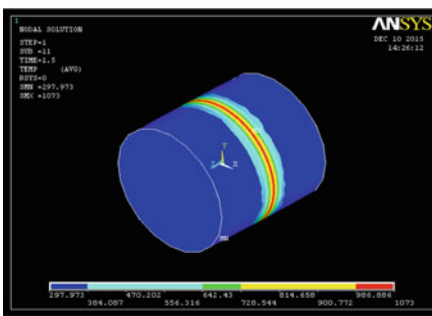


(a) Temperature distribution

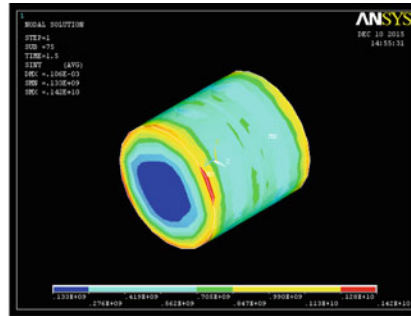


(b) Stress intensity

Fig. 4 Diffusion-bonded joint of Ti-6Al-4V—SS304L stainless steel (1073 K, 50 bar, and 1 h)

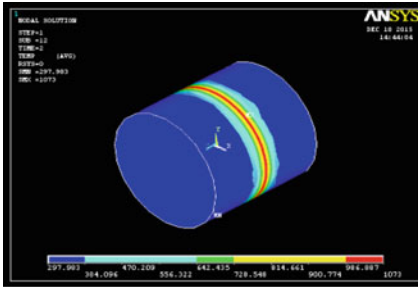


(a) Temperature distribution

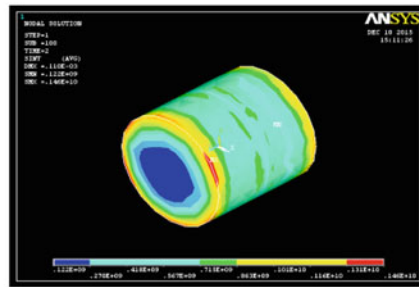


(b) Stress intensity

Fig. 5 Diffusion-bonded joint of Ti-6Al-4V—SS304L stainless steel (1073 K, 100 bar, and 1.5 h)

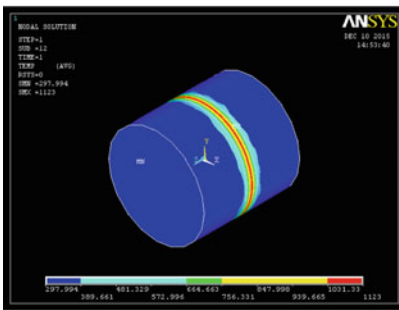


(a) Temperature distribution

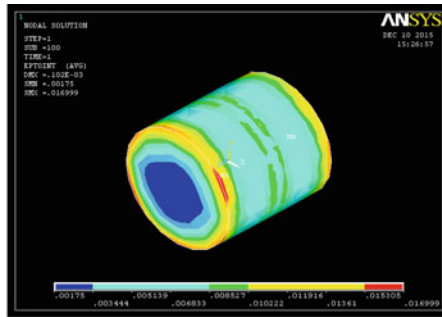


(b) Stress intensity

Fig. 6 Diffusion-bonded joint of Ti-6Al-4V—SS304L stainless steel (1073 K, 150 bar, and 2 h)

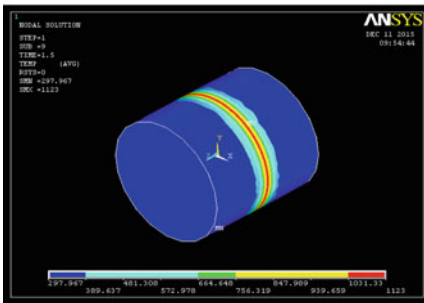


(a) Temperature distribution

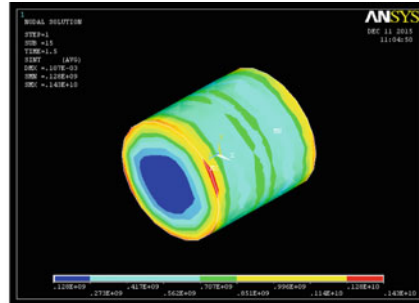


(b) Stress intensity

Fig. 7 Diffusion-bonded joint of Ti-6Al-4V—SS304L stainless steel (1123 K, 50 bar, and 1 h)



(a) Temperature distribution



(b) Stress intensity

Fig. 8 Diffusion-bonded joint of Ti-6Al-4V—SS304L stainless steel (1123 K, 100 bar, and 1.5 h)

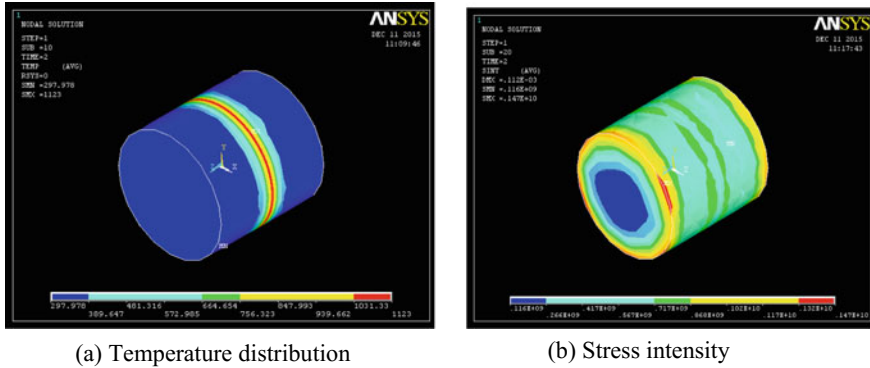


Fig. 9 Diffusion-bonded joint of Ti–6Al–4V—SS304L stainless steel (1123 K, 150 bar, and 2 h)

Table 5 Experimental readings for Ti–6Al–4V—SS304L stainless steel diffusion-bonded joints

No.	<i>T</i> (K)	<i>P</i> (bar)	<i>t</i> (h)	Tensile stress (MPa)	Hardness (HV)
1	1023	50	1	69	243
2	1023	100	1.5	84	251
3	1023	150	2	102	248
4	1073	50	1.5	89	236
5	1073	100	2	136	240
6	1073	150	1	121	260
7	1123	50	2	180	275
8	1123	100	1	163	264
9	1123	150	1.5	227	259

and hardness of the diffusion bonding joints were completed. Table 6 showed the calculated values of the diffusion-bonded joints for all the experiments using the regression equation of the tensile stress and hardness.

Figure 10 obviously showed about the main effect plot for the tensile stress of the diffusion-bonded joints corresponding to the temperature, pressure, and time. It demonstrated that the temperature of the diffusion-bonded joint affects the tensile stress. The experimental temperature and pressure were directly proportional to tensile stress of the joint.

The main effect plot for the hardness of the joint Ti–6Al–4V and SS304L was without a doubt showed in Fig. 11. The experimental temperatures influence the hardness variation of diffusion bonded joints. When the temperature increases, the hardness of the material is also increases. From the Table 6, results, 23rd parameter from the run order, the factors’ temperature 1073 K, pressure 150 bar, and holding time 1.5 h in the experiment are carried out and the testing is also done and the observation and accuracy of experiment are tabulated in Table 7.

Table 6 Calculated values for Ti-6Al-4V—SS304L Stainless steel diffusion-bonded joints

No.	<i>T</i> (K)	<i>P</i> (bar)	<i>t</i> (h)	Tensile stress (MPa)	Hardness (HV)
1	1073	150	2	159.27	254.415
2	1123	50	1.5	163.64	260.08
3	1073	50	1.5	111.14	250.745
4	1023	100	1	66.46	244.235
5	1073	50	2	121.97	250.085
6	1123	50	1	152.81	260.74
7	1023	50	1	47.81	242.07
8	1123	150	1.5	200.94	264.41
9	1073	100	1	118.96	253.57
10	1023	150	1.5	95.94	245.74
11	1073	50	1	100.31	251.405
12	1023	50	1.5	58.64	241.41
13	1123	150	1	190.11	266.12
14	1123	150	2	213.64	263.75
15	1023	100	2	88.12	242.915
16	1023	150	1	85.11	246.4
17	1123	100	2	193.12	261.585
18	1023	100	1.5	77.29	243.575
19	1073	100	1.5	129.79	252.91
20	1073	100	2	140.62	252.25
21	1123	100	1.5	182.29	262.245
22	1123	50	2	174.47	259.42
23	1073	150	1.5	148.44	255.075
24	1073	150	1	137.61	255.735
25	1023	50	2	69.47	240.75
26	1123	100	1	171.46	262.905
27	1023	150	2	106.77	245.08

Table 7 Validation of experiments of Ti-6Al-4V—SS304L stainless steel joints

Response	Theoretical value	Experimental value	% of accuracy
Tensile strength (MPa)	148.44	139	93.64
Hardness (HV)	255.075	235	92.12

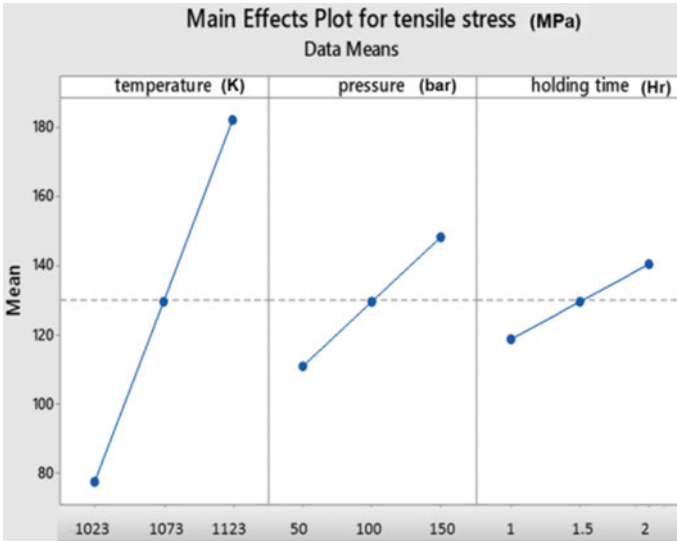


Fig. 10 Main effect plots for tensile stress of Ti-6Al-4V—SS304L diffusion-bonded joints

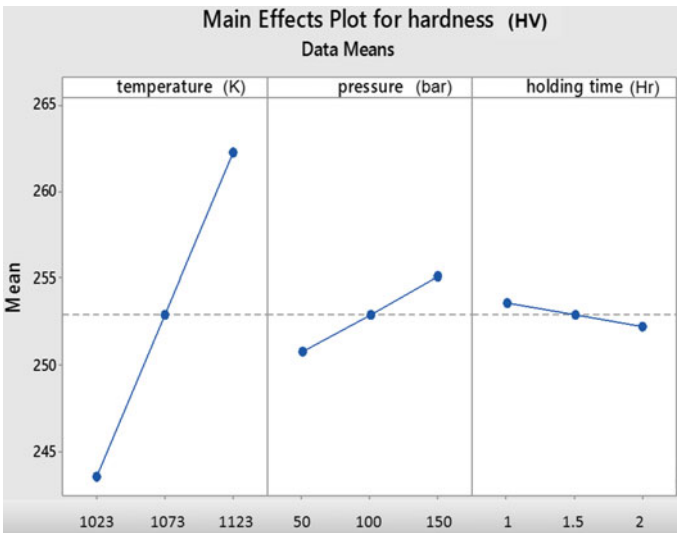


Fig. 11 Main effect plots for hardness for Ti-6Al-4V—SS304L diffusion-bonded joints

5 Conclusion

By this investigation, following conclusion were listed.

- By using diffusion bonding process, Ti–6Al–4V and SS304L stainless Steel can be able to weld.
- From these ANSYS diagrams the maximum, minimum temperature variation of joints showed in temperature distribution diagrams similarly maximum, minimum stresses of joints were showed in the stress intensity diagrams.
- Temperature influence in both tensile strength and hardness is in directly proportional manner.
- Among these combinations of diffusion bonding joint conditions maximum tensile strength (213.64 MPa) was obtained at temperature 1123 K, pressure 150 bar, and time 2 h.
- Similarly, 266.12 HV of maximum hardness was reached at 1123 K, pressure 150 bar, and time 1 h.

References

1. Orhan N, Aksoy M, Eroglu M (1999) A new model for diffusion bonding and its application to duplex alloys. *Mater Sci Eng A* 271:458–468
2. Balasubramanian M, Ramesh G, Balasubramanian V (2015) Diffusion bonding of titanium alloy Ti–6Al–4V and AISI304 stainless steel—an experimental investigation. *J Eng Sci Technol* 10(10):1342–1349
3. Kurt B, Orhan N, Hasçalık A (2007) Effect of high heating and cooling rate on interface of diffusion bonded gray cast iron to medium carbon steel. *Mater Design* 28:2229–2233
4. Kurta Bulent, Çalik Adnan (2009) Interface structure of diffusion bonded duplex stainless steel and medium carbon steel couple. *Mater Charact* 60:1035–1040
5. Orhan N, Khanand TI, Eroglu M (2001) Diffusion bonding of a micro duplex SS to Ti–6Al–4V. *Scripta Mater* 45:441–446
6. Islam MF, Ridley N (1998) Isostatic diffusion bonding of a microduplex Stainless steel. *Scripta Mater* 38(8):1187–1193
7. Elrefaey A, Tillmann W (2009) Solid state diffusion bonding of titanium to steel using a copper base alloy as interlayer. *J Mater Process Technol* 209:2746–2752
8. Ghosh M, Das S, Banarjee PS, Chatterjee S (2005) Variation in the reaction zone and its effects on the strength of diffusion bonded titanium–stainless steel couple. *Mater Sci Eng A* 390:217–226
9. Fielding J, Needham JC (1970) *Advances in welding processes*. Abington Hall, Cambridge, pp 72–77
10. Yuan XJ, Sheng GM, Qin B, Huang WZ, Zhou B (2008) Impulse pressuring diffusion bonding of titanium alloy to stainless steel. *Mater Charact* 59:930–936
11. He P, Feng JC, Zhang BG, Qian YY (2003) A new technology for diffusion bonding inter-metallic Ti Al to steel with composite barrier layers. *Mater Charact* 50:87–92
12. Kothandaraman CP, Subramaniyan S *Heat and mass transfer data book*, 7th edn. New Age International Publication

Optimization of Tribological Properties of Al6061/9% Gr/WC Hybrid Metal Matrix Composites Using FGRA



Gangadhara Rao Ponugoti, Pandu R. Vundavilli and Alluru Gopala Krishna

Abstract In the present work, Hybrid MMCs are developed using Al6061 as a matrix with graphite (Gr) and tungsten carbide (WC) as reinforcements. This investigation is motivated to estimate the tribological properties such as wear phenomenon and coefficient of friction. The composites produced through stir casting route, initially 3, 6, 9, and 12% of Gr are produced and the investigation of these composites for mechanical and microstructural properties indicates that 9% Gr shows better performance. So, hybrid composite of Al6061/9%Gr/WC (WC varies from 1, 2, 3%) produced. Thereafter in view of modeling and optimization of the tribological property of the composites, the wear tests are conducted on pin-on-disk tribometer under varying conditions of reinforcement percentage, load, sliding distance, and sliding velocity according to face-centered central composite design that consists of 30 experimental runs. The wear rate and coefficient of friction are recorded as the tribological property indicators. Regression models for each response in terms their control variables were developed and checked their adequacy with ANOVA. Consequently, these models were used for optimization. Fuzzy gray relational analysis (FGRA) was used to derive the values of optimal control variable. The suitability of this multi-response optimization approach which minimizes the wear rate and coefficient of friction simultaneously was analyzed and reported. Finally, the derived optimal tribological conditions of the composites were confirmed through the validation experimental results.

Keywords Al6061/Gr/WC hybrid composites · Mechanical properties · Wear rate · Coefficient of friction · Multi-response optimization · Fuzzy gray relational analysis (FGRA)

G. R. Ponugoti (✉)

Nalanda Institute of Engineering and Technology, Sattenapalli 522403, AP, India
e-mail: audibalav@gmail.com

P. R. Vundavilli

School of Mechanical Sciences, Indian Institute of Technology Bhubaneswar, Bhubaneswar 752050, Odisha, India

A. G. Krishna

Department of Mechanical Engineering, JNTU, Kakinada 533001, AP, India

© Springer Nature Singapore Pte Ltd. 2019

S. S. Hiremath et al. (eds.), *Advances in Manufacturing Technology*,

Lecture Notes in Mechanical Engineering,

https://doi.org/10.1007/978-981-13-6374-0_54

1 Introduction

Metal matrix composites (MMCs) are the most emerging area of research in the field of material science. Researchers are interested in developing various new materials to fulfill the requirement of diverse engineering applications. To introduce various tailor-made properties in MMCs, investigators focus on the design and development of various hybrid composites with aluminum and its alloys as matrix [1]. In the hybrid composites, the reinforcement helps in enhancing the properties of the pure metal or alloy so that these composites will replace the existing alloys. The scope of replacement of the heavyweight alloy components is mentioned in the literature [2]. Stojanovic [3] used silicon carbide as reinforcement to enhance the tribological properties of aluminum metal matrix composites (AlMMCs) and observed an increase in its wear resistance. Further, Reddy [4] developed Al hybrid MMCs by adding SiC and B₄C as reinforcements and achieved an improvement in hardness, tensile strength, and flexural rigidity of aluminum hybrid MMCs. Similar research was done on stir casting while preparing these composites [5]. However, Umasankar et al. [6] experimentally evaluated the influence of process parameters on the mechanical properties of Al–SiC particle-reinforced MMCs. It was observed that the compacting pressure was having a positive influence on the sintering density and micro-hardness of the component. It was also observed that the sintering temperature and time had shown a negative influence on the said mechanical properties of the component. Moreover, Patel [7] and Beffort [8] prepared MMCs by using squeeze casting; even though, the composite preparation method is different, this research was aimed at enhancing the mechanical and tribological properties of Aluminum hybrid MMCs. With the best of the authors' knowledge, limited literature is available on the optimization of tribological properties of MMCs. However, Ghosh [9] applied Taguchi methodology to optimize the wear and coefficient of friction (COF). Later on, Shouvik [10] used gray relational analysis to optimize the tribological properties of LM6/SiCp MMCs. They used the concept of gray-Taguchi approach to optimize the wear phenomenon of said composite by varying the input process parameters, namely percentage of SiCp, applied load, sliding velocity, and sliding time. A very few researchers had used this gray fuzzy relational grade in optimizing the tribological properties. In the present research, an attempt is made to optimize this tribological properties using FGRA hybrid optimization tool.

2 Experimental Procedure

During the preparation of these composites, initially the graphite crucible with specified amount of matrix material in it is placed in a pit furnace and heated till the temperature rises to 750 °C. Once the melt is reached to 750 °C, the stirring started with maximum stirrer speed of 300 rpm. At this stage, the preheated (200 °C) reinforcement of 3% graphite is fed into the crucible. The stirring action was continued

Table 1 Table showing the ranges of the variables used in the study

S. No.	Factors	Symbol	Range low (-1)	Ranges high (+1)
1	WC reinforcement (%)	%WC	1	3
2	Load (N)	Load	10	30
3	Sliding distance (m)	Sd	500	2500
4	Sliding velocity (m/s)	Sv	1	3

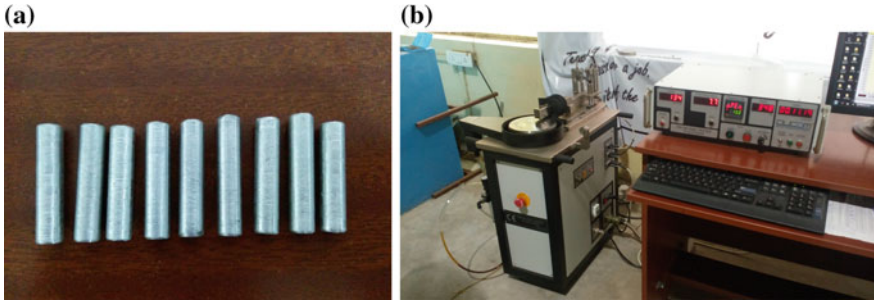


Fig. 1 Schematic diagram showing **a** hybrid Al6061/9%Gr/WC MMCs and **b** wear tester

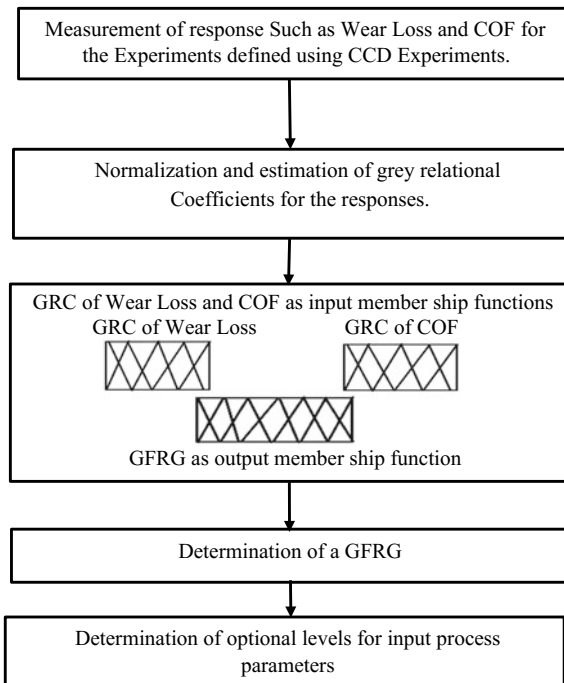


Fig. 2 Schematic diagram showing the flowchart of FGRA

for 15 min. After conforming uniform distribution of reinforcement particles, the liquid melt is poured into dies. The entire process is carried out under inert gas environment. Similar procedure was repeated by changing the percentage of reinforcement of graphite of 6, 9, and 12%. Further similar procedure was adopted to produce hybrid composite of Al6061/9%Gr/WC, by varying the WC (1, 2, and 3%).

During wear test, a statistical technique named face-centered central composite design is used to decide the number of experiments required to analyze the experiment. Table 1 shows the range of input process parameters used in the present study.

The hybrid MMCs specimens prepared and the wear testing machine used in this study are shown in Fig. 1a, b, respectively.

Once the experimental data is obtained, the FGRA algorithm as shown in Fig. 2 is used to perform the multi-objective optimization.

3 Results and Discussions

The experimental data and other information related to the algorithm are given in Table 2.

The calculation of FGRG values from the fuzzy reasoning after using the GRC values of the WR and COF is given in Fig. 3.

Once the FGRG values are obtained, the response table is prepared for the input process parameters to determine the influence of level of a particular process parameter on the responses.

From Table 3, it has been concluded that the levels of the input process parameters A2, B3, C1, and D4 are found to have maximum values for the average fuzzy gray relational grades when compared with the other levels of the parameters. From this analysis, it is concluded that the combination A2-B3-C1-D4 is found to be the best

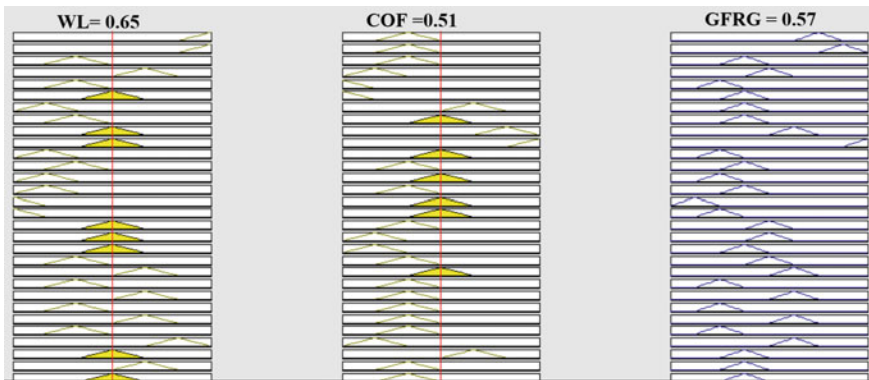


Fig. 3 Schematic diagram showing the fired rules and the corresponding membership function distributions for a given input

Table 2 Table showing the normalized, deviation sequence, GRC, and FGRA values

S. No.	%WC	Load	SD	SV	WL	COF	Norm. Seq.		Dev. Seq.		GRC		FGRA
							WL	COF	WL	COF	WL	COF	
1	1	10	500	1	0.036	0.410	0.921	0.448	0.079	0.552	0.864	0.475	0.606
2	3	10	500	1	0.005	0.443	1.000	0.300	0.000	0.700	1.000	0.417	0.7
3	1	30	500	1	0.083	0.399	0.802	0.497	0.198	0.503	0.716	0.499	0.592
4	3	30	500	1	0.051	0.485	0.883	0.111	0.117	0.889	0.811	0.360	0.587
5	1	10	2500	1	0.084	0.420	0.799	0.403	0.201	0.597	0.714	0.456	0.587
6	3	10	2500	1	0.056	0.413	0.871	0.436	0.129	0.564	0.794	0.470	0.625
7	1	30	2500	1	0.125	0.329	0.695	0.811	0.305	0.189	0.621	0.726	0.596
8	3	30	2500	1	0.095	0.363	0.772	0.660	0.228	0.340	0.686	0.595	0.589
9	1	10	500	3	0.086	0.353	0.794	0.704	0.206	0.296	0.709	0.628	0.604
10	3	10	500	3	0.055	0.330	0.873	0.807	0.127	0.193	0.798	0.722	0.775
11	1	30	500	3	0.132	0.287	0.678	1.000	0.322	0.000	0.608	1.000	0.775
12	3	30	500	3	0.097	0.300	0.766	0.942	0.234	0.058	0.682	0.896	0.775
13	1	10	2500	3	0.133	0.510	0.675	0.000	0.325	1.000	0.606	0.333	0.53
14	3	10	2500	3	0.105	0.503	0.746	0.031	0.254	0.969	0.663	0.340	0.535
15	1	30	2500	3	0.185	0.354	0.543	0.699	0.457	0.301	0.523	0.624	0.55
16	3	30	2500	3	0.164	0.362	0.596	0.665	0.404	0.335	0.553	0.599	0.56
17	2	20	1500	2	0.090	0.404	0.784	0.473	0.216	0.527	0.699	0.487	0.58
18	2	20	1500	2	0.070	0.410	0.835	0.448	0.165	0.552	0.752	0.475	0.62
19	2	20	1500	2	0.075	0.390	0.822	0.538	0.178	0.462	0.738	0.520	0.63
20	2	20	1500	2	0.085	0.380	0.797	0.583	0.203	0.417	0.711	0.545	0.63

(continued)

Table 2 (continued)

S. No.	%WC	Load	SD	SV	WL	COF	Norm. Seq.		Dev. Seq.		GRC		FGRA
							WL	COF	WL	COF	WL	COF	
21	1	20	1500	2	0.090	0.378	0.784	0.592	0.216	0.408	0.699	0.551	0.63
22	3	20	1500	2	0.068	0.421	0.840	0.397	0.160	0.603	0.758	0.453	0.61
23	2	10	1500	2	0.051	0.418	0.883	0.413	0.117	0.587	0.811	0.460	0.64
24	2	30	1500	2	0.110	0.389	0.734	0.543	0.266	0.457	0.652	0.523	0.6
25	2	20	500	2	0.049	0.433	0.888	0.345	0.112	0.655	0.817	0.433	0.63
26	2	20	2500	2	0.090	0.441	0.784	0.308	0.216	0.692	0.699	0.419	0.54
27	2	20	1500	1	0.351	0.420	0.122	0.404	0.878	0.596	0.363	0.456	0.43
28	2	20	1500	3	0.399	0.385	0.000	0.561	1.000	0.439	0.333	0.532	0.42
29	2	20	1500	2	0.143	0.393	0.651	0.526	0.349	0.474	0.589	0.513	0.54
30	2	20	1500	2	0.151	0.390	0.629	0.538	0.371	0.462	0.574	0.520	0.53

Table 3 Response table for the FGRA of Al6061/9%Gr/WC MMCs

Level	%WC (A)	Load (B)	SD (C)	SV (D)
1	0.54156	0.62244	0.67156	0.59022
2	0.56583	0.56483	0.57167	0.59833
3	0.63956	0.62489	0.568	0.61378
Max-min	0.098	0.06006	0.103556	0.023556
Rank	2	3	1	4

combination of input process parameters for optimizing the wear behavior of the hybrid Al6061/9%Gr/WC MMCs.

4 Conclusions

In the present research, Al6061/9%Gr/WC hybrid MMCs are prepared with the help of stir casting method. The concept of design of experiments is applied to conduct the experiments related to wear test. Once the data is obtained, multi-objective optimization of the responses such as WL and COF is carried out using a hybrid approach named FGRA. It is observed that the optimal values of input process parameters, namely percentage of WC, load, sliding distance, and sliding velocity that are responsible for minimizing both the wear rate and coefficient of friction are found to be equal to 3%, 30 N, 500 m, and 3 m/s, respectively.

References

1. Bodunrin MO, Alaneme KK, Chown LH (2015) Aluminum matrix hybrid composites: a review of reinforcement philosophies; mechanical, corrosion and tribological characteristics. *J Mater Res Technol* 4(4):434–445
2. Shibata K, Ushio H (1994) Tribological application of MMC for reducing engine weight. *Tribol Int* 27(1):39–44
3. Stojanovic B, Babic M, Mitrovic S, Vencel A, Miloradovic NM, Pantic M (2013) Tribological characteristics of aluminium hybrid composites reinforced with silicon carbide and graphite: a review. *J Balkan Tribol Assoc* 19(1):83–96
4. Reddy PS, Kesavan R, Vijaya Ramnath B (2018) Investigation of mechanical properties of aluminium 6061-silicon carbide. *Boron Carbide Metal Matrix Compos, Silicon* 10(2):495–502
5. Kaushik N, Singhaal S (2017) Mechanical and metallurgical examinations of stir cast aluminum matrix composites: a review study. *Int J Eng Technol* 9(4):3201–3217
6. Umashankar V, Anthony Xavier M, Karthikeyan S (2014) Experimental evaluation of the influence of processing parameters on the mechanical properties of SiC particle reinforced AA6061 aluminium alloy matrix composite by powder processing. *J Alloy Compd* 582(5):380–386
7. Patel GCM, Krishna P, Vundavilli PR, Parappa Goudar MP (2016) Multi-objective optimization of squeeze casting process using genetic algorithm and particle swarm optimization. *Arch Foundry Eng* 16(3):172–186

8. Beffort O, Long S, Cayron C, Kuebler J, Buffat PA (2007) Alloying effects on microstructure and mechanical properties of high volume fraction SiC-particle reinforced Al-MMCs made by squeeze casting infiltration. *Compos Sci Technol* 67(3):737–745
9. Ghosh S, Sutradhar G, Sahoo P (2011) Wear performance of Al-5%SiC metal matrix composite using Taguchi method. *J Tribol Res* 11(4):33–40
10. Shouvik G, Prasanth S, Goutam S (2012) Wear behavior of Al–SiCp metal matrix composites and optimization using Taguchi method and grey relational analysis. *J Miner Mater Charact Eng* 11(11):1085–1094

Experimental Study on Mechanical Properties of Superelastic Alloy



M. Sangeetha, P. Ponnusamy, Durgajeevitha and S. Shiva Ganesh

Abstract This work deals with the fabrication of titanium-free superelastic alloy for mechanical applications, and it summarizes the fabrication of superelastic alloys and various tests conducted on the fabricated specimen. Based on its fabrication and testing, the shape memory alloys are improved in some of the properties such as ultimate tensile strength, wear resistance, and corrosion resistance damping properties. There are various superelastic materials; out of these, nickel titanium is best suited for the medical field since there is a requirement of the annealing process. The honeycomb nickel titanium is the good replacement of steel bar in concrete structures. Copper–nickel–aluminum is best suited for damping purpose, and it is economical due to the absence of titanium. Mechanical applications can make use of titanium-free superelastic alloys due to low cost.

Keywords Aluminum · Copper · Elastic material · Mechanical properties · Nickel

1 Introduction

Superelastic materials spread over a wide range in mechanical, medical, and civil structures due to its improved properties, and the cost of this alloy is reduced by replacing the titanium with aluminum and copper. It is having applications such as morphing, health monitoring, active vibration control, self-healing, flexible skins, distributed actuators, and sensors.

M. Sangeetha · S. Shiva Ganesh
School of Mechanical Engineering, Sathyabama Institute of Science and Technology,
Chennai 600119, India

P. Ponnusamy (✉)
School of Mechanical Engineering, Vellore Institute of Technology (VIT), Vellore 632014, India
e-mail: sreepons@gmail.com

Durgajeevitha
Vins Christian College of Engineering, Nagercoil, India

© Springer Nature Singapore Pte Ltd. 2019
S. S. Hiremath et al. (eds.), *Advances in Manufacturing Technology*,
Lecture Notes in Mechanical Engineering,
https://doi.org/10.1007/978-981-13-6374-0_55

Superelasticity is also called as pseudo-elasticity which is an elastic response to an applied stress, and it is caused by phase transformation between austenite and martensite. The transformation from austenite to martensite is said to be an exothermic reaction, and similarly, the transformation from martensite to austenite is termed as an endothermic reaction; there is a strong coupling between the thermal and mechanical phenomena. Regularly arranged austenite subjected to cooling resulted in twinned martensite which deforms further to generate detwinned martensite. When the detwinned structure subjected to a temperature of above austenite, it returns to its original structure and it is explained in Fig. 1.

This work deals with the fabrication of titanium-free superelastic alloy for mechanical applications, and it summarizes the fabrication of superelastic alloys and various tests conducted on the fabricated specimen. Based on its fabrication and testing, the shape memory alloys are improved in some of the properties such as ultimate tensile strength, wear resistance, and corrosion resistance damping properties. There are various superelastic materials; out of these, nickel titanium is best suited for medical field since there is a requirement of the annealing process. The honey-comb nickel titanium is Kim (2008) [1] analyzed the mechanical performance of nickel-titanium wires and proved that the nickel-titanium wires with low flexibility and high hysteresis failed to compress. When the nitinol wire sent into a blocked channel it won't remove the block instead applied more stress along the channel walls, to overcome this polymer coating is to be done over the nitinol wire.

Sardmezhad (2009) [2] conducted the thermal hydrogen test to fabricate nickel-titanium shape memory alloy, and it reached Young's modulus of 19.8 GPa and high tensile strength of 255 MPa; it is similar to human bone, and 1.2% of strain is recoverable. The properties are checked under the ASTM E8 standard using servo-hydraulic test.

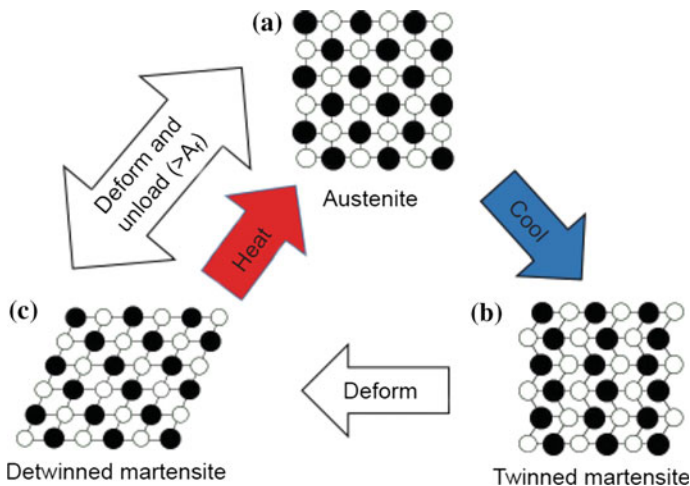


Fig. 1 Different stages or transformation of shape memory alloy

Bigdeli (2009) [3] compared the hardness of Ni–P alloy with silicon-carbide-coated Ni–P. The microhardness of coated Ni–P shows the higher value of hardness of 721 HV (Vickers hardness number). After heat treatment with 400 °C for one hour, the microhardness value is further increased to 1122 HV.

Bernard (2012) [4] studied the fatigue behavior of shape memory alloy and concluded that fatigue is more complex and sensitive to a large number of parameters than alloys. Under cyclic compression test with varying load, it shows the similar property as metal foams and it sustains cyclic compression fatigue stresses without failure. Nickel-titanium shapes memory alloy and their mechanical and thermomechanical properties and concludes that under stress loading nickel-titanium alloy shows better fatigue property and proper mixing of nickel titanium in the microstructure.

Jaureguizar (2015) [5] conducted a test on nine different combinations of the superelastic specimen. In all specimens, the stress value remained below 600 MPa and stress amplitude 89 MPa. In fully austenite stage, the material reached lives up to 7×10^6 cycles without fracture, while in the martensite stage, the specimen fractured at a finite number of cycles. It is proved that the life is more for full austenite followed by partial martensite and the lowest life for full martensite, and it is explained in Fig. 2.

Jaureguizar (2016) [6] conducted pseudo-elastic cycling test which was carried out at different ambient temperature ranges from 25 to 50 °C and at different strain rate and proved that the fatigue life is nearer to 10,000 cycles at low strain rate for a long time; fatigue life is not dependent on strain range, and this material shows the behavior of resistance to intrinsic damage mechanism.

Di Cocco (2016) [7] carried out the pseudo-elastic test in superelastic alloys using the machine shown in Fig. 3. The motor is used to apply the load on the specimen, and the load applied is indicated in the load cell; the deformation of the specimen is

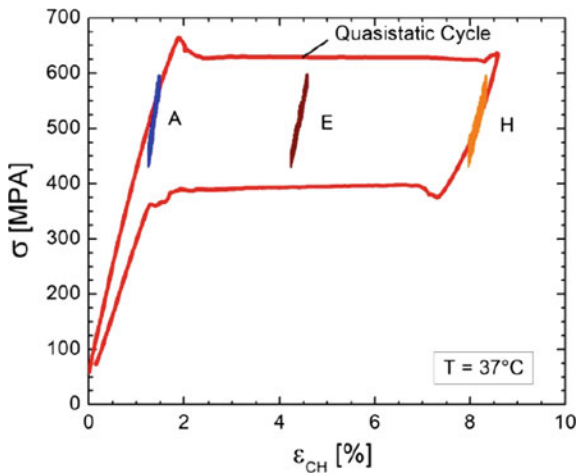


Fig. 2 Pseudo-elastic effect performed at same temperature [5], A—full austenite, E—partial martensite, H—fully martensite

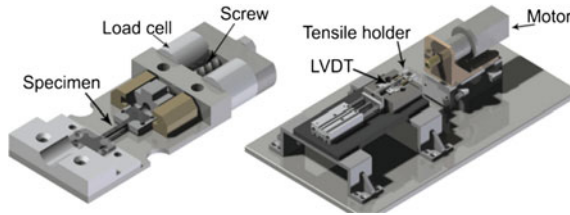


Fig. 3 Fatigue testing machine [7]

recorded in a linear variable differential transducer (LVDT). Microstructural evaluation of nickel-titanium alloy is characterized by a pseudo-elastic behavior. Austenite spectrum gets recovered at each investigated cycle. There is a change in lattice structure without changing the boundaries, and the recovery of the initial shape takes place above the critical temperature which is termed as crystallographic structure transition.

DesRoches (2004) [8] performed the cyclic loading both in quasi-static and dynamic loading to study the properties of nickel-titanium alloys. The density, elongation, and Poisson’s ratio are similar for both austenite and martensite. The density is 6.45 g/cm^3 , the percentage elongation is up to 8%, and the Poisson’s ratio is 0.33 with excellent corrosion property compared to stainless steel. Young’s modulus of austenite ranges from 30 to 83 GPa, and for martensite, it is about 21–41 GPa and the yield strength ranges from 895 to 1900 MPa. The loading stress ranges between 350 and 550 MPa, and the corresponding frequencies range from 0.025 to 1 Hz. In plastic deformation, the temperature greater and equal to martensite temperature, in superelastic state the temperatures is greater than austenite temperature and for shape memory alloy the temperature is below the finishing state of martensite and it is explained in Fig. 4.

Shaw (2007) [9] prepared the honeycomb superelastic alloy by brazing the structures of nickel-titanium alloys together and compared with monolithic nickel-titanium alloys. The brazed joint allowed isothermal recovery of compressive strain

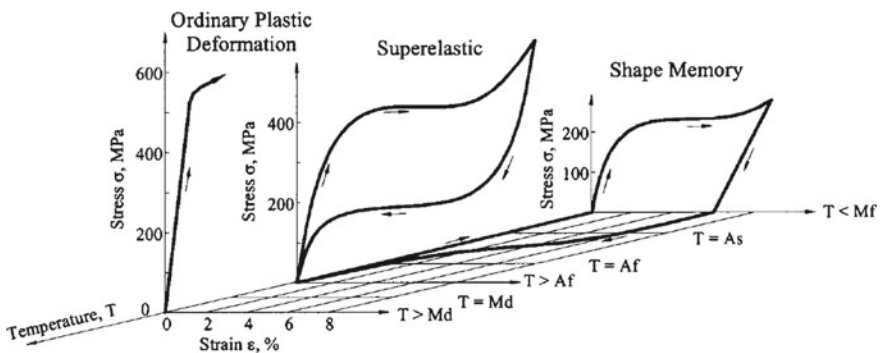


Fig. 4 Stress–strain diagram for plastic deformation, superelastic, and shape memory alloy [8]

ten times greater than monolithic nickel-titanium alloy, and it is significant for certain properties such as lightweight, armor, and energy absorption; it is having application in high displacement actuators and biomedical implants.

Fukuta (2004) [10] conducted the tensile test for both steel and shape memory alloys, and it is proved that shape memory alloys have extremely large deformation, whereas Young's modulus and yield stress are less. Stress-strain details of the compressive test are different from a tensile test. The strain for a tensile strain is 5% which is not in the case of compressive strain due to the presence of residual stress. The composition of a superelastic alloy that can be replaced by steel in concrete structures is 54.51% of nickel, 1.48% cobalt, and remaining titanium, and their properties are checked with the loading frequency of 0.066, 0.33, 1.64, and 3.3 Hz.

2 Materials and Methods

2.1 Copper

Copper alloy is highly adaptable for engineering applications and has properties such as strength, corrosion resistance, highly conductive, ductile, and easily machinable. Since it is capable of corroding slowly, it is used as electrical wires and motors. It is also having applications in roofing and guttering.

2.2 Aluminum

Due to its high strength-to-weight ratio, it is applied mostly in aerospace industries. It is well known for its lightweight, less dense, less corrosion, high strength, highly ductile, and machinable.

2.3 Nickel

Nickel is meant for its excellent corrosion resistance, and it is used under water. It has high pressure and temperature resistance, and it is having applications in jet engine blades; it is hard, malleable, and ductile.

Fig. 5 Fabricated specimen polished in a grinding machine

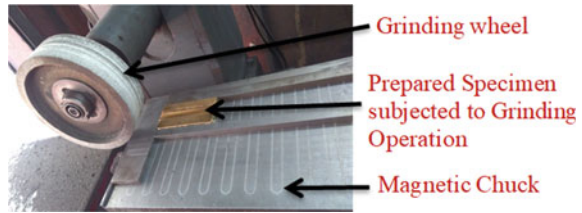


Table 1 Different combinations of materials

Composition	Copper	Aluminum	Nickel
1	82.11	13.7	4.19
2	83.31	3.8	12.89

2.4 Stir Casting Method

The melting point of nickel, copper, and aluminum are high the specimen is fabricated by stir casting process. Figure 5 represents the specimen fabricated using stir casting process, and the surface of the workpiece is polished using a grinding machine before subjected to various testing; it is a suitable method compared to the powder metallurgy process. Two different combinations of materials (Table 1) are prepared based on an L_4 array, and they are polished using a grinding machine before the testing process.

2.5 Mechanical Tests

Mechanical Properties include hardness test, Impact Charpy test. In hardness test, the load is increased and the ball indenter made an indentation on the surface of the specimen; the scale value denotes the hardness number, and it is termed as resistance against indentation. In the Charpy test, the specimen is fixed in the simply supported form, the sudden load is applied at the center of the specimen, and the corresponding impact value is recorded from the scale.

2.6 Morphological Study

This study is carried out using the optical microscope in order to determine proper mixing of the three different metal powders in certain magnification based on the size of the powders.

3 Results and Discussions

3.1 Results of Hardness Test

The prepared specimen is placed on a specimen holder, the load of 10 kg is applied, and the specimen is lifted up by means of a lever until it reaches the ball indenter; the corresponding load value is measured. Figure 6 and Table 2 revealed that the combination of 82.11% of copper, 13.7% of aluminum, and 4.19% of nickel shows the highest value of Brinell hardness number in L4 (Table 2) array compared to other combinations followed by the third combination.

3.2 Results of Impact Tests

This test is also termed as Charpy V notch test. Least count of capacity (dial) scale = 2 J. The specimen is prepared by mixing copper, aluminum, and nickel in various proportions. The maximum impact strength is obtained at the higher percentage of copper followed by aluminum or nickel. The amount of reinforcement for specimen 1 and 4 varies up to 1%, and hence, the difference is less. A heavy pendulum is tending to strike the center of the simply supported beam at the center (Fig. 7), and the corresponding value is noted from the dial gauge in terms of a joule. The

Fig. 6 Variation in hardness value for various combinations of alloys

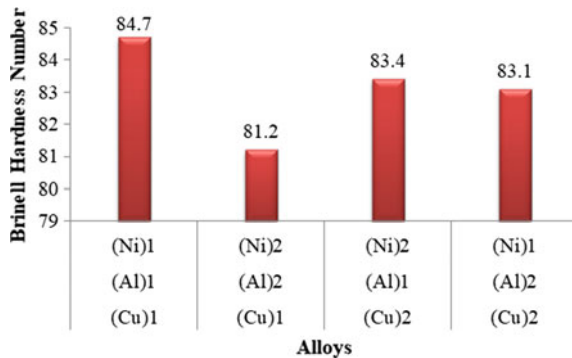


Table 2 L4 array with Brinell hardness number

Copper	Aluminum	Nickel	Brinell hardness number (BHN)
1	1	1	84.7
1	2	2	81.2
2	1	2	83.4
2	2	1	83.1

Fig. 7 Specimen subjected to impact load

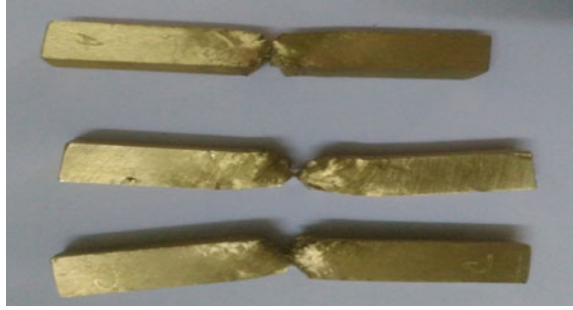
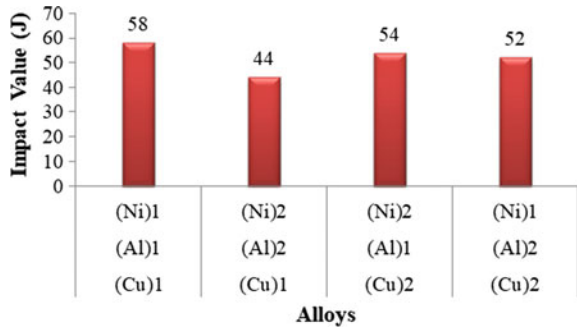


Table 3 L4 array with impact values

Copper	Aluminum	Nickel	Impact test (J)
1	1	1	58
1	2	2	44
2	1	2	54
2	2	1	52

Fig. 8 Variation in impact value for various combinations of alloys



combination of 82.11% of copper, 13.7% of aluminum, and 4.19% of nickel shows the highest value of impact value, and it is shown in Table 3 and Fig. 8.

3.3 Morphological Analysis

The microstructure of the specimen is taken in 500× magnification which clearly reveals the proper distribution of nickel and aluminum in the copper alloys as shown in Fig. 9.

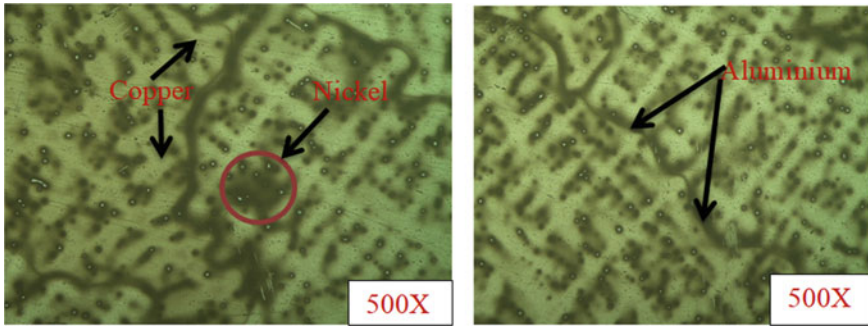


Fig. 9 Microstructural view of fabricated specimen

4 Conclusion

From the study, it was concluded that the various applications of superelastic alloys widely spread in the field of medicine, structures, and mechanics. The superelastic alloy is essential for its superelastic nature and high tensile strength. Superelastic alloys are used in mechanical field replacing the titanium alloys with aluminum–copper alloys which is less expensive compared to the titanium alloy used in medical applications.

It is also proved that the combination of 82.11% of copper, 13.7% of aluminum, and 4.19% of nickel is best suited for mechanical structures.

References

1. Kim JH, Kang TJ, Yu WR (2008) Mechanical modeling of a self-expandable stent fabricated using braiding technology. *J Biomech* 41(15):202–212
2. Sadrnezhad SK, Arami H, Keivan H, Khalifezadeh R (2006) Powder metallurgical fabrication and characterization of nanostructured porous NiTi shape-memory alloy. *Mater Manuf Process* 21:727–735
3. Bigdeli F (2008) The corrosion behavior of electroless Ni–P–SiC nano-composite coating. *Int J Mod Phys B* 22:3031
4. Bernard S, Krishna Balla V, Bose S, Bandyopadhyay A (2012) Compression fatigue behavior of laser processed porous NiTi alloy. *J Mech Behav Biomed Mater* 13:62–68
5. Jaureguizar S, Soul H, Chapetti M, Yawny A (2015) Characterization of fatigue life of ultra-fine grained NiTi superelastic wires under uniaxial loading. *Proced Mater Sci* 9:326–334
6. Jaureguizar S, Soul H, Chapetti M, Yawny A (2016) Fatigue of NiTi Shape Memory Wires. *Proced Struct Integr* 2:1427–1434
7. Di Cocco V, Iacoviello F, Natali S (2016) Fatigue microstructural evaluation in pseudo elastic NiTi alloy. *Proced Struct Integr* 2:1457–1464
8. DesRoches R, Asce M, McCormick J, Delemont M (2004) Cyclic properties of superelastic shape memory alloy wires and bars. *J Struct Eng* 130:38–46

9. Shaw JA, Grummon DS, Foltz J (2007) Superelastic NiTi honeycombs: fabrication and experiments. *Smart Mater Struct* 16:S170–S178
10. Fukuta T, Iiba M, Kitagawa Y, Sakai Y (2004) Experimental study on stress-strain property of shape memory alloy and its application to self-restoration of structural members. In: 13th world conference on earthquake engineering, Vancouver, B.C., Canada, Paper No. 610, 1–6 Aug 2004

Framework Execution and Schematic of Jounce Bumper in Two-Wheeler Fork



T. Babu, R. Sudharshan, Mohammed Suhail, K. Pradeep and S. Sanjay Arun

Abstract A two-wheeler fork connects the front wheel and the axle to its frame, via a pair of triple tree clamps. It typically incorporates the front suspension and front brake, which allows the front wheel to rotate about the steering axis so that the two-wheeler may be steered effectively. The front suspension is either hydraulic or pneumatic shock absorption type. The common type of the front suspension in motorcycle is telescopic forks which are now replaced by mono-shocks that gives a superior vehicle handling and provides safety while braking. The existing front fork suspension assembly consists of fork tubes, sliders, spring, damper rod, spacer, and gaiters to absorb and dampen the shock impulses. The front suspension contributes to the vehicle's handling, thus providing safety and comfort by keeping the vehicle's passengers comfortably isolated from bumps, vibration, and road noise. The objective of our work is to enhance the overall suspension efficiency of the front suspension system by introducing jounce bumper (bump stopper) between the spring and damper rod. The jounce bumper is a polymeric component usually made of polyurethane that can improve the noise, vibration, and harshness performance of the entire vehicle. Polyurethane is known for its low density, flexibility, and resistance to fatigue. Hence with the added absorption capacity of the jounce bumper, the effects of front suspension will get enhanced, which will result in reduction in noise, vibration, and harshness (NVH) leading to improved ride quality and vehicle handling.

Keywords Jounce suspension · Jounce bumper · Polyurethane

1 Introduction

Jounce bumpers play a key role in automobile suspension systems. These are typically mounted between the absorber and its base which is located inside the suspension coil spring. Moreover, jounce bumpers are commonly manufactured from

T. Babu (✉) · R. Sudharshan · M. Suhail · K. Pradeep · S. Sanjay Arun
Department of Mechanical Engineering, Sri Sai Ram Engineering College, Chennai, India
e-mail: babu.prabu@gmail.com

© Springer Nature Singapore Pte Ltd. 2019
S. S. Hiremath et al. (eds.), *Advances in Manufacturing Technology*,
Lecture Notes in Mechanical Engineering,
https://doi.org/10.1007/978-981-13-6374-0_56

503

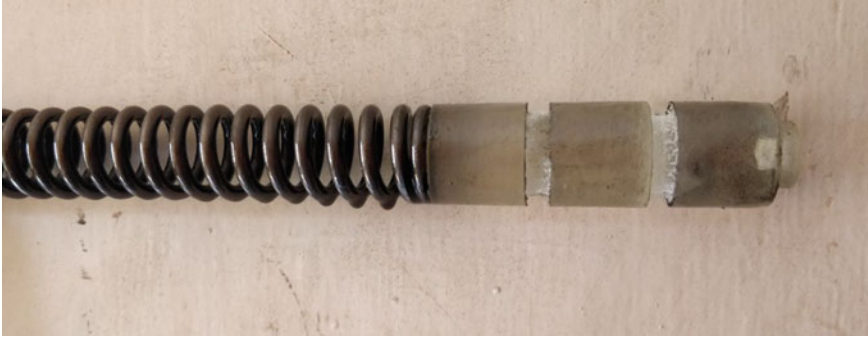


Fig. 1 Fitment of jounce bumper

polyurethane (PU) elastomer, and they primarily serve to absorb the impact energy and to improve the noise, vibration, and harshness (NVH) aspects by preventing suspension components from being fully compressed during transient impacts caused by heavy loads, potholes, curbs, or objects on the road. The jounce bumpers can limit the maximum jounce height of wheels to prevent the spring and absorber from being striking themselves. Aidy Ali [1] determined the maximum load that a jounce bumper can withstand under fatigue conditions and also the displacement control of the jounce bumper before and after fatigue. Using this study, he made an improvement in the quality and design of the jounce bumper. To achieve this result, he used Malaysian car, the Proton saga which consists of butadiene rubber 10% and natural rubber 90%. Sidhu [2] experimented rubber jounce for twelve sets of displacement for the fatigue comparison test in 20 °C ambient temperature. Instron 8871 table model fatigue system was employed for the fatigue test. Yuanlong Wang [3] introduced negative Poisson's ratio in his study, and the finite element method showed the enlargement in the loading velocity and material density that can improve the efficiency.

Our work mainly explains the positioning of jounce bumper inside the two-wheeler fork suspension. Figure 1 shows the fitment of jounce bumper with the suspension spring.

2 Results and Discussion

After the fitment of jounce inside the suspension, load–displacement tests were performed using UTM. The model of spring assembly in suspension without jounce was initially analyzed using ANSYS. After that, the suspension with polyurethane jounce was analyzed and results are depicted in Figs. 2 and 3.

The suspension springs without the jounce were not able to withstand more sprung masses in various terrains considering that it would result in much more increased natural frequencies while traveling on-roads. Thereby, it results in more deflection

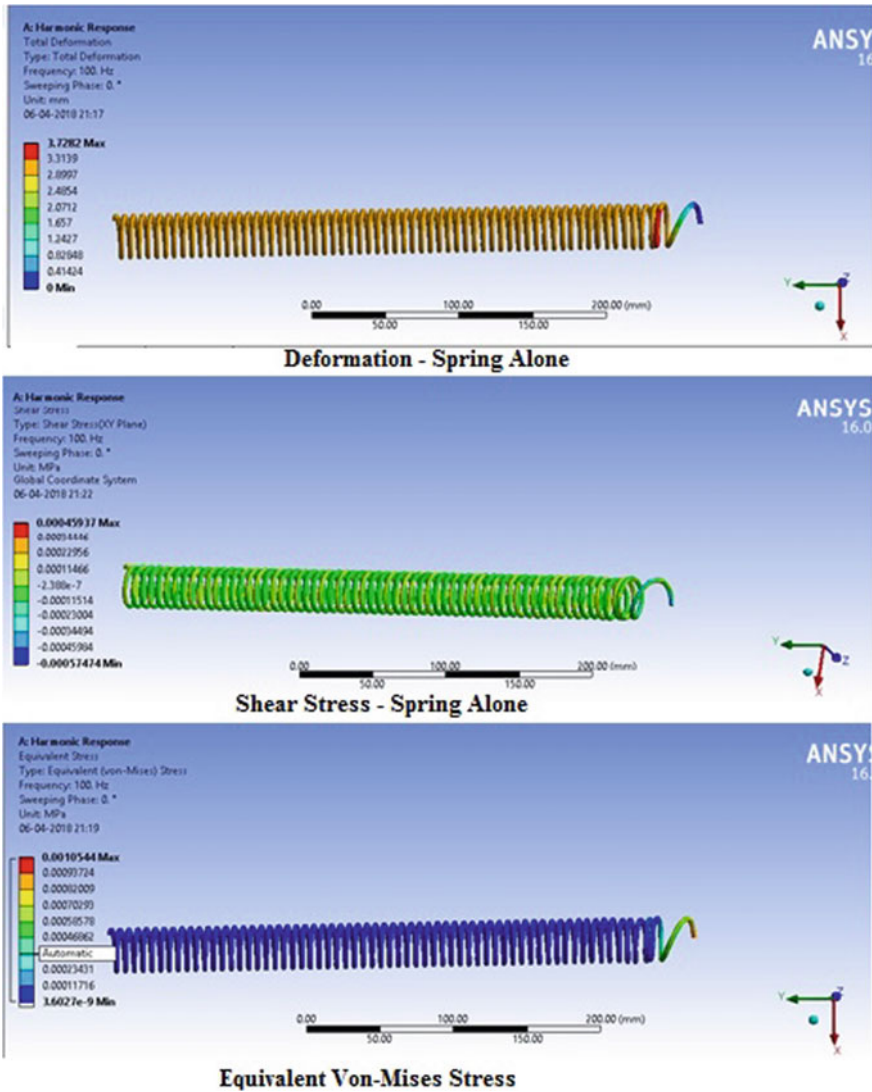


Fig. 2 Analysis results of suspension without jounce

resulting in an uncomfortable and unsafe condition for the driver that prevails while driving in high speeds. So, a spring was designed without jounce and assumed that the spring mass would be 500 N and analysis resulted in a maximum shear of 0.00045937 and a maximum equivalent stress of 0.0010544. So, a spring assembly with a jounce was designed to increase the efficiency and also to withstand the transient impacts caused by the vehicles and the terrains.

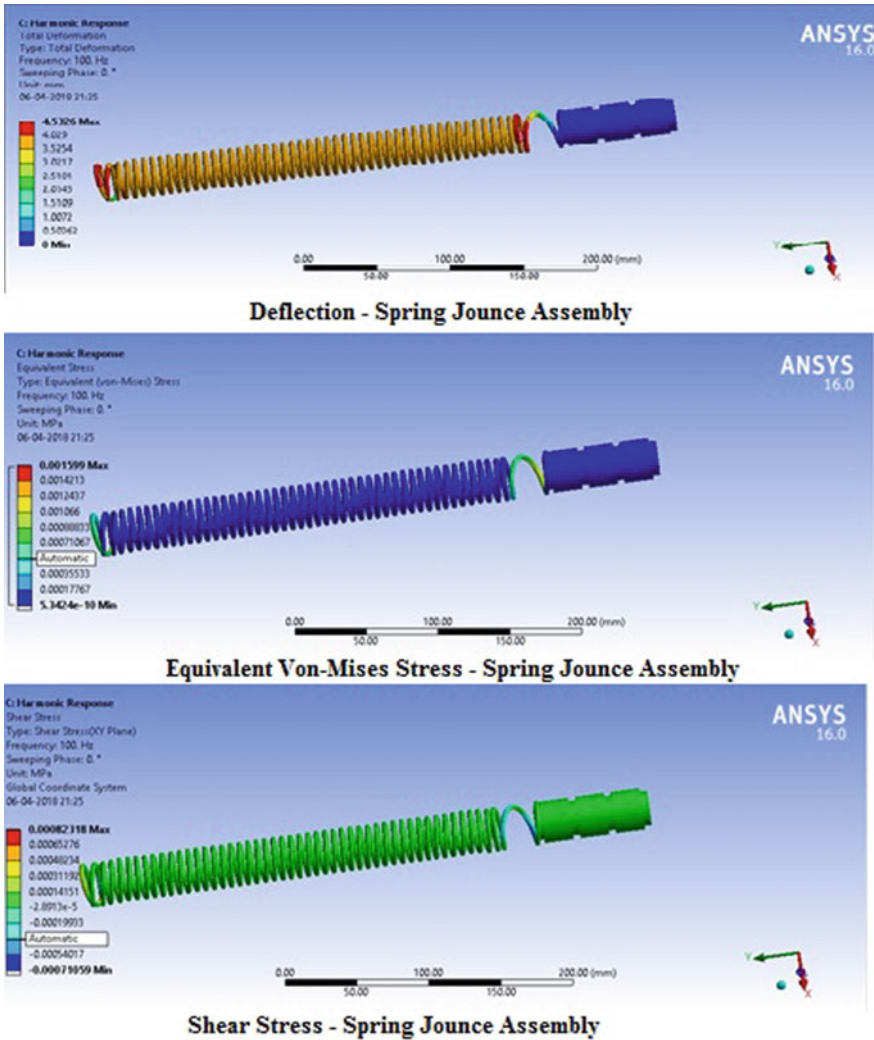


Fig. 3 Analysis results—spring with jounce

Design of Jounce bumpers:

Three things were considered while designing the jounce bumpers. The driver needs to be comfortable and also should be safeguarded in any type of terrains. The objective of this design was to make the jounce bumper as compact as possible and also to control the deflections that are produced in the transient impact load conditions.

This design is able to withstand more sprung masses so that these forces are passed through their springs and absorbed by the polyurethane elastomers which has

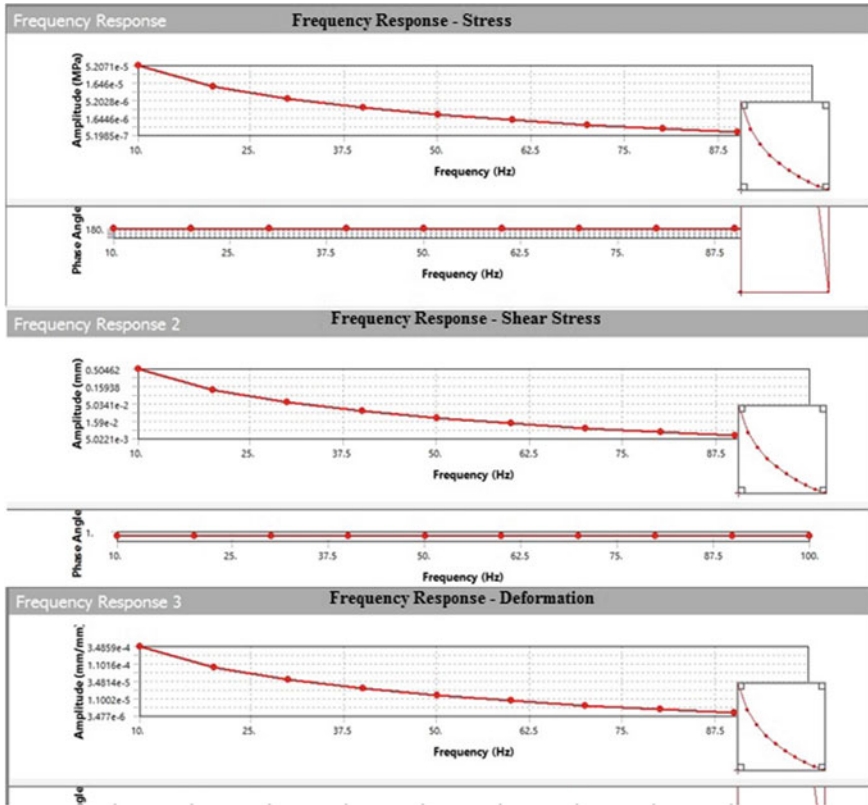


Fig. 4 Frequency response

the potential strength to keep the deflection in the normal range and a frequency around 100 Hz (Fig. 4).

For the same value of 500 N, the spring without jounce showed a maximum equivalent stress value of 0.001599 and shear value of 0.00082318. The factor of safety value was greater than 1. The maximum deformation was 0.001 mm which was comparatively small and negligible. The maximum stress was found to be within the maximum ultimate stress value of the material (Fig. 5 and Table 1).

The frequency range with respect to stress–strain deformation is also shown for comparison. As the frequency increases, the deformation, the stress, and the strain decrease. This is because of the sudden impact of 500 N force at the start, which is opposed by the spring, and hence, the deformation, stress, and strain decreases. After the shock absorber was analyzed, it had undergone a deflection test in the UTM, and the results were plotted. It is inferred that the deflection of the suspension with jounce bumper gives better results and the graph clearly shows the gradual increase of deflection under the different load conditions. But in case of the suspension without jounce bumper, it is found to deviate without an uniformity.

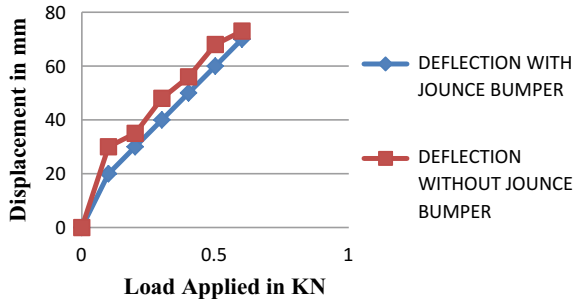


Fig. 5 Displacement plot

Table 1 UTM test results

Force (kN)	Deflection with jounce bumper (mm)	Deflection without jounce bumper (mm)
0	0	0
0.1	20	30
0.2	30	35
0.3	40	48
0.4	50	56
0.5	60	68
0.6	70	74

3 Conclusion

Thus by introducing the jounce bumper made of polyurethane inside a front fork, assembly will obviously improve the noise, vibration, and harshness (NVH) of the vehicle. The test results obtained using the universal testing machine clearly depicts the uniform displacement that occurred in the assembly with the jounce with the gradual increment in the load of 0.1 kN. The impulse absorption is more when it is compared with an existing front fork assembly (without jounce). The above test results clearly show that the maximum shear stress value is higher in front fork assembly with jounce, which is clearly more stable and efficient compared to the existing design. The frequency response and analysis of the spring jounce assembly were proven effective compared to the existing design. Due to the added absorption capacity and the effective damping characteristics of the jounce bumper, the effects of front suspension were enhanced which resulted in the reduction of NVH, leading to improved ride quality and vehicle handling.

References

1. Ali A, Sidhu RS, Samad MSA (2011) Fatigue characteristic of automotive jounce bumper. *New Trends Dev Autom Syst Eng* 298–306
2. Sidhu RS, Ali A (2010) Fatigue life of automotive rubber jounce bumper. *Mater Sci Eng* 11:1–6
3. Wang Y, Wang L, Ma Z, Wang T (2017) Finite element analysis of a jounce bumper with negative Poisson's ratio structure. *J Mech Eng Sci* 231(23):4374–4387
4. Pinjarla P, Lakshmana KT (2012) Design and analysis of a shock absorber. *Int J Res Eng Technol* 1(4):578–592
5. Wang Y, Wang L, Ma Z, Wang T (2016) A negative Poisson's ratio suspension jounce bumper. *Mater Des* 103:90–99
6. Wang Y, Zhao W, Zhou G, Gao Q, Wang C (2018) Suspension mechanical performance and vehicle ride comfort applying a novel jounce bumper based on negative Poisson's ratio structure. *Adv Eng Softw* 122:1–12
7. Samad MSA, Ali A, Sidhu RS (2011) Durability of automotive jounce bumper. *Mater Des* 32:1001–1005
8. Wang Y, Ma Z, Wang L (2016) A finite element stratification method for a polyurethane jounce bumper. *J Automob Eng* 230(7):983–992
9. Zhang J, Li H (2015) Optimization design on dynamic characteristics and fatigue life of automotive suspension system. *J VibroEng* 17(5):2547–2558

Finite Element Analysis of Bending and Dynamic Response of a Power Transmission Spur Gear



A. Saravanan and P. Suresh

Abstract The spur gears are the simplest model and widely used in power transmission and weight lifting mechanism, etc. In this paper describes the selection of the materials is based on the increasing efficiency in bending, torque, velocity during heavy load application. The challenge is to develop a high-strength spur gear that can safely withstand required load. Bronze alloy was chosen for the spur gear application because of its toughness, strength, low coefficient of friction, corrosion resistance, high fatigue strength, and fine grain. One set of spur gear arrangement like one gear mesh with one pinion arrangement taken into consideration. Usually, the gear made up of steel that can be replaced by Bronze alloy. In this numerical analysis for the steel spur gear pair, the gear and pinion both are made up of AISI 4340 Steel. For the Bronze alloy gear pair, the gear is made up of phosphorus bronze copper alloy (UNS C51000) and pinion is made up of bronze sand cast. The model of spur gear was created using Creo-parametric software and the bending and torque analysis was obtained using FEA code ANSYS 15.0 software. The dynamic analysis was obtained by using FEA code ANSYS 15.0 (LS-DYNA) software. That performance of both materials numerically investigated and verified analytically. Bronze alloy gear provides better mechanical properties such as beam strength, high velocity, high dynamic load carrying capacity, and very low stress. Finally it was concluded that the Bronze alloy gears showed better performance when compared to steel alloy gears and this bronze alloy gear could be used as the better alternative gears for weight lifting applications.

Keywords Spur gear · AISI 4340 Steel · Bronze alloy · FEA · LS-DYNA

Nomenclature

Z_1 and Z_2 Number of teeth on Pinion and Gear

A. Saravanan (✉) · P. Suresh
Mechanical Engineering Department, Sona College of Technology, Salem, Tamil Nadu, India
e-mail: ansyssaran@gmail.com

© Springer Nature Singapore Pte Ltd. 2019
S. S. Hiremath et al. (eds.), *Advances in Manufacturing Technology*,
Lecture Notes in Mechanical Engineering,
https://doi.org/10.1007/978-981-13-6374-0_57

511

m	Module
r, R	Pitch circle Radius of Pinion and Gear
d, D	Pitch circle Diameter of Pinion and Gear
C	Center Distance
P_c	Circular pitch
P_d	Diametral pitch
G	Gear ratio
r_A, R_A	Addendum circle radius of Pinion and Gear
a_p, a_w	Addendum of Pinion and Gear
N_1	Speed of Gear
DVS	Displacement vector sum (Over all displacement of the gear)
v	Velocity of gear
P	Power
F_t	Tangential load on tooth
V	Pitch line Velocity
F_s	Beam Strength
F_d	Dynamic Load
F_w	Maximum Wear Load
φ	Pressure Angle
b	Face width
y	Lewis form factor
Q	Ratio factor
K_w	Load Stress factor

1 Introduction

Nowadays it is mandatory to operate machines at varying load and speed. Especially, load-carrying machines must operate different loads with different speed conditions. Load-carrying capacity for static and dynamic conditions and reducing stress due to bending and torque is the major criteria for load-carrying machines. Spur gears are simple, easily manufactured gears and are usually the first choice when exploring gear options. Transmitting power between parallel axes, the teeth project radially on the disk. Spur gears are regularly used for speed reduction or increase, torque multiplication, resolution, and accuracy enhancement for positioning systems. The teeth run parallel to the gear axis and can only transfer motion between parallel axis gear sets. Spur gears mate only one tooth at a time, resulting in high stress on the mating teeth and noisy operation. The gear is a device which is to transmit torque by applying force to another gear [1]. Recently, MMC (metal matrix composite) materials have been developed for mechanical components due to their unique properties such as lightweight, high beam strength, dimensional stability, and corrosion resistance [2]. When compared to polymer base materials, MMC material cost is high [3, 4] because of material and manufacturing cost. AL-Sic composite materials can be produced by powder metallurgy method, and it provides improve hardness and high strength and weight reduction [5]. While designing a gear, there are various standards and factors are available [6, 7] that all factors should be considerate. While dynamic load of gear

is minimized, its result the gear noise can be minimized, increase gear efficiency, improve pitting fatigue life, and prevent gear tooth fracture [8]. The pressure angle of gear is a very important factor, because changing of pressure angle will impact the tooth mesh characteristic such as tooth contact zone and contact ratio. Increase in pressure angle in gear teeth and making different profile cause decrease or reduce the bending stress and the contact stress [9]. Here the material of gear is changed according to load and speed applications for better strength and velocity and wear resistance. In this paper, the FEM is using to analyze the gear characteristics because it is capable of providing information on bending stress, transmission errors, which require for designing a gear pair system.

Bronze is an alloy that consists primarily of copper with the addition other ingredients in most cases the ingredient added typically tin, but arsenic, phosphors, aluminum, manganese, and silicon can also be used to produce different properties of the material. Phosphors bronze alloy typically has a tin content ranging from 0.5 to 1.0% and a phosphors range of 0.01–0.35%. These alloys preferable for its toughness, strength, low coefficient of friction, high fatigue strength and fine grain. The composition content for phosphor bronze copper alloy (UNS C51000) is copper (95%), tin (5%) and phosphorus (trace). The tin content increases the corrosion resistance and tensile strength, while the phosphor content increases the wear resistance and stiffness. Phosphor bronze is an alloy of copper, tin (3.5–20%), and phosphors (<1%); these materials exhibit high fatigue strength, corrosion resistance, and low coefficient of friction [10]. Because of addition of cu with the Phosphors bronze alloy, it has good wear resistance, good machinability, cold workability, fatigue resistance, corrosion resistance, and it can operate in most severe conditions and up to temperatures nearly 450 °C [10]. C51910 phosphor bronze gives excellent mechanical properties, high wear and corrosion resistance, low-temperature resistance, inability to generate an electrical spark under impact, and good walkability and is often used to produce metal parts like connector and pin parts in aerospace and electrical motor applications [11].

2 Materials and Properties

The material properties of steel and bronze alloy are tabulated in Table 1.

- AISI 4340 Steel (Gear and Pinion) [12]

Table 1 Material properties for steel and bronze alloy

S. No.	Properties	Unit	Steel (gear and pinion)	Bronze alloy	
				C51000	Sand cast
1	Density	kg/m ³	7850	8860	7500
2	Modulus of elasticity	Gpa	200	117	117
3	Poisson’s ratio	–	0.30	0.34	0.34
4	Tensile yield strength	Mpa	300	552	530
5	Tensile ultimate strength	Mpa	645	965	760

- Phosphor bronze copper alloy (UNS C51000) (Gear—C51000 and Pinion-Sand cast) [12]

3 Numerical Analysis of Gear

In the numerical analysis, the following data and specifications are taken into consideration. The model calculation and results are given below.

3.1 Model Calculation

The following data are taken into consideration for analysis of gear material

- Power $P = 32 \times 10^3$ W
- Speed $N_1 = 600$ rpm
- No. of teeth on pinion $Z_1 = 22$
- Angle $\varphi = 20^\circ$
- Velocity $v = 12$ m/s

Spur gear made up of Bronze

Module = 9 mm No. of teeth on pinion $Z_1 = 22$ mm No. of teeth on Gear $Z_2 = 88$ mm Pitch circle radius of pinion $r = 99$ mm	Pitch circle radius of gear $R = 396$ mm Center distance $C = 495$ mm Circular pitch $P_c = 28.27$ mm Diametral pitch $P_d = 0.1$ tooth/mm
Beam strength (F_s) $F_s = \pi * m * b * \sigma_b * y$ $= \pi * 9 * 90 * 84 * 0.1125$ $= 24047.32$ N	Dynamic load (F_d) $F_d = \frac{F_t}{C_v} = \frac{6431.90}{0.333}$ $= 19315.02$ N
Bending stress due to torque (σ_b) $\sigma_b = \frac{i+1}{a.m.b.y} [M_t]$ where $[M_t] = M_t * k * d$ also $M_t = \frac{60 * P}{2 * \pi * N_1} = 713.01 * 10^3$ N/mm $\sigma_b = \frac{4 + 1}{495 * 9 * 90 * 0.402} \{713.01 * 10^3\}$ $\sigma_b = 22.11$ N/mm ²	Maximum Wear Load (F_w) $F_w = d_1 * b * Q * K_w$ where $Q =$ Ratio factor $= \frac{2 * i}{i + 1} = \frac{2 * 4}{4 + 1} = 1.6$ $K_w =$ Load stress factor $= 1.211$ N/mm ² $F_w = 198 * 90 * 1.6 * 91.211$ $= 34528.05$ N

Table 2 Numerical result for steel and bronze gear materials

S. No.	Material	Pitch line velocity (V) (m/s)	Beam strength (F_s) (N)	Dynamic load (F_d) (N)	Bending stress due to torque (N/mm ²)	Max wear load (F_w) (N)
1	Steel	5.52	19,000	17383.5	31.492	27281.4
2	Bronze	6.22	24,047	19315.02	22.11	34528.05

Fig. 1 Pitch line velocity (V) curve

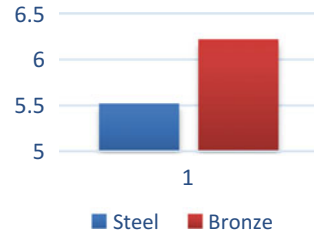
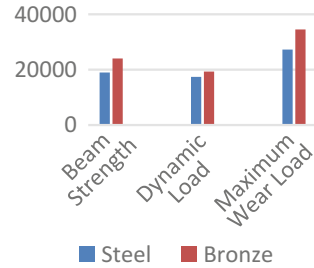


Fig. 2 Beam strength (F_s), dynamic load (F_d) and max wear load (F_w) curve



4 Result (Numerical)

The pitch line velocity, beam strength, bending stress, and maximum wear load are numerically calculated and tabulated in Table 2.

The pitch line velocity for both the materials is plotted in the curve as shown in Fig. 1. The beam strength, dynamic load, and maximum wear load for both the materials are plotted in the curve as shown in Fig. 2.

5 Analysis of Gear (Analytical)

The spur gear dimensions are taken from the above details and created FEA model of gear using Creo 2.0 parametric design software and it's imported to FEA code ANSYS 15.0 software for analyzing analytical method. In this, analytical method for steel gear AISI 4340 Steel and for the bronze alloy phosphor bronze copper alloy (UNS C51000) is taken into consideration. The FEA model of spur gear created

using Creo 2.0 parametric design software. The boundary condition for the bending analysis of gear is the center surface of gear is arrested and 10 Pa pressure loads applied on tooth of gear surface. The meshed view model of spur gear created using ANSYS 15.0 software.

6 Bending Analysis

The bending analysis of spur gear can be obtained using FEA code ANSYS 15.0 software. The figures are shown, and values are tabulated below.

6.1 Stress Value from FEA (10 Bar Pressure)

The 10 Pa pressure load applied on the surface of the gear tooth for bending analysis and stress (Figs. 3 and 4) values are obtained from FEA as shown below for both the materials.

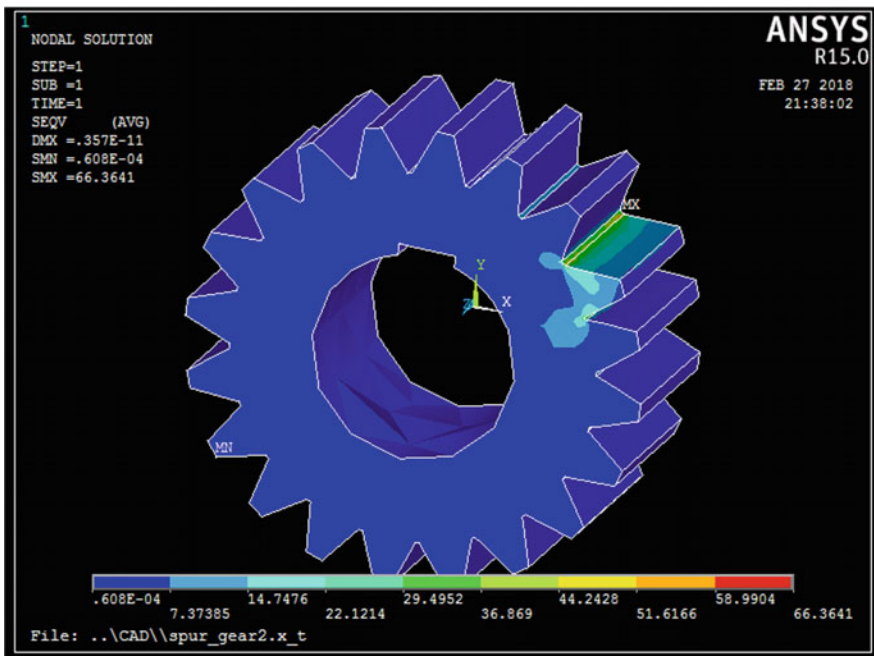


Fig. 3 Bending stress for steel gear

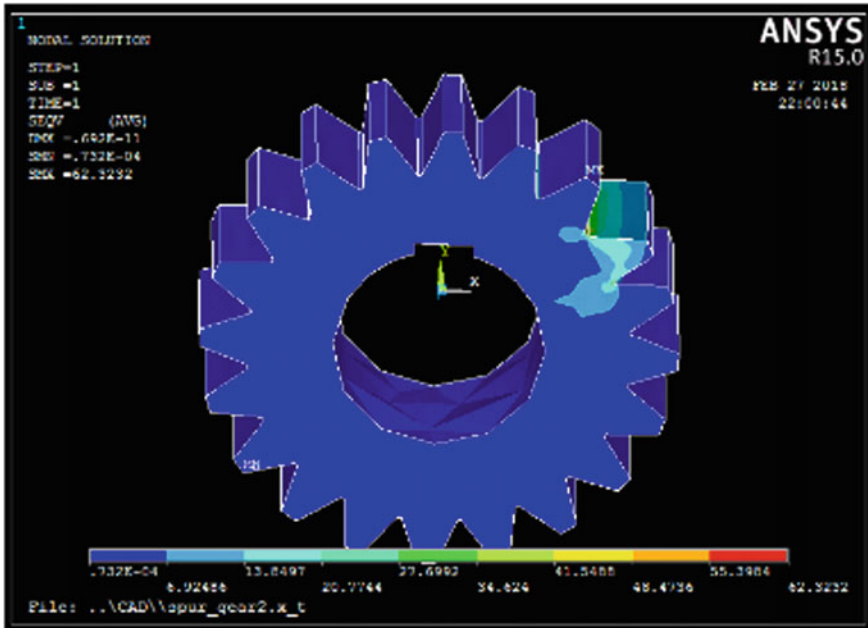


Fig. 4 Bending stress for bronze gear

7 Torsion Analysis

The 10,000 Pa pressure load applied on one pitch of the gear tooth for torque analysis. The boundary condition, stress, and strain values are obtained from FEA as shown below for both the materials. The boundary condition for the torque analysis of gear is the center surface of gear is arrested and 10,000 Pa pressure loads applied on pitch of gear surface as torque load.

7.1 Torsion Stress

The 10,000 Pa pressure load applied on the surface of the gear tooth for torque analysis and stress (Figs. 5 and 6) values are obtained from FEA as shown below for both the materials.

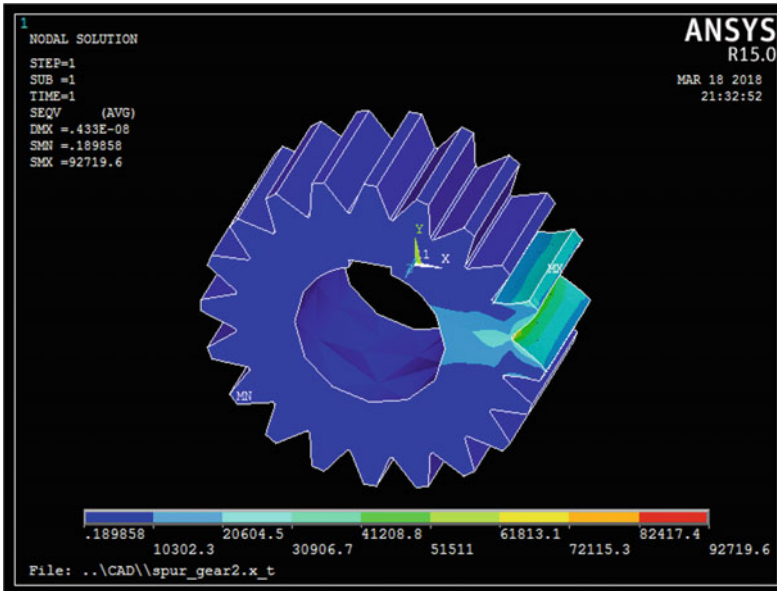


Fig. 5 Stress due torque for steel gear

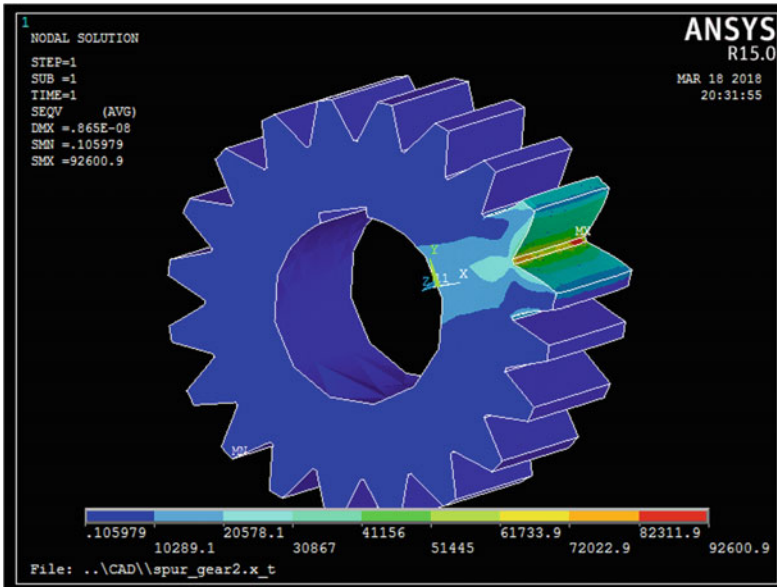


Fig. 6 Stress due torque for bronze alloy gear

8 Results (Analytical)

The bending stress and torsional stress are calculated from FEA code ANSYS 15.0 software and tabulated in Tables 3 and 4. It is given in Table 3. Analytical result of bending stress for steel and bronze material.

The DVS value and stress from Table 3 are plotted in the graph, given in Figs. 7 and 8. The stress value from Table 4 is plotted in the graph, given in Fig. 9.

Table 3 Analytical result for bending stress for steel and bronze materials

S. No.	Material	Load (pressure) (N/m ²)	DVS (mm)	V. Stress (N/m ²)
1	Steel	10	6.78	66.36
2	Bronze	10	5.22	62.32

Table 4 Analytical result for torsional stress for steel and bronze materials

S. No.	Material	Load (pressure) (N/m ²)	V. Stress (N/m ²)
1	Steel	10,000	92719.6
2	Bronze	10,000	92600.9

Fig. 7 DVS curve (due to bending)

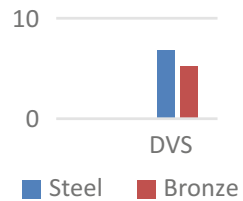


Fig. 8 V. Stress curve (due to bending)

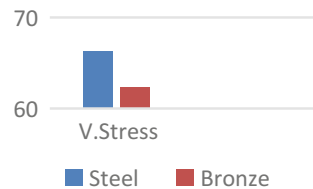
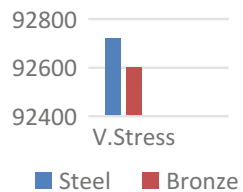


Fig. 9 V. Stress curve (due to torque)



9 Dynamic Analysis

The 52 rad/s (500 rpm) rotating speed applied in the spur gear for dynamic analysis in the FEA code ANSYS 15.0 (LS-DYNA). The boundary condition, stress, and maximum rotating velocity values are obtained from FEA as shown below for both the materials. The boundary condition for the dynamic analysis of gear is rotated about Z-axis by 52 rad/s.

9.1 Stress Value from FEA (Dynamic Analysis)

The 52 rad/s speed applied on the gear for dynamic analysis and stress (Figs. 10 and 11) values are obtained from FEA as shown below for both the materials.

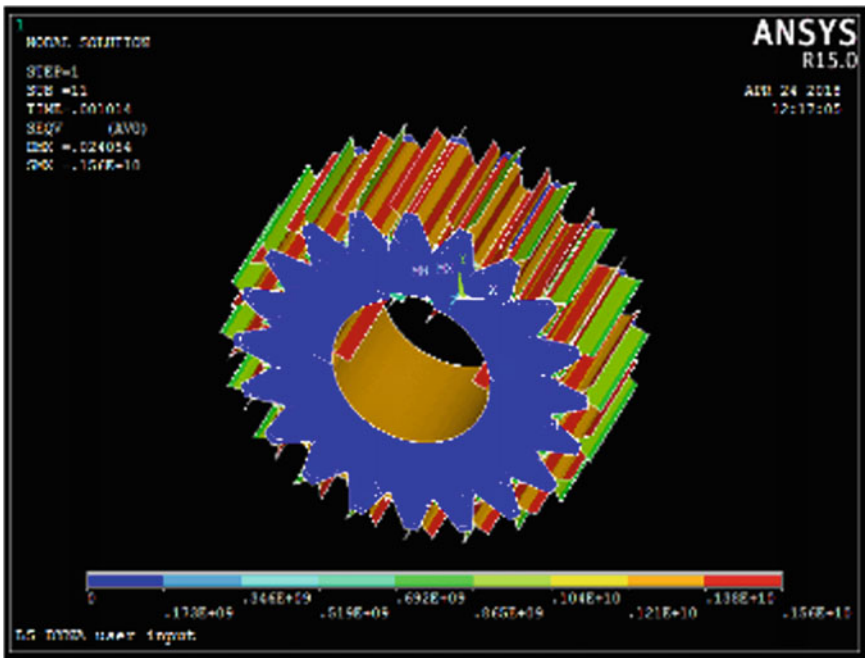


Fig. 10 V. Stress for steel (dynamics)

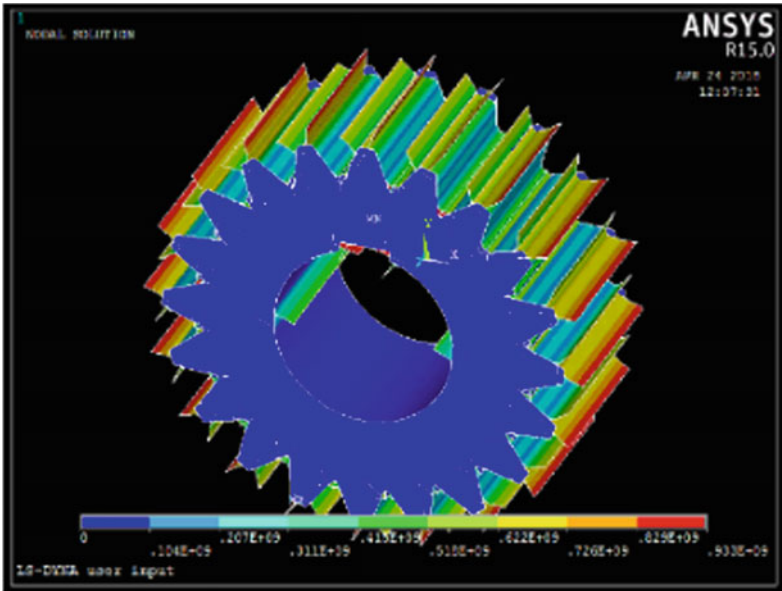


Fig. 11 V. Stress bronze alloy (dynamics)

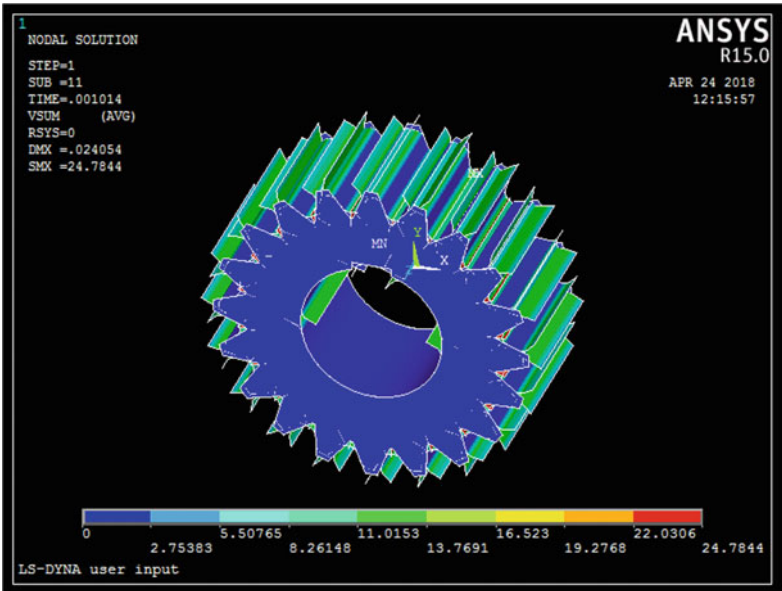


Fig. 12 Velocity for steel (dynamics)

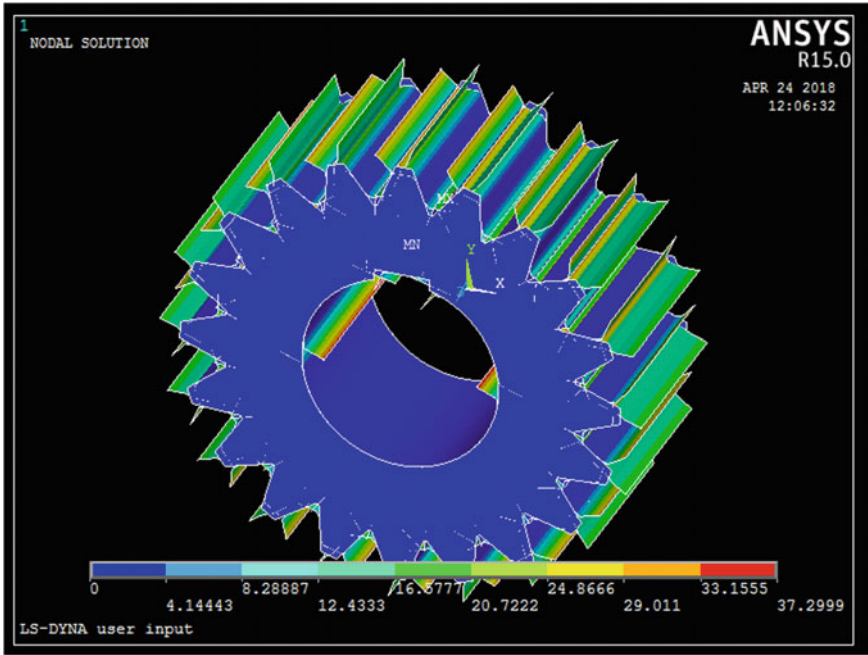


Fig. 13 Velocity for bronze alloy (dynamics)

9.2 Velocity Value from FEA (Dynamic Analysis)

The 52 rad/s speed applied on the gear for dynamic analysis and velocity (Figs. 12 and 13) values are obtained from FEA as shown below for both the materials.

10 Results (Dynamic Analysis)

The dynamic stress and maximum velocity are calculated from FEA code ANSYS 15.0 software and tabulated in Table 5.

Table 5 Analytical result for dynamic analysis for steel and bronze materials

S. No.	Location	Angular velocity (Rad/s)	Time of response (s)	Steel	Bronze
1	V. Stress (N/m ²)	52	0.001	0.156e10	0.933e9
2	Max. rotating velocity (Rad/s)	52	0.001	28.7844	37.2999

Fig. 14 V. Stress curve (dynamics)

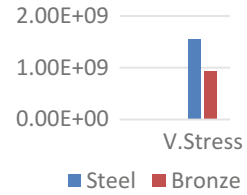
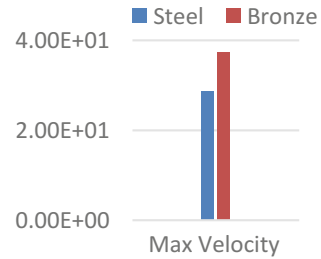


Fig. 15 Velocity curve (dynamics)



The stress value and velocity taken from Table 5 and plotted in the graph, it is given in Figs. 14 and 15.

11 Result and Discussion

- Result of the study revealed that the gear made up of phosphorus bronze alloy gave better value for velocity, strength, dynamic load, and minimum stress than that of steel gear.
- Table 1 shows the numerical study of both the materials, its demonstrate enormously the gear made up of phosphorus bronze and pinion made up of sand cost pair giving better value for velocity and beam strength and dynamic load than that of steel gear.
- The analytical study of displacement vector sum and von Misses stress for steel and bronze material are obtained and presented in Tables 3 and 4.
- Table 5 shows that von Misses stress and maximum rotating velocity for steel and bronze material in dynamic condition.
- For evaluating strength, velocity, dynamic load, stress for the bronze material, it gave better result due to ingredient added, typically tin, phosphors, and copper.
- Because of tin added corrosion resistance and fatigue strength increased while phosphorus added wear resistance and stiffness increased in bronze alloy material. Also, copper added to bronze alloy material, it exhibits good machinability, cold workability, and fatigue resistance.
- Finally, the investigation of performance of the bronze alloy and steel alloy materials is successfully completed using numerical and analytical method, and both methods gave the similar result.

12 Conclusion

In this present work, the existing gear made up of steel is replaced by bronze alloy material and various mechanical tests are conducted for evaluating properties of gear. The following conclusions are drawn from the numerical and analytical analyses on gears.

- From that the numerical analyses, the spur gear pair, gear is made up of phosphor bronze copper alloy (UNS C51000) and pinion is made up of bronze sand cast gets less chance to failure while its operating in various load and speed condition over the gear and pinion made up of AISI 4340 Steel.
- From the analytical (FEA) analysis, the phosphor bronze copper alloy (UNS C51000) material is suitable for high load, torque, and speed applications over the AISI 4340 Steel gear.
- Also, the phosphor bronze copper alloy (UNS C51000) gave almost 3–4% better result than that of AISI 4340 Steel gear, it has been observed from the numerical and analytical results.
- These gears can be used for transmitting almost 34 kW power.
- Further research work is needed to determine whether phosphor bronze copper alloy (UNS C51000) material gave wear resistance, corrosion resistance, good machinability, and cold workably with real-time testing.

References

1. Chawathe DD (2012) Handbook of gear technology. Int J Mech Civ Eng 1(1):15–25 (New Age International Publication)
2. Devi N, Mahesh V, Selvaraj N (2011) Mechanical characterization of aluminium silicon carbide composite. Int J Appl Eng Res 1(4):126–131
3. Shigley JE, Mischke CR, Mechanical engineering design, 6th edn.
4. Wang H, Zhang R, Hu X, Wang C-A, Huang Y (2008) Characterization of a powder metallurgy SiC/Cu–Al composite. J Mater Process Technol 43–48
5. Saravanan A, Suresh P (2018) Static analysis and weight reduction of aluminum casting alloy connecting rod using finite element method. Int J Mech Prod Eng Res Dev (IJMPERD) 08(3). ISSN: 2249-8001
6. Chironis NP, Sclater N (1996) Mechanisms & mechanical devices sourcebook, 2nd edn. McGraw-Hill, New York
7. Hsieh WH (2007) An experimental study on cam-controlled planetary gear trains. Mech Mach Theory 42:513–525
8. Hsieh WH, Lee IC (2011) Modelling and control of cam-controlled planetary gear trains. Int J Model Ident Control 12:272–279
9. Yan HS, Chen WR (2000) On the output motion characteristics of variable input speed servo-controlled slider-crank mechanisms. Mech Mach Theory 35:541–561

10. Sharma SC, Satish BM, Grish BM, Somasekar DR (2001) Wear characteristics of phosphor-bronze/silicon carbide particulate composites. *J Mater Process Technol* 118:65–68
11. Liu P, Ren F, Jia S (2007) Copper alloy and its application. Chemical Industry Press, Beijing, p 73 (in Chinese)
12. Hashim J, Looney L, Hashmi MSJ (1999) Metal matrix composites: production by the stir casting method. *J Mater Process Technol* 17

Design and Analysis of Composite Parabolic Leaf Spring Under Fatigue Load Condition



Priyadarshi Dutt, T. Babu, M. Murugan, P. Anbarasu and Bala Subramani

Abstract Suspension is considered as a link between the wheels and the body. It absorbs fatigue loading and energy. Leaf spring is one of the oldest suspension types. Nowadays, parabolic leaf spring is mainly used in heavy load vehicles and machines. Design fundamentals of parabolic leaf spring are based on the strength and comfort. The strength properties of leaf spring are usually determined based on the suspension type and loading. The advantage of the parabolic leaf spring is due to its simple construction, low cost, and easy maintenance. The design also helps in providing the axle support. This paper mainly deals with the suspension uses of parabolic leaf spring. The difference between the normal leaf spring and the parabolic leaf spring is the total number of leaves. A parabolic leaf does not need of more number of leafs because the stress is distribution to the leaf are equally due to its parabolic shape.

Keywords Leaf spring · Parabolic leaf spring · Fatigue analysis · Suspension · GFRP

1 Introduction

Basically, a parabolic spring is a spring that consists of two or more leaves. The leaves touch only in the center where they are fixed to the axle and at the outer ends, they are fixed to the vehicle. In between those two points, the leaves do not touch each other as they do with conventional leaf springs. To increase the riding comfort, leaf springs are used widely. This paper mainly deals about the parabolic leaf spring. Comparing normal leaf spring, the number of leaves is less in parabolic leaf spring. This helps us in reducing the material which leads to less in cost. Also, the main advantage of using parabolic leaf spring is its load carrying capacity and energy

P. Dutt (✉) · T. Babu · M. Murugan · P. Anbarasu
Department of Mechanical Engineering, Sri Sai Ram Engineering College, Chennai, India
e-mail: dutt.priyadarshi25@gmail.com

B. Subramani
Department of Mechanical Engineering, Sri Sai Ram Institute of Technology, Chennai, India

© Springer Nature Singapore Pte Ltd. 2019
S. S. Hiremath et al. (eds.), *Advances in Manufacturing Technology*,
Lecture Notes in Mechanical Engineering,
https://doi.org/10.1007/978-981-13-6374-0_58

absorption. This helps us in getting good suspension and good riding comfort. Dubey et al. [1] have studied that composite materials have more elasticity, energy storage capacity, and high strength-to-weight ratio as compared to the normal steel. By using composite materials like GFRP, the weight of the parabolic leaf spring without reducing on load carrying capacity and probable stiffness can be achieved. Therefore, analysis of composite material parabolic leaf springs has become essential in getting required possible results [2]. In general, the most of the engineering components are subjected to non-constant amplitude proportional loading like fatigue loads at which stress–strain cycles fluctuate with time [3]. At this condition, component leads to fail under various loading conditions. Fatigue failure of mechanical components like leaf springs is a process of periodic stress–strain conditions [4]. Using the finite element method approach, the life of parabolic spring under fatigue load is estimated for stress–strain life of leaf spring. Parabolic spring is widely used in many automobile vehicles and is one of the major components of suspension system. Chandrabose et al. [5] studied that FEA model is developed and material geometry with improved material is based on the life, shear stress, and spring rate.

2 Experimental Procedure

2.1 Material Properties

The material of the steel parabolic leaf spring was according to the spring's manufacturer. Standard comparison indicated that the SUP 9 spring steel is equal to the 55Cr3 spring steel. SAE number for the 55Cr3 is 5160. Fatigue properties of the steel were determined according to SAE from the GlyphWorks material properties' database. The material properties of the SAE5160/SUP 9/55Cr3 have been given in Table 1. Tables 2 and 3 represent the parameters of the leaf spring.

Table 1 Material properties steel

SAE5160/SUP 9/55Cr3	Values	Unit
Elastic modulus, E	207	GPa
Ultimate tensile strength, R_m	1600	MPa
Yield strength, R_{el}	1250	MPa
Work hardening coefficient, K	1940	MPa
Cyclic strength coefficient, K'	2432	MPa
Fatigue strength exponent, b	−0.08	
Fatigue ductility exponent, c	−1.05	
Fatigue ductility coefficient, E_f	9.56	

Table 2 Dimensions of leaf spring and properties of GFRP

Parameters	Values
Total length (eye-to-eye) (mm)	1150
Arc height at axle seat (Camber) (mm)	175
Spring rate (N/mm)	20
Number of full length leaves	2
Number of graduated leaves	5
Width of the leaves (mm)	34
Thickness of the leaves (mm)	5.5
Full bump loading (N)	3250
Spring weight (kg)	13.5

Table 3 Material properties of GFRP

Properties	Values
Modulus of elasticity (GPa)	E_{11} , 38.6
Modulus of elasticity (GPa)	E_{22} , 8.27
Modulus of shear (GPa)	G_{12} , 4.14
Poisson ratio (ν_{xy})	0.26
Tensile strength (MPa)	σ_{t11} , 1062
Tensile strength (MPa)	σ_{t22} , 31
Compressive strength (MPa)	σ_{c11} , 610
Compressive strength (MPa)	σ_{c22} , 118
Shear strength (MPa)	σ_{c12} , 71

2.2 Boundary Conditions

Consideration of both the steel and GFRP parabolic leaf springs boundary conditions chosen in the following manner: Both the ends of leaf springs were fixed and the force is applied on the bottom of the leaf spring. In this, the force value applied is 3750 N.

3 Results and Discussions

The suspension obtained for the GFRP parabolic leaf spring using the deformation is comparably much higher than the parabolic leaf spring made of steel which is evident in Fig. 1.

The deformation value of the GFRP parabolic leaf spring is 2.0478 mm, whereas for the steel parabolic leaf spring is 0.0028431 mm. This is because the ductile property for the steel material is lower than the GFRP material. Figures 1 and 2 show the deformation of steel parabolic leaf spring and GFRP parabolic leaf spring. Figure 2

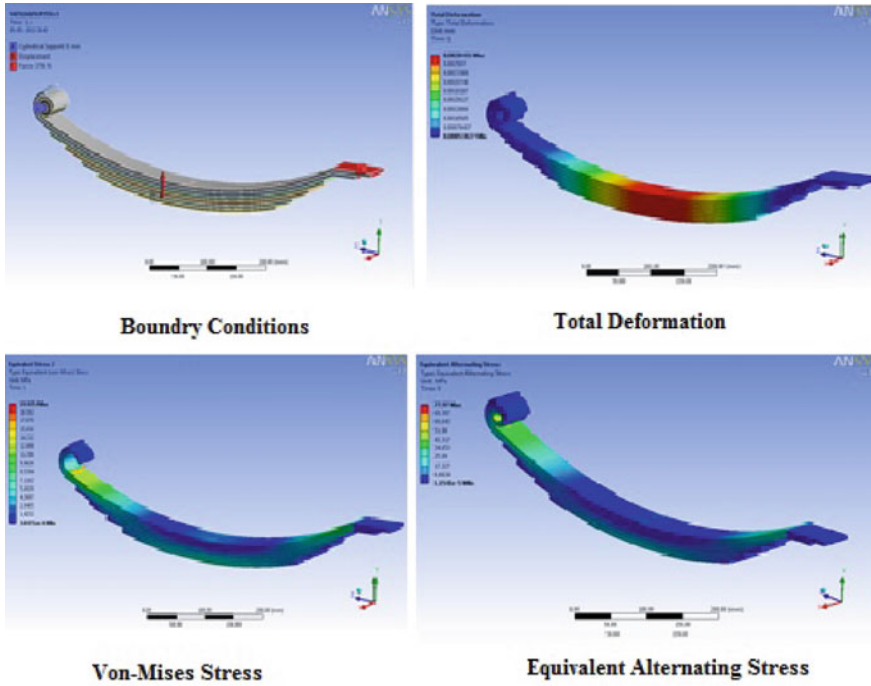


Fig. 1 Results of steel

Table 4 Comparison of deformation and stress for steel and GFRP

Value level	Deformation (mm)	Stress (MPa)
<i>Steel</i>		
Maximum	0.0028431	19.925
Minimum	0.0053827	19.9253.8471E-6
<i>GFRP</i>		
Maximum	2.0478	78.338
Minimum	0.00029898	0.032328

represent the stress plot for steel and GFRP parabolic leaf spring, respectively. The stress value of GFRP is much lower than steel leaf spring which has been evident in Fig. 2. The stress value of GFRP leaf spring is 78.338 N/mm², whereas for the steel leaf spring is 19.925 N/mm². This is because toughness factor of GFRP parabolic leaf spring is comparably better than steel parabolic leaf spring (Tables 4 and 5).

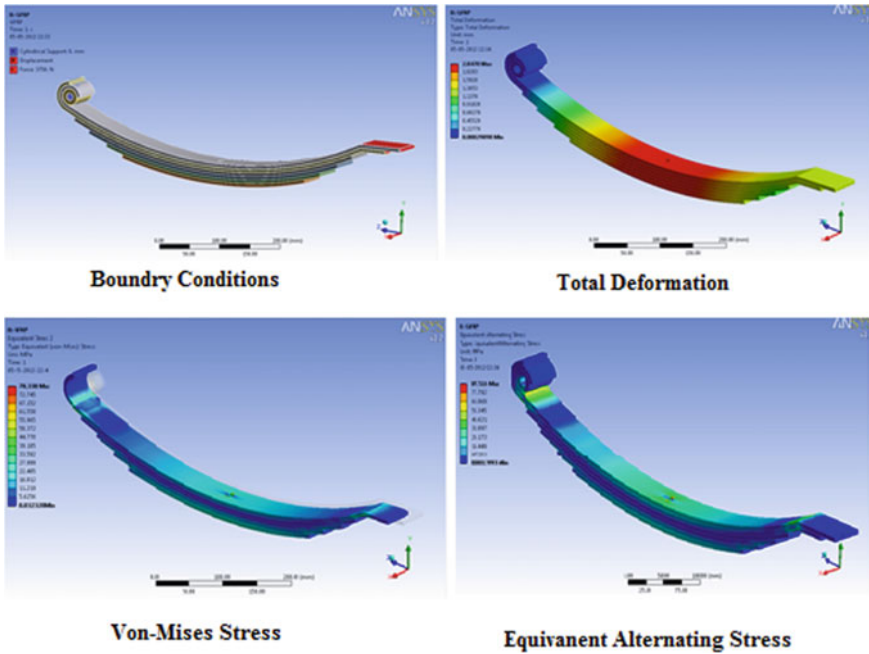


Fig. 2 Results of GFRP

Table 5 Mass details of steel and GFRP parabolic leaf spring

S. No.	Material for leaf spring	Mass (kg)
1	Parabolic leaf spring with steel	723
2	Parabolic leaf spring with GFRP	267

4 Conclusion

This research paper deals with the analyzing of the design and strength of the parabolic leaf spring along with structural and fatigue load analysis. By observing the results, the analyzed stress values have been lesser than their respective yield stress values in the GFRP parabolic leaf spring. So, the proposed design is safe. By comparing the results for both GFRP and steel, the stress value for the steel parabolic leaf spring is higher than GFRP parabolic leaf spring. Also, while comparing the mass of both parabolic leaf springs, it clearly shows that the mass of GFRP spring is low comparing to steel leaf spring. So, it has been concluded that as per the standard analysis using material, GFRP for parabolic leaf spring is considered.

References

1. Dubey DN, Mahakalkar SG (2013) Stress analysis of a Mono-parabolic leaf spring—a review. *Int J Mod Eng Res India* 769–772
2. Varvani-Farahani A, Sharma M, Kianoush MR (2005) Fatigue damage analysis and life assessment under variable amplitude loading conditions. *Mater Sci Eng A* 403:42–47
3. Li B, Reis L, de Freitas M (2006) Simulation of cyclic stress/strain evolutions for multiaxial fatigue life prediction. *Int J Fatigue* 28:451–458
4. Leevy G, Cao K (2004) Evaluation of a multi-leaf hybrid springs for automotive suspensions. *SAE Technical Paper Series* 2004-01-0782
5. Chandrabose S, Thamodharan C, Naveenchandran P, Anbazhagan R (2014) Design optimization and analysis of a parabolic leaf spring. *Middle-East J Sci Res* 20(11):1590–1596
6. Karlus EN, Himte RL, Rathore RK (2014) Optimization of mono parabolic leaf spring. *Int J Adv Eng Technol* 7(1):284–291
7. Chauhan A, John F (2016) Static analysis of parabolic leaf spring with that of conventional leaf spring by finite element analysis using Ansys. *Imp J Interdiscip Res* 2(6):1022–1028
8. Vijayarangan S, Ganesan N (1994) Static stress analysis of a composite bevel gear using a three-dimensional finite element method. *Comput Struct* 51(6):771–783
9. Tanabe K, Seino T, Kajio Y (1982) Characteristics of carbon/glass fiber reinforced plastic leaf spring. *SAE 820403*, pp 1628–1634
10. Yu WJ, Kim HC (1998) Double tapered FRP beam for automobile suspension leaf spring. *Compos Struct* 279–300

Optimizing Headlamp Focusing Through Intelligent System as Safety Assistance in Automobiles



S. K. Rajesh Kanna, N. Lingaraj, P. Sivasankar, C. K. Raghul Khanna and M. Mohanakrishnan

Abstract One of the major challenges faced by the automobile industries is to reduce the chance of occurring accidents and also to enhance the production of the safest automobiles. Even though many safety devices are available in the vehicles, the highest fatal terrific accidents occur on curved roads and junctions at nighttime. Also, the accidents occur due to glare from the fore coming vehicles. Because, in most of the cases, late recognition of objects in the zone plays a key role, and this happens due to improper forward lighting. So the main aim of this research is to provide enhanced nighttime safety measures by developing steerable dynamic headlights by considering most of the cases such as glare, curved roads, hill curves, and junctions. Also to react optimally based on the surrounding environment by interpreting the surrounding properly, an intelligent system has been developed to control the optimal movement of the headlight. Different kinds of tests were done on critical parts of the system, in order to determine its accuracy, its response time, and the system impact. Finally, the results acquired from these various tests are found satisfactory. It is a low-cost setup with minor modification on the doom of the headlight which will prevent the accidents due to improper lighting at nighttime.

Keywords Headlamp · Intelligent system · Optimized lighting system

1 Introduction

Due to the revolution in the automobile sector and enhancement of the economic status of the society, the number of on-road vehicles increases drastically and in turn leads to many accidents, and some may be fatal. These types of accidents are mainly due to technical failure, human mistakes, and wrong interpretation of the surrounding environment. Nowadays automobile sector is more conscious of the

S. K. Rajesh Kanna (✉) · N. Lingaraj · P. Sivasankar · C. K. Raghul Khanna · M. Mohanakrishnan
Rajalakshmi Institute of Technology, Chennai, India
e-mail: skrkanna@gmail.com

© Springer Nature Singapore Pte Ltd. 2019
S. S. Hiremath et al. (eds.), *Advances in Manufacturing Technology*,
Lecture Notes in Mechanical Engineering,
https://doi.org/10.1007/978-981-13-6374-0_59

533

Fig. 1 Reflector type headlamp



technical failures by providing safety systems. The second category of the failure is due to human mistakes, which is more dependable on the driver. Even though sleep detection, drunken detection, auto navigation, smoke alarm, etc., are available, human failures became unavoidable. But the third category can be avoidable and reduced by facilitating the proper surrounding interpretation. Especially the ability to perceive and judge the exact distance of the objects and vehicles on the road is severely impaired at night, as the human eye requires light to clearly view, and improper lighting at nighttime became a top cause of accidents. In general, drivers are in the position of making instant decisions based on what they see in the combination of headlights and road lights, with the darkness around them. Thus, it is clear that the primary reason, in order to make the correct decision, is by providing a clear vision for the drivers through proper lighting. Therefore, drivers can make proper decisions and can avoid auto accidents during the night.

Lighting system in the automobiles is mainly by its headlamps. Headlamp is a set of lamps fitted on either side of the front portion of a vehicle to light the road ahead and is powered by the battery. The first electric headlamps were introduced in 1898 on the Columbia Electric Car from the Electric Vehicle Company of Hartford, Connecticut. Bulbs such as xenon bulb, halogen bulb, and LED bulb are considered as the heart of the headlamps, and a sample headlight is shown in Fig. 1. It has the multi-functional bulb, doom as outer casing, front glass to avoid dazzle and bulb safety, reflector parabolic disk to reflect the light toward roadside, and the doom has been controlled in this research to distribute the light based on the road conditions dynamically.

Therefore, the drivers can interpret the required information on the road and the surrounding environments, especially during nighttime. The major parameters influencing the design of headlights for an automobile are brightness, illumination, throw, and divergence. Higher the brightness, more clear the road vision, but it will affect the vision of the fore coming vehicle driver. So that the brightness control such as parking, dimmer, dim-tip, and brighter options is provided for the drivers. Any mal selection of brightness options by a driver on the road may leads to accidents, and a necessity arises to optimally control the brightness of headlamp based on the surrounding environment. The second parameter is the illumination; headlamp illumination performance has been steadily improving, and the illumination may create glare and reduce the vision of the fore coming vehicle drivers. Thus, the

headlamp glasses are designed such a way to reduce the illumination, and the design controversy reduces the brightness. The third parameter considered in designing the headlamp is the throw or “main beams.” In order to maximize the viewing distance of the driver, throw of the light should be longer, and on the other hand, the throw is proportional to the glare for fore coming vehicles. So a necessity arises to control the throw optimally by considering the surrounding.

So in this research, an attempt has been made to control the headlight motion optimally through sensors and the Arduino board, in which the main beam and low beams shift automatically in highways based on fore coming vehicle, more diverging light projection on the turn side, adaptively changing the throw based on the speed of the vehicle, weather beam projection, and an increase in the divergence projection in junction to indicate the vehicle movement and to identify the other vehicles. Thus, the drivers can get a clear vision on the surrounding environment, thereby leading to the right decision, which indirectly reduces the road accidents. The various researches carried out in the area are discussed in the following section.

2 Literature Review

The reduction in the cost and globalization of the automobiles leads to rise in the usage of motorization and creates a proportional increase in road accidents, in specific, 42% of road accidents occur after in night, whereas 58% of the above are fatal accidents, and 67% are pedestrian casualties [1]. Automobile industries are implementing and upgrading their system to avoid accidents and safeguard life [2]. Nighttime vehicle lighting is a vast research area where the researchers and the R and D engineers working to develop useful driver assistance systems. Researches were carried out with both non-vision-based approaches [3, 4] and vision-based approaches for traffic surveillance and driver assistance systems [5–13]. In most of the above researches, headlight control has been widely analyzed and enhanced for detecting surrounding at night. Some of the implemented headlight control systems are multi-functional bulbs, multi-beam LED, multi-LED bulb [14], smart beam with CMOS image sensor [15], adaptive headlight control with camera [16], etc. Apart from headlight control, many researches focused on headlight glare and brake light detection using sensors [17]. Other than improving the systems in the automobiles, the researcher also tried with the system to identify the humans [18, 19], edges [20], and objects [21]. Also, it has been identified that the timed braking will reduce many accidents and developed an intelligent braking system, to avoid accidents [22]. In recent researches, automated vehicles are being developed with its own visual system [23]. Even though many researches are going on, the adaptive control of the doom of the headlight is one of the low-cost methods for providing desired lighting system to the driver at the nighttime, and the same have been implemented in this research.

3 Need for Intelligent Adaptive Head Light

Reasons for the accidents and especially most of the accidents occur during night rides are due to lack of proper lighting and false interpretation by the drivers in poor illumination. Even though many reasons and factors are influencing the accidents, in this research, major six accident-causing factors have been considered for experimentation and developed an optimized intelligent system to overcome those accident-causing factors, and the six conditions are as follows.

Case a. Normally, in highway riding and longtime riding, some of the drivers have not used to switch the low and high beam with respect to oncoming vehicles. So the high beam of the vehicle projected over the approaching vehicle and causes glare to the approaching driver. So accidents may occur and a necessity arises to change from high to low beam, whenever any vehicle approaches the other vehicle.

Case b. Generally, national highways are having many curves and bends. The light beam distributed from the fixed headlight might not focus in accordance with the curvy roads, instead, it projects straight and the light falls over the object in the front. Thus, the driver in the night rides will find difficulty in finding the exact objects and the road in the curves. This may lead to accidents. So a necessity arises to illuminate the curves so that the driver can predict the surrounding environments and act accordingly to prevent the accidents.

Case c. In the signals and in the junction roads, the vehicles can approach on any roads. So the drivers should know the objects and the vehicles in each corner because, while taking a turn, the objects or humans in the corners may hit by the side of the vehicles. Also, the driver has to decide the turning radius based on the objects in the corners. So a necessity arises to project the light beam in the corners at the junctions to identify the objects in the corners to make the proper decision in turning the vehicles.

Case d. Also in junctions, especially during the nighttime, vehicles may cross the junctions randomly. So the drivers should be aware of the approaching vehicles at the corners of the junction. As the vehicles approaching the junction in perpendicular direction may not be able to view the indicator signals. So a necessity arises to project the beam in the corners of the junctions.

Case e. In highway driving, the vehicles are moving with high speed, and the projection of the headlamp remains the same in all the speed. So the distance covered by the headlamp remains constant. In low speed, more projection is required for the nearby front region of the vehicle and the existing headlamps are sufficient to predict the environment and road conditions at low speed. On the other hand, for the high speed, it requires to project or to throw the light to a longer distance. So that the driver can easily predict the approaching vehicles, road conditions, signals, direction signs, speed breakers, etc. So a necessity arises to focus the light beam based on the speed of the vehicles.

Case f. During rainy and foggy conditions, the penetration of the headlight is less and might not sufficient for the drivers to predict the objects in the road. So the vehicles are provided with yellow light, which can penetrate through the fog. But the yellow light emits the constant light intensity and independent of the fog or rainwater density and day condition. So it may lead to accidents at high speed. So a necessity arises to project the penetrating light beams based on the surrounding environments.

To overcome these situations, projector lights for better focusing, a vertical swiveling mechanism to increase or decrease the range, and adaptive front lighting system are also expensive as it requires a separate controller, sensors, and many electronic types of equipment. These are also subjected to high maintenance. These technologies should be made affordable and adaptable to all the vehicles so that drivers can feel the pleasure of driving, and the accident rates can be decreased in low levels became the main objective of this research. In this research, all the above-mentioned issues have been satisfied by developing an intelligent adaptive doom control system for optimally control the doom movement and indirectly providing a clear vision to the drivers.

4 Intelligent System for Optimal Doom Control

In order to interpret the surrounding environment, sensors like ultrasonic sensor, light sensor, IR sensor, humidity sensor, rotary POT, and tachogenerator have been used in this research, and the similar output from the same sensor will have different meaning with respect to other sensors output. So a necessity arises for a decision-making system to finalize with the optimal solution from the available solutions. Thus, in this research, an artificial neural network (ANN) module has been implemented to identify the optimal movement of the doom. ANN is a network of processing elements interconnected with each other and capable of doing processing in parallel and in a distributed manner [23]. Each unit has input/output characteristics and implements a local computation through its developed transfer function. The output of any unit is determined by its input/output characteristics and its interconnections to other units and external inputs. The developed network is shown in Fig. 2.

The input vector $I = s_1, s_2, s_3, \dots s_{24}$, and the connections of the long-term memory forms a vector $W = W_{1-1}, W_{1-2}, W_{1-3}, \dots W_{2-75}$, where W represents the weight from the node i to $i + 1$. There is an additional parameter θ , internal threshold value modulated by the weight W used for activating the processing elements. The transfer function used to compute the activation and the output is given in Eqs. 1 and 2, respectively [24].

$$A_i = \Sigma W_{ij} * O_{ij} + \theta_j \tag{1}$$

$$O_i = 1/(1 + \exp - A_i) \tag{2}$$

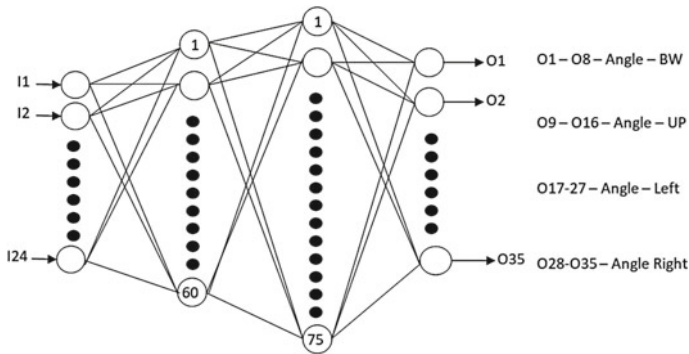


Fig. 2 Developed ANN network model

In this research, after sensitivity analysis, it has been decided to have 24 neurons in the input layer which receives distributed values in the range of 0–1 from sensors (signal conditioning unit). Two hidden layers with 60 and 75 neurons, respectively, have been constructed for deep learning and finally with 32 output neurons as output. Even a small angle variation in doom, the larger the difference in the light throw, so the number of neurons in the hidden layers increased to 135. The output is in the predefined coding to control the doom angle in three axes with four motors activation. The back-propagation network had been adopted for training the ANN with the step size of 0.01 and learning speed of 0.25. A fixed threshold of 0.01 has been used to stop the procedure if the error is below it. Equations 3 and 4 are used to update the network weight and threshold values [23].

$$\Delta W_{ij} = \beta * D_j * O_i \tag{3}$$

whereas

$$\begin{aligned} D_j &= (D_{op} - O_i) * (1 - O_i) * O_i \\ W_{ij} &= W_{ij} + \Delta W_{ij} \\ \Delta T_i &= D_j * T_j \end{aligned} \tag{4}$$

The output is in the pre-defined format of 32 digits, and each eight-digit represents the movement of the four different motors for forward, backward, upward, and downward, respectively. The sample input is of the format as shown below.

00000000100000000010000100110000

The first four digits denote 0°, and the next four digits represent zero step angle for the forward motor. A total of 9–12th digits denote 8° movement for the backward motor and with zero step angle denoted by 13–16th digits. A total of 17–20th digits

Table 1 Sample weight for training

Before training	After training
0.628111239; 0.882353887; 0.546025434; 0.405960441; 0.00329928; 0.19896787; 0.723132279; 0.390514195; 0.932794101; 0.08139515; 0.76352662; 0.517657204; 0.06095037; 0.976935686; 0.967969577; 0.113708026; 0.810559431; 0.385500752; 0.032610272; 0.176036632; 0.957355018; 0.206441133; 0.5294077; 0.859103821; 0.56545771; 0.947923357; 0.029644406; 0.615979568; 0.384897227; 0.498480959; 0.778166955; 0.383212612; 0.455124515; 0.056785464; 0.571900903; 0.141739218; 0.394884394; 0.30808898; 0.583501845; 0.426964702; 0.741165408; 0.419610668; 0.882419896; 0.712943125; 0.653096491; 0.892074965; 0.028644673; 0.429733037; 0.864221652; 0.00841715; 0.818498548; 0.363896144; 0.287151386; 0.210469645; 0.251625803; 0.875689297; 0.782738285; 0.635571692; 0.266417323; 0.290005105; 0.362406098; 0.857968244; 0.69171705; 0.538029395; 0.715932918; 0.895588335; 0.708024343; 0.247315824; 0.403986741; 0.274683062; 0.02370676; 0.760819492; 0.943271824; 0.674407548; 0.467988302; 0.865236058; 0.298261826; 0.262681679; 0.712639561; 0.725861179; 0.854292716; 0.296133819; 0.700951231; 0.355871423; 0.795312789; 0.186223181; 0.292114902; 0.631544329; 0.901921685; 0.35200597; 0.367360493; 0.586576604; 0.741140533; 0.422797156; 0.250962026; 0.603032822; 0.840664843; 0.309960388; 0.838892789	0.659094976; 0.942337979; 0.021090339; 0.992534346; 0.81415626; 0.320838909; 0.342771927; 0.728743822; 0.3391888; 0.856240966; 0.154283158; 0.372093126; 0.089627762; 0.660192242; 0.144976858; 0.155182542; 0.440762194; 0.253979897; 0.810744308; 0.164864451; 0.466783572; 0.720323246; 0.620140067; 0.074206371; 0.718847161; 0.426103035; 0.106178316; 0.706721548; 0.872127193; 0.372834618; 0.206466123; 0.796914085; 0.502883559; 0.042185689; 0.621989887; 0.629818744; 0.961184528; 0.898018383; 0.201078696; 0.647265567; 0.334673962; 0.704188606; 0.012211072; 0.054958927; 0.795580185; 0.847022895; 0.755075839; 0.179145993; 0.432301265; 0.672844941; 0.796489354; 0.529268068; 0.359906948; 0.505378517; 0.913611147; 0.913234274; 0.593068392; 0.014879899; 0.766485843; 0.074975722; 0.974190825; 0.524696967; 0.005282176; 0.356520223; 0.001546428; 0.252264865; 0.217100209; 0.588659704; 0.043317103; 0.935137719; 0.568807749; 0.108058467; 0.599187047; 0.467418732; 0.331071773; 0.858209255; 0.370168732; 0.998524484; 0.689292079; 0.388541927; 0.533675606; 0.197015201; 0.992103802; 0.771294909; 0.977400278; 0.258201854; 0.206313322; 0.63699658; 0.53576357; 0.709077376; 0.774363266; 0.531480672; 0.582392332; 0.174520381; 0.077457551; 0.547004108; 0.166279032; 0.450640709; 0.756992633; 0.955358053; 0.84806404; 0.39882287



Fig. 3 Headlamp doom and actuator

denote 2° movement of one step angle denoted by 21–24th for the upward motor. A total of 25–28th digits denote 3° and zero step angle denoted by 29th–32nd digit for the downward motor. The sample weight table before and after training is given in Table 1. The combined movements of all these motors give the three-axis movement of the doom. The rectangular/circular reflector plate of the headlamps is connected with four geared motor on four sides to actuate left, right, upward, and downward motion. The 12-V DC geared motors are controlled by means of PIC 40 pin controller with a relay and driver interface unit to get the desired motion even though all the motors actuated simultaneously. The PIC controller is coded in embedded C programming. Geared DC motors have been used to get high torque with very low speed. The headlamp motor gives translation motion as the output, instead of rotary motion using inbuilt rack arrangements.

The headlamp doom and the actuator are shown in Fig. 3. The entire intelligent and the mechatronics system coding have been done such a way that the developed system will not override the driver control, and the module can be switched off and on as desired. Also, the system is developed to fit into the vehicles without any modifications, so the dashboard control has not been included in decision making.

5 Experimental Implementation

The implementations include six different cases and are explained as follows.

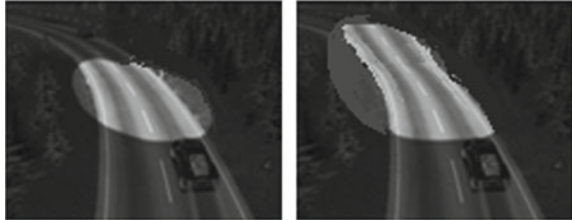
Case a: Vertical Swiveling Mechanism. Automatic low- and high-beam shifting based on the approaching vehicles are controlled by means of the vertical swelling mechanism of the headlamp reflector plate. The bumper of the vehicle has been fitted with four light sensors. In normal situations, the headlight focusing is based on the driver control and when the approaching vehicles head beam falls on the light sensor, it generates emf, and the generated emf is given as input to the controller, if the generated emf is more than 0.5 V, then only the controller sends signal to ANN. Therefore, the headlamp doom moves downward proportional to the voltage level and behaves like a dimmer lamp with the same high-beam light distribution. Thus, it avoids the glare to the approaching vehicles and avoids the accidents due to light glaring. The limitation is that the sensors emit high voltage of 0.8–1 V during daytime and in city roads having bright light. But the limitation has not affected the safety. The comparison of the high beam and low beam for 8° inclination is shown in Fig. 4.

Case b: Dynamic Curve Light. High-end automobiles are having dynamic curve light technology, which is costlier. In this research, the rotary potentiometer is attached to the steering rod, and the steering angle is given as input to the PIC controller and to ANN. In turn, right and left motors are actuated proportionally. So that for the slightly curvy and deep curvy roads the headlight reflector plate turns to a degree and maximum of 4° , respectively. On the other hand, if the steering angle is high and the indicator is switched on, the reflector plate can deflect to 8° . In this research, to reduce the cost and complexity of the system, instead of measuring the velocity

Fig. 4 Low-beam and high-beam projection



Fig. 5 Dynamic curve light



of yaw, the indicator lamp control signal has been used. Therewith, the visibility range can be increased up to 70% compared with conventional lighting systems. The comparison of the light beam before and after implementation is shown in Fig. 5.

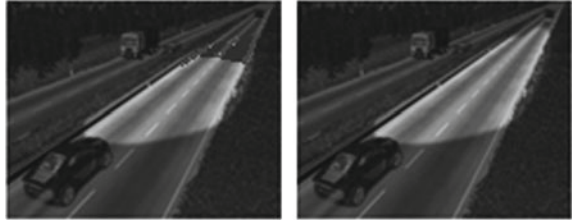
Case c: Cornering Light for Turning. As it became very essential to illuminate the light on the turning corners, in this research, with the actuation of the turn indicator and the speed of the vehicle is less than 20 kmph, the controller activates the left or right motor based on the turn signal indicator activation direction. The driving lane and the verge are becoming obviously better illuminated. Instead of having separate cornering light is integrated either directly in the headlamp or also in the bumper outside of the headlamp, the reflector plates only turned. With the activation of the cornering light for 2° – 8° , the verge is illuminated from 30° to 60° . The comparison of projection of light beam before and after illumination is shown in Fig. 6.

Case d: Cornering Light without tuning. In the signals and in junctions, especially during nighttime, the drivers should know the approaching vehicles in all the directions. So in this research, if the driver turns on both the turn signals, i.e., both the left and right signal, the controller actuates the left and right motors to a maximum of

Fig. 6 Cornering beam projection



Fig. 7 Motorway beam projection



0° – 8° and to 0° in sequence. Therefore, the light projected to 60° on either side of the vehicle and helps the driver to predict the approaching vehicles on all the sides of the junction. Also, this mechanism became an indicator for the approaching vehicles by throwing the light all around. Also, the driving lane obviously better illuminated.

Case e: Motorway light Intensity. The driving velocity of an automobile is above 60 km/h and continuous for more than a minute, and the motorway light intensity module has been activated. The module is having two modes. In the former mode, the controller actuates the reflector plate top motor and moves the doom to 2° – 4° upward proportional to 60–120 kmph above the high-beam angle, which helps to throw the light for a longer distance. When the light throws for a longer distance, its intensity reduces, and to compensate, in the later mode, the controller increases the voltage supplied to the headlight proportional to the speed of the vehicle. As the voltage increases, the intensity of the light increases and illuminates the road for a longer distance. The comparison of the light projection is shown in Fig. 7. With increasing speed, the power of the xenon lamp is raised the illumination range from 3 m up to 5 m.

Case f: Adaptive Weather Light. Adaptive weather light is used to support the driver during the adverse weather conditions due to mist, fog, rain, etc. This module will get actuated, once the driver switches ON either the yellow light or the wiper. With the actuation, in this research, the controller actuates the sequence of operations and is as follows: It actuates the yellow light lamp, activates the downward doom motor, distributes the high-beam bright light, and increases the voltage supplied to the headlight. Thus, the bright illumination from the headlight lightens the nearby road conditions to the driver. Also, the controller supplies the voltage to the yellow light which is inversely proportional to the voltage supplied to the wiper and on the other hand, if it is in ON state. If the wiper is in OFF state, the voltage supplied is proportional to the speed of the vehicle. Thus, the yellow light can penetrate in the rainy and foggy environment and illuminate to the driver for easy prediction of the road conditions. This also avoids the glare for the approaching vehicles, but with brighter illumination. The condition is shown in Fig. 8.

Different kinds of experimentations were performed with various test cases by actuating various sensors and conformed to the accuracy, its response time, and the system impact for various test cases in the laboratory for both the rectangular and

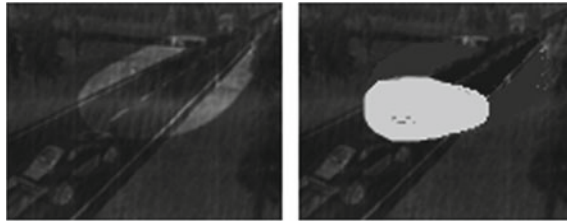


Fig. 8 Weather beam projection

Table 2 Experimental results

Case	Sensor	Volt (0–1)	Motor	Angle (1°–8°)
a	Light sensors	<0.5 V	Downward motor	–
		>0.5 V		1°
		>0.8 V		2°
		=1 V		4°
b	Rotary POT	<0.3 V	Right/left motor	–
		>0.6 R/L volt		2°
		>0.9 R/L volt		4°
		>0.9, Ind = High		8°
c	Tachogenerator	<0.2 V, Ind = High (R/L)	Right/left motor	2° ++/3 s
d	–	Ind = High-R&L	Right/left motor	1° ++/1 s, –/1 s
e	Tachogenerator	>0.6 V, timer >60	Upward motor	2°, HLV ++
		>0.7 V, timer >60		3°, HLV ++
		>0.8 V, timer >60		4°, HLV ++
f	–	Wiper/yellow = high	Downward motor	4°, HLV ++
g	Ultrasonic sensor	Any object within 3 meters	Up/downward motor	Alternate actuation

circular dooms. The performance of the ANN has also been found satisfactory, and the data table constructed for the implementation is given in Table 2 for the circular doom.

6 Conclusions

With the increased number of vehicles on roads and increasing accident rates, an adaptive expert swiveling mechanism for headlight has become an essential feature in all the automobiles. In this research, the developed module is of very low cost, and all the controls are with the reflector plates and voltage level, so it can be implemented

in all the vehicles with minor modifications, i.e., rotating the doom is independent of the type, orientation, size, and shape of the headlight. Thus the developed intelligent lighting system optimizes sifting of low and high beam, dynamic light distribution at turnings, corner lighting at junctions with and without turning of vehicles, high speed lighting and adaptive lighting. Thus, from the system, the accident rates during nights will be minimized as the lighting explores the surrounding road conditions clearly to the drivers and supports in decision making.

References

1. Alcantarilla PF (2011) Automatic light beam controller for driver assistance. *Mach Vis Appl* 22(5):819–835
2. Tripathy AK, Kayande D, George J, John J, Jose B (2015) Wi Lights—a wireless solution to control headlight intensity. In: IEEE international conference on technologies for sustainable development (ICTSD-2015), 04–06 Feb 2015, Mumbai, India
3. Chen YL, Chiang CY (2010) Embedded vision-based nighttime driver assistance system. In: 2010 international symposium on computer communication control and automation (3CA), vol 2. IEEE, pp 199–203
4. Juric D, Loncaric S, A method for on-road night-time vehicle headlight detection and tracking. In: 2014 international conference on IEEE connected vehicles and expo (ICCVE), Vienna, 3–7 Nov 2014, pp 655–660
5. Luo F, Hu F (2014) A comprehensive survey of vision based vehicle intelligent front light system. *Int J Smart Sens Intell Syst* 7(2):701–723
6. Fossati A, Schonmann P, Fua P (2011) Real-time vehicle tracking for driving assistance. *Mach Vis Appl* 22(2):439–448
7. Li Y, Haas N, Pankanti S (2011) Intelligent headlight control using learning-based approaches. In: 2011 IEEE on intelligent vehicles symposium (IV). IEEE, pp 722–727
8. Lopez A, Hilgenstock J, Busse A, Baldrich R, Lumbreras F, Serrat J (2008) Nighttime vehicle detection for intelligent headlight control. In: Advanced concepts for intelligent vision systems. Springer, pp 113–124
9. Alsumady M, Alboon SA (2013) Intelligent automatic high beam light controller. *J Act Passiv Electron Dev* 1–8 (Old City Publishing, Inc.)
10. New Headlight Sensors Make Night Driving Safer, Road and travel magazine. [Online]. Available: <http://www.roadandtravel.com/autoadvice/2007/highbeams.html>
11. O'Malley R, Jones E, Glavin M (2010) Rear-lamp vehicle detection and tracking in low-exposure color video for night conditions. *IEEE Trans Intell Transp Syst* 11(2):453–462
12. Eum S, Jung HG (2013) Enhancing light blob detection for intelligent headlight control using lane detection. *IEEE Trans Intell Transp Syst* 14(2):1003–1011
13. Zhang W, Wu QMJ, Wang G, You (2012) Tracking and pairing vehicle headlight in night scenes. *IEEE Trans Intell Transp Syst* 13(1):140–153
14. Multibeam LED brings light into the darkness [Online]. Available: <https://www.mercedes-benz.com/en/mercedes-benz/innovation/multibeam-led-brings-light-into-the-darkness/>
15. Lighting Assist—SmartBeam® [Online]. Available: <https://www.gentex.com/automotive/products/forward-driving-assist>
16. Mobileye Binary Headlamp Control [Online]. Available: <http://www.mobileye.com/technology/applications/head-lamp-control/binary-headlamp-control/>
17. Chen D-Y, Lin Y-H, Peng Y-J (2012) Nighttime brake-light detection by nakagami imaging. *IEEE Trans Intell Transp Syst* 13(4):1627–1637
18. Ahonen T, Hadid A, Pietikainen M (2004) Face recognition with local binary patterns. In *Proc Eur Conf Comput Vis* 469–481

19. Dalal N, Triggs B (2005) Histograms of oriented gradients for human detection. In Proc IEEE Conf Comput Vis Pattern Recogn 1(12):886–893
20. Kuang H, Chong Y, Li Q, Zhenge C (2014) MutualCascade method for pedestrian detection. Neurocomputing 137:127–135
21. Dollar P, Zitnick CL (2015) Fast edge detection using structured forests. IEEE Trans Pattern Anal Mach Intell 37(1):1–1
22. Rajesh Kanna SK, Manigandan S (2012) Intelligent vision inspection system for IC engine head: an ANN approach. J Adv Mater Res 479(12):2242–2245
23. Rajesh Kanna SK, Vignesh S, Sivashankar P, Vishwanath (2017) Intelligent handbraking system using artificial neural network. Int J Emerg Technol Adv Eng 7(9):734–739
24. Vignesh, Rajesh Kanna SK, Lingaraj N (2017) Intelligent automated guided vehicle using visual servoing. Am J Eng Res 6(11):16–20

Modeling and Validation of Ride Characteristics of All-Terrain Vehicle (ATV)



Mallikarjuna Reddy, Sanyam Kakkar, Prabhu Pal Singh
and Uma Shankar Lath

Abstract The performance of the vehicle is defined by considering the criteria of ride comfort. Mathematical models are proposed for studying the ride comfort of the car. In this study, the quarter-car model and half-car model are developed for all-terrain vehicle (ATV), and the sinusoidal excitation is taken as most of the bumps on the off-road are in the form of sinusoidal function, and therefore, results are discussed. Data were filtered using a Butterworth filter, and power spectrum analysis was done in MATLAB. Subsequently, the transmissibility ratio versus frequency graph was plotted, and the trend was compared with the theoretically obtained curves to validate the model. Further, composite weighted level, maximum transient vibration, and fourth power vibration dose were calculated using the weighting factor defined in ISO 2631-4: 2001.

Keywords Ride comfort · All-terrain vehicle (ATV) · MATLAB

1 Introduction

To understand the ride characteristics of a vehicle, models such as quarter-car model, half-car model with two degrees of freedom as well as four degrees of freedom were prepared by the various authors in their respective research work [1–4]. The aim of these studies was to study transmissibility of the suspension [5] and ride comfort characteristics of passenger cars. Much later with the introduction of MATLAB, mathematical modeling was done using Simulink [6] to create the respective mathematical model and obtain the results. In the present work, sprung mass RMS acceleration was calculated using Simulink, this value must be within range as specified in ISO2631 [7], and similar work was performed by Pawar et al. in their work [8]. Also, the results were obtained by varying the various parameters of suspension like shock stiffness, damping coefficient, sprung mass, and unsprung mass. The mathematical

M. Reddy (✉) · S. Kakkar · P. P. Singh · U. S. Lath
School of Mechanical Engineering, VIT University, Vellore 632014, India
e-mail: dmreddy@vit.ac.in

© Springer Nature Singapore Pte Ltd. 2019
S. S. Hiremath et al. (eds.), *Advances in Manufacturing Technology*,
Lecture Notes in Mechanical Engineering,
https://doi.org/10.1007/978-981-13-6374-0_60

547

model was modeled in order to study the riding behavior of passive and active suspension using half-car model in [9]. The aim of modeling the vehicle is to enhance the ride characteristics and assist in the design for the comfortable ride. Generally, to improve the ride comfort of the car, the parameters like sprung mass, unsprung mass, the stiffness of shock, and the damping ratio of shocks are adjusted in order to get optimum ride comfort, but also more emphasis was put on the suspension geometry of the car [10, 11]. The contribution analysis of the seat and suspension system in the ride comfort was investigated [12, 13] in order to get the optimum combination and reduce the seat transmissibility. Studies like [14] were also done on mini ATVs cars, where accelerometers were bonded before and after the rear suspension to measure the transmissibility characteristics. In this work, theoretical model was validated using a simple data acquisition system. Measured data were filtered using a Butterworth filter, and power spectrum analysis was done in MATLAB. Subsequently, the transmissibility ratio versus frequency graph is plotted, and the trend was compared with the theoretically obtained curves to validate the model.

2 Vehicle Ride Modeling

The purpose of a vehicle suspension is to eliminate or reduce the road disturbances transmitted to the driver and the passengers. To ensure the ride comfort, soft spring and damper setup are desirable. The simple measure for ride comfort is the vertical RMS acceleration of the chassis. So to measure the vertical RMS acceleration, again quarter-car model is studied, and graphs for RMS acceleration versus cutoff frequency are plotted. The data required for ATV are given in Table 1.

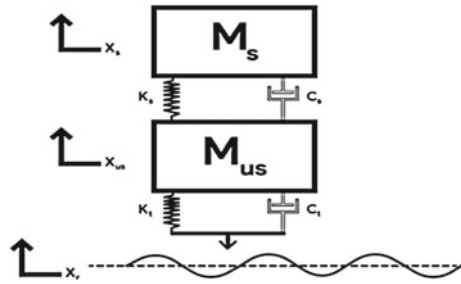
2.1 Quarter-Car Model

Quarter-car model has two degrees of freedom as shown in Fig. 1. First is the translational motion of sprung mass (m_s), and second is the translational motion of unsprung mass (M_{us}). The sprung mass (M_s) and unsprung mass (M_{us}) are interconnected by suspension spring having a stiffness (K_s) and a damper having a damping coeffi-

Table 1 Data taken for ATV are as follows

Parameter	Value
Sprung mass	11.2 kg
Unsprung mass	13.8 kg
Shock stiffness	26,000 N/m
Tire stiffness	208,000 N/m
Sprung mass	11.2 kg

Fig. 1 Quarter-car model with sinusoidal excitation



cient (C_S). The unsprung mass mainly consists of the wheel assembly. The stiffness of tire is also considered as it is not the completely rigid body, but its damping is neglected for the sake of simplicity. This stiffness of tire is taken as (K_t). To study the response of disturbance that comes from the road, displacement of sprung mass (X_s) and unsprung mass (X_{us}) is considered. The disturbance coming from the road is taken as (X_r).

$$M\ddot{x} + C\dot{x} + kx = Fxr \tag{1}$$

where

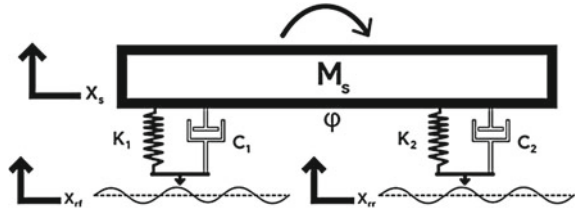
$M = \begin{bmatrix} M_s & 0 \\ 0 & M_{us} \end{bmatrix}$, $C = \begin{bmatrix} C_s & -C_s \\ C_s & C_s \end{bmatrix}$, and $K = \begin{bmatrix} K_s & K_s \\ -K_s & K_s + K_t \end{bmatrix}$ are the mass, damping, and stiffness matrix, respectively, $F = \begin{bmatrix} 0 \\ K_t \end{bmatrix}$ is the forcing matrix, and $x = \begin{bmatrix} X_s \\ X_{us} \end{bmatrix}$ is the displacement vector.

To understand the vibrational characteristics of the vehicle, Newton’s equation of motion is taken for each sprung and unsprung mass. After solving equations, the natural frequencies and amplitude ratios are determined by considering principal modes of the system.

2.2 Half-Car Model

In half-car model of a vehicle, vertical motion of combined front and rear half-car as well as pitching motion is considered. Half-car model has two degrees of freedom. Useful information about the half-car model is shown in Fig. 2. Equations are formulated using Newton’s second law and static equilibrium origin in which (M_S) is taken as combined mass for both front and rear half-car. (K_1) is taken as the stiffness of front shock absorber and (C_1) as damping coefficient of the respective shock absorber. In the same method (K_2) is taken as rear shock stiffness, and (C_2) is damping coefficient of the respective shock absorber. The vertical displacement

Fig. 2 Half-car model with sinusoidal excitation



of the chassis is taken as (X_s), and the pitching motion which is denoted in angle is taken as (φ). The distance of the center of gravity from front axle is denoted as (l_1), and similarly, distance of the center of gravity from rear axle is denoted as (l_2). These distances and (l_1) and (l_2) are used to get moment arm for the moment equation which governs pitching motion of the car. Moment of inertia is denoted as (J). The excitation input is given individually for both the half-cars. The front excitation is taken as (X_{rf}), and excitation is taken as (X_{rr}).

$$M\ddot{x} + C\dot{x} + kx = F_1u_1 + F_2U_2 \tag{2}$$

where

$$M = \begin{bmatrix} M_s & 0 \\ 0 & J \end{bmatrix}, C = \begin{bmatrix} C_1 + C_2 & C_2l_2 - C_1l_1 \\ C_2l_2 - C_1l_1 & C_1l_1^2 + C_2l_2^2 \end{bmatrix}, \text{ and}$$

$$K = \begin{bmatrix} K_1 + K_2 & K_2l_2 - K_1l_1 \\ K_2l_2 - K_1l_1 & K_1l_1^2 + K_2l_2^2 \end{bmatrix} \text{ are mass, damping, and stiffness matrix}$$

$$F_1 = \begin{bmatrix} C_1 & C_2 \\ -C_1l_1 & C_2l_2 \end{bmatrix} \text{ and } F_2 = \begin{bmatrix} K_1 & K_2 \\ -K_1l_1 & K_2l_2 \end{bmatrix} \text{ are the force matrix.}$$

$$u_1 = \begin{bmatrix} \dot{X}_{rf} \\ \dot{X}_{rr} \end{bmatrix} \text{ and } u_2 = \begin{bmatrix} X_{rf} \\ X_{rr} \end{bmatrix} \text{ are road displacements}$$

$$x = \begin{bmatrix} X_s \\ \varphi \end{bmatrix} \text{ is the displacement vector.}$$

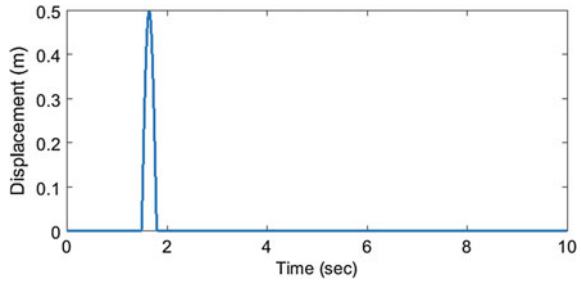
Using these equations in Simulink, the displacement and sprung mass acceleration can be calculated.

3 Ride Comfort

To know the ride comfort of the vehicle, vertical RMS acceleration is calculated.

The value of vertical acceleration gives us the measure of the ride comfort. Higher the vertical acceleration, lower will be the ride comfort. Again vertical RMS acceleration can be calculated for both random excitations as well as sine wave excitation. The excitation here is taken as half-sinusoidal function as shown in Fig. 3. The time delay between the front and rear wheel is taken as 2 s. The velocity with which the

Fig. 3 Road excitation graph for sinusoidal type



car to be moved is taken as 10 m/s. The distance before the bump starts is taken as 15 m. The height of the bump is taken as 0.5 m, and length of the bump is 3 m.

4 Results and Discussion

Simulation results of the quarter-car model are shown in Figs. 1 and 2. Frequency response functions of transmissibility and suspension travel are presented. The ratio of unsprung mass to sprung mass, damping ratio, and the ratio of tire stiffness to suspension stiffness are considered as design parameters. From Fig. 4, at the low excitation frequency, it can be observed that transmissibility is almost independent of unsprung-mass-to-sprung-mass ratio.

For excitation frequency lower than the natural frequency of sprung mass the transmissibility is lower, and on the other hand, at higher excitation frequency, the transmissibility lowers at a much high rate and also dependent on the mass ratio. From Fig. 5, it can be observed that at lower excitation frequency, the transmissibility is independent of damping ratio, once the excitation frequency reaches the sprung mass natural frequency, higher damping ratio lowers the transmissibility, and once the excitation frequency reaches the unsprung mass natural frequency, the transmissibility is the same for all the damping ratios. Beyond this frequency, the transmissibility lowers with frequency.

Fig. 4 Transmissibility versus frequency graph for the quarter-car model showing variation with change in mass ratio

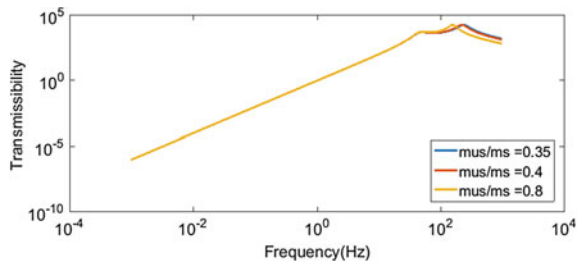


Fig. 5 Transmissibility versus frequency graph for the quarter-car model showing variation with change in damping ratio

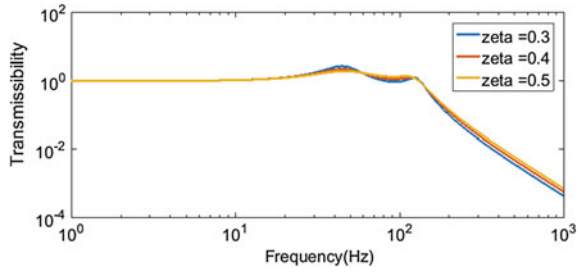


Fig. 6 Transmissibility versus frequency graph for the quarter-car model showing variation with change in stiffness ratio

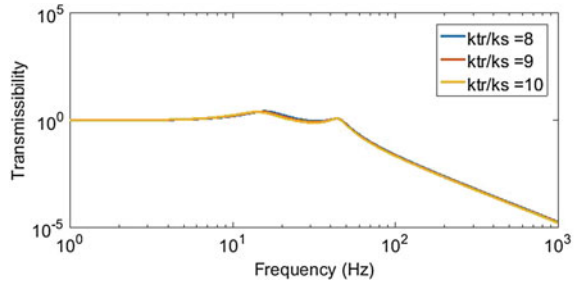
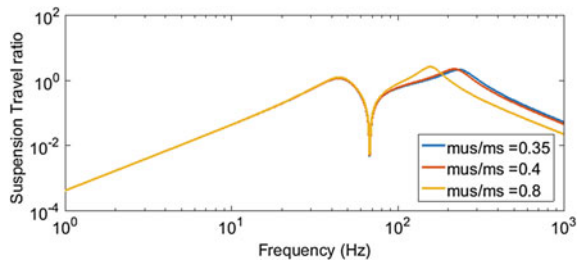


Fig. 7 Suspension travel versus frequency graph for the quarter-car model showing variation with change in mass ratio



From Fig. 6, it can be observed at low excitation frequencies, the transmissibility varies with different stiffness ratios, but as the excitation frequencies increase, the transmissibility is the same for all the stiffness ratios, also it can be seen at the higher excitation frequencies the transmissibility lowers. For frequency higher than sprung mass frequency, a higher stiffness ratio gives lower transmissibility.

From Fig. 7, it shows that at lower excitation frequencies, suspension travel is independent of frequencies. Also for the frequency between sprung mass and unsprung mass natural frequency the higher the ratio, higher is the suspension travel. And on further increasing the excitation frequency, the suspension travel lowers down.

From Fig. 8, it can be observed that suspension travel is lower for excitation frequencies less than sprung mass natural frequency, and as the excitation frequency goes above than the sprung mass natural frequency, the suspension travel becomes higher for lower stiffness ratio.

From Fig. 9, simple conclusion that can be drawn from this graph is we get low suspension travel for high values of damping ratio whether it is low or high excitation

Fig. 8 Suspension travel versus frequency graph for the quarter-car model showing variation with change in stiffness ratio

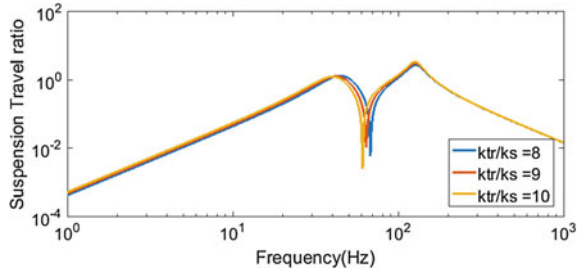
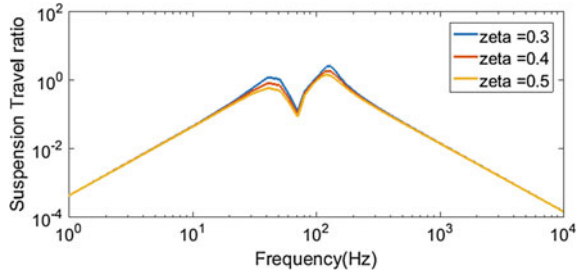


Fig. 9 Suspension travel versus frequency graph for the quarter-car model showing variation with change in damping ratio



frequency. A conclusion is a certain range of damping coefficient and stiffness of the shocks within which it should be operated in order to sustain good road holding characteristics. The other event is endurance. Endurance racing is done to determine how well the components of the buggy and participant can hold up for long hours. To get the RMS acceleration, data values for random vibration are taken from Theory of Ground Vehicles.

The graph of power spectral density which was taken is shown in Fig. 10. From Fig. 10, it characterizes the surface profile of the rough runway. It shows the spectral density as a function of spatial frequency of the path. Every path has a certain set of frequencies, and accordingly, the function of spectral density is determined. The above graph shows the same for the rough runway. The calculation is done for the RMS acceleration for quarter-car model taking random vibration. The result for which can be seen in Fig. 11, when speed was taken 12.5 m/s. It denotes the RMS acceleration for the vehicle which is exposed to set off the frequencies corresponding to the spectral density function.

5 Validation

A simple data acquisition system was used to validate the theoretical results obtained during the research work. An accelerometer was rigidly mounted on the upright using double-sided tape to accurately measure the acceleration reading of unsprung mass while for the sprung mass another accelerometer was mounted using a screw to the

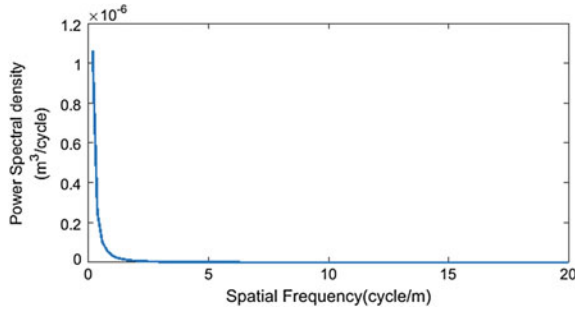


Fig. 10 Power spectral density versus spatial frequency for the rough runway (track for the off-road vehicles)

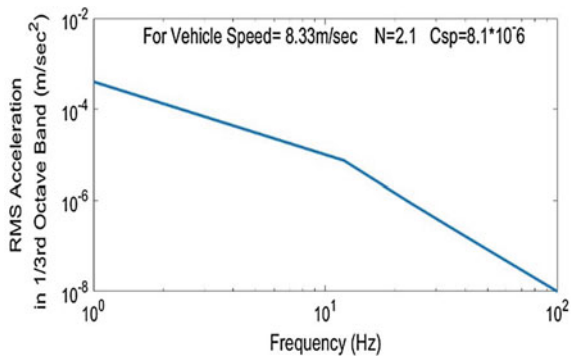


Fig. 11 RMS acceleration versus frequency for the quarter-car model

chassis as shown in Fig. 12. It must be ensured that the accelerometers are rigidly mounted on a flat surface with their axes correctly aligned with axes of the car. Both the accelerometers were connected with the analog input of Arduino Uno. To measure vibration phenomenon the data should be logged at a frequency of around 500 Hz with due technical problem and time constraint during the research work, the sampling rate of 100 Hz was achieved.

Testing was done on a straight track with a single sinusoidal bump in the middle of the track having a height approximately equal to the theoretical input signal used in a simulation, and actual weight of the sprung and unsprung mass of the vehicle was found to be 11.2 and 13.8 kg, respectively. Once the data is logged the post-processing phase starts with fast Fourier analysis of data. Figure 13a shows the power spectral density of accelerometer data mounted on the upright plotted using MATLAB. Power spectral density of both the accelerometer data was calculated using MATLAB, using that result transmissibility ratio was calculated. The relationship between sprung mass frequency and transmissibility is shown in Fig. 13. Throughout the frequency range, the value of transmissibility was observed approximately equal to 1 with an expected peak of 2.8 at a frequency 43.5 Hz. The actual curve closely

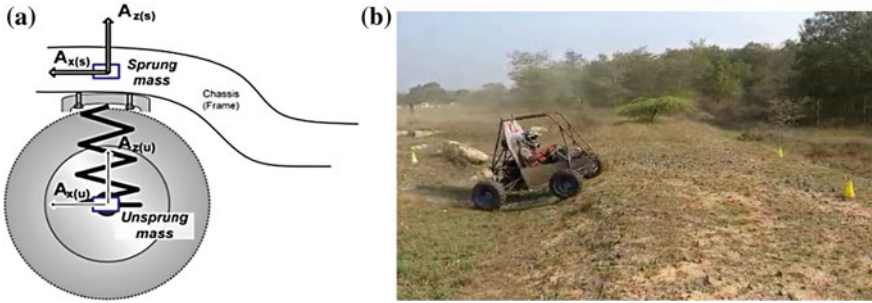


Fig. 12 a Schematic showing accelerometer mounting position [15]. b Testing of ATV on the track

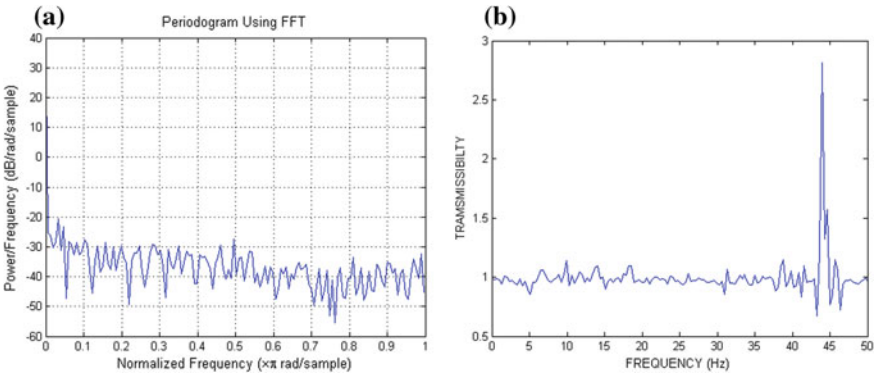


Fig. 13 a Power spectral density of accelerometer data. b Transmissibility versus frequency plot obtained from sensor data

follows the theoretical trends as shown in Fig. 13b. Uneven damping performance by damper due to fatigue, compliance in the suspension system, random error in measurement, and external noise in data can be the reason behind slight deviation of actual transmissibility ratio value from the expected value.

6 Conclusion

MATLAB codes made to perform a succession of band-pass filtering operations for consecutive, non-overlapping bands on sprung mass accelerometer data. Composite weighted level, maximum transient vibration, and fourth power vibration dose were found to be 4.697 m/s^2 , 4.697 m/s^2 , and 6.948 m/s^2 , respectively. As the ratio of maximum transient vibration and composite weighted level is less than 1.5, so according to ISO2631, the value found is well under the accepted norms defined. And therefore, it was concluded that the ride comfort for the theoretically optimized damper setting and mass configuration will give a satisfactory ride in real life also.

Also, the power spectral density shows the resemblance with the trainability and having a peak in between the 10 and 100 Hz with the transmissibility value of 2.5 approximately which validates our theoretical assumption of the damping coefficient of zeta 0.3. Subsequently, the transmissibility ratio versus frequency graph was plotted, and the trend was compared with the theoretically obtained curves to validate with the model.

References

1. Talukdar S, Mazumdar A, Mullasseril M, Kalita K, Ujjwal A (2012) Mathematical modeling in vehicle ride dynamics. No. 2012-01-0056. SAE Technical Paper
2. Kulkarni A, Ranjha S, Kapoor A (2017) A quarter-car suspension model for dynamic evaluations of an in-wheel electric vehicle. Proc Inst Mech Eng Part D: J Automob Eng 0954407017727165
3. Prabakar RS, Sujatha C, Narayanan S (2016) Response of a half-car model with optimal magnetorheological damper parameters. J Vib Control 22(3):784–798
4. Faheem A, Alam F, Thomas V (2006) The suspension dynamic analysis for a quarter car model and half car model. In: 3rd BSME-ASME international conference on thermal engineering, pp 20–22
5. Wong JY (2008) Theory of ground vehicles. Wiley, New York. ISBN: 978-0-470-17038-0
6. Phalke Trupti P, Mitra Anirban C (2017) Analysis of ride comfort and road holding of quarter car model by Simulink. Mater Today: Proc 4(2):2425–2430
7. Kropac Oldrich, Mucka Peter (2008) Indicators of longitudinal unevenness of roads in the USA. Int J Veh Des 46(4):393–415
8. Pawar PR, Saraf MR (2007) Ride comfort evaluation of different three-wheelers based on the probability density distribution. No. 2007-26-073. SAE Technical Paper
9. Soliman AMA, Moustafa SM, Shogae AOM (2008) Parameters affecting vehicle ride comfort using half vehicle model. No. 2008-01-1146. SAE Technical Paper
10. Boggs C, Ahmadian M, Southward S (2008) Application of system identification for efficient suspension tuning in high-performance vehicles: quarter-car study. SAE Int J Passeng Cars-Mech Syst 1(2008-01-2962):1298–1310
11. Kim M-G (2011) Transfer function analysis of rear multi-link suspension to improve ride vibration and road noise. No. 2011-01-1571. SAE Technical Paper
12. Kim BS, Joo KJ, Bae KI (2011) Ride comfort improvement of a compact SUV considering driving maneuver and road surface. No. 2011-01-0558. SAE Technical Paper
13. Wu X, Rakheja S, Boileau P-É (1999) Dynamic performance of suspension seats under vehicular vibration and shock excitations. No. 1999-01-1304. SAE Technical Paper
14. Pacheco PMCL, Kenedi PP, Vieira RD, Jorge JCF, Danninger W (2002) Analysis of the transmissibility of the rear suspension of a Mini-Baja vehicle. No. 2002-01-3506. SAE Technical Paper
15. Shokrollahi S et al (2017) An investigation into the accelerometer mounting effects on signal transmissibility in modal measurements. Sci Iran 24:2436–2444

Influence of Tool Rotation Speed on Soundness of Water-Cooled Friction Stir Welded Armour Grade Al–Cu Joint



S. Sree Sabari, J. S. Binoj, Felix Xavier Muthu, S. Malarvizhi and V. Balasubramanian

Abstract Need of AA2519-T87 aluminium alloy in the military application leads to explore the possibility of efficient joining technique. The fusion weldability of Al–Cu alloy is poor because of the formation of residual stress, distortion, and solidification defects. The solid-state welding process, friction stir welding (FSW), can be remedy for the above-said shortcomings which does not have melting and solidification of material. However, the elevated temperature experienced in the thermo-mechanical heat affected zone (TMAZ) and heat-affected zone (HAZ) will coarsen and dissolve Al_2Cu precipitates. The undesired precipitate transformation can be controlled by adopting the in-process water-cooling technique. The material flow behaviour and joint characteristics for the water cooling are different from conventional FSW. To explore the usefulness of water-cooling technique, the joining mechanism and resultant joint characteristics have to be studied. Hence, an attempt is made to investigate the influence of predominant process parameter, tool rotational speed (TRS) on microstructure features and joint soundness. This investigation reports that joint fabricated using lower TRS of 1200 rpm is sound due to the lower extent of Al_2Cu precipitate coarsening and narrowing of weaker TMAZ and HAZ regions.

Keywords Friction stir welding · Water cooling · Tool rotation speed · Precipitation · Joint strength

S. Sree Sabari (✉) · J. S. Binoj
Department of Mechanical Engineering, Micromachining Research Centre, Sree Vidyanikethan Engineering College (Autonomous), Tirupati 517102, India
e-mail: sreesabaridec2006@yahoo.co.in

F. X. Muthu
St. Xavier's Catholic College of Engineering, Nagercoil 629003, India

S. Malarvizhi · V. Balasubramanian
CEMAJOR, Annamalai University, Annamalai Nagar, Chidambaram 608002, India

© Springer Nature Singapore Pte Ltd. 2019
S. S. Hiremath et al. (eds.), *Advances in Manufacturing Technology*,
Lecture Notes in Mechanical Engineering,
https://doi.org/10.1007/978-981-13-6374-0_61

1 Introduction

In recent days, the mobility of the lightweight combat military vehicles is improved by replacing the conventional materials with new materials which have better properties like high ballistic strength and fracture toughness [1]. AA2519 is a new grade aluminium alloy having required properties for military applications [2]. Friction stir welding (FSW) is a solid-state joining technique capable of joining the aluminium material with better joint strength over fusion welding process [3, 4]. The heat generated during FSW does not involve in melting of materials; however, it will modify the microstructural characteristic which deteriorates the joint properties by grain coarsening and precipitate dissolution [5, 6]. The grain coarsening and precipitate dissolution results in lower hardness of the TMAZ and HAZ, and thus, these regions are named as the lower hardness distribution region (LHDR) [7, 8]. By controlling the thermal cycles prevailing during FSW, the grain coarsening, precipitate dissolution, and LHDR widening can be controlled and thereby the hardness and the joint strength can be enhanced. It was reported in the literatures that hardness measured along the LHDR was nearly 50% inferior to the parent metal, and it was reported that the tensile fracture exactly occurred predominantly in the HAZ and TMAZ [9, 10]. Hence, improving the hardness in HAZ and TMAZ is very important to enhance the soundness of the joint.

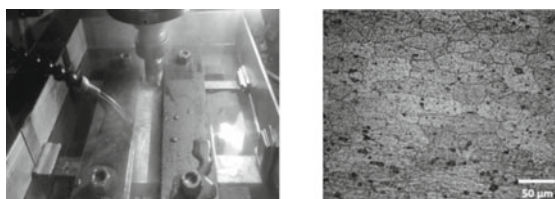
Underwater friction stir welding (UWFSW) is a modification of the FSW process where the welding is done in the submerged water environment instead of open air environment [11]. The high heat transfer capacity of water limits the heat-related problems like grain coarsening and precipitate transformations. Moreover, the thickness of the TMAZ and HAZ can be minimized and thus the joint properties can be improved. The possibility of joining of aluminium materials using water-cooled FSW process with enhanced joint properties than the FSW process was demonstrated in the previous studies [12, 13]. But the relationship between the process parameters on the joint formation and joint soundness was not systematically studied by any of the researchers. The TRS was varied from 1100 to 1500 rpm for joint fabrication, and the variations on stir zone characteristics, microhardness, and tensile properties of the water-cooled FSW joints were studied.

2 Experimental Details

AA2519-T87 armour aluminium alloy of 6-mm-thick rolled plates was used for the fabrication of joints. The parent metal chemical composition and the mechanical properties are listed in Table 1. Figure 1 shows the UWFSW setup which is used to fabricate the joints and the parent metal microstructure. The dimension of the joint is $150 \times 150 \times 6$ mm. The welding was done by varying TRS from 1000 to 1400 rpm. The details of the various process parameters and the welding conditions used for welding are listed in Table 2. Optical microscope was employed to examine the

Table 1 Chemical composition (wt%) of AA 2519 T87 aluminium alloy

Cu	Mg	Mn	Fe	V	Si	Ti	Al
5.71	0.47	0.27	0.1	0.05	0.04	0.02	Balance

Fig. 1 Experimental details**(a)** Photograph of the UWFSW setup**(b)** Optical microstructure of AA2519 Al**Table 2** UWFSW parameters and tool dimensions used in this investigation

Process parameters	Values
TRS (rpm)	1100, 1200, 1300, 1400, 1500
Welding speed (mm/min)	30
Tool shoulder diameter (mm)	18
Pin length (mm)	6
Pin diameter (mm)	6–5
Axial force (kN)	14
Tool tilt angle (°)	2°
Pin profile	Taper threaded cylindrical
Pin thread pitch (mm)	1.5
Tool material	Hardened super high speed steel

microstructural features of the joints. The metallographic specimens were made in accordance with the ASTM E407-09 standard procedures. The samples were polished and etched with the Keller's reagent, in order to reveal the macro- and microstructures. Transverse tensile specimens were prepared and tested as per the ASTM E8M standard guidelines. Scanning electron microscope (SEM) was employed to characterize the tensile fracture samples. Microhardness measurements were acquired along the cross section (3 mm below the top surface). Vickers microhardness tester was employed, and the measurements were made by indenting with a load of 0.05 N for the dwell period of 15 s.

3 Results

3.1 Macrographs

Figure 2 shows the top view of the joints made using varying TRS. Defect-free top surface is observed in all the joints. The weld surfaces are smooth and exhibited equally spaced ripples in all the joints. Table 3 shows the macrostructural features of the joints made using various TRS. Of the five joints, defects are observed in the joints made using TRS of 1110 and 1500 rpm. The stir zones observed in the joints made using TRS of 1200, 1300, and 1400 rpm are free from defects. The stir zone is classified into shoulder-influenced region (SIR), mid-thickness region (MIR), and pin-influenced region (PIR). The defect is observed in the SIR of the joint welded using TRS of 1100 rpm, and the defect is also observed in the PIR of the joint welded using TRS of 1500 rpm. The defect-free joints obtained using TRS of 1200, 1300, and 1400 rpm are considered for the further testing and characterization.

3.2 Microstructure

Figure 3 presented the optical micrographs of the various joints made using TRS of 1200, 1300, and 1400 rpm. The stir zone exhibits fine recrystallized equi-axed grains in all the three joints (Fig. 3a–c). The average grain diameters of the various regions are shown in Table 4. The grain sizes of stir zones are fine; however, the grain sizes are remarkably varied for the three defect-free joints. The joint fabricated using TRS of 1200 rpm exhibits fine-grained microstructure than the other two joints made

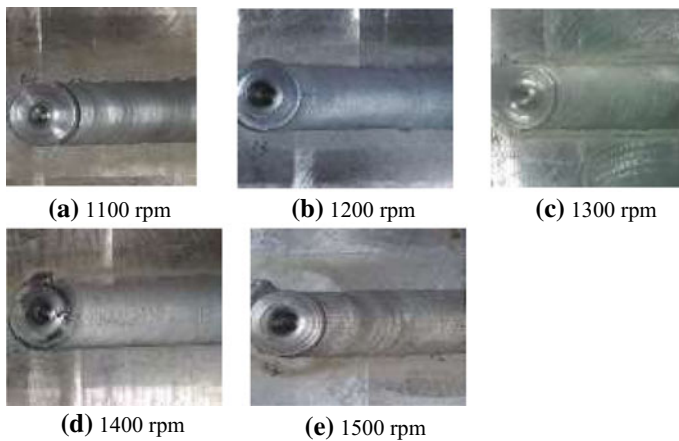
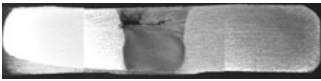
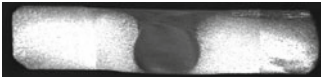
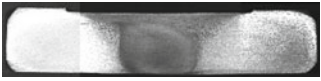
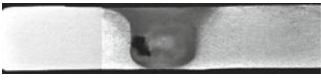



Fig. 2 Photographs of joints at top surface

Table 3 Effect of tool rotation speed on cross-sectional macrographs

TRS (rpm)	Macrograph	TRS (rpm)	Macrograph
1100		1400	
1200		1500	
1300			

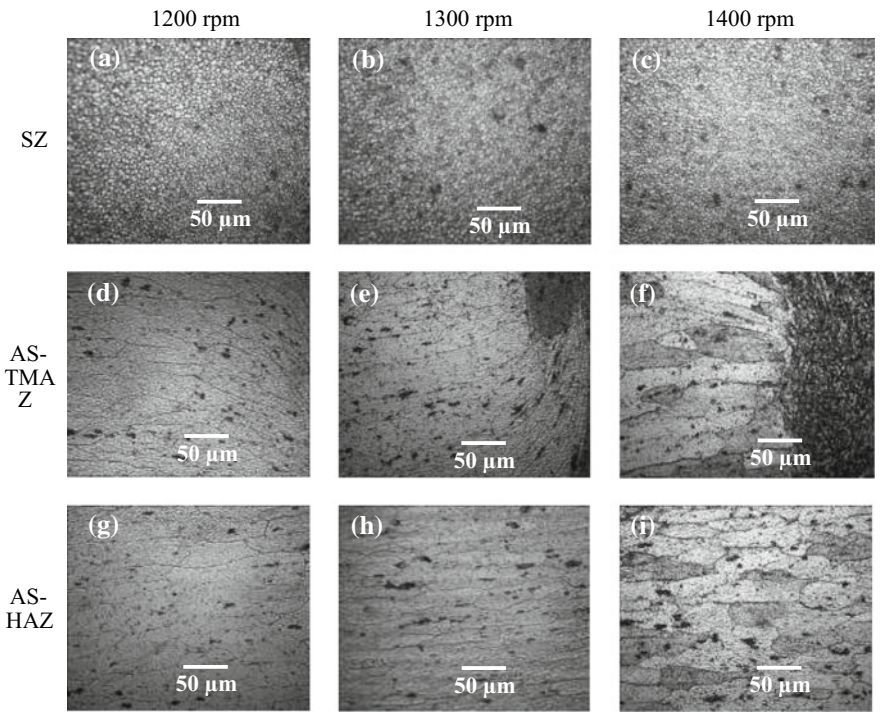


Fig. 3 Optical micrographs of various regions

using TRS of 1300 and 1400 rpm. The average grain diameter in the SZ is measured as 2.5, 3.3, and 4.2 μm for the joint fabricated using 1200, 1300, and 1400 rpm, respectively.

Table 4 Average grain diameter

Tool rotation speed	SZ (μm)	AS-TMAZ (μm)	RS-TMAZ (μm)	AS-HAZ (μm)	RS-HAZ (μm)	PM (μm)
1200	2.5	49	50	49	49	49
1300	3.3	50	50	49	49	
1400	4.2	54	54	51	51	

In all the three joints, the TMAZ exhibits coarse elongated grains. The AS-TMAZ (advancing-side thermomechanically affected zone) and RS-TMAZ (retreating-side thermomechanically affected zone) of all the three joints show coarse and deformed grains towards the stir zone. The average grain diameters of TMAZ at advancing and retreating sides are same in size and measured as 50 μm and 54 μm for the joints made using TRS of 1300 and 1400 rpm, respectively. The extent of deformation and grain size are equal on both sides, and therefore, the microstructure seems to more or less symmetric. Among the three joints, the average grain diameter of HAZ is lower for the joint made using TRS of 1300 rpm. The HAZ grain sizes are measured as 49 μm , 49 μm , and 51 μm for the joint fabricated using TRS of 1200 rpm, 1300 rpm, and 1400 rpm, respectively.

3.3 Microhardness

The microhardness is measured across the MTR and along the cross section which is plotted in Fig. 4. Typical W-shaped graphs are recorded for all the three joints. The TMAZ at both AS and RS exhibits lower hardness in all the three joints. The hardness, width of LHDR, and the location of the LHDR are varying with varying TRS.

The lowest hardness is recorded as 95 HV, 93 HV, and 88 HV for the joint fabricated using TRS of 1200, 1300, and 1400 rpm, respectively. The stir zone is harder than the TMAZ and HAZ in all the three joints. The hardness of the SZ is recorded as 107 HV, 105 HV, and 101 HV for the joint made using TRS of 1200, 1300, and 1400 rpm, respectively. It is also observed that, as the TRS increases, the location of the LHDR is shifting away from the weld centre.

3.4 Tensile Properties

The transverse tensile properties were evaluated and compared in the form of stress–strain plots. The yield strength, ultimate tensile strength, percentage of elongation, and joint efficiency of various joints are interpreted from the stress–strain plot and

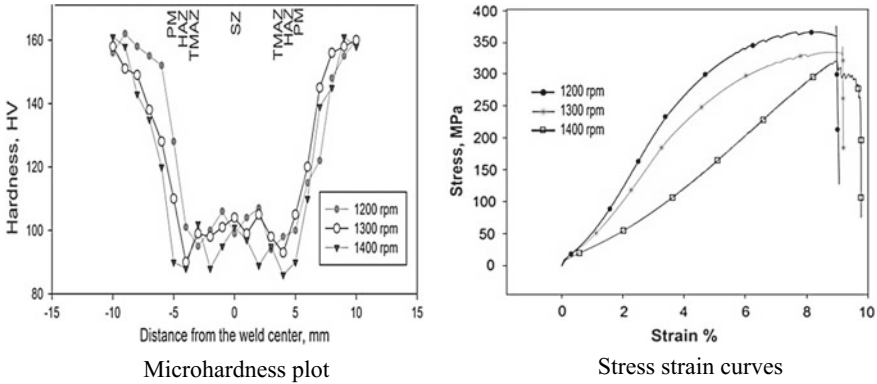


Fig. 4 Mechanical properties

Table 5 Tensile properties

	0.2% yield strength (MPa)	Tensile strength (MPa)	Elongation in 50 mm gauge length (%)	Joint efficiency (%)
Parent metal	427	452	11.2	—
1200 rpm	344	372	9.01	82
1300 rpm	322	345	9.17	76
1400 rpm	295	319	9.85	70

listed in Table 5. The joint made using TRS of 1200 rpm exhibited the highest tensile strength of 372 MPa. The other two joints made using TRS 1300 and 1400 rpm resulted in tensile strength of 345 and 319 MPa, respectively. It is observed that the increase in TRS decreases the tensile properties. In addition, it is observed that all the three joints exhibit lesser tensile strength than the PM. The joint efficiency is found as 82, 76, and 70%, respectively, for the joints made using TRS of 1200, 1300, and 1400 rpm. The percentage of elongation of the joint made using TRS of 1200, 1300, and 1400 rpm is 9.01, 9.17, and 9.85%, respectively, which is also lower than the PM.

3.5 Fracture Surface

The tensile fracture paths at cross section of the joints are shown in Fig. 5. In all the three joints, the tensile fracture path falls in the TMAZ of the joints. Generally, in UWFSW joints, the width of the TMAZ is very narrow. Therefore, the fracture seems to occur in the SZ-TMAZ interface. Fracture path is following outer periphery of the stir zone in all the joints. Figure 6 shows the typical fracture surface at

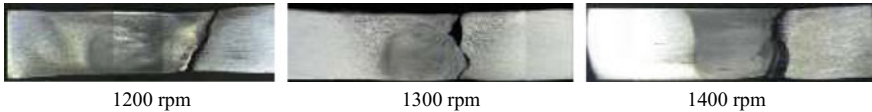


Fig. 5 Effect of tool rotation speed on fracture path

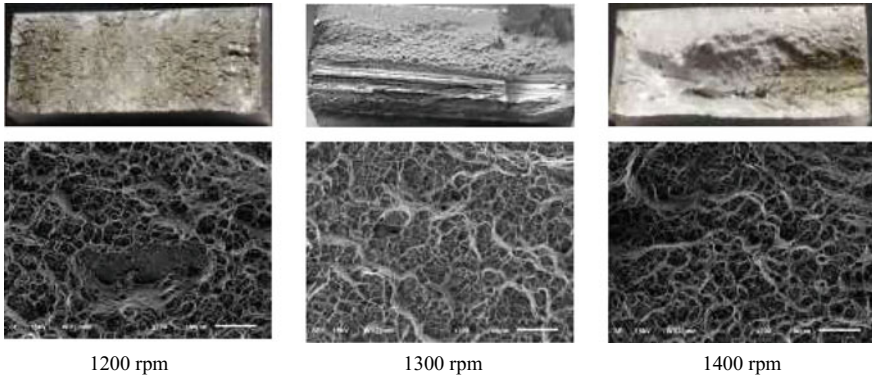


Fig. 6 Fracture analysis

macro- and microlevel examinations. The macro-level fracture surface shows two different patterns in the joint fabricated using TRS of 1300 and 1400 rpm. In both the joints, SIR exhibits ductile type of fracture and PIR exhibits mixed mode of (ductile and cleavage) fracture. But a flat macro-level fracture surface is seen for the joint fabricated using TRS of 1200 rpm. At microlevel examination, all the three joints exhibited fine colonized dimples in the fractographs. The dimples are fine, equally sized, and oriented towards the loading direction in all the joints. The presence of dimples represents ductile mode of failure of weld joints.

4 Discussion

The defect formation is noticed in the joints made using both lower TRS and higher TRS. The stable state of heat is only experienced while using the TRS of 1200, 1300, and 1400 rpm, and thus, it results in defect-free joints. At the lower TRS of 1100 rpm, insufficient state of heat is prevailed in the SZ, and at the TRS of 1500 rpm, excess state of heat is prevailed in the stir zone. It can be inferred that the defect formation is primarily due to the achievement of inadequate or excess heat state in the stir zone. In UWFSW process, the heat is generated due to three reasons, namely rubbing of tool shoulder with the workpiece, rubbing of tool probe with the workpiece, and the plastic deformation of materials. Among the three reasons, the frictional heat generated owing to tool shoulder rubbing plays the primary contribution for the

plasticization of material. By increasing the TRS, the extent of rubbing of the tool with workpiece increases. Increase in TRS increases the number of rubbing per second. So increase in TRS increases the heat input and vice versa. At lower TRS of 1100 rpm, the rate of tool rubbing is low. Therefore, insufficient heat is attained because of the low frictional heat. The poor thermal softening of material results in improper material which in turn forms defect in the stir zone. During tool rotation, initially, the material is transported from AS to RS in the leading edge of the tool. At the tool back, the material is transported from RS to AS to compensate the vacant created during excavation. Due to poor plasticization of material, it is hard to fill the vacant created in the AS. So the defect is occurred in the AS of the stir zone. On increasing the TRS to 1200, 1300, and 1400 rpm, enough plasticization can be achieved. The amount of material transported from RS to AS to fill the vacant is equal to or higher than the amount of material transported from AS to RS. At these TRSs, the tool rubbing rate is sufficient to create balance heat and material flow state. At higher TRS of 1500 rpm, defect was occurred in the stir zone irrespective of the high heat generation. The defect occurrence at higher TRS is attributed due to two reasons. Firstly, at higher TRS, the excess heat state is attained which will create turbulent material flow in which the flow of material is improper and end up in defect formation. Secondly, due to high thermal softening of materials, the extent of friction between the tool and softened materials is greatly reduced. The drop in friction results in sliding over sticking condition in the tool-material interface. Therefore, the slippage of material results in defect in the stir zone. By this way the TRS influence the quality of the joint.

The mechanical performances of the joints rely on the microstructural features available in various zones. According to the Hall–Petch relation, the finer grain size yields higher hardness and vice versa. The TMAZ exhibits coarse grains, and so it exhibits lower hardness in the joint made using TRS of 1200, 1300, and 1400 rpm. Because of fine grains, massive amount of grain boundaries is available in the stir zone. Grain boundaries are capable of hindering the dislocation motion. Therefore, the SZ exhibits greater hardness than the softer TMAZ region in all the cases. The joint made using TRS of 1200 rpm exhibits higher hardness than the other two joints which was attributed to the presence of finer grains in all the respective regions. In the same way, the joint fabricated using TRS of 1200 rpm results in higher tensile strength than the other two joints. The greater tensile strength is owing to the presence of finer grains in the stir zone and narrowed LHDR. The increase in the number of grain boundaries increases the grain boundary strengthening of the joint. During tensile loading, the grain boundary offers resistance to the dislocation motion. During tensile pulling, the weakest zone will undergo severe deformation. The TMAZ is the weakest region in the joint, and thus, the load was concentrated in the TMAZ and the fracture happened in that region. This can correlate with the microhardness plots. Thus, the fracture happened at the weakest SZ-TMAZ and followed a zigzag path. Moreover, the grain orientation variance at the SZ-TMAZ boundary limits the fracture, and thus, the fracture surface is not smooth. The load concentration phenomenon is called strain localization. Because of strain localization, the weakest region alone contributes to joint deformation. Thus, lower elongation values were observed for the UWFSW

joints compared to the PM. From the macro- and microfracture surface images, it can be concluded that at all the joint conditions, mixed mode of failure was observed.

5 Conclusions

The effect of TRS on microstructure features and joint soundness was studied, and it is concluded as,

- (1) The joints made using TRS of 1200, 1300, and 1400 rpm showed defect-free weld top surface and cross-sectional stir zone. It is owing to the attainment of stable state of heat generation and material flow.
- (2) The joint fabricated using TRS of 1200 rpm exhibited maximum tensile strength of 372 MPa and joint efficiency of 82%, which is 7 and 14% higher than the joint fabricated using TRS of 1300 and 1400 rpm, respectively.
- (3) The existence of relatively fine grains in the stir zone, marginally greater hardness of stir zone, and noticeably lower width of lower hardness distributed region (LHDR) are the prime causes for the soundness of joint made using TRS of 1200 rpm than the counter parts.

References

1. Cheeseman A, Gooch WA, Burkins MS (2008) Ballistic evaluation of aluminum 2139-T8. In: Bless SJ, Walker JW (eds) Proceedings of the 24th international symposium on ballistics, New Orleans, USA, p 651
2. Fisher J Jr, James J, Lawrence SK, Joseph RP (2002) Aluminum alloy 2519 in military vehicles. *Adv Mater Process* 160:43–46
3. Quintino L, Miranda R, Dilthey U, Iordachescu D, Banasik M, Stano S (2012) Laser welding of structural aluminium. *Adv Struct Mater* 8:33–57
4. Mishra RS, Ma ZY (2005) Friction stir welding and processing. *Mater Sci Eng: R* 50:1–78
5. Fuller CB, Murray Mahoney W, Calabrese M, Miconi L (2010) Evolution of microstructure and mechanical properties in naturally aged 7050 and 7075 Al friction stir welds. *Mater Sci Eng, A* 527(9):2233–2240
6. Rui-dong F, Zeng Qiang S, Rui Cheng S, Ying L, Hui Jie L, Lei L (2011) Improvement of weld temperature distribution and mechanical properties of 7050 aluminum alloy butt joints by submerged friction stir welding. *Mater Des* 32:4825–4831
7. Liu HJ, Zhang HJ, Huang YX, Lei Y (2010) Mechanical properties of underwater friction stir welded 2219 aluminum alloy. *Trans Nonferrous Met Soc China* 20:1387–1391
8. Zhang Z, Xiao BL, Ma ZY (2014) Influence of water cooling on microstructure and mechanical properties of friction stir welded 2014 Al-T6 joints. *Mater Sci Eng, A* 614:6–15
9. Zhang HJ, Liu HJ, Yu L (2012) Effect of water cooling on the performances of friction stir welding heat-affected zone. *J Mater Eng Perform* 21:1182–1187
10. Fonda RW, Bingert JF (2014) Microstructural evolution in the heat-affected zone of a friction stir weld. *Metall Mater Trans A* 35A:1487–1499

11. Xu WF, Liu JH, Chen DH, Luan GH, Yao JS (2012) Improvements of strength and ductility in aluminum alloy joints via rapid cooling during friction stir welding. *Mater Sci Eng, A* 548:89–98
12. Fratini L, Buffa G, Shivpuri R (2010) Mechanical and metallurgical effects of in process cooling during friction stir welding of AA7075-T6 butt joints. *Acta Mater* 58:2056–2067
13. Zhang HJ, Liu HJ, Yu L (2011) Microstructure and mechanical properties as a function of rotation speed in underwater friction stir welded aluminum alloy joints. *Mater Des* 32:4402–4407

Investigation of Hardness and Tribological Behaviour of Aluminium Alloy LM30 Reinforced with Silicon Carbide, Boron Carbide and Graphite



P. Shanmugaselvam, R. Sasikumar and S. Sivaraj

Abstract The present paper deals with the study of hardness and wear characteristics of SiC (microsize)-, B₄C (microsize)- and graphite (microsize)-reinforced aluminium LM30 metal matrix composites (MMC). Matrix alloy with (5, 7 and 13%) of SiC and B₄C, and (5, 7 and 10%) of graphite were made using stir casting technique. A pin-on-disc wear testing machine was used to find out the wear rate in which E24 steel disc under dry condition and Brinell hardness testing machine was used to find the hardness of the casted material. This work mainly emphasizes on the investigation of the hardness and wear property of the casted material. The wear properties are tested in both loading and unloading conditions. Wear resistance and hardness of the material are increased when adding the SiC, B₄C and graphite. The result shows that properties of stir casting material are good due to the complete dispersion of micropowder.

Keywords Aluminium · Metal matrix composites · Stir casting · Wear rate · Hardness

1 Introduction

Aluminium alloy is widely used in automotive, aerospace and mineral processing industries to make their products due to its excellent properties such as low density and high thermal conductivity [1]. Dry sliding wear characteristics of MMC-based aluminium alloys have been studied by Rana and Purohit [2] in with load conditions. Wear characteristics of MMCs in no load condition and hardness have been studied by Ramesh et al. [3]. The effect of parameters such as reinforcement weight fraction and speed, applied load, sliding speed, hardness of the counter face and the properties of

P. Shanmugaselvam (✉) · S. Sivaraj
Department of Mechanical Engineering, Chennai Institute of Technology, Chennai 600069, India
e-mail: sunface.selvam@gmail.com

R. Sasikumar
Department of Mechanical Engineering, Selvam College of Technology, Namakkal 637003, India

© Springer Nature Singapore Pte Ltd. 2019
S. S. Hiremath et al. (eds.), *Advances in Manufacturing Technology*,
Lecture Notes in Mechanical Engineering,
https://doi.org/10.1007/978-981-13-6374-0_62

569

reinforcement phase on dry sliding wear behaviours was examined in [1–3]. Hence, the present study was attempted to improve the dry sliding wear behaviour of Al-LM30 alloy reinforced with SiC, B₄C and graphite at load and no load with the help of varying proportion of adding reinforcement. The wear and hardness results are reported in this paper. Further related works on aluminium based metal matrix composites works are carried out by the different researchers are augmenting the present work [4–10].

2 Experimental Procedure

2.1 Manufacturing of Aluminium Using Stir Casting Process

LM30 was first super-heated to its melting point in a ceramic crucible. Subsequently, the SiC, B₄C and graphite are preheated to a temperature of 850 °C. Subsequently, the TiB₂ micropowder is preheated to a temperature of 850 °C. After preheating the micro powder (5, 7 and 13%) of SiC and B₄C, and (5, 7 and 10%) of Graphite for every weight fraction were then added to the molten metal. Stirring was carried out using an automatic stainless steel (SS) stirrer rate of 750 rpm for 15 min. Finally, specimens fabricated in four various conditions were prepared for subsequent mechanical analyses.

2.2 Pin-on-Disc Wear Test

Wear tests were conducted on CSEM pin-on-disc tribometer. The wear resistance was determined for all materials using a pin-on-disc test in air under dry sliding conditions and at room temperature, without load, at a disc velocity of 2.77 ms⁻¹. The pin, which had a diameter of 8 mm ± 0.1 mm with ball end, was machined using a cooled lubricant and slow machining speeds to avoid influencing the microstructure. Two disc materials were investigated, cast iron and EN 31 steel. Of those two materials, we had chosen EN 31.

The pin-on-disc tester was of a simple design, and the pin was in contact with the same disc track. The steel discs were cleaned prior to testing and before and after each weighing. A new disc was used for each material tested. The pin was ultrasonically cleaned by immersing in methanol for five minutes before and after each measurement followed by remounting in the tester in the same location. The test duration was up to 395 s with a total sliding distance of approximately 1097 m without any load.

By using the above data and wear value from the graph, we can find the wear rate by using the following formula. Wear rate = $\frac{\text{wear volume}}{\text{sliding distance}}$ mm³/m, wear volume = $\pi r^2 h$, sliding distance = $\frac{\pi DN}{60} \times t$, D = drag diameter, N = disc rotating speed, t = time, r = pin radius and h = wear.

Remove burrs from the test specimen pin by using emery paper. The wear disc with 8 mm thickness was thoroughly cleaned with solvent and clamped it on the holder using four screws. Fix the specimen pin in the holder and tighten set the height of the test specimen pin above the wear disc using height adjustment block ensures the loading arm is always parallel. Tighten clamping screws of hardened jaws to clamp the specimen pin firmly. The wear track diameter is set to 60 mm. The RPM is set at 885, and the time duration is set to 395 s (Fig. 1).

The test specimens with various % of SiC, B₄C and Graphite reinforced with LM30 Aluminium alloy (Figs. 2 and 3).

- Pin length—30 mm
- Sliding speed—885 rpm
- Pin diameter—8 mm with ball end
- Load—no load, 1 and 2 kg condition
- Temperature—room temperature
- Track diameter—60 mm.



Fig. 1 Pin-on-disc apparatus and wear testing set-up



Fig. 2 Wear test specimens



Fig. 3 Experimental set-up of pin-on-disc tribometer

2.3 Model Calculation

No load condition

$$\text{Wear rate} = \frac{\pi r^2 h}{\frac{\pi DN}{60} \times t} = \frac{3.14 \times (4^2) \times (290 \times 10^3)}{\frac{3.14 \times 60 \times 885}{60} \times 395}$$

Wear rate for no load condition = 0.0132 mm³/m.

The calculating procedures have been followed for all compositions with no load, 1 and 2 kg.

3 Result and Discussion

3.1 Wear Test Result

The results of this study have shown that microsized SiC, B₄C particulates (5, 7 and 13%) and graphite (5, 7 and 10%) volume are able to bring appreciable improvement to the wear resistance of pure aluminium matrix alloy, especially under higher sliding speeds. The small volume fraction of reinforcement used presently is significant, because the earlier studies have found that there exists an optimum level of

Table 1 Wear test result with no load

Composition	Wear (μm)	Wear rate (mm^3/m)
Pure Al LM30	290	0.0132
Al LM30 85% + SiC 5% + B ₄ C 5% + graphite 5%	95	0.00434
Al LM30 79% + SiC 7% + B ₄ C 7% + graphite 7%	95	0.00434
Al LM30 64% + SiC 13% + B ₄ C 13% + graphite 10%	115	0.00526

Table 2 Wear test result with 1 kg load

Composition	Wear (μm)	Wear rate (mm^3/m)
Pure Al LM30	350	0.01601
Al LM30 85% + SiC 5% + B ₄ C 5% + graphite 5%	265	0.01212
Al LM30 79% + SiC 7% + B ₄ C 7% + graphite 7%	290	0.0132
Al LM30 64% + SiC 13% + B ₄ C 13% + graphite 10%	290	0.0132

Table 3 Wear test result with 2 kg load

Composition	Wear (μm)	Wear rate (mm^3/m)
Pure Al LM30	425	0.0194
Al LM30 85% + SiC 5% + B ₄ C 5% + graphite 5%	310	0.0141
Al LM30 79% + SiC 7% + B ₄ C 7% + graphite 7%	350	0.016
Al LM30 64% + SiC 13% + B ₄ C 13% + graphite 10%	370	0.0169

reinforcement for a given particulate size and sliding condition. On the other hand despite an increase in hardness, results in wear rates comparable to or even higher than the unreinforced material.

The graph shows that 5% of (SiC + B₄C + graphite) of LM30 alumina withstands the low wear rate due to their increase in hardness (Tables 1, 2 and 3).

3.2 Wear Test Result Discussion

Wear test was performed on specimens in pin on disc; the wear rate decreases while increasing the reinforcement of (SiC, B₄C and graphite) percentage.

Thirteen percentage of silicon carbide-reinforced, 13% of boron carbide-reinforced and 10% of graphite-reinforced LM30 Al. alloys have high hardness; it reduces the wear rate LM30 Al. Alloy has higher tensile strength. The same is shown in Figs. 4, 5 and 6.

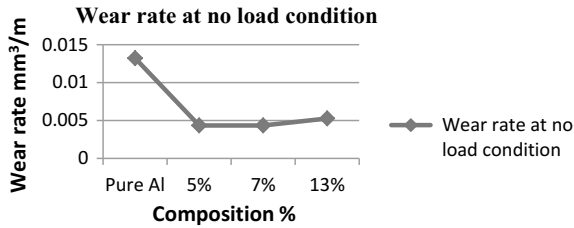


Fig. 4 Composition versus wear rate at no load condition

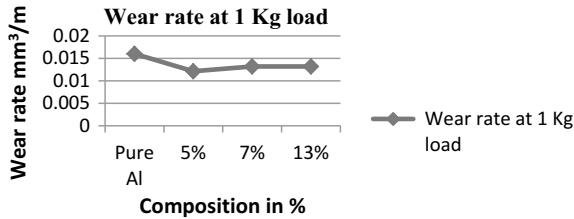


Fig. 5 Composition versus wear rate at 1 kg load condition

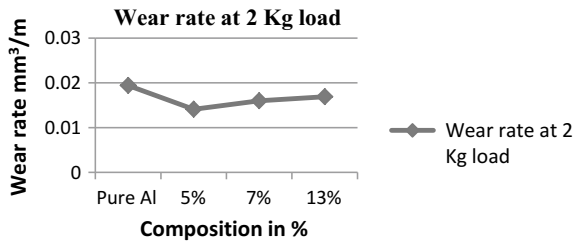


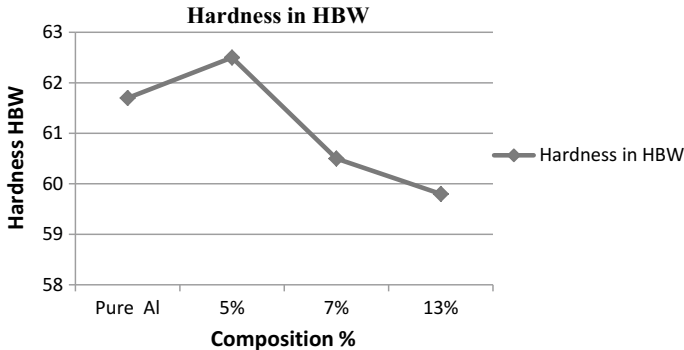
Fig. 6 Composition versus wear rate at 2 kg load condition

3.3 Hardness Test Results

Brinell hardness test was performed on the polished sample of the aluminium alloy. The dimension of the specimen for hardness test was 100 mm × 50 mm × 10 mm. Hardness test was conducted on test specimen for the applied load 500 kgf for a given time period, and the indenter diameter was 10 mm. It was observed that the MMC samples with a higher percentage of reinforcement show higher hardness. The hardness values of the test samples are shown in Table 4, indicates that the composition of [5% of (SiC) + 5% of (B₄C) + 5% of (graphite)] gives the increased hardness value when compared to other compositions.

Table 4 Hardness values

Composition	Hardness values in HBW			Average value
Pure aluminium LM30	61.7	61.3	61.3	61.4
85% Al LM30 + 5% SiC + 5% B ₄ C + 5% graphite	62.5	62.1	62.1	62.2
79% Al LM30 + 7% SiC + 7% B ₄ C + 7% graphite	60.5	60.9	60.9	60.7
64% Al LM30 + 13% SiC + 13% B ₄ C + 10% graphite	59.8	60.1	60.1	60.1

**Fig. 7** Comparison of hardness of LM30 Al. alloy with variable compositions

3.4 Hardness Test Result Discussion

Brinell hardness test was done on the specimens, the percentage of reinforcements increases its the hardness also increases in proportional manner due to the presence of strong ionic inter-atomic bonding which would improves its Hardness value of the LM30 Al Alloy Metal matrix composites 5% SiC + 5% B₄C + 5% Graphite—reinforced LM30 MMNC gives the higher hardness value with impact values of 1 J and further increase in reinforcements about 5% it starts to reduces the hardness value decreases (Fig. 7).

4 Conclusion

The different samples were fabricated by stir casting process by varying the composition of micro sized silicon carbide (SiC), boron carbide (B₄C) and graphite particles reinforced LM30 aluminium alloy. The best wear resistance is observed in the 13% of composition (13% SiC + 13% B₄C + 10% graphite) casted material.

Finally, there is a gradual reduction in the wear rates and improvement in hardness when adding the SiC-, B₄C- and graphite-reinforced materials. The impact test results

have shown that there is a considerable rise in the impact strength at 5% composition. The hardness test results reveal that there is a considerable hike in the hardness value at 5% composition. The tensile test results have shown increase in the tensile strength at 7% composition.

References

1. Das S (2004) Development of aluminium alloy composites for engineering applications. *Trans Indian Inst Met* 57–4:325–334
2. Rana RS, Purohit R (2012) Effect of Magnesium enhancement on mechanical property and wear behaviour of LM6 Aluminum alloy. *Int J Sci Eng Res* 3(7). ISSN 2229-5518
3. Ramesh A, Prakash JN, Gowda ASS, Appaiah S (2009) Comparison of the mechanical properties of AL6061/albite and AL6061/graphite metal matrix composites. *J Miner Mater Charact Eng* 8(2):93–106. JMMCE.Org
4. Singla M (2009) Development of aluminium based silicon carbide particulate metal matrix composite. *J Miner Mater Charact Eng* 8(6):455–467. JMMCe.org
5. Doel TJA, Lorretto MH, Bowen P (1993) Mechanical properties of aluminium based particulate metal matrix composites. *J Compos* 24:270–275
6. Lucas JP, Stephens JJ, Greulich FA (1991) The effect of reinforcement stability on composition redistribution in cast aluminium metal matrix composites. *Mater Sci Eng* 131(2):221–230
7. Naher S, Brabazon D, Looney L (2004) Development and assessment of a new quick quench stir caster design for the production of metal matrix composites. *J Mater Process Technol* 166:430–439
8. Kumar GBV (2011) Mechanical and tribological behavior of particulate reinforced aluminum metal matrix composites. *Rev J Miner Mater Charact Eng* 10(1):59–91. jmmce.org
9. Alaneme KK (2011) Corrosion behavior of alumina reinforced aluminium (6063) metal matrix composites. *J Miner Mater Charact Eng* 10(12):1153–1165. JMMCE.org
10. Nunes RCR, Ramanathan LV (1995) Corrosion behaviour of alumina-aluminium and silicon carbide-aluminium metal-matrix composites. *Corrosion* 51(8):610–617. <https://doi.org/10.5006/1.3293621>
11. Hassan SF, Gupta M (2005) Development of high performance Magnesium nano composites using nano—Al₂O₃ as reinforcement. *Mat Sci Eng A* 392:163–168

Friction and Wear Properties of Bio-Based Abrasive in a High-Friction Composite Material



S. Stephen Bernard, Md. Javeed Ahmed, J. Dasaprakash, M. R. Saroj Nitin, S. Vivek and G. K. Kannan

Abstract The objective of the work is to analyse the function of bio-based abrasive in a high-friction composite materials. Cashew dusts are cheaper when compared to other frictional brake materials which stimulated the idea of exploring their possible incorporation into friction materials. The effect of cashew dust loading on physical, mechanical and tribological properties of brake pad composite is evaluated. Cashew dust is loaded with 0, 4, 8, 12, 16 and 20% as an alternate of alumina by varying the pressure and speed in a pin on disc tribometer. By increasing cashew dust content's heat swell, porosity and specific gravity decrease and also hardness and loss on ignition increase. By increasing the pressure, 8, 12 and 16% shows high friction stability at all speeds. Finally, the effect of environment on the composites was investigated in water, salt water and oil.

Keywords Cashew dust · Wear · Friction stability · Heat swell · SEM

1 Introduction

Abrasives and lubricants are considered as friction additives in brake pad to enhance the friction stability and low wear rate. Abrasive removes iron oxides from the counter-friction material as well as other undesirable surface films formed during braking. Lubricant stabilizes developed friction coefficient at high temperature. The role of abrasive in the brake pad material is to maintain the friction level in brake control and clean the glaze on the disc at the friction interface. A large number of abrasives are used with varying strength, size, shape, surface reactivity, hardness

S. Stephen Bernard (✉) · J. Dasaprakash · M. R. Saroj Nitin · S. Vivek
Rajalakshmi Institute of Technology, Chennai, Tamil Nadu, India
e-mail: ssbstephen@gmail.com

Md. Javeed Ahmed
B.S Abdur Rahman University, Vandalur, Tamil Nadu, India

G. K. Kannan
Chennai Institute of Technology, Kundrathur, Chennai, Tamil Nadu, India

© Springer Nature Singapore Pte Ltd. 2019
S. S. Hiremath et al. (eds.), *Advances in Manufacturing Technology*,
Lecture Notes in Mechanical Engineering,
https://doi.org/10.1007/978-981-13-6374-0_63

and toughness in brake pad [1]. Cashew dust is used to improve friction stability at elevated temperature, and it is an organic ingredient. A fine powder alumina is also used, as its wear debris is ground up in the wear process. Abrasive in brake lining determines friction optimization under a dynamic set of operating variables such as braking force, sliding speed, braking duration and braking temperature [2–4]. In general, metals and plastics can deform plastically to relieve high contact stress before fracture occurs. Alumina can deform plastically under the hydrostatic stress associated with concentrated contacts, but the plastic deformation involved is very small, when compared with metals and polymers [5]. Here both organic ingredient and alumina powder are used to find the optimization between them in a brake pad.

Brake pad materials are essentially constructed by four components: a binder, filler, friction modifier and reinforcement. The main task of the binder is that it holds the components of a brake pad together to prevent its constituents from crumbling apart [6–9]. Fillers are essentially used to reduce the overall cost of the material and partly to alter the brake pad properties. The role of abrasive in the brake pad is to control the friction level during braking and cleaning the glaze on the disc at the friction interface. Solid lubricant in brake pad plays the role of developing the friction film on the brake drum surface which influences the brake performances such as brake drum wear, torque variation, stopping distance and noise propensity [10].

Cashew dust is available in India in large quantity, and there is no clear awareness of the frictional properties. Cashew dust elements are equally found in asbestos; therefore, cashew dust can be used as a replacement for asbestos in frictional composites. Cashew dust can be used in brake pad material by considering its low ash, low wear rate and high strength [11]. By incorporating cashew dust in the composites, the properties like thermal stability, hardness and dielectric constant of the composites enhanced. This motivates the current work to study the influence of cashew dust on the frictional properties of the brake pad materials.

2 Experiment Procedure

2.1 Preparation of Friction Materials

Six different compositions were prepared for friction test. The formulation of friction material is given in Table 1. Raw materials are formulated as a weight percentage of the total formulation for ease of fabrication depending on batch size. All the materials were weighed using an analytical balance instrument to an accuracy of 0.1 g. The ingredients are mixed using a blender (electron EBR 100) for 16 min at 4000 rpm at room temperature (30 °C). In order to obtain a homogeneous mixture, a sequential mixing procedure derived from the experience was adopted as per the following procedure [12]:

All the fibres were added initially to produce a large mass of cutting particles to optimize the volume of the mixture for 10 min. It is followed by the required

Table 1 Formulation of friction material by varying cashew dust content

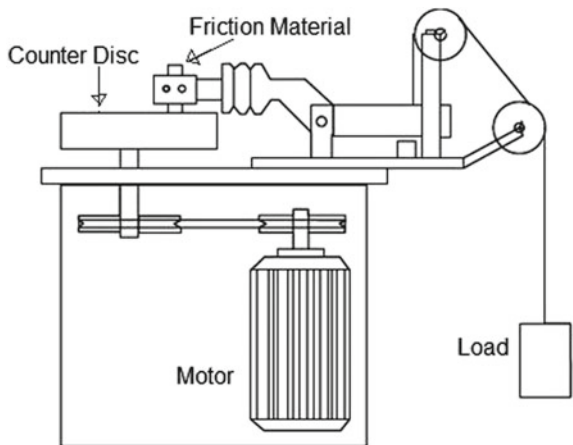
Raw materials (% in weight)	20 A	4 CD	8 CD	12 CD	16 CD	20 CD
Cardanol resin	15	15	15	15	15	15
Phenolic resin	5	5	5	5	5	5
Palm fibre	8	8	8	8	8	8
Rockwool fibre	4	4	4	4	4	4
Cashew dust	0	4	8	12	16	20
Alumina	20	16	12	8	4	0
Steel fibre	8	8	8	8	8	8
CaCO ₃	20	20	20	20	20	20
Calcium silicate, vermiculate, silicon	12	12	12	12	12	12
Antimony trisulphide	8	8	8	8	8	8

quantity of filler and friction modifiers simultaneously. Finally, the binder materials were added and mixed for a further 3 min at the same speed, giving a total of 16-min mixing time for each composite.

2.2 Testing

Dry sliding wear test for six specimens was conducted using Ducom wear and friction monitor—TR 20 with grey cast iron as the counterpart with a diameter of 120 mm. All the testing procedures were operated by a WinDucom data acquisition system on a computer using the ASTM G-99 standard (Fig. 1).

Fig. 1 a WinDucom wear and friction tester



The dimension of a single composite material was 8 mm diameter and a length of 32 mm. The disc was ground to a smooth surface finish and renewed for each test. The samples were placed on the wear disc, and the sliding wear tests were carried out at various times and speeds. The test was conducted in a load range of 20 N at a sliding velocity of 2–4 m/s and at sliding distance of 6.3 km. For each specimen, the testing time is 2100 s by varying the speed (300, 500, 700 rpm) with respect to 700 s. After each test, the specimens were removed, cleaned in acetone and weighed with an electronic balance within an accuracy of 0.1 mg.

3 Results and Discussions

3.1 Physical and Mechanical Properties of Cashew Dust Abrasive Composites

The cashew dust is loaded at different loading levels of 4, 8, 12, 16 and 20% in the optimized friction material containing 15% cardanol and 8% palm fibre with other ingredients. The composites were subjected to hardness, porosity, heat swell, specific gravity and loss on ignition tests, and the results are presented in Fig. 2. It shows that the increase in cashew dust content increases the hardness and loss of ignition significantly. Addition of cashew dust increases the hardness up to 2.3% and their loss of ignition up to 3%.

Decrease in the alumina content can be considered to be a reason for deformation of the material during friction. For heat swell, without cashew dust the material has

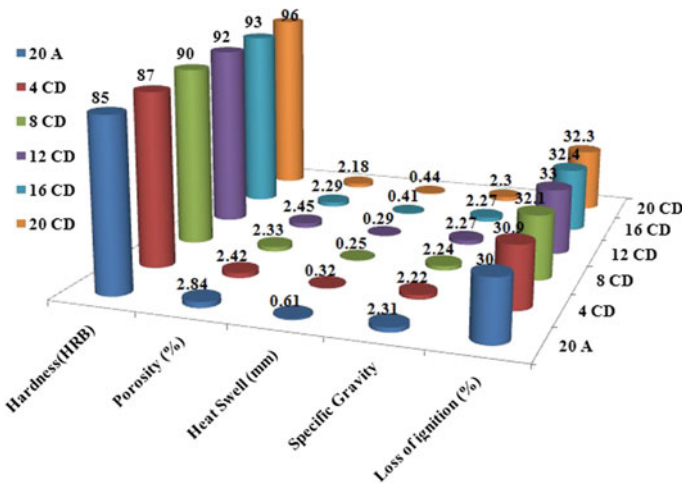


Fig. 2 Properties of cashew dust material as a brake pad

higher value of 0.61 and it is drastically reduced to 47.5% when 4% of cashew dust is added. It clearly indicates that thickness of the brake pad is reduced by adding cashew dust because of low porosity as well as deformation of cashew dust suppresses the increase of thickness in the composite material [8].

3.2 Friction Performance of the Cashew Dust Composite

The friction test was carried out at a constant pressure of 2 MPa for 35 min to investigate the effect of μ at different speed. Figure 3 shows μ for three different speeds (300, 500 and 700 rpm) as a function of time. The figure shows strong influence of the relative amount of cashew dust and alumina exhibiting different friction curves with the sliding velocity. The coefficient of friction from the high content of cashew dust (16 CD and 20 CD) showed a sharp increase after 1300 rpm. This is due to the inability of formation of oxides at higher rate due to high rpm and temperature at the interface, which leads to increase in COF [5].

Figure 4 shows the friction performance of the composite materials loaded for 2, 3 and 4 MPa. The average COF increased to 0.4 and does not change with pressure, in 8 CD composite at 700 rpm. This behaviour can be explained by the perfect binding of alumina and cashew dust in the composite; as a result, the porous structure of material crumbled easily during the friction tests [9]. From the results, it is apparent that a small decrease or increase in pressure and speed from the optimum range can provide considerable change in the tribological properties of the friction materials. Therefore, material selection must be limited between the optimum rates given by the test. Therefore, in this study, 8 CD and 12 CD were selected to evaluate tribological performance.

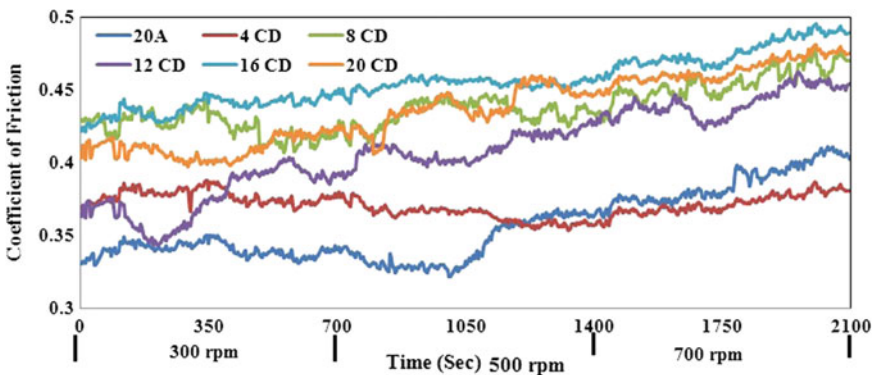


Fig. 3 Effect of varying cashew dust composite for COF (2 MPa)

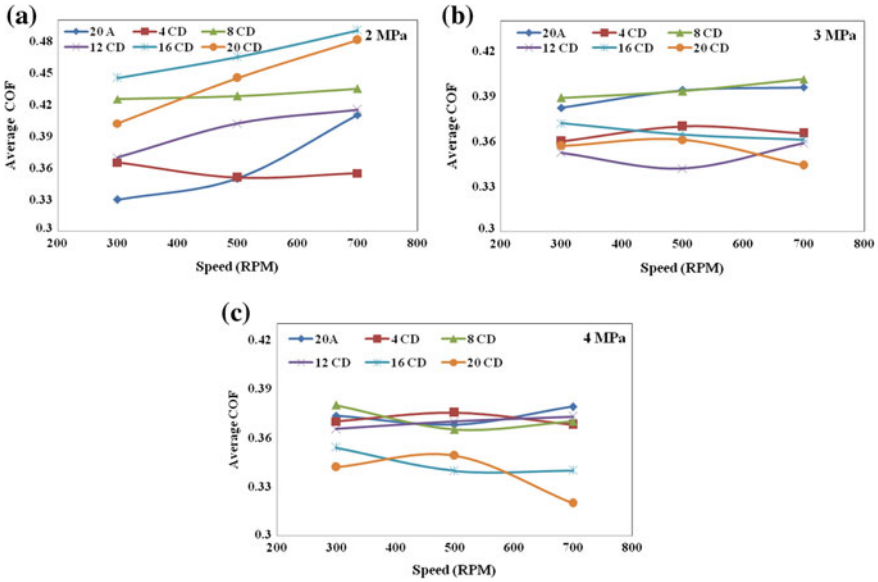


Fig. 4 Friction performance of cashew dust composites under various speeds and pressures: **a** 2 MPa, **b** 3 MPa and **c** 4 MPa

3.3 Friction Stability of Cashew Dust Composite

Figure 5a, b, c shows that the friction stability was improved when large quantity of cashew dust with a low amount of alumina was used. Figure 5a indicates that the FS for the 12 CD and 16 CD shows good behaviour as it has greater than 93% for all the speed. This stabilization indicates that the destruction of the effective contact area at elevated temperature is reduced [9]. At high speed and applied pressure, FS was increased in all the composites compared to previous speed and pressure. For 8 CD, the FS of 3 MPa was increased to 9.2% compared to 2 MPa. The increase of FS is attributed to the thermal decomposition of ingredients and followed by the subsequent destruction of contact areas at the sliding interface. The FS was most significant in the case of 20A at lower rpm for all pressure as it has high value (greater than 95%) than the other composite material. This high FS at low rpm will scratch the disc which increases the wear of the composite [11].

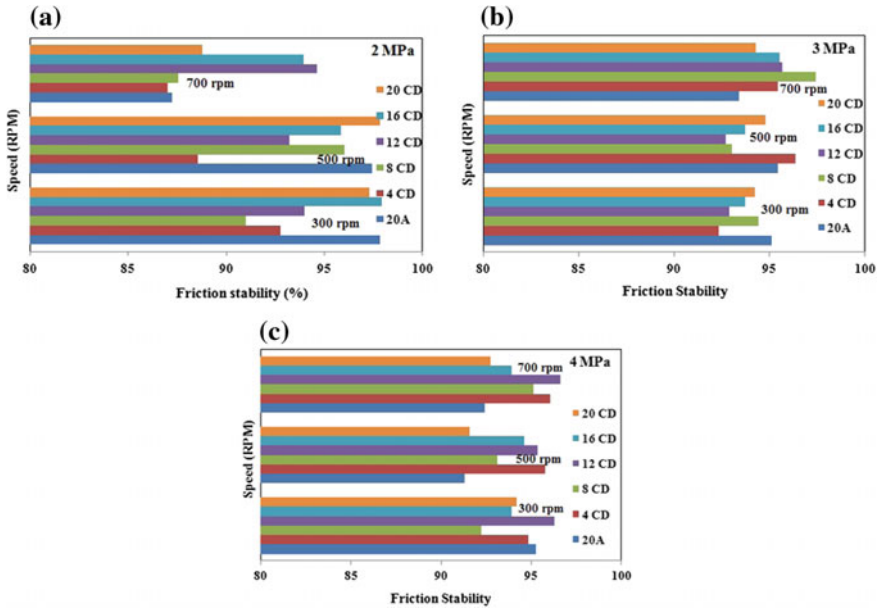


Fig. 5 Friction stability of cashew dust for various operating pressures and speeds: **a** 2 MPa, **b** 3 MPa and **c** 4 MPa

3.4 Wear Performance of Cashew Dust Composite

Figure 6 shows the specific wear rate of cashew dust friction material for varying speed as a function of time. 20 A and 4 CD showed slight improvement in wear resistance by producing wear-resistant contact plateaus in the friction surface. However, the wear rate of the composite increased much at a higher speed (500 and 700 rpm).

Increase in wear rate is due to high content of alumina which reduces the counter face friendliness of the disc at increased speed. Excellent high-speed wear resistance was found in the composites 12 CD and 16 CD. The wear rate of composite 12 CD was constant for all the speed. This was particularly interesting because friction materials normally exhibit excessive wear as the speed increases due to thermal decomposition of organic ingredients. The 16 CD composition exhibits a significant improvement in wear resistance, the reason for which may be attributed to the quantity of cashew dust and its influence on the formation of contact plateaus, which offsets thermal degradation of the composite [3].

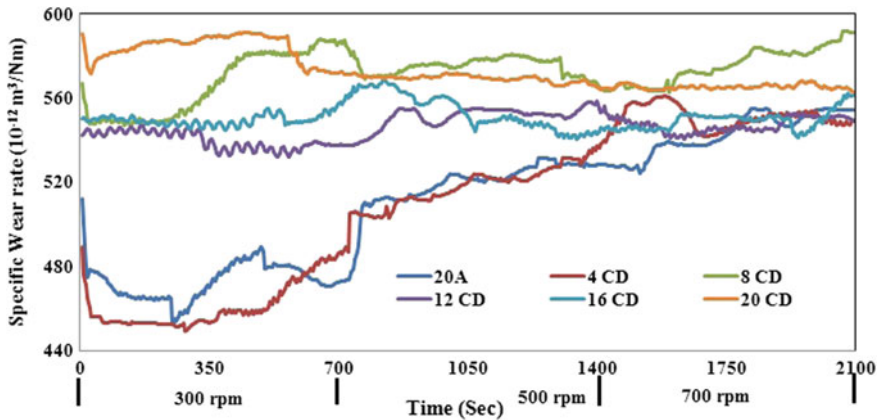


Fig. 6 Effect of varying cashew dust for specific wear rate (2 MPa)

4 Conclusion

The present research involved the study of mechanical, physical and tribological properties of the friction materials. The following conclusions are drawn from this study.

Hardness, porosity, loss on ignition and specific gravity values none of the friction material was best in all properties. From the investigation, it was observed that 4 CD and 8 CD show the lower COF value less than 0.36 throughout the sliding. It forms a poor contact between the pad and the rotor. Friction stability of cashew dust composite is high at high pressure, and therefore reduces fluctuation for continuous sliding. 12 CD exhibited the best wear performance compared to other friction material, and this type of reinforced sample has a longer life. This may be due to the fact that cashew dust is nearly equal in proportion to that of the alumina.

References

1. El-Tayeb NSM, Liew KW (2008) Effect of water spray on friction and wear behaviour of noncommercial and commercial brake pad materials. *Wear* 208:135–144
2. Han Y, Tian X, Yan Y (2008) Effect of ceramic fiber on the friction performance of automotive brake lining materials. *Tribol Trans* 51:779–783
3. Stephen Bernard S, Jayakumari LS (2014) Effect of the properties of natural resin binder in a high friction composite material. *Polimeros- Ciencia Tecnologia* 24(2):149–152
4. Stephen Bernard S, Jayakumari LS (2018) Pressure and temperature sensitivity analysis of Palm fiber as a biobased reinforcement material in brake pad. *J Brazilian Soc Mech Sci Eng* 40:152
5. Malhotra VM, Valimbe PS, Wright MA (2002) Effects of fly ash and bottom ash on the frictional behaviour of composites. *Fuel* 81:235–244

6. Ikpambese KK, Gundu DT, Tuleun LT (2016) Evaluation of Palm Kernel Fibers (PKFs) for production of asbestos-free automotive brake pads. *J King Saud Univ Eng Sci* 28:110–118
7. Stephen Bernard S (2009) Investigation on performance, combustion and emission characteristics of a turbocharged low heat rejection DI diesel engine with extended expansion concept. SAE technical paper 2009-28-0006
8. Mohanty S, Chugh YP (2007) Development of fly ash-based automotive brake lining. *Tribol Int* 40:1217–1224
9. Suresh G, Jayakumari LS (2015) Evaluating the mechanical properties of E-Glass fiber/carbon fiber reinforced interpenetrating polymer networks. *Polimeros* 1:49–57
10. Rosa AGDA, Moreto JA, Manfrinato MD, Rossino LS (2015) Study on friction and wear behavior of SAE 1045 steel, reinforced nylon 6.6 and NBR rubber used in clutch disks. *Mater Sci* 17:1397–1403
11. Jang H, Lee JS, Fash JW (2001) Compositional effects of the brake friction material on creep groan phenomena. *Wear* 251:1477–1483
12. Stephen Bernard S, Jayakumari LS (2016) Effect of rockwool and steel fiber on the friction performance of brake lining materials. *Materia- Rio de Janeiro* 21:656–665

Parametric Optimization of Single-Cylinder Four-Stroke Spark Ignition Engine Crankshaft Using Four Different Materials—AISI 1040, AISI 4340, AISI 4140 and AISI 4615



A. Pandiyan, G. Arun Kumar, S. Shaik Asif and Amit Patel

Abstract The aim of the study is to design and optimize crankshaft for a single-cylinder four-stroke overhead valve (OHV) spark ignition engine. This paper used reverse engineering techniques, in order to obtain an existing physical model. A three-dimensional crankshaft has been created with the help of SOLIDWORKS, and it is imported to ANSYS environment for the coupled steady-state thermal structural analysis. The material used for crankshaft is AISI 1040, AISI 4340, AISI 4140 and AISI 4615. The objective of this paper is to focus on the lightweight crankshaft design through coupled steady-state thermal structural analysis and to optimize the crankshaft design within the design domain using parametric optimization. The results obtained from finite element analysis and parametric optimization concluded, the modified design is safe along the selected materials for AISI 1040 and shows the maximum von Mises stresses 145.66 MPa, factor of safety (n) is 2.8491, and reduced weight of the crankshaft was 63 g which is 4.054% less as compared to the existing crankshaft model without compromising the strength-to-weight ratio.

Keywords OHV · Crankshaft · Reverse engineering · Finite element analysis · Parametric optimization

1 Introduction

In order to obtain a compression ratio of 16.5 in a diesel engine the pressure versus crank angle was investigated experimentally. To know the equations of equilibrium from free body diagram of slider crank, dynamic and kinematic analysis was ana-

A. Pandiyan (✉) · S. Shaik Asif · A. Patel
Department of Mechanical Engineering, Saveetha School of Engineering, SIMATS, Thandalam,
Saveetha Nagar, Chennai 602105, Tamil Nadu, India
e-mail: pandiyan@saveetha.com

G. Arun Kumar
Department of Mechanical Engineering, Sathyabama Institute of Science and Technology,
Chennai 600119, Tamil Nadu, India

© Springer Nature Singapore Pte Ltd. 2019
S. S. Hiremath et al. (eds.), *Advances in Manufacturing Technology*,
Lecture Notes in Mechanical Engineering,
https://doi.org/10.1007/978-981-13-6374-0_64

lyzed. Based on the obtained results, the forces were applied along with boundary conditions to AISI E4340 forged steel crankshaft. From the stress analysis result, critical regions have identified crankshaft and von Mises stresses and deformation were used to find the factory of safety [1].

An internal combustion engine crankshaft is a difficult geometry, which converts the sliding motion of the piston into a rotary motion by using four-bar linkage mechanism. Design and development of the crankshaft are significant roles in the fabrication unit, to achieve lightweight with low cost, good fatigue with optimum fuel efficiency and greater output power [2]. To reduce weight of the crankshaft through design optimization of crank web, hollow crank pins, journal of connecting rod and reducing the diameters have been discussed in this research work. The crankshaft optimization method explains the reduction in mass by 22% and shows increase in factor of safety as compared to existing crankshaft [3].

Many research papers have discussed these three traditional methods by which a crankshaft is been manufactured: forging, casting and machining. There are some disadvantages of these methods like waste of material and time spent in post-processing which ultimately increases the manufacturing cost. The main objective of this paper is to focus on weight reduction in crankshaft design through reverse engineering practices, selection of material and parametric optimization in order to increase the engine performance and control the emission parameters, higher the strength-to-weight ratio and to reduce the total cost of production.

2 Materials and Methods

2.1 Engine Specification

This paper attention is on crankshaft; the geometry and the requirements of the crankshaft solely depend upon the engine. A 4 stroke single cylinder air cooled engine is used with a bore of 68 mm, and stroke of 45 mm. The displacement is 163 cm³, and the rated output is 2.83 kW @ 3600 rpm. The maximum torque obtained is 10.3 N-m @ 2500 rpm. The compression ratio is 9:1, and the total weight of the engine is 15.1 kg.

2.2 Crankshaft: Material

Compact weight and high structural rigidity are the key factors essential for all components of an IC engine. AISI 1040 carbon steel has high carbon content and can be hardened by heat treatment followed by quenching and tempering to achieve

Table 1 Chemical structure of selection materials % by weight, physical and mechanical properties

Designation	Materials			
	AISI 1040	AISI 4340	AISI 4140	AISI 4615
Elements	Content (%)	Content (%)	Content (%)	Content (%)
Iron (Fe)	98.6–99	95.19–96.33	96.785–97.77	96.495–97.42
Manganese (Mn)	0.60–0.90	0.60–0.80	7.5–1.0	0.45–0.65
Carbon (C)	0.370–0.440	0.370–0.430	0.380–0.430	0.13–0.18
Sulfur (S)	≤0.050	0.040	≤0.040	≤0.040
Phosphorous (P)	≤0.040	0.035	≤0.035	≤0.035
Chromium (Cr)	–	0.700–0.900	0.80–1.10	–
Molybdenum (Mo)	–	0.20–0.30	0.15–0.25	0.20–0.30
Silicon (Si)	–	0.15–0.30	0.15–0.30	0.15–0.30
Nickel (Ni)	–	1.65–2.00	–	1.65–2
Density (Kg/M ³)	7845	7850	7850	7850
Yield strength (MPa)	415	470	415	350
Ultimate strength (MPa)	620	745	655	650

150–250 ksi tensile strength. Alloy steels are labeled by AISI four-digit numbers which contain various steel types having the margins of B, C, Mn, Mo, Ni, Si, Cr and Va set for carbon steels. AISI 4340 alloy steel contains nickel, chromium and molybdenum and is heat treatable. This AISI 4340 alloy steel provides good toughness and strength [5]. The chemical structure of crankshaft materials is used in this project work, and the physical and mechanical properties of used materials are shown in Table 1.

2.3 Reverse Engineering

Reverse engineering (RE) is a technique to attain 3D CAD model from physical model by using 3D scanner [4]. It follows the procedure of data collection, preprocessing, cleaning and the use of CAD/CAM/CAE tools. They are commonly used in automotive, aircraft, marine, medical life science, software industries, etc. The reverse engineering techniques is used in the paper with accurate measurements of the steinbichler comet L3D scanner having resolution of 2Mpx and 1600 × 1200 pixels, in order to obtain existing physical model. The scanned model and CAD model are shown in Fig. 1.

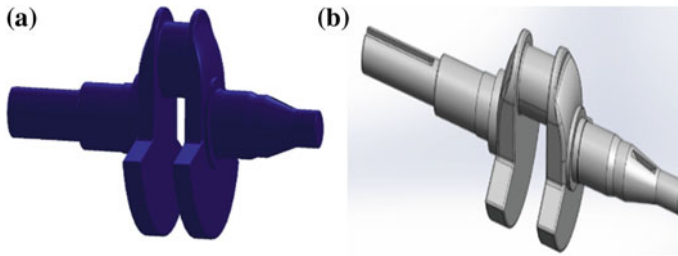


Fig. 1 Crankshaft model—**a** scanned model and **b** CAD model

2.4 Finite Element Analysis

A three-dimensional crankshaft has been created with the help of SOLIDWORKS 2016, and it is imported to ANSYS 16.2 environment for coupled steady-state thermal structural analysis. Maximum pressure of 23 bar is generated inside the cylinder due to burning of air–fuel mixture. This pressure will be transmitted into crankshaft via piston and connecting rod. Figure 2a shows the crankshaft model imported to ANSYS, and Fig. 2b shows fine meshed crankshaft; it consists of 285,208 nodes and 172,986 triangular elements. The thermal loads at 60 °C and the boundary conditions are applied through convective mode temperature 22 °C, and the obtained results are maximum temperature of 60 °C. The heat transferred per unit area is maximum of 0.64455 W/mm² at web fillet. The applied compressive load of 2.34 MPa, fixed support at the bearing region and moment of 10300 N-m was at the output shaft key. The maximum deformation is 0.017114 mm, stress is 152.74 MPa, shear stress is 152.74 MPa, and the minimum FOS for the crankshaft is 2.717.

2.4.1 Analysis Results Before Optimization

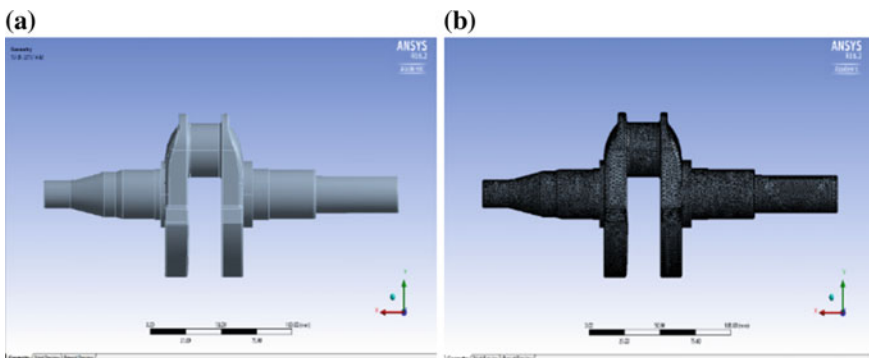


Fig. 2 Crankshaft model front view—**a** imported to ANSYS and **b** meshed model

3 Parametric Optimization

At first finite element analysis was conducted and shown that the low stress region on crankshaft counterweight, web and journal of connecting rod. Counterweight is experiencing insignificant stress so that this portion cannot be modified because crankshaft is dynamically stable. The most significant way during parametric optimization either adds material or removes out symmetry to the principal axis. So, the parametric changes were analyzed for optimization on the crankpin region of 14-mm diameter hole and penetrate through end so that the crankshaft attains considerable mass reduction under working conditions. Increasing fillet radius at the knuckle arm in journal of connecting rod, which does not affect the connecting rod geometry.

Figure 3a displays the fully optimized model, and Fig. 3b displays meshed crankshaft model; it consists of 284,797 nodes and 169,725 triangular elements. The maximum equivalent (von Mises) stress acting near the crankpin bottom surface close to web fillet is shown as 145.66 MPa. The minimum factor of safety is 2.8491.

3.1 Analysis Results After Parametric Optimization

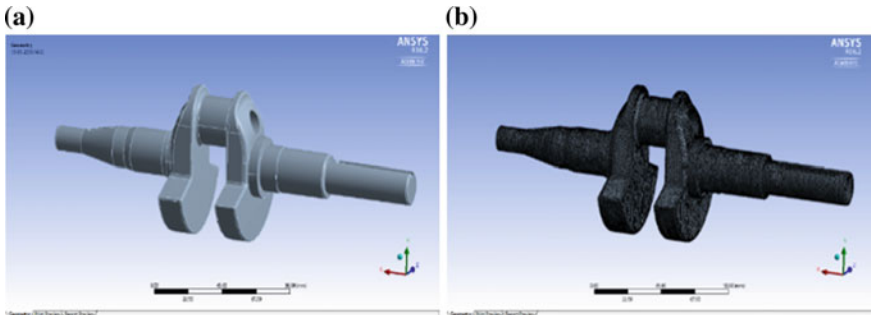


Fig. 3 Crankshaft model side view—**a** imported to ANSYS and **b** meshed model

4 Results and Discussion

Maximum von Mises stresses, deformation and factor of safety were originated out in finite element analysis. Maximum stress raised up in the web fillet near the crankpin for compressive loading at crank journal. After optimizing the geometry, the high localized stress occurs near the bottom fillet region of crankpin. From the results obtained the graphs were plotted before and after optimization, Fig. 4a Displays the total heat flux of AISI 4615 and AISI 4340 is almost equal before and after optimization, AISI 4140 is less than AISI 1040, AISI 4140 is the lowest among all the others before optimization and after optimization, and Fig. 4b describes the total deformation in which AISI 4340 is having the maximum deformation and AISI 4140 deformation which is close to AISI 1040, AISI 4615 shows the lowest deformation among all the others. Figure 4c shows the maximum von mises stress developed in AISI 4340 and AISI 4615 is the lowest, AISI 1040 and AISI 4615 is almost equal and AISI 1040 is less than AISI 4140 and Fig. 5a AISI 4340 is having the highest shear stress and AISI 4615 is having the lowest shear stress among these four materials. AISI 1040 is having the highest factor of safety among the others after optimization, AISI 4615 is the lowest among all the other materials, and AISI 1040 is having little less factor of safety than AISI 4340 before optimization (Fig. 5b). And AISI 4140 is having greater factor of safety than AISI 4615. The mass of the initial model for AISI 1040, AISI 4340, AISI 4140 and AISI 4615 is 1.554, 1555, 1.555 and 1.555 Kg, and after optimized model is reduced to 1.491, 1.492, 1492 and 1.492 kg.

4.1 Comparison of Results Before and After Optimization

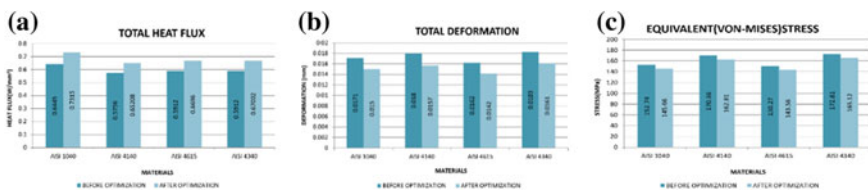


Fig. 4 Results for a total heat flux, b total deformation and c von Mises stress

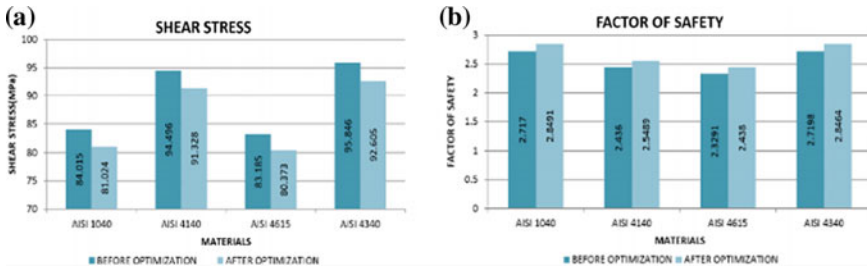


Fig. 5 Results for a shear stress and b factor of safety

5 Conclusion

It is observed that conducting the coupled steady-state thermal structural analysis shows total heat flux, total deformation, von Mises stresses, shear stress and factor of safety as per the known loading circumstances. Based on the coupled field analysis, additional material can be removed on the possible regions.

The high localized stress occurs at first near the bottom fillet region of crankpin, by increasing area by providing fillets in this region, problem can be solved. The second problem is during built-up; conventional manufacturing methods like casting, molding and forming are not feasible with the design. Meanwhile, additive manufacturing will give a better result. After parametric optimization, AISI 1040 reduced the weight of the crankshaft by 63 g from the 1554 g or intern of 4.054%. AISI 1040 is the best material for crankshaft which can sustain or withstand engine load cycles, based on the yield strength, von Mises stress and factor of safety for the optimized crankshaft design. Factor of safety for AISI 1040 is more as compared to other three materials, meaning that design is much stronger.

References

1. Satyanarayana K, Viswanath AK, Hanumanta Rao TV, Uma maheswara rao SV (2017) Investigation of the stresses induced in crankshaft AISI E4340 forged steel. In: 11th international symposium on plasticity and impact mechanics, vol 173. Procedia Engineering, pp 1672–1677
2. Montazersadgh FH, Fatemi A (2007) Stress analysis and optimization of crankshafts subject to dynamic loading. A final project report submitted to the Forging Industry Educational Research Foundation (FIERF) and American Iron and Steel Institute (AISI), The University of Toledo
3. Thirunavukkarasu G, Sriraman A (2016) Design optimization and analysis of crankshaft for light commercial vehicle. Indian J Sci Technol 9(36)
4. Kumar A, Jain PK, Pathak PM (2013) Reverse engineering in product manufacturing: an overview. DAAAM International Scientific Book, chapter 39, pp. 665–678
5. AZo Materials, AZo Network, AISI 1040 Carbon Steel (UNSG10400), 13 Sept 2012. <https://www.azom.com/article.aspx?ArticleID=6525>

Evaluation and Optimization of Surface Roughness and Metal Removal Rate Through RSM, GRA, and TOPSIS Techniques in Turning PTFE Polymers



N. Sathiya Narayanan, N. Baskar, M. Ganesan, M. P. Jenarthanan and S. Praveen

Abstract The performance of any component depends on the surface finish which helps in proper working of the assembly. To achieve the higher machining rate which gives the adequate surface finish is crucial. This research work is concentrated to find the optimum turning parameters which end up with higher metal removal rate and better surface finish for –polytetrafluoroethylene (PTFE) polymers which have broad applications in the field of petrochemical, electrical components, food and beverages, bearing pads and laboratory components. The Central composite response surface methodology based 31 number of pilot experiments conducted by considering the cutting speed (v), feed rate (f), depth of cut (a_p), and coolant flow rate (C_f) as input machining parameters. The analysis of variance is used to prove the adequacy of the quadratic regression model of output responses. Gray relational analysis (GRA) and Technique for Order of Preference by Similarity to Ideal Solution (TOPSIS) algorithm are used to get the optimum parameters, and the results are compared.

Keywords Response surface methodology · Desirability function · GRA · TOPSIS

1 Introduction

Selecting the machining parameters is considered to be the most important criteria in the manufacturing industry [1]. Experiments based on trial and error are the act of non-technical way of conducting the experiments and end up with time and cost consumption [2]. In order to meet the requirements of the customer and maximum utilization of the resources, the economic usage of machines is in high demand [3]. Sanci et al. [4] carried out turning operations on carbon-filled and glass fiber-filled PTFEs. Authors insisted that the fillers improve the mechanical properties but

N. Sathiya Narayanan (✉) · N. Baskar · M. Ganesan
Department of Mechanical Engineering, Saranathan College of Engineering, Trichy, India
e-mail: sathyasairam89@gmail.com

M. P. Jenarthanan · S. Praveen
School of Mechanical Engineering, SASTRA Deemed University, Tanjore, India

© Springer Nature Singapore Pte Ltd. 2019
S. S. Hiremath et al. (eds.), *Advances in Manufacturing Technology*,
Lecture Notes in Mechanical Engineering,
https://doi.org/10.1007/978-981-13-6374-0_65

also reduce the machinability of PTFEs. Tushar and Hemant [5] conveyed that the mechanical properties of some polymers are quite similar to conventional metals; therefore, the replacement of polymers in the particular field can be carried out. Xiao and Zhang [6] assessed the chip formation, cutting force, and surface roughness while machining thermosetting and thermoplastic kind of polymers. Authors conclude that the increase in cutting speed has a significant effect of rise in temperature between tool and workpiece interactions but improves the surface roughness. Davim and Mata [7] carried out turning experiments in PA 6 and PA66 polymer materials with cutting insert of cemented carbide. The cutting force values of PA 66 polymers are comparatively higher in range for turning PA 6 polymers. Fetecau and Stan [8] investigated the turning parameters of PTFE composites using PCD diamond tool for cutting force and surface integrity. Oktem et al. [9] modeled and optimized the milling parameters of POMC to obtain minimum surface integrity using artificial neural network model. Ansari [10] considered cutting force and surface roughness for optimizing the turning parameters of PTFE filled with MoS_2 bronze. Authors used Taguchi method and GRA for modeling and optimization. Sanjeev Kumar [11] achieved the minimum surface roughness while machining PTFE using a genetic algorithm to find the optimal solution. Yadav [12] carried out duplex turning on alloy steel with conventional high-speed steel as a cutting tool. Taguchi–RSM hybrid plan of experiments is conducted by considering cutting velocity, feed rate, primary and secondary depths of cut as turning parameters. Results show that the hybrid approach showed major improvement in surface roughness than Taguchi design of experiments. Salmasnia et al. [13] used DF-neuro-fuzzy logic hybrid technique for multi-response optimization. Ray [14] compared the GA, SA, and Tabu search results for the multi-response optimization of CNC grinding parameters. Experiments were carried out in RSM-DF plan of experiments. Chabbi et al. [15] determined the optimum turning parameters for polyoxymethylene polymer POM C using RSM desirability function. Authors considered the minimization of surface roughness, cutting force and power consumption and maximization of metal removal. They reached the multi-objective optimization desirability value of 91.5% for the combined output response by optimizing the V_c , f , and a_p . In this context, researches were carried out for many works for the optimization of turning and other machining parameters on different workpiece and tool insert combinations. Comparative studies in the usage of semi-synthetic coolant and optimization of coolant flow rate are very limited in machining of PTFE polymer materials. In this research, work is focused on optimizing the turning parameters (V_c, f, a_p, C_f) with metal removal rate (MRR), surface roughness (Ra), cutting force (Fc), and power consumption (Pc) for turning PTFE polymer material with carbide cutting insert by considering the semi-synthetic RATAK Soluble 10 as cutting fluid.

2 Experimental Details

PTFE polymer materials having good corrosion resistance and low friction coefficient make it possible to be used in mass production industries. Carbide insert

Table 1 Machining parameters in various levels

Levels	V (m/min)	f (mm/rev)	a_p (mm)	C_f (lpm)
-2	31.5	0.1	0.1	0.358
-1	63	0.15	0.2	0.66
0	94.5	0.2	0.3	0 (Dry)
1	126	0.25	0.4	0.261
2	157.5	0.3	0.5	1.45

(CNMG120408), and a tool holder (CSDPN 2525M12) of positive rake angle is used for turning 31 number of experiments suggested by the response surface methodology central composite design. Table 1 shows the four factors (cutting speed, feed, depth of cut, and coolant flow rate) considered at five different levels. The machining is carried out in CNC turning center controlled by FANUC system with the initial dimensions of $\phi 25$ mm and turned for 40 mm. The weight of the before and after machining workpieces is measured using AUX 220 digital weighing machine to find the metal removal rate. Mitutoyo Surf tester SJ-210 is used for measuring the surface roughness of the turned workpieces at three different areas, and the average is considered.

3 Results and Discussion

3.1 Analysis of Variance and Effect of Parameters

Table 2 shows the experimental results based on the design of experiments. Tables 3 and 4 shows that the models were significant and the individual and interaction effect of the parameters for MRR and surface roughness. Further, the regression coefficient values (R^2) are high and close to 1. R^2 values of 0.9541 and 0.9444 are obtained for surface roughness and metal removal rate. Equations (1) and (2) are the regression equations for the metal removal rate and surface roughness.

$$\begin{aligned}
 \text{MRR} = & +0.21 + 0.025^*A + 0.071^*B + 9.527E - 003^*C - 0.014^*D \\
 & + 3.277E - 003^*A^*B + 0.012^*A^*C - 0.023^*A^*D \\
 & + 0.010^*B^*C - 0.012^*B^*D - 6.819E - 003^*C^*D + 0.013^*A^2 \\
 & + 0.014^*B^2 - 4.304E - 003^*C^2 + 5.975E - 003^*D^2
 \end{aligned} \tag{1}$$

$$\begin{aligned}
 \text{Ra} = & +3.06 + 0.013^*A + 0.52^*B - 0.022^*C \\
 & - 0.47^*D - 0.020^*A^*B + 0.051^*A^*C - 0.17^*A^*D \\
 & - 0.10^*B^*C + 0.14^*B^*D - 0.11^*C^*D + 1.1321^*A^2 \\
 & - 0.3711^*B^2 - 0.40145^*C^2 + 0.10154^*D^2
 \end{aligned} \tag{2}$$

Table 2 Experimental results based on the design of experiments

Exp no	Machining parameters				Responses	
	Vc (m/min)	f (mm/rev)	a _p (mm)	C _f (lpm)	Ra (μm)	MRR (g/s)
1	63	0.15	0.2	0.261	2.5850	0.1091
2	126	0.15	0.2	0.261	3.0907	0.1441
3	63	0.25	0.2	0.261	3.7453	0.2614
4	126	0.25	0.2	0.261	4.1553	0.3305
5	63	0.15	0.4	0.261	2.7820	0.1588
6	126	0.15	0.4	0.261	3.4473	0.1905
7	63	0.25	0.4	0.261	3.4147	0.3707
8	126	0.25	0.4	0.261	3.5760	0.4143
9	63	0.15	0.2	0.66	3.7880	0.1724
10	126	0.15	0.2	0.66	2.7657	0.1827
11	63	0.25	0.2	0.66	4.6957	0.2523
12	126	0.25	0.2	0.66	4.5710	0.2334
13	63	0.15	0.4	0.66	2.6983	0.1422
14	126	0.15	0.4	0.66	2.8877	0.1592
15	63	0.25	0.4	0.66	4.2887	0.2662
16	126	0.25	0.4	0.66	3.8543	0.3436
17	31.5	0.2	0.3	0	2.6600	0.1819
18	157.5	0.2	0.3	0	4.2473	0.5104
19	94.5	0.1	0.3	0	2.8140	0.1402
20	94.5	0.3	0.3	0	3.6527	0.5533
21	94.5	0.2	0.1	0	2.6603	0.2251
22	94.5	0.2	0.5	0	3.5737	0.3252
23	94.5	0.2	0.3	0.358	3.3777	0.2798
24	94.5	0.2	0.3	1.45	3.2713	0.2805
25	94.5	0.2	0.3	0	4.7927	0.2802
26	94.5	0.2	0.3	0	4.6080	0.2684
27	94.5	0.2	0.3	0	4.6367	0.2596
28	94.5	0.2	0.3	0	4.6497	0.2893
29	94.5	0.2	0.3	0	4.7427	0.2617
30	94.5	0.2	0.3	0	4.6483	0.2812
31	94.5	0.2	0.3	0	4.8177	0.2848

Table 3 Analysis of variance results for MRR

Source	SS	DF	MS	F value	P value	Remarks*
					Prob > F	
Model	0.2737	14	0.0196	10.7699	<0.0001	Yes
A	0.0417	1	0.0417	23.1667	0.0227	Yes
B	0.0916	1	0.0916	50.4316	<0.0001	Yes
C	0.0584	1	0.0584	32.4444	0.0007	Yes
D	0.0155	1	0.0155	8.5227	0.01	Yes
AB	0.0002	1	0.0002	0.0946	0.7623	No
AC	0.0022	1	0.0022	1.1845	0.2926	No
AD	0.0237	1	0.0237	13.042	0.0023	Yes
BC	0.0017	1	0.0017	0.9223	0.3512	No
BD	0.0068	1	0.0068	3.7276	0.0714	No
CD	0.0021	1	0.0021	1.1375	0.302	No
A ²	0.0048	1	0.0048	2.6671	0.122	No
B ²	0.0049	1	0.0049	2.7262	0.1182	No
C ²	0.0005	1	0.0005	0.2735	0.6082	No
D ²	0.0169	1	0.0169	9.3326	0.0076	Yes
Error	0.029	16	0.0018	0.909	0.3546	No
Total	0.3028	30				

*Remarks for significance

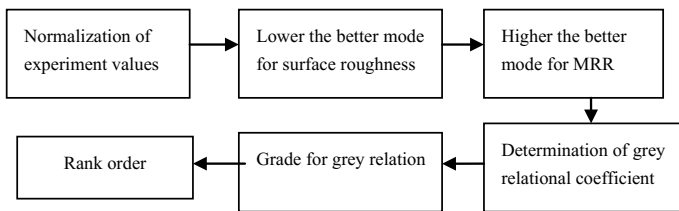


Fig. 1 Process flow of gray relational analysis

3.2 GRA Analysis

GRA approach is used to transform the multi-objective problems to a single objective function. Figure 1 shows the process flow of the gray relational analysis. Table 5 represents the normalized data and gray grade ranks. Higher the gray grade provides better multi-objective optimum parameters. Table 5 and Fig. 2 shows that, the experiment number 20 (gray grade = 0.7556, $v = 94.5$ m/min, $f = 0.30$ m/min, $a_p = 0.3$ mm) is the optimum values to achieve better surface finish with higher metal removal.

Table 4 Analysis of variance results for surface roughness

Source	SS	DF	MS	F value	P value	Remarks*
					Prob > F	
Model	17.9174	20	0.8959	64.088	<0.0001	Yes
A	0.0029	1	0.0029	0.207	0.6587	No
B	4.8940	1	4.8940	350.107	<0.0001	Yes
C	0.0011	1	0.0011	0.075	0.7892	No
D	2.9333	1	2.9333	209.840	<0.0001	Yes
AB	0.0066	1	0.0066	0.474	0.5067	No
AC	0.0413	1	0.0413	2.955	0.1163	No
AD	1.3523	1	1.3523	96.740	<0.0001	Yes
BC	0.1640	1	0.1640	11.729	0.0065	Yes
BD	0.8255	1	0.8255	59.052	<0.0001	Yes
CD	0.1881	1	0.1881	13.459	0.0043	Yes
A ²	1.5912	1	1.5912	113.831	<0.0001	Yes
B ²	3.5589	1	3.5589	254.593	<0.0001	Yes
C ²	0.5290	1	0.5290	37.843	<0.0001	Yes
D ²	1.2748	1	1.2748	91.199	<0.0001	Yes
Error	0.1398	10	0.0140	3.501	0.0837	No
Total	18.0572	30				

*Remarks for significance

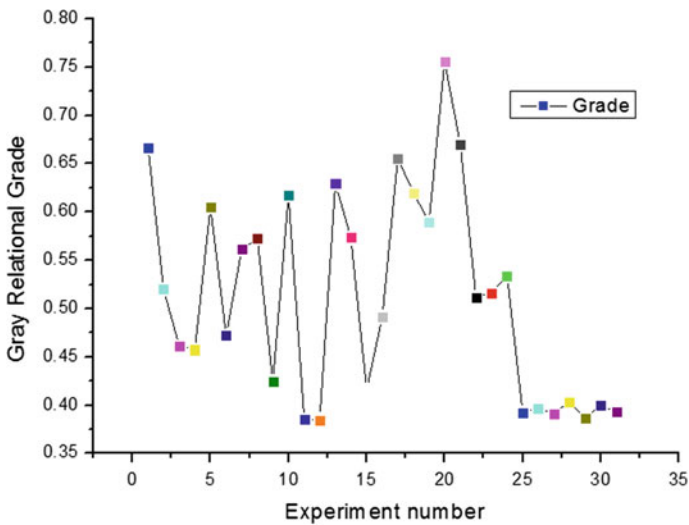


Fig. 2 Gray relational grade at the respective experiments

Table 5 Gray relational coefficients and gray grades of conducted experiments

Exp. No.	Gray relational coefficient		Gray relational grade	Rank
	Ra	MRR		
1	1	0.3333	0.6667	3
2	0.6882	0.3518	0.52	14
3	0.4903	0.4321	0.4612	19
4	0.4155	0.4992	0.4574	20
5	0.85	0.3602	0.6051	8
6	0.5642	0.3797	0.4719	18
7	0.5736	0.5488	0.5612	12
8	0.5297	0.6151	0.5724	11
9	0.4813	0.3683	0.4248	21
10	0.8607	0.3747	0.6177	7
11	0.3459	0.4246	0.3853	30
12	0.3598	0.4097	0.3848	31
13	0.9079	0.3507	0.6293	5
14	0.7867	0.3604	0.5736	10
15	0.3959	0.4361	0.416	22
16	0.4679	0.5144	0.4912	17
17	0.937	0.3742	0.6556	4
18	0.4018	0.838	0.6199	6
19	0.8298	0.3496	0.5897	9
20	0.5111	1	0.7556	1
21	0.9368	0.4036	0.6702	2
22	0.5303	0.4933	0.5118	16
23	0.5848	0.4481	0.5164	15
24	0.6193	0.4488	0.534	13
25	0.3358	0.4485	0.3922	27
26	0.3556	0.438	0.3968	25
27	0.3524	0.4306	0.3915	28
28	0.3509	0.4568	0.4039	23
29	0.341	0.4324	0.3867	29
30	0.3511	0.4494	0.4003	24
31	0.3333	0.4527	0.393	26

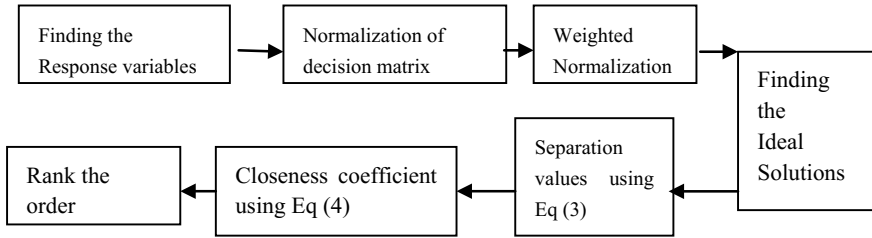


Fig. 3 Process flow of technique for order of preference by similarity to ideal solution

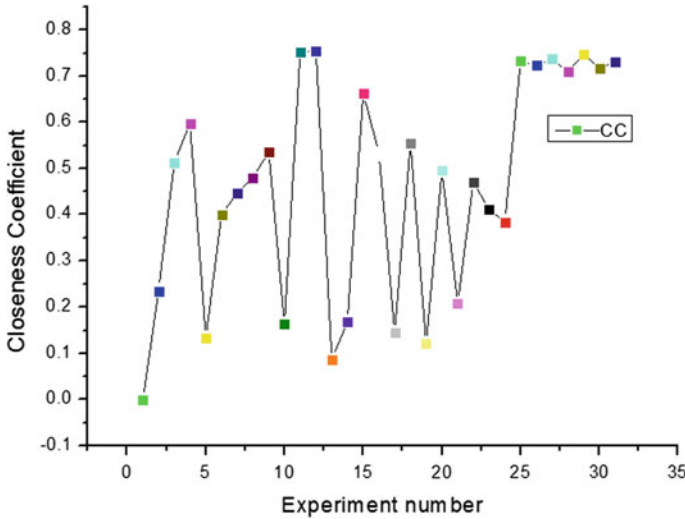


Fig. 4 Closeness coefficients at the respective experiments

3.3 Technique for Order of Preference by Similarity to Ideal Solution (TOPSIS)

The weighted normalized values are calculated by considering the equal weights for all the responses. Figure 3 shows the process flow of the TOPSIS algorithm. Separation measures and closeness coefficient are found out with Eqs. (3), (4), and (5). Table 6 provides the rank order based on TOPSIS approach. It is found out that the experiment number 12 obtained the highest rank ($v = 126.5$ m/min, $f = 0.25$ m/min, $a_p = 0.2$ mm, $C_f = 0.66$ lpm) and is considered to be optimum solutions for achieving the multi-objectives. Figure 4 depicts the graph between the closeness coefficients with the respective experiment numbers.

Table 6 TOPSIS separation measure and closeness coefficients

Exp. No.	Weighted normalized data		Separation measures		Closeness coefficient	Rank
	Ra	MRR	Si*	Si	CC _i	
1	0.5000	0.0000	0.7071	0.0000	0.0000	31
2	0.3868	0.0394	0.3888	0.1199	0.2357	23
3	0.2402	0.1714	0.2951	0.3113	0.5134	15
4	0.1483	0.2492	0.2900	0.4310	0.5978	11
5	0.4559	0.0559	0.4593	0.0712	0.1342	28
6	0.3069	0.0916	0.3203	0.2137	0.4002	21
7	0.3142	0.2945	0.4306	0.3482	0.4471	19
8	0.2781	0.3436	0.4420	0.4090	0.4806	17
9	0.2306	0.0712	0.2414	0.2787	0.5359	13
10	0.4595	0.0828	0.4669	0.0922	0.1649	26
11	0.0273	0.1612	0.1635	0.4994	0.7534	2
12	0.0552	0.1399	0.1504	0.4662	0.7561	1
13	0.4746	0.0372	0.4761	0.0450	0.0864	30
14	0.4322	0.0564	0.4359	0.0882	0.1682	25
15	0.1185	0.1768	0.2128	0.4205	0.6640	10
16	0.2157	0.2640	0.3409	0.3879	0.5322	14
17	0.4832	0.0819	0.4901	0.0836	0.1457	27
18	0.1277	0.4517	0.4694	0.5853	0.5550	12
19	0.4487	0.0349	0.4501	0.0620	0.1212	29
20	0.2609	0.5000	0.5640	0.5542	0.4956	16
21	0.4831	0.1306	0.5005	0.1317	0.2083	24
22	0.2786	0.2432	0.3698	0.3289	0.4707	18
23	0.3225	0.1921	0.3754	0.2616	0.4107	20
24	0.3463	0.1929	0.3964	0.2467	0.3836	22
25	0.0056	0.1926	0.1927	0.5306	0.7336	5
26	0.0470	0.1793	0.1853	0.4872	0.7245	7
27	0.0405	0.1694	0.1741	0.4897	0.7377	4
28	0.0376	0.2028	0.2062	0.5049	0.7100	9
29	0.0168	0.1718	0.1726	0.5128	0.7482	3
30	0.0379	0.1937	0.1974	0.5010	0.7174	8
31	0.0000	0.1977	0.1977	0.5377	0.7311	6

$$S_i^+ = \sqrt{\sum_{i=1}^n (v_{ij} - v_j^+)^2} \quad (3)$$

$$S_i^- = \sqrt{\sum_{i=1}^n (v_{ij} - v_j^-)^2} \quad (4)$$

$$CC_i = \frac{S_i^-}{S_i^+ + S_i^-} \quad (5)$$

where $i = 1, 2, 3, \dots, n$.

4 Inferences and Conclusion

Modeling, prediction, and multi-objective optimization of parameters for turning PTFE polymer in order to minimize the Ra and maximize the MRR are considered in the work. From the works carried out, the following conclusions were drawn. The quadratic regression model shows the significance, and the correlation coefficient (R^2) for surface roughness and metal removal rate was obtained as 0.9541 and 0.9444. ANOVA is used to find the effect of individual and combined effects of machining parameters. For the metal removal rate and surface roughness, the feed rate is most significant followed by the other individual and interaction effects. From gray relational analysis (GRA), the parameters $v = 94.5$ m/min, $f = 0.30$ m/min, $a_p = 0.3$ mm and $C_f = 0$ lpm are to be maintained for the optimum results. According to TOPSIS algorithm, $v = 126.5$ m/min, $f = 0.25$ m/min, $a_p = 0.2$ mm, $C_f = 0.66$ lpm are the optimum values for achieving the multi-objective. GRA and TOPSIS algorithm approaches are used for the optimization which are the experimentally and analytically proven methods for achieving the multi-objectives.

References

1. Raja SB, Narayanan NS, Pramod CVS (2012) Optimization of constrained machining parameters in turning operation using firefly algorithm. *J Appl Sci* 12:1038–1042
2. Raja SB, Baskar N (2012) Application of particle swarm optimization technique for achieving desired milled surface roughness in minimum machining time. *Expert Syst Appl* 39:5982–5989
3. Raja SB, Baskar N (2010) Investigation of optimal machining parameters for turning operation using intelligent techniques. *Int J Mach Mater* 8:146–166
4. Sanci Me, Halis S, Kaplan Y (2017) Optimization of machining parameters to minimize surface roughness in the turning of carbon-filled and glass fiber-filled polytetrafluoroethylene. *Mater Des Appl* 65:295–305
5. Tushar UJ, Hemant AM (2015) Machining of plastics: a review. *Int J Eng Gen Sci* 3:577–581
6. Xiao KO, Zhang LC (2002) The role of viscous deformation in the machining of polymers. *Int J Mech Sci* 44:2317–2336

7. Davim JP, Mata F (2007) A comparative evaluation of the turning of reinforced and unreinforced polyamide. *Int J Adv Manuf Technol* 33:911–914
8. Fetecau C, Stan F (2012) Study of cutting force and surface roughness in the turning of polytetrafluoroethylene composites with a polycrystalline diamond tool. *Measurement* 45:1367–1379
9. Oktem H, Erzurumlu T, Erzincanli F (2006) Prediction of minimum surface roughness in end milling mold parts using neural network and genetic algorithm. *Mater Des* 27:735–744
10. Ansari MS, Sharma D, Nikam S (2014) Study of cutting forces and surface roughness in turning of bronze filled polytetrafluoroethylene. *Int J Adv Mech Eng* 4(2):151–160
11. Sanjeev kumar M, Kaviarasan V, Venkatesan R (2012) Machining parameter optimization of PTFE using genetic algorithm. *Int J Mod Eng Res* 2(1):143–149
12. Yadav RN (2017) A hybrid approach of Taguchi-response surface methodology for modeling and optimization of duplex turning process. *Measurement* 100:131–138
13. Salmasnia A, Kazemzadeh RB, Tabrizi MM (2012) A novel approach for optimization of correlated multiple responses based on desirability function and fuzzy logics. *Neurocomputing* 91:56–66
14. Mukherjee I, Ray PK (2008) Optimal process design of two-stage multiple responses grinding processes using desirability functions and metaheuristic technique. *Appl Soft Comput* 8:402–421
15. Chabbi A, Yaltese MA, Meddour I, Nouioua M, Mabrouki T, Girardin F (2017) Predictive modeling and multi-response optimization of technological parameters in turning of polyoxymethylene polymer (POM C) using RSM and desirability function. *Measurement* 95:99–115

Effect of Sintering Temperature on the Microstructure and Forming Behavior of AA8079 (Al–Cu–Fe–Si–Zn)



M. Meignanamoorthy, M. Ravichandran, A. Elmariung
and S. Dinesh Kumar

Abstract In this study, an attempt has been made to examine the influence of sintering temperature on the microstructure and forming behavior of AA8079 synthesized through powder metallurgy route. The AA8079 powders were milled using high-energy ball mill. The green compacts were prepared using suitable punch and die by applying a compaction pressure of 400 MPa using hydraulic press. The green compacts were sintered at three different temperatures 400, 500, and 600 °C. The sintering was done with the aid of electric muffle furnace under the controlled atmosphere. The sintered samples were subjected to microstructure analysis by using a scanning electron microscope (SEM). The cold upset tests were conducted in stages of 10 kN and the true axial stress, the true hoop stress, the true hydrostatic stress, and the true effective stresses were identified, and their behavior besides the true axial strain was systematically investigated.

Keywords Aluminum · Alloys · Sintering · Forming behavior

1 Introduction

Powder metallurgy is a familiar method to fabricate metal matrix composites with homogenous dissemination of the reinforcements [1]. Aluminum alloy possesses tremendous applications in the field of aerospace and automobile industries due to

M. Meignanamoorthy · A. Elmariung
Department of Mechanical Engineering, Mother Teresa College of Engineering Technology,
Pudukkottai 622102, India

M. Ravichandran (✉)
Department of Mechanical Engineering, K.Ramakrishnan College of Engineering,
Tiruchirappalli 621112, Tamil Nadu, India
e-mail: smravichandran@hotmail.com

S. Dinesh Kumar
Department of Mechanical Engineering, Chendhuran College of Engineering and Technology,
Pudukkottai 622507, Tamil Nadu, India

their superior mechanical properties such as tensile strength, relative density, ductility properties, formable feasibility, workability, wear properties, and corrosion resistance [2]. Aluminum and its alloys with their intrinsic properties of lightweight mixed with high specific strength have their extensive area of applications [3]. Several types of research have been focused on the fabrication of aluminum alloys through powder metallurgy route due to the easy fabrication of parts with net shape with reasonable cost [4]. Umasankar et al. investigated the consequence of sintering temperature and time on SiC-reinforced AA6061 composites [5]. Mehdi Rahimian et al. studied the effect of production parameters on microstructure of Al–Al₂O₃ composite and reported that sintering temperature reduces the porosity, and sintering time increases the grain area [6]. Ravichandran et al. described that increasing the sintering time and temperature leads to the homogenous distribution of reinforcement particle with the matrix material [7]. Gokce et al. synthesized the Al–Cu–Mg via powder metallurgy route and investigated their microstructure [8]. Perianayagam et al. studied the sintering behavior of iron–carbon–copper compacts [9]. Balamurugan investigated the effect of process parameters on Cu–fly ash composite and reported that an increase in sintering temperature results in increased strength and improved wear resistance [10]. Ravichandran investigated the forming characteristics of Al–TiO₂ powder metallurgy composites through cold upsetting under plane stress state conditions and reported that the accumulation of TiO₂ reinforcement to the Al matrix material leads to rises in strength coefficient (K) and decreases the strain hardening index (n) [11]. Anandakrishnan et al. studied the forming behavior of in situ AA7075–TiC composites, and several stress parameters were estimated [12]. Narayanasamy et al. [13] examined the strain hardening behavior in three dimensions of Al–Fe powder metallurgy composite through cold upsetting. Ramesh et al. investigated the workability studied on Al–20% SiC powder metallurgy composites during cold upsetting. It was concluded that stress ratio parameters ($\sigma_{\theta}/\sigma_{\text{eff}}$) greater for Al–SiC composites compared to pure Al and (σ_z/σ_m) decreases for Al–SiC composites compared to pure Al [14]. Ravichandran et al. [15] studied the hot upset studies on sintered (Al–TiO₂–Gr) powder metallurgy hybrid composite and concluded that maximum true axial stress and minimum axial strain attained for hybrid composite preforms are greater than those witnessed in unreinforced Al preforms. Hence, the present work aims to synthesize AA8079 through the powder metallurgy technique. The effect of three different levels of sintering temperature on microstructure and forming behavior was analyzed and reported. Most of the researchers investigated the mechanical properties of the synthesized material. Limited work has been conducted on an effect of sintering temperature on the forming behavior of Al alloys. Henceforth, this research work made an effort to analyze the effect of sintering temperature on the microstructure and forming behavior of AA8079.

2 Experimental Details

Aluminum powder of particle size less than $350\ \mu\text{m}$ with 99.5% purity was used as a matrix material, and the elemental powders such as copper, iron, silicon, zinc, and magnesium of particle size less than $20\ \mu\text{m}$ with 99% purity are shown in Fig. 1. The AA8079 alloy powders were exactly weighted using an electronic weighing machine. The powders were milled using ball mill. The speed of the drum was 120 rpm, and the milling was carried out for a time period of 15 h. The 5-mm-diameter steel ball was used. The ball-to-powder ratio was 10:1. The SEM image of the AA8079 is shown in Fig. 1. The milled powders were compacted into cylindrical billets of diameter 20 mm and height 10 mm by using suitable punch and die. The essential pressure was applied using hydraulic press of 200 kN capacities hydraulic press as shown in Fig. 1. To avoid friction between punch and die, graphite was used as a lubricant. The green compacts were sintered in an electric muffle furnace at three different temperatures 400, 500, and 600 °C as shown in Fig. 1. After completed the sintering process, the sintered compacts were kept in the furnace for furnace cooling by switching off the furnace. Microstructure examination was carried out on the sintered samples by using scanning electron microscope. Cylindrical samples were fabricated with customary measurements of initial diameter (D_0) of 24 mm and height of 12 mm to provide an aspect ratio of 0.5. Further, the sample is exposed to traditional compression test at

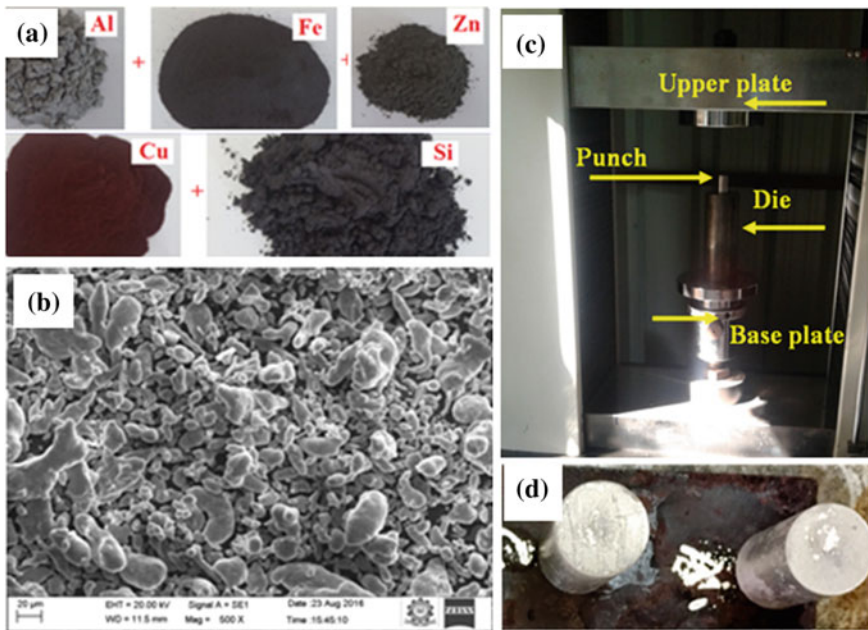


Fig. 1 a Images of Al, Fe, Cu, Si, and Zn, b SEM image of AA8079, c compaction process setup, and d sintered samples

room temperature with an additional compressive load step of 10 kN. The upsetting of the sample was carried out between two flat, mirror finished open dies on a 50 kN capacity universal testing machine. The deformation was conducted till the presence of first peripheral shear crack on the free surface. In order to get a fairly uniform deformation, graphite lubricant was smeared on both sides of the die contact surfaces during cold deformation, which also confirmed the entire least friction state. The true axial stresses, true hoop stress, true hydrostatic stress, true effective stress and true axial strain was calculated from the upsetting test.

3 Results and Discussions

Figure 2a–c shows the microstructure of AA8079 sintered at various temperatures such as 400, 500, and 600 °C. Figure 2a shows the SEM image of the AA8079 sintered at 400 °C. It shows some pores, and it is expected for the materials produced via powder metallurgy route by using various alloying elements. It is evident that 400 °C temperature is not sufficient to sinter the AA8079. From Fig. 2b, some improvement can be clearly seen, and little amount of pores has been observed due to an increase in sintering temperature. From Fig. 2c, it is clearly understood that pores have been eliminated when increasing the sintering temperature from 400 to 600 °C. It could be understood that increase in the temperature pores can be reduced due to the proper diffusion of surfaces along grain boundaries. The reason is that the increase in sintering temperature enhances the sufficient sintering cycle. The bonding between the particles enlarges and merges during high-temperature sintering process. Here, the presence of Zn is melted during this temperature and infiltrated in between the pores. During sintering, the initial point contact of particles and early stage of neck formation is possible for the sintering at high temperatures.

The variations of true axial stress with reference to true axial strain of AA8079 sintered at different temperatures are shown in Fig. 3. It is apparent that AA8079 sintered at 400 °C exhibits the lowest true axial stress for any true axial strain. The increase in sintering temperature from 400 to 500 °C increases the true axial stress for the true axial strain. The raise in sintering temperature reduces the deformation

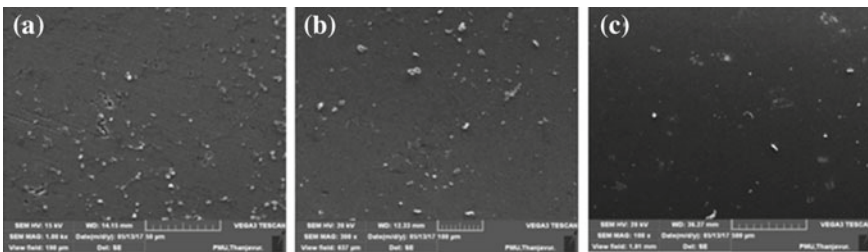


Fig. 2 SEM images of alloy sintered at different temperatures **a** 400 °C, **b** 500 °C, and **c** 600 °C

Fig. 3 True axial stress versus true axial strain

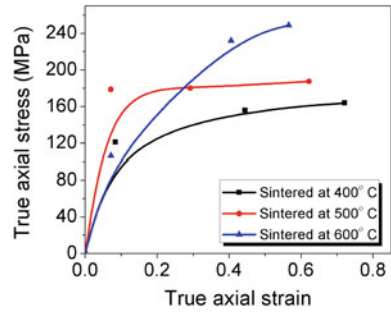
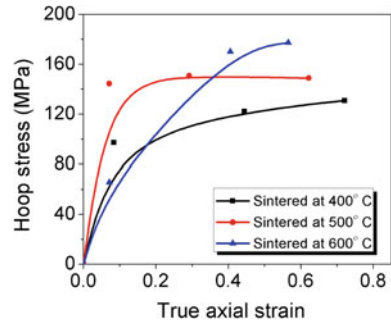


Fig. 4 True hoop stress versus true axial strain



due to work hardening effect and also reduces the pore size of the AA8079 preforms. The increase in sintering temperature from 500 to 600 °C increases the true axial stress for a given true axial strain. The reason for the increase in true axial stress is the existence of elemental particles that ultimately conquer the pores thus making further applied load essential for deforming through cold upsetting [11]. The increased sintering temperature increases the densification of the preforms and leads to good microstructure as shown in Fig. 2c. The improved microstructure definitely increases the strength of the materials. Here, the preforms sintered at 600 °C resist the applied compressive load, and the induced axial stress is high for the sample. As discussed earlier in microstructure, the bonding between the particles is good when the preforms are sintered at high temperature and this is also one of the reasons to increase the strength of the alloy [7]. The relationships between true hoop stress and true axial strain for AA8079 preforms sintered at 400, 500, and 600 °C are shown in Fig. 4. The AA8079 preforms sintered at 600 °C display the highest true hoop stress among the samples tested, whereas in the case of preforms sintered at 400 °C, true hoop stress is the lowest owing to the presence of larger pore sizes. It is detected that increasing the sintering temperature from 500 to 600 °C increases the strength of the AA8079 preforms [12].

The interactions between true hydrostatic stress and true axial strain for AA8079 preforms sintered at 400, 500, and 600 °C are shown in Fig. 5. The extreme true hydrostatic stress was attained for the preforms sintered at 600 °C and the minimum for the preforms sintered at 400 °C. AA8079 preforms sintered at 500 °C fall in

Fig. 5 True hydrostatic stress versus true axial strain

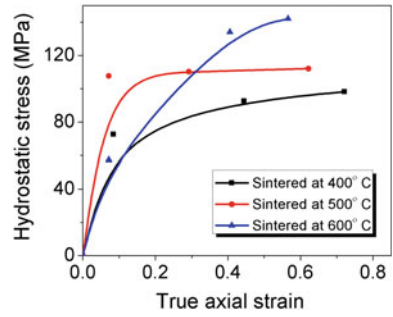
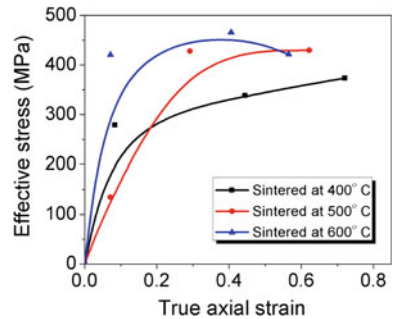


Fig. 6 True effective stress versus true axial strain



between the preforms sintered at 400 °C and 600 °C. It is also detected that true hydrostatic stress increases with small increases in true axial strain. The interactions between true effective stress and true axial strain for AA8079 preforms sintered at 400, 500, and 600 °C are shown in Fig. 6. The extreme true hydrostatic stress was attained for the preforms sintered at 600 °C, and slightly it falls down at 500 °C. The same behavior was attained for the true hydrostatic stress.

4 Conclusion

The aluminum alloy (AA8079) has been successfully synthesized via powder metallurgy route, and the effect of sintering temperature on the microstructure and forming behavior was analyzed, and the following conclusions are drawn: The microstructure analysis results revealed that increase in sintering temperature leads to the reduction in pores. The maximum true axial stresses, true hoop stress, true hydrostatic stress, true effective stress, and true axial strain were obtained for the samples sintered at 600 °C. The increase in true axial stresses, true hoop stress, true hydrostatic stress, and true effective stress was observed for the increase in sintering temperature for all the true axial strain. The future work will be carried out to investigate the effect of other PM parameters on the microstructure and forming behavior of AA8079.

References

1. Ravichandran M, Manikandan A, Omkumar MS (2016) Investigations on properties of Al-B₄C composites synthesized through powder metallurgy route. In: Applied Mechanics and Materials 852:93–97 (2016)
2. Ashwath P (2016) Xavier MA (2016) Processing methods and property evaluation of Al₂O₃ and SiC reinforced metal matrix composites based on aluminium 2xxx alloys. J Mater Res 31(9):1201–1219
3. Dhadsanadhep C, Luangvaranunt T, Umeda J, Kondoh K (2008) Fabrication of Al/Al₂O₃ composite by powder metallurgy method from aluminium and rice husk ash. J Metals, Mater Miner 18(2):99–102
4. Solay Anand S, Mohan B (2012) Effect of particle size, compaction pressure on density and mechanical properties of elemental 6061Al alloy through powder metallurgical process. Int J Mater Eng Innovation 3(4):259–268
5. Umasankar V (2014) Experimental evaluation of the influence of processing parameters on the mechanical properties of SiC particle reinforced AA6061 aluminium alloy matrix composite by powder processing. J Alloy Compd 582:380–386
6. Rahimian M, Parvin N, Ehsani N (2011) The effect of production parameters on microstructure and wear resistance of powder metallurgy Al–Al₂O₃ composite. Mater Design 32(2):1031–1038
7. Ravichandran M, Anandkrishnan V (2015) Optimization of powder metallurgy parameters to attain maximum strength coefficient in Al–10 wt% MoO₃ composites. J Mater Res 30(15):2380–2387
8. Gokce A, Findik F, Kurt AO (2011) Microstructural examination and properties of premixed Al–Cu–Mg powder metallurgy alloy. Mater Charact 62:730–735
9. Perianayagam P-D-AR, Kichenaradjao P, Alluru GK (2016) Sintering studies on Iron- Carbon-Copper Compacts. Sci Sintering 48:237–246
10. Balamurugan P, Uthayakumar M (2015) Influence of process parameters on Cu-Fly ash composite by powder metallurgy technique. Mater Manuf Proc 30(3):313–319
11. Ravichandran M, Naveen Sait A, Anandkrishnan V (2014) Synthesis and forming characteristics of Al–TiO₂ powder metallurgy composites during cold upsetting under plane stress state conditions. J Sandwich Struct Mater 17(3):278–294
12. Anandkrishnan V, Baskaran S, Sathish S (2013) Synthesis and forming behavior of In-Situ AA 7075-TiC composites. Adv Mater Res 651:251–256
13. Narayanasamy R, Ramesh T, Pandey KS (2006) Some aspects on strain hardening behaviour in three dimensions of Aluminium-Iron powder metallurgy composite during cold upsetting. Mater Des 27:640–650
14. Ramesh T, Prabhakar M, Narayanasamy R (2010) Workability studies on Al-20%SiC powder metallurgy composites during cold upsetting. Adv Prod Eng Manag 5(1):33–44
15. Ravichandran M, Anandkrishnan V (2016) Hot upset studies on sintered (Al–TiO₂–Gr) powder metallurgy hybrid composite. Strength Mater 48(3):450–459

Studies on the Influence of Welding Parameters in Cladding of ERNiCrMo-10 on AISI 4140 Using GMAW Process



G. Britto Joseph, T. N. Valarmathi, G. Mageshwaran, Jeya Jeevahan, V. Sriram and R. B. Durai Raj

Abstract Welding process parameters and the interaction between them show a major effect on the clad bead shape. This work focuses on an experimental study of clad bead shapes and analyzes the interaction between the welding process parameters by depositing ERNiCrMo-10 cladding on AISI 4140 steel by gas metal arc welding (GMAW) process. The experiment is performed with three factors and three levels, and mathematical models are developed using the response surface methodology (RSM), and the adequacy is checked using ANOVA. The model developed using RSM is analyzed using interaction surface plots.

Keywords Clad bead geometry · ERNiCrMo-10 · AISI 4140

1 Introduction

Steel structures are widely used for many industrial applications. During working, these structures are affected by corrosion and wear leading to a reduction in the strength. Hence, preventing these problems is very much important. Although eliminating corrosion fully is not possible, it can be brought down to some levels by applying some mechanical processes such as weld cladding. This practice can be efficiently used to facilitate the improvement in the life of constituents and to minimize the cost. Recently, weld cladding techniques are flourished hastily and used in several fields such as food processing and petrochemical industries [1]. Many welding processes such as GMAW and oxyacetylene are used for making cladding. Nowadays, GMAW is widely used in industries for almost all applications. The strength of the clad metal depends upon the composition and shape [2]. Bead geometry is indicated by the shape of the bead, and the accurate clad bead geometry depends upon the current, arc voltage, etc.

G. B. Joseph (✉) · T. N. Valarmathi · G. Mageshwaran · J. Jeevahan · V. Sriram · R. B. Durai Raj
School of Mechanical Engineering, Sathyabama Institute of Science and Technology, Chennai,
India
e-mail: britto619@yahoo.co.in

© Springer Nature Singapore Pte Ltd. 2019
S. S. Hiremath et al. (eds.), *Advances in Manufacturing Technology*,
Lecture Notes in Mechanical Engineering,
https://doi.org/10.1007/978-981-13-6374-0_67

This research work investigates the relationship between the welding process parameters through the experimental work and the mathematical models developed in cladding using ERNiCrMo-10 on AISI 4140 steel by GMAW process. The experiment is performed with 3 levels and 3 factors, and the mathematical model is derived using RSM method. The derived mathematical models are tested for their competence and connotation.

2 Experimental Work

The experiments are performed using a THYRO μ P 400 using DC electrode positive. Specimens of size $200 \times 100 \times 15$ mm are cut and the scales and dirt are cleaned before cladding. Keeping the base metal as AISI 4140, the weld beads are made using ERNiCrMo-10 solid filler wire of diameter 1.6 mm. The composition of AISI 4140 and ERNiCrMo-10 filler wire is presented in Tables 1 and 2. Argon and O₂ mixture is supplied for shielding. The experiments are performed by laying a single bead using the stringer bead technique. Current, welding speed and nozzle-to-plate distance are considered as inputs and welded bead width, depth of penetration, and height of reinforcement are studied as outputs. After conducting trial runs, working range is fixed by changing one of the parameters and keeping others constant [3]. Based on the quality of the obtained surface, the range is selected. The upper-limit and the lower-limit coded values for intermediate values are determined using relation (1).

$$Y_i = \frac{2[2Y - (Y_{\max} + Y_{\min})]}{Y_{\max} - Y_{\min}} \quad (1)$$

where Y_i is the needed coded value of a parameter Y . Y is any value of the parameter from Y_{\min} to Y_{\max} . Y_{\min} is the lower limit of the parameter, and Y_{\max} is the upper limit of the parameter.

A central composite rotatable design is considered as the design matrix. The number of deposits is made by different combinations of clad run. After the end of every run, settings for all parameters are changed and rearranged for the subsequent overlay [4]. Table 3 shows the chosen welding process parameters and their levels.

Table 1 Chemical composition of AISI 4140

Element	C	Mn	Cr	Si	Mo	S	P	Fe
AISI 4140	0.4	0.9	1	0.25	0.23	0.04	0.029	Bal

Table 2 Chemical composition of ERNiCrMo-10

Element	C	Si	Mn	P	S	V	Cu	Cr	Ni	Mo	Co
ERNiCrMo-10	0.015	0.08	0.50	0.02	0.002	0.35	0.5	21.5	56	13.8	1.8

Table 3 Range of process parameters

Parameters	Notation	Unit	Factor levels		
			-1	0	+1
Welding speed	A	mm/min	160	170	180
Nozzle-to-plate diameter	B	mm	4	6	8
Current	C	A	140	150	160

Table 4 Experimental values

Std	A: Current (A)	B: Welding speed (mm/min)	C: Nozzle-to-plate distance (mm)	Penetration (mm)	Reinforcement (mm)	Width (mm)
1	140	160	4	0.99	1.46	9.71
2	160	160	4	1.2	1.61	14.07
3	140	180	4	0.92	1.28	8.46
4	160	180	4	1.09	1.4	12.71
5	140	160	8	0.89	1.59	10.16
6	160	170	8	1.16	1.59	12.44
7	140	180	8	0.83	1.34	9.71
8	160	180	8	1.01	1.54	12.85
9	140	180	6	0.95	1.37	9.19
10	160	180	6	1.09	1.54	12.84
11	150	160	6	1.07	1.65	12.11
12	150	180	4	0.94	1.39	10.89
13	150	170	4	1.08	1.43	10.93
14	150	170	8	0.98	1.53	11.23
15	150	170	6	1.14	1.44	11.12
16	150	170	6	1.14	1.52	11.16
17	150	170	6	1.13	1.58	11.13

The specimens of transverse sections are prepared for all the weld overlays. They are polished and etched with 2% Nital [5]. The weld bead profiles were detected by using optical profile projector of reflective type with a magnification of 10. The profile images are traced in 2D form to measure responses. The values are presented in Table 4.

The response values obtained for the weld bead parameters can be expressed using the equation [4].

$$Z = f(Y_1, Y_2, Y_3) \quad (2)$$

where Z is the response (e.g., weld bead width), and Y_1 , Y_2 , and Y_3 are the current, welding speed, and nozzle-to-plate distance, respectively.

The second-order polynomial equation used for the three factors can be represented in the following equation

$$Y = \lambda_0 + \lambda_1 A + \lambda_2 B + \lambda_3 C + \lambda_{11} A^2 + \lambda_{22} B^2 + \lambda_{33} C^2 + \lambda_{12} AB + \lambda_{13} AC + \lambda_{23} BC \quad (3)$$

where λ_0 is the free coefficient of polynomial equation. λ_1 , λ_2 , and λ_3 are linear terms. λ_{11} , λ_{22} , and λ_{33} are quadratic terms. λ_{12} , λ_{13} , and λ_{23} are interaction terms.

The analysis of variance (ANOVA) technique is used to test the adequacy of the developed models [6, 7]. Above 95% level of confidence is favored for any design of experimental work. The values of ANOVA are presented in Table 5. It is observed that all models are adequate.

$$\begin{aligned} \text{Penetration} = & 1.13 + 0.095A - 0.046B - 0.046C - 0.013AB + 0.0028AC \\ & + 0.0022BC + 0.06A^2 - 0.10B^2 - 0.081C^2 \end{aligned} \quad (4)$$

3 Results and Discussions

3.1 Direct Influence of Process Parameters

All the three responses are increased when only the current is increased. Since the current increases, the welding power/length also increases by this clad bead length, and the higher density of current is the reason for deeper penetration. An increase in the current results in an increase in the rate of deposition and increases the size and shape of the weld bead [5].

The decrease in voltage reduces the weld bead width and height of the reinforcement due to lesser heat input per unit length. When the speed increases, the penetration depth is also increased. Penetration depth is prevented when the welding speed is low because the position of the arc is nearly vertical and the effect of arc is cushioned by the weld pool [8].

When the distance between the nozzle and plate increases, the penetration of the weld bead shape decreases, but weld shape width and reinforcement increases when the distance between the nozzle and plate increases. This is due to an increase in the circuit resistance in between the welding torch and the weld plate. So heat input is reduced when the distance between the nozzle and plate increased.

Table 5 ANOVA values for penetration

Sources	Sum of squares	DoF	Mean square	F value	p-value	
Model	0.179358	9	0.019929	67.915	<0.0001	significant
A-Current	0.066695	1	0.066695	227.2904	<0.0001	
B-Welding speed	0.017166	1	0.017166	58.49924	0.0001	
C-Nozzle-to-plate distance	0.017656	1	0.017656	60.17156	0.0001	
AB	0.001097	1	0.001097	3.73773	0.0945	
AC	5.48E-05	1	5.48E-05	0.186871	0.6785	
BC	3.04E-05	1	3.04E-05	0.103711	0.7568	
A ²	0.00656	1	0.00656	22.35536	0.0021	
B ²	0.018582	1	0.018582	63.32604	0.0045	
C ²	0.021	1	0.021	71.56605	0.0054	
Residual	0.002054	7	0.000293			
Lack of fit	0.001987	5	0.000397	11.92427	0.0792	Not significant
Pure error	6.67E-05	2	3.33E-05			
Cor total	0.181412	16				
Std. dev.	0.01713	R-squared	0.988677			
Mean	1.035882	Adj R-squared	0.97412			
C.V. %	1.653657	Pred R-squared	0.951063			
PRESS	0.008878	Adeq precision	28.49767			

3.2 Interaction Effects

The interaction effects of process parameters on penetration are shown in Fig. 1. From Fig. 1a, it is clear that the decrease in speed and current decreases the penetration.

From Fig. 1b, it is noted that the penetration is decreased with a decrease in the current and a decrease in the distance between the nozzle and plate. It is because of low heat input/unit length of the base metal, and it is the negative effect of speed and distance between the nozzle and plate. From Fig. 1c, it is observed that penetration decreases with an increase in speed and the distance between the nozzle and plate. It is because of lesser heat input when the speed and distance between the nozzle and plate increases. It is the positive effect of the increase in the distance between the nozzle and plate.

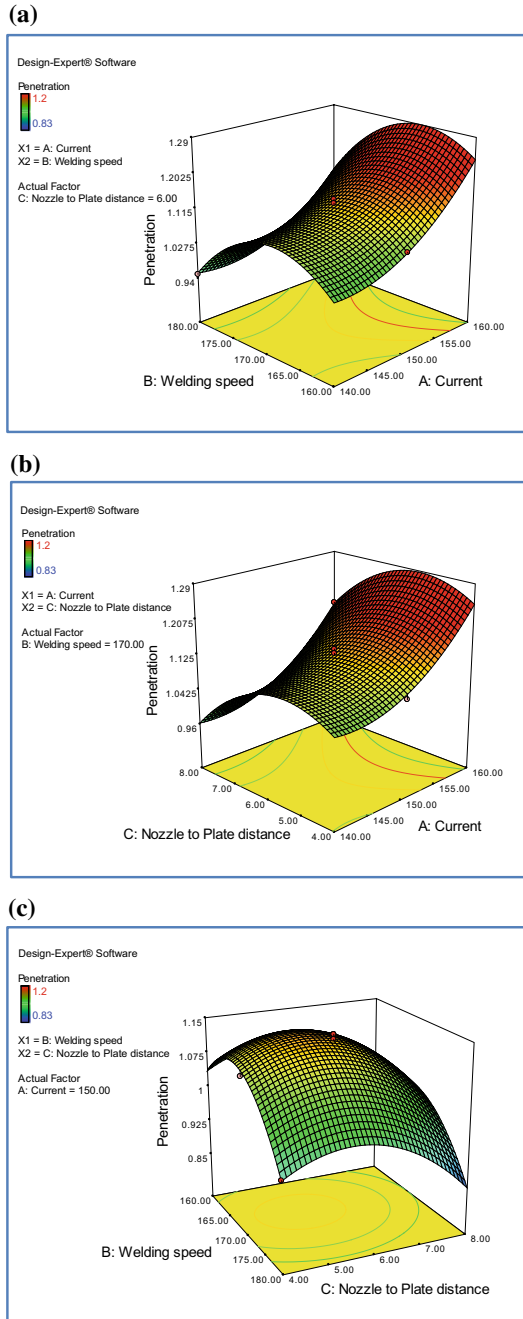


Fig. 1 Interaction effects of process parameters on penetration

4 Conclusions

A three-level, three-factor full-factorial design matrix based on the RSM central composite rotatable design technique is used to develop mathematical models to predict the clad bead geometry and shape relationships for cladding deposited by GMAW on AISI 4140 steel with ERNiCrMo-10 filler material. ANOVA is used to check the adequacy of the models. From experimental results and RSM-based analysis and ANOVA, it is concluded that the developed models are in good agreement with the experiment results. All the process parameters have an influence on clad bead geometry. From the surface plots it is concluded that the interaction between the process parameters have significant effect on the weld penetration.

References

1. ASM Handbook Welding, Brazing, and Soldering (1993) vol 6. ASM, USA
2. Kannan T, Murugan N (2006) Sensitivity analysis of flux cored arc cladding parameters using response surface methodology. *Int J Manuf Sci Prod* 7:3–4
3. Cochran WG, Cox GM (1987) *Experimental designs*. Wiley, New York
4. Joseph GB, NarendraKumar G, Mageshwaran G, Jeevahan J, Sriram V, Durai Raj RB (2018) Optimisation of process parameters for electroless nickel plating on SS316L for refrigeration systems. *Int J Ambient Energy*. <https://doi.org/10.1080/01430750.2018.1437564>
5. Davies OL (1978) *The design and analysis of industrial experiments*. Longmen, New York
6. Dhinakaran V, Shanmugam NS, Sankaranarayanan K (2017) Some studies on temperature field during plasma arc welding of thin titanium alloy sheets using parabolic Gaussian heat source model. *Proc Inst Mech Eng Part C: J Mech Eng Sci* 231(4):695–711
7. Dhinakaran V, Shanmugam NS, Sankaranarayanan K (2017) Experimental investigation and numerical simulation of weld bead geometry and temperature distribution during plasma arc welding of thin Ti-6Al-4V sheets. *J Strain Anal Eng Design* 52(1):30–44
8. Ghosh PK, Gupta PC, Goyal VK et al (1998) Stainless steel cladding of structural steel plate using the pulsed current GMAW process. *Weld J* 77(7):307–s–314-s

Review on Corrosion Behavior of Copper–Brass Weldment Samples During Welding with the Different Corrosive Environment



Sourabh S. Nair, Aparna Vinayan, Raghuraman Srinivasan and Sivachidambaram Pichumani

Abstract The work intends to review the study of the fundamental properties of brass and copper, the behavior of the weldment formed by the combination of brass and copper, effects of tribology in the weldment, and the types of welding techniques available for the welding purpose. The literature review helped us to engage in the study covering the fundamental aspects. In this research article, we have attempted to study the basics of the corrosion phenomenon, wide aspects of types of welding, properties of brass and copper, and the terminologies in tribology.

Keywords Corrosion · Brass · Copper · Welding · Tribology

1 Introduction

Brass is a combination of copper, in a dominant proportion, usually coupled with zinc. However, admission of other metals in trace proportions is induced for the desired range of functionality and application, for example, lead. The proportions of copper may vary from 55 to 95%; while that of zinc, the range would be a shift between 5 and 40%. Extensive brass utilization is mandated in certain domains as a result of some unique properties; therefore, features and responsive characteristics have been noted for beneficial usages. Brass adopt various classifications and, thus, brasses are categorized as alpha, alpha–beta, beta, and gamma brasses. Similar to copper, brass also has the potential to be engaged in various mechanical applications like extrusion, forgings, wires, sheets, strips, etc. Brass used for marine applications comprise of examples like naval brass and admiralty brass, which when used with traces of tin can improve corrosion resistance, high tensile brasses, and dezincification resistant brasses. Tungum tubes used for hydraulic lines in the aircraft control systems are a combination of brass with other metals like aluminum, nickel, and silicon which proved to be corrosion resistant and dealt with fatigue issues effectively. Similarly, several combinations of brass with other elements tend to impart specific

S. S. Nair · A. Vinayan · R. Srinivasan · S. Pichumani (✉)
School of Mechanical Engineering, SASTRA Deemed University, Thanjavur 613401,
Tamil Nadu, India
e-mail: sivaumaphd@gmail.com

© Springer Nature Singapore Pte Ltd. 2019
S. S. Hiremath et al. (eds.), *Advances in Manufacturing Technology*,
Lecture Notes in Mechanical Engineering,
https://doi.org/10.1007/978-981-13-6374-0_68

properties and, thus, are employed in several applications. Brass with 39% weight composition and with 3% lead are used in components like switch terminals. While a mixture of 24% zinc and 12% nickel is used in resistance wires, connectors, etc. Gearbox components would invite brass in tandem with a series of elements like manganese, aluminum, lead, and silicon [1]. Copper (reddish-brown color atomic number 29), as we all know, has a wide range of applications. The innumerable properties would encompass an FCC crystal structure, application-based qualities of conductivity, ductility, malleability, and also lower chemical reactivity. Several engineering purposes entail copper in domains of electrical applications, constructions, and industrial tools as well as to be used concurrently with other metals in the form of alloys and other materials. Copper is used in tandem to fabricate alloys like bronze (copper with tin and often other metals like aluminum, magnesium, manganese, etc.), brass (copper and zinc), gunmetal (a combination of copper, tin, and zinc), cupronickel (copper and nickel), etc. Wrought and cast products can be molded from copper and its subsequent alloys with the wrought product being manufactured from hot-worked, annealed, cold-worked processes, etc. Extrusion and forging are examples of hot-worked processes and soldering will be illustrations of cold-worked processes. Under joining, we have several methods which also include welding, which is a successful method for copper and its alloys. For instance, thin sheets of copper can be dealt with using spot welding technique. Copper has several uses and it can be found to be used in the making of coins, or along with other chemical elements to be used in agriculture and even available in laboratories for multiple purposes [2].

2 Welding

The possibilities of employing copper and brass for various applications with their reliable properties have been discussed in earlier sections. Thus, enough evidence is available for the use of these materials in mechanical, electrical, and construction-based applications. However, such applications pose questions as to how these materials can be used in confluence with materials of the same genre, might be with different compositions or other parameters such as joining of copper alloys with its pure metal form, and with other materials that have complete dissimilarities. Now, welding is one such mechanical operation which in simple terms is supposedly engaged in joining any two given metals or alloys or both. The materials, though, need to be tested for their response to such a mechanical process. Welding imparts a permanent joint aided by the application of heat or pressure as the materials to be joined are melted and allowed to solidify [3]. Weldability is affected by factors like crack formation, oxidation, hardness, etc. There are several types of welding processes:

1. Arc welding
2. Gas welding
3. Resistance welding
4. High-energy beam welding
5. Solid-state welding

2.1 TIG Welding

TIG welding also referred to gas tungsten arc welding (GTAW) is an appropriate welding method due to quality weld that promises improved resistance to faults and mechanical properties such as high strength, cleanliness, and additional economic benefits. TIG welding requires optimization on factors like welding speed, arc length on the weld profile, and weld bead appearance to achieve desired results. It is further categorized as pulsed current TIG, constant current TIG, activated TIG, and pulsed current activated TIG welding.

Mechanism of TIG welding

It is an arc welding process, TIG welding employs a tungsten electrode. An inert gas such as argon or helium shields the weld area from atmospheric exposure. The tungsten electrode derives power through a welding torch essentially from the power source. The metal, also called a workpiece, engages in forming an arc with the electrode during the welding process. This arc generation is aided by a constant current welding power-supply-generating energy. The temperature of the arc can go up to 20,000 °C and the heat, thus, generated helps to melt the workpieces and are firmly joint upon solidification.

Disadvantages

Though TIG is identified with certain positive attributes as mentioned, other factors like coarse grain structure formation during welding of materials like, in case of aluminum alloys and composites and intermetallic formation in the welded region tends to produce weak mechanical properties. Weld strength is below par in case of arc welding, due to excessive heat in the weld zone and the longer time periods the weld pools took to get cool, which in turn promoted the development of stresses and the coarse grain structure in case of metal like aluminum, as mentioned earlier. An identified technique to support the issue of weld strength is weld alloying among others.

2.2 Dissimilar Welding

Dissimilar metal welding is a welding technique involved in fitting together two metals in possession of separate chemical and mechanical properties. Dissimilarity in nature of the materials is easily established due to the geological conditions under which they are formed. This is done so as to extract as many benefits from the combination and thereby reducing the frailties. Several combinations like that of aluminum and steel, stainless steel and copper, etc. are carved keeping in mind the positive outcomes and objectives [4]. Several examples can be put forth wherein dissimilar welding is administered on the materials:

1. Aluminum and steel possessing different characteristics like varying boiling point, thermal conductivity, etc. are joined with the help of a coated layer, like

zinc, over steel that is compatible with aluminum and thus joined. The technique used here is buttering layer technique. Even a combination of aluminum and stainless steel employs the same method and technique.

2. Aluminum is welded with copper with the help of a transition material that is compatible with the two metals.
3. Alloys of aluminum can similarly invite dissimilar welding benefits.
4. Copper is also, like aluminum, used in tandem with stainless steels. Fillers of the copper alloy is employed for thinner metallic sections while stainless steel would use a buttering layer of such fillers for metallic sections that are thicker. Copper surfaces can be covered with substances like nickel [5].

2.3 Dissimilar Welding Process

The parameters are initially to be determined as a presupposition before carrying out the dissimilar welding process. The process involves melting of two dissimilar metals at the requisite conditions especially that of temperature to let the metals fuse into each other under the action of heat that is applied through laser beams as one of the mechanisms. However, it is possible that such a method could produce intermetallic compounds in the transition zone and that could limit the efficacy of this process in forming a strong reliable bond. Generally, a layer called a buttering layer is administered to supply an easy transition between the two parent materials and, thus, advocating further efficiency of the process [6]. The selection of buttering layer depends on factors like thickness of the coating required, the metals involved in the coating, and whether it could culminate in a successful bonding with the employed metals compared to another layering. For example, nickel is engaged as a buttering layer for a combination of copper and steel due to the fact that it is soluble with both the metals and imparts strong bondage. The nickel, thus, used may either be smaller in dimensions or a larger one depending on the requirements.

2.4 ATIG and PCTIG

Following sections would be dealing with a brief account of the types of TIG welding:

A-TIG:

Activated TIG welding is directed to coat a layer of active flux which could involve any metal oxide and is useful when adequate weld penetration, as it tends to impart twice the penetration as observed under normal TIG conditions which are attributed to the arc constriction effect, is desired to weld thicker sections. This technique is also advantageous in terms of the heat to be supplied as input [7]. A-TIG has two working mechanisms, namely the reverse Marangoni convection effect and the arc constriction effect. Certain parameters to be closely observed with A-TIG welding

would be activated flux particle size and the coating thickness. Other factors like active flux thickness under the optimal conditions could be influenced to have better penetration of the weld. Apart from optimizing a few parameters, some of them need to be effectively kept under check to ensure a stronger weld as, for example, the excessive supply of current required for coating process could lead to a weld break. Fluxes like SiO_2 , Al_2O_3 , iO_2 , CaO , etc. are used [8]. Among them, A-TIG welding with SiO_2 active flux is promising in terms of the weld depth and width in addition to resistance to cracking tendency.

PCTIG:

There are several welding types in TIG category that are preferred to overcome the shortcomings in plain TIG welding of the components [9]. Pulsed current TIG welding (PCTIG) can be employed in applications at the industrial scale as it requires minimal adjustments to available systems. There are several parameters to take into account which enhances the effectivity of PCTIG welding. Welding parameters, include peak current, base current, pulse on time, pulse frequency, etc. which invoke constructive aspects in terms of narrowed heat input, better cooling rates and finer grain microstructure, better entrance, and globule shape that tends to display the motive in preferring PCTIG over simpler TIG welding for these factors that have improvised effect on the microhardness of the material. The concise focus of the improvising factors includes apt penetration and bead contour which are attributed to peak current with stable arc attributed to base current, and pulse frequency takes care of appropriate heat transfer [10]. For an ideal understanding of PCTIG welding parameters, the consequence of each pulsed current TIG welding parameters and the interface between two or more parameters on the bending strength, ultimate tensile strength, the percentage of elongation, and yield strength are evaluated. The consistency and validation are done using the experimental verification of the predicted values.

3 Corrosion

Corrosion can be simply defined as the erosion of any given material when subjected to certain environments that have been ascertained to be instrumental in aiding or initiating corrosion. This erosion of material, or corrosion, is common in metals and, thus, it becomes one of the major parameters to establish the quality of a material. Corrosion is a mechanical–physical–chemical process that involves dissolution, diffusion, reactions in solid and liquid, and wear among the materials. Corrosion–wear is a tribological process where the total material removal results in concurrent mechanical wear and chemical corrosion. Corrosion is speeded up by wear and wear is speeded up by corrosion. The synergism where both corrosion and wear are appreciably increased by the exchanges between them can extensively amplify total material losses. Corrosion occurs essentially through two types of oxidation which occur under diverse conditions like passive and active. Passive oxidation

occurs at relatively low temperatures and high partial pressures of oxidizing species through the formation of a passive surface layer which then protects the underlying material, drastically reducing the rate of further corrosion. Active corrosion happens in the presence of active radicals which enhances the rate of corrosion.

There are several types of corrosion categorized based on several factors. A few of them have been noted here:

1. General attack corrosion: The weakening of a metal due to its entire surface experiencing an electrochemical reaction initiated by an acid. It is more disastrous in comparison to any other form of corrosion but is considered safe as it can be predicted and prevented.
2. Localized corrosion: This form of corrosion can be further categorized into pitting corrosion, crevice corrosion, and filiform corrosion. Here, a specific area of the metal is under the attack of corrosion unlike a general attack, which is uniform throughout the surface of the metal.
3. Galvanic corrosion: A type of corrosion induced by the presence of two dissimilar metals in a corrosive medium. Here, the metals assume anodic and cathodic terminals wherein the anodic metal is the sacrificial metal for its eroded.
4. Pitting corrosion: A type of corrosion characterized by the formation of small pits but damaging.
5. Erosion corrosion: As the name suggests, is the subsequent deterioration of a material by the erosion that is initiated, which could be due to an abrasive interaction or movement between any two surfaces. Damage due to cavitation is another form of erosion–corrosion wherein formation of vapor bubbles on subsequent changes with pressure-based systems in a fluid–solid enclosed environment results in erosion.
6. Fretting corrosion: Two surfaces subjected to load in along with the tendency of slip and vibration exhibit fretting corrosion and is common in engine parts.
7. Stress corrosion cracking: A corroding medium and tensile stress are influencing factors for SSC. Hydrogen embrittlement is many a time a form of SSC.

Corrosion Prevention

Since corrosion is a binding problem for any application, there exists several tools and mechanisms to deal with the harmful effects of the same. Following are the techniques available to deal with corrosion effectively:

1. Painting, plating, and even enamel application are surface treatment techniques useful to deal with corrosion. For example, the outer bodies of ships being painted in order to thwart the corrosion due to salty water of the seas. These applied coatings act as barrier layer preventing the corroding agents from reacting with main material surface.
2. Corrosion inhibitors are a very common alternative and they are examples of reactive coatings administered to prevent electrochemical reactions.
3. Anodization performs as a sacrificial technique wherein electrochemical poles of cathode and anode are engaged. The metal with more potential to behave as

an anode attracts corrosion by letting the desired metal to stay from corrosion attack by converting the same as a cathode.

There are several other techniques that are currently available and can be opted depending upon preference after taking into consideration the factors involved. The focus of this paper revolves around, on a general note, the response of the selected metal and alloy (combined with welding) against acid-based corrosion. Henceforth, a brief elucidation can be narrowed in, acknowledging the same.

Acidic corrosion is identified during the wear and damage of a metal under perilous acidic environments. The source of the acid could be from anywhere, for example, soil, industrial air or water, or subsequent reactions due to the contact of certain reactants. The acid corrosion is basically an electrochemical reaction wherein there exists an electric potential difference on the metal surface, a charge transfer and established a continuous conduction mechanism between the anode and the cathode. Acid concentration, temperature, and as well as alloy composition determine how the rate of corrosion will be evaluated. Other factors like aeration, the presence of impurities in the acid such as chlorine could also affect the corrosion rate.

Nitric Acid (HNO_3 , molecular weight: 63.012 g/mol) is a strong mineral acid having suffocating and pungent odor with a pH of about 3 that has widespread use in the industrial sector. The pure form is generally colorless, but it acquires a yellow tinge due to subsequent decomposition into oxides of nitrogen and water over time. Nitric acid is used in the production of fertilizers, organic chemicals explosives like nitroglycerin and trinitrotoluene (TNT), dye intermediates, uranium recovery, metal pickling, and plastics and is thus identified as an essential industrial acid with a utility concentration of 68% in water which may change as per use. Being a powerful oxidizing agent, it shows violent behavior against non-metallic compounds, dissolves metals, and initiates metal oxide formation. Constant exposure to this chemical has been proven hazardous.

4 Tribology—Wear, Friction, and Lubrication

Tribology is attributed to the analysis of the three facets, namely friction, lubrication, and wear. It helps to study the surfaces of materials that are in interaction with each other. Being interdisciplinary in nature, tribology is employed in ensuring safety, reliability, stability, etc. with several economic benefits. The knowledge of tribology helps to deal with issues like energy loss, losses developed economically due to breakdowns, machine depreciation, etc. and thus has a conclusive effect on the service life of materials [11]. Type of lubricant used, additive usage, and installation of bearings are the very few examples where the knowledge of tribology is essential. Most common example of tribology use is in the case of bearings, cams, gears, breaks, seals, and many more. As already mentioned, the interdisciplinary aspect tends to enhance its employment in almost all aspects of engineering and construction like automotive, railways, shipping, electronic goods, aerospace, etc.

4.1 Wear

Wear refers to the erosion of material which could be damaging in terms of measurable wear and a positive effect in terms of zero wear which renders a polished outlook to the material surface. Mechanical and chemical wear would mean erosion and corrosion, respectively. The extent of wear depends upon lubrication, the load that is born by the equipment, surface hardness, etc. Tribology includes wearing under its umbrella. Wear can be classified as adhesive wear, abrasive wear, fretting wear, erosive, corrosive and oxidative wear, and even surface fatigue. Surface fatigue is when the material tends to be on the weaker side of continuous exposure to heavy loads. The erosion is initiated as soon as the cracks tend to appear. All the above classifications have only slight variations and thus are classified accordingly.

4.2 Friction

Friction, as is known, is a necessary evil. It is essential in several instances, but equally undesirable in many other cases. The unwanted friction is usually associated with machinery wherein long operating hours renders the machine less efficient. Wear, loss of energy, and eventually weak performance are the ultimate irreversible conclusions for most machinery. However, every problem requires a solution and here, the frictional losses are overcome by opting for remedial measures like lubrication and change in machine design. Coefficient of friction is an estimate to understand the frictional effects. This estimating parameter depends on factors like temperature, surface roughness, and even hardness. Metals used for welding shall not possess tendency for extra adhesion which in turn will reflect on the frictional loss. Dry friction, fluid friction, lubricated friction, skin friction, and internal friction are the classifications for friction. Dry friction, which is further divided into static friction, refers to the opposition to motion between solid surfaces that are in contact. Fluid friction opposes the smooth movement between viscous fluid layers. The remaining classifications of friction adopt similar descriptions. Friction results in the conversion of kinetic energy to thermal energy and thus considerable energy is lost in this way. Wear is another problem that cannot be neglected.

4.3 Lubrication

Lubrication is the concept of administering lubricants wherein there is an established interaction between two surfaces and this is a sub-categorisation of tribology. Solids, liquids, solid-liquid dispersions, liquid-liquid dispersions, and even gaseous lubricants are available and are put to use depending upon the conditions involved. Grease, oil, water, etc. all are examples of lubricants. Lubrication is basically a smoothen-

ing tool in rigorous mechanical operations, equipment, fittings, etc. The interaction between two solid surfaces mostly necessitates liquid lubricants for they handle the physical load, manage stresses, and eventually have a positive influence on friction and wear. Lubrication proves to be a good option to deal with friction and wear of materials. In addition, it can reduce fatigue and surface failures and so does prevents concentration of stress at localized junctions. As is for any tribology category, lubrication is also associated with bearings, transmission parts, surfaces involving metallic contact, and more. Lubricants are administered depending upon its usage and the application. However, lubricants necessitate a few common requirements like:

- (1) Lubricants need to act as a barrier between the interacting surfaces by forming films and thereby reduce frictional wear and tear.
- (2) Lubricants need to cling to the surfaces and not get grind away with successive use.
- (3) It shall deal with corrosive agents effectively.
- (4) Lubricants need to be employed under severe conditions like high temperatures and thus shall be able to withstand the same.

Solid lubricants have the primary purpose of taking in the additional load over the surface and thus prevent distortion, strength loss, etc. Oil is the best example of liquid lubrication. Oil has classifications depending upon the conditions it has been employed. The classifications include vegetable oils, animal fats, and mineral oils. Castor is a good example of vegetable oil. However, vegetable oils have the disadvantage of being less stable at higher temperatures compared to mineral oils. Animal fat products are derived from animals and marine species like fish. Also called as fixed oils due to their non-volatility, they consist of fatty acids and are also used in tandem with mineral oils to enhance the formation of films. Tallow oil and fish oil are examples. However, the drawback seems to be their availability. Mineral oils are subsidiaries from crude oil and therefore comprise of hydrocarbons in addition to traces of sulfur and nitrogen compounds. Grease is the best example of a semi-solid lubricant with good performance under normal environmental conditions but with the inapt dissipation of heat. Gas lubricants like air, nitrogen, and helium are administered when the separation between two surfaces has a very hairline gap between them. Low viscosity, high-temperature usage. etc. fall under its advantages.

5 Conclusion

The focal point of this paper revolves around the selection of brass–copper weldment for the study of its corrosion behavior in acidic environments. A combination of copper and brass has invited limited studies and hence such a pursuit will unravel this alloy combination as to whether such a manufactured product will suffice current material needs and standards in several domains and applications. The choice of material as well as the technique to fabricate the same has been guided by the advantages they offer, and the account of which has been briefed up. The choice of TIG

welding has been substantiated through its innumerable benefits and the subsequent selection of ATIG and PCTIG welding has been clearly set over the requirements for this work. Brass especially seems to be falling behind in its action against a corroding agent like nitric acid. Brass and especially copper continue to be used extensively in the day-to-day applications and thus blending the two metals shall give enhanced output consisting of advantageous results of both the metals. However, even though fusing the two may reflect positives, as in the case of alloys, these need to be tested for all the requisite parameters. The commingling of the metals shall not be devoid of strength and resistant properties of the parent material. Tribological studies have been an important aspect of any industrial operation. Therefore, the authors have paid attention to the same considering that optimization of tribological elements like wear, friction, and lubrication will enable to impart favored results when employed in tandem with the materials considered so far in this work. Thus, corrosion rate based on weight loss can be adopted as an estimate for the effect of corrosion. This corrosion rate will help to elaborate the deficiency in the copper–brass weldment and it thereby can be evaluated in comparison with many other alloys as well as welded samples. The scope of this work is, thus, wide as corrosion still remains one of the most fundamental problems and simple in nature but is absolutely essential for ensuring longer lifespan of the material. Finally, the separate estimate of surface roughness for both copper and brass is just an indication to map the effect of nitric acid and thereby acidic effects on the material under study on the surface aspects of the metals. Thus, the authors have left enough ground to be taken up for further research in this domain. The vitality of the analysis is laid down through the proposed work.

References

1. American Society For Testing Materials, "Copper and Copper Alloys." Annual Book of ASTM Standards, vol 2.1(2), ASTM International, West Conshohocken, PA
2. Mendenhall JH (1986) Understanding Copper Alloys. In: Robert E (ed) Krieger Publishing Co., Malabar, FL
3. Tyler DE (1990) Wrought copper and copper alloy products, properties and selection: nonferrous alloys and special-purpose material, ASM Handbook, 10th edn, vol 2: 244 ASM International, Materials Park, OH
4. American Society For Metals (1990) properties, and selection: nonferrous alloys and special-purpose materials, ASM Handbook, 10th edn vol 2, ASM International, Materials Park, OH
5. Breedis JF, Caron RN (1993) Copper alloys (wrought), Kirk-Othmer encyclopaedia of chemical technology, vol 7, 4th edn. Wiley, Hoboken, pp 429–473
6. Michels HT (2006) Antimicrobial characteristics of copper. ASTM Standard News 11:28–31
7. Gould et al (2009) The antimicrobial properties of copper surfaces against a range of clinically important pathogens. *Ann Microbiol* 59(1):151–156
8. Sivachidambaram P, Srinivasan R, Ramamoorthi V (2015) Developing regression model to predict the tensile strength, bending load and microhardness and to optimize the wt.% of SiC in Al-SiC composite. *ARPN J Eng App Sci* 10(18):8096
9. Sivachidambaram P, Srinivasan R (2017) Weld profile optimization on weld speed & arc length parameters of TIG welding on Al-SiC composite. *J Adv Res Dyn Control Syst, Special Issue* (11)

10. Sivachidambaram P, Srinivasan R (2017) Study and optimization on the effect of welding current and active flux coating thickness in the weld profile of Al-SiC composite weldment using A-TIG Welding. *J Adv Res Dyn Control Syst*, Special issue (11)
11. Sivachidambaram P, Balachandar K (2015) Optimization of pulsed current TIG welding parameters on Al-SiC metal matrix composite—an empirical approach. *Indian J Sci Technol*, Vol 8(23), IPL0288

Effect on Mechanical Properties of Aluminum Composites by Inclusion of Silicon Carbide



V. Senthil Kannan and K. Lenin

Abstract In this paper, the mechanical properties of new composite material aluminum with silicon carbide were analyzed. The composite with various proportions of silicon carbide (2, 4 and 6%) with aluminum 2017 was prepared by stir casting process. For the analysis of mechanical properties for aluminum composite included by silicon carbide, the hardness test, impact tests and tensile tests were conducted. The results showed that the inclusion of silicon carbide particles increased the hardness and impact strength of the composites. It was also found that only small amount of increment was found in all results. From this, it was clearly known that if the increase in % of silicon carbide inclusion increases mechanical properties of aluminum composite for a certain level.

Keywords Reinforcement · Stir casting

1 Introduction

Aluminum composites are most widely used composites in the automotive and aerospace application for their low weight, high strength, high stiffness and low cost. Aluminum 2017 alloy is used as a key material for production of composites. Silicon carbide microparticles of size 37 μm (400 meshes) were used for reinforcement of composite. To analyze the mechanical properties, different weight proportions (2, 4 and 6%) of silicon carbide particles were reinforced in the Al2017 alloy. Rana et al. [1] fabricated Al/SiC composites by ultrasonic-assisted stir casting and observed that the tensile and compressive strength of composites increased with increase in addition of silicon carbide particles. The author used 6% of silicon carbide for analysis.

V. Senthil Kannan (✉)

Department of Mechanical Engineering, Paavai Engineering College, NH44,
Pachal, Namakkal, India
e-mail: vsktgp@gmail.com

K. Lenin

Department of Mechanical Engineering, K.Ramakrishnan College of Engineering,
Samayapuram, Tiruchirappalli, India

© Springer Nature Singapore Pte Ltd. 2019

S. S. Hiremath et al. (eds.), *Advances in Manufacturing Technology*,

Lecture Notes in Mechanical Engineering,

https://doi.org/10.1007/978-981-13-6374-0_69

Harichandran et al. [2] added boron carbide particles to aluminum and reported that increase in B₄C beyond 6% leads to porosity and particle agglomeration, thereby decreasing the strength and ductility of composites. Suresha [3] studied wear characteristics of hybrid aluminum matrix composites reinforced with graphite and silicon carbide particulates and found that hybrid composites exhibit better mechanical properties and wear characteristics. From the above literature views, the composites were not prepared by using the Al2017 alloy. From the above research works, it was found that reinforcement of silicon carbide more than 6% of weight composition leads porosity and low hardness. Therefore, an attempt was made to prepare the composite with Al2017 alloy.

2 Materials and Method

2.1 Matrix Material

For the analysis, the effect of reinforcement particles on mechanical properties of Al2017 alloy was considered as the parent material. Table 1 shows the composition, and Table 2 shows the mechanical properties of the Al2017 alloy. Silicon carbide particles of 37 μm were used as reinforced material for making the composite. To investigate the mechanical properties two combinations, 2 and 4% of weight, of silicon carbide particles based on Al2017 were used to prepare the composites.

2.2 Preparation of Composite

Initially, the Al2017 was charged in the graphite crucible furnace and heated to 750° until the entire material in the crucible was changed into liquid state. The silicon

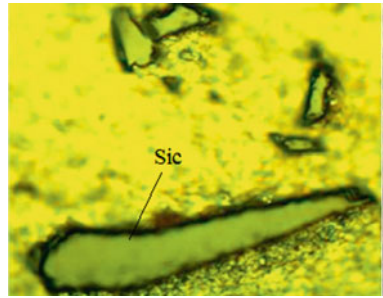
Table 1 Chemical composition of Al2017

Element	Cu	Mn	Mg	Fe	Si	Zn	Cr	Ti
wt%	4.19	0.59	0.45	0.19	0.59	0.21	0.02	0.021

Table 2 Mechanical properties of Al2017

Properties	Al2017
Density (g/cm^3)	8.47
Melting point ($^{\circ}\text{C}$)	1413
Coefficient of expansion ($\mu\text{m}/\text{m}^{\circ}\text{C}$)	13.3
Brinell hardness number	105 BHN
Rockwell hardness number	43 HRB

Fig. 1 Optical micrograph of composite



carbide particle with different compositions according to the weight combination was preheated to 700° to completely remove the moisture content. After the molten metal was fully melted, a stainless steel stirrer was used to stir the molten metal at a constant speed of 700 rpm. During stirring process, the preheated silicon carbide particles were poured into the molten metal with constant rate. Once the preheated reinforcement silicon carbide particles were added to the molten metal, they were stirred 10 min to equal distribution of silicon carbide in molten metal. The above molten slurry was poured into the mold which is already prepared for impact and hardness tests; the mold was preheated to 500° to avoid porosity during solidification. Thus, the composite specimens of 2 and 4% weight proportion of silicon carbide-reinforced composites were prepared.

2.3 Microstructural Characterization

The microstructure of the hybrid composites was examined using an optical microscope (model: Olympus) which is in J. J. College of Engineering and Technology. For visualizing the structure, the specimen was grounded by abrasive sheets followed by rotating disk cloth polishing. The structure is shown in Fig. 1.

3 Testing Method of Composites

3.1 Hardness Test

For the analysis of the mechanical properties of the composites, the hardness test was carried out. The specimens for hardness test were prepared by the size of $50 \times 50 \times 5$ mm. The test was conducted by Brinell hardness tester. The maximum capacity of the Brinell hardness tester was 10,000 kgf, the testing was conducted, and results were obtained from the Brinell hardness tester available at J. J. College of Engineering and Technology, Trichy. A load of 1000 kgf was applied for 20 s to

the specimen. The diameter of the steel ball indenter 5 mm used for the test. The diameter of the indentation on the specimen is measured by the optical microscope. The Brinell hardness number was calculated by Eq. 1. The average value of hardness number was found by three trials of test.

$$\text{BHN} = \frac{2P}{D(D - \sqrt{D^2 - d^2})} \quad (1)$$

where P is the applied load on the specimen, D is the diameter of the indenter, and d is the diameter of the indentation on the specimen.

3.2 Impact Test

Impact test was conducted on the composites for calculating the strength of the composites under suddenly applied load. Here, the specimen of size $55 \times 10 \times 10$ mm was prepared with 'V' notch with 5 mm-thickness with 5 mm-depth. The Izod impact test was conducted on the composite specimens by the impact testing machine which is in J. J. College of Engineering and Technology, Trichy. The impact strength of the specimen at the notch area was calculated by Eq. 2 given below.

$$I = \frac{F}{A} J/\text{mm}^2 \quad (2)$$

where F is the impact load and A is the area of cross section of the specimen.

4 Results and Discussion

4.1 Microstructural Characterization

The reinforcement of 2% weight composition of silicon carbide particles in to the Al2017 alloy was shown by the optical micro graph in Fig. 1. It was clear that the uniform distribution of silicon carbide particle in the composite. It was also found that there would not contain any voids and uneven particles in the composites.

4.2 Measurement of Hardness and Impact Strength

From Table 3, it was clear that the Brinell hardness value of the composites increased with the increasing percentage contribution of silicon carbide particles. The reason for increasing the hardness values is due to the increasing density of the composites.

Table 3 Brinell and Rockwell hardness number of Al2017 and composites

S. No.	Description of material	Brinell hardness number (BHN)	Rockwell hardness number (HRB)
1.	Aluminum 2017 with 0% SiC (Al2017 alloy)	105	43
2.	Al2017 with 2% weight of SiC	107	45
3.	Al2017 with 4% weight of SiC	109	47
4.	Al2017 with 6% weight of SiC	111.25	48.75

Table 4 Impact strength values of Al2017 and composites

S. No.	Description of material	Impact strength J/mm ²
1.	Aluminum 2017 with 0% SiC (Al2017 alloy)	0.2
2.	Al2017 with 2% weight of SiC	0.218
3.	Al2017 with 4% weight of SiC	0.234
4.	Al2017 with 6% weight of SiC	0.254

The impact strength of the composites with reinforcement was not changed much more. They are almost the same with all the composition % of silicon carbide. This could be varied if the % of reinforcement of the silicon carbide increases. Table 4 shows that the impact strength values of pure Al2017 and composites which were obtained from the Izod impact test.

5 Conclusions

1. From the micrograph of aluminum composites, stir casting process was suitable for creating new composites with aluminum as base material.
2. From the hardness test, it was clearly understood that increase in inclusion percentage of silicon carbide would increase the hardness of the aluminum composites for a certain level of increasing in percentage of silicon carbide. After that, it would be reduced due to uneven distribution of silicon carbide particles.
3. It should note that the hardness values might be increased due to the increases of densities of composites than that of Al alloy.
4. From the impact test, it was found that the increase in percentage of silicon carbide inclusion in aluminum alloy does not produce much more changes in impact strength of the composites. If the percentage of silicon carbide inclusion increased further the result may be increased.

References

1. Rana RS, Purohit R, Soni VK, Das S (2015) Characterization of mechanical properties and microstructure of aluminum alloy-SiC composites. *Mater Today* 2:1149–1156
2. Harichandran R, Selvakumar N (2016) Effect of nano/micro B4C particles on the mechanical properties of aluminum metal matrix composites fabricated by ultrasonic cavitation-assisted solidification process. *Arch Civ Mech Eng* 16:147–158
3. Suresha S, Sridhara BK (2010) Wear characteristics of hybrid aluminum matrix composites reinforced with graphite and silicon carbide particulates. *Compos Sci Technol* 70:1652–1659
4. Mahendra KV, RadhaKrishna K (2010) Characterization of stir cast Al Cu (fly ash + SiC) hybrid metal matrix composites. *J Compos Mater* 44(8):989–1005
5. Balakumar S, Selvam MD, Nelson AJR (2018) Wear and friction characteristics of aluminium matrix composites reinforced with flyash/Cu/Gr particles. *Int J ChemTech Res* 11(01):121–133
6. Singh J, Chauhan A (2016) Characterization of hybrid aluminum matrix composites for advanced applications—a review. *J Mater Res Technol* 5(2):159–169